

THIS WEEK

EDITORIALS

NEUROSCIENCE There is something stirring in the fields of Transylvania **p.312**

WORLD VIEW Why is it that postdocs must move around so much? **p.313**

ZOOLOGY The sticky bridge building secrets of fire ants **p.314**

Present danger

There is much hype about predicting and preventing future pandemics, but not enough is being done about a threat sitting under our noses.

If the deadly disease MERS-CoV evolves to spread easily between humans and cause a global outbreak, hard questions will be asked. Why did health authorities and scientists allow a virus with clear pandemic potential to fester for so long, and what more could have been done to nip it in the bud? Those questions need to be asked now, when there is still time to deal with the crisis.

As of 16 June, the World Health Organization (WHO) had reported 701 lab-confirmed cases of MERS-CoV (Middle East respiratory syndrome coronavirus), including 249 deaths, since the virus was first identified in September 2012. The reported cases are largely confined to the Middle East, with most in Saudi Arabia.

MERS-CoV is, in principle, eminently stoppable. It remains an animal-borne virus that sporadically infects humans: there have been large hospital outbreaks in which patients have infected health-care workers and others, but so far the virus does not spread easily between people. By tracking down its animal sources and the routes through which people contract it, authorities should be able to dam the stream of infections.

But there is a risk that MERS-CoV, like the coronavirus SARS (severe acute respiratory syndrome), might mutate to spread easily between humans and so propagate rapidly around the world. SARS was detected in late 2002 and stamped out in July 2003; in those few months, it caused more than 8,000 infections and 700 deaths. Key to the defeat of SARS was a tightly coordinated international public-health effort, led by the WHO. The organization assembled an effective in-house outbreak-response team and quickly put together an international network of scientists that for the most part set competition aside in favour of collaboration.

Partly as a result of SARS, in 2005 the WHO's member states agreed on legally binding International Health Regulations to strengthen the international response to public-health events that occur in individual countries but potentially pose a global threat. The rules, for example, require countries to strengthen their disease surveillance and outbreak-response infrastructure, and to report all cases of possible international concern to the WHO within 24 hours.

TRY HARDER

When it comes to MERS-CoV, the lessons of SARS success have too often been ignored. This is perhaps due in part to a mistaken perception that MERS-CoV is less urgent than was SARS, because it does not yet spread easily between people. Research groups have tended to compete rather than cooperate. From the outset, conflict and distrust over credit, patents and sharing of specimens and data have marred efforts. (see *Nature* <http://doi.org/s75>; 2013).

Saudi Arabia's response to MERS-CoV has been better than many of its critics give it credit for. Tackling the outbreak is challenging: with only a few hundred cases to go on, tracking down clues to the source of infections is not easy in a country that is almost three and a half times the size of France. But even so, response efforts have suffered from

ineptitude, infighting and inadequate transparency. Saudi Arabia may be rich, but it is on a steep learning curve when it comes to international research collaboration and dealing with a complicated outbreak.

In April, Saudi Arabia replaced its health minister as case numbers surged, and last month it created a Command and Control Center that brings together scientists and public-health officials to better coordinate control efforts, and acts as a focal point for international collaboration.

“Diplomacy and trust are key to building an effective outbreak response.”

This month, it removed deputy health minister Ziad Memish — the most prominent public face of Saudi MERS-CoV efforts — and announced 113 cases and 92 deaths that had occurred since 2012 but had gone unreported (these cases are not included in the WHO's latest totals). It is too soon to say how effective the Command and Control Center will be, but

domestic pressure to stop MERS-CoV is at an all-time high.

The WHO has been much less prominent and decisive on MERS-CoV than it was on SARS. Its outbreak-response division is underfunded and understaffed, and effective leadership has been lacking.

On the positive side, researchers have obtained a lead, finding the virus in camels in Saudi Arabia, Egypt, Oman and Qatar. Antibodies to the pathogen — evidence of past infection — have been detected in camels in many countries in the Middle East and North Africa. Last week, researchers reported finding the virus in unpasteurized camel milk. But almost two years after MERS-CoV was first identified, no one has definitively pinned down its routes of transmission to humans. Scientists and authorities could, and should, do better.

The many cases caused by hospital outbreaks, for instance, could have been prevented by rigorous infection-control measures. Rapid identification and isolation of cases, decontamination of surfaces and use of protective clothing such as masks can all help to block infection of people in contact with patients.

Outbreak response cannot always be decreed by international rules. There is tension between the sovereign right of nations to handle the situation in their own countries and the desire of the international community to intervene and prevent the disease crossing borders. Diplomacy and trust are key to building an effective outbreak response. Saudi Arabia needs to be encouraged, not alienated.

The International Health Regulations say little about research, but a separate WHO agreement sets out clear rules for sharing samples and sequences of pandemic influenza viruses. Similar rules for all infectious diseases that have pandemic potential are needed.

What is most lacking in the fight against MERS-CoV is global leadership. The WHO, as an intergovernmental agency with a direct line to health ministries, remains best placed to bang heads together and get things done cooperatively, but its efforts must be well funded and staffed. Politicians everywhere must wake up to the fact that the world has another Middle East problem. ■

Quandrum

Does reality exist? Fifty years on, Bell's theorem still divides (and confuses) physicists.

When it comes to Bell's theorem, a cornerstone of modern quantum mechanics, there is one thing that everyone agrees on: it was published 50 years ago. Everything else is open to debate — especially its interpretation — and there is little prospect of these matters being settled soon. Indeed, Bell's theorem has become synonymous with the most puzzling meeting of metaphysics and physics that science has to offer.

Nature prides itself on writing for the general reader, but explaining the idea published by Northern Irish physicist John Stewart Bell in 1964 poses a stiff challenge to that mantra of accessibility. But confused readers can be consoled by the fact that they are not alone: even the best quantum physicists are left bewildered by Bell's theorem. Still, to unlock the secrets of the Universe, a little effort seems worthwhile.

In short, Bell predicted that measurements on entangled quantum particles will be incompatible with one of two common world views. The first is locality — the idea that a measurement on a London desk cannot be influenced by the setting of a measuring device in New York. The second is realism — that there is a reality that is independent of what we measure or observe.

Before Bell, both were common assumptions in science. For most people, they still are. But for physicists who step from the physical world into the quantum universe, Bell's theorem poses a real challenge. They must accept either that entangled quantum particles can influence each other instantaneously, even if they are light years apart, or that in the quantum world there is no Moon if nobody looks. Bell's

predictions have withstood all experimental tests so far, so it looks like we have to give up at least one dearly held, intuitive concept.

The reluctance of physicists to choose either of the possible options is illustrated by the fact that they still disagree on what exactly to make of Bell's theorem. For example, a conference in Vienna this week to celebrate the 50th anniversary of Bell's big idea will not merely issue a few historic outlooks and then move on to the hot topics of today. Rather, the theorem itself remains hot. (Sample talk title in Vienna: 'My struggle to face up to unreality'.)

"Even the best quantum physicists are bewildered by Bell's theorem."

It is not that quantum physics has gone nowhere over the past 50 years. On the contrary: in the 1990s, quantum physics experienced a boost that has been coined the 'second quantum revolution', when the theories developed in the first revolution were translated into practical quantum technologies such as unbreakable cryptography protocols and ultrafast computing concepts. After all, we can simply use the equations of quantum mechanics to invent new technology without understanding their deeper meaning.

Still, the second quantum revolution was at least partially triggered by contemplations about the meaning of it all. Quantum physicist Artur Ekert, for instance, devised one of the key ingredients for secure quantum communication while pondering the meaning of Bell's theorem (A. K. Ekert *Phys. Rev. Lett.* **67**, 661; 1991).

Today's quantum-physics agenda holds great promise for such fruitful collaboration between fundamental research and practical applications. For example, the search for the biggest objects that can be subject to quantum superposition is not only motivating theorists to think about possible universal distinctions between the macroscopic classical and the microscopic quantum world, but also prompting the improvement of experimental tools that will probably become useful in other contexts.

See, that wasn't too hard. Was it? ■

Summer skills

A fledgling neuroscience programme is a rare beacon of research excellence in Romania.

Readers of vampire fiction might hesitate to peer inside an isolated house in a remote part of the Romanian region of Transylvania. Indeed, something strange was happening there this month, in the Pike Lake Pension. Much of the gently rolling farmland around the house is still worked by horsepower, but within its walls stand a couple of twenty-first-century two-photon microscopes. They were built by a group of young neuroscientists who also write the software needed to operate them. The team has used the microscopes in behavioural experiments involving specially bred mice — having gained ethical approval from the University of Medicine and Pharmacy in Transylvania's capital, Cluj. The researchers aim to identify neural circuits in the brain, and use optical-genetics techniques at the cutting edge of modern neuroscience.

The students are part of the third annual Transylvanian Experimental Neuroscience Summer School (TENSS), established by two idealistic Romanians who had, as school children, witnessed the demise of their country's scientific base in the political chaos that followed the collapse of communism in 1989. One of these idealists is Florin Albeanu, an assistant professor at the Cold Spring Harbor Laboratory in New York; the other is Raul Muresan, a principal investigator at the Center for Cognitive and Neural Studies in Cluj. TENSS might not be quite enough to raise the country's science from the dead. But it may yet help to return some of the lifeblood drained from the system.

The scheme shows young scientists that it is possible to achieve

uncompromising, international standards of science on Romanian soil. And this is no local-scale project. The students that participate do so only after fierce international competition for places. This year, just two students from Romanian institutions joined the 13 chosen from 122 applicants.

Muresan and Albeanu are determined that the summer school will have an experimental aspect as well as a theoretical one, partly to compensate for the dearth of experimental biology in Romania. But it also speaks to the programme's global 'yes we can' philosophy. Students are, in part, selected for their likelihood of contributing to similar research when they return home — whether or not their labs are wealthy. Learning to build expensive equipment, such as two-photon microscopes, which can cost hundreds of thousands of dollars, gives students the confidence to build, repair or modify whatever apparatus might be required to address the neuroscientific research questions they wish to pose.

The inspiring story has spurred many scientists from leading institutions around the world — from Harvard University in Cambridge, Massachusetts, to the National Centre for Biological Sciences in Bangalore, India — to lecture at the course. And so far, several research foundations and commercial companies in different countries have stumped up financial or in-kind support.

TENSS will clearly continue to need such generosity in years to come. But the Romanian government must emulate some of the school's lofty aims — and carve out a rational, meritocratic system to educate and support homegrown scientists and science. The TENSS experience has shown that talent and enthusiasm will be available, as will the required curiosity — in whatever form. One day during last year's summer school, a villager stared mystified through the open door. After some thought, he ventured: "That's a fine-looking sewing machine you have there." ■

➔ **NATURE.COM**
To comment online,
click on Editorials at:
go.nature.com/xhbnq

LEE BARRETT



Uprooting researchers can drive them out of science

*Making early-career scientists change institutions frequently is disruptive and — with modern technology — unnecessary, says **Russell Garwood**.*

Many people have to move jobs and homes to build their careers. Relocation is a common disruption, sometimes desired and sometimes not. But how many careers demand that people move every few years, as science does? In how many other fields are promising recruits — who often already have a decade's education behind them — expected to uproot their families and move repeatedly for the best part of another decade?

Such frequent changes of location are unsettling and detrimental to people's personal lives. Yet there is a widespread expectation that early-career researchers should move around, to demonstrate their independence or work with new people.

This attitude partly serves as an uncomfortable reminder that some academics view junior scientists as expendable sources of cheap labour whose lives and happiness are secondary considerations. But it is also outdated, reflecting the world in which many senior scientists developed their own careers: a world in which graduates and young researchers needed to move between labs and institutions to spread their knowledge and skills and, in doing so, keep science innovative and collaborative.

The information-technology revolution of the twenty-first century has changed that. For many scientists in 2014, the physical location of a laboratory is less important than the speed of its Internet connection. If they wish, researchers can now communicate more often, and just as easily, with colleagues in a different time zone than with those in the next office.

During my current fellowship, I have worked with colleagues in the United States, Germany, Australia, Sweden and France, many of whom I have never met in person. If face-to-face interaction is essential, budget airlines allow for multiple short visits to other labs and collaborators. (I am writing this on a plane to Uppsala in Sweden for such a trip.) The day-to-day work of science has become similarly diffuse. Standardized lab equipment allows researchers to replicate experiments and results more easily than in the past, wherever the work is performed.

For some scientists, of course, the opportunity to move around is wonderful. It is perfect for people with wanderlust, who lack personal ties or who thrive in varied surroundings and on ephemeral contracts.

However, for many others this migration-centred system is hugely disruptive, and can add to the forces that squeeze talented scientists out of academia and into other careers.

The 'young' people whom science labels as in their early careers can actually be in their late twenties or thirties. Many are in long-term relationships, which causes a 'two-body

problem'. It is often not possible, or wise, for them to drop everything and move every few years, especially if they have children. Yet making the best decision for their families can harm their careers. For example, my current fellowship is based in Manchester, UK, but my partner has a job in London — a few hours away by train — and is understandably reluctant to leave. We have been very lucky: the terms of my fellowship mean that I have a degree of independence and can travel a lot, allowing us to live together. But having made the choice to reduce the amount of time spent at my institution, I find it hard to contribute to many aspects of departmental life. I worry that this might limit my future options. The effect is surely even greater for female scientists, whose careers often already suffer as a result of family obligations.

Simply put, the career framework for young scientists was established at a time when wives and partners did not necessarily work and were expected to follow the — generally male — breadwinner as he worked his way up. That (thankfully) is not the world we live in now. Society has changed and science should change with it.

Institutional policies can ease the move. In the United States, for instance, a number of universities make an effort to help to find jobs for researchers' partners. But relocation should not be necessary. In the long term, cultural change is required — just as it is to address, for example, the under-representation of women in science, which is exacerbated by the two-body problem.

There are some straightforward steps that we can take. First, guidelines for grant reviewers, job panels and academics should make clear that personal factors are as important and legitimate as professional ones when it comes to making

career choices. Instead of demanding that all young researchers move institutions, funding agencies could consider personal motivations on a case-by-case basis, just as they currently judge the strength of an applicant's science.

Second, principal investigators could ensure that young scientists have the chance to pursue independent research without leaving the lab, and to publish the results. Early-career researchers should push for such opportunities, and institutions should encourage and nurture them. For example, one afternoon a week could be set aside for early-career scientists to conduct self-directed research.

Staying in one place has the potential to stifle independence. But that risk should be measured against the danger that the scientist will be forced out of research — and that ultimately, science will lose out. ■

Russell Garwood is an 1851 research fellow at the University of Manchester, UK.
e-mail: russell.garwood@manchester.ac.uk

IN 2014, THE
**PHYSICAL
LOCATION**
OF A LABORATORY
IS LESS IMPORTANT
THAN THE
**SPEED OF ITS
INTERNET.**

➔ **NATURE.COM**
Discuss this article
online at:
go.nature.com/lxst9c



RESEARCH HIGHLIGHTS

Selections from the
scientific literature



GLACIOLOGY

Refrozen water warms glacier

Meltwater flowing beneath Greenland's glaciers refreezes into large ice units that could be distorting and even warming the overlying ice layers.

Robin Bell of Columbia University's Lamont-Doherty Earth Observatory in Palisades, New York, and her team used radar data to identify subglacial ice units across northern Greenland. The authors found significant warping of the surrounding layers, which they attribute to the refreezing meltwater below.

Moreover, these ice units were found in areas of fast glacier flow. The authors suggest that energy released from the meltwater as it refreezes is warming the ice above, and thus speeding up the glacier's march towards the ocean.

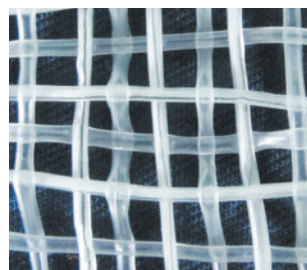
Nature Geosci. <http://doi.org/s7j> (2014)

ELECTRONICS

Stretchy battery woven into fabric

Researchers in China have incorporated relatively powerful lithium-ion wire batteries into textiles — a step towards better power sources for wearable electronics.

Lithium-ion batteries in general are more powerful than current wearable energy storage devices, but can



short-circuit and combust if stretched or distorted during use. Huisheng Peng, Yonggang Wang and their team at Fudan University, Shanghai, overcame this by incorporating safer lithium-oxide nanoparticles into carbon nanotube yarns. These yarns, which form the batteries' electrodes, were twisted around a piece of elastic, creating a stretchable structure that could be woven into textiles (pictured).

The wire battery produced 10 times more power per cubic centimetre than non-stretchable, thin-film lithium batteries and maintained 84% of its capacity after being

stretched 200 times.

Angew. Chem. <http://doi.org/f2r6pv> (2014)

ECOLOGY

Stick together to fight disease

Isolated plant populations are more vulnerable to disease than highly connected ones, contrary to popular thinking.

Diseases are thought to spread more quickly in dense populations, which facilitate the transfer of disease from one group to another. But Anna-Liisa Laine of the University of Helsinki and

her team found a different pattern when they tracked more than 4,000 populations of the weed *Plantago lanceolata* over 12 years on the Åland Islands in the Baltic Sea. Rather than being protected, isolated populations were infected by the mildew *Podosphaera plantaginis* more often than weeds in dense networks.

The team then studied samples from 22 plant populations in the lab and found that plants from highly connected populations were generally more disease resistant than their counterparts from fragmented populations, possibly because resistance



ZOOLOGY

How ants link up to build bridges

Fire ants band together into rafts and bridges by each making an average of 14 connections with adjacent ants.

The insects (*Solenopsis invicta*) form networks (pictured) to cross streams and deal with floods. To study the networks' structure, David Hu and his team at the Georgia Institute of Technology in Atlanta froze clumps of ants with liquid nitrogen, coated them with vaporized glue and imaged them with a micro-computed-tomography

scanner. The team found that the ants grab hold of each other using adhesive pads on their legs. The insects also tend to orient themselves perpendicularly to one another, with smaller ants slotted in between larger ones to maximize the number of connections between them.

The ants could inspire the development of robots and smart materials that assemble into new structures, the authors say.

J. Exp. Biol. 217, 2089–2100 (2014)



DAVID L. HU/TIM NOWACK PHOTOGRAPHY

SCOTT LESLIE/MINDEN PICTURES/CORBIS

JING REN

genes are more readily exchanged among populations located near each other. *Science* 344, 1289–1293 (2014)

PHYSICS

Global quantum clock proposed

A set of atomic clocks linked together using the principles of quantum physics could be the authoritative world clock — more accurate and stable than any atomic clock today.

Mikhail Lukin of Harvard University in Cambridge, Massachusetts, and his team propose combining ultra-precise atomic clocks using quantum entanglement, which links the quantum states of particles separated over large distances. Entangling the clocks would allow scientists to combine measurements in a way that reduces the overall noise, rendering the combined signal more accurate. The resulting space-based network could be used to synchronize timekeeping standards globally, the authors say.

Building the clock will require technological advances, such as improving the stability of clock signals sent through Earth's turbulent atmosphere. *Nature Phys.* <http://doi.org/s7k> (2014)

MOLECULAR BIOLOGY

Genome editing of stem cells

A genome-editing system allows researchers to introduce multiple gene alterations into human stem cell lines.

A team led by Danwei Huangfu at Memorial Sloan-Kettering Cancer Center in New York used the recently developed genome-editing systems TALEN and CRISPR-Cas9 to efficiently create human embryonic stem (ES) cells and induced pluripotent stem (iPS) cells containing up to three different gene alterations. The researchers used their approach to introduce various mutations linked to Alzheimer's disease

into iPS cells, as well as to delete certain genes in pancreatic cells derived from ES cells.

The method should make it faster and easier to determine the effects of disease-related gene changes on cell and tissue development, the authors say. *Cell Stem Cell* <http://doi.org/s6w> (2014)

PARTICLE PHYSICS

Exotic four-quark particle confirmed

A team have confirmed the existence of a four-quark particle, named Z(4430). The finding, together with other exotic particles, challenges the idea that quarks only combine in pairs (mesons) or triplets.

Z(4430) was first spotted in 2008 at the Belle detector in Japan, but another detector in California failed to see it, casting doubt on the initial observations. A team working on the LHCb experiment at CERN, Europe's particle physics laboratory near Geneva in Switzerland, analysed about a billion high-energy proton–proton collisions. The scientists noticed that in about 4,000 cases there was a highly significant Z(4430) signal — about 14 standard deviations above background levels.

The authors determined that the particle is composed of four quarks because of its observed decay patterns, and is not an artefact of interactions between ordinary two-quark mesons. *Phys. Rev. Lett.* 112, 222002 (2014)

REGENERATIVE BIOLOGY

Love hormone revitalizes muscles

The hormone involved in social bonding also enables old muscles to rejuvenate.

Wendy Cousin, Irina Conboy and their colleagues at the University of California, Berkeley, injected the hormone oxytocin into old mice, and found that after an injury the muscles in these animals had similar regeneration levels to muscles in young mice. The hormone improves repair by

SOCIAL SELECTION

Popular articles on social media

Lab animals spark debate

Social media is hosting the latest round of the debate over medical studies involving animals. Writing in the *British Medical Journal*, Yale University epidemiologist Michael Bracken and UK medical sociologist Pandora Pound argued that too many animal trials investigating medical treatments are poorly designed, and called for better use of systematic reviews to maximize their benefit. Lenny Verkooijen, a clinical epidemiologist at University Medical Center Utrecht in the Netherlands, tweeted that there is “insufficient systematic evidence for the clinical benefits of animal research”. But in a letter to the journal, pharmacologist Fernando Martins do Vale at the University of Lisbon noted that animal research has benefited medicine and has led to “seminal discoveries in the field of physiology, biochemistry, pharmacology and genetics”. Pound, P. & Bracken, M. B. *Br. Med. J.* 348, g3387 (2014)



Based on data from altmetric.com. Altmetric is supported by Macmillan Science and Education, which owns Nature Publishing Group.

➔ **NATURE.COM**
For more on popular papers:
go.nature.com/hyvsvi

activating a signalling pathway in muscle stem cells — thereby boosting the cells' proliferation. Moreover, mice engineered to lack oxytocin showed decreased muscle repair and greater loss of muscle tissue compared with normal mice of the same age.

Oxytocin could be used as a drug to prevent or slow down muscle ageing, the authors say. *Nature Commun.* 5, 4082 (2014)

ANIMAL BEHAVIOUR

Apes cooperate on their own

Without any prior training, captive chimpanzees team up on a task, suggesting that the primates are more cooperative than previously thought.

Malini Suchak, now at Canisius College in Buffalo, New York, and her colleagues designed a device that required one or two chimps (*Pan troglodytes*) to remove a barrier in order for another individual to simultaneously obtain a tray of food. The researchers placed the device in a large enclosure in which 11 chimps lived, and found that the animals



spontaneously worked together in groups of two or three to complete the task (pictured) more than 3,000 times — an average of 38 per one-hour session. Unlike most previous studies, the apes were free to choose their own partners, which could have allowed them to avoid competitors that might impede cooperation. Complex cooperative behaviour is not a uniquely human trait, the authors suggest.

PeerJ 2, e417 (2014)

➔ **NATURE.COM**
For the latest research published by Nature visit:
www.nature.com/latestresearch

SEVEN DAYS

The news in brief

PEOPLE

Urologist sentenced

Austrian urologist Hannes Strasser will have to serve a two-year sentence for crimes relating to his use of an unauthorized stem-cell therapy to treat urinary incontinence, an appeals court confirmed on 11 June. The treatment was ineffective in many patients, and harmed others. The scandal was exposed six years ago, when Strasser was a professor at the Medical University of Innsbruck (see *Nature* **454**, 922–923; 2008). The university was not allowed to dismiss him because of a ruling from a national employment committee, but the court judgment means that he now has to be dismissed.

POLICY

Drug data freed

The European Medicines Agency has agreed in principle to publish clinical-trial reports on any drug that receives marketing approval in the European Union. It announced the move on 12 June and is the first major drug regulatory agency to take such a step. The agency says that the shift will improve transparency in the medicine approval process and make it easier for academics to conduct non-commercial research. See go.nature.com/obsicm for more.

Chile axes dam plan

The Chilean government said on 10 June that it had rejected plans for a controversial hydroelectric project in southern Patagonia. The 2,750-megawatt HidroAysén project won partial government approval in 2011, but was dogged by concerns about the environmental and social effects of building five new dams on Patagonian

rivers. The government's latest move may not spell the end for the dam, however. Its backers, power companies Endesa Chile and Colbún, could revise their plans and seek permission to go forward with an updated version of the project, media reports say.

TB drug too costly

The high cost of treating a form of tuberculosis that is resistant to many drugs could allow the disease to spread, physicians warn. An effective new drug, bedaquiline, is available, but costs up to US\$30,000 for one course of treatment. On 12 June Caitlin Reed of the Olive View–University

of California, Los Angeles, Medical Center told the 2014 National TB Conference in Atlanta, Georgia, that the drug would be too expensive. Reed is currently using bedaquiline to treat a patient who, she said, has the most drug-resistant form of tuberculosis ever seen in the United States.

Biofuel cap

By 2020, biofuels made from food crops should be limited to providing only 7% of all transport fuel in the European Union, European ministers agreed on 13 June. The limit is more generous than the 5% cap originally proposed by the European Commission, but awaits a vote from the

that will exacerbate the decline of the African elephant population. The report also shows a rise in seizures of large ivory shipments (weighing more than 500 kilograms). For the first time, more large seizures were made in Africa than in Asia, 80% of which occurred in Kenya, Tanzania and Uganda. The results will be discussed at a CITES meeting in Geneva, Switzerland, on 7–11 July.



JOSEPH OKANGA/REUTERS/CORBIS

Ivory poaching continues apace in Africa

More than 20,000 African elephants were poached across the continent last year, finds a report by the Convention on International Trade in Endangered Species of Wild Fauna and Flora (CITES). Published on 13 June, the report uses the latest figures from CITES programmes that monitor poaching. Overall poaching numbers were lower in 2013 than in the previous two years, but continue at levels

newly elected European Parliament. Scientists have long warned that fuels such as biodiesel made from palm oil can produce more carbon emissions than the fossil fuels they replace (see *Nature* **499**, 13–14; 2013).

Integrity audit

Scientists in Ireland should expect their research processes to be audited by outside consultants, according to plans outlined by Mark Ferguson, director-general of the basic-research funding agency Science Foundation Ireland. Ferguson told *Nature* that the aim of the audit is to ensure that work funded by the agency is being conducted

ASAHI SHIMBUN VIA GETTY

with integrity. He hopes that the first annual audits will begin by the end of the year. See page 325 for more.

EVENTS

Park oil-drilling axed

Oil company SOCO International is suspending explorations in Virunga National Park in the Democratic Republic of the Congo, it announced on 11 June. Virunga is Africa's oldest national park and is home to the critically endangered mountain gorilla (*Gorilla beringei beringei*). The move came after conservation groups led by the WWF filed a complaint with the Organisation for Economic Co-operation and Development. SOCO, which is based in London, has agreed not to drill in the park or in any other site given World Heritage status by the United Nations.

FACILITIES

RIKEN report

An independent committee has recommended that the RIKEN Centre for Developmental Biology in Kobe, Japan, should close because of its role in the publication of two problematic papers in *Nature*. The research in question purported to describe a new method for generating



embryonic stem cells, but the papers were found to include duplicated images, among other problems. On 12 June, a committee looking into research misconduct told a press conference (pictured, with committee head Teruo Kishi speaking) that it had found structural flaws in the running of the Kobe centre and called for it to be dismantled. RIKEN is planning structural reforms and intends to appeal against the judgement.

RESEARCH

Cancer trial

A groundbreaking clinical trial in lung cancer began enrolling patients on 16 June. The five-year Lung Cancer Master Protocol trial will assign up to 1,000 patients per year to receive one of five experimental treatments, depending on the genetic mutations in their tumours (see *Nature* 498, 146–147; 2013). It unites five

pharmaceutical companies, and will be led by the SWOG Cancer Research consortium in Portland, Oregon, and administered by the US National Cancer Institute. It is intended to serve as a model for how clinical trials can be streamlined and personalized.

Hubble search

The Hubble Space Telescope has begun searching for an icy world in the outer Solar System that NASA's New Horizons mission can visit after its fly-by of Pluto in July 2015. The search was announced on 16 June by the NASA committee that allocates observing time on Hubble. Mission scientists were unable to identify a suitable candidate in the Kuiper belt using ground-based telescopes, and they hope that Hubble's vantage point will give them a better view. See go.nature.com/nayaec for more.

H7N9 predictions

Researchers have developed a model that accurately predicts which live-poultry markets are at risk of becoming infected with the H7N9 avian influenza virus that has swept across China. Most human cases of the virus have occurred through exposure at such markets. The research team conducted a census of 8,943 live-poultry markets in China, and found that local density

COMING UP

21–26 JUNE

The Euroscience Open Forum meets in Copenhagen to discuss the future direction of research and science policy in Europe. esof2014.org/info

23–27 JUNE

The first meeting of the United Nations Environment Assembly takes place in Nairobi. Discussions will include the sustainable development goals that aim to reduce global poverty. www.unep.org/unea/en

is the most important factor in predicting the risk of outbreaks (M. Gilbert *et al.* *Nature Commun.* 5, 4116; 2014). The findings should help authorities to develop better control measures.

Child-study hold-up

A US study of 100,000 children that was authorized by Congress 14 years ago may face further delays. An external review released on 16 June found that planning for the National Children's Study lacked proper scientific input. See page 323 for more.

BUSINESS

Tesla opens patents

Electric-car company Tesla Motors has announced that it will let other firms use the technology it has patented. The company, headquartered in Palo Alto, California, said on 12 June that it would not initiate patent lawsuits, apparently in an effort to promote growth in the market for electric vehicles and to encourage common standards for supporting infrastructure, such as battery chargers.

► NATURE.COM

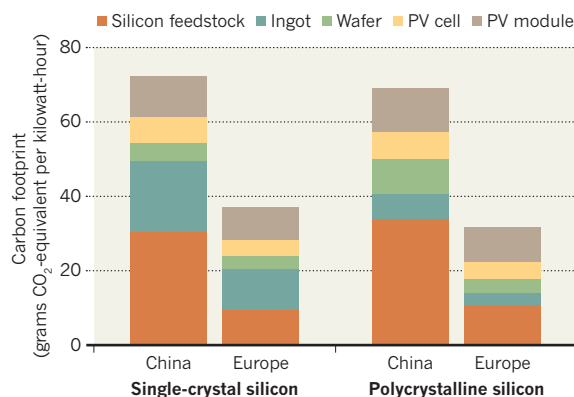
For daily news updates see: www.nature.com/news

TREND WATCH

China's coal-intensive electricity grid means that making a silicon solar panel there — although cheaper — leaves a carbon footprint almost twice as large as that from making one in Europe, according to a study led by Fengqi You at Northwestern University in Evanston, Illinois (D. Yue, F. You and S. B. Darling *Sol. Energy* 105, 669–678; 2014). But emissions per kilowatt-hour of electricity produced by even the 'dirtiest-made' solar panel are some 16 times lower than those from a typical coal plant.

SOLAR POWER'S CARBON FOOTPRINT

The carbon dioxide emissions created when photovoltaic (PV) solar panels are made in China are twice as high as for those made in Europe.

SOURCE: D. YUE ET AL. *SOL. ENERGY* 105, 669–678 (2014)

NEWS IN FOCUS

ECOLOGY Tree travelled halfway across globe in extreme long-distance dispersal **p.320**

PUBLIC HEALTH Report finds flaws in long-delayed US National Children's Study **p.323**

POLICY Irish funding agency plans independent audits of university labs **p.325**

RESOURCES Nations tap unconventional sources of fresh water **p.326**

PAUL SOUDERS/COREIS



The terracotta army, which consists of individually sculpted warriors, was found inside the mausoleum of China's first emperor, Qin Shi Huang.

ARCHAEOLOGY

3D images remodel history

Digital-photo software promises to offer unprecedented access to artefacts and sites.

BY EWEN CALLAWAY

It took hundreds of thousands of workers decades to create China's terracotta army, but digital avatars made in minutes could solve the lingering mystery of one of the country's most famous relics. By creating three-dimensional (3D) models of the 2,200-year-old collection of statues, archaeologists hope to confirm whether the soldiers were intended to represent a real army of distinct individuals.

Known broadly as computer vision, the

technology was developed to enable machines such as factory robots and the Mars rovers to map a 3D world from camera images. But now it is quietly revolutionizing archaeology and palaeontology, allowing virtual bones, artefacts and whole excavation sites to be shared and studied without risk of damage.

"In the future, it's highly likely that these sorts of methods will be the standard thing you do to record an archaeological site," says Andrew Bevan, an archaeologist at University College London, who is part of a team using

computer vision to build digital models of the terracotta army's life-size warriors.

Since the army was discovered in 1974 in an emperor's mausoleum near Xian, historians have debated whether the soldiers' facial details were modelled on actual militiamen. "Are the warriors portraits of individual people? Or are they a 'Mr Potato Head' approach to individualism, where you slap on different noses and moustaches and ears?" Bevan says.

Computer-vision models might offer the answer, Bevan suggests. Digital photos ►

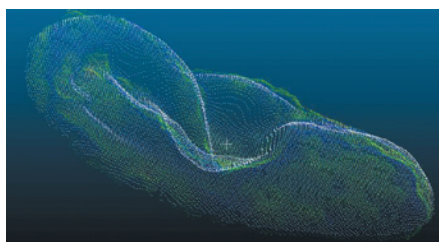
► can be taken quickly, cheaply and without disturbing the statues. Several dozen high-quality photos of a soldier, taken from multiple perspectives, can provide a computer algorithm with enough data to determine where each image was taken from and create a 3D map in a few minutes. The model — a set of *x*, *y* and *z* coordinates — can be plotted against other models, analysed and even used to make a cast with a 3D printer.

In a pilot study published on 4 June, Bevan's team modelled the faces of 30 warriors and found that no two ears were identical — evidence that the army consists of individuals (A. Bevan *et al.* *J. Archaeol. Sci.* <http://doi.org/s7v>; 2014). The researchers compared ears because these are unique and may have been modelled on real people. But they plan to analyse other anatomical features to see whether the soldiers vary in ethnicity or bear the hallmarks of distinct craftsmen. Bevan stresses that the work is at an early stage.

Archaeologists and palaeontologists have used computer modelling for decades, to map digs with laser scanners or study bones with computed tomography (CT), for example. But proponents of computer vision argue that these technologies are costly and not made for routine use in the field.

"You're talking about having a camera versus having a £30,000 [US\$50,000] piece of kit ready," says Sarah Duffy, an archaeologist at the University of York, UK. When

"We can expect to see entire collections of hundreds of thousands of objects digitally available."



Superimposed 3D models (one in green, the other in white) reveal minute differences in ear shape.

900,000-year-old footprints were found on eastern England's Norfolk coast last year, she was part of a team that raced to photograph the scene and capture the footprints in 3D. The resulting model revealed that they had been left by a human ancestor — the oldest such relics discovered outside Africa (N. Ashton *et al.* *PLoS ONE* <http://doi.org/rd2>; 2014). The prints had nearly vanished by the time the researchers lugged a laser scanner to the site a week later.

Benjamin Dücke at the German Archaeological Institute in Berlin agrees that the technology has the potential to preserve sites that are disappearing. Last October, he used a drone equipped with a video camera to create a 3D map of a large pre-Columbian settlement in Mexico in a couple of days. His team, called Project Archaeocopter, plans to analyse sites in Uzbekistan and at Pompeii in Italy. With an infrared camera mounted on a drone, the technology could map archaeological sites obscured by dense forests, he says.

Powerful computer-vision software is affordable and readily available, but advocates such as Heinrich Mallison, a palaeontologist

at Berlin's Natural History Museum, see the technology as more than a time and money saver. "It means we can expect to see entire collections of hundreds of thousands of objects digitally available in a decade, so everybody can use these for research," he says. Dücke thinks that the technology has the potential to break the "interpretative monopoly" of scholars whose theories prevail because others lack access to particular artefacts or remains.

Jean-Jacques Hublin, a palaeoanthropologist at the Max Planck Institute for Evolutionary Anthropology in Leipzig, Germany, expects museums to limit the creation and distribution of such models in their collections, in the same way as some have done for CT scans. Museums worry about losing control over their collections, but Hublin thinks that demand among scientists will inevitably push more collections online. With computer-vision technology in mind, in May the European Union began accepting applications for a €14-million (\$19-million) fund to create 3D models of examples of Europe's cultural heritage.

But data theft is a worry, Mallison says. "I can go to a museum in Beijing, pull out my Canon, play tourist and do research on a high-resolution 3D model of their fossils." Academics might not risk the backlash of collecting data without permission, but replica sellers could pillage museum collections with computer-vision software, says Mallison. He thinks that international rules are needed to prevent this. Nevertheless, he predicts that it is only a matter of time before 3D models of museum collections are widely available. "The question is, do we see it in 5 years or 10 years or 15 years?" he says. ■

A. BEVAN ET AL. / J. ARCHAEOLOGICAL SCI. <http://doi.org/s7v> (2014) CC BY

ECOLOGY

Tree hitched a ride to island

Acacia analysis reveals globetrotting seed trekked 18,000 kilometres from Hawaii to Réunion.

BY EMMA MARRIS

In what is probably the farthest single dispersal event ever recorded, researchers have shown using genetic analysis that an acacia tree endemic to Réunion Island in the Indian Ocean is directly descended from a common Hawaiian tree known as the koa. In fact, these two trees on small specks of land on opposite sides of the globe turn out to be the same species.

The event is remarkable not just for the sheer distance covered — some 18,000 kilometres, almost the farthest apart that any two points on land can be — but that it occurred between two small islands. Koa seeds are unlikely to have

floated to Réunion — they will not germinate after being soaked in seawater, and the trees grow in the mountains, not near the shore. The researchers, led by Johannes Le Roux, a molecular ecologist at Stellenbosch University in Matieland, South Africa, propose in a study published this week that a sea bird brought a seed from Hawaii to Réunion in its stomach or stuck to its feet in a one-off event some 1.4 million years ago (J. J. Le Roux *et al.* *New Phytol.* <http://dx.doi.org/10.1111/nph.12900>; 2014).

Le Roux notes that the physical similarities between the two trees, *Acacia heterophylla* from Réunion and *Acacia koa* from Hawaii, have been known for decades. "To me the most exciting thing is that we have solved this

riddle," he says. "And how improbable is it?"

Le Roux and his team sequenced the DNA from 88 trees, including *A. heterophylla*, *A. koa* and a closely related acacia species from Australia, where the family originated. They found that all the acacias on Réunion share a genetic signature that is just one mutational step away from that of some Hawaiian koas. Using the slight differences between the trees' sequences, they developed a family tree, which clearly showed that all *A. heterophylla* are more closely related to one type of Hawaiian koa than some other types of koa are to each other.

To work out when the dispersal event took place, the team used a 'molecular clock'. This counts up genetic changes between populations

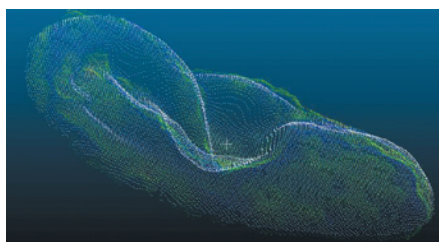
► can be taken quickly, cheaply and without disturbing the statues. Several dozen high-quality photos of a soldier, taken from multiple perspectives, can provide a computer algorithm with enough data to determine where each image was taken from and create a 3D map in a few minutes. The model — a set of *x*, *y* and *z* coordinates — can be plotted against other models, analysed and even used to make a cast with a 3D printer.

In a pilot study published on 4 June, Bevan's team modelled the faces of 30 warriors and found that no two ears were identical — evidence that the army consists of individuals (A. Bevan *et al.* *J. Archaeol. Sci.* <http://doi.org/s7v>; 2014). The researchers compared ears because these are unique and may have been modelled on real people. But they plan to analyse other anatomical features to see whether the soldiers vary in ethnicity or bear the hallmarks of distinct craftsmen. Bevan stresses that the work is at an early stage.

Archaeologists and palaeontologists have used computer modelling for decades, to map digs with laser scanners or study bones with computed tomography (CT), for example. But proponents of computer vision argue that these technologies are costly and not made for routine use in the field.

"You're talking about having a camera versus having a £30,000 [US\$50,000] piece of kit ready," says Sarah Duffy, an archaeologist at the University of York, UK. When

"We can expect to see entire collections of hundreds of thousands of objects digitally available."



Superimposed 3D models (one in green, the other in white) reveal minute differences in ear shape.

900,000-year-old footprints were found on eastern England's Norfolk coast last year, she was part of a team that raced to photograph the scene and capture the footprints in 3D. The resulting model revealed that they had been left by a human ancestor — the oldest such relics discovered outside Africa (N. Ashton *et al.* *PLoS ONE* <http://doi.org/rd2>; 2014). The prints had nearly vanished by the time the researchers lugged a laser scanner to the site a week later.

Benjamin Dücke at the German Archaeological Institute in Berlin agrees that the technology has the potential to preserve sites that are disappearing. Last October, he used a drone equipped with a video camera to create a 3D map of a large pre-Columbian settlement in Mexico in a couple of days. His team, called Project Archaeocopter, plans to analyse sites in Uzbekistan and at Pompeii in Italy. With an infrared camera mounted on a drone, the technology could map archaeological sites obscured by dense forests, he says.

Powerful computer-vision software is affordable and readily available, but advocates such as Heinrich Mallison, a palaeontologist

at Berlin's Natural History Museum, see the technology as more than a time and money saver. "It means we can expect to see entire collections of hundreds of thousands of objects digitally available in a decade, so everybody can use these for research," he says. Dücke thinks that the technology has the potential to break the "interpretative monopoly" of scholars whose theories prevail because others lack access to particular artefacts or remains.

Jean-Jacques Hublin, a palaeoanthropologist at the Max Planck Institute for Evolutionary Anthropology in Leipzig, Germany, expects museums to limit the creation and distribution of such models in their collections, in the same way as some have done for CT scans. Museums worry about losing control over their collections, but Hublin thinks that demand among scientists will inevitably push more collections online. With computer-vision technology in mind, in May the European Union began accepting applications for a €14-million (\$19-million) fund to create 3D models of examples of Europe's cultural heritage.

But data theft is a worry, Mallison says. "I can go to a museum in Beijing, pull out my Canon, play tourist and do research on a high-resolution 3D model of their fossils." Academics might not risk the backlash of collecting data without permission, but replica sellers could pillage museum collections with computer-vision software, says Mallison. He thinks that international rules are needed to prevent this. Nevertheless, he predicts that it is only a matter of time before 3D models of museum collections are widely available. "The question is, do we see it in 5 years or 10 years or 15 years?" he says. ■

A. BEVAN ET AL. / J. ARCHAEOLOGICAL SCI. <http://doi.org/s7v> (2014) CC BY

ECOLOGY

Tree hitched a ride to island

Acacia analysis reveals globetrotting seed trekked 18,000 kilometres from Hawaii to Réunion.

BY EMMA MARRIS

In what is probably the farthest single dispersal event ever recorded, researchers have shown using genetic analysis that an acacia tree endemic to Réunion Island in the Indian Ocean is directly descended from a common Hawaiian tree known as the koa. In fact, these two trees on small specks of land on opposite sides of the globe turn out to be the same species.

The event is remarkable not just for the sheer distance covered — some 18,000 kilometres, almost the farthest apart that any two points on land can be — but that it occurred between two small islands. Koa seeds are unlikely to have

floated to Réunion — they will not germinate after being soaked in seawater, and the trees grow in the mountains, not near the shore. The researchers, led by Johannes Le Roux, a molecular ecologist at Stellenbosch University in Matieland, South Africa, propose in a study published this week that a sea bird brought a seed from Hawaii to Réunion in its stomach or stuck to its feet in a one-off event some 1.4 million years ago (J. J. Le Roux *et al.* *New Phytol.* <http://dx.doi.org/10.1111/nph.12900>; 2014).

Le Roux notes that the physical similarities between the two trees, *Acacia heterophylla* from Réunion and *Acacia koa* from Hawaii, have been known for decades. "To me the most exciting thing is that we have solved this

riddle," he says. "And how improbable is it?"

Le Roux and his team sequenced the DNA from 88 trees, including *A. heterophylla*, *A. koa* and a closely related acacia species from Australia, where the family originated. They found that all the acacias on Réunion share a genetic signature that is just one mutational step away from that of some Hawaiian koas. Using the slight differences between the trees' sequences, they developed a family tree, which clearly showed that all *A. heterophylla* are more closely related to one type of Hawaiian koa than some other types of koa are to each other.

To work out when the dispersal event took place, the team used a 'molecular clock'. This counts up genetic changes between populations

and uses an estimated mutation rate to derive the date that populations first split. The team knew that the koa tree originally came from Australia, and that the earliest point at which it could have become established on Hawaii was when Kauai, one of the older Hawaiian islands with the high elevations that koas prefer, formed 5.1 million years ago. Comparison of the Hawaiian koa and the trees on Réunion then showed that mutations that occurred in the subsequent 3.7 million years were present in both lineages. But mutations that occurred after that were found in either the Réunion trees or the Hawaiian trees, but not in both; this genetic divergence suggests that the dispersal event took place 1.4 million years ago.

Le Roux has ruled out the possibility of humans transferring the seed, because the molecular clock suggests that genetic changes began long before humans arrived in Réunion. “Despite its close genetic relatedness to koas from Hawaii, you see there is already diversification that is unique to Réunion,” he says.

The startling finding is the latest in a string of improbable long-distance dispersal events that have been uncovered in the past 15 years or so. These include the proposed movement of New World (flat-nosed) monkeys on a raft from Africa to South America less than 50 million years ago, long after the two continents split; and the transfer of sundew carnivorous plants (*Drosera* species) from western Australia to Venezuela, probably by birds (see ‘Far and wide’). Such findings have shaken up the field of biogeography, which concerns itself with why species are found where they are.

In the past, similar species found on different land masses were presumed to be the result of the continents slowly drifting apart, says Alan de Queiroz, an evolutionary biologist at the University of Nevada, Reno, and author of *The Monkey’s Voyage* (Basic, 2014), a book about long-distance dispersal. And islands were thought to be largely dead ends when it came to species dispersal. “Things don’t go from islands,” he says, “or at least that was the general thought.”

But the newly discovered long-distance events are changing that opinion, and



Ecologists have now shown that these acacia trees on Réunion are the same species as those on Hawaii.

biogeographers are increasingly stressing the role of improbable events and serendipity in shaping which species occur where. “The event [of the koa dispersal] is a giant fluke, but that’s part of the message of a lot of recent biogeographic studies: that giant flukes happen,” de Queiroz says.

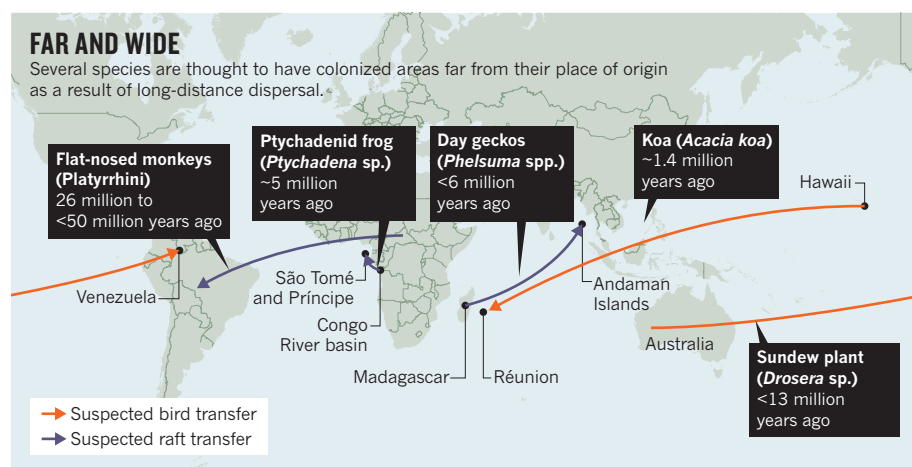
As these accounts of long-distance dispersal accumulate, some ecologists say that the next challenge is to make predictive generalizations

about how often such events occur and which mechanisms (such as bird dispersal or rafting) are most important. “What we need to do is go beyond this accumulation of anecdotal evidence,” says Ran Nathan, a movement ecologist at the Hebrew University of Jerusalem.

But the problem is that the rarity and accidental nature of such events may defy categorization. “There could be an argument that you get an endless list of very, very strange and peculiar mechanisms,” says Nathan. “There will be a long list, but there will be some mechanisms that are much more frequent.”

Ecologist Jon Waters of the University of Otago in Dunedin, New Zealand, says that despite the potentially large role of long-distance dispersals in organizing global flora and fauna, such dispersals are not completely random or unpredictable. “As well as thinking about geographic proximity in making predictions about dispersal, there are numerous other factors to consider, such as oceanographic connectivity patterns, prevailing winds, storm tracks and even bird migrations,” he says.

In other words, the distribution of some species may be the result of chance, time and luck — but there are still patterns. And science still has a part to play in elucidating them. ■



PUBLIC HEALTH

US child study hits buffers

Launch date for cohort study set to be delayed as data problems are identified.

BY HEIDI LEDFORD

Like proud new parents, US researchers had high hopes for the National Children's Study (NCS). It would track 100,000 children from birth to age 21, provide a wealth of data about environmental effects on health and yield a greater understanding of health disparities between different ethnicities and income levels. It might even reveal links between exposures and conditions such as asthma, autism and attention deficit hyperactivity disorder, which are increasingly common in children.

But 14 years after planning began, with more than US\$1 billion spent and 5,050 children enrolled in a pilot phase, the study still lacks the scientific grounding it would need to be fully implemented next year as scheduled, a review by the US National Research Council has found.

"The study has great promise," says Greg Duncan, an economist at the University of California, Irvine, and chair of the review committee. "But we did identify a number of problems that need to be addressed."

HISTORY OF SETBACKS

The council's report, released on 16 June, is the latest blow to a study mired in controversy. During the 2000s, the administration of then-president George W. Bush repeatedly attempted to cancel the NCS, only for Congress to restore its funding. In 2012, the study was scaled back in the face of projections that it would cost more than twice the initial estimate of \$3 billion over 25 years.

The latest report finds that the study's protocols for data collection have not yet been finalized or tested, and administrators failed to back up important decisions with scientific documentation. The review panel also says that the scientific hypotheses used to guide study design were poorly defined. "The hypotheses were just silly," says Nigel Paneth, an epidemiologist at Michigan State University in East Lansing, who



The wait for the study's launch has been prolonged.

was involved with the study before it was scaled back. "They bore no relationship to any public-health goal that I could recognize."

The panel traces many of the study's problems to a lack of expertise in the programme's management office at the US National Institute of Child Health and Human Development. The authors note that the office does not seem to have incorporated feedback from scientists on key decisions, and they highlight a series of ensuing concerns, including an insufficient model for comparing the effectiveness of different study designs. "The panel is concerned that the Program Office may not have sufficient in-house expertise in relevant scientific and survey research disciplines to enable it to function effectively," the committee writes.

Funding problems and design issues have

plagued the study since it was authorized by the Children's Health Act of 2000. When the pilot study suggested that the initial strategy of going door to door to enlist participants would be too expensive and slow, study planners began recruiting volunteers through group health-care providers. That raised concerns that the study would exclude rural areas not served by such groups. The drive to cut costs also led the programme to contract out data collection to private consulting groups instead of academic investigators.

UNDER REVIEW

In March 2013, amid concerns about the effects of these changes, Congress requested that the National Research Council and the Institute of Medicine review the NCS and withhold payment on contracts related to the study until 60 days after the review was completed.

The resulting report raises valid issues, says Francis Collins, director of the US National Institutes of Health: "They had substantive concerns about the study design and oversight and we ought to take that seriously."

Collins plans to convene a panel of experts to assess the study's next steps and to gauge whether it is time, given the project's long history, to update its design to incorporate technological advances in electronic medical records and ways to assess environmental exposures. "If we're going to be doing this for 21 years, let's make sure we're making the very best use of everything that's available to us," he says.

Duncan declines to speculate on how long it will take the study's organizers to incorporate the committee's recommendations, which include soliciting input from outside researchers and incorporating a scientific review-and-approval process. But given the information provided to the review committee, he says that the study was already unlikely to start on time. "We expected to see a lot of completed protocols for sampling and early data collection," he says. "We didn't." ■

DAVID ELLIS/AURORA PHOTOS/CORBIS



**MORE
ONLINE**

TOP STORY



Dinosaurs were 'mesotherms' — neither warm- nor cold-blooded
go.nature.com/ssolwr

MORE NEWS

- Quantum-entangled network could make ultra-precise clock go.nature.com/etg5kf
- Disabled physicist joins European Parliament go.nature.com/zhc8rd
- Genes reveal diversity of pre-Columbian Mexico go.nature.com/i83ecq

NATURE PODCAST



A controversial stem-cell therapy, the gravitational constant, and unusual ways to get water nature.com/nature/podcast



Women in sub-Saharan Africa are often not tested for HIV until they become pregnant.

clinical trial to protect infants any better than Option B, acknowledges Jennifer Cohn, medical director of the Médecins Sans Frontières Access Campaign in Geneva, Switzerland. But “the movement is towards treatment simplification”, she says, and Option B requires choices to be made about when treatment should be restarted.

In places where lab facilities are scarce and women have an average of five to six children, doctors often find it difficult to follow protocols that require regular immune-cell testing and resumption of treatment if levels drop or the woman becomes pregnant again. Partly for that reason, countries such as Uganda, Malawi, Tanzania and Zambia have now opted for the simplicity of Option B+. But this means that some women who enrol in the PROMISE trial will receive less-aggressive treatment than is recommended in their countries.

INFORMED CONSENT

“It is inconceivable that properly informed HIV-infected pregnant women would accept enrolment in a study where they might receive treatment that is inferior to that offered by their national ministry of health,” wrote paediatrician Arthur Ammann, founder of Global Strategies, a capacity-building organization based in Albany, California, in a 7 June letter to officials at the US National Institutes of Health (NIH) in Bethesda, Maryland.

However, Fowler says that the ministries of health at all PROMISE sites agreed to continue the trial after the WHO revised its guidelines, with the exception of Tanzania, which is still considering the decision.

A 2012 review of PROMISE’s design commissioned by the NIH concluded that it was ethical to continue testing older regimens in countries that now use Option B+ because there was no evidence at the time that Option B+ was any better than those regimens.

But public-health officials believe that because it provides greater coverage, Option B+ is more effective at protecting infants than the other treatments. According to statistics from the United Nations, the number of HIV infections in children up to 14 years old halved between 2009 and 2012 in Malawi and Zambia, and during that period, Option B+ was widely adopted in both countries.

Dieffenbach says that no one aside from the independent review board has seen the PROMISE data, and that the board has repeatedly said that the trial continues to provide useful information. He also says that any plan to end the trial would have to ensure that the women and children who were enrolled would continue to receive care.

“These are the kinds of things that need to be thought out,” Dieffenbach says, “such as how you would change this trial in a way that is both useful for research and deals in a respectful and ethical way with these women.” ■

PUBLIC HEALTH

HIV trial attacked

Critics question ethics of allowing pregnant women to receive treatment that falls below the standard in their country.

BY ERIKA CHECK HAYDEN

Treatment of people with HIV has advanced so much that some doctors and activists are urging the US National Institute of Allergy and Infectious Diseases (NIAID) to stop a trial that compares how well older and newer protocols keep mothers from passing HIV on to their newborn babies.

The Promoting Maternal–Infant Survival Everywhere (PROMISE) study is comparing three ways of delivering antiretroviral drugs to pregnant women. In Option B+, women receive a three-drug cocktail called highly active antiretroviral therapy (HAART) and stay on it indefinitely. In Option A, the women take a single drug during pregnancy and in Option B, they take the triple-drug therapy, but stop shortly after delivery or finishing breastfeeding as long as their immune-cell counts have not dropped to unhealthy levels.

Mary Glenn Fowler, the leader of the trial and a physician at the Johns Hopkins Bloomberg School of Public Health in Baltimore, Maryland, says that the study will provide crucial evidence about whether exposing pregnant women to the aggressive antiviral treatment

used in options B and B+ puts them and their newborns at unnecessary risk. “It is critical to be sure we’re doing no harm,” she says.

But last year, the World Health Organization (WHO) recommended that, where feasible, all pregnant women with HIV receive Option B+. “The PROMISE trial has become almost redundant,” says physician Erik Schouten, who works for the non-profit advisory organization Management Sciences for Health in Malawi, one of 15 countries in which the trial is being conducted.

Yet in December, leaders of the group conducting the study — known as the International Maternal Pediatric Adolescent AIDS Clinical Trials network — decided to continue PROMISE but stop other trials in the face of a 32% budget cut. And in May, an independent review board said that the trial’s output so far justified its continuation. “We’re kind of in between a rock and a hard place,” says Carl Dieffenbach, director of the NIAID’s Division of AIDS.

Option B+ has not been shown in a large

“The PROMISE trial has become almost redundant.”

POLICY

Irish university labs face external audits

Funding agency aims to affirm best practice with independent checks on research methods.

BY RICHARD VAN NOORDEN

Scientists in Ireland will soon have to open up their lab notebooks and explain their research processes to outside auditors, according to plans outlined by the head of the country's basic-research funding agency.

Mark Ferguson, the director-general of Science Foundation Ireland (SFI), says that he has invited independent consultancy firms to bid for an unusual and unique annual auditing exercise to start before the end of this year. The firms will check whether SFI-funded institutions, including all of Ireland's leading universities, have procedures in place for reporting and investigating misconduct; whether management has followed those procedures in real cases; and whether any investigations have been carried out to a satisfactory standard.

For a small, random selection of SFI-funded grants, auditors will also check how experimental details have been recorded in lab notebooks and signed off by supervisors. In addition, they might ask to see the data behind particular papers.

"I don't want to cast us in the role of Big Brother. I want this to be constructive, polite and educative," Ferguson says. But he notes that checking that research is conducted with integrity is just as important as running routine financial audits. "It's to pick up mistakes and promulgate best practice. We are all in the business of making sure we are getting the best research for our money," he adds.

The plans follow the release on 4 June of the National Policy Statement on Ensuring Research Integrity in Ireland (go.nature.com/lxvreq), which outlines common standards for Irish research. It was signed by major research institutions and funders, and is closely modelled on similar European and British agreements.

But whereas funders in other nations ask research organizations to assure them only that they are following the rules — and in some cases to report data on matters such as misconduct investigations — Ferguson says that annual external audits are needed to check compliance and to maintain public trust that money is well spent. "We have the right to withdraw a grant if there is serious mishandling," he says, although he does not expect to see anything beyond minor issues.

But some researchers question whether the audits are worthwhile. "This is an interesting idea but I am not sure it will really work. It may serve the profile of funders to say superficially that 'We have done our job well,' but I doubt that the sample of audited work will be large enough and in depth enough to make any material difference," says John Ioannidis, a physician who studies research methodology at Stanford University in California. "It may add only another layer of bureaucratic checks."



"I don't want to cast us in the role of Big Brother. I want this to be constructive, polite and educative."

Mark Ferguson

The US National Institutes of Health in Bethesda, Maryland, a major funder of biomedical research, takes a similar view. Although it has rules that organizations must abide by, it is not considering external audits, says Sally Rockey, the deputy director for extramural research at the agency. Instead, it is focusing on enhancing researcher training to improve the reproducibility of research.

Ferguson admits that exhaustive audits would not be cost-effective for the SFI, an agency that gives out only around €150 million (US\$203 million) a year in grants. Auditors will not have a deep scientific knowledge or be expected to reinvestigate misconduct cases, so the auditing will be "fairly procedural", he says. The SFI would publish the broad findings of its audits, but not the fine details, which would be shared only with universities. "I don't want to stigmatize particular grant holders," Ferguson says.

Beyond early discussions, he has not talked through the plans in detail with research institutions. *Nature's* news team asked four universities for comment; they directed a reply through the Irish Universities Association. "We look forward to further discussing with SFI how the practical implementation of the policy may be best effected," a spokesperson said. ■

WATER ON TAP

Researchers are exploring unconventional sources of fresh water to quench the globe's growing thirst.

BY QUIRIN SCHIERMEIER

In an effort to combat his country's long-standing water crisis, Iran's president took to Twitter last year. "We need plan to save water in agriculture, prevent excessive tap water use, protect underground sources of water and prevent illegal drilling," Hassan Rouhani tweeted in November.

Iran is far from alone. From the southwest United States to southern Spain and northern China, water shortages threaten many parts of the world. Nearly 800 million people lack access to safe drinking water and 2.5 billion have no proper sanitation.

The situation will probably get worse in coming decades. The world's population is expected to swell from 7 billion today to more than 9 billion by 2050, even as climate change robs precipitation from many parched parts of the planet. If the world warms by just 2°C above the present level by the end of the century, which scientists believe is exceedingly likely, up to one-fifth of the global population could suffer severe shortages of fresh water.

"Even without global environmental change, feeding 9 billion people by 2050 will require an additional 2,000–3,000 cubic kilometres of fresh water in agriculture — more than the total global use of water in irrigation," says Johan Rockström, a specialist on water resources at Stockholm University and director of the Stockholm Resilience Centre. "This equates to nothing less than a new agricultural revolution. Novel approaches, such as water-harvesting practices, are absolutely critical in the future."

Most countries are seeking to expand access by tapping the underground aquifers that already supply the bulk of the fresh water for the global population. At the same time, some are experimenting with recycling waste water for agriculture and other uses. But many nations hope to tap unconventional sources — ranging from fog to the ocean — to quench their thirst. Some approaches involve billion-dollar deals; others are local efforts that require little in the way of costly technology. Here *Nature* looks at five ways to produce fresh water from unusual sources.

DESALINATION AT A COST

Like all Mediterranean countries, Israel receives most of its precipitation during the winter months. But last winter, almost no rain fell. In the past, such a drought would have caused severe problems for Israel's 8.2 million people. But thanks to the seawater desalination plants that Israel has built over the past decade, the country's taps did not run dry.

Israel's four large 'reverse osmosis' plants rank among the biggest and most efficient desalination facilities in the world. By next year, they are expected to provide more than 500 million cubic metres of fresh water per year — about half of Israel's needs. In 2012, IDE Technologies in Kadima, the company behind three of the existing Israeli plants, signed a deal to design a US\$1-billion desalination facility near Carlsbad, California. When completed by 2016, it will supply fresh water to about one-tenth of the 3.2 million people living in San Diego county.

A rapidly growing global industry, desalination has become in the past 20 years an essential source of fresh water for the Middle East, Australia, the United States, South Africa, Spain and, increasingly, India and China. In 2012, the total amount of installed desalination capacity exceeded 80 million cubic metres per day, enough to supply some 200 million people.

"With nearly half of the global population living within 100 kilometres of the ocean coast, you just can't avoid desalination," says Gary Amy, director of the Water Desalination and Reuse Center at the King Abdullah University of Science and Technology (KAUST) in Thuwal, Saudi Arabia. "Desalination is here to stay and it will inevitably become bigger."

But by any method, desalination consumes much more energy than conventional water sources. It takes just over 3 kilowatt hours (kWh) of energy to produce 1 cubic metre of potable water at the most efficient commercial reverse osmosis desalination plants — where pre-filtered sea water is forced under pressure through a series of semi-permeable membranes. A process that evaporates ocean water in thermal plants requires about 10 kWh to produce the same amount of potable water. Some oil-rich countries do not mind the high price: Saudi Arabia's desalination industry, for example, currently burns some 300,000 barrels of oil per day.

Engineers are trying to improve reverse-osmosis technology using components such as low-energy pumps and advanced membranes. Some are experimenting with membranes made of graphene to replace the polymers currently used. And efforts are under way globally to shift from fossil fuels to renewable energies in the desalination process.

Even with those advances, desalination will remain costly, says Maria Kennedy, a water-treatment specialist at the United Nations' Institute for Water Education in Delft, the Netherlands. "Nobody decides to do desalination unless they're out of other options."



RIVERBANK FILTRATION

Every July and August, millions of Hindu pilgrims flock to the holy city of Haridwar in India, to visit its temples and fetch water from the Ganges river. The aquifers that supply fresh water to the city cannot keep up with the annual influx of people, so another source is needed. The banks of the Ganges offer a solution.

Germans along the Rhine have been using riverbanks to filter water since the 1870s. The method is straightforward: when wells are dug next to a river in regions with suitable geology, the river water filters through sand and gravel that strips out most of the chemical and biological pollutants, and so emerges relatively clean.

"The treated water may not always meet the water-quality requirements," says Saroj Sharma, an environmental engineer at the UN's

water institute. But when the river is relatively clean and the geological conditions are favourable, as in Haridwar, it may need only a minor amount of disinfection, says Sharma.

India will have to increase its use of natural water-treatment systems. Groundwater currently provides 85% of the country's domestic water, but supplies are rapidly declining: in 20 years, about 60% of all of India's aquifers will be critically degraded, according to the World Bank.

Researchers are now looking to improve the efficiency of technologies for natural water filtration and reuse in India as part of the Saph Pani project, a \$6.5-million collaboration at nine sites in the country, funded by the European Union. The studies range from riverbank filtration in Haridwar to wastewater treatment in artificial wetlands in Hyderabad.

Hindu pilgrims gather to bathe in the Ganges.

DANIEL BEREJULAK/GETTY

ANCIENT TECHNOLOGY

The Tigray region of northern Ethiopia is notoriously dry, and as a result has experienced repeated famines. But the villagers of Koraro no longer face water shortages, thanks to an imported ancient technology.

Upmanu Lall, director of Columbia University's water centre in New York City, brought the method to Koraro as part of the university's Millennium Villages Project, which seeks to fight poverty and hunger in Africa through community-led efforts. While searching for a way to supply the community with water, Lall sought inspiration from waterworks known as qanats, invented by Persian engineers more than 2,000 years ago. These elaborate tunnels carry groundwater from high elevations down to dry valleys and plains; some ancient systems are still in use in Iran and parts of the Arabian Peninsula. In 2009, with \$250,000 funding from the Ceil and Michael E. Pulitzer Foundation, Lall's engineering students began to design a modern version of a qanat in Koraro.

The village and surrounding fields are on a sandy slope, just a few kilometres away from the steep cliffs of a mountain. The region receives scant rainfall, except in July and August, when flash floods badly erode soil. In the past, villagers have stored rainwater in tanks, but much of that water evaporated quickly and the rest often became polluted.

To get around these problems, the Columbia students, aided by Ethiopian engineers and local villagers, designed a system of small

rock dams at the top of the mountain to control surface run-off and allow the rainwater to seep into the subsurface.

The water then flows down through the mountain into a trench measuring 3 metres wide by 3 metres deep, which stretches from the foot of the mountain down the slope to the village 4 kilometres away. The system, which can hold 36,000 cubic metres of water, has been working for three years. The trench recharges the groundwater around Koraro, thus supplying villagers with water for drinking and agriculture. The water has enabled villagers to add an extra planting season, and it supplements irrigation during breaks in the rainy season.

"Just like the master-builders of ancient Persian qanats, we have created an aquifer where actually there wasn't one," says Lall. "And, filtered by the sand, the water we produce is of pure drinking quality."

"Water scarcity is often caused by sporadic rainfall rather than actual lack of water," says Alberto Montanari, a hydrologist at the University of Bologna in Italy. "The challenge then is to devise sustainable solutions for storing water to make a reserve for the dry season. The Koraro project is an excellent example how this can be done."

As word spreads about the success of the scheme, other communities in Tigray are planning to adopt similar techniques. The method, says Lall, could be applied in many locations with appropriate topography and hydrology, including most of Africa's semi-arid highlands. And Lall is already looking beyond Africa: he is in talks with the state of Jharkhand in northeast India to develop a qanat there.

GREENING THE DESERT

Agriculture uses more than two-thirds of Earth's fresh water, so the idea of a farming practice that produces more water and energy than it consumes seems too good to be true. But in the desert of Qatar, scientists are showing that salt water and sunlight can yield food and clean water in a self-sustaining cycle.

The Sahara Forest Project (SFP), a Norwegian company launched in 2009 and supported by the Oslo-based fertilizer company Yara and the Qatar Fertilizer Company of Mesaieed, operates an \$8.5-million pilot facility outside Doha. Last year, the 700-square-metre greenhouse produced a crop of vegetables comparable to that of commercial greenhouses in Europe, according to SFP.

Greenhouses normally trap heat, but the reverse is required in hot places such as Qatar. At the SFP facility, sea water does the trick. The water, piped from the ocean just 100 metres away, trickles over a lattice at the windward side of the greenhouse. As the water evaporates, it humidifies the air entering the greenhouse and cools it by some 10°C, creating an indoor climate suitable for growing vegetables such as cucumbers and tomatoes. Other crops, such as barley, salad rocket and useful desert plants, grow between hedges downwind of the greenhouse.

When the desert cools at night, water condenses on surfaces inside the greenhouse and is collected for irrigation and drinking. A desalination facility at the site produces further fresh water. And the electricity needed to run the entire installation comes from solar power.

Joakim Hauge, chief executive of the SFP in Oslo, believes that the concept can be scaled up to create green oases in desert climates that are otherwise hostile to farming. "With

Agriculture uses more than two-thirds of Earth's fresh water.

60 hectares of greenhouse production we could match the yearly import of cucumbers, tomatoes, peppers and aubergines to Qatar," he says.

The company is working with the government of Jordan to set up a 20-hectare pilot facility, including a commercial greenhouse unit and a research and innovation centre, in Aqaba. A larger commercial facility, says Hauge, would be able to produce excess electricity that could be exported to the grid.

The concept might work in any dry and sunny location that is near sea level, and therefore has low pumping costs. Even so, saltwater greenhouses remain an experiment for now, says Nina Fedoroff, director of the Center for Desert Agriculture at KAUST. "The concept is intriguing," she says. "But it is still a rather pricey way of producing food that might not gain huge commercial traction."



FOG HARVESTING

For as long as people can remember, women in the small mountain village of Tojquia, Guatemala, have had to trek down to the valley bottom during the dry winter months and haul fresh water back uphill to their families. But now they can get their water by wringing moisture from the fog that often envelops their community.

One cubic metre of fog can contain up to 0.5 grams of liquid water, and harvesting it is relatively easy. A large vertical mesh panel can collect water droplets as the wind pushes clouds of moisture through its fibres. Tiny at first, the droplets coalesce and grow, then run into a gutter at the bottom and into a storage tank.

At 3,300 metres above sea level, where winters are windy and dry but often foggy, Tojquia is an ideal site for this technique. With the help of researchers from the non-profit FogQuest project in Kamloops, Canada, the residents of Tojquia have installed 35 collectors since 2006. These produce an average of 6,300 litres of potable water per day — enough for about 30 families during the dry season — and considerably more in the wet season when rainwater, too, is collected in the storage tanks.

Fog collection is catching on in seasonally dry regions that lack other sources of fresh water. The first simple mesh panels were built in the 1960s in the port town of Antofagasta in northern Chile. Today, 35 countries are using the technique, particularly along the Pacific coast of South and Central America, in the Atlas Mountains in Morocco and on the high plateaux of Eritrea and Nepal.

Improvements could come from advanced mesh materials, such as the permeable fibres developed by scientists at the Massachusetts Institute of Technology in Cambridge; when tested in Chile, these collected fog at a rate five times that of conventional mesh. And in the Namib Desert in Namibia, three-dimensional meshes developed at the Institute of Textile Technology and Process Engineering in Denkendorf, Germany, have achieved up to three times higher water yields than normal meshes.

Even with those kinds of gains, fog harvesting will not solve Chile's — or any other country's — water shortages. But it can provide a simple and sustainable method of producing fresh water in semi-arid regions that are short of other options, says Otto Klemm, a climatologist at the University of Münster in Germany.

"If the climatic conditions are right — and, importantly, if local people are trained to independently maintain the facilities," he says, "it does have the potential of supplying rural communities with precious fresh water year-round." ■

Quirin Schiermeier reports for Nature from Munich in Germany.

A fog collector in the hills above Lima, Peru.

MARIANA BAZZO/REUTERS/CORBIS

The *inside* track

Members of the US National Academy of Sciences have long enjoyed a privileged path to publication in the body's prominent house journal. Meet the scientists who use it most heavily.

BY PETER ALDHOUS

In April, the US National Academy of Sciences elected 105 new members to its ranks. Academy membership is one the most prestigious honours for a scientist, and it comes with a tangible perk: members can submit up to four papers per year to the body's high-profile journal, the venerable *Proceedings of the National Academy of Sciences* (PNAS), through the 'contributed' publication track. This unusual process allows authors to choose who will review their paper and how to respond to those reviewers' comments.

For many academy members, this privileged path is central to the appeal of PNAS. But to some scientists, it gives the journal the appearance of an old boys' club. "Sound anachronistic? It is," wrote biochemist Steve Caplan of the University of Nebraska, Omaha, in a 2011 blogpost that suggested the contributed track could be used as a "dumping ground" for some

papers. Editors at the journal have strived to dispel that perception.

With PNAS currently celebrating its centenary, the news team at *Nature* decided to examine the contributed track, both to assess its scientific impact and to see which members use it most heavily and why. After analysing a decade's worth of PNAS papers, we found that only a small number of scientists have used the track at close to the maximum allowable rate. The group includes some of the biggest names in science, and six are past or current members of the journal's editorial board. These scientists say that the main motivator for using the contributed track is an intense frustration with the peer-review process at other high-profile journals, which they argue has become excessive and laborious.

Our analysis also suggests that the efforts by PNAS to prevent abuse of the contributed track and to boost the quality of papers published by




this route are bearing fruit. Although contributed PNAS papers attract fewer citations than those handled through the journal's standard review process, the gap has narrowed in recent years. "We have worked really hard at this," says Alan Fersht, a biophysicist at the University of Cambridge, UK, one of PNAS's associate editors and a heavy user of the contributed track.

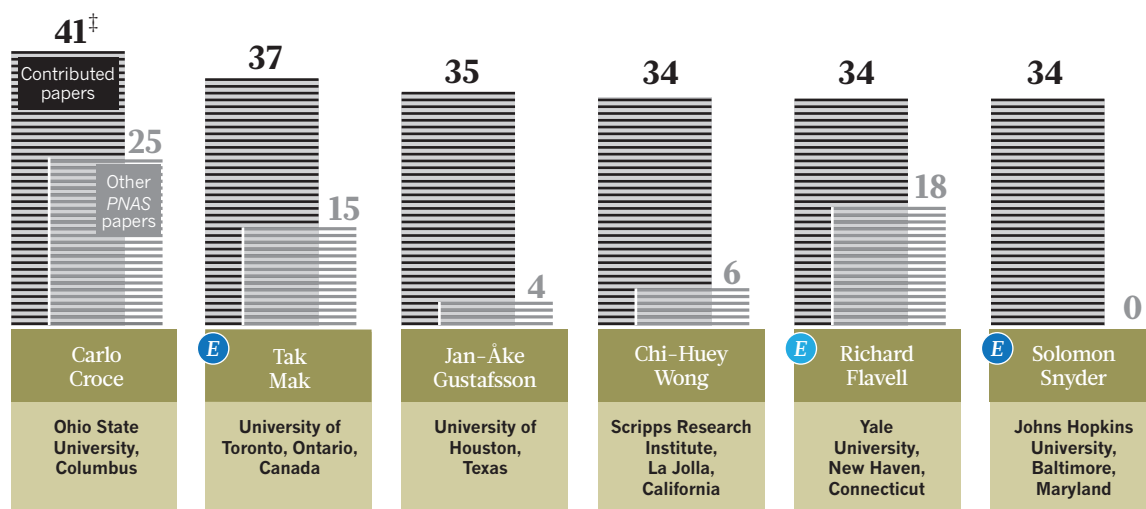
A PRIVILEGE TO PUBLISH

An inside track to publication for academy members rests deep in PNAS's DNA. The journal was established in 1914 with the explicit goal of publishing members' "more important contributions to research" in addition to "work that appears to a member to be of particular importance". That remit led to the creation of two publishing tracks: contributed and 'communicated' papers (manuscripts sent by non-members to colleagues in the academy, who would shepherd them through review).

Who are the power users?

Just 13 members of the US National Academy of Sciences consistently published three or more papers per year in the 'contributed track' at PNAS* during the past decade. 'Other' papers include direct submissions, reviewed in the normal way, and papers contributed or communicated by other members.

-  Nobel prizewinner
-  Member of PNAS editorial board
-  Former member of editorial board



*Proceedings of the National Academy of Sciences; [‡]Total includes one paper submitted in 2003.

These two tracks were the only ways to get a paper into *PNAS* until 1995, when biochemist Nicholas Cozzarelli of the University of California, Berkeley, took over as editor-in-chief and introduced 'direct submissions', which are handled more like papers at other journals. Direct submissions must pass an initial screen by a member of the editorial board, after which they are assigned to an independent editor — either an academy member or a guest editor — who organizes peer review.

Starting in 1972, the journal placed limits on the number of contributed papers that an academy member could submit, and the current annual cap of four was imposed in 1996. Then in 2010, *PNAS* abolished the communicated track, which was already declining in popularity¹. Today, more than three-quarters of the papers published in the journal are direct submissions. These papers are much less likely to be accepted than those contributed by academy members. Only 18% of direct submissions were published in 2013, whereas more than 98% of contributed papers were published, according to figures on the journal's website. (The one caveat is that *PNAS* has no data on how many papers intended for the contributed track receive negative reviews and never get submitted.)

Despite the impressive acceptance rate for contributed papers, the data collected show that many eligible scientists choose not to submit papers through this track. Of the more than 3,100 academy members who could have used the contributed track between 2004 and 2013, fewer than 1,400 scientists did so. (This might in part reflect where researchers from different fields prefer to publish their work; the academy draws its members from all disciplines, including researchers from fields such as astronomy and mathematics, who rarely send their papers to *PNAS*.) Most members who used the contributed track did so sparingly: the majority published on average fewer than one contributed paper per year. Only a small group consistently used the track at close

to the allowable maximum: from 2004 to 2013, 13 scientists each contributed more than 30 of their own papers. This roster includes some of the best-known people in contemporary science (see 'Who are the power users?').

Some of these researchers, such as Solomon Snyder, a neuroscientist at Johns Hopkins University in Baltimore, Maryland, rarely or never publish in *PNAS* except through the contributed track. But others, including immunologist Tak Mak at the University of Toronto in Canada and cancer researcher Carlo Croce at

at *PNAS*. *Cell* declined to provide figures. However, comparing across journals is difficult because each has different policies on when a revised manuscript is considered a 'new' submission.

Still, many of the contributed track's power users believe that increased competition for space in high-profile journals has allowed editors and reviewers to become more demanding. "Being able to publish four high-profile papers with much less grief than the usual high-prestige journal — that's worth some-

Editors have been dogged by the view that **PNAS** is a club for academy members

Ohio State University in Columbus, also regularly send in direct submissions.

Having control over the review process brings advantages. Those who work across disciplinary boundaries say that being able to choose your own reviewers is the best way to ensure that referees actually understand the material. "Chemists have no idea about glyco-biology," says Chi-Huey Wong of the Scripps Research Institute in La Jolla, California, who studies the chemistry and biology of sugars.

But for others, including Croce, who consistently hits his annual allocation of four contributed papers per year, the track's appeal boils down to one word: speed. Several of the contributed track's most regular users say that they have had papers held in limbo for up to two years at *Nature*, *Science* or *Cell* while the manuscripts went through multiple reviews and revisions. "In two years, you can be scooped over and over and over," says Croce.

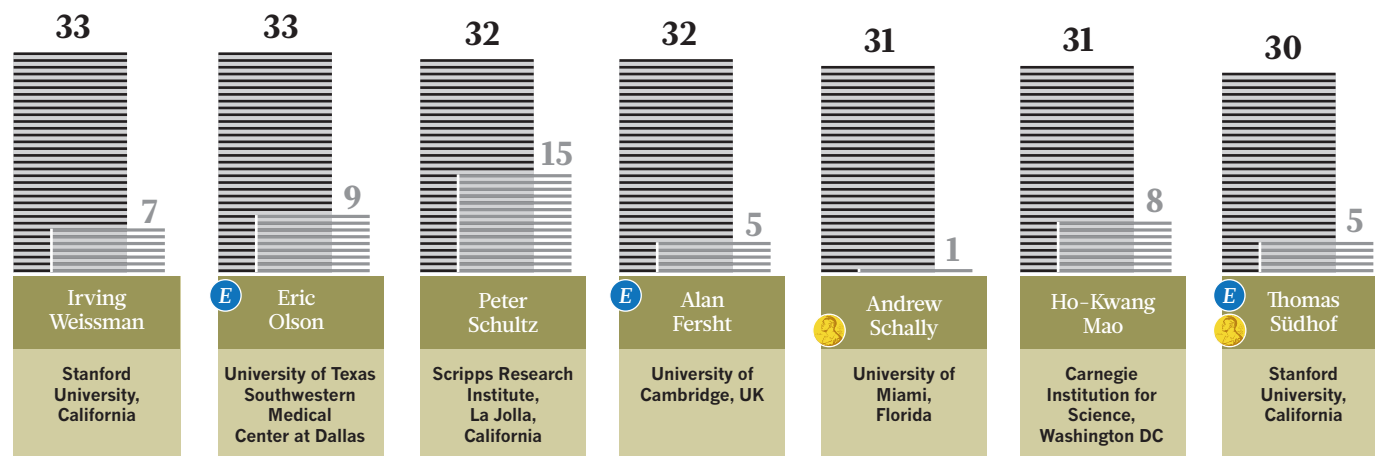
Science and *Nature* each provided figures for median time passed between submission and publication for recent papers, which suggest lag times greater than for contributed articles

thing," says Snyder. Some of the power users, including Snyder and Mak, add that the contributed track benefits postdoctoral researchers or students in their laboratories who are searching for jobs and need high-profile publications more quickly than the review time at *Nature* or *Science* would allow.

Complaints about nitpicking reviews at *Nature* and *Science* go hand-in-hand with the charge that the editors at these journals are in thrall to trendy areas of research. "Very often what seems to be fashionable is not very good science," says Croce.

SPECIAL ACCESS

The problem for most scientists looking to advance their career, however, is that they do not have the option of turning to *PNAS*'s contributed track. No wonder, then, that successive editors-in-chief have been dogged by the view that *PNAS* is a club for academy members. "We want to remove this perception," says current editor-in-chief Inder Verma, a gene-therapy researcher at the Salk Institute for Biological Studies in La Jolla.



The steady growth of direct submissions bears witness to efforts by Verma and his predecessors to make the journal attractive to scientists who are not academy members (see 'A changing journal'). "When I was editor, I was very concerned about the abuse of members' privilege," says Randy Schekman of the University of California, Berkeley, a former *PNAS* editor-in-chief, under whose watch communicated papers were abolished (see *Nature* <http://doi.org/d22bqx>; 2009). Academy members were consulted on that decision, and it was a popular one — probably because it freed members from having to deal with submission requests from colleagues.

But it would be far more difficult to convince members to give up their own publishing privileges. Even the contributed track's critics accept that it is here to stay, at least for the foreseeable future. "I'd just do away with it," says applied physicist David Weitz of Harvard University in Cambridge, Massachusetts. "But it's something that many members of the academy have viewed as their prerogative." Weitz, who sits on the *PNAS* editorial board, publishes some of his best work in the journal, but has a policy of never using the contributed track. "I don't want to have a special 'in,'" he says.

The contributed track's most enthusiastic users argue that their papers get thoroughly reviewed. "The referees I choose are people I hardly know but who can give the best review of the papers — so I don't get egg on my face," says Fersht. "It's not a free ride," agrees Mak, who adds that his haul of contributed *PNAS* papers should be viewed against his high productivity overall. His laboratory published more than 300 original research papers over the same decade. Many of the other power users head similarly productive labs.

PNAS has also tried to limit conflicts of interest by barring members from picking recent collaborators to referee their papers. Current rules prohibit members from choosing any scientist they have worked with in the past four years. The journal's editorial board can also step in to block contributed papers if it feels that members are abusing their privileges, a process that Schekman says took a considerable amount of time and effort during his tenure. Telling big-name scientists — some with egos to match — that their work isn't up to snuff can be difficult. "We would challenge these papers, and people would take umbrage and personally attack me," says Schekman. "It was discouraging to have to deal with that, but I was unbowed." Verma continues the fight, taking a wry view.

"Every member of the academy is a legend in their own mind," he jokes.

As well as providing oversight for the contributed track, the nearly 200-strong *PNAS* editorial board includes some of the track's most enthusiastic users. Our analysis shows that almost half of those who contributed more than 30 papers over the past decade are current or former members of the board — including Fersht, Mak and Snyder. These scientists work hard for *PNAS*: none more so than Snyder, who has organized the review of hundreds of direct-submission papers over the past decade.

Verma is adamant that there is no preferential treatment for those who sit on the journal's editorial board. Still, he acknowledges that the perk of the contributed track helps to

and communicated papers². (By the time Rand and Pfeiffer published their analysis, *PNAS* had already decided to abolish the communicated track.)

Although citations are not the only way to judge the impact of papers, they are the most readily available and widely researched measure. We repeated and extended Rand and Pfeiffer's analysis, considering papers published from 2004 to 2011. Overall, the conclusion was the same: the difference between citation rates for directly submitted and contributed papers was not large — controlling for other factors such as discipline, contributed papers garnered about 4.5% fewer citations — but it was statistically significant. *Nature's* analysis also suggests that the gap in citation rates between directly submitted and contributed papers has been narrowing, and this does not seem to be because more-recent papers have yet to acquire enough citations for the difference to show.

Viewed in this light, the journal seems to be making progress with its efforts to eliminate the abuse of publishing privileges by academy members. And Verma vows to keep up the pressure. He is now encouraging academy members to list the reviewers for contributed papers, taking the lead by doing so for his own most recent contribution³. Such transparency, he hopes, will hold everyone to rigorous standards.

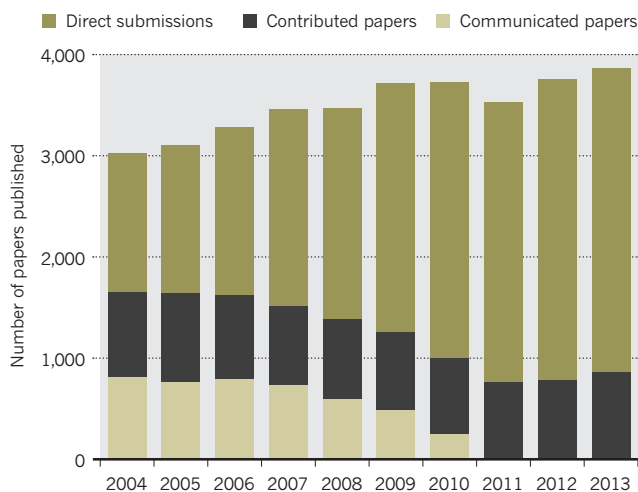
Verma also wants to eliminate what some scientists see as a vestige of the old communicated track — an option to request a 'prearranged editor' from the academy. One in five direct submissions published in 2013 used a prearranged editor, and the acceptance rate for these papers is higher than for other direct submissions. "More and more the playing field will be levelled," says Verma.

As *PNAS* marches into its second century, debate about its idiosyncratic publishing mechanisms is sure to continue. But for those who benefit from the journal's distinctive approach, *PNAS's* quirks are inherent to its appeal. "The last thing we need, I think, is less diversity," argues Nobel-prizewinning neuroscientist Thomas Südhof of Stanford University in California. "Turning *PNAS* into a standard journal, in my view, would make it unnecessary." ■

Peter Aldhous is a science journalist in San Francisco, California.

A changing journal

The number of direct submissions to *Proceedings of the National Academy of Sciences* has been increasing steadily over the past decade. Communicated papers were phased out in 2010, but the contributed track has remained constant.



explain how the journal can operate without professional editors. Fersht agrees: "Members are willing to act as editors, and part of it is because they know they are able to publish their own papers." Verma says that more than 1,200 members of the academy responded to the call to edit one or more papers in 2013, and he argues that collective editing by leading scientists is the journal's main strength.

But all of that does not quell criticism of the contributed track, and there is evidence that contributed papers have less impact than those reviewed in the usual way. In 2009, psychologist David Rand and evolutionary biologist Thomas Pfeiffer, then both at Harvard University, looked at citations to papers published in *PNAS* between June 2004 and April 2005. Controlling for factors such as scientific discipline and time elapsed since publication, the pair found that contributed papers were cited less often than direct submissions

NATURE.COM
For more information
on how the analysis
was done, see:
go.nature.com/gm7ode

1. Schekman, R. *Proc. Natl Acad. Sci. USA* **106**, 15518 (2009).
2. Rand, D. G. & Pfeiffer, T. *PLoS ONE* **4**, e8092 (2009).
3. Firth, A. L. et al. *Proc. Natl Acad. Sci. USA* **111**, E1723–E1730 (2014).

COMMENT

MEDICINE Deregulation lobby is using stem-cell therapies to push its cause **p.336**



BIOLOGY A hymn to symbiosis and those who work on it **p.338**

FIGURES Colour-blind correspondents find too many red-green images **p.340**

POLICY Is NIH mandate on the sex of cells and animals too much or too little? **p.340**

ALBERTO CRISTOFARI/CONTRASTO/EYEVINE



Italian stem-cell researcher Elena Cattaneo.

Taking a stand against pseudoscience

Elena Cattaneo and **Gilberto Corbellini** are among the academics working to protect patients from questionable stem-cell therapies. Here, they share their experiences and opinions of the long, hard fight for evidence to prevail.

Scientists get the most satisfaction from working long hours at the bench with like-minded colleagues, but sometimes their duty lies elsewhere, even if it means missing grant deadlines and receiving threatening letters. When lax clinical standards endangered Italy's health-care system and patients, we were among those who left

the comfort of our labs and offices to fight for evidence to prevail.

Since its creation in 2009, the Stamina Foundation, a private organization in Italy, has been claiming that stem cells collected from human bone marrow can be transformed into neural cells by exposure to retinoic acid, an important molecule in

embryonic development. Stamina's founder Davide Vannoni, who has not trained as a scientist or physician, holds that injections with these cells can treat conditions as diverse as Parkinson's disease, muscular dystrophy and spinal muscular atrophy. He has not published in the peer-reviewed literature. (PubMed searches for Vannoni ►

STAMINA SAGA

The ups and downs of Italy's struggle with stem-cell-therapy claims.



2011

The Stamina Foundation, founded by Davide Vannoni (pictured) sets up operations in a public hospital in Brescia, Italy.

MAY 2012

The Italian Medicines Agency shuts down Stamina operations because of safety concerns.

MARCH 2013

Italian health minister allows Stamina treatments to continue; 13 leading Italian stem-cell scientists write a letter in protest.

MAY 2013

Italian government agrees to sponsor clinical trial of Stamina's procedure.

JULY 2013

Data in Stamina patent application found to be flawed.

AUGUST 2013

Elena Cattaneo appointed as lifetime senator in Italian Senate; Stamina investigations continue.

OCTOBER 2013

Trial plans halted after scientific committee identifies problems with Stamina's protocol.

DECEMBER 2013

Decision made to form new committee to re-investigate Stamina protocol.

JANUARY 2014

Paolo Bianco, Cattaneo and Michele De Luca win public-service award from the International Society for Stem Cell Research.

APRIL 2014

Public prosecutor accuses Stamina founder of attempted fraud, and him and others of criminal conspiracy.

MAY 2014

European court rules that 'compassionate therapy' requires scientific evidence.

▶ with the key words 'stem cell' or 'neuron' return nothing.) He has moved his laboratory around and outside Italy, stating a desire to work where regulations are less strict.

Multiple scientists and government officials have found that Stamina's cell-preparation protocols are flawed and that evidence that the treatments work is wanting. Nonetheless, Italy's national health services paid for some of these procedures, and the Italian parliament even agreed to sponsor a €3-million (US\$3.9-million) clinical trial.

For most of the past two years, we and others (especially stem-cell specialists Paolo Bianco and Michele De Luca) have spoken out against these treatments. We have had to miss grant deadlines and professional meetings to make our case. We have learned to apply our investigational abilities outside our disciplines, and have come to appreciate the skills involved in helping non-scientists to grasp the value of evidence, rigour and risk assessment.

Our most recent victory came on 28 May, with the release of a ruling from the European Court of Human Rights that patients have no right to receive therapies for which there is no scientific evidence. But we are not ready to relax. Earlier this month, Marino Andolina, the Stamina Foundation's vice-president, was appointed acting commissioner of the public hospital in Brescia, in northern Italy, where the foundation still operates; a court gave him the go-ahead to give a child the 'Stamina treatment'.

Desperate patients will always be vulnerable to exploitation. We hope that sharing our experience — and we learned some lessons the hard way — will help other investigators to join the fight against predatory pseudoscience.

INTO THE FRAY

We first became aware of Stamina's claims in August 2012. Three months before, inspectors from the Italian Medicines Agency had shut down Stamina's operations at the hospital in Brescia, deeming its cell-preparation methods unsafe. Patient groups responded with lawsuits, demanding that the 'Stamina method' be made available for anyone with a terminal illness and for its costs to be covered by Italy's public health services.

In August 2012, one Italian court ruled that a child with spinal muscular atrophy could receive the treatment. Since then, the majority of the 500 courts that patients turned to decided in favour of the treatment and ordered its administration in the Brescia hospital.

In winter 2012, we and others began alerting patients, politicians and the press — writing articles and giving dozens of interviews every week — to the view that the method lacked both regulatory

precedent and scientific rationale and did not qualify for compassionate use.

Together with De Luca and Bianco, we began scrutinizing websites and Facebook pages into the small hours. We found that although Stamina presented itself as a private charitable organization, its address was that of a commercial company, Medestea, which had been fined for misleading advertising for dietary supplements. We began to collect evidence that Vannoni was trying to lobby government officials and members of parliament to have his operations exempted from regulatory oversight and to have national health plans cover untested protocols. We found that Stamina's patent applications had been rejected because the US patent office found they lacked specificity, stating in part that it was unlikely that collected cells could be induced to form desired types under the conditions described. But no one — not the journalists, public-health authorities or hospital physicians — had bothered to dig. We began talking daily with officers in the health unit of the Italian police.

By early 2013, those of us objecting to Stamina were being vilified by Vannoni and by some media outlets as keeping children from life-saving treatments. The evidence, which a small group of us had spent months collecting and distributing, was largely ignored. We knew that there can be no compassion without safety and efficacy, and that we needed to stay vocal, lucid and rational. Most of all, we had to avoid succumbing to the feeling that we had done all that we could be expected to do.

ON TRIAL

We prepared 40-page dossiers for every politician whom we could reach, and the legislature held hearings for Stamina advocates and challengers to make their cases. Vannoni was unable even to remember the names of the clinicians with whom he worked.

In May 2013, the government promised to pay for a \$3.9-million clinical trial, even though Vannoni had not presented evidence from animal or cell-based studies, or even established cell-preparation protocols that guard against contamination. Here was a dilemma: the trial would be an appalling waste of meagre public money, yet some of us thought that it would be better than unknown cells being injected into children. At least for a rigorous trial, cells would be prepared by an authorized laboratory under strict quality controls and the protocol could be scrutinized.

In August 2013, the Italian President Giorgio Napolitano appointed one of us (E.C.) and the Nobel-prizewinning physicist Carlo Rubbia as Senators for Life in the upper house of the legislature — positions that are usually reserved for politicians.

FILIPPO MONTEFORTE/AFP/GETTY



Patient advocates campaigning in November 2013 for access to the Stamina method.

The appointments, part of an effort to strengthen science in Italy, gave our band of researchers investigating Stamina greater access to politicians.

As part of the requirements for the clinical trial, Vannoni revealed his putative method for preparing cells. A scientific committee appointed by Italy's health minister found, among other shortcomings, that the method included flawed techniques to assess cells' identity and lacked basic screens for pathogens. An earlier analysis of frozen cells collected from Stamina found only blood cells, and no neurons. Plans to begin the trial were cancelled in October 2013.

In December 2013, another court ruled that any committee members who had previously spoken publicly against Stamina were biased, and called for the creation of another committee to re-examine the protocols. That same month, the health ministry said that the condition of three dozen patients treated with Stamina's protocols had not improved. (Vannoni maintains that patients' conditions did improve.)

Last month, the *International Journal of Stem Cells* published a single-author paper by Andolina, describing a boy with a severe neurodegenerative disease who had been injected with cells from his father (M. Andolina *Int. J. Stem Cells* 7, 30–32; 2014). The three-page paper contains no figures, no detailed methods and no supplementary materials, yet states that the boy's "movements [and] relationship with the parents", improved. Even more bafflingly, the author declares that he has "no conflicting financial interest". Last week, some scientists wrote to the journal about these concerns.

Meanwhile, Stamina's case continues to unravel. Italian police are looking into accusations against the foundation from patients' relatives. In April, after a four-year investigation, a public prosecutor accused Vannoni of attempting to fraudulently obtain public money, and along with some physicians and civil servants, also of criminal conspiracy. A judge will determine whether the cases will go to trial. Vannoni maintains that he is innocent of this and other charges.

FIGHTING FOR RIGHT

Our crusade has come at a high personal cost. The past 18 months have been a roller coaster of hope, disappointment, triumph and outrage. We have spent countless hours talking to each other and to politicians on the phone, in person and on video conferences. We prepared and shared at least six dossiers and dozens of slides. We have given interviews to newspapers and written commentaries almost weekly. We exchanged letters and comments with patient organizations; we established relationships with doctors at the public hospital that had housed Stamina, which has now distanced itself from Vannoni.

Every morning, we reviewed the battlefield in detail. We had to be prepared to change plans at the last minute when Stamina won a media, political or regulatory skirmish. Since June 2013, both of us, along with De Luca and Bianco, have been repeatedly asked by students' associations, university professors, science-festival organizers, patient associations and other groups to give lectures on the Stamina case. We never turn down these requests. Those of us who run research groups (E.C., De Luca and Bianco) estimate

that we have each sacrificed 60–80 weeks of lab time so far and have delayed submitting papers. We often catch up with our students and lab members at night and by e-mail.

We learned to avoid appearing on television shows on which cool reason is drowned out by strong emotional messages. Over several months, some of us received threatening letters and insults from people who felt that we lacked compassion for dying patients. Several of these letters were serious enough that we forwarded them to police. Our institutions filed complaints against unknown people hanging around our labs. Our universities were the target of e-mail and other cyberattacks.

Gathering support from the international community has proved invaluable. It underlined that we were not just local troublemakers, but had worldwide backing. An advocacy award given to E.C., Bianco and De Luca by the International Society for Stem Cell Research boosted our credibility in Italy, as did statements from Nobel laureate and stem-cell pioneer Shinya Yamanaka and publications in the scientific literature.

At home, finding the right allies and getting the best from them was key. We need to be able to talk with everyone, regardless of their scientific knowledge — from taxi drivers to lawyers. Some people welcome the documentation and persistence that comes naturally to a scientist. Others want to debate values and opinions; it is important to respect and engage with this, steadily explaining the difference between beliefs and facts.

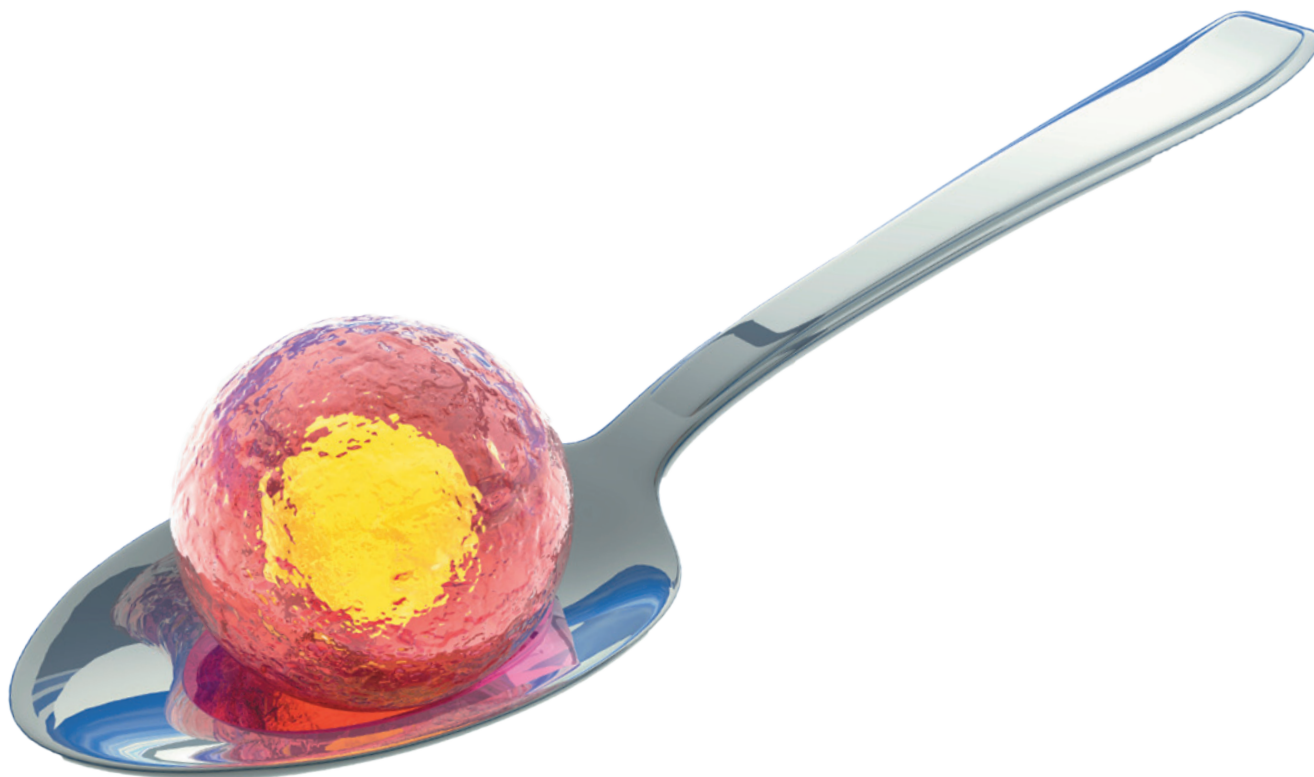
Nurturing relationships with fellow scientists involved in the battle was also key. We

had to learn to be generous and to remember that we shared a single goal. In public advocacy, the *prima donna* attitude is not helpful. Maintaining

valid and effective political and communicative actions requires a united front.

But it has all been worth it. Now, thanks to the European Court ruling and a Senate investigation into the case that launched three months ago, we are hopeful that these dubious treatments will soon be banished from Italy; they were displaced from Switzerland in 2011 and from Cape Verde earlier this year. We recommend that all scientists stand up for the scientific method. Science depends on public institutions and is done in the public interest — we have a duty to defend both. ■

Elena Cattaneo is at the Department of Biosciences and director of the Centre for Stem Cell Research at the University of Milan, Italy. **Gilberto Corbellini** is a historian of medicine and a bioethicist at the University of Rome La Sapienza, Italy. e-mail: elena.cattaneo@unimi.it



Sell help not hope

Stem cells are being used as a wedge in calls to allow unproven medical interventions onto the market, warn **Paolo Bianco** and **Douglas Sipp**.

Modern medicine depends on products that must pass rigorous tests for safety and efficacy before being marketed to patients. Such requirements are in place for drugs and other medical products across the world. Over the past decade, however, some have called to weaken or even undo this key protection.

Think tanks in the United States are using stem cells to promote broader deregulation; these moves are influencing policy in other countries. Some argue that stem-cell products and procedures should not be governed by drug regulatory agencies at all; others want to bypass requirements that treatments must be shown to work before they are sold.

'Free-to-choose' reasoning pits the scientific method against unrestrained market forces. But there is little correlation between business success and efficacy in poorly regulated markets; the billions of dollars in revenue from nutritional supplements and homeopathy bear testament to that.

A loosening of the regulatory strictures would enable companies and practitioners to generate revenue from untested products

and procedures. Patients would, in effect, pay to serve as research subjects. Worse, with no requirement to demonstrate efficacy, there would be less need for research, so new treatments might not be discovered and developed. What is needed are better business models for bringing innovative medical technologies to market, not lower standards.

BUYER BEWARE

Three key documents give a sense of what is at stake. Under the Free to Choose Medicine campaign put forward in 2010 by the Heartland Institute in Chicago, Illinois, US companies would be able to sell drugs after small clinical trials that are insufficient to establish either safety or efficacy.

The campaign's language is echoed in the bill for the Compassionate Freedom of Choice Act put forward to the US Congress in April. This would exempt from liability those who sell investigational products to people who are terminally ill and prohibit the US Food and Drug Administration (FDA) from requiring companies

even to report clinical information.

The Right to Try legislation proposed by the Goldwater Institute in Phoenix, Arizona, goes even further. Written as a template for state legislatures, the document calls for criminal penalties for public employees who seek to enforce regulations on physicians who are selling investigational drugs, biological products and devices to people who are terminally ill.

Although the above proposals target medical products and practice in general, in the past three years, stem cells and regenerative medicine have become the rallying cry of the free-to-choose lobby. In an opinion piece published¹ in 2012 in *The Wall Street Journal*, former FDA commissioner Andrew von Eschenbach, who now heads Project FDA at the Manhattan Institute for Policy Research in New York, wrote that regenerative-medicine products and other 'promising' therapies should be allowed onto the market after proof-of-concept and safety testing, and be evaluated only afterwards for efficacy. In the same newspaper, another former senior FDA official, Scott Gottlieb, now at the American

Enterprise Institute for Public Policy Research in Washington DC, also called² for loosening approval standards specifically for stem-cell products, warning readers that “the FDA wants to regulate your cells”.

The fiercest arguments are over autologous cells — those collected from and delivered back to the same patient. Courts, scientists, clinicians and ethicists have argued that stem-cell-based products should be regulated as drugs if they are processed or if their intended therapeutic behaviour differs from that in their original location.

Proponents of deregulation counter that autologous cell products should be treated as part of medical practice and thus not subjected to marketing approval. For example, in legal battles against the FDA, Regenerative Sciences of Broomfield, Colorado, argued that the agency did not have oversight over its human-cell-based products. Two conservative medical groups filed arguments in the company's defence, and the Manhattan Institute published a legal analysis supporting the company's position. US courts ultimately upheld the FDA's authority, sustaining its ability to regulate products based on human cells and tissues.

In a separate case in 2012, the FDA issued a warning letter to Celltex Therapeutics in Houston, Texas, after the state had moved to allow physicians to market investigational stem-cell products. The company subsequently shifted its clinical operations to Mexico; it posts the Manhattan Institute's position paper on its website.

RELAXED MARKETS

Several countries in Asia, Latin America and the Caribbean have already punted stem cells straight onto the market, often in concert with state-backed initiatives to promote medical tourism. Australia has exempted autologous cells from the purview of its drug regulatory agency, the Therapeutic Goods Administration, unleashing offers of unproven treatments from at least a dozen clinics.

In the controversy surrounding the Stamina Foundation in Italy³, which offers an unproven stem-cell treatment for a range of conditions, US advocates of free-to-choose-medicine last year pressed the Italian government to allow entities to market stem cells for diseases such as ischaemic heart disease and multiple sclerosis without requiring any proof of efficacy, and only a small phase I clinical trial to evaluate safety. This prompted alarm and counter-arguments from scientists (see page 333). Earlier this year, a nearly identical deregulatory proposal was published⁴ as a call for stem-cell products to be placed on the market first, and tested for clinical effectiveness later.

In November 2013, Japan enacted a regulatory regime that allows companies to market ‘regenerative-medicine’ products

that have shown nominal safety and inklings of efficacy in phase I trials for up to seven years without presenting further evidence of efficacy. How efficacy would be determined after this period is unclear. Foreign stem-cell companies are already lining up to enter Japan's lucrative market⁵.

BACKWARD STEP

Even the idea of putting products up for sale and into consumers' bodies on the basis of phase I data is disturbing. Early-stage clinical trials reveal only whether a product is safe enough for continued testing, not for widespread use. Some 80% of products that make it through phase I clinical trials fail in later studies — about half of those proving to be insufficiently effective and one-fifth insufficiently safe⁶.

When test subjects are paying for the product under investigation, establishing efficacy is hard: controls, randomization, masking and other hallmarks of clinical research break down⁷. Many stem-cell clinics offer their procedures for disparate conditions, further complicating post-market studies.

Under the guise of ‘patient-funded clinical trials’, clinics in the United States and Mexico persuade people who are seriously ill to pay tens of thousands of dollars for procedures⁸. Because such patients have been told that a product is experimental, they have little recourse when hoped-for cures fail to materialize. Companies can thus profit from selling hope. With their products already on the market, they have little reason to conduct rigorous, conclusive research.

Advocates of deregulation suggest that databases of patient information could provide the data needed to tease out efficacy. Aside from the fact that such databases are not in place, and their construction would require massive outlays of public money (something conservative groups ordinarily bemoan), there are also no means of ensuring compliance. More than 360 registered studies at ClinicalTrials.gov are listed as using mesenchymal stem cells as an intervention. None lists results.

In short, proposals for deregulation come shrouded in appealing messages that shift adroitly in response to critiques: freedom of choice, giving hope to dying patients, fighting bureaucratic obstructionism and, of course, innovating medicine. But it is a business model that removes the incentives to make drugs and treatments ever better. It offloads financial risk from investors and companies to patients, and requires the very ill to pay for interventions that are unlikely to work.

A BETTER WAY

The pressure to deregulate comes from the failure of current business models as engines of innovation. In the United States

and Europe, regulatory structures actively support therapeutic development, even for rare or orphan diseases. The gene-therapy product Glybera (alipogene tiparvovec), approved by the European Medicines Agency in 2012 for a condition that can cause life-threatening pancreatitis, is an example of establishing efficacy for a complex, innovative product with a small, but rigorous trial⁹.

However, many companies are not equipped, scientifically or technologically, to develop therapies from promising biological advances in the five or so years that their

“It is a business model that removes the incentives to make drugs and treatments ever better.”

investors demand. Much longer and deeper commitment is needed to bring stem-cell and other complex therapies to market.

Regulatory agencies face a growing challenge in gauging the merits of stem-cell therapies. Meanwhile, governments need better mechanisms to identify and support radical innovation. Untapped tools include public investment banks and equity shares¹⁰.

For stem-cell research to achieve its therapeutic potential, science, medicine, economy and policy all must work together. If, as has been widely asserted, stem cells represent the future of medicine, then we need to ensure that that future is one in which patients can reasonably expect treatments to be both safe and effective. ■

Paolo Bianco is a stem-cell biologist and professor of pathology at the University of Rome La Sapienza, Italy, and is an editor of Stem Cell Research. **Douglas Sipp** is head of the Office for Research Communication at the RIKEN Center for Developmental Biology in Kobe, Japan.
e-mails: paolo.bianco@uniroma1.it

- von Eschenbach, A. ‘Medical Innovation: How the US Can Retain its Lead’ *The Wall Street Journal* (14 February 2012).
- Gottlieb, S. & Klasmeier, C. ‘The FDA Wants to Regulate Your Cells’ *The Wall Street Journal* (7 August 2012).
- Bianco, P. et al. *EMBO J.* **32**, 1489–1495 (2013).
- Caplan, A. I. & West, M. D. *Stem Cells Transl. Med.* **3**, 560–563 (2014).
- Hara, A., Sato, D. & Sahara, Y. *Ther. Innov. Regul. Sci.* <http://dx.doi.org/10.1177/2168479014526877> (2014).
- Allison, M. *Nature Biotechnol.* **30**, 41–49 (2012).
- London, A. J., Kimmelman, J. & Carlisle, B. *Science* **336**, 544–545 (2012).
- Sipp, D. *Regen. Med.* **7**, 105–111 (2012).
- Melchiorri, D. et al. *Nature Rev. Drug Discov.* **12**, 719 (2013).
- Mazzucato, M. *The Entrepreneurial State: Debunking Public vs. Private Sector Myths* (Anthem Press, 2013).

The views expressed are those of the authors alone, and do not necessarily reflect those of any institution with which they are affiliated.



The chloroplast (pale green oval) originated when a cyanobacterium formed a symbiotic partnership with an ancestral plant cell.

EVOLUTION

The complexity chronicles

Nancy Moran enjoys a treatise on symbiosis — the intimate association of species that transformed life and Earth.

In *One Plus One Equals One*, John Archibald melds two epic stories. One is the 3.8-billion-year tale of the fundamental biochemical inventions that underlie life on Earth, and how they were swapped and merged to produce complex life forms. The second follows the scientists who first mapped the domains of life and finally proved the central evolutionary role of symbiosis — the intimate associations between two or more distinct species.

Cells originated, became complex and expanded their capabilities: events that, as Archibald puts it, “led to a transformation of ocean, land, and atmosphere”. He relates the scientific struggles behind the discoveries of these events with an appreciation of the strategies used. The microbiologist Carl Woese, for example, catalogued ribosomal RNA fragments harvested from large volumes of microbial cultures to transform our understanding of the tree of life. He delineated the ancient lineages that were later recognized as the fundamental players in the symbiotic formation of complex cells.

Archibald also offers glimpses into the

personalities of these pioneers. I loved the story of how, in 1978, Woese was so eager to see how the first determined ribosomal RNA gene sequence (from *Escherichia coli*) fitted with his own data that he could not wait for his issue of *FEBS Letters* to arrive in Illinois by post. Instead, he called biochemist Ford Doolittle in Halifax, Canada — who already had a copy — and got him to read out the 1,542-letter sequence over the telephone.

The origins of mitochondria and chloroplasts from bacterial ancestors are arguably the two biggest innovations in the history of life. In eukaryotes, organisms in which the genomic DNA of each cell is packaged in a membrane-bound nucleus, mitochondria serve as energy factories; plants and algae also have chloroplasts

that allow the harvest and storage of energy from sunlight. As their remnant genomes show, mitochondria and chloroplasts each arose from a specific bacterial group (α -proteobacteria and cyanobacteria, respectively). And each arose from a single endosymbiotic event in which the bacterium was engulfed by an ancestral cell that ‘chose’ to coexist with it, rather than digest it. Those two choices made all the difference.

From 1905, when Constantin Mereschkowsky first postulated that higher plants depend on “little green slaves” (chloroplasts), until the 1980s, the endosymbiotic theory provoked controversy. The evolutionary biologist Lynn Margulis was a proponent from the late 1960s onwards, along with botanist Peter Raven and microbiologist Jostein Gøksøyr; botanist Arthur Cronquist was among the detractors. Proof came with the molecular era. As Archibald describes, a constellation of biologists, biochemists and bioinformaticians — prominently Michael Gray, Doolittle and Margaret Dayhoff — exploited molecular technologies as they became available.



One Plus One Equals One: Symbiosis and the Evolution of Complex Life
JOHN ARCHIBALD
Oxford University Press: 2014.

GEORGE CHAPMAN/VISUALS UNLIMITED/CORBIS

The consequences of symbiosis are ubiquitous and ongoing. Symbiotic cells have themselves been engulfed as symbionts of hosts, from algae to insects. Archibald gives many examples, including the citrus mealybug *Planococcus citri*, which contains one bacterial symbiont nested within another. And sequencing data are revealing many ghosts of symbioses past, in the form of genes transferred between interacting genomes. Many nuclear genes in plants were transferred from the chloroplast ancestor, for example.

Mysteries remain. A central one is the origin of eukaryotic cells. Their distinctive nuclei, as well as other attributes such as a cytoskeleton and endomembrane system, clearly show that these cells arose only once. The few eukaryotes that lack recognizable mitochondria, such as the protozoan parasite *Giardia lamblia*, descend from ancestors that had them, as evidenced by sprinklings of mitochondrion-derived genes in their nuclear genomes. If any proto-eukaryote had a nucleus but no mitochondrion, it left either no descendants, or descendants so few or secluded that they remain undiscovered.

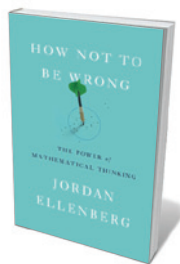
Why would the ancestral mitochondrion have been retained? The 'ox-tox' hypothesis posits that the mitochondrion provided an 'oxygen antidote' for the anaerobic host cell, which would have struggled to thrive in conditions of rising atmospheric oxygen. This seems paradoxical, because modern mitochondria generate oxygen by-products that would have been toxic to the host.

An alternative idea is the hydrogen hypothesis. This posits that the eukaryotic cell evolved from a separate-but-equal partnership between a hydrogen-producing α -proteobacterium and a methane-producing archaean. In this idea, the nuclear envelope arose after the symbiosis. Archibald weighs up the arguments, but the jury is still out.

Just as distinct organismal lineages swap and combine biochemical inventions, generating ecological breakthroughs, scientific disciplines exchange technology and ideas, instigating unexpected leaps forward. One could venture that molecular biology did for evolutionary biology what chloroplasts did for the eukaryotic ancestor of plants. In both cases, it is hard to say which side benefited more from the partnership. And with time, the merger has become so complete that the original duality is not evident. But tracing the origins of the threads from which the present is spun is exhilarating, for both cells and science. *One Plus One Equals One* is an eloquent account, at times verging on the poetic. With serious scholarship, it illuminates a rare scientific endeavour. ■

Nancy A. Moran is professor of integrative biology at the University of Texas at Austin. e-mail: nancy.moran@austin.utexas.edu

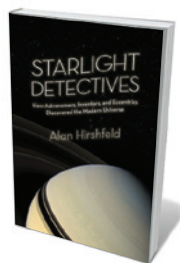
Books in brief



How Not to Be Wrong: The Power of Mathematical Thinking

Jordan Ellenberg PENGUIN (2014)

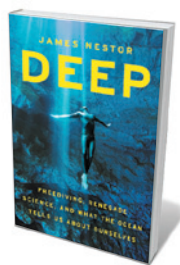
Mathematicians from Charles Lutwidge Dodgson to Steven Strogatz have celebrated the power of mathematics in life and the imagination. In this hugely enjoyable exploration of everyday maths as "an atomic-powered prosthesis that you attach to your common sense", Jordan Ellenberg joins their ranks. Ellenberg, an academic and *Slate*'s 'Do the Math' columnist, explains key principles with erudite gusto — whether poking holes in predictions of a US "obesity apocalypse", or unpicking an attempt by psychologist B. F. Skinner to prove statistically that Shakespeare was a dud at alliteration.



Starlight Detectives: How Astronomers, Inventors, and Eccentrics Discovered the Modern Universe

Alan Hirshfeld BELLEVUE LITERARY PRESS (2014)

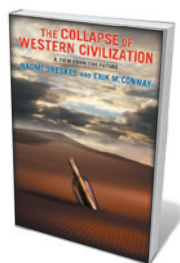
From 1850 to 1930, a handful of technological adepts transformed astronomy. That race to see deep space is told with palpable relish by physicist Alan Hirshfeld. Among the brilliant amateurs whose work he showcases are William Bond, Harvard University's 'astronomical observer', and astrophotographic pioneer Henry Draper. No less rousing is Hirshfeld's rendition of the coda, as Edwin Hubble — using the 2.5-metre reflector telescope at Mount Wilson, California — discovered the expansion of the Universe and opened up the cosmos.



Deep: Freediving, Renegade Science and What the Ocean Tells Us About Ourselves

James Nestor HOUGHTON MIFFLIN HARCOURT (2014)

Freediving, the sport that harnesses the mammalian dive reflex to survive deep plunges, can be a boon for marine researchers, avers James Nestor. We meet a salty cast of them, such as the "aquanauts" of Aquarius, a marine analogue of the International Space Station submerged off the Florida Keys. Equally mesmeric are Nestor's own adventures, whether spotting bioluminescent species from a submarine in the bathypelagic zone, or freediving himself — and voyaging into humanity's amphibious origins in the process.



The Collapse of Western Civilization: A View from the Future

Naomi Oreskes and Erik M. Conway COLUMBIA UNIVERSITY PRESS (2014)

In *Merchants of Doubt* (Bloomsbury, 2010), science historians Naomi Oreskes and Erik Conway laid out the costs of science denialism. In this trenchant sci-fi novella, they carry the consequences to their illogical conclusion. A future historian in the "Second People's Republic of China" looks back at the last gasp of Western culture in 2093, drowned, burnt and broken by climate change, neoliberal-powered ignorance and market failure. Packed with salient science, smart speculation and flashes of mordant humour.



Is the Planet Full?

Ian Goldin OXFORD UNIVERSITY PRESS (2014)

Indefatigable economist Ian Goldin follows up *The Butterfly Defect* (Princeton University Press, 2014), on the risks of globalization, with this edited volume on the equation of planetary resources and human population. Standouts among the agile analyses are Ian Johnson's reappraisal of the Club of Rome's trailblazing 1972 *The Limits to Growth*, in which Massachusetts Institute of Technology researchers tackled the same overall question; and Goldin's discussion of governance, ever the elephant in this particular room. **Barbara Kiser**

Correspondence

NIH policy: mandate goes too far

The planned mandate of the US National Institutes of Health (NIH) to include both sexes in effectively all preclinical studies could undermine its own objective by wasting resources, slowing down research or even provoking a backlash (see J. A. Clayton and F. S. Collins *Nature* **509**, 282–283; 2014). Instead of a blanket mandate, the NIH should be promoting research into the sex differences that are important to science and in disease.

Duplicating studies to “compare and contrast experimental findings in male and female animals and cells” is rarely practical, affordable, prudent, scientifically warranted or ethically justifiable. Researchers use both sexes because this roughly halves the costs of breeding and maintenance. Sometimes one sex is excluded if results are likely to differ between sexes, and possibly for well-known reasons — for instance, male rats run faster than female rats through a maze. If there is no justification for studying both sexes, then it should not be done.

Clayton and Collins suggest that statistical variability will not be increased by using equal numbers of male and female cells or animals in studies, but this is questionable and undermines the premise for the NIH's argument. If the sexes were not different, there would be no need to use both. Variances are additive, so using both sexes halves sample size while increasing variance, making it less likely that an observed difference not due to sex can be detected at a statistically significant level. Thus, an increased number of samples would be needed to reach firm conclusions.

Understanding gender differences in disease is a goal in itself, but this will not be attained as a by-product of mandating its intrusion into every hypothesis under investigation.

R. Douglas Fields *Bethesda, Maryland, USA.*
douglas.fields@gmail.com

NIH policy: status quo is also costly

Researchers have raised concerns about the cost of requiring applicants for US National Institutes of Health (NIH) grants to use male and female animals or cells in preclinical research (see J. A. Clayton and F. S. Collins *Nature* **509**, 282–283; 2014). But they should also consider the costs of not taking sex into account: these include failed clinical trials, misdiagnosis and inappropriate therapies for women, and omission of fundamental biological principles.

Many researchers are still unfamiliar with the distinction between sex and gender. Gender combines self- and societal perceptions of a person's sex, so applies only to humans. Sex is the biological result of interplay between sex chromosomes and gonadal hormones.

The impact of sex is dynamic, changing throughout lifespan and in response to injury and disease. Ruling out the influence of sex on a particular endpoint will sometimes be as difficult as identifying it. Sex must be evaluated in the context of other variables, such as age, experience, genetics and environment.

Age-appropriate medicine is a well-accepted idea that is reflected in the formation of NIH centres studying ageing and child health. The factor of sex deserves an equally integrative approach. **Louise D. McCullough, Margaret M. McCarthy, Geert J. de Vries** *Organization for the Study of Sex Differences, Washington DC, USA.*
lmccullough@uchc.edu

Sharing your data is easier than you think

Geoffrey Goodhill questions some of the practicalities of open data-sharing policies (*Nature* **509**,

33; 2014), but I believe that his concerns are largely unfounded.

Storing large volumes of raw data is costly, but many items destined for sharing are highly processed and relatively small. The mouse-brain connectome, for example, is available as a 3-megabyte file derived from many gigabytes of raw data (S. W. Oh *et al. Nature* **508**, 207–214; 2014). Neither is there a shortage of repositories: many institutional databases are freely available and well supported (such as zenodo.org, maintained by CERN, Europe's particle-physics lab in Geneva, Switzerland). More repositories will come online as researchers learn how to share data more effectively.

Contrary to Goodhill's suggestion, sharing computer code does not necessarily demand much time investment (see, for example, D. C. Ince *et al. Nature* **482**, 485–488; 2012). Code is a valuable part of a paper, so everyone benefits if its authors assume from the start that it will be shared or reused. Also, people releasing code are under no obligation to maintain it. **Stephen Eglen** *University of Cambridge, UK.*
sje30@cam.ac.uk

Justifying embryo research in Europe

It was a relief last month when the European Commission decided not to modify legislation on research involving the destruction of human embryos in response to a petition by the One of Us pro-life group. Even so, it is time to put a stop to this ‘democracy carousel’ (see *Nature* **508**, 287; 2014).

Such citizen campaigns against embryo destruction disregard the births of more than 5 million babies as a result of advances in reproductive medicine. Moreover, selective abortion following an adverse genetic diagnosis can often be avoided, owing to advances in screening embryos before implantation. And embryonic stem-cell research

is opening up regenerative medicine, which may eventually provide therapies for conditions such as pancreatic failure and age-related macular degeneration.

Central to the debate is the ethical status of the human embryo between fertilization and implantation. Many believe that, although a zygote has the potential to develop into a person, it is not yet a person. On this basis, destruction of donated embryos for medical research can be justified provided the work is subject to strict regulation and supervision. Indeed, a recent (unpublished) study shows that donation of spare embryos is widely supported by couples undergoing *in vitro* fertilization in Europe.

Joep Geraedts *Maastricht University, the Netherlands.*
joep.geraedts@mumc.nl

Still too many red–green figures

People with red–green colour blindness cannot interpret figures in research papers that use these colours. We call for all journals to provide alternative versions of figures that are more accessible to such individuals.

We searched *Nature* papers published in January–April 2014 that contained at least one image requiring colour discrimination: roughly three-quarters used a red–green combination. Some journals now recommend that authors recolour their figures — green and magenta, say (see, for example, B. Wong *Nature Methods* **8**, 441; 2011).

It would be preferable if journals could include a weblink to a colour-accessible version of red–green figures, and do so retroactively for archived figures. These would also be useful for making slideshows and posters. **S. Colby Allred, William J. Schreiner, Oliver Smithies** *University of North Carolina School of Medicine, Chapel Hill, North Carolina, USA.*
samuel_allred@med.unc.edu

CANCER

Natural-born killers unleashed

The finding that phosphoinositide-3-OH kinase δ restrains the antitumour immune response by promoting the action of suppressive immune cells may broaden the applicability of drugs targeting this enzyme to multiple cancers. [SEE LETTER P.407](#)

EMILIO HIRSCH & FRANCESCO NOVELLI

Cancer cells carry mutations that lead to the production of tumour-associated antigen molecules, against which the immune system can react. In principle, this response allows the elimination of cells that have undergone cancer-causing changes. But tumours often escape this action by tweaking immune reactions and by promoting activities usually associated with the resolution of these responses. Typically, this involves the cancer cells influencing immune cells that have a regulatory function, such as regulatory T cells and myeloid-derived suppressor cells. On page 407 of this issue, Ali *et al.*¹ report that, to escape the immune response, tumours require the action of the intracellular enzyme phosphoinositide-3-OH kinase δ . They also demonstrate that inhibiting this enzyme blocks the suppressive activity of immune-regulatory cells, thus strengthening the anticancer immune response.

Phosphoinositide-3-OH kinases (PI(3)Ks) are involved in the intracellular amplification of extracellular cues and, therefore, in many cellular functions, including proliferation, migration and metabolic control². Mutated forms of PI(3)Ks often directly drive cancer formation, and their function in cells surrounding a tumour might also indirectly favour cancer growth³. PI(3)K δ , the p110 δ isoform of PI(3)K, is primarily expressed by white blood cells (leukocytes), including lymphocytes (the class to which T and B cells belong) and myeloid cells. For example, PI(3)K δ functions in lymphocyte proliferation and migration⁴, and is implicated in cancers of these cells, such as chronic lymphocytic leukaemia and indolent B-cell lymphomas.

Recently developed drugs that inhibit PI(3)K δ have shown particular effectiveness in the treatment of lymphocyte cancers and are expected to be approved by governmental regulatory agencies soon⁵. Nonetheless, the leukocyte-specific expression of PI(3)K δ means that these drugs have been expected to be ineffective against solid tumours. Ali and colleagues' findings challenge this concept, widening the clinical application of PI(3)K δ -targeting drugs and suggesting that they may be used to support cancer immunotherapy — an increasingly

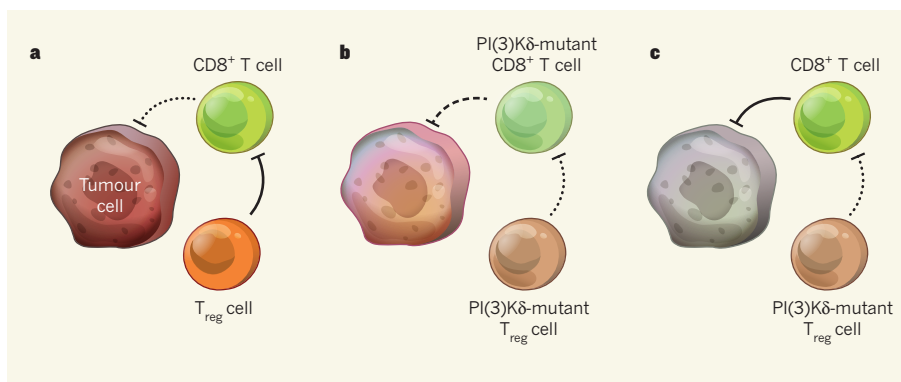


Figure 1 | Inhibition of PI(3)K δ releases immune suppression. **a**, Immune-suppressive T cells, called regulatory T cells (T_{reg} cells), block the recognition and elimination of tumour cells by cytotoxic CD8⁺ T cells. **b**, Ali *et al.*¹ show that when both T_{reg} and cytotoxic CD8⁺ T cells carry a mutation that inhibits the activity of the enzyme PI(3)K δ , T_{reg}-cell-mediated immune suppression is released. Although the cytotoxic CD8⁺ T cells themselves require PI(3)K δ for their tumour-killing activity, the release of T_{reg}-cell suppression is sufficient to induce a heightened anticancer response. **c**, Accordingly, when PI(3)K δ is inhibited only in T_{reg} cells, the anticancer effect mediated by cytotoxic CD8⁺ T cells is maximal.

successful anticancer strategy that aims to boost immune responses against tumour cells⁶.

These immune responses are driven by the CD8⁺ class of T cells. The cell-killing activity of these cells can be restrained by immune-suppressive CD4⁺ regulatory T cells (T_{reg} cells), which are normally responsible for maintaining T-cell tolerance of self-antigens, preventing autoimmune reactions and dismantling immune responses, for example after successful elimination of a pathogen⁷. However, T_{reg} cells also inhibit CD8⁺ T-cell-mediated killing of cancer cells, thus representing a major obstacle to cancer immunotherapy.

Ali and colleagues show that the growth and metastatic spread of different types of tumour transplanted into mice in which PI(3)K δ is genetically inactivated is significantly inhibited compared with the tumours' behaviour in normal mice. Because PI(3)K δ is not expressed by the tumour cells themselves, this effect seems to be linked to a disturbed suppression of anticancer immunity. The researchers demonstrate that PI(3)K δ activity is required for the proliferation and differentiation of suppressive T_{reg} cells induced by tumour cells, and that deletion of PI(3)K δ only in the T_{reg}-cell population blocks tumour growth and prolongs the survival of mice after inoculation with cancer cells.

Previous studies have suggested that PI(3)K δ functions in cells other than T_{reg} cells. For example, a lack of PI(3)K δ activity reduces the differentiation of cytotoxic CD8⁺ T cells, thus, paradoxically, reducing tumour-cell killing⁸. However, Ali *et al.* show that the effect of PI(3)K δ inhibition is stronger on T_{reg} cells than on CD8⁺ T cells, and that blocking T_{reg}-cell-dependent inhibition of CD8⁺ T cells overcomes the reduction in CD8⁺ T-cell-mediated cytotoxicity (Fig. 1).

T_{reg} cells are not alone in inhibiting the cytotoxic immune response — other leukocytes, including polymorphonuclear myeloid-derived suppressor cells (PMN-MDSCs), are stimulated by tumour cells to block cytotoxic CD8⁺ T-cell function. Ali and colleagues show that PI(3)K δ inhibition not only reduces the number of T_{reg} cells but also impairs the function of PMN-MDSCs to limit T-cell proliferation. These synergistic effects explain the greatly enhanced anticancer immune reaction observed in mice lacking active PI(3)K δ .

To assess whether these observations could be of therapeutic value, the authors investigated pharmacological inhibition of PI(3)K δ in a model of spontaneously developed cancer in mice, focusing on one of the most deadly cancers, pancreatic ductal adenocarcinoma. Strikingly, they found prolonged survival in

these animals, as a result of the expected blockade of T_{reg} -cell activity and the accumulation of tumour-killing $CD8^+$ T cells in the pancreas.

Although these results highlight the potential of PI(3)K δ inhibition in cancer therapy, they do not clarify how PI(3)K δ inhibition blocks the immune-modulating activity of T_{reg} cells. Clues may come from Ali and colleagues' finding that PI(3)K δ inhibition impairs PMN-MDSC production of soluble messenger molecules that cause immune suppression and tumour growth. But how this occurs is still unclear, and future studies should more precisely define the intracellular mechanisms by which PI(3)K δ controls immune suppression.

This strong proof of concept that PI(3)K δ inhibition can boost the immune response against a wide range of tumours will probably fuel the already-intense testing of drugs that

target this enzyme. Early clinical trials show that PI(3)K δ inhibitors, such as idelalisib, are effective in and tolerated by humans⁶. However, little is known about the long-term effects of PI(3)K δ inhibition and whether chronic treatment is sufficiently safe. For example, more work is required to exclude the possibility that long-term blockade of immune suppression leads to unwanted lymphocyte-mediated responses, such as autoimmunity. But if safety is demonstrated, PI(3)K δ inhibition to unleash our spontaneous predisposition to eliminate cancer cells may become a valid option for cancer treatment. ■

Emilio Hirsch is at the Molecular Biotechnology Center, Department of Molecular Biotechnology and Health Sciences, University of Turin, 10126 Turin, Italy. **Francesco Novelli** is at the Center for

Experimental Research and Medical Studies, Department of Molecular Biotechnology and Health Sciences, University of Turin.

e-mails: emilio.hirsch@unito.it;

franco.novelli@unito.it

1. Ali, K. *et al.* *Nature* **510**, 407–411 (2014).
2. Vanhaesebroeck, B., Guillemet-Guibert, J., Graupera, M. & Bilanges, B. *Nature Rev. Mol. Cell Biol.* **11**, 329–341 (2010).
3. Hirsch, E., Ciraolo, E., Franco, I., Ghigo, A. & Martini, M. *Oncogene* <http://dx.doi.org/10.1038/onc.2013.265> (2013).
4. Okkenhaug, K. *Annu. Rev. Immunol.* **31**, 675–704 (2013).
5. Fruman, D. A. & Cantley, L. C. *N. Engl. J. Med.* **370**, 1061–1062 (2014).
6. Couzin-Frankel, J. *Science* **342**, 1432–1433 (2013).
7. Sakaguchi, S., Miyara, M., Costantino, C. M. & Hafler, D. A. *Nature Rev. Immunol.* **10**, 490–500 (2010).
8. Putz, E. M. *et al.* *PLoS ONE* **7**, e40852 (2012).

This article was published online on 11 June 2014.

APPLIED MATHEMATICS

How chaos forgets and remembers

“It is difficult to make predictions, especially about the future,” goes the proverb. A study of the dynamics of chaotic systems in the context of information theory adds a twist to this saying.

P.-M. BINDER & R. M. PIPES

The chaos revolution is now more than 50 years old¹. Long anticipated by mathematicians, beginning with Henri Poincaré in the 1880s, the field finally emerged on the science stage in the early 1960s following the identification of chaotic behaviour in computer simulations of atmospheric and astronomical systems. Since then, many experimental observations of chaotic dynamics (such as in fluids, electric circuits, lasers and insect populations) and parallel theoretical developments have transformed the field into a fully fledged area of research. The central tenet of chaos is that simple deterministic systems — those in which the past uniquely determines the present and the present pegs down the future — can display behaviour that seems random. Writing in *Physics Letters A*, James and co-workers² present a study that adds a layer of subtlety to this statement: they show that measurements on a deterministic system that evolves in time may contain information that is specific to its past, present and future.

In the early days of nonlinear science and chaos, several branches of knowledge from within mathematics, physics and computer science helped to create a terminology that has become the lingua franca of a broad

community of scientists from the physical, life and social sciences. Geometry and information theory stand out among these contributors. The first interprets the dynamics of a chaotic system as motion in an abstract space of system states, leading to the characterization of beautiful and elegant swirling trajectories called strange attractors. The second, inspired by the work of physicist Ludwig Boltzmann and mathematician Claude Shannon, focuses on calculations based on the probabilities of

specific realizations of a chaotic system. A central finding of the latter approach is that information is produced by chaotic systems as they evolve in time. Strong connections between geometry and information theory have helped to unify the field of chaos (see, for example, ref. 3). James and colleagues' study is based on information theory.

In principle, a chaotic system is as predictable as clockwork, although much less regular. In practice, the famous butterfly effect⁴ amplifies exponentially into the future any uncertainty about the initial state of a dynamical system. But what James *et al.* found is deeper. Working within the larger context of how to infer models from data, they selected several examples of one- and two-dimensional chaotic systems for which a measurement can be made as coarse as possible — taking a value of either zero or one — through a technique called symbolic dynamics⁵. Consequently, records of the dynamics of these systems are represented as strings of zeros and ones. The authors then performed information-based calculations on these strings that allowed them



Figure 1 | Chaos measurements in time. A real-life chaotic system, such as an electric circuit with an alternating-current power supply and several nonlinear elements (left), produces a time series of states (middle) that may not be fully accessed by an experimentalist but can be codified as a binary sequence of zeros and ones (right). The most salient regularity of the sequence produced in this case is that no two consecutive zeros occur. In accordance with James and colleagues' results², the binary outcomes of measurements of this system provide, on average, some knowledge of the past and the future of the system. Outcomes of '1' allow previous information about the system to be forgotten, and '0' outcomes guarantee that both the previous and subsequent measurements are '1'.

to correlate a present measurement to its past and future. They found that, typically, some of the information measured in the present comes from the past (redundant or predicted) and the rest is newly created. Focusing on the created information, they further found that some of it (ephemeral) does not carry into the future — in other words, it is readily forgotten, with the rest (bound) being remembered and carried into the future. This fine-graining of information sheds new light on how chaotic processes work.

To illustrate these concepts, consider a real-life chaotic system, such as an electric circuit, for which coarse measurements can be made but the true states of which are inaccessible (Fig. 1). In this example, any sequence with two consecutive zeros cannot happen. Without performing any calculations, some manifestations of the types of information identified in James and co-workers' study can be gleaned. A sequence '01' is an example of redundant information, because the zero always implies a one. A measurement of '1' can be preceded by either '0' or '1'; this exemplifies ephemeral information, because what came before it becomes irrelevant and is forgotten. Finally, a measurement of '0' carries bound information because the system remembers and evolves to '1'.

James and colleagues' results show how the past and future of an evolving chaotic system become intertwined with its present. This feature may be at the heart of one of the most enigmatic of physical principles: the second law of thermodynamics, which states that the entropy of an isolated system never decreases with time. The statistical, irreversible character of this law is at odds with the underlying deterministic and reversible dynamics of such isolated systems at the microscopic level^{6,7}. The idea of applying the information-based methods presented here to thermodynamic systems, such as collections of gas molecules, is promising. Considering the entropy of such a collection as a property of its state might lead to insight into the 'arrow of time' in the second law, especially because, as James and co-workers show, chaos both forgets and remembers. ■

P.-M. Binder and R. M. Pipes are in the Department of Physics and Astronomy, University of Hawaii, Hilo, Hawaii 96720-4091, USA. e-mail: pbinder@hawaii.edu

1. Motter, A. E. & Campbell, D. K. *Phys. Today* **66**(5), 27–33 (2013).
2. James, R. G., Burke, K. & Crutchfield, J. P. *Phys. Lett. A* <http://dx.doi.org/10.1016/j.physleta.2014.05.014> (2014).
3. Binder, P.-M. & Wissman, B. D. *Chaos* **20**, 013106 (2010).
4. Lorenz, E. N. *The Essence of Chaos* (Univ. Washington Press, 1995).
5. Morse, M. & Hedlund, G. A. *Am. J. Math.* **60**, 815–866 (1938).
6. Sklar, L. *Physics and Chance* (Cambridge Univ. Press, 1995).
7. Hoover, W. G. *Time Reversibility, Computer Simulation, and Chaos* (World Scientific, 1999).

POPULATION HEALTH

Immaturity in the gut microbial community

Undernourished children fall behind not only on growth, but also on maturation of their intestinal bacterial communities, according to a study comparing acutely malnourished and healthy Bangladeshi children. SEE LETTER P.417

ELIZABETH K. COSTELLO & DAVID A. RELMAN

Effective assessments of child growth rely on a knowledge of underlying processes, appropriate standards and accurate measurements. These elements form a comparative framework with which trajectories can be charted and developmental milestones marked, providing 'actionable intelligence' on health and disease in individuals and populations. In this issue, Subramanian *et al.*¹ (page 417) chart a different path — one in which the milestones are microbial — for young children living in the Mirpur urban slum of Dhaka, Bangladesh, many of whom suffer from undernutrition (Fig. 1). The authors find evidence for delays in the development of gut bacterial communities in acutely malnourished children compared with healthy children, and that these delays are only fleetingly ameliorated by standard treatment. The team's approach for classifying and tracking gut microbiota may enhance assessments of childhood health and development, and improve therapeutic strategies.

Growth faltering in early childhood is the hallmark of undernutrition, a pervasive condition in the developing world that arises from insufficient intake, absorption or assimilation of nutrients. Undernutrition results from scarce and nutrient-poor food, poor-quality water and unsanitary living conditions. Recurrent bouts of gastrointestinal infections exacerbate and perpetuate the problem². Positive feedback loops can ensue both in individuals, when intestinal damage reinforces poor growth and susceptibility to infection, and over generations, when maternal undernutrition causes undernutrition in children. Over time, these cycles can impair learning, limit productivity and ultimately perpetuate poverty. Maternal and child undernutrition were a factor in 3.1 million (45% of all) deaths in children under 5 years of age in 2011³. Children under 2 are particularly vulnerable to undernutrition (and infection), but are also the most responsive to treatment⁴.

In early childhood, assembly of gut microbial communities results from the sequential arrival of taxa from external sources and the extinction of taxa already present, in part in response to age-associated events such as

weaning. Progression towards an adult-like, 'mature' state occurs over the first 2–3 years of life. These postnatal events prompt the terminal maturation of intestinal structures, stimulate immune responses and provide resistance to invasion by pathogens; aberrant or delayed assembly is associated with altered metabolism and immune function. Thus, because they affect and are affected by similar factors, undernutrition and gut-microbiota development are closely intertwined. Unravelling the two and discerning the role of host and environmental factors are daunting but important goals⁴.

Anthropometric indicators — physical measurements, such as weight for height, which are scored relative to a reference population — are indispensable tools in the assessment and treatment of undernutrition. Not surprisingly, equivalent international standards for gut-microbiota development are not yet available: few individuals have been followed in detail over the requisite time frame, and it also seems that microbiota composition in early childhood differs across populations^{5,6}. In light of this, Subramanian and colleagues examined healthy and malnourished children from the same urban area, ostensibly minimizing genetic and environmental differences between the two groups.

To derive a model of gut-microbiota development in the Bangladeshi children, the researchers collected faecal samples from 50 well-nourished subjects at monthly intervals over the first 2 years of life. Next, they surveyed the bacterial communities in the samples by sequencing 16S ribosomal RNA genes, which are used to define and enumerate bacterial taxa. The taxa from 12 of the subjects were then assessed and ranked according to their ability to discriminate between different host ages. The authors found that the 24 most age-discriminatory taxa could predict the ages of the remaining 38 healthy children from their gut microbial composition.

In keeping with the tradition of anthropometric indicator scores, the authors defined two indicators of gut-microbiota maturation: relative microbiota maturity and a microbiota-for-age Z-score (MAZ). The overall gist is this: if the model classifies your gut microbiota as that of a 6-month-old when you are actually



Figure 1 | Children from the Mirpur slum of Dhaka, Bangladesh.

18 months old, then your gut microbiota is probably 'immature' — its composition looks 'younger' than that of most healthy people of your age (although it may be different in other ways, too). Applying these indicators to their well-nourished cohort, the authors found that microbiota maturity decreased during diarrhoeal episodes, increased with infant-formula consumption, was unchanged by recent antibiotic use and was correlated among family members.

Subramanian and colleagues then applied their microbiota-maturation indices to 64 children aged 6–20 months at the start of the study who were sampled during and after inpatient treatment for severe acute malnutrition. The children were participating in a randomized trial comparing two therapeutic foods, in combination with supportive therapy that included antibiotics. Compared with healthy children, the malnourished children showed significant microbiota immaturity during treatment, regardless of treatment group. Notably, in the 2–3 months following treatment, the children's microbiota-maturation scores improved significantly; however, after this period, much of this catch-up maturation was lost. These patterns mirrored the anthropometric outcomes of the study: although they gained weight initially, children in both groups remained severely underweight compared with healthy children at the end of the follow-up period. The results also support previous studies of undernutrition in humanized mouse models⁷.

Degraded ecosystems are notoriously difficult to restore. Often, such efforts focus on restoring environmental conditions (akin to the food intervention in Subramanian and colleagues' study) and eliminating unwanted species (akin to the antibiotic therapy), then

waiting for assembly processes to play out 'naturally' to restore the desired community⁸. But degraded communities can be resistant or resilient to change^{8,9}, and although host health can be restored, youth cannot. The composition of mature communities may depend on the timing and order of earlier species introductions (and extinctions)¹⁰ and may prove difficult to reconstitute (by the use of probiotics, for example). Thus, an ounce of prevention is likely to be worth a pound of cure and, as with other types of developmental delays, early intervention may be crucial.

The approach presented by Subramanian *et al.* could be used to develop standards across

the globe, and then to monitor gut colonization during early childhood, as an early-warning system for microbiotas that are falling 'off track' (and there may be many such tracks to health). A detailed analysis of microbiota maturation in well-nourished populations will complement this work, and allow further deconvolution of some of the common microbiota insults that were unavoidably layered and repeated in the current study. It is becoming clear that recognizing which features of microbiota assembly are associated with health, and understanding whether and how healthy communities bounce back after disturbance, are key requirements for future human-development roadmaps. ■

Elizabeth K. Costello and David A. Relman are in the Departments of Medicine and of Microbiology & Immunology, Stanford University, Stanford, California 94305-5124, USA, and at the Veterans Affairs Palo Alto Health Care System, Palo Alto, California. e-mails: costello@stanford.edu; relman@stanford.edu

1. Subramanian, S. *et al.* *Nature* **510**, 417–421 (2014).
2. Mondal, D. *et al.* *Clin. Infect. Dis.* **54**, 185–192 (2012).
3. Black, R. E. *et al.* *Lancet* **382**, 427–451 (2013).
4. Gordon, J. I., Dewey, K. G., Mills, D. A. & Medzhitov, R. M. *Sci. Transl. Med.* **4**, 137ps12 (2012).
5. De Filippo, C. *et al.* *Proc. Natl Acad. Sci. USA* **107**, 14691–14696 (2010).
6. Yatsunenkov, T. *et al.* *Nature* **486**, 222–227 (2012).
7. Smith, M. I. *et al.* *Science* **339**, 548–554 (2013).
8. Suding, K. N., Gross, K. L. & Houseman, G. R. *Trends Ecol. Evol.* **19**, 46–53 (2004).
9. Costello, E. K., Stagaman, K., Dethlefsen, L., Bohannan, B. J. M. & Relman, D. A. *Science* **336**, 1255–1262 (2012).
10. Fukami, T. in *Community Ecology: Processes, Models, and Applications* (eds Verhoeve, H. A. & Morin, P. J.) 45–54 (Oxford Univ. Press, 2009).

This article was published online on 4 June 2014.

QUANTUM COMPUTING

Powered by magic

What gives quantum computers that extra oomph over their classical digital counterparts? An intrinsic, measurable aspect of quantum mechanics called contextuality, it now emerges. [SEE ARTICLE P.351](#)

STEPHEN D. BARTLETT

For decades, researchers have struggled with the question of what makes quantum computers so powerful, and the answer has been as elusive as an understanding of quantum physics itself. Is there some unique feature of quantum physics that is responsible for enabling quantum computers to perform certain computations faster than their conventional digital counterparts? Many of the more exotic properties of quantum mechanics have

been put forward as possible candidates, but so far none has held up to scrutiny. On page 351 of this issue, Howard *et al.*¹ uncover a remarkable connection between the power of quantum computers and one of the stranger properties of quantum theory known as contextuality.

Designs for quantum computers often mirror those of conventional computers, in that they are built out of basic components such as logic gates that perform elementary operations on quantum bits of information. A commonly used set of operations for a quantum processor

is known as the stabilizer operations². These operations are designed using the rules of quantum physics, but are in many ways similar to those used by a classical machine. For example, initializing quantum bits to a value of 0 or 1, reading out these binary values or flipping them are all stabilizer operations (as well as more-exotic ones). In fact, within this limited set of building blocks, it is often possible to imagine that the quantum bits are simply described by pairs of bits (0's and 1's) that are initialized, processed and measured by stabilizer operations much like the bits in a digital computer^{3,4}. The restricted 'classical' nature of the stabilizer operations lets quantum engineers design error-correcting codes and logic gates that are tolerant when things go wrong.

Any quantum machine that computes using only these stabilizer operations is no more powerful than your desktop computer^{5,6}. So how can we supplement this set to build a quantum computer? There are several approaches, but by far the most common is to provide the computer with a large number of additional quantum bits that are initialized in a peculiar way, using a quantum superposition of the usual stabilizer initializations⁷. A quantum bit described by a superposition possesses characteristics of both binary values 0 and 1 simultaneously. This way of initializing the quantum bits is called magic — a rather suitable name for some of the quantum weirdness that contradicts our everyday experience. Supply a processor that uses only stabilizer operations with quantum bits initialized as magic states and — hey presto! — that limited machine is endowed with the full power of a quantum computer.

If a quantum computer that uses only stabilizer operations is stuck in the slow lane together with today's run-of-the-mill digital computers, but can be 'boosted' to a powerful quantum computer by being supplied with magic states, then these magic states must hold the key to the quantum computer's increased performance. So what is so special about magic states? The answer provided by Howard *et al.* comes from studying how these states might also be described using pairs of bits for each quantum bit, as we could for stabilizer operations. The authors formalize this perspective by using a non-contextual hidden-variable theory, which is a way of describing the properties of a quantum particle or device using the values (hidden variables) of a number of bits. The non-contextuality comes from the desire to have these bits take consistent values throughout the computation, regardless of when and how we might hypothetically take a peek at their values (the context in which we measure the bits).

We have long known that not all of quantum physics can be described by a non-contextual hidden-variable theory, and there are experimental tests that can be used to prove that quantum systems are contextual and so evade

any possible classical description. In their study, Howard and colleagues show that what makes magic states special is precisely their contextuality. Specifically, they find that magic states possess exactly the properties needed to prove that quantum physics is contextual using an experimental test that relies only on stabilizer operations. That is, the authors demonstrate that this particular measurable aspect of quantum weirdness — contextuality — is the source of a quantum computer's power.

A few curious details remain unresolved. First, there are some subtleties that limit what these results can say about quantum bits — the most elementary quantum systems — as opposed to larger quantum systems. The limitations could simply be a vagary of the proof technique used by the authors, or could be a hint of something deeper. There also remain some unanswered questions regarding the power of states with vanishingly small amounts of magic. And finally, does contextuality power other quantum-computing architectures that supplement stabilizer operations in other ways than supplying magic states, such as those designed around quantum measurements⁸? Further refinements of the possible tests of contextuality to the most general situations could clarify these outstanding issues.

Knowing that contextuality supplies the magic for quantum computers is much more than a satisfying connection. This finding also promises to help researchers design better architectures for quantum machines. In many of the most sophisticated models for a potential quantum computer, just manipulating magic states into a usable form consumes most of the processor time. New architectures that are thriftier in their use of this contextuality resource may be much easier to build. ■

Stephen D. Bartlett is at the Centre for Engineered Quantum Systems and the School of Physics, The University of Sydney, Sydney 2006, Australia.

e-mail: stephen.bartlett@sydney.edu.au

- Howard, M., Wallman, J., Veitch, V. & Emerson, J. *Nature* **510**, 351–355 (2014).
- Gottesman, D. *Phys. Rev. A* **54**, 1862–1868 (1996).
- Gibbons, K. S., Hoffman, M. J. & Wootters, W. K. *Phys. Rev. A* **70**, 062101 (2004).
- Spekkens, R. W. *Phys. Rev. A* **75**, 032110 (2007).
- Aaronson, S. & Gottesman, D. *Phys. Rev. A* **70**, 052328 (2004).
- Veitch, V., Ferrie, C., Gross, D. & Emerson, J. *New J. Phys.* **14**, 113011 (2012).
- Bravyi, S. & Kitaev, A. *Phys. Rev. A* **71**, 022316 (2005).
- Raussendorf, R. *Phys. Rev. A* **88**, 022322 (2013).

This article was published online on 11 June 2014.

CELL BIOLOGY

Balancing act

The enzyme parkin is known to promote disposal of organelles called mitochondria that have suffered damage. The identification of an enzyme that opposes parkin demonstrates how a delicate balance is maintained in the cell. [SEE ARTICLE P.370](#)

ALBAN ORDUREAU & J. WADE HARPER

Cells have a love–hate relationship with mitochondria. As the power plants of cells, these organelles provide the energy required for life, but mitochondrial defects can lead to the production of reactive oxygen species that disrupt crucial cellular functions. Cells therefore use a specialized program, mitophagy, to eliminate damaged mitochondria and so maintain cellular health. Although a mitophagy signalling pathway comprised of two enzymes, PINK1 and parkin, has been identified, it is not clear what factors inhibit the pathway. In this issue, Bingol *et al.*¹ (page 370) report that USP30, a deubiquitinating enzyme, puts the brakes on mitophagy.

In cells with healthy mitochondria, parkin is located in the cytoplasm and is thought to be inactive^{2,3}, whereas PINK1 is associated with mitochondria. Activation of PINK1 in response to mitochondrial damage causes migration of parkin, a ubiquitin ligase, to the outer membrane of the mitochondrion, and its

subsequent activation by PINK1 (refs 2, 4, 5). Activated parkin then transfers a small protein called ubiquitin to one or more lysine amino-acid residues on dozens of proteins bound to the mitochondrial outer membrane^{6,7}. Following this ubiquitination process, the ubiquitin tags are recognized by the cell's mitophagy machinery², leading to mitochondrial degradation. Defects in mitochondrial quality control, brought about by mutations in PINK1 and parkin are the cause of certain neurodegenerative disorders, such as some early-onset familial forms of Parkinson's disease².

The pathways downstream of ubiquitination at the mitochondrial outer membrane are far from clear, but specific ubiquitinated targets and the total number of ubiquitin modifications on target proteins have been offered as possible factors in the recruitment of the mitophagy machinery to mitochondria^{2,7}. Protein ubiquitination is a reversible modification — indeed, the human genome encodes more than 100 deubiquitinating enzymes. Bingol and colleagues therefore reasoned that

inhibiting deubiquitination of parkin targets could be a tool to restore the balance of mitophagy in cells in which the PINK1–parkin pathway is defective (Fig. 1). The authors induced mitophagy experimentally in cells by triggering mitochondrial depolarization, which activates PINK1, and performed a screen for deubiquitinating enzymes that could prevent parkin-dependent mitophagy. This quest resulted in the identification of USP30.

The authors found that USP30 not only prevented the mitophagy machinery from recognizing damaged mitochondria, but also reversed the accumulation of ubiquitin on proteins bound to the mitochondrial outer membrane, indicating that USP30 directly opposes parkin function. In a cell-wide analysis of ubiquitin-tagged proteins, Bingol and co-workers identified 41 targets of parkin ubiquitination that could be deubiquitinated by USP30, including TOM20, a subunit of the mitochondrial translocase enzyme, which is responsible for transport of proteins across the outer mitochondrial membrane. Surprisingly, the 'classic' parkin target protein, mitofusin, was resistant to USP30-driven deubiquitination. An understanding of how USP30 selectively removes ubiquitin from some but not other parkin targets will require further work, but it is conceivable that the proteins that are not targeted by USP30 are simply those that are most efficiently ubiquitinated.

Although the PINK1–parkin pathway is known² to promote mitophagy in response to chemical or genetic disruption in cell-culture samples, its role in neurons — which are critically affected in Parkinson's disease — has been controversial⁶. In an experimental tour de force, Bingol *et al.* examined USP30 and its role in mitophagy in cultured rat neurons and in fruit flies genetically engineered to model Parkinson's disease.

By tracking mitochondria in rat neurons as they underwent mitophagy in 'normal' situations (without the need to artificially activate the pathway), the authors demonstrated that levels of mitophagy were reduced by loss of PINK1 and parkin, and increased by depletion of USP30. Thus, USP30 opposes PINK1–parkin-dependent mitophagy in healthy neurons, in which defective mitochondria probably arise as a result of the oxidative stress that occurs during normal cellular function.

Fruit flies that model Parkinson's disease have defective mitochondria in flight-muscle cells, a reduced ability to climb and reduced

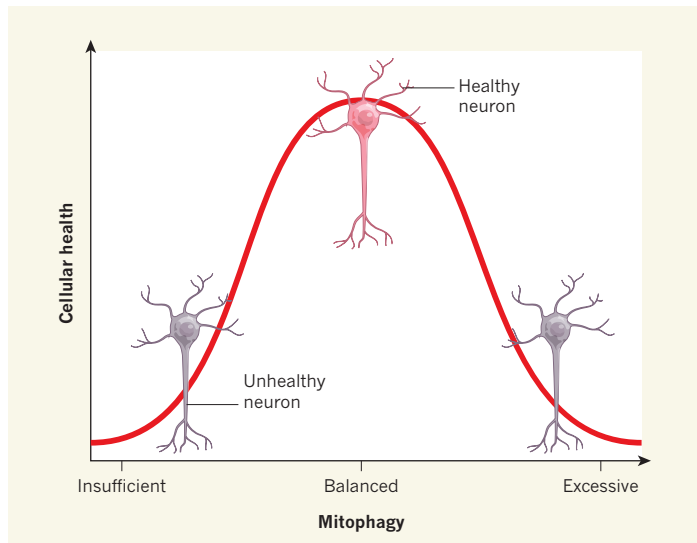


Figure 1 | Maintaining balance in mitophagy. A graphical representation of how cellular health can be affected by changes in the levels of mitophagy — the process by which cells dispose of mitochondria that have become defective or damaged. Insufficient or excessive mitophagy reduces cellular health, owing to accumulation of defective mitochondria or disposal of too many mitochondria, respectively. PINK1–parkin signalling promotes mitophagy, and Bingol *et al.*¹ now find that an enzyme, USP30, opposes the action of the parkin enzyme and inhibits mitophagy (not shown). Thus, in cells that express both parkin and USP30, a balanced level of mitophagy is maintained.

levels of the neurotransmitter dopamine^{9,10}. Bingol and colleagues found that these defects were largely reversed when USP30 was removed throughout the animal. To examine the dopamine-producing neurons that are affected by Parkinson's disease, the authors genetically deleted USP30 in these cells specifically, and treated the insects with paraquat, a mitochondrial toxin that elicits Parkinson's-disease-like symptoms in humans, and reduces dopamine levels in fruit flies. Depletion of USP30 in dopamine-producing neurons largely reversed dopamine loss and behavioural defects, and increased survival, indicating that USP30 might actively oppose the PINK1–parkin pathway in cell types affected by Parkinson's disease.

This study may have implications for the treatment of defective PINK1–parkin signalling in Parkinson's disease, and gives us a deeper understanding of this form of mitophagy in general. Inhibitors of USP30 might increase mitochondrial health under conditions in which this system is impaired, for example in patients with mutations in *PINK1* or *PARKIN*. Indeed, Bingol and co-workers found that depletion of USP30 increased mitophagy in human cell lines altered to express a mutant form of *PARKIN*.

If this activity can be extended to neurons, it is possible that USP30 inhibitors could be beneficial to patients. The development of effective USP14 inhibitors¹¹ suggests that selective targeting of this enzyme class is a possibility. USP30 inhibitors might also improve

mitochondrial health in cells with other types of defect, by reducing the threshold for PINK1–parkin-dependent mitochondrial clearance.

Precisely why dopamine-producing neurons are more sensitive to familial mutations in the PINK1–parkin pathway than other cells in the body is unclear. This work raises the interesting possibility that relative levels of USP30 and parkin in various cell types could determine the sensitivity of cells to defects in this pathway. However, a recent report¹² suggests that a different family member, USP15, can similarly reverse the PINK1–parkin pathway. Further studies will be needed to understand the relationship between these two pathways.

Finally, Bingol and colleagues provide evidence that ubiquitination of TOM20 is required for mitophagy, providing a new potential link between mitochondria and the mitophagy machinery. Exploring whether TOM20 ubiquitination promotes assembly of the mitophagy machinery on mitochondria may help us to understand what continues to be a central puzzle in the field: the mechanism by which ubiquitinated mitochondria are recognized by autophagosomes, the vesicles that transport damaged mitochondria to be degraded¹. Now the race is on to determine whether releasing the parkin brake will benefit patients. ■

Alban Ordureau and J. Wade Harper are in the Department of Cell Biology, Harvard Medical School, Boston, Massachusetts 02115, USA. **J.W.H.** is on sabbatical at Biogen-Idec, Cambridge, Massachusetts.

1. Bingol, B. *et al.* *Nature* **510**, 370–375 (2014).
2. Narendra, D., Walker, J. E. & Youle, R. *Cold Spring Harb. Perspect. Biol.* <http://dx.doi.org/10.1101/cshperspect.a011338> (2012).
3. Trempe, J.-F. *et al.* *Science* **340**, 1451–1455 (2013).
4. Shiba-Fukushima, K. *et al.* *Sci. Rep.* **2**, 1002 (2012).
5. Kondapalli, C. *et al.* *Open Biol.* **2**, 120080 (2012).
6. Chan, N. C. *et al.* *Hum. Mol. Genet.* **20**, 1726–1737 (2011).
7. Sarraf, S. A. *et al.* *Nature* **496**, 372–376 (2013).
8. Exner, N., Lutz, A. K., Haass, C. & Winklhofer, K. F. *EMBO J.* **31**, 3038–3062 (2012).
9. Greene, J. C. *et al.* *Proc. Natl Acad. Sci. USA* **100**, 4078–4083 (2003).
10. Sang, T.-K. *et al.* *J. Neurosci.* **27**, 981–992 (2007).
11. Lee, B.-H. *et al.* *Nature* **467**, 179–184 (2010).
12. Cornelissen, T. *et al.* *Hum. Mol. Genet.* <http://dx.doi.org/10.1093/hmg/ddu244> (2014).

This article was published online on 4 June 2014.

QUANTUM PHYSICS

Feel the force

An approach based on quantum sensing, in which controlled quantum systems serve as precision sensors, has enabled measurement of the weak magnetic interaction between two electrons bound to two separate ions. **SEE LETTER P.376**

FERDINAND SCHMIDT-KALER

That electrons have negative charge and repel each other are concepts familiar to most readers. Less well known is that they also possess a magnetic moment associated with their spin, and therefore exert magnetic forces on one another. However, interactions between individual electron spins have hitherto not been measured. This is mainly because they are dwarfed by other effects: for small, atomic-scale separation between electrons, the Pauli exclusion principle, which states that two electrons cannot occupy the same quantum state, and the Coulomb electric interaction dominate; and for large separation, the strength of the magnetic interaction is vastly reduced and typically fully masked by the force that an electron's magnetic moment experiences in an ambient fluctuating magnetic field. On page 376 of this issue, Kotler *et al.*¹ report how they have succeeded in detecting the minuscule magnetic interaction between two electrons bound to two ions separated by about 2 micrometres, using ideas from the emerging field of quantum sensing.

The quantum states of single photons, atoms and ions, and of impurity ions in crystals, can be controlled almost perfectly in the laboratory. Initially, the development of experimental techniques to control and manipulate such quantum states was motivated by an interest in testing the fundamental principles of quantum physics. Nowadays, advances in quantum-state manipulation are also targeted towards applications such as quantum computing, quantum simulation and quantum sensing. Whereas quantum computing and simulation require exquisite control of interactions between large numbers of quantum particles, sensing applications, in which quantum systems serve as sensing devices, are much less demanding in that regard.

In their study, Kotler *et al.* control and manipulate the valence electrons of two strontium ions confined in an electrical device known as a Paul trap. To understand their work, think of the spin of a strontium ion's valence electron as a tiny magnet with a north and a south pole — like the needle of a magnetic compass — that aligns with external magnetic fields. But imagine what happens if two such compass needles are placed close to each other. Now, one needle may interact with the other and rotate slightly, depending on the orientation of

the other needle. It is exactly this small effect — the magnetic interaction of two single spins — that Kotler and colleagues measured in their experiment.

To perform their measurements, the researchers first used laser pulses to cool the ions and initialize them such that the magnetic moments of the valence electrons pointed in opposite directions. Returning to the magnetic-compass analogy, both south poles are now facing and repelling each other (Fig. 1a). In addition, the interactions of the two electrons with a uniform external magnetic field — which should be eliminated in order to measure the tiny spin–spin interaction strength — are balanced out, because they are of the same magnitude but opposite sign.

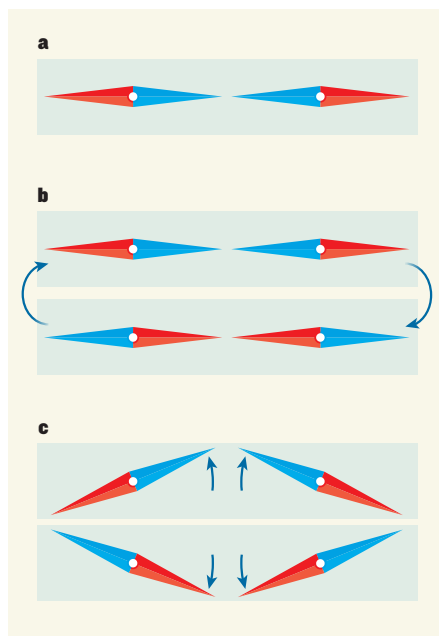


Figure 1 | Measuring magnetic forces. Kotler *et al.*¹ have measured the tiny interaction between two electron spins bound to two strontium ions about 2 micrometres apart. **a**, The electron spins of both ions can be illustrated by magnetic-compass needles, here aligned opposite to each other; blue indicates a south pole and red a north pole. **b**, By repeatedly flipping the needles' directions rapidly and simultaneously, the authors could cancel out the interactions of the ions with a fluctuating external magnetic field (not shown). **c**, This allowed them to measure the magnetic interaction between both needles from the rotation that they undergo in the previous configurations.

Next, the directions of both compass needles were rapidly and continuously flipped simultaneously (Fig. 1b). This step helped to compensate for fluctuations of the external magnetic field, which are different in strength at the two ion locations. On average, any interactions of the ions with the fluctuating external magnetic field essentially vanished, and Kotler and co-workers were set to measure the spin–spin interaction strength.

In the two configurations described above (south poles or north poles facing one another), the spin–spin interaction causes the magnetic moments to repel each other and start turning (Fig. 1c). In the experiment, the magnetic moments turn but do so in a 'coherent quantum superposition'. This is a neat quantum trick, in which the electrons' magnetic moments are forced to align with each other and eventually become quantum entangled. By measuring the properties of this carefully designed state, which is immune to magnetic noise and has a lifetime of almost 1 minute, the authors could measure the rotation of the moments and thus the spin–spin interaction strength. Owing to the extremely small strength of the interaction and associated rotation rate (only 0.0009 hertz), the authors had to wait 15 seconds before they could determine the rotation.

Kotler and colleagues' study has broad ramifications for quantum sensing. The experimental sequence adopted by the authors may be readily applied to other atomic systems, as well as to molecular, optical and solid-state systems, with the prospect of using them as sensitive magnetic probes. The approach may be relevant for developing clocks based on trapped ions or atoms² and for sensing small interactions in hybrid systems, such as mixtures of cold ions and atoms^{3,4}. Applying the technique to solid-state systems will be particularly interesting, because these systems offer prospects for commercial applications such as magnetic sensors operating in 'noisy' environments. Magnetic sensors based on single-nitrogen-atom impurities in diamond have already been produced^{5,6} and are close to reaching the sensitivity needed to detect a single nuclear spin. Physicists await further advances in quantum sensing with great interest. ■

Ferdinand Schmidt-Kaler is at *QUANTUM, Institute of Physics, Johannes Gutenberg University of Mainz, 55128 Mainz, Germany.* e-mail: fsk@uni-mainz.de

1. Kotler, S., Akerman, N., Navon, N., Glickman, Y. & Ozeri, R. *Nature* **510**, 376–380 (2014).
2. Roos, C. F., Chwalla, M., Kim, K., Riebe, M. & Blatt, R. *Nature* **443**, 316–319 (2006).
3. Härter, A. & Hecker Denschlag, J. *Contemp. Phys.* **55**, 33–45 (2014).
4. Schmidt-Kaler, F. & Gerritsma, R. *Europhys. Lett.* **99**, 53001 (2012).
5. Zhao, N. *et al. Nature Nanotechnol.* **7**, 657–662 (2012).
6. Maletinsky, P. *et al. Nature Nanotechnol.* **7**, 320–324 (2012).

Contextuality supplies the ‘magic’ for quantum computation

Mark Howard^{1,2}, Joel Wallman², Victor Veitch^{2,3} & Joseph Emerson²

Quantum computers promise dramatic advantages over their classical counterparts, but the source of the power in quantum computing has remained elusive. Here we prove a remarkable equivalence between the onset of contextuality and the possibility of universal quantum computation via ‘magic state’ distillation, which is the leading model for experimentally realizing a fault-tolerant quantum computer. This is a conceptually satisfying link, because contextuality, which precludes a simple ‘hidden variable’ model of quantum mechanics, provides one of the fundamental characterizations of uniquely quantum phenomena. Furthermore, this connection suggests a unifying paradigm for the resources of quantum information: the non-locality of quantum theory is a particular kind of contextuality, and non-locality is already known to be a critical resource for achieving advantages with quantum communication. In addition to clarifying these fundamental issues, this work advances the resource framework for quantum computation, which has a number of practical applications, such as characterizing the efficiency and trade-offs between distinct theoretical and experimental schemes for achieving robust quantum computation, and putting bounds on the overhead cost for the classical simulation of quantum algorithms.

Quantum information provides unique new capabilities for computation such as Shor’s factoring algorithm¹ and quantum simulation algorithms². This naturally raises the fundamental question: what unique resources of the quantum world enable the advantages of quantum information? There have been many attempts to answer this question, with proposals including the hypothetical ‘quantum parallelism’³ some associate with quantum superposition, the necessity of large amounts of entanglement⁴, and much ado about quantum discord⁵. Unfortunately none of these proposals have proven satisfactory^{6–9}, and, in particular, none have helped resolve outstanding challenges confronting the field. For example, on the theoretical side, the most general classes of problems for which quantum algorithms might offer an exponential speed-up over classical algorithms are poorly understood. On the experimental side, there remain significant challenges to the design of robust, large-scale quantum computers, and an important open problem is to determine the minimal physical requirements of a useful quantum computer^{10,11}. A framework identifying relevant resources for quantum computation should help clarify these issues—for example, by identifying new simulation schemes for classes of quantum algorithms and by clarifying the trade-offs between the distinct physical requirements for achieving robust quantum computation. Here we establish that quantum contextuality, a generalization of non-locality identified^{12,13} almost 50 years ago, is a critical resource for quantum speed-up within the leading model for fault-tolerant quantum computation, known as magic state distillation (MSD)^{14–16}.

Contextuality was first recognized as an intrinsic feature of quantum theory via the Bell–Kochen–Specker ‘no-go’ theorem. This theorem implies the impossibility of explaining the statistical predictions of quantum theory in a natural way. In particular, the actual outcome observed under a quantum measurement cannot be understood as simply revealing a pre-existing value of some underlying ‘hidden variable’¹⁷. A key observation is that the non-locality of quantum theory is a special case of contextuality. Under the locality restrictions motivating quantum communication, non-locality is a quantifiable cost for classical simulation complexity¹⁸ and a fundamental resource for practical applications

such as device-independent quantum key distribution^{19–21}. Locality restrictions can be made relevant to measurement-based quantum computation¹¹, for which non-locality quantifies the resources required to evaluate non-linear functions^{22,23}. However, locality restrictions are not relevant in the standard quantum circuit model for quantum computation, and, in this context, a large amount of entanglement has been shown to be neither necessary nor sufficient for an exponential computational speed-up⁹.

Here we consider the framework of fault-tolerant stabilizer quantum computation²⁴ which provides the most promising route to achieving robust universal quantum computation thanks to the discovery of high-threshold codes in two-dimensional geometries^{25–29}. In this framework, only a subset of quantum operations—namely, stabilizer operations—can be achieved via a fault-tolerant encoding. These operations define a closed subtheory of quantum theory, the stabilizer subtheory, which is not universal and in fact admits an efficient classical simulation³⁰. The stabilizer subtheory can be promoted to universal quantum computation through MSD^{14–16} which relies on a large number of ancillary resource states. Here we show that quantum contextuality plays a critical role in characterizing the suitability of quantum states for MSD. Our approach builds on recent work^{31,32} that has established a remarkable connection between contextuality and graph-theory. We use the framework of refs 31 and 32 to identify non-contextuality inequalities such that the onset of state-dependent contextuality, using stabilizer measurements, coincides exactly with the possibility of universal quantum computing via MSD. The scope of our results differs depending on whether we consider a model of computation using qubits (systems of even prime dimension) or qudits (systems of odd prime dimension). We note that some authors use the term qudit to describe a system with an arbitrary number of levels. Whereas in both cases we can prove that violating a non-contextuality inequality is necessary for quantum-computational speed-up via MSD, in the qudit case we are able to prove that a state violates a non-contextuality inequality if and only if it lies outside the known boundary for MSD.

¹Department of Mathematical Physics, National University of Ireland, Maynooth, Ireland. ²Institute for Quantum Computing and Department of Applied Mathematics, University of Waterloo, Waterloo, Ontario N2L 3G1, Canada. ³Department of Statistics, University of Toronto, 100 St George Street, Toronto, Ontario M5S 3G3, Canada.

Graph-based contextuality

Interpreting measurements on a quantum state as merely revealing a pre-existing property of the system leads to disagreement with the predictions of quantum theory. In quantum mechanics, a projective measurement can be decomposed as a set of binary tests. Contradictions with models using pre-existing value assignments can arise when these tests appear in multiple measurement scenarios—that is, in multiple contexts. In other words, we cannot always assign a definite value to tests appearing in multiple contexts and consequently quantum mechanics cannot be described by a non-contextual hidden variable (NCHV) theory. The earliest demonstrations of quantum contextuality used sets of tests such that no NCHV model could reproduce the quantum predictions, regardless of what quantum state was actually measured. Recently, a more general framework has been derived in which a given set of tests can be considered to have non-contextual value assignments only if the measured state satisfies a non-contextuality inequality³¹. We briefly review this framework below.

Consider a set of n binary tests, which can be represented in quantum mechanics by a set of n rank-1 projectors $\{\Pi_1, \dots, \Pi_n\}$. Two such tests are compatible, and so can be simultaneously performed on a quantum system, if and only if the projectors are orthogonal. We define the witness operator Σ for a set of tests to be

$$\Sigma = \sum_{i=1}^n \Pi_i \quad (1)$$

and the associated exclusivity graph Γ to be a graph wherein each vertex corresponds to a projector and two vertices are adjacent (connected) if the corresponding projectors are compatible. Only one outcome can occur when a measurement of a set of orthogonal projectors is performed, so we require that a value of 1 will be assigned to at most one projector in each measurement. Since two vertices of Γ are adjacent if and only if the corresponding projectors are compatible, the maximum value of Σ in an NCHV model, $\langle \Sigma \rangle_{\max}^{\text{NCHV}}$, is the independence number $\alpha(\Gamma)$, that is, the size of the largest set of vertices of Γ such that no two elements of the set are adjacent.

The maximum quantum mechanical (QM) value of Σ can be obtained by varying over projectors satisfying the appropriate compatibility relations and over quantum states. This quantity is bound above by the Lovasz number, ϑ , of the exclusivity graph, that is,

$$\langle \Sigma \rangle_{\max}^{\text{QM}} \leq \vartheta(\Gamma) \quad (2)$$

where ϑ can be calculated as the solution to a semidefinite program. Graphs for which $\alpha(\Gamma) < \vartheta(\Gamma)$ indicate that appropriately chosen projectors $\{\Pi_i\}$ and states ρ may reveal quantum contextuality by violating the non-contextuality inequality:

$$\text{Tr}(\Sigma \rho) \leq \alpha(\Gamma) \quad (3)$$

For generalized probabilistic theories, an important class of ‘post-quantum’ theories, the maximum value of Σ is given by the fractional packing number of the exclusivity graph $\alpha^*(\Gamma)$, that is:

$$\langle \Sigma \rangle_{\max}^{\text{GPT}} = \alpha^*(\Gamma) \quad (4)$$

Note that if $\alpha(\Gamma) < \langle \Sigma \rangle_{\max}^{\text{QM}} = \alpha^*(\Gamma)$, then the optimal choice of quantum state and projectors is maximally contextual, in that no greater violation of the non-contextuality inequality can be obtained in any generalized probabilistic theory.

The stabilizer formalism

Quantum information theory relies heavily on a family of finite groups usually called the (generalized) Pauli groups. The most promising and well understood quantum error correcting codes—stabilizer codes—are built using the elements of these groups, that is, Pauli operators. Qubits are the most commonly used building blocks for quantum computing, but a circuit using qudits has the same computational power. While qudits with larger dimensionality may pose new experimental challenges, these

may be offset by a lower overhead for fault-tolerant computation¹⁶. In this section we outline the mathematical structure associated with the generalized Pauli group and the geometrical characterization of probabilistic mixtures of stabilizer states.

The stabilizer formalism for p -dimensional systems (where p is a prime number) is defined using the generalized X and Z operators

$$X|j\rangle = |j+1\rangle \quad Z|j\rangle = \omega^j|j\rangle \quad (5)$$

where $\omega = \exp\left(\frac{2\pi i}{p}\right)$. The set of Weyl-Heisenberg displacement operators is defined as

$$\mathbf{D}_p = \left\{ D_{x,z} = \omega^{2^{-1}xz} X^x Z^z : x, z \in \mathbb{Z}_p \right\} \quad (6)$$

where 2^{-1} is the multiplicative inverse of 2 in the finite field $\mathbb{Z}_p = \{0, 1, \dots, p-1\}$. For $p=2$, one can replace $\omega^{-2^{-1}}$ with i in equation (6) to recover the familiar qubit Pauli operators. The Clifford group $\mathbf{C}_{p,n}$ is defined to be the normalizer of the group $\langle \mathbf{D}_p^{\otimes n} \rangle$ (that is, the group generated by the set of displacement operators), that is,

$$\mathbf{C}_{p,n} = \left\{ U \in \mathcal{U}(d^n) : U \langle \mathbf{D}_p^{\otimes n} \rangle U^\dagger = \langle \mathbf{D}_p^{\otimes n} \rangle \right\} \quad (7)$$

and the set of stabilizer states is the image of the computational basis under the Clifford group $\mathbf{C}_{p,n}$.

The stabilizer polytope is the convex hull of the set of stabilizer states. For a single system, the stabilizer polytope³³ is defined by the following set of simultaneous inequalities

$$\mathcal{P}_{\text{STAB}} = \left\{ \rho : \text{Tr}(\rho A^{\mathbf{q}}) \geq 0, \mathbf{q} \in \mathbb{Z}_p^{p+1} \right\} \quad (8)$$

where $A^{\mathbf{q}} = -\mathbb{I}_p + \sum_{j=1}^{p+1} \Pi_j^{q_j}$ and $\Pi_j^{q_j}$ is the projector onto the eigenvector with eigenvalue ω^{q_j} of the j th operator in the list $\{D_{0,1}, D_{1,0}, D_{1,1}, \dots, D_{1,p-1}\}$ (the eigenbases of these operators form a complete set of mutually unbiased bases). In the preceding expression \mathbb{I}_p is the $p \times p$ identity matrix and \mathbf{q} is a vector of length $p+1$ with entries from $\{0, 1, \dots, p-1\}$.

Magic state distillation

The stabilizer formalism of the previous section was developed in the search for quantum error-correcting codes, that is, codes allowing the robust, fault-tolerant storage and manipulation of quantum information stored across many subsystems^{15,24}. Surface codes^{25–29}, in particular, admit a comparatively high fault-tolerance threshold within an experimentally realistic planar physical layout. Codes such as these have a finite non-universal set of transversal (that is, manifestly fault-tolerant) operations that must be supplemented with an additional resource—a supply of so-called magic states—in order to attain universality. MSD refers to the subroutine, described below, wherein almost pure resource states are constructed using large numbers of impure resource states^{14–16}.

An MSD protocol consists of the following steps: (1) prepare n copies of a suitable (see below) input state, that is, $\rho_{\text{in}}^{\otimes n}$; (2) perform a Clifford operation on $\rho_{\text{in}}^{\otimes n}$; (3) perform a stabilizer measurement on all but the first m registers, postselecting on a desired outcome. With appropriate choices of stabilizer operations, the resulting output state in the first m registers, $\rho_{\text{out}}^{\otimes m}$, is purified in the direction of a magic state $|\nu\rangle$, so that $\langle \nu | \rho_{\text{out}} | \nu \rangle > \langle \nu | \rho_{\text{in}} | \nu \rangle$. This process can be reiterated until ρ_{out} is sufficiently pure, at which point the resource ρ_{out} is used up to approximate a non-Clifford operation (via ‘state injection’)—for example, the $\pi/8$ gate or its qudit generalizations^{16,34}. Supplementing stabilizer operations with the ability to perform such gates enables fault-tolerant and universal quantum computation.

For which states ρ_{in} does there exist an MSD routine purifying ρ_{out} towards a non-stabilizer state? A large subset of quantum states have been ruled out by virtue of the fact that efficient classical simulation schemes are known for noiseless stabilizer circuits supplemented by access to an arbitrary number of states from the polytope $\rho_{\text{in}} \in \mathcal{P}_{\text{SIM}}$ (refs 30, 35, 36). This polytope \mathcal{P}_{SIM} of the known simulable states is described by^{33,37}

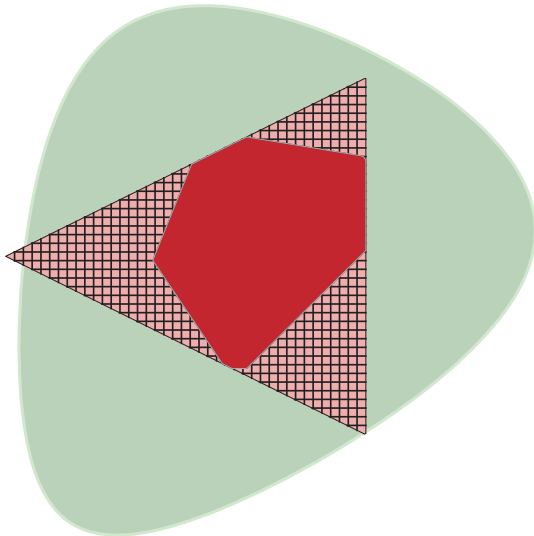


Figure 1 | A two-dimensional slice through qutrit state space. Three distinct regions in the space of 3×3 matrix operators: the region shaded in pale green describes quantum state space (valid density operators); region \mathcal{P}_{SIM} , with hatched shading, corresponds to ancillas known to be efficiently simulable (and hence useless for quantum computation via MSD); and the dark red region $\mathcal{P}_{\text{STAB}}$ describes mixtures of stabilizer states. The strict inclusion $\mathcal{P}_{\text{STAB}} \subset \mathcal{P}_{\text{SIM}}$ identifies a large class of bound magic states³⁵.

$$\mathcal{P}_{\text{SIM}} = \begin{cases} \{\rho : \text{Tr}(\rho A^{\mathbf{r}}) \geq 0, \mathbf{r} \in \mathbb{Z}_2^3\} & p=2, \\ \{\rho : \text{Tr}(\rho A^{\mathbf{x}\mathbf{a} + \mathbf{z}\mathbf{b}}) \geq 0, \mathbf{x}, \mathbf{z} \in \mathbb{Z}_p\} & p>2 \end{cases} \quad (9)$$

where $\mathbf{a} = [1, 0, 1, \dots, p-1]$ and $\mathbf{b} = -[0, 1, 1, \dots, 1]$ (ref. 38). Note that $\mathcal{P}_{\text{SIM}} = \mathcal{P}_{\text{STAB}}$ for qubits (giving an octahedron inscribed within the Bloch sphere) whereas $\mathcal{P}_{\text{SIM}} \supset \mathcal{P}_{\text{STAB}}$ is a proper superset for all other primes. Subsequently we refer to the set of facets enclosing \mathcal{P}_{SIM} as

$$\mathcal{A}_{\text{SIM}} = \{A^{\mathbf{r}} | p=2 : \mathbf{r} \in \mathbb{Z}_2^3, p \neq 2 : \mathbf{r} = \mathbf{x}\mathbf{a} + \mathbf{z}\mathbf{b}\} \quad (10)$$

In Fig. 1 we plot the geometric relationship between arbitrary quantum states and sets of states contained within \mathcal{P}_{SIM} and $\mathcal{P}_{\text{STAB}}$ for the case of qutrits ($p=3$).

By prior results^{35,39}, we know that the set of states \mathcal{P}_{SIM} coincides exactly with the set of states that are non-negatively represented within a distinguished quasiprobability representation—a discrete Wigner function^{40–42}. Are the states in the set \mathcal{P}_{SIM} , the set excluded from MSD by the known efficient simulation schemes, the complete set of non-distillable states? We now address this fundamental question by demonstrating a remarkable relationship between non-distillability, non-negativity and non-contextuality.

Contextuality as a computational resource

We will prove that all states $\rho \notin \mathcal{P}_{\text{SIM}}$ exhibit state-dependent contextuality with respect to stabilizer measurements. Our definition of stabilizer measurement is quite inclusive; we allow all projective measurements wherein elements are rank-1 projectors onto stabilizer states. Rearranging the definition of $A^{\mathbf{r}}$ given in equation (8) gives

$$\sum_{j=1}^{p+1} \sum_{\substack{s_j \in \mathbb{Z}_p \\ s_j \neq \mathbf{r}_j}} \Pi_j^{s_j \neq \mathbf{r}_j} = p \mathbb{I}_p - A^{\mathbf{r}} \quad (11)$$

that is, the set of projectors $\{\Pi_j^{s_j \neq \mathbf{r}_j}\}$ is a set of projectors whose sum, $\Sigma^{\mathbf{r}}$, is such that:

$$\text{Tr}(\Sigma^{\mathbf{r}} \rho) > p \Leftrightarrow \text{Tr}(A^{\mathbf{r}} \rho) < 0 \quad (12)$$

The left-hand side of this equivalence is a witness for contextuality if and only if the independence number of the associated graph $\Gamma^{\mathbf{r}}$ satisfies

$\alpha(\Gamma^{\mathbf{r}}) = p$ as in equation (3). In fact, this simple construction fails to identify any quantum states as contextual because $\text{Tr}(\Sigma \rho) \leq \alpha(\Gamma^{\mathbf{r}})$ for all ρ . This is not surprising, given that every single-qudit stabilizer projector is part of exactly one context, namely the basis (one of the complete set of mutually unbiased bases) in which it is contained.

Stabilizer projectors appear in multiple contexts only when two or more subsystems are involved. Consequently, we introduce two-qudit stabilizer projectors such that the structure of $A^{\mathbf{r}}$ as in equation (11) is reflected on the first qudit only. We can limit consideration to two-qudit projectors since this approach characterizes as contextual all single-qudit states that do not have an NCHV model via the discrete Wigner function, that is, we find two-qudit projectors are sufficient to achieve the best possible result.

Our construction uses a different set of projectors for each facet $A^{\mathbf{r}}$. For a fixed facet $A^{\mathbf{r}}$, we define a set of separable projectors

$$\{\Pi\}_{\text{sep}}^{\mathbf{r}} = \{\Pi_j^{s_j \neq \mathbf{r}_j} \otimes |k\rangle\langle k| : 1 \leq j \leq p+1, s_j, k \in \mathbb{Z}_p\} \quad (13)$$

that is, we take the $p(p^2-1)$ separable projectors consisting of all tensor products of projectors in equation (11) for the first qudit and computational basis states for the second qudit. We also define the set $\{\Pi\}_{\text{ent}}$ to be the set of all two-qudit entangled projectors.

The sum of the combined set of separable and entangled projectors $\{\Pi\}^{\mathbf{r}} = \{\Pi\}_{\text{sep}}^{\mathbf{r}} \cup \{\Pi\}_{\text{ent}}$ is

$$\Sigma^{\mathbf{r}} = (p^3 \mathbb{I}_p - A^{\mathbf{r}}) \otimes \mathbb{I}_p \quad (14)$$

so that for any state $\sigma \in \mathcal{H}_p$ of the second system (even the maximally mixed state) we have:

$$\text{Tr}[\Sigma^{\mathbf{r}}(\rho \otimes \sigma)] \leq p^3 \Leftrightarrow \text{Tr}[A^{\mathbf{r}} \rho] \geq 0 \quad (15)$$

Forming the exclusivity graph $\Gamma^{\mathbf{r}}$ of $\{\Pi\}^{\mathbf{r}}$ and applying the results of refs 31 and 32 identifies the left-hand side of equation (15) as a witness for the contextuality of ρ . The following theorem shows that the inequality on the left-hand side of equation (15) is indeed a non-contextuality inequality.

Theorem 1. The independence number of the exclusivity graph associated with $\Sigma^{\mathbf{r}}$ is $\alpha(\Gamma^{\mathbf{r}}) = p^3$ for all $A^{\mathbf{r}} \in \mathcal{A}_{\text{SIM}}$ and all prime $p \geq 2$. Furthermore, for $p > 2$, a state exhibits contextuality if and only if it violates one of our non-contextuality inequalities and maximally contextual states saturate the bound on contextuality associated with post-quantum generalized probabilistic theories, that is,

$$\langle \Sigma^{\mathbf{r}} \rangle_{\text{max}}^{2-\text{QUDIT}} = \vartheta(\Gamma^{\mathbf{r}}) = \alpha^*(\Gamma^{\mathbf{r}}) = p^3 + 1 \quad (p > 2) \quad (16)$$

Theorem 1 says that, relative to our construction, exactly the states $\rho \notin \mathcal{P}_{\text{SIM}}$ are those that exhibit contextuality. For qudits of odd prime dimension there does not exist any construction using stabilizer measurements that characterizes any $\rho \in \mathcal{P}_{\text{SIM}}$ as contextual, so that the conditions for contextuality and the possibility of quantum speed-up via MSD coincide exactly.

Proof. For $p=2$, a software package⁴³ can be used to obtain:

$$\alpha(\Gamma^{\mathbf{r}}) = 8 < \vartheta(\Gamma^{\mathbf{r}}) < \alpha^*(\Gamma^{\mathbf{r}}) \leq 9$$

The exclusivity graph $\Gamma^{\mathbf{r}}$ and an independent set of 8 vertices is depicted in Fig. 2. The maximal violation of our non-contextuality inequality is achieved by the state $|T\rangle\langle T| \otimes \sigma$, where $|T\rangle$ is the magic state introduced in ref. 14 and σ is arbitrary.

For $p > 2$, we will now show that $\vartheta(\Gamma^{\mathbf{r}}) = \alpha^*(\Gamma^{\mathbf{r}}) = p^3 + 1$. To do this, we use the graph theoretical inequality

$$\alpha(\Gamma) \leq \langle \Sigma \rangle_{\text{max}}^{\text{QM}} \leq \vartheta(\Gamma) \leq \alpha^*(\Gamma) \leq \bar{\chi}(\Gamma) \quad (17)$$

where $\bar{\chi}(\Gamma) \in \mathbb{N}$ is the clique cover number, which is the minimum number of cliques needed to cover every vertex of Γ . (A clique is a subset of a graph's vertices wherein every pair of vertices is connected.) The clique cover number cannot be greater than the number of distinct bases in $\{\Pi\}^{\mathbf{r}}$, which contains $p+1$ separable bases and p^3-p entangled bases. Therefore $\vartheta(\Gamma) \leq \alpha^*(\Gamma) \leq p^3 + 1$. Then, since there exist⁴⁰ quantum

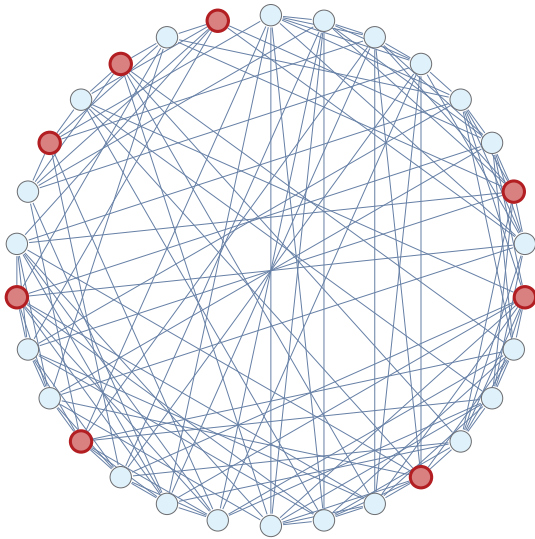


Figure 2 | Our construction applied to two qubits. Each of the 30 vertices in this graph Γ corresponds to a two-qubit stabilizer state; connected vertices correspond to orthogonal states. A maximum independent set (representing mutually non-orthogonal states) of size $\alpha(\Gamma) = 8$ is highlighted in red. As described in Theorem 1 (main text), this value of α identifies all states $\rho \notin \mathcal{P}_{\text{SIM}}$ as exhibiting contextuality with respect to the stabilizer measurements in our construction.

states ρ such that $\text{Tr}(A^r \rho) = -1$, $\langle \Sigma^r \rangle_{\max}^{\text{QM}} \geq p^3 + 1$ by equation (15) and so $\beta(\Gamma^r) = \alpha^*(\Gamma^r) = p^3 + 1$.

The statement that no non-contextuality inequality constructed from stabilizer measurements can be violated by any state $\rho \in \mathcal{P}_{\text{SIM}}$ for odd prime dimensions follows from the existence of a NCHV model, namely, the discrete Wigner function^{35,40–42}, for all stabilizer measurements and states $\rho \in \mathcal{P}_{\text{SIM}}$.

We defer the proof that $\alpha(\Gamma^r) = p^3$ to Supplementary Information.

Significance and outlook

For qudits (which we defined as systems of odd prime dimension), a state is non-contextual under the available set of measurements—stabilizer measurements—if and only if it lies in the polytope \mathcal{P}_{SIM} (the set of ancilla states known to be useless for any MSD routine). The same construction applied to qubits also identifies all $\rho \notin \mathcal{P}_{\text{SIM}}$ as contextual. These results establish that contextuality is a necessary resource for universal quantum computation via MSD.

For qudits, the set of states proven to be contextual by our construction have been previously conjectured to be sufficient⁴⁴ to promote stabilizer circuits to universality. Proving this conjecture would require proving that any state $\rho \notin \mathcal{P}_{\text{SIM}}$ can be distilled to a magic state. While substantial progress in this direction has been made¹⁶, it is still an open problem.

For qubits, the mere presence of contextuality cannot be sufficient to promote stabilizer circuits to universality since any state $\rho \in \mathcal{P}_{\text{SIM}}$ (which includes the maximally mixed state) can violate a non-contextuality inequality constructed from stabilizer measurements. For example, converting the Peres–Mermin magic square^{45,46} to a 24-ray (projector) proof of contextuality and applying the formalism of refs 31 and 32 gives a non-contextuality inequality that is violated by all two-qubit states, including states of the form $\rho \otimes \sigma = \mathbb{I}/4$.

The crucial difference between qubits and qudits is that state-independent contextuality (like that of the Peres–Mermin square) is never manifested within the qudit stabilizer formalism. Consequently, for qudits, any contextuality is necessarily state-dependent and our results show that this contextuality has an operational meaning as a necessary and possibly sufficient resource for the ‘magic’ that makes quantum computers work. In the case of qubits, it is a pressing open question whether a suitable

operationally motivated refinement^{47,48} or quantification of contextuality can align more precisely with the potential to provide a quantum speed-up.

METHODS SUMMARY

Here we outline the argument that we use to prove that, for odd-prime p , the independence number of Γ^r is p^3 . Recall that the independence number of a graph Γ is the size of the largest independent set of Γ , where an independent set is a set of vertices of which no two are connected. Since two vertices are connected if and only if the associated projectors commute, an independent set in Γ^r is equivalent to a set of mutually non-commuting projectors in $\{\Pi\}^r$. Because the elements of $\{\Pi\}^r$ are all rank 1, two elements are non-commuting if and only if they are non-orthogonal.

We prove $\alpha(\Gamma^r) = p^3$ by proving $\alpha(\Gamma^r) \geq p^3$ and $\alpha(\Gamma^r) < p^3 + 1$. This completes the proof since $\alpha(\Gamma^r)$ is an integer. In Theorem 2 we show that $\alpha(\Gamma^r) \geq p^3$ by showing that there exists a set of p^3 mutually non-orthogonal elements of $\{\Pi\}^r$ for any $A^r \in \mathcal{A}_{\text{sim}}$. In Lemmas 3–5 we parametrize the set of stabilizer projectors using the symplectic representation of the Clifford group in order to transform a condition of mutual non-orthogonality of projectors into a set of algebraic constraints on parameters. In Theorem 6 we then show that $\alpha(\Gamma^r) < p^3 + 1$ by showing that no subset of $p^3 + 1$ elements of $\{\Pi\}^r$ can satisfy the constraints established in Lemmas 3–5, that is, there cannot exist a subset of $p^3 + 1$ mutually non-orthogonal elements of $\{\Pi\}^r$.

Received 16 January; accepted 30 April 2014.

Published online 11 June 2014.

- Shor, P. W. in *Proc. IEEE Foundations of Computer Science (FOCS)* (ed. Goldwasser, S.) 124–134 <http://dx.doi.org/10.1109/SFCS.1994.365700> (IEEE Computer Society, 1994).
- Lloyd, S. Universal quantum simulators. *Science* **273**, 1073–1078 (1996).
- Deutsch, D. Quantum theory, the Church-Turing principle and the universal quantum computer. *Proc. R. Soc. A* **400**, 97–117 (1985).
- Vidal, G. Efficient classical simulation of slightly entangled quantum computations. *Phys. Rev. Lett.* **91**, 147902 (2003).
- Datta, A., Shaji, A. & Caves, C. M. Quantum discord and the power of one qubit. *Phys. Rev. Lett.* **100**, 050502 (2008).
- Steane, A. M. A quantum computer only needs one universe. Preprint at <http://arxiv.org/abs/quant-ph/0003084> (2000).
- Vedral, V. The elusive source of quantum speedup. *Found. Phys.* **40**, 1141–1154 (2010).
- Brodutch, A. Discord and quantum computational resources. *Phys. Rev. A* **88**, 022307 (2013).
- Van den Nest, M. Universal quantum computation with little entanglement. *Phys. Rev. Lett.* **110**, 060504 (2013).
- Knill, E. & Laflamme, R. Power of one bit of quantum information. *Phys. Rev. Lett.* **81**, 5672–5675 (1998).
- Briegleb, H. J., Browne, D. E., Dür, W., Raussendorf, R. & Van den Nest, M. Measurement-based quantum computation. *Nature Phys.* **5**, 19–26 (2009).
- Bell, J. On the problem of hidden variables in quantum mechanics. *Rev. Mod. Phys.* **38**, 447–452 (1966).
- Kochen, S. & Specker, E. P. The problem of hidden variables in quantum mechanics. *J. Math. Mech.* **17**, 59–87 (1968).
- Bravyi, S. & Kitaev, A. Universal quantum computation with ideal Clifford gates and noisy ancillas. *Phys. Rev. A* **71**, 022316 (2005).
- Knill, E. Quantum computing with realistically noisy devices. *Nature* **434**, 39–44 (2005).
- Campbell, E. T., Anwar, H. & Browne, D. E. Magic state distillation in all prime dimensions using quantum Reed-Muller codes. *Phys. Rev. X* **2**, 041021 (2012).
- Mermin, N. D. Simple unified form for the major no-hidden-variables theorems. *Phys. Rev. Lett.* **65**, 3373–3376 (1990).
- Buhrman, H., Cleve, R., Massar, S. & de Wolf, R. Nonlocality and communication complexity. *Rev. Mod. Phys.* **82**, 665–698 (2010).
- Acín, A. *et al.* Device-independent security of quantum cryptography against collective attacks. *Phys. Rev. Lett.* **98**, 230501 (2007).
- Reichardt, B. W., Unger, F. & Vazirani, U. Classical command of quantum systems. *Nature* **496**, 456–460 (2013).
- Vazirani, U. & Vidick, T. Fully device independent quantum key distribution. Preprint at <http://arxiv.org/abs/1210.1810> (2012).
- Raussendorf, R. Contextuality in measurement-based quantum computation. *Phys. Rev. A* **88**, 022322 (2013).
- Hoban, M. J., Wallman, J. J. & Browne, D. E. Generalized Bell-inequality experiments and computation. *Phys. Rev. A* **84**, 062107 (2011).
- Gottesman, D. Theory of fault-tolerant quantum computation. *Phys. Rev. A* **57**, 127–137 (1998).
- Kitaev, A. Yu. Fault-tolerant quantum computation by anyons. *Ann. Phys.* **303**, 2–30 (2003).
- Raussendorf, R., Harrington, J. & Goyal, K. A fault-tolerant one-way quantum computer. *Ann. Phys.* **321**, 2242–2270 (2006).
- Dennis, E., Kitaev, A., Landahl, A. & Preskill, J. Topological quantum memory. *J. Math. Phys.* **43**, 4452–4505 (2002).
- Anwar, H., Brown, B. J., Campbell, E. T. & Browne, D. E. Efficient decoders for qudit topological codes. Preprint at <http://arxiv.org/abs/1311.4895> (2013).

29. Fowler, A. G., Mariantoni, M., Martinis, J. M. & Cleland, A. N. Surface codes: towards practical large-scale quantum computation. *Phys. Rev. A* **86**, 032324 (2012).
30. Aaronson, S. & Gottesman, D. Improved simulation of stabilizer circuits. *Phys. Rev. A* **70**, 052328 (2004).
31. Cabello, A., Severini, S. & Winter, A. (Non-)Contextuality of physical theories as an axiom. Preprint at <http://arxiv.org/abs/1010.2163> (2010).
32. Cabello, A., Severini, S. & Winter, A. Graph-theoretic approach to quantum correlations. *Phys. Rev. Lett.* **112**, 040401 (2014).
33. Cormick, C., Galvão, E. F., Gottesman, D., Pablo Paz, J. & Pittenger, A. O. Classicality in discrete Wigner functions. *Phys. Rev. A* **73**, 012301 (2006).
34. Howard, M. & Vala, J. Qudit versions of the qubit $\pi/8$ gate. *Phys. Rev. A* **86**, 022316 (2012).
35. Veitch, V., Ferrie, C., Gross, D. & Emerson, J. Negative quasi-probability as a resource for quantum computation. *N. J. Phys.* **14**, 113011 (2012).
36. Mari, A. & Eisert, J. Positive Wigner functions render classical simulation of quantum computation efficient. *Phys. Rev. Lett.* **109**, 230503 (2012).
37. van Dam, W. & Howard, M. Noise thresholds for higher-dimensional systems using the discrete Wigner function. *Phys. Rev. A* **83**, 032310 (2011).
38. Appleby, D. M., Bengtsson, I. & Chaturvedi, S. Spectra of phase point operators in odd prime dimensions and the extended Clifford group. *J. Math. Phys.* **49**, 012102 (2008).
39. Wallman, J. J. & Bartlett, S. D. Non-negative subtheories and quasiprobability representations of qubits. *Phys. Rev. A* **85**, 062121 (2012).
40. Gross, D. Hudson's theorem for finite-dimensional quantum systems. *J. Math. Phys.* **47**, 122107 (2006).
41. Wootters, W. K. The discrete Wigner function. *Ann. NY Acad. Sci.* **480**, 275–282 (1986).
42. Gibbons, K. S., Hoffman, M. J. & Wootters, W. K. Discrete phase space based on finite fields. *Phys. Rev. A* **70**, 062101 (2004).
43. Östergård, P. R. J. A fast algorithm for the maximum clique problem. *Discrete Appl. Math.* **120**, 197–207 (2002).
44. Veitch, V., Mousavian, S. A. H., Gottesman, D. & Emerson, J. The resource theory of stabilizer computation. *N. J. Phys.* **16**, 013009 (2014).
45. Howard, M., Brennan, E. & Vala, J. Quantum contextuality with stabilizer states. *Entropy* **15**, 2340–2362 (2013).
46. Peres, A. Two simple proofs of the Kochen-Specker theorem. *J. Phys. A* **24**, L175–L178 (1991).
47. Spekkens, R. W. Contextuality for preparations, transformations, and unsharp measurements. *Phys. Rev. A* **71**, 052108 (2005).
48. Acín, A., Fritz, T., Leverrier, A. & Sainz, A. B. A combinatorial approach to nonlocality and contextuality. Preprint at <http://arxiv.org/abs/1212.4084> (2012).

Supplementary Information is available in the online version of the paper.

Acknowledgements M.H. was supported by the Irish Research Council (IRC) as part of the Empower Fellowship programme, and all authors acknowledge support from CIFAR and the Government of Canada through NSERC.

Author Contributions All authors made significant contributions to the results, interpretation and presentation of this Article.

Author Information Reprints and permissions information is available at www.nature.com/reprints. The authors declare no competing financial interests. Readers are welcome to comment on the online version of the paper. Correspondence and requests for materials should be addressed to J.E. (jemerson@math.uwaterloo.ca)

The genome of *Eucalyptus grandis*

Alexander A. Myburg^{1,2}, Dario Grattapaglia^{3,4}, Gerald A. Tuskan^{5,6}, Uffe Hellsten⁵, Richard D. Hayes⁵, Jane Grimwood⁷, Jerry Jenkins⁷, Erika Lindquist⁵, Hope Tice⁵, Diane Bauer⁵, David M. Goodstein⁵, Inna Dubchak⁵, Alexandre Poliakov⁵, Eshchar Mizrahi^{1,2}, Anand R. K. Kullán^{1,2}, Steven G. Hussey^{1,2}, Desre Pinar^{1,2}, Karen van der Merwe^{1,2}, Pooja Singh^{1,2}, Ida van Jaarsveld⁸, Orzenil B. Silva-Junior⁹, Roberto C. Togawa⁹, Marilia R. Pappas³, Danielle A. Faria³, Carolina P. Sansaloni³, Cesar D. Petrolis³, Xiaohan Yang⁶, Priya Ranjan⁶, Timothy J. Tschaplinski⁶, Chu-Yu Ye⁶, Ting Li⁶, Lieven Sterck¹⁰, Kevin Vanneste¹⁰, Florent Murat¹¹, Marçal Soler¹², Hélène San Clemente¹², Najib Saidi¹², Hua Cassan-Wang¹², Christophe Dunand¹², Charles A. Hefer^{8,13}, Erich Bornberg-Bauer¹⁴, Anna R. Kersting^{14,15}, Kelly Vining¹⁶, Vindhya Amarasinghe¹⁶, Martin Ranik¹⁶, Sushma Naithani^{17,18}, Justin Elser¹⁷, Alexander E. Boyd¹⁸, Aaron Liston^{17,18}, Joseph W. Spatafora^{17,18}, Palitha Dharmawardhana¹⁷, Rajani Raja¹⁷, Christopher Sullivan¹⁸, Elisson Romanel^{19,20,21}, Marcio Alves-Ferreira²¹, Carsten Külheim²², William Foley²², Victor Carocha^{12,23,24}, Jorge Paiva^{23,24}, David Kudrna²⁵, Sergio H. Brommonschenkel²⁶, Giancarlo Pasquali²⁷, Margaret Byrne²⁸, Philippe Rigault²⁹, Josquin Tibbits³⁰, Antanas Spokevicius³¹, Rebecca C. Jones³², Dorothy A. Steane^{32,33}, René E. Vaillancourt³², Brad M. Potts³², Fourie Joubert^{2,8}, Kerrie Barry⁵, Georgios J. Pappas Jr³⁴, Steven H. Strauss¹⁶, Pankaj Jaiswal^{17,18}, Jacqueline Grima-Pettenati¹², Jérôme Salse¹¹, Yves Van de Peer^{2,10}, Daniel S. Rokhsar⁵ & Jeremy Schmutz^{5,7}

Eucalypts are the world's most widely planted hardwood trees. Their outstanding diversity, adaptability and growth have made them a global renewable resource of fibre and energy. We sequenced and assembled >94% of the 640-megabase genome of *Eucalyptus grandis*. Of 36,376 predicted protein-coding genes, 34% occur in tandem duplications, the largest proportion thus far in plant genomes. *Eucalyptus* also shows the highest diversity of genes for specialized metabolites such as terpenes that act as chemical defence and provide unique pharmaceutical oils. Genome sequencing of the *E. grandis* sister species *E. globulus* and a set of inbred *E. grandis* tree genomes reveals dynamic genome evolution and hotspots of inbreeding depression. The *E. grandis* genome is the first reference for the eudicot order Myrtales and is placed here sister to the eurosids. This resource expands our understanding of the unique biology of large woody perennials and provides a powerful tool to accelerate comparative biology, breeding and biotechnology.

A major opportunity for a sustainable energy and biomaterials economy in many parts of the world lies in a better understanding of the molecular basis of superior growth and adaptation in woody plants. Part of this opportunity involves species of *Eucalyptus* L'Hér, a genus of woody perennials native to Australia¹. The remarkable adaptability of eucalypts coupled with their fast growth and superior wood properties has driven their rapid adoption for plantation forestry in more than 100 countries across six continents (>20 million ha)², making eucalypts the most widely planted hardwood forest trees in the world. The subtropical *E. grandis* and the temperate *E. globulus* stand out as targets of breeding programmes worldwide. Planted eucalypts provide key renewable resources for the production of pulp, paper, biomaterials and bioenergy, while mitigating human pressures on native forests³. Eucalypts also have a large diversity

and high concentration of essential oils (mixtures of mono- and sesquiterpenes), many of which have ecological functions as well as medicinal and industrial uses. Predominantly outcrossers¹ with hermaphroditic animal-pollinated flowers, eucalypts are highly heterozygous and display pre- and postzygotic barriers to selfing to reduce inbreeding depression for fitness and survival⁴.

To mitigate the challenge of assembling a highly heterozygous genome, we sequenced the genome of 'BRASUZI', a 17-year-old *E. grandis* genotype derived from one generation of selfing. The availability of annotated forest tree genomes from two separately evolving rosoid lineages, *Eucalyptus* (order Myrtales) and *Populus* (order Malpighiales⁵), in combination with genomes from domesticated woody plants (for example, *Vitis*, *Prunus*, *Citrus*), provides a comparative foundation for addressing

¹Department of Genetics, Forestry and Agricultural Biotechnology Institute (FABI), University of Pretoria, Private bag X20, Pretoria 0028, South Africa. ²Genomics Research Institute (GRI), University of Pretoria, Private bag X20, Pretoria 0028, South Africa. ³Laboratório de Genética Vegetal, EMBRAPA Recursos Genéticos e Biotecnologia, EPQB Final W5 Norte, 70770-917 Brasília, Brazil. ⁴Programa de Ciências Genômicas e Biotecnologia - Universidade Católica de Brasília SGAN 916, 70790-160 Brasília, Brazil. ⁵US Department of Energy Joint Genome Institute, 2800 Mitchell Drive, Walnut Creek, California 94598, USA. ⁶Biosciences Division, Oak Ridge National Laboratory, Oak Ridge, Tennessee 37831, USA. ⁷HudsonAlpha Institute for Biotechnology, 601 Genome Way, Huntsville, Alabama 35801, USA. ⁸Bioinformatics and Computational Biology Unit, Department of Biochemistry, University of Pretoria, Pretoria, Private bag X20, Pretoria 0028, South Africa. ⁹Laboratório de Biotecnologia, EMBRAPA Recursos Genéticos e Biotecnologia, EPQB Final W5 Norte, 70770-917 Brasília, Brazil. ¹⁰Department of Plant Biotechnology and Bioinformatics (VIB), Ghent University, Technologiepark 927, B-9000 Ghent, Belgium. ¹¹INRA/UBP UMR 1095, 5 Avenue de Beaulieu, 63100 Clermont Ferrand, France. ¹²Laboratoire de Recherche en Sciences Végétales, UMR 5546, Université Toulouse III, UPS, CNRS, BP 42617, 31326 Castanet Tolosan, France. ¹³Department of Botany, University of British Columbia, 3529-6270 University Blvd, Vancouver V6T 1Z4, Canada. ¹⁴Evolutionary Bioinformatics, Institute for Evolution and Biodiversity, University of Münster, Huefferstrasse 1, D-48149, Münster, Germany. ¹⁵Department of Bioinformatics, Institute for Computer Science, University of Duesseldorf, Universitätsstrasse 1, 40225 Düsseldorf, Germany. ¹⁶Department of Forest Ecosystems and Society, Oregon State University, Corvallis, Oregon 97331, USA. ¹⁷Department of Botany and Plant Pathology, Oregon State University, 2082-Cordley Hall, Corvallis, Oregon 97331, USA. ¹⁸Center for Genome Research and Biocomputing, Oregon State University, Corvallis, Oregon 97331, USA. ¹⁹Laboratório de Biologia Evolutiva Teórica e Aplicada, Departamento de Genética, Universidade Federal do Rio de Janeiro (UFRJ), Av. Prof. Rodolpho Paulo Rocco, 21949900 Rio de Janeiro, Brazil. ²⁰Departamento de Biotecnologia, Escola de Engenharia de Lorena-Universidade de São Paulo (EEL-USP), CP116, 12602-810, Lorena-SP, Brazil. ²¹Laboratório de Genética Molecular Vegetal (LGMV), Departamento de Genética, Universidade Federal do Rio de Janeiro (UFRJ), Av. Prof. Rodolpho Paulo Rocco, 21949900 Rio de Janeiro, Brazil. ²²Research School of Biology, Australian National University, Canberra 0200, Australia. ²³ICT/MNE; Palácio Burnay - Rua da Junqueira, 30, 1349-007 Lisboa, Portugal. ²⁴IBET/ITQB, Av. República, Quinta do Marquês, 2781-901 Oeiras, Portugal. ²⁵Arizona Genomics Institute, University of Arizona, Tucson, Arizona 85721, USA. ²⁶Dep. de Fitopatologia, Universidade Federal de Viçosa, Viçosa 36570-000, Brazil. ²⁷Centro de Biotecnologia, Universidade Federal do Rio Grande do Sul, 91501-970 Porto Alegre, Brazil. ²⁸Science and Conservation Division, Department of Parks and Wildlife, Locked Bag 104, Bentley Delivery Centre, Western Australia 6983, Australia. ²⁹GYDLE, 1363 av. Maguire, suite 301, Québec, Québec G1T 1Z2, Canada. ³⁰Department of Environment and Primary Industries, Victorian Government, Melbourne, Victoria 3085, Australia. ³¹Melbourne School of Land and Environment, University of Melbourne, Melbourne, Victoria 3010, Australia. ³²School of Biological Sciences and National Centre for Future Forest Industries, University of Tasmania, Private Bag 55, Hobart, Tasmania 7001, Australia. ³³Faculty of Science, Health, Education and Engineering, University of the Sunshine Coast, Queensland 4558, Australia. ³⁴Departamento de Biologia Celular, Universidade de Brasília, Brasília 70910-900, Brazil.

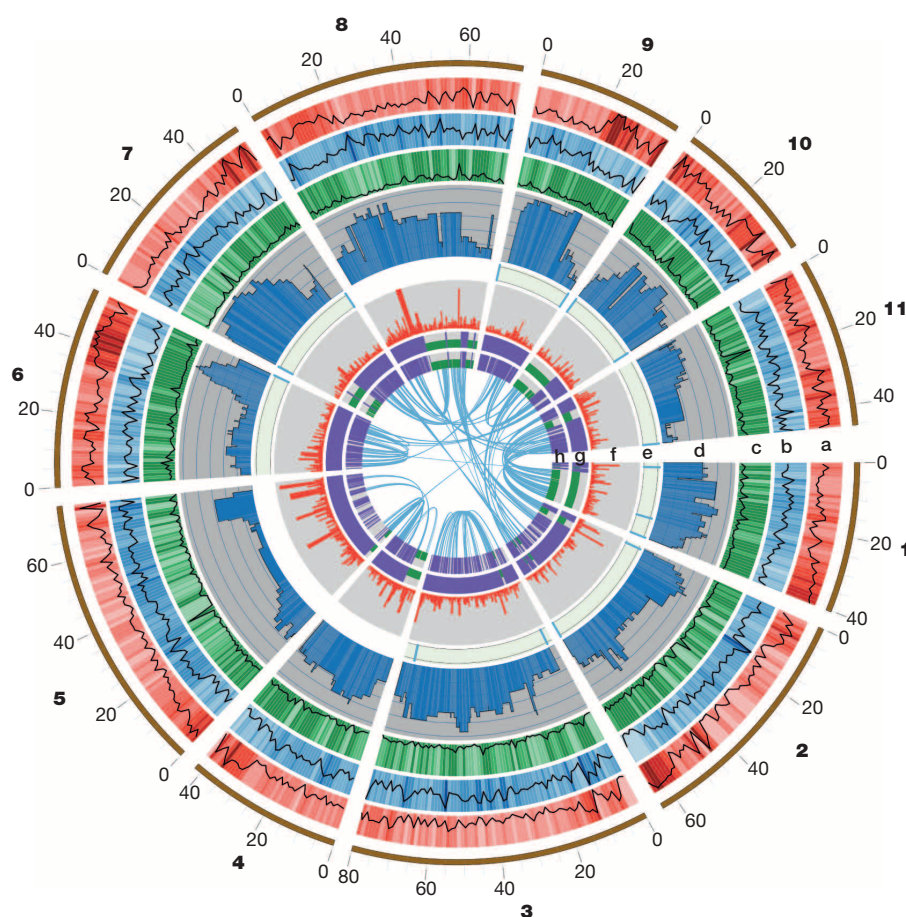


Figure 1 | *Eucalyptus grandis* genome overview. Genome features in 1-Mb intervals across the 11 chromosomes. Units on the circumference show megabase values and chromosomes. **a**, Gene density (number per Mb, range 6–131). **b**, Repeat coverage (22–88% per Mb). **c**, Average expression state (fragments per kilobase of exon per million sequences mapped, FPKM, per gene per Mb, 6–41 per Mb). **d**, Heterozygosity in inbred siblings (proportion of 28 S_1 offspring heterozygous at position, 0.39–0.93). **e**, Telomeric repeats. **f**, Tandem duplication density (2–50). **g**, **h**, Single nucleotide polymorphisms (SNPs) identified by resequencing BRASUZ1 in 1-Mb bins (**g**) and per gene (**h**, 11,656 genes); homozygous regions (~24%) and genes in green and heterozygous regions and genes in purple. Central blue lines connect gene pairs from the most recent whole-genome duplication event (Supplementary Data 1).

fundamental evolutionary questions related to the biology of woody perennials. Moreover, the unique palaeogeographic evolution of *Eucalyptus*, that is, isolation from other members of the rosoid clade, enables disentangling of the events that led to the modern members of the rosoids by characterizing shared and unique whole-genome duplication events and syntenic gene space with other sequenced genomes. The draft genome of *E. grandis* suggests that the *Eucalyptus* genome has been shaped by an early lineage-specific genome duplication event and a subsequent high rate of tandem gene duplication.

Sequencing, assembly and annotation

We assembled a non-redundant chromosome-scale reference (V1.0) sequence for BRASUZ1 based on 6.7× whole-genome Sanger shotgun coverage, paired bacterial artificial chromosome (BAC)-end sequencing and a high-density genetic linkage map⁶ (see Methods and Supplementary Information section 1). An estimated 94% of the genome is organized into 11 pseudomolecules (605 megabases (Mb), Fig. 1). Anchoring the genome assembly to an independent linkage map⁷ revealed that the remaining 4,941 smaller unanchored scaffolds (totalling 85 Mb) correspond largely to repeat-rich sequences and segments of alternative haplotypes of the assembled chromosomes derived from regions of residual heterozygosity in the otherwise inbred BRASUZ1 genome.

The *E. grandis* genome encodes a large number of predicted protein-coding loci (36,376) of which 89% are expressed in vegetative and reproductive tissues (Extended Data Fig. 1) plus various classes of non-coding genes (Supplementary Information section 2). Of the 36,376 predicted proteins, 30,341 (84%) are included in gene clusters shared with other rosoid lineages (Extended Data Fig. 2). Retrotransposons account for the major portion of the genome (44.5%), with long terminal repeat retrotransposons being the most pervasive class (21.9%). DNA transposons encompass only 5.6% of the genome. For this class, Helitron elements

are the most abundant with an estimated 15,000 copies or 3.8% of the genome (Supplementary Information section 2).

Genome evolution and phylogeny

To address the phylogenetic position of *Eucalyptus*, we performed genome-wide analysis of 17 sequenced plant genomes, generating a matrix of 697,423 aligned amino acid positions from 3,268 orthologue gene clusters (Methods and Supplementary Information section 3). Studies employing broad taxon sampling but a modest number of genes⁸ have consistently recovered two very well-supported clades of eurosids—the fabids and malvids—and grouped *Eucalyptus* and other Myrtales with the malvids. Our analysis alternatively places *Eucalyptus* as a sister taxon to the eurosids (Extended Data Fig. 3) and supports the grouping of *Populus* and *Jatropha* (order Malpighiales) with malvids rather than fabids, in agreement with other recent whole-genome studies^{9,10}. The discrepancy between our genome-wide analyses and the angiosperm phylogeny group (APG) consensus highlights important methodological trade-offs between sampling more characters (as in our genome-wide study) versus more taxa (as per APG)^{11,12}.

The evolutionary history of the *Eucalyptus* genome is marked by a lineage-specific palaeotetraploidy event newly revealed by our genomic analysis, superimposed on the earlier palaeohexaploidy event shared by all eudicots (Fig. 2). The whole-genome duplication (WGD) is estimated to have occurred ~109.9 (105.9–113.9) million years (Myr) ago (Supplementary Information section 3 and Extended Data Fig. 4) in a Gondwanan ancestor around the time when Australia and Antarctica began to separate from East Gondwana. This WGD event is considerably older than those typically detected in other rosoids¹³ and could have played a pivotal part in the evolution of the Myrtales lineage and its subsequent diversification from other rosoid ancestors. The coincidence of the estimated WGD timing and the origin of the Myrtales¹⁴ leads to speculation

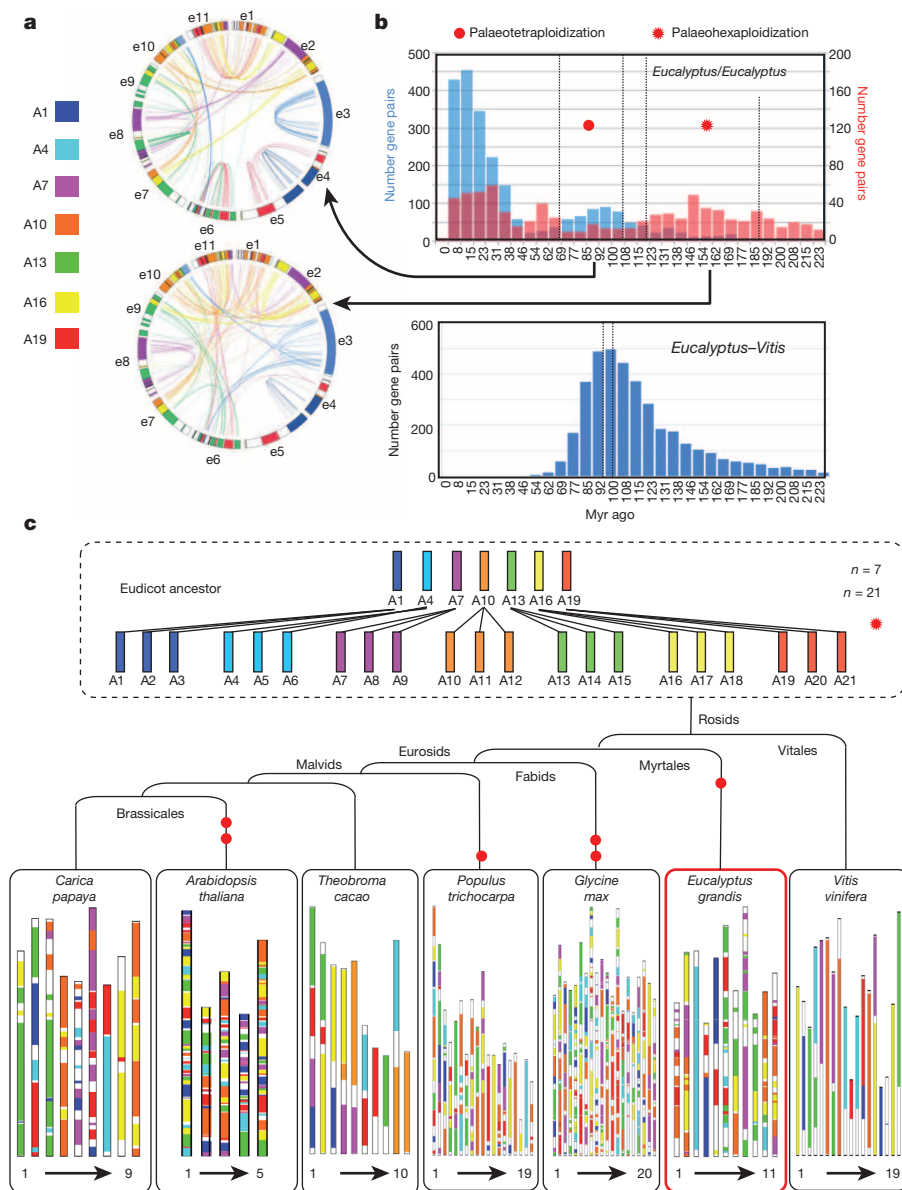


Figure 2 | *Eucalyptus grandis* genome synteny, duplication pattern and evolutionary history. **a**, Paralogous gene pairs in *Eucalyptus* for the identified palaeohexaploidization (bottom) and palaeotetraploidization (top) events. Each line represents a duplicated gene, and colours reflect origin from the seven ancestral chromosomes (A1, A4, A7, A10, A13, A16, A19). **b**, Number of synonymous substitutions per synonymous site (K_s) distributions of *Eucalyptus* paralogues (top) and *Eucalyptus*–*Vitis* orthologues (bottom). Blue bars (top) indicate K_s values for 378 gene pairs from the palaeotetraploidization WGD event (red dot), and red bars show K_s values for 274 gene pairs of the palaeohexaploidization event (red star). **c**, Evolutionary scenario of genome rearrangements from the Eudicot ancestor to *Eucalyptus* and other sequenced plant genomes; palaeohistory modified from ref. 49.

that the WGD event could be directly related to the origin of the clade. More precise timing will require genomic analysis of other families and genera from the Myrtales.

The *Eucalyptus* genome exhibits substantial conservation of synteny with other rosids as has been demonstrated for the basal rosid lineage represented by *Vitis vinifera*¹⁵. Extending the method previously described⁵ we identified 480 pairwise segments of conserved synteny between *Eucalyptus* and *Vitis* (Supplementary Information section 3). These segments include 68% of *Eucalyptus* genes and 76% of *Vitis* genes used in the analysis. The WGD in the *Eucalyptus* lineage relative to *Vitis* is clearly revealed by the 2:1 pattern in which two different *Eucalyptus* regions are typically collinear with a single region in *Vitis*. However, the gene content of these segments varies, as more than 95% of the paralogues in *Eucalyptus* have been lost subsequent to the WGD (a total of 5,896 *Vitis* genes have 6,158 synteny-confirmed orthologues in *Eucalyptus*). Half of the total length of the orthologous segments is contributed by segments longer than 1.83 Mb in *Eucalyptus* and 2.35 Mb in *Vitis*, suggesting that the loss of redundant genes after the WGD in *Eucalyptus* was accompanied by a compaction of those parts of the genome.

Eucalyptus chromosome 3, the largest single chromosome in the *Eucalyptus* genome, is the only chromosome that does not contain inter-chromosomal segmental duplications (Fig. 1), having fused with

its WGD homologue. A similar situation occurs in *Populus* chromosome XVIII. Interestingly, *Eucalyptus* chromosome 3 and *Populus* chromosome XVIII nearly exclusively contain the ancestral eudicot chromosome 2 (Fig. 2c), despite their independent WGDs. There are no other examples among the currently sequenced dicotyledon genomes that contain a sole single copy of an ancestral chromosome. Moreover, in *Eucalyptus* and *Populus*, all other ancestral chromosomes appear to be dispersed and rearranged among the extant chromosomes (Fig. 2c). The conserved gene content and order (Supplementary Information section 3) on these chromosomes in two distantly related species could be due to: (1) convergent selection and positional stoichiometry of genes related to long-lived perennial woody habit that favours preservation of certain genes in syntenic order; and/or (2) merged ancestral chromosome structure (that is, multiple telomeres and centromeres on one chromosome) that suppresses gene expression, recombination and/or successive rearrangement. *Eucalyptus* chromosome 3 has the lowest average gene expression metrics of any of the *Eucalyptus* chromosomes (Fig. 1c), favouring the second hypothesis. Alternatively, there are several clusters of shared syntenic genes that appear to be related to perennial habit, including homologues of NAM (no apical meristem, PF02365) and senescence-associated protein (PF02365), several syntenic sets of disease-resistance genes, as well as genes related to cell-wall formation (Supplementary Data 2).

Table 1 | Tandem duplicate statistics for selected plant genomes

Species	Number of tandem expanded regions	Total number of retained tandem genes (%)
<i>Physcomitrella patens</i>	885	1,949 (6%)
<i>Arabidopsis thaliana</i>	1,821	5,038 (18%)
<i>Populus trichocarpa</i>	2,575	8,104 (18%)
<i>Vitis vinifera</i>	1,818	6,033 (23%)
<i>Eucalyptus grandis</i>	3,185	12,570 (34%)

Eucalyptus has more tandem duplicates and more tandem expanded regions (clusters) than other plant genomes.

We also find that *E. grandis* has the largest number of genes in tandem repeats (12,570, 34% of the total) reported among sequenced plant genomes (Table 1 and Supplementary Information section 3). The low frequency of contig breaks separating tandem gene pairs (Extended Data Fig. 5) and conserved gene order on independent BAC clones spanning two large tandem gene arrays (Supplementary Data 3 and Supplementary Information 1) support the accuracy of the assembly across highly similar tandem copies. Tandem duplication often involves stress-response genes that are retained in a lineage-specific fashion, suggesting that tandem duplication is important for adaptive evolution in dynamically changing environments¹⁶. For example, more than 80% of the S-domain receptor-like kinase (SDRLK) subfamily occurs in tandem arrays (Supplementary Data 4). There also seems to be a bias in gene retention following tandem duplication in comparison to segmental and whole-genome duplication¹⁷. Even within the genus *Eucalyptus*, tandem duplication appears to be dynamic, for example, a cluster of MYB transcription factor genes in *E. globulus* lacks four of the nine tandem duplicates found in *E. grandis* (Extended Data Fig. 6).

Despite having the same number of chromosomes ($n = 11$) and highly co-linear genomes¹⁸, eucalypts vary considerably in genome size. *E. grandis* (640 Mb¹⁹) and *E. globulus* (530 Mb¹⁹) represent different sections (*Latoangulatae* and *Maidenaria*) within the subgenus *Symphomyrtus*²⁰, estimated to have diverged in the past 36 million years²¹. Resequencing of the subtropical *E. grandis* (BRASUZ1) and a representative of the temperate *E. globulus* ('X46', Supplementary Information section 3) revealed that many small, non-transposable element (TE)-derived changes distributed throughout the genome (164,813 regions; mean length 538 bp, median 230 bp, maximum 30,610 bp, total 88.7 Mb) account for nearly all of the genome size difference between the two species. Recent TE activity accounts for only 2 Mb of the size difference. This is in contrast to other studies in closely related plant species that report a predominant role for TEs in genome size evolution²². Using sequence data from other *Eucalyptus* species taxonomically positioned around the *E. grandis*–*E. globulus* split (J. Tibbits, unpublished data), we estimate that since divergence, *E. grandis* has gained 58 Mb and lost 12 Mb, while *E. globulus* has gained 15 Mb and lost 24 Mb, suggesting more active genome size evolution than was apparent from previous estimates.

Genetic load and heterozygosity

Eucalypts are preferentially outcrossing with late-acting post-zygotic self-incompatibility resulting in outcrossing rates that can exceed 90%¹, high levels of nucleotide variation^{23,24} and accumulation of genetic load and expression of inbreeding depression⁴. A microsatellite survey of BRASUZ1 and its inbred siblings indicated putative hotspots of genetic load (Supplementary Information section 4). To investigate the distribution of preserved heterozygosity further, we resequenced an unrelated (outbred) *E. grandis* parental genotype M35D2 and 28 of its S_1 offspring. The offspring were genotyped using 308,784 high-confidence heterozygous sites (within 22,619 genes) identified in M35D2 (Methods and Supplementary Information section 4). Contrary to Mendelian expectation of 50% retained heterozygosity after selfing, we observed 52% to 79% heterozygosity in the 28 S_1 offspring (average of 66%). In all chromosomes except 5 and 11, heterozygosity was high (>80%) in long chromosome segments with peaks at >90% on chromosomes 6, 7 and 9 (Fig. 1d). Despite the strong bias towards heterozygosity in these regions, a small proportion of either homozygous haplotype was always present, suggesting

that there are genetic backgrounds in which homozygosity of any particular gene is not lethal. One exception is on chromosome 4, where a 25-Mb region is completely devoid of one homozygous class across all surveyed genotypes (Extended Data Fig. 7 and Supplementary Information section 4).

The genetic architecture of genetic load and contribution of individual loci to inbreeding depression are largely unknown for woody perennials and present a barrier to rapid domestication via recurrent inbred mating. Our results suggest that a model of genome-wide cumulative effects of many small recessive alleles affecting overall fitness and survival best explains the architecture of inbreeding depression in *Eucalyptus*. This result is consistent with recent genome-wide selection experiments in *Eucalyptus* showing that a multifactorial model of a few hundred small effects throughout the genome contribute additively to height growth²⁵, in contrast to earlier suggestions of the existence of a relatively small number of loci of larger effect as reported in several biparental QTL mapping studies²⁶.

Lignocellulosic biomass production

Whereas woody growth habit (the ability to produce radial secondary tissues from a vascular cambium) is polyphyletic, having appeared and disappeared multiple times across more than 30 diverse taxa²⁷, secondary cell wall formation itself is highly conserved across vascular plants. Large woody plants produce secondary cell walls on a vastly different scale from that of herbaceous plants. Approximately 80% of woody biomass comprises cellulose and hemicellulose, with the remaining biomass primarily composed of lignin^{28–30}. A major determinant of industrial processing efficiency lies in secondary cell wall ultrastructure, which is dependent on interactions among these biopolymers. We identified putative functional homologues of genes encoding 18 enzymatic steps of cellulose and heteroxylan biosynthesis (Supplementary Information section 5). Despite the lineage-specific WGD event and the high number of genes in tandem duplications, relative and absolute expression levels (See Methods) suggest that most of the key enzymatic steps involve only one or two functional homologues (Fig. 3), which are highly and specifically expressed in xylem tissue. The xylem expression pattern of genes involved in sucrose catabolism suggests that *Eucalyptus* uses both direct (SUSY) and indirect (INV) pathways for the production of UDP-glucose (Fig. 3). Notably, the two *sucrose synthase 4* homologues (Eucgr.C03199 and Eucgr.C00769) are expressed at high levels in xylem tissue and account for 70% and 18% of total sucrose synthase expression, respectively. These genes, found on chromosome 3 in *Eucalyptus*, are part of a syntenic set of genes found on *Populus* chromosome XVIII, indicating that these genes pre-date the speciation events that separate these genera. There are 10 multigene families encoding phenylpropanoid biosynthesis genes that have expanded, mostly through tandem duplication, to include 174 genes in *E. grandis* (Supplementary Information section 5). Phylogenetic analysis and expression profiling have allowed us to define a core set of 24 genes, as well as five novel lignification candidates, preferentially and highly expressed in developing xylem (Extended Data Fig. 8 and Supplementary Information section 5). These results highlight the central role of tandem gene duplication in shaping functional diversity in *Eucalyptus* and suggest that subfunctionalization within these expanded gene families has prioritized specific genes for wood formation.

Secondary metabolites and oils

It is generally thought that the extremely diverse array of secondary metabolites observed within *Eucalyptus* defends against a comparably diverse array of biotic pests, pathogens and herbivores encountered across its natural range. Many of the defence compounds are terpenoid based, including the commercially valuable eucalyptus oil, which is composed largely of 1,8-cineole. The conjugation of terpenes with phloroglucinol derivatives³¹, as well as the formation of monoterpene glucose esters³², leads to the myriad of defence compounds that vary across the genus. *E. grandis* has the largest observed number of terpene synthase genes among all sequenced plant genomes ($n = 113$ compared to a range of

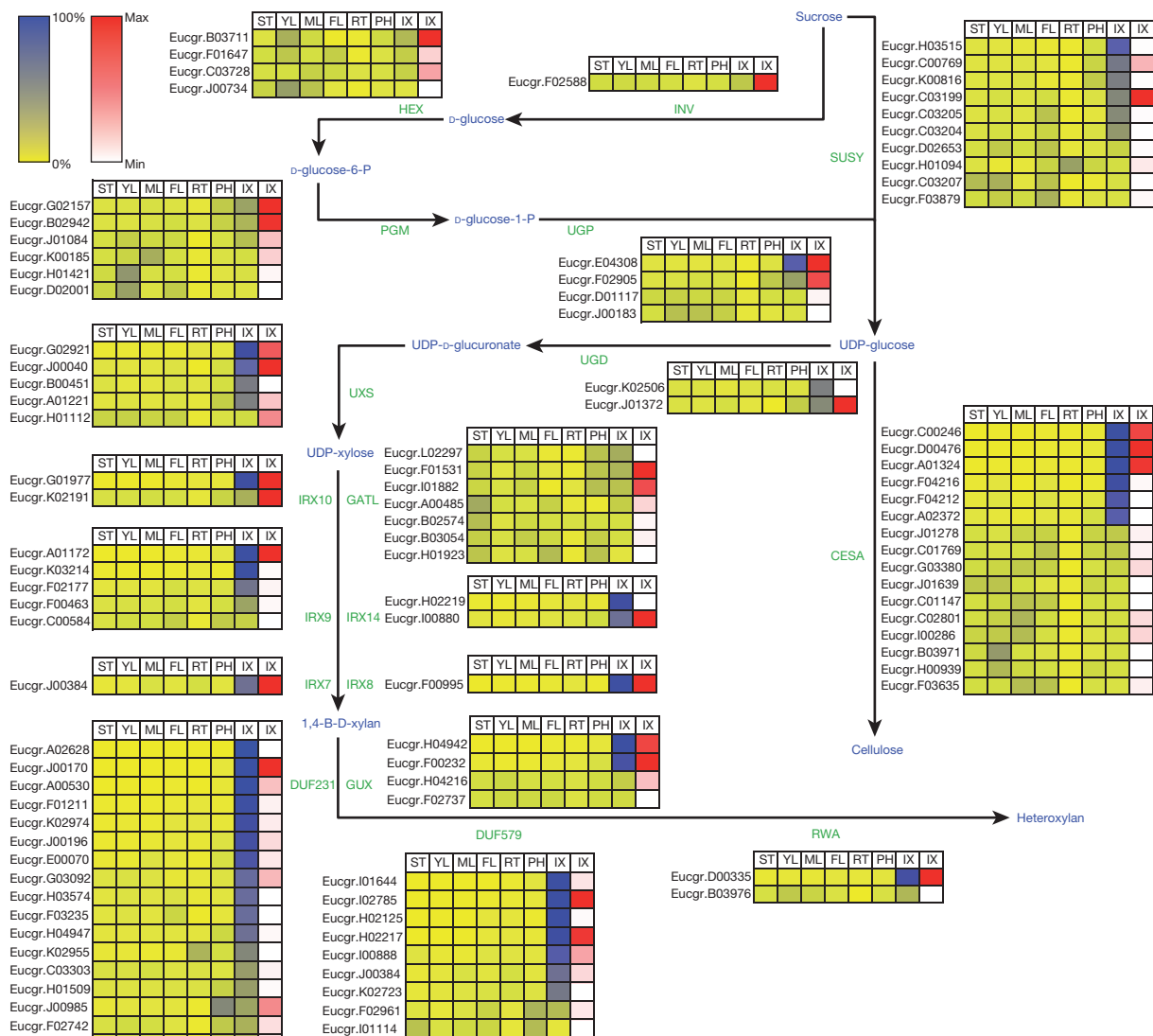


Figure 3 | Genes involved in cellulose and xylan biosynthesis in wood-forming tissues of *Eucalyptus*. Relative (yellow–blue scale) and absolute (white–red scale) expression profiles of secondary cell-wall-related genes implicated in cellulose and xylan biosynthesis²⁹. Sugar and polymer intermediates are shown in green, while the proteins (enzymes) involved in each step are shown in blue. Detailed protein names, annotation and mRNA-seq expression data are provided in Supplementary Data 5. ST, shoot tips; YL, young leaves; ML, mature leaves; FL, floral buds; RT, roots; PH, phloem, IX, immature xylem. Absolute expression level (FPKM⁵⁰) is only shown for immature xylem, the target secondary cell-wall-producing tissue. DUF, domain of unknown function; GATL, galacturonosyl transferase-like; GUX, glucuronic acid substitution of xylan; HEX, hexokinase; INV, invertase; IRX, irregular xylem; PGM, phosphoglucosyl transferase; SUSY, sucrose synthase; RWA, reduced wall acetylation; UGD, UDP-glucose dehydrogenase; UGP, UDP-glucose pyrophosphorylase; UXS, UDP-xylose synthase.

$n = 2$ in *Physcomitrella* to 83 in *Vitis*, Fig. 4), as well as a marked expansion of several phenylpropanoid gene families (Supplementary Information section 5). Furthermore, a subgroup of R2R3-MYB transcription factor genes known to be involved in the regulation of the phenylpropanoid pathway in *Arabidopsis* is expanded by tandem duplication in *Eucalyptus* to yield 16 genes with diverse expression profiles (Extended Data Fig. 9) possibly associated with the wide range of phenylpropanoid-derived compounds found in *Eucalyptus*.

Reproductive biology

The genus *Eucalyptus* is named for its unusual floral structure derived from the Greek *eu-*, well, and *kaluptos*, covered, which refers to the operculum that covers the floral buds before anthesis. The ability to produce large amounts of pollen and seed over long generation times increases the reproductive success of woody perennials³³ and impacts on adaptation and population genetics. Interestingly, the evolution and genetic control of the unique floral structure in *Eucalyptus* may be reflected in the expansion and deletion of genes typically associated with floral structure (for example, the APETALA1/FRUITFUL-like clade, Supplementary

Information section 7). *SOC1*, a type II MADS-box gene that integrates multiple signals related to initiation of flowering, including long days, vernalization and pathways related to gibberellin signalling³⁴, has been markedly expanded in *E. grandis* compared to other angiosperms (Extended Data Fig. 10). *Eucalyptus* is a diverse genus of over 700 species distributed in a wide range of environments ranging from tropical, subtropical and temperate forests¹. This environmental heterogeneity encompasses extensive variation in the onset, season and intensity of flowering³⁵. Because of *SOC1*'s diverse roles in environmental control of flowering, the expansion and subfunctionalization of the *SOC1* subfamily may have contributed to the evolutionary diversification of *Eucalyptus* by integrating multiple signals into flowering responses relevant to different geographical zones. *Eucalyptus* may thus provide a model for the evolution of responses to divergent sets of flowering cues required for wide colonization and speciation.

Conclusions and future directions

The availability of a high-quality reference represents a timely step forward in fundamental studies of adaptation across the diversity of habitats

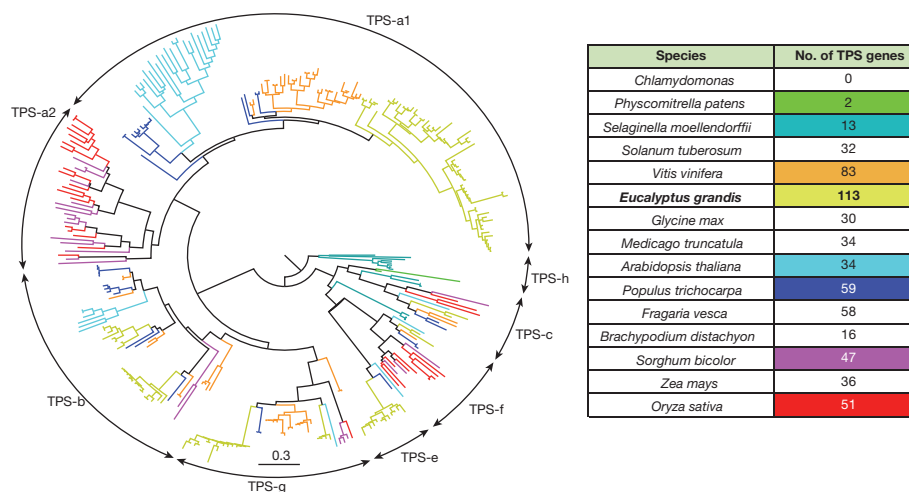


Figure 4 | Interspecific phylogenetic analysis and classification of terpene synthase (TPS) genes from *Eucalyptus grandis* and other sequenced plant genomes. The phylogenetic tree shows all TPS genes found in eight plant genomes (Supplementary Data 6). TPS subfamilies are indicated on the circumference of the circle. The tree has been rooted between the two major groups of type I and type III TPS. The table shows the number of TPS genes from several species obtained from a Pfam search for the two Pfam motifs (PF01397 and PF03936) found in the TPS genes. Colour coding in the table corresponds to that in the tree. The scale bar (0.3) shows the number of amino acid substitutions per site.

occupied by eucalypt species. The unique biology and evolutionary history of *Eucalyptus* are reflected in its genome, for example, the expansion of terpene synthesis genes and the large number of tandem repeats, respectively. The coincidence of a lineage-specific WGD with the origin of the Myrtales reinforces the proposed role of genome duplication in angiosperm evolution and underscores the value of additional genome sequencing of families and genera in this important rosoid lineage. Future studies of variation in functional genes will provide insights into the relative influences of drift and selection on *Eucalyptus* evolution and identify mechanisms of speciation and adaptive divergence. Such insight will lead to improved understanding of the response of eucalypts to environmental change. Comparative analysis of the *E. grandis* genome with those of other large perennials will add crucial insights into the evolutionary innovations that have made eucalypts keystone species that shape biodiversity in diverse ecosystems. The prospect of accelerating breeding cycles for productivity and wood quality via genomic prediction of complex traits²⁵ and association genetics is enhanced by the release of the *Eucalyptus* genome. Genome-enabled derivation of an integrative data framework based on large-scale genotypic and phenotypic data sets will offer increasingly valuable insights into the complex connections between individual genomic elements and the extraordinary phenotypic variation in *Eucalyptus*.

METHODS SUMMARY

We used whole-genome shotgun sequencing (6.73× final sequence coverage from 7.7 million Sanger reads) followed by assembly in Arachne v.20071016 (ref. 36) and high-density genetic linkage mapping to produce chromosome-scale pseudomolecule sequences of the 11 nuclear chromosomes of BRASU1. Protein-coding loci were identified using homology-based FgenesH and GenomeScan predictions and ~260,000 PASA³⁷ EST assemblies from *E. grandis* and sister species. Gene family clustering was performed with the Inparanoid algorithm^{38,39} and peptide sequences analysed with Interproscan⁴⁰, SignalP⁴¹, Predotar⁴², TMHMM⁴³ and orthology-based projections from *Arabidopsis*. We performed maximum-likelihood-based phylogenetic reconstruction⁴⁴ of the green plant phylogeny based on 174,020 peptides encoded by single copy orthologous genes from 17 plant genomes. Protein domains and domain arrangements were analysed to identify a core set of domains and arrangements present in rosoid lineages represented by *Eucalyptus*, *Vitis*, *Populus* and *Arabidopsis*. Genome-wide gene expression profiling was performed using Illumina RNA-seq analysis of seven developing tissues from *E. grandis*. We identified whole-genome duplications using an approach^{45,46} based on paralogue- and orthologue-specific comparisons of the 36,376 predicted protein-coding genes and further refined the estimated age of the lineage-specific WGD event using a phylogenetic dating approach¹³. Genome synteny between *E. grandis* and *P. trichocarpa* was evaluated using the VISTA pipeline infrastructure^{47,48}. Genome resequencing of *E. grandis* (BRASU1) and sister species *E. globulus* (X46) genomes was performed with Illumina PE100 DNA sequencing. Lignin, cellulose, xylan, terpene and flowering-related gene families were analysed using a combination of gene annotation, phylogenetic analysis and mRNA-seq expression profiling.

Online Content Any additional Methods, Extended Data display items and Source Data are available in the online version of the paper; references unique to these sections appear only in the online paper.

Received 8 September 2013; accepted 2 April 2014.

Published online 11 June 2014.

- Byrne, M. Phylogeny, diversity and evolution of eucalypts. in *Plant Genome: Biodiversity and Evolution, Part E: Phanerogams-Angiosperm* Vol. 1 (eds Sharma, A. K. & Sharma, A.) 303–346 (Science Publishers, 2008).
- Iglesias, I. & Wilmertmann, D. in *Eucalyptologics Information Resources on Eucalypt Cultivation Worldwide* <http://www.git-forestry.com> (GIT Forestry Consulting, retrieved, 29 March 2009).
- Bauhus, J., van der Meer, P. J. & Kanninen, M. *Ecosystem Goods and Services from Plantation Forests* 254 (Earthscan, 2010).
- Costa e Silva, J., Hardner, C., Tilyard, P. & Potts, B. M. The effects of age and environment on the expression of inbreeding depression in *Eucalyptus globulus*. *Heredity* **107**, 50–60 (2011).
- Tuskan, G. A. *et al.* The genome of black cottonwood, *Populus trichocarpa* (Torr. & Gray). *Science* **313**, 1596–1604 (2006).
- Kullan, A. R. K. *et al.* High-density genetic linkage maps with over 2,400 sequence-anchored DArT markers for genetic dissection in an F2 pseudo-backcross of *Eucalyptus grandis* × *E. urophylla*. *Tree Genet. Genomes* **8**, 163–175 (2012).
- Petrol, C. D. *et al.* Genomic characterization of DArT markers based on high-density linkage analysis and physical mapping to the *Eucalyptus* genome. *PLoS ONE* **7**, e44684 (2012).
- Wang, H. *et al.* Rosid radiation and the rapid rise of angiosperm-dominated forests. *Proc. Natl Acad. Sci. USA* **106**, 3853–3858 (2009).
- D'Hont, A. *et al.* The banana (*Musa acuminata*) genome and the evolution of monocotyledonous plants. *Nature* **488**, 213–217 (2012).
- Shulaev, V. *et al.* The genome of woodland strawberry (*Fragaria vesca*). *Nature Genet.* **43**, 109–116 (2011).
- Martin, W., Deusch, O., Stawski, N., Grunheit, N. & Goremykin, V. Chloroplast genome phylogenetics: why we need independent approaches to plant molecular evolution. *Trends Plant Sci.* **10**, 203–209 (2005).
- Jeffroy, O., Brinkmann, H., Delsuc, F. & Philippe, H. Phylogenomics: the beginning of incongruence? *Trends Genet.* **22**, 225–231 (2006).
- Fawcett, J. A., Maere, S. & Van de Peer, Y. Plants with double genomes might have had a better chance to survive the Cretaceous-Tertiary extinction event. *Proc. Natl Acad. Sci. USA* **106**, 5737–5742 (2009).
- Bell, C. D., Soltis, D. E. & Soltis, P. S. The age and diversification of the angiosperms re-visited. *Am. J. Bot.* **97**, 1296–1303 (2010).
- Jaillon, O. *et al.* The grapevine genome sequence suggests ancestral hexaploidization in major angiosperm phyla. *Nature* **449**, 463–467 (2007).
- Hanada, K., Zou, C., Lehti-Shiu, M. D., Shinzaki, K. & Shiu, S. H. Importance of lineage-specific expansion of plant tandem duplicates in the adaptive response to environmental stimuli. *Plant Physiol.* **148**, 993–1003 (2008).
- Freeling, M. Bias in plant gene content following different sorts of duplication: tandem, whole-genome, segmental, or by transposition. *Annu. Rev. Plant Biol.* **60**, 433–453 (2009).
- Hudson, C. J. *et al.* High synteny and colinearity among *Eucalyptus* genomes revealed by high-density comparative genetic mapping. *Tree Genet. Genomes* **8**, 339–352 (2012).
- Grattapaglia, D. & Bradshaw, H. D. Nuclear DNA content of commercially important *Eucalyptus* species and hybrids. *Can. J. For. Res.* **24**, 1074–1078 (1994).
- Brooker, M. I. H. A new classification of the genus *Eucalyptus* L'Her. (Myrtaceae). *Aust. Syst. Bot.* **13**, 79–148 (2000).
- Crisp, M. D., Burrows, G. E., Cook, L. G., Thornhill, A. H. & Bowman, D. M. Flammable biomes dominated by eucalypts originated at the Cretaceous-Palaeogene boundary. *Nature Commun.* **2**, 193 (2011).

22. Ågren, J. A. & Wright, S. I. Co-evolution between transposable elements and their hosts: a major factor in genome size evolution? *Chromosome Res.* **19**, 777–786 (2011).
23. Külheim, C., Hui Yeoh, S., Maintz, J., Foley, W. & Moran, G. Comparative SNP diversity among four *Eucalyptus* species for genes from secondary metabolite biosynthetic pathways. *BMC Genomics* **10**, 452 (2009).
24. Novaes, E. *et al.* High-throughput gene and SNP discovery in *Eucalyptus grandis*, an uncharacterized genome. *BMC Genomics* **9**, 312 (2008).
25. Resende, M. D. *et al.* Genomic selection for growth and wood quality in *Eucalyptus*: capturing the missing heritability and accelerating breeding for complex traits in forest trees. *New Phytol.* **194**, 116–128 (2012).
26. Grattapaglia, D. *et al.* Progress in Myrtaceae genetics and genomics: *Eucalyptus* as the pivotal genus. *Tree Genet. Genomes* **8**, 463–508 (2012).
27. Groover, A. T. What genes make a tree a tree? *Trends Plant Sci.* **10**, 210–214 (2005).
28. Boerjan, W., Ralph, J. & Baucher, M. Lignin biosynthesis. *Annu. Rev. Plant Biol.* **54**, 519–546 (2003).
29. Mizrachi, E., Mansfield, S. D. & Myburg, A. A. Cellulose factories: advancing bioenergy production from forest trees. *New Phytol.* **194**, 54–62 (2012).
30. Scheller, H. V. & Ulvskov, P. Hemicelluloses. *Annu. Rev. Plant Biol.* **61**, 263–289 (2010).
31. Eschler, B. M., Pass, D. M., Willis, R. & Foley, W. J. Distribution of foliar formylated phloroglucinol derivatives amongst *Eucalyptus* species. *Biochem. Syst. Ecol.* **28**, 813–824 (2000).
32. Goodger, J. Q. & Woodrow, I. E. α,β -Unsaturated monoterpene acid glucose esters: structural diversity, bioactivities and functional roles. *Phytochemistry* **72**, 2259–2266 (2011).
33. Petit, R. J. & Hampe, A. Some evolutionary consequences of being a tree. *Annu. Rev. Ecol. Syst.* **37**, 187–214 (2006).
34. Lee, J. & Lee, I. Regulation and function of SOC1, a flowering pathway integrator. *J. Exp. Bot.* **61**, 2247–2254 (2010).
35. House, S. M. Reproductive biology of eucalypts. in *Eucalypt Ecology: Individuals to Ecosystems* (ed. Woinarski, J.) 30–56 (Cambridge Univ. Press, 1997).
36. Jaffe, D. B. *et al.* Whole-genome sequence assembly for mammalian genomes: Arachne 2. *Genome Res.* **13**, 91–96 (2003).
37. Haas, B. J. *et al.* Improving the *Arabidopsis* genome annotation using maximal transcript alignment assemblies. *Nucleic Acids Res.* **31**, 5654–5666 (2003).
38. Remm, M., Storm, C. E. & Sonnhammer, E. L. Automatic clustering of orthologs and in-paralogs from pairwise species comparisons. *J. Mol. Biol.* **314**, 1041–1052 (2001).
39. Östlund, G. *et al.* InParanoid 7: new algorithms and tools for eukaryotic orthology analysis. *Nucleic Acids Res.* **38**, D196–D203 (2010).
40. Hunter, S. *et al.* InterPro: the integrative protein signature database. *Nucleic Acids Res.* **37**, D211–D215 (2009).
41. Bendtsen, J. D., Nielsen, H., von Heijne, G. & Brunak, S. Improved prediction of signal peptides: SignalP 3.0. *J. Mol. Biol.* **340**, 783–795 (2004).
42. Small, I., Peeters, N., Legeai, F. & Lurin, C. Predotar: A tool for rapidly screening proteomes for N-terminal targeting sequences. *Proteomics* **4**, 1581–1590 (2004).
43. Sonnhammer, E. L., von Heijne, G. & Krogh, A. A hidden Markov model for predicting transmembrane helices in protein sequences. *Proc. Int. Conf. Intell. Syst. Mol. Biol.* **6**, 175–182 (1998).
44. Stamatakis, A. RAxML-VI-HPC: maximum likelihood-based phylogenetic analyses with thousands of taxa and mixed models. *Bioinformatics* **22**, 2688–2690 (2006).
45. Salse, J., Abrouk, M., Murat, F., Quraishi, U. M. & Feuillet, C. Improved criteria and comparative genomics tool provide new insights into grass paleogenomics. *Brief. Bioinform.* **10**, 619–630 (2009).
46. Salse, J. *et al.* Reconstruction of monocotyledonous proto-chromosomes reveals faster evolution in plants than in animals. *Proc. Natl Acad. Sci. USA* **106**, 14908–14913 (2009).
47. Frazer, K. A., Pachter, L., Poliakov, A., Rubin, E. M. & Dubchak, I. VISTA: computational tools for comparative genomics. *Nucleic Acids Res.* **32**, W273–W279 (2004).
48. Dubchak, I., Poliakov, A., Kislyuk, A. & Brudno, M. Multiple whole-genome alignments without a reference organism. *Genome Res.* **19**, 682–689 (2009).
49. Salse, J. *In silico* archeogenomics unveils modern plant genome organisation, regulation and evolution. *Curr. Opin. Plant Biol.* **15**, 122–130 (2012).
50. Trapnell, C. *et al.* Transcript assembly and quantification by RNA-Seq reveals unannotated transcripts and isoform switching during cell differentiation. *Nature Biotechnol.* **28**, 511–515 (2010).

Supplementary Information is available in the online version of the paper.

Acknowledgements The work conducted by the US Department of Energy Joint Genome Institute is supported by the Office of Science of the US Department of Energy under Contract No. DE-AC02-05CH11231. The research and writing of the manuscript was supported, in part, by the Office of Biological and Environmental Research in the US Department of Energy Office of Science under contract DE-AC05-00OR22725 as part of the US DOE Bioenergy Center. Funding for additional components of the study was provided by the Brazilian Ministry of Science, Technology and Innovation (MCTI) through its research funding agencies (CNPq and FINEP), the Brazilian Federal District Research Foundation (FAP-DF), the public-private Genolyptus network of Brazilian forestry companies, the Tree Biosafety and Genomics Research Cooperative (TBGRC, Oregon State University), South African forestry companies Sappi and Mondi, the Technology and Human Resources for Industry Programme (THRIP, UID 80118), the South African Department of Science and Technology (DST) and National Research Foundation (NRF, UID 18312 and 86936), the Laboratoire d'Excellence (LABEX TULIP ANR-10-LABX-41), the Agence Nationale pour la Recherche (Project Tree For Jolies ANR-2010-KBBE-007-01; Fundação para a Ciência e Tecnologia (FCT, P-KBBE/AGR/GPL/0001/2010), the Centre National pour la Recherche Scientifique (CNRS), the University Paul Sabatier Toulouse III (UPS). Part of this work was carried out using the Stevin Supercomputer Infrastructure at Ghent University, funded by Ghent University, the Hercules Foundation, and the Flemish Government-department EWI. We also acknowledge S. Oda and E. Gonzalez of Suzano Paper and Pulp for providing genetic material of *E. grandis* genotypes BRASUZI, G7J1, M35D2 and their progeny used for genome sequencing and resequencing, Forestal Mininco (Chile) for genetic material of X46, the *E. globulus* genotype used for genome resequencing, M. Hinchee and W. Rottmann of ArborGen for EST sequences used to support gene annotation, Sappi (South Africa) for genetic material of the population used for genetic linkage mapping, and Sappi and Mondi (South Africa) for *E. grandis* tissues used for RNA sequencing. We acknowledge M. O'Neill of the University of Pretoria for technical assistance with *E. grandis* RNA sequencing.

Author Contributions A.A.M., D.G. and G.A.T. are the lead investigators and contributed equally to the work. J.Sc., J.J., J.G., R.D.H., D.M.G., I.D., A.P., U.H., D.S.R., E.L., H.T., D.B. and K.B. contributed to the assembly, annotation and sequence analysis, S.H.B., D.K. and D.G. to BAC library construction, G.P., S.H.B., M.R.P., D.A.F. and D.G. to various parts of biological sample collection, preparation and quality control, U.H., K.V., L.S., Y.V.d.P., F.M. and J.Sa. to genome duplication analyses, D.M.G., P.J. and J.E. to gene family clustering, U.H., P.J., J.E., A.L., A.E.B. and J.W.S. to green plant phylogeny, R.D.H., D.M.G., P.J., S.N. and R.R. to InterPro and Gene Ontology based functional annotation, X.Y., C.-Y.Y., T.L., T.J.T., M.R.P. and G.J.P. to non-coding RNA analyses, I.v.J., E.M., F.J. and A.A.M. to 5' UTR analysis, M.R., E.M., C.A.H., K.V.d.M., F.J. and A.A.M. to RNA sequencing and expression profiling, A.R.K., E.B.-B., E.M. and A.A.M. to protein domain and arrangement analysis, D.A.S., J.T., P.R. and A.S. to *E. globulus* genome resequencing and analysis, U.H., M.S., V.C., H.S.C., J.P., J.G.-P. and G.J.P. to tandem duplicate analysis, K.V., V.A., P.D., C.S., C.A.H., E.R., M.R., A.A.M., S.H.S., R.C.J. and M.A.-F. to MADS box analyses, E.M., D.P., P.J., F.J. and A.A.M. to cellulose, xylan and CAzyme analysis, V.C., J.P., C.D., E.M., A.A.M. and J.G.-P. to lignin biosynthesis genes analysis, J.G.-P., S.G.H., C.A.H., M.S., N.S., H.C.-W., H.S.C., J.T. and P.R. to NAC and MYB analysis, C.K., P.J. and W.F. to terpene synthase gene family analysis, G.J.P. and R.C.T. to transposable elements analysis, U.H., A.R.K.K., C.P.S., C.D.P., D.A.F., O.B.S.-J., D.G. and A.A.M. to genetic mapping, U.H., D.A.F., M.R.P., P.S. and D.G. to genetic load and heterozygosity analysis, and S.N. and P.J. to SDRK gene family analysis. B.M.P., D.A.S., R.E.V. and M.B. contributed to taxonomic and biological background text. G.A.T. headed and K.B. managed the sequencing project. D.S.R. coordinated the bioinformatics activities, A.A.M., D.G. and G.A.T. wrote and edited most of the manuscript. All authors read and commented on the manuscript.

Author Information The *E. grandis* whole-genome sequences are deposited in GenBank under accession number AUSX00000000. A genome browser and further information on the project are available at <http://www.phytozome.net/eucalyptus.php>. Reprints and permissions information is available at www.nature.com/reprints. The authors declare no competing financial interests. Readers are welcome to comment on the online version of the paper. Correspondence and requests for materials should be addressed to A.A.M. (zander.myburg@up.ac.za).



This work is licensed under a Creative Commons Attribution-NonCommercial-ShareAlike 3.0 Unported licence. The images or other third party material in this article are included in the article's Creative Commons licence, unless indicated otherwise in the credit line; if the material is not included under the Creative Commons licence, users will need to obtain permission from the licence holder to reproduce the material. To view a copy of this licence, visit <http://creativecommons.org/licenses/by-nc-sa/3.0>

METHODS

Whole-genome shotgun sequencing and assembly. All sequencing reads were collected with standard Sanger sequencing protocols on ABI 3730XL automated sequencers at the Joint Genome Institute, Walnut Creek, CA. Three different sized libraries were used for the plasmid subclone sequencing process and paired-end sequencing. A total of 3,446,208 reads from the 2.6-kb sized libraries, 3,479,232 reads from the 6.0-kb sized libraries and 518,016 reads from a 36.2–40.6-kb library were sequenced. Two BAC libraries (EG_Ba, 127.5-kb insert and EG_Bb, 155.0-kb insert) were end sequenced to add an additional 294,912 reads for long-range linking.

The sequence reads were assembled using a modified version of Arachne v.20071016 (ref. 36) with parameters `maxcliq1 = 100`, `correct1_passes = 0`, `n_haplotypes = 2` and `BINGE_AND_PURGE = True`. The resulting output was then passed through Rebuilder and SquashOverlaps with parameters to merge adjacent assembled alternative haplotypes and subsequently run through another complete Arachne assembly process to finalize the assembly. This produced 6,043 scaffold sequences, with a scaffold L50 of 4.9 Mb and total scaffold size of 692.7 Mb. Scaffolds were screened against bacterial proteins, organelle sequences, GenBank nr and were removed if found to be a contaminant. Additional scaffolds were removed if they (1) consisted of >95% of base pairs that occurred as 24mers four other times in the scaffolds larger than 50 kb; (2) contained a majority of unanchored RNA sequences; or (3) were less than 1 kb in length.

For chromosome-scale pseudomolecule construction, markers from the genetic map were placed using two methods. SSR-based markers were placed using three successive rounds of e-PCR with $N = 0$, $N = 1$ and $N = 3$. Markers that had sequence associated with them, including SNP markers, were placed with BLAT⁵¹ and blastn⁵². A total of 19 breaks (16 in high coverage (>6x), 3 in low coverage (≤6x)) were made in scaffolds based on linkage group discontinuity; a subset of the broken scaffolds were combined using 257 joins to form the 11 pseudomolecule chromosomes. Map joins were denoted with 10,000 repeats of the letter N (Ns). The pseudomolecules contained 605.9 Mb out of 691.3 Mb (88%) of the assembled sequence. The final assembly contains 4,952 scaffolds with a contig L50 of 67.2 kb and a scaffold L50 of 53.9 Mb. The completeness of the resulting assembly was estimated using 1,007,962 ESTs from BRASUZI. The goal of this analysis was to obtain an estimate of the completeness of the assembly, rather than to do a comprehensive examination of gene space. Briefly, ESTs <300 bp were removed, along with chloroplast, mitochondrial or rDNA ESTs. All duplicate ESTs were placed against the genome using BLAT⁵¹. The remaining ESTs were screened for alignments that had ≥90% identity and ≥85% EST coverage. The screened alignments indicated that 98.98% of available expressed gene loci were included in the 11 chromosome assemblies.

Gene prediction. To produce the current gene set, we used the homology-based FgenesH and GenomeScan predictions. The best gene prediction at each locus was selected and integrated with EST assemblies using the PASA program³⁷. The gene set shown in the browser was generated from the input gene models at JGI. The gene prediction pipeline was structured as follows: peptides from diverse angiosperms and ~260,000 EST assemblies (from ~2.9 M filtered *E. grandis* ESTs and ~2.4 M EST sequences from other closely related ("sister") *Eucalyptus* species, assembled with PASA) were aligned to the genome and their overlaps used to define putative protein-coding gene loci. The corresponding genomic regions were extended by 1 kb in each direction and submitted to FgenesH and GenomeScan, along with related angiosperm peptides and/or ORFs from the overlapping EST assemblies. These two sets of predictions were integrated with expressed sequence information using PASA³⁷ against ~260,000 *Eucalyptus* EST assemblies. The results were filtered to remove genes identified as transposon-related.

Gene family cluster and gene ontology analysis. The Inparanoid algorithm^{38,39} was used to identify orthologous and paralogous genes that arose through duplication events. Clusters were determined using a reciprocal best pair match and then an algorithm for adding in-paralogues was applied. The peptide sequences used were from *Arabidopsis lyrata*, *Arabidopsis thaliana*, *Brachypodium distachyon*, *Caenorhabditis elegans*, *Chlamydomonas reinhardtii*, *Danio rerio*, *Ectocarpus siliculosus*, *Escherichia coli*, *Eucalyptus grandis*, *Fragaria vesca*, *Glycine max*, *Homo sapiens*, *Jatropha curcas*, *Mus musculus*, *Neurospora crassa*, *Nostoc punctiforme*, *Oryza sativa*, *Phoenix dactylifera*, *Physcomitrella patens*, *Populus trichocarpa*, *Saccharomyces cerevisiae*, *Schizosaccharomyces pombe*, *Selaginella moellendorffii*, *Solanum tuberosum*, *Sorghum bicolor*, *Synechocystis pcc6803*, *Theobroma cacao*, *Vitis vinifera* and *Zea mays*. The sequences were downloaded from Gramene^{53,54}, Phytozome (<http://www.phytozome.net>) and Ensembl (<http://www.ensembl.org>). A functional annotation pipeline similar to the one used for strawberry genome annotation¹⁰ was used to infer Gene Ontology⁵⁵ assignments to 29,841 protein coding genes (~82%). Peptide sequences were analysed through an integrated approach involving Interproscan⁴⁰, SignalP⁴¹, Predotar⁴², TMHMM⁴³ and orthology-based projections from *Arabidopsis*.

Green plant phylogeny. We used an integrated approach of gene orthology clustering⁴⁰ and an automated workflow for phylogenomic analyses⁵⁶ to reconstruct land plant phylogeny of peptide sequences. A total of 174,020 peptides encoded by single-copy

protein coding orthologous nuclear genes from 17 plant genomes (Supplementary Data 7) were identified, aligned and assembled into a supermatrix resulting from conservative and liberal superalignments that retained 42.26% (697,423 amino acids) and 46.35% (764,978 amino acids) of the original 1,650,340 amino acid concatenated alignment for maximum likelihood phylogenetic reconstruction⁴⁴, respectively (Supplementary Data 7). These alignments come from 3268 orthologous gene clusters with each cluster carrying single copy genes from at least 9 (50%) species.

Protein domain analysis. Domains and domain arrangements were compared within the rosids to distinguish a core set of domains and arrangements present in all rosids and those shared by one or more of the four rosid lineages included in the analysis (Supplementary Data 8). Domains occurring at twice the frequency in *Eucalyptus* compared to the average abundance in the rosids were defined as overrepresented. If several splice variants were present for one protein, we excluded all but the longest transcript. All proteomes were scanned for domains with the Pfam_scan utility and HMMER 3.0 against the Pfam-A and Pfam-B databases⁵⁷. For the annotation of Pfam-A domains, we used the model-defined gathering threshold and query sequences were required to match at least 30% of the defining model⁵⁸. Pfam-B domains were annotated using an e-value cutoff of 10^{-3} . When possible, Pfam-A domains were mapped to clans and consecutive stretches of the same domain were collapsed into one large pseudo-domain^{59,60}. We defined domain arrangements as ordered sets of domains for each protein. For the analysis of arrangements, only Pfam-A domains were used.

Genome-wide mRNA expression profiling. To study the expression of predicted protein-coding and ncRNA genes, RNA-seq reads obtained from Illumina sequencing of seven *Eucalyptus* tissues (that is, shoot tips, young leaf, mature leaf, flower, roots, phloem and immature xylem, <http://www.eucgenie.org/>, Hefer *et al.*, unpublished data) were mapped to the *Eucalyptus* genome using TopHat⁶¹ with the Bowtie algorithm⁶² for performing the alignment. The aligned read files were processed by Cufflinks⁵⁰, with RNA-seq fragment counts (that is, fragments per kilobase of exon per million fragments mapped (FPKM)) to measure the relative abundance of transcripts. Differential ncRNA expression between the seven *Eucalyptus* tissues was determined using Cuffdiff⁵⁰.

ncRNA analysis. To predict ncRNAs in *Eucalyptus*, the genome sequence was scanned using Infernal⁶³ with the covariance models (that is, a combination of sequence consensus and RNA secondary structure consensus) of 1,973 RNA families in the RFam database v10.1 (refs 64, 65). The bit score cutoff of the Infernal search was set as the TC cutoff value that was used by RFam curators as the trusted cutoff. The Infernal search result was further filtered by an e-value cutoff of 0.01. To examine the ncRNA conservation between *Eucalyptus* and other plant genomes, the *Eucalyptus* ncRNA candidate sequences obtained from the Infernal search were used as queries to search against the genome sequences listed above using BLAT⁵¹ with a minimum coverage (that is, minimum fraction of query that must be aligned) of 80% and a minimum identity of 60%.

5' UTR empirical curation. Approximately 2.9 million *E. grandis* ESTs and ~700 million RNA-seq reads from seven diverse tissues were used to empirically curate 5' UTR annotations. At each locus, the predicted, EST and RNA-seq derived 5' UTR lengths were compared. An empirical annotation was prioritized over an *in silico* prediction and the longest empirical transcript was preferred. Those loci which had a 5' UTR reported by only FgenesH retained their annotation as the best current annotation.

Genome evolution. We used the *E. grandis* genome sequence information (<http://www.phytozome.net/eucalyptus.php>) to unravel the Myrtales evolutionary palaeo-history leading to the modern *Eucalyptus* genome structure of 11 chromosomes. Independent intraspecific (that is, paralogue) and interspecific (that is, orthologue) comparisons were necessary to infer gene relationships between *Eucalyptus* and the other rosid genomes. We applied a robust and direct approach^{45,46} allowing the characterization of genome duplications by aligning the available genes (36,376) on themselves with stringent alignment criteria and statistical validation.

We used the VISTA pipeline infrastructure^{47,48} for the construction of genome-wide pairwise DNA alignments between *E. grandis* and *Populus trichocarpa*. To align genomes we used a combination of global and local alignment methods. First, we obtained an alignment of large blocks of conserved synteny between the two species by applying Shuffle-LAGAN global chaining algorithm⁶⁶ to local alignments produced by translated BLAT⁵¹. After that we used Supermap, the fully symmetric whole-genome extension to the Shuffle-LAGAN. Then, in each syntenic block we applied Shuffle-LAGAN a second time to obtain a more fine-grained map of small-scale rearrangements such as inversions.

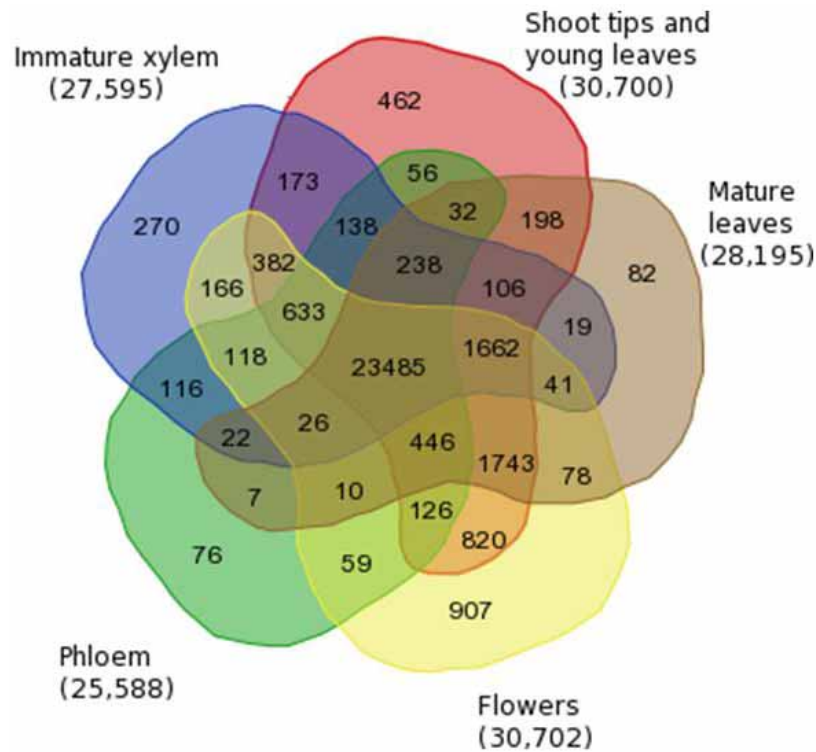
Syntenic regions between *Eucalyptus* chromosome 3 and *Populus* chromosome XVIII were defined as segments of contiguous sequence. Each contiguous block of DNA was annotated and cross-compared between the two species. Gene models within the syntenic blocks were compared based on a sliding window representing 10 gene models with an allowance of two intercalated gene models. Genes occurring in tandem repeats on either the *Eucalyptus* or *Populus* chromosomes were counted as a single locus in either case. The constructed genome-wide pair-wise alignments can

be downloaded from <http://pipeline.lbl.gov/downloads.shtml> and are accessible for browsing and various types of analysis through Phytozome (<http://phytozome.org>).

For comparative analysis of the *E. grandis* and *E. globulus* genomes, enriched nuclei were extracted using a modified BAC library preparation protocol⁶⁷ and DNA extracted following Tibbits *et al.*⁶⁸. DNA was prepared for sequencing using Illumina TruSeq kits and 100-bp paired-end sequencing was performed on a HiSeq2000. NUCLEAR software (Gyde Inc.) was used to filter for high-quality reads that were then mapped to the *E. grandis* genome scaffold assembly. The VISION software was used to visualize assemblies and assembly metrics were computed using custom Perl, R and Shell scripts.

Genome function analysis. Using homology to *Arabidopsis* genes and Pfam domain analysis we identified candidate homologues for lignin, cellulose and xylan biosynthetic genes. All possible family members were identified and their gene expression evaluated in seven developing tissues of *E. grandis* using Illumina RNA-seq analysis. In particular, we analysed each gene's expression relative to other family members/isoforms in xylem, as well as relative to the median (~90,000 FPKM) of xylem expression in the entire transcriptome. Considering each gene's relative and absolute expression levels, all members expressed over median in xylem were noted (Supplementary Data 5 and Supplementary Data 9). Similarly, a search for conserved protein motifs for the terpene synthase gene family was conducted in eight plant genomes, including *E. grandis* (Supplementary Information section 6 and Supplementary Data 6). The amino acid sequences were aligned and truncated to compare homologous sites. A maximum likelihood tree was created, rooted by the split between two major types of terpene synthase genes, and nodes were coloured by species.

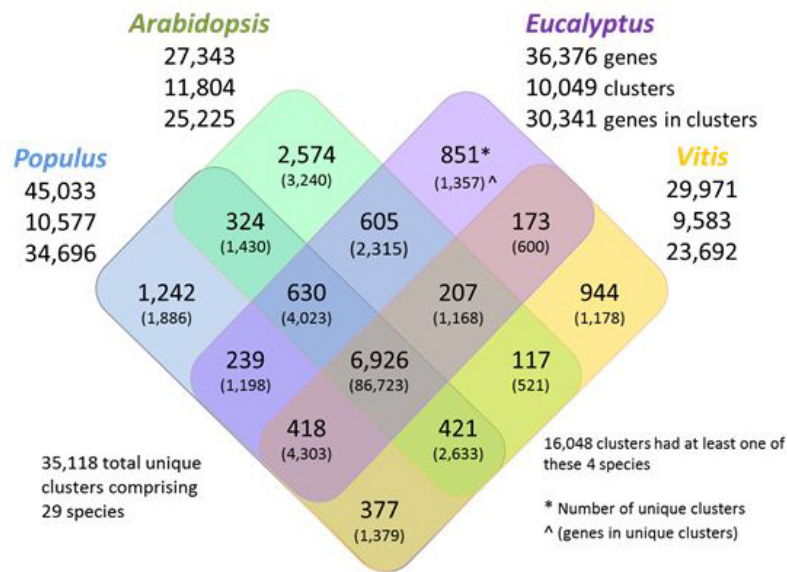
51. Kent, W. J. BLAT—the BLAST-like alignment tool. *Genome Res.* **12**, 656–664 (2002).
52. Altschul, S. F. *et al.* Gapped BLAST and PSI-BLAST: a new generation of protein database search programs. *Nucleic Acids Res.* **25**, 3389–3402 (1997).
53. Youens-Clark, K. *et al.* Gramene database in 2010: updates and extensions. *Nucleic Acids Res.* **39**, D1085–D1094 (2011).
54. Jaiswal, P. Gramene database: a hub for comparative plant genomics. *Methods Mol. Biol.* **678**, 247–275 (2011).
55. Ashburner, M. *et al.* Gene ontology: tool for the unification of biology. The Gene Ontology Consortium. *Nature Genet.* **25**, 25–29 (2000).
56. Robbertse, B., Yoder, R. J., Boyd, A., Reeves, J. & Spatafora, J. W. Hal: an automated pipeline for phylogenetic analyses of genomic data. *PLoS Curr.* **3**, RRN1213 (2011).
57. Finn, R. D., Clements, J. & Eddy, S. R. HMMER web server: interactive sequence similarity searching. *Nucleic Acids Res.* **39**, W29–W37 (2011).
58. Buljan, M., Frankish, A. & Bateman, A. Quantifying the mechanisms of domain gain in animal proteins. *Genome Biol. Evol.* **11**, R74 (2010).
59. Ekman, D., Bjorklund, A. K., Frey-Skott, J. & Elovsson, A. Multi-domain proteins in the three kingdoms of life: orphan domains and other unassigned regions. *J. Mol. Biol.* **348**, 231–243 (2005).
60. Forslund, K., Henricson, A., Hollich, V. & Sonnhammer, E. L. Domain tree-based analysis of protein architecture evolution. *Mol. Biol. Evol.* **25**, 254–264 (2008).
61. Trapnell, C., Pachter, L. & Salzberg, S. L. TopHat: discovering splice junctions with RNA-Seq. *Bioinformatics* **25**, 1105–1111 (2009).
62. Langmead, B., Trapnell, C., Pop, M. & Salzberg, S. L. Ultrafast and memory-efficient alignment of short DNA sequences to the human genome. *Genome Biol.* **10**, R25 (2009).
63. Nawrocki, E. P., Kolbe, D. L. & Eddy, S. R. Infernal 1.0: inference of RNA alignments. *Bioinformatics* **25**, 1335–1337 (2009).
64. Griffiths-Jones, S., Bateman, A., Marshall, M., Khanna, A. & Eddy, S. R. Rfam: an RNA family database. *Nucleic Acids Res.* **31**, 439–441 (2003).
65. Gardner, P. P. *et al.* Rfam: Wikipedia, clans and the “decimal” release. *Nucleic Acids Res.* **39**, D141–D145 (2011).
66. Brudno, M. *et al.* LAGAN and Multi-LAGAN: efficient tools for large-scale multiple alignment of genomic DNA. *Genome Res.* **13**, 721–731 (2003).
67. Peterson, D. G., Kevin, S. & Stephen, M. Isolation of milligram quantities of nuclear DNA from tomato (*Lycopersicon esculentum*), a plant containing high levels of polyphenolic compounds. *Plant Mol. Biol. Rep.* **15**, 148–153 (1997).
68. Tibbits, J. F. G., McManus, L. J., Spokevicius, A. V. & Bossinger, G. A rapid method for tissue collection and high-throughput isolation of genomic DNA from mature trees. *Plant Mol. Biol. Rep.* **24**, 81–91 (2006).
69. Katoh, K., Misawa, K., Kuma, K. & Miyata, T. MAFFT: a novel method for rapid multiple sequence alignment based on fast Fourier transform. *Nucleic Acids Res.* **30**, 3059–3066 (2002).
70. Tamura, K., Dudley, J., Nei, M. & Kumar, S. MEGA4: Molecular evolutionary genetics analysis (MEGA) software version 4.0. *Mol. Biol. Evol.* **24**, 1596–1599 (2007).



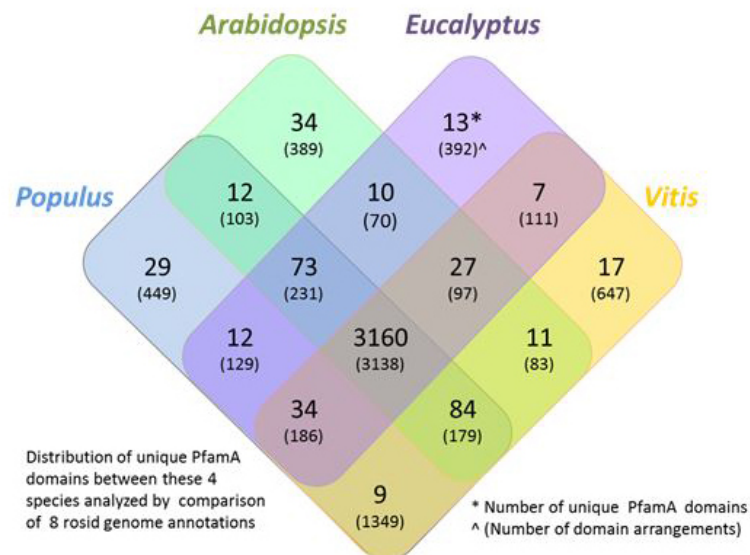
Extended Data Figure 1 | RNA-seq-based expression evidence for predicted *Eucalyptus grandis* gene models. Gene expression was assessed with Illumina RNA-seq analysis (240 million RNA sequences from six tissues, mapped to 36,376 *E. grandis* genes, V1.1 annotation). Genes were counted as expressed in a tissue if a minimum of FPKM = 1.0 was observed in the tissue. A total of 23,485

gene models (64.6%) were detected in all six tissues compared here and 32,697 (89.9%) in at least one of the six tissues. Expression profiles for individual genes are accessible in the *Eucalyptus* Genome Integrative Explorer (EucGenIE, <http://www.eucgenie.org/>).

a Gene Family Clusters Across Tree of Life

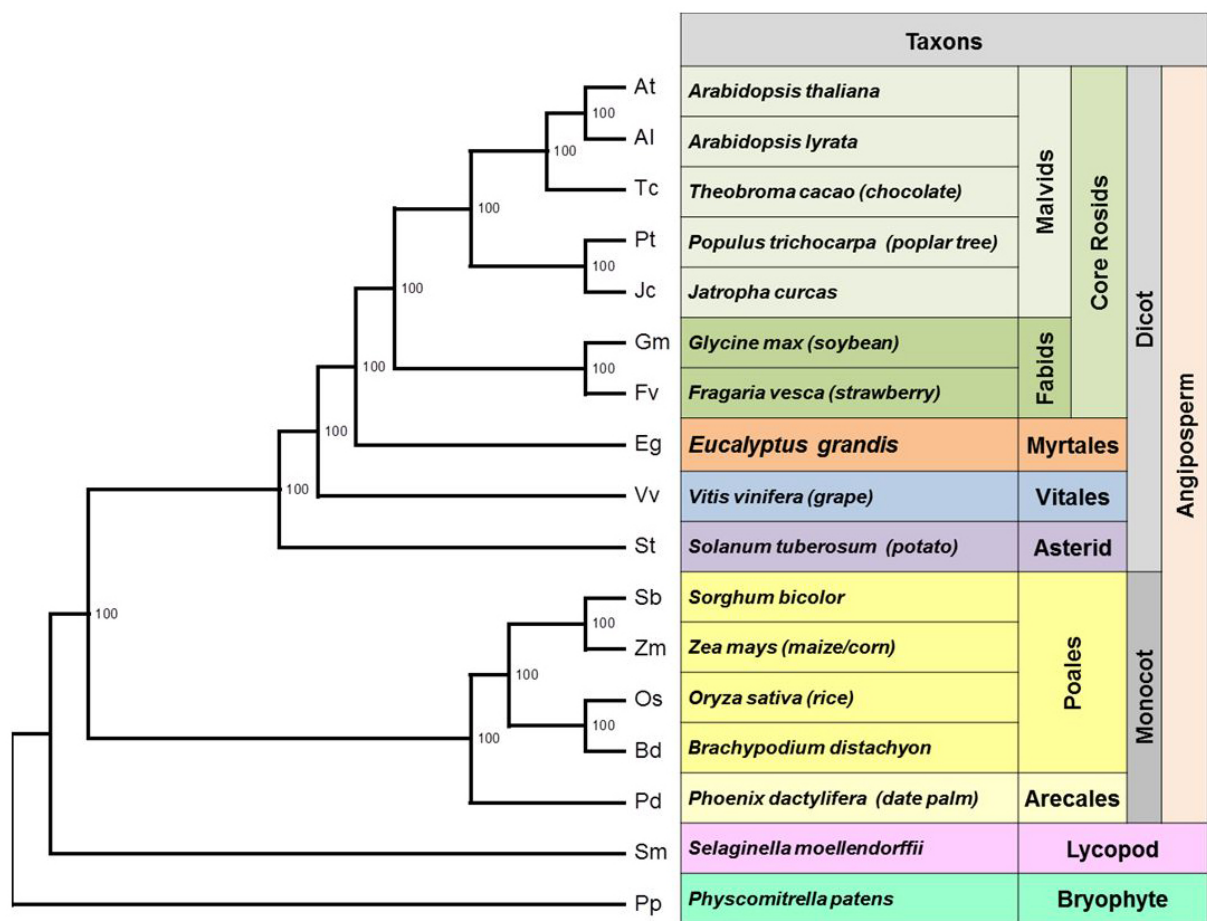


b PfamA Domain and Arrangements



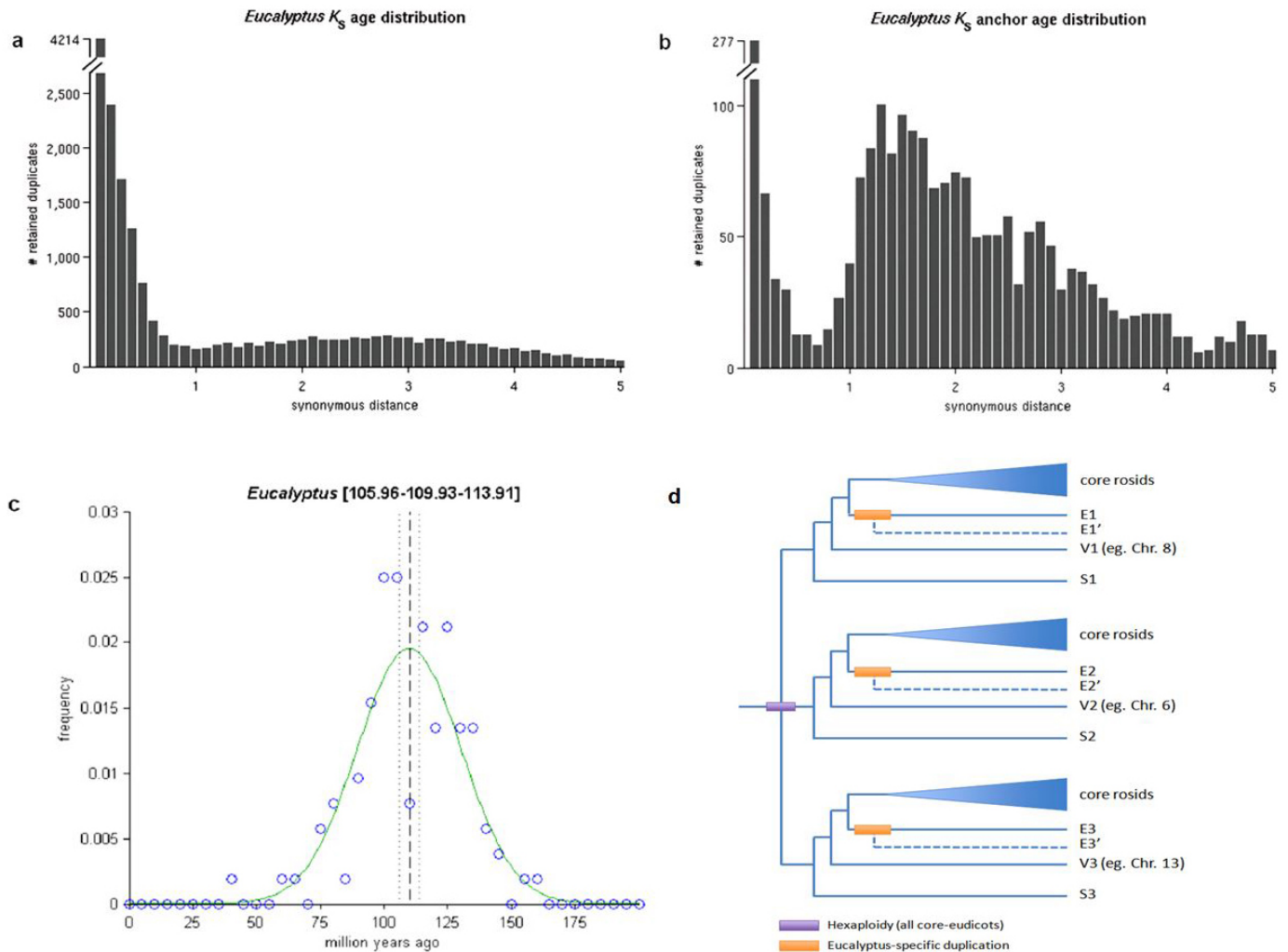
Extended Data Figure 2 | Sharing of protein-coding gene families, protein domains and domain arrangements in *Eucalyptus*, *Arabidopsis*, *Populus* and *Vitis*. **a**, The four rosids lineages have a total of 16,048 protein coding gene clusters (from a total of 35,118 identified in 29 sequenced genomes; see Methods and Supplementary Information section 3) of which a core set of 6,926 clusters are shared among all four lineages. Of the 36,376 high-confidence annotated gene models in *E. grandis*, 30,341 (84%) are included in 10,049

clusters. *E. grandis* has 851 unique gene clusters (that is, not shared with any of the three other rosids genomes, but shared with at least one other of the 29 genomes). **b**, A total of 3,160 Pfam A domains are shared among the four rosids lineages, the majority of which are single-domain arrangements (3,138 shared among the four lineages). Thirteen PfamA domains were only detected in *Eucalyptus* and 392 domain arrangements are specific to *Eucalyptus* in this four-way comparison.



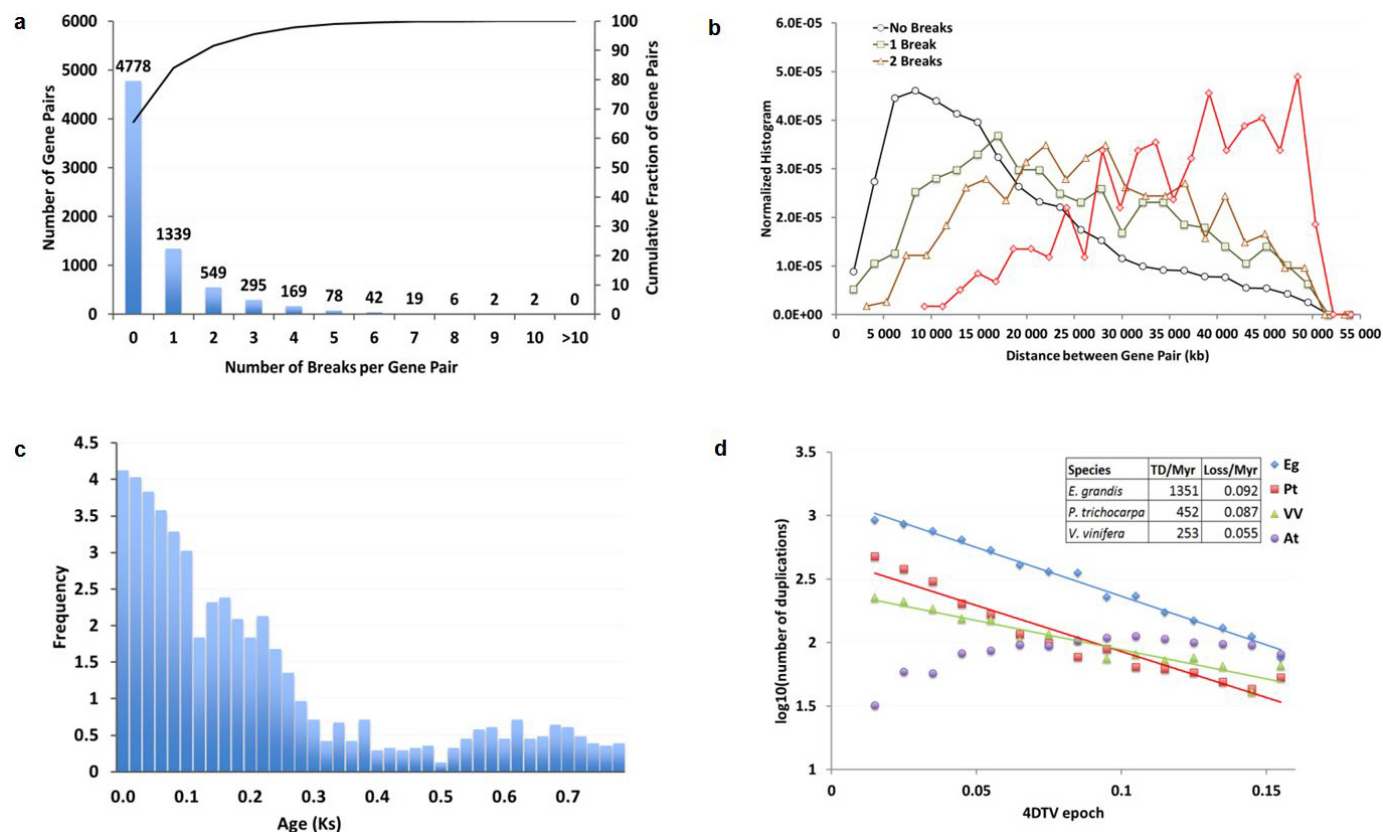
Extended Data Figure 3 | Green plant phylogeny based on shared gene clusters from 17 sequenced plant genomes. The phylogenetic tree was generated by RAxML analysis including at least one protein from at least half of the species per protein cluster in a concatenated MUSCLE alignment adjusted by Gblocks with liberal settings (Supplementary Data 7). The corresponding

bootstrap partitions are provided at each node. The tree was rooted with *Physcomitrella* (a moss) as outgroup. The Myrtales lineage represented by *Eucalyptus grandis* is supported as sister to fabids and malvids (core rosid) clades together with the basal rosid lineage Vitales, whereas *Populus trichocarpa* (Malpighiales) is grouped with malvids.



Extended Data Figure 4 | Dating of the *Eucalyptus* lineage-specific whole-genome duplication event. **a**, *Eucalyptus* K_s whole-paranome (the set of all duplicate genes in the genome) age distribution. On the x axis the K_s is plotted (bin size of 0.1); on the y axis the number of retained duplicate paralogous gene pairs is plotted. **b**, *Eucalyptus* K_s anchor age distribution. On the x axis the K_s is plotted (bin size of 0.1); on the y axis the number of retained duplicate anchors is plotted. Anchors falling within the K_s range of 0.8–1.5 were used for absolute dating. **c**, *Eucalyptus* absolute dated anchors from the most recent WGD. The smooth green curve represents the maximum likelihood normal fit of dated anchors derived from the most recent WGD in *Eucalyptus*, whereas the blue dots represent a histogram of the raw data. The dashed line indicates

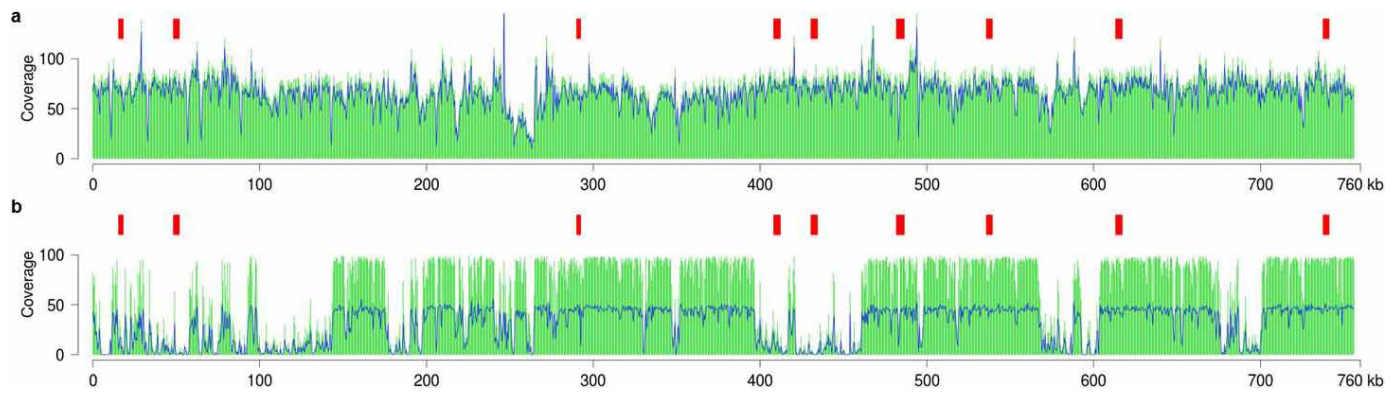
the ML estimate of the distribution mode, whereas the dotted lines delimit the corresponding 95% confidence intervals. The mode of dated anchors is estimated at 109.93 Myr ago with its lower and upper 95% boundaries at 105.96 and 113.91 Myr ago, respectively. **d**, Genome duplication pattern in the core eudicot (rosid and asterid) ancestor and lineages leading to *Solanum* (asterid), *Vitis* and *Eucalyptus* (basal rosids) and the core rosids. The three *Eucalyptus* (E1–E3), *Vitis* (V1–V3) and *Solanum* (S1–S3) orthologues were generated by the shared hexaploidy event (purple box, ~130 to 150 Myr ago) and an additional set of *Eucalyptus* orthologues (E1'–E3') were created in the lineage-specific WGD (orange boxes, ~110 Myr ago).



Extended Data Figure 5 | Genome-wide analysis of tandem gene assemblies.

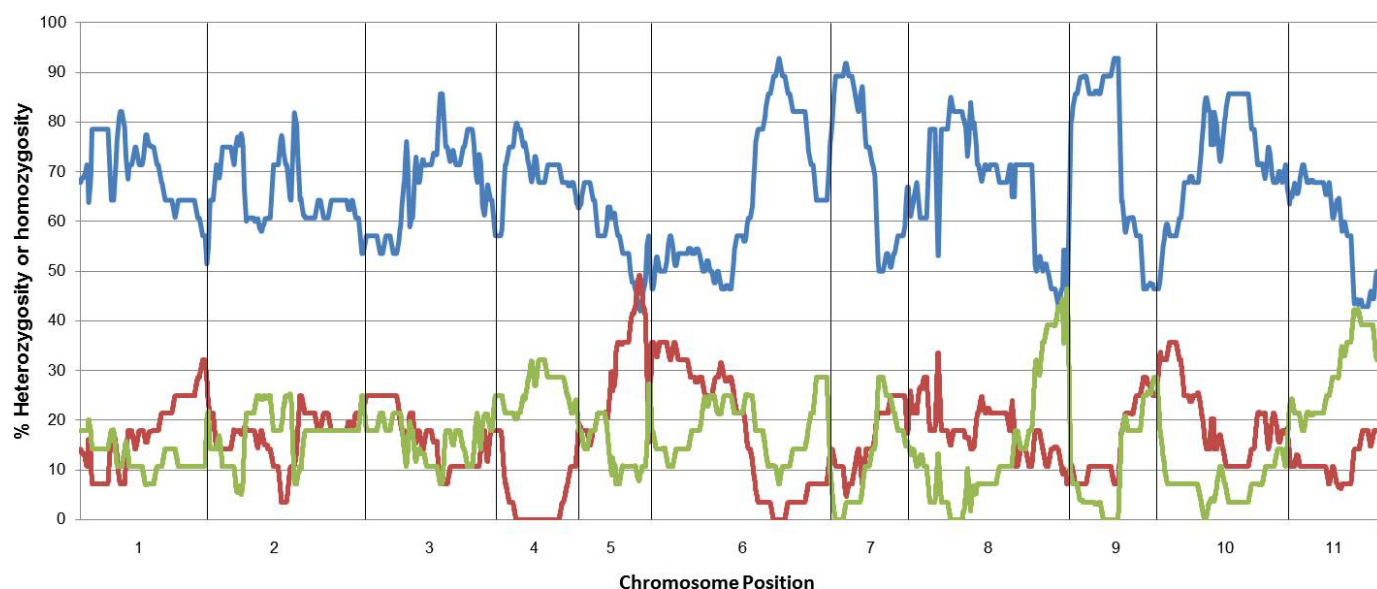
The number and distribution of contig breaks was evaluated for pairs of tandem genes (located within 50 kb of each other). **a**, Distribution of the number of contig breaks between gene pairs (blue bars) and cumulative proportion of gene pairs separated by contig breaks (black line). **b**, Distribution of the number of contig breaks per separation distance showing that the number of breaks is positively correlated with separation distance. The red line shows the distribution of distance between gene pairs with three or more contig breaks. **c**, Distribution of K_s divergence of tandem gene pairs in clusters with exactly

two tandem genes showing a gradient of similarity (that is, age of duplication) expected for authentic tandem gene pairs. **d**, Rate of tandem gene duplication (TD) and gene loss in *Eucalyptus grandis* (Eg), *Populus trichocarpa* (Pt), *Vitis vinifera* (Vv) and *Arabidopsis thaliana* (At). All of the rosoid genomes (except *Arabidopsis*) exhibit constant rates of tandem duplication and loss. The rate of tandem gene duplication in *Eucalyptus* has been stable and consistently higher than in *Populus* and *Vitis*. 1 Myr \sim 0.0026 transversions at fourfold degenerate sites, consistent with *Populus* and *Eucalyptus* having diverged \sim 100 Myr ago.



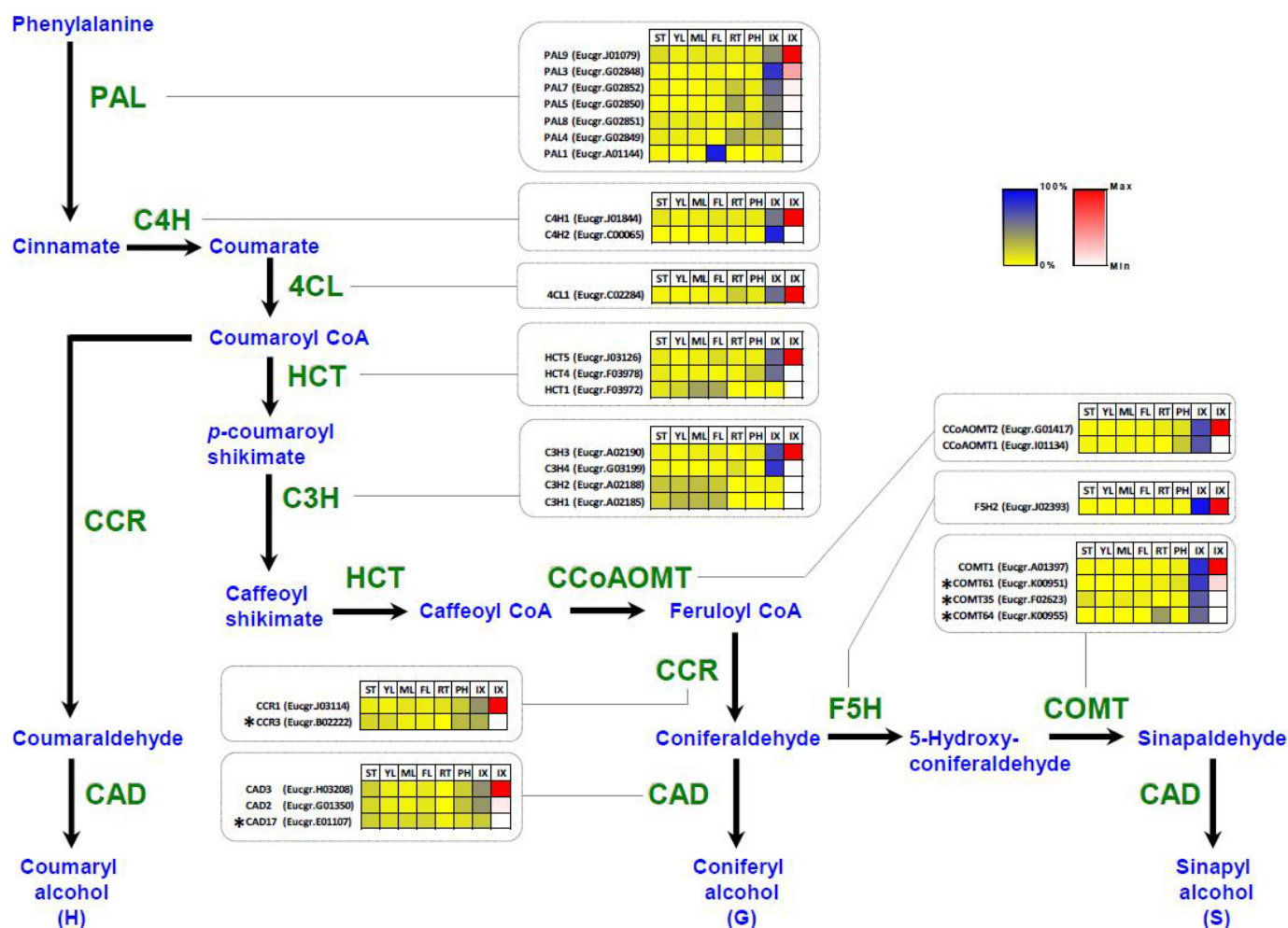
Extended Data Figure 6 | Illumina PE100 read coverage of the ~760-kb region containing a R2R3-MYB tandem gene array. Illumina PE100 reads generated from BRASUZ1 (*E. grandis*) and X46 (*E. globulus*) were aligned to the *E. grandis* (BRASUZ1, V1.0) genome assembly, and insert (green bars) and sequence (blue line) coverage investigated for the ~760-kb region including a R2R3-MYB tandem array (details in Supplementary Data 3) in the *E. grandis* genome assembly. **a**, Read coverage profile of the BRASUZ1 reads mapped

to the region showing 1× relative coverage across all nine of the tandem duplicates (red blocks) in the region, and **b**, X46 (*E. globulus*) reads mapped to the region showing 1× relative coverage on approximately half of the region with some tandem duplicates apparently absent from the *E. globulus* genome. Note that insert coverage (green bars) is relatively higher for *E. globulus* (X46, panel **b**) due to the larger insert size of the genomic library sequenced for X46 (~300 bp) than for BRASUZ1 (~150 bp).



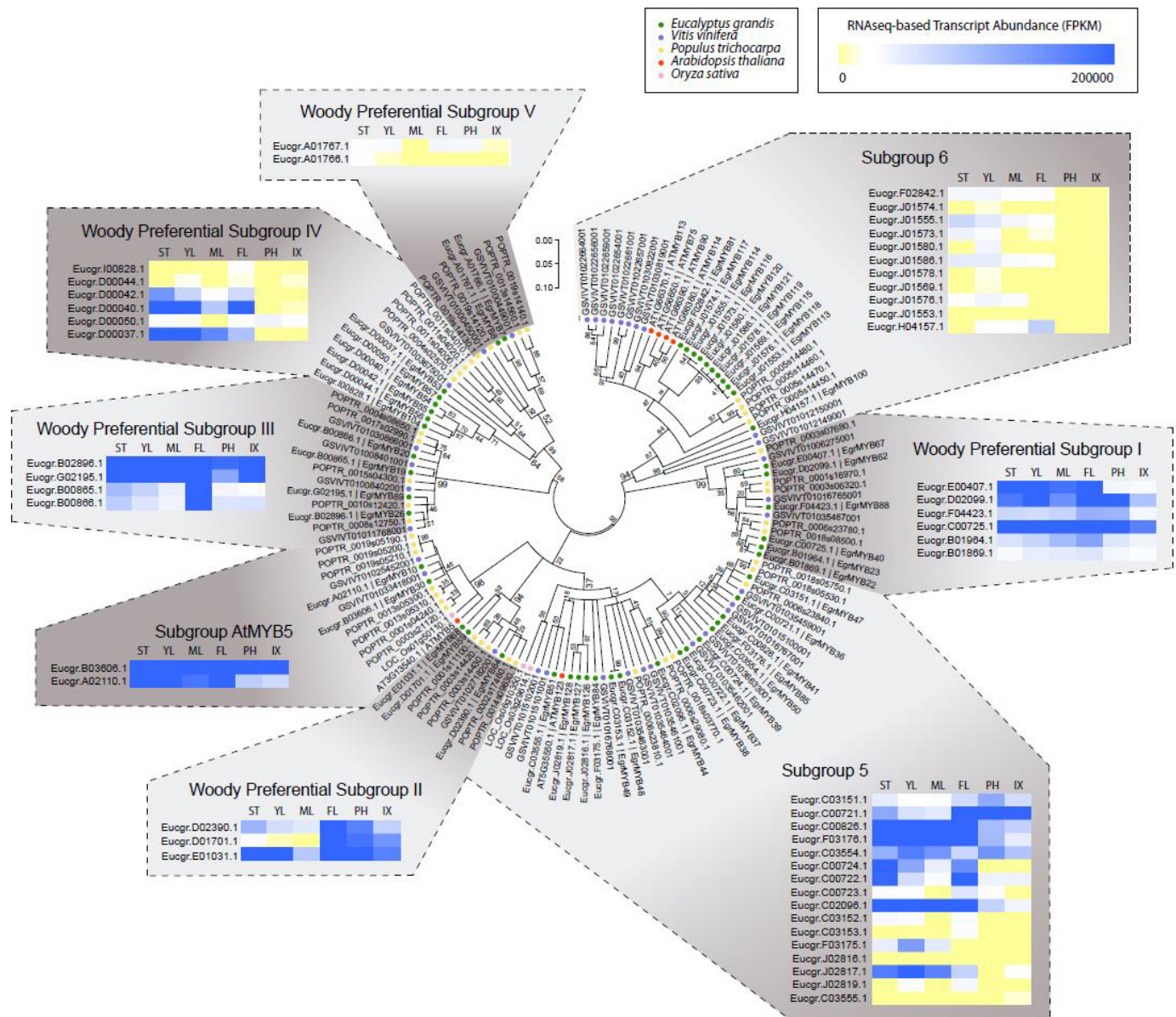
Extended Data Figure 7 | Alternative homozygous classes observed in the 28 M35D2 siblings as a function of position on chromosomes 1–11. Several peaks of conserved heterozygosity (peaks $>80\%$) are seen on all chromosomes except 5 and 11. A region of 25 Mb on chromosome 4 from 11 to 36 Mb is completely devoid of homozygous versions of one of the alleles (red line), but has roughly 25–32% of the siblings homozygous for the other allele (green line) and the rest heterozygous in a roughly 1:4 ratio. The blue line is the total

proportion of siblings out of 28 that are heterozygous in the region. One would expect 50% under the null model, but almost the entire chromosome is biased towards heterozygosity. In several other regions (for example, chromosomes 6, 7, 9 and 10) both homozygous classes are depleted, suggesting the presence of genetic load at different loci along the two parental homologues and explaining the strong selection for heterozygosity in such regions.



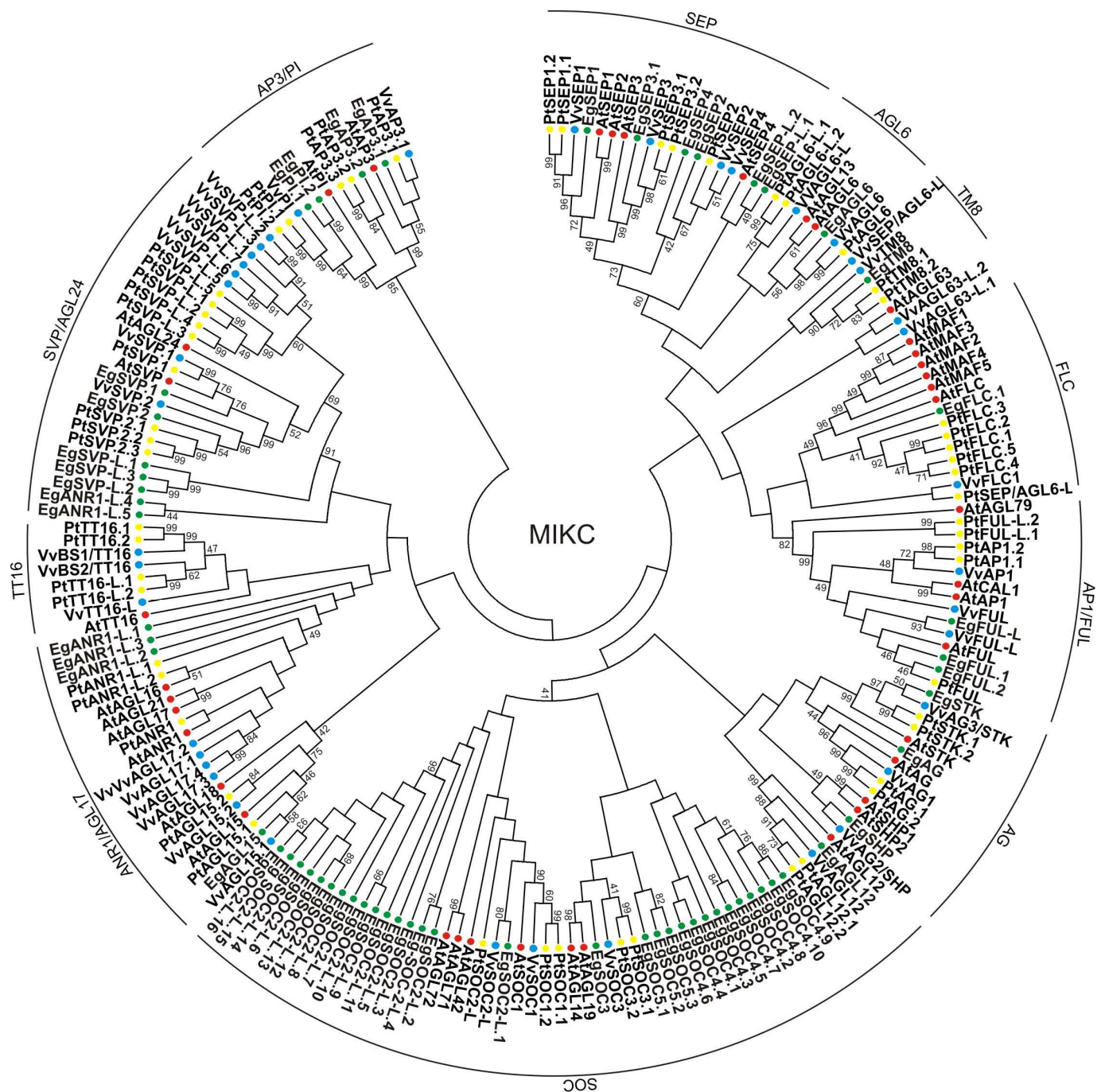
Extended Data Figure 8 | Genes involved in lignin biosynthesis in woody tissues of *Eucalyptus*. Relative (yellow–blue scale) and absolute (white–red scale) expression profiles of secondary cell-wall-related genes implicated in lignin biosynthesis. Detailed gene annotation and mRNA-seq expression data are provided in Supplementary Data 9. Five novel *Eucalyptus* candidates that

have not previously been associated with lignification are indicated by asterisks (Carocha *et al.*, unpublished data). ST, shoot tips; YL, young leaves; ML, mature leaves; FL, floral buds; RT, roots; PH, phloem; IX, immature xylem. Absolute expression level (FPKM⁵⁰) is only shown for immature xylem.



Extended Data Figure 9 | Phylogenetic tree of R2R3 MYB sequences from subgroups expanded and/or preferentially found in woody species. A total of 133 amino acid sequences from *Eucalyptus grandis* (50), *Vitis vinifera* (34), *Populus trichocarpa* (40), *Arabidopsis thaliana* (6) and *Oryza sativa* (3) corresponding to three woody-expanded (subgroups 5, 6 and AtMYB5 based on *Arabidopsis* classification) and five woody-preferential subgroups (I through V). The latter do not contain any *Arabidopsis* nor *Oryza* sequences. Sequences were aligned using MAFFT with the FFT-NS-i algorithm⁶⁹ (Supplementary Data 10). Evolutionary history was inferred constructing a Neighbour-joining tree with 1,000 bootstrap replicates (bootstrap support is shown next to branches) using MEGA5 (ref. 70). The evolutionary distances

were computed using the Jones-Taylor-Thornton substitution model and the rate variation among sites was modelled with a gamma distribution of 1. Positions containing gaps and missing data were not considered in the analysis. The tree is drawn to scale, with branch lengths in the same units as those of the evolutionary distances used to infer the phylogenetic tree. RNA-seq-based relative transcript abundance data for six different tissues, expressed in FPKM values (fragments per kilobase of exon per million fragments mapped), are shown for each *Eucalyptus* gene next to each subgroup. ST, shoot tips; YL, young leaves; ML, mature leaves; FL, flowers; PH, phloem; and IX, immature xylem.



Extended Data Figure 10 | Phylogenetic tree of type II MIKC MADS box proteins. Neighbour-joining consensus tree of the type II MIKC sub-clade using protein sequences from *Eucalyptus grandis*, *Arabidopsis thaliana*, *Populus trichocarpa* and *Vitis vinifera* (Supplementary Data 11). Bootstrap values from 1,000 replicates were used to assess the robustness of the tree.

Bootstrap values lower than 40% were removed from the tree. *Eucalyptus* genes are denoted with green dots, *Arabidopsis* genes with red dots, *Populus* genes with yellow dots and *Vitis* genes with blue dots. The gene model numbers from *Populus* and *Vitis* were abbreviated to better fit in the figure (*P. trichocarpa*, Pt; *V. vinifera*, Vv).

Single-cell RNA-seq reveals dynamic paracrine control of cellular variation

Alex K. Shalek^{1,2,3*}, Rahul Satija^{3*}, Joe Shuga^{4*}, John J. Trombetta³, Dave Gennert³, Diana Lu³, Peilin Chen⁴, Rona S. Gertner^{1,2}, Jellert T. Gaublotme^{1,2}, Nir Yosef³, Schraga Schwartz³, Brian Fowler⁴, Suzanne Weaver⁴, Jing Wang⁴, Xiaohui Wang⁴, Ruihua Ding^{1,2}, Raktima Raychowdhury³, Nir Friedman⁵, Nir Hacohen^{3,6}, Hongkun Park^{1,2,3}, Andrew P. May⁴ & Aviv Regev^{3,7}

High-throughput single-cell transcriptomics offers an unbiased approach for understanding the extent, basis and function of gene expression variation between seemingly identical cells. Here we sequence single-cell RNA-seq libraries prepared from over 1,700 primary mouse bone-marrow-derived dendritic cells spanning several experimental conditions. We find substantial variation between identically stimulated dendritic cells, in both the fraction of cells detectably expressing a given messenger RNA and the transcript's level within expressing cells. Distinct gene modules are characterized by different temporal heterogeneity profiles. In particular, a 'core' module of antiviral genes is expressed very early by a few 'precocious' cells in response to uniform stimulation with a pathogenic component, but is later activated in all cells. By stimulating cells individually in sealed microfluidic chambers, analysing dendritic cells from knockout mice, and modulating secretion and extracellular signalling, we show that this response is coordinated by interferon-mediated paracrine signalling from these precocious cells. Notably, preventing cell-to-cell communication also substantially reduces variability between cells in the expression of an early-induced 'peaked' inflammatory module, suggesting that paracrine signalling additionally represses part of the inflammatory program. Our study highlights the importance of cell-to-cell communication in controlling cellular heterogeneity and reveals general strategies that multicellular populations can use to establish complex dynamic responses.

Variation in component molecules between individual cells^{1–7} may have an important role in diversifying population-level responses^{8–11}, but also poses therapeutic challenges^{4,5}. Although pioneering studies have explored heterogeneity within cell populations by focusing on small sets of preselected markers^{1,2,4–6,8,12}, single-cell genomics promises unbiased exploration of the molecular underpinnings and consequences of cellular variability^{13–17}.

We previously¹⁶ used single-cell RNA-seq to identify substantial differences in messenger RNA (mRNA) transcript structure and abundance across 18 bone-marrow-derived mouse dendritic cells 4 h after stimulation with lipopolysaccharide (LPS, a component of Gram-negative bacteria). Many highly expressed immune response genes were distributed bimodally amongst single cells, originating, in part, from closely related maturity states and the variable activation of a key antiviral circuit. As these observations focused on a single pathogenic stimulus and time point, they raised several questions about the causes and roles of single-cell variability during the innate immune response. Examining the dynamics of cellular heterogeneity, its pathogen-specificity, and its intra- and intercellular control required new approaches to profile large numbers of cells from diverse conditions and genetic perturbations.

Here we use a microfluidic device to help prepare over 1,700 SMART-seq¹⁵ single-cell RNA-seq libraries along time courses of bone-marrow-derived dendritic cells responding to different stimuli (Fig. 1 and Extended Data Fig. 1a). Combining computational analyses with diverse perturbations—including stimulation of individual cells in isolated, sealed microfluidic chambers and genetic and chemical alterations of paracrine signalling—we show how both antiviral and inflammatory response

modules in dendritic cells are controlled by positive and negative intercellular paracrine signalling that both promote and restrain variation.

Microfluidics-based single-cell RNA-seq

We used the C₁ single-cell Auto Prep System (Fluidigm; Fig. 1b) and a transposase-based library preparation strategy to perform SMART-seq¹⁵ (Supplementary Information) on 1,775 single dendritic cells, including both stimulation time courses (0, 1, 2, 4 and 6 h) for three pathogenic components¹⁸ (LPS, PIC (viral-like double-stranded RNA), and PAM (synthetic mimic of bacterial lipopeptides)) and additional perturbations (Fig. 1, Extended Data Fig. 1 and Supplementary Information). For most conditions, we captured up to 96 cells (87 ± 8 (average \pm s.d.)), and generated a matching population control (Fig. 1c, Supplementary Information and Supplementary Table 1). We prepared technically matched culture and stimulation replicates for the 2 h and 4 h LPS stimuli, and independent biological replicates for the unstimulated (0 h) and 4 h LPS experiments (Supplementary Information). We sequenced each sample to an average depth of 4.5 ± 3.0 million read pairs, as single-cell expression estimates stabilized at low read-depths^{13,19} (Extended Data Fig. 2). The quality of our libraries was comparable to published SMART-seq data^{15,16} (Extended Data Fig. 1b, Supplementary Tables 1 and 2). Overall, we successfully profiled 831 cells in our initial time courses and 944 cells in subsequent experiments (Extended Data Fig. 1a and Supplementary Tables 1 and 2). We excluded another 1,010 libraries with stringent quality criteria (Supplementary Information and Extended Data Fig. 1c).

Aggregated *in silico*, single-cell expression measurements agreed with the matching population controls ($R = 0.87 \pm 0.05$), with correlations

¹Department of Chemistry & Chemical Biology, Harvard University, 12 Oxford Street, Cambridge, Massachusetts 02138, USA. ²Department of Physics, Harvard University, 17 Oxford Street, Cambridge, Massachusetts 02138, USA. ³Broad Institute of MIT and Harvard, 7 Cambridge Center, Cambridge, Massachusetts 02142, USA. ⁴Fluidigm Corporation, 7000 Shoreline Court, Suite 100, South San Francisco, California 94080, USA. ⁵School of Computer Science and Engineering, Hebrew University, 91904 Jerusalem, Israel. ⁶Center for Immunology and Inflammatory Diseases & Department of Medicine, Massachusetts General Hospital, Charlestown, Massachusetts 02129, USA. ⁷Howard Hughes Medical Institute, Department of Biology, Massachusetts Institute of Technology, Cambridge, Massachusetts 02140, USA.

*These authors contributed equally to this work.

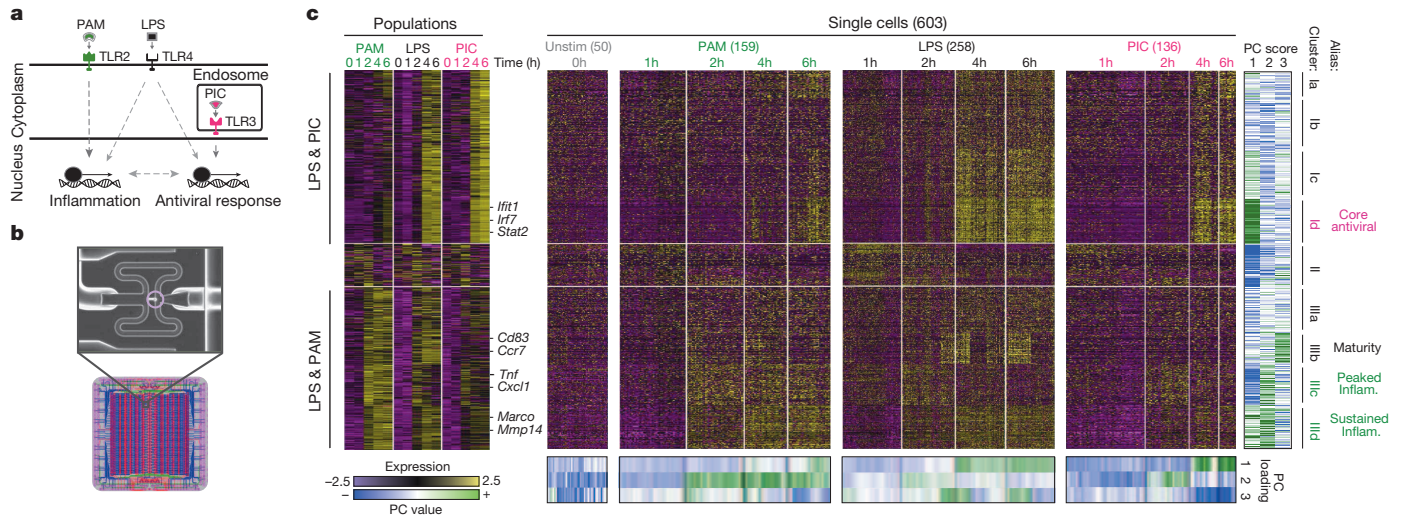


Figure 1 | Microfluidic-enabled single-cell RNA-seq of dendritic cells stimulated with pathogenic components. **a**, Schematic of Toll-like receptor (TLR) sensing of PAM by TLR2, LPS by TLR4, and PIC by TLR3 (Supplementary Information). **b**, Microfluidic capture of a single dendritic cell (top, cell circled in purple) on a C_1 chip (CAD drawing, bottom). **c**, Time-course expression profiles for induced genes (rows) in dendritic cells

plateauing once we had sampled ~ 30 cells (Supplementary Information, Extended Data Fig. 1d–g). Technical and biological replicates were reproducible (technical: aggregate $R > 0.90$, biological: aggregate $R > 0.87$; Extended Data Fig. 3) and our results were robust to variations in several aspects of sample preparation (Supplementary Information and Extended Data Fig. 1h–j). We removed 537 ‘cluster-disrupted’ dendritic cells¹⁶, a distinct subpopulation that matures as an artefact of isolation and culturing (Supplementary Information and Extended Data Fig. 4), retaining 1,238 dendritic cells for further analyses (Supplementary Tables 1 and 2).

Variability during immune responses

Principal components analysis (PCA) of gene expression profiles from all three time courses together showed that dendritic cells spread along a continuum of expression variation in each principal component (PC) (Fig. 1c and Extended Data Fig. 1k–n). For example, although PC1 distinguished early from late time points for each stimulus, its scores also varied substantially between cells within any single stimulus and time point (Fig. 1c and Extended Data Fig. 1k–n), suggesting that some cells were ahead of others, especially early (1–2 h).

Consistent with previous studies¹⁸, pathogen-responsive genes partitioned into co-regulated modules based on their population-level expression profiles (Fig. 1c, left; Supplementary Information). Genes induced in cells stimulated with LPS or PIC (cluster I, Fig. 1c) were enriched for antiviral defence factors, including interferons and their targets (Bonferroni-corrected $P < 10^{-5}$), whereas genes induced in cells stimulated with LPS or PAM (cluster III, Fig. 1c) were enriched for inflammatory genes and NF- κ B targets (Bonferroni-corrected $P < 10^{-6}$; Supplementary Table 3).

We used the single-cell gene expression profiles to partition these main clusters into finer modules (Fig. 1c, black lines, right; Supplementary Table 3; Supplementary Information) and applied a resampling method²⁰ (Supplementary Information, Extended Data Fig. 5d) to identify four modules significantly associated with the three major PCs (Fig. 1c): Cluster I_d (core antiviral module; enriched for annotated antiviral and interferon response genes; for example, *Ifit1*, *Irf7*; Bonferroni-corrected $P < 10^{-8}$, Supplementary Table 3, Fig. 1c and Extended Data Fig. 5a) was significantly associated with PC1; cluster III_c (peaked inflammatory module; showing rapid, yet transient, induction under LPS; for example, *Tnf*, *Il1a*, *Cxcl2*) and cluster III_d (sustained inflammatory module; exhibiting continued rise in expression under LPS; for example, *Mmp14*,

(columns) at 0, 1, 2, 4 and 6 h post-stimulation with PAM (green), LPS (black), or PIC (magenta) within populations (left) and individual cells (right). Far right: gene projection scores onto the first three principal components (PCs) (columns); bottom: contributions of each cell (columns) to the first three PCs (rows).

Marco, *Il6*) were associated with PC2; and cluster III_b (‘maturity’ module; containing markers of dendritic cell maturation; for example, *Cd83*, *Ccr7*, and *Ccl22*; Supplementary Information) was associated with PC3.

Digital and analogue expression variability

Genes from these four modules displayed distinct patterns of variation that changed with time and stimulus (Fig. 2a, Extended Data Figs 5 and 6). For example, early after LPS stimulation, core antiviral response genes were detectably expressed only in some cells (that is, were bimodal) (Fig. 2a, Extended Data Figs 5a and 6), but were turned on in most cells between 2 and 4 h (that is, became unimodal). In contrast, many peaked inflammatory genes were induced by LPS in all cells early, but were only detectable in some cells later (Fig. 2a, Extended Data Figs 5b and 6). Finally, sustained inflammatory genes were induced early in most cells and persisted at equal or elevated levels later (Fig. 2a, Extended Figs 5c and 6). Some variation patterns changed between stimuli (for example, peaked inflammatory genes remained detectably expressed in most cells late (6 h) in PAM), whereas other patterns were similar for distinct pathogens (for example, the antiviral modules I_a–I_d under LPS and PIC) (Figs 1 and 2a and Extended Data Fig. 5a–c).

As noted previously from single-cell quantitative real-time polymerase chain reaction (qRT-PCR) data²¹, we distinguished two types of heterogeneity: (1) digital (on/off) variation, reflecting the percentage of cells detectably expressing a transcript; and (2) analogue variation, representing expression level variability among detectably expressing cells. Using the variance calculated over all cells as a metric of heterogeneity^{6,16} conflates these two types of variation. We therefore explicitly modelled our data using three parameters (Fig. 2b and Extended Data Fig. 7): the mean (μ) and variance (σ^2) of a gene’s expression among detectably expressing cells, and the fraction of detectably expressing cells (α)²¹: in this scheme, σ^2 and α signify analogue and digital variation, respectively.

We computed α based on a fixed threshold for appreciable expression ($\ln(\text{TPM} + 1) > 1$, Supplementary Information and Extended Data Fig. 7a, f), and then estimated μ and σ^2 across appreciably expressing cells. This three-parameter model effectively described most (91%) of our single-cell data (Fig. 2c, d, Supplementary Information and Extended Data Fig. 7b). Our data did not support fitting with either a single log-normal or a mixture of two, fully parameterized lognormals (modelling high and low expression states; Supplementary Information and Extended Data Fig. 7c–e). Computed α values were consistent between technical

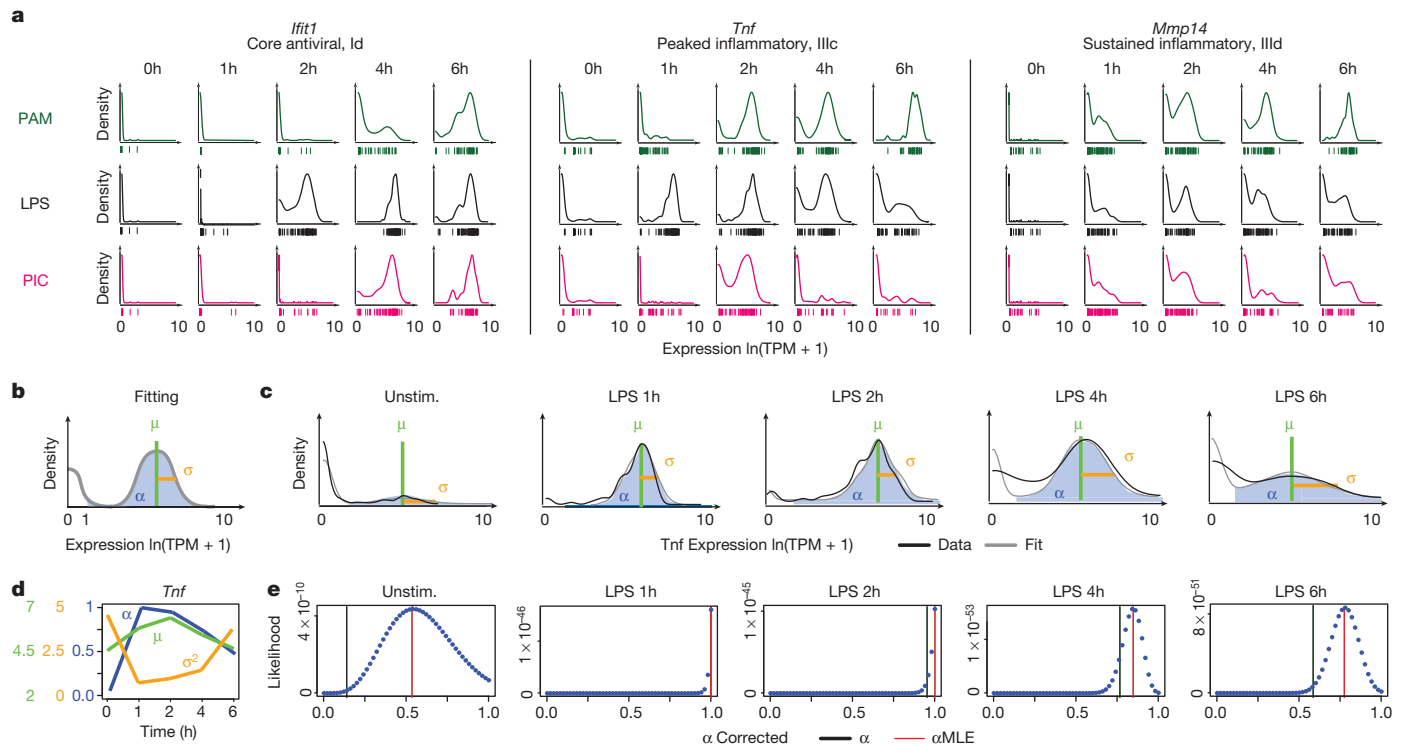


Figure 2 | Time-dependent behaviours of single cells. **a**, Single-cell expression distributions for three genes at each time point after stimulation with PAM (top, green), LPS (middle, black), or PIC (bottom, magenta). Distributions are scaled to have the same maximum height. Individual cells are plotted as bars underneath each distribution. **b**, Three parameters describing single-cell gene expression distributions: μ (green) and σ^2 (gold), the mean and variance of RNA abundance in detectably expressing cells, respectively, and

α (blue), the fraction cells with detectable expression (at $\ln(\text{TPM} + 1) > 1$). **c**, Examples of fit (grey) and measured *Tnf* expression distributions (black). **d**, The values of μ , σ^2 , and α (y axes, left to right) computed for *Tnf* at each time point (x axis). Units for μ and σ^2 are $\ln(\text{TPM} + 1)$. **e**, Maximum likelihood estimate α (α_{MLE}). Shown are the likelihood functions (dotted blue line) for *Tnf* (matching **c**) used to determine α_{MLE} (red line; vertical black line: nominal α ; Supplementary Information).

and biological replicates, but μ and σ^2 estimates were reproducible only when genes were expressed in at least 10 or 30 cells, respectively (Supplementary Note, Supplementary Information, Extended Data Figs 2c–e, 7g and 8).

Our nominal α estimates are likely deflated due to the detection limits of single-cell RNA-seq. Indeed, we observe higher α values when examining our existing RNA fluorescence *in situ* hybridization (RNA-FISH) data¹⁶ (Extended Data Fig. 6g–j). By comparing our single-cell RNA-seq and RNA-FISH, we estimate that the transcript detection efficiency for our single-cell RNA-seq is $\sim 20\%$, consistent with previous reports^{14,22}. We and others^{15,23} have also observed a strong relationship between the average expression of a gene and its probability of detection (Extended Data Fig. 7h). We thus used a conservative null model, where this relationship results solely from technical limitations (Supplementary Information, Extended Data Fig. 7h), and determined the maximum likelihood estimate of α (α_{MLE}) for each gene after correcting for this relationship (Fig. 2e, Extended Data Fig. 7j–l and Supplementary Information). From this analysis, we estimate that $\sim 45\%$ of core antiviral genes and 30% of peaked inflammatory genes are significantly bimodal in at least one measured time point in the LPS response (likelihood ratio test (LRT), Bonferroni-corrected $P < 0.01$; Supplementary Information and Extended Data Fig. 7i).

Chromatin mark levels correlate with α

As the presence of a chromatin mark is, by definition, discrete in a single cell, we reasoned that population ChIP-seq profiles of active histone marks (for example, histone 3 lysine 27 acetylation (H3K27ac)) should more closely reflect the fraction of cells with detectable transcripts (α) than population-level expression. Supporting this hypothesis, the observed α for a gene was strongly correlated (mean R for binned data = 0.89; Supplementary Information) to its promoter-associated ChIP-seq

density (collected under identical conditions²⁴), even within a fixed population expression range (Fig. 3a top/middle, rows). In contrast, a gene's population-level expression was not correlated (mean R for binned data = -0.02) to H3K27ac promoter levels within a fixed α range (Fig. 3a top, middle; columns). We note that H3K27ac and population-level expression remained correlated within a fixed range of μ (instead of α , Fig. 3b). A partial correlation analysis focussed on either all immune response genes or 'bimodal' genes (LRT, $P < 0.01$) yielded similar results ($P > 0.1$, after controlling for α , Fig. 3c). Digital variation did not correlate with histone 3 lysine 4 trimethylation (H3K4me3) levels (Fig. 3a, bottom), in line with previous observations²⁴ that H3K4me3 is not as tightly correlated with active transcription. Emerging single-cell epigenomic technologies²⁵ should help to further explore this relationship.

Dynamic responses via shifts in α and μ

An average (population) increase in the expression of bimodally expressed genes may represent changes in the amount of transcript made by expressing cells (shifts in μ), the proportion of expressing cells (shifts in α), or both. For each pair of consecutive time points, we examined the proportion of genes in each module with a significant change in: (1) μ (Wilcoxon rank-sum test); (2) α (LRT, controlling for the aforementioned confounding relationship between average expression and detection efficiency, Supplementary Information); or (3) both. Given our limitations in estimating α and μ , we only considered genes that were annotated as bimodal in at least one time point in the relevant time course and expressed in at least 10 cells in both time points (Supplementary Information). We excluded the unstimulated time point when most immune response genes were not yet expressed.

Under LPS stimulation, core antiviral and sustained inflammatory genes had the strongest increases in α (alone or with μ) at early time points (Fig. 3d, top; Extended Data Fig. 5e, f), and transitioned to high

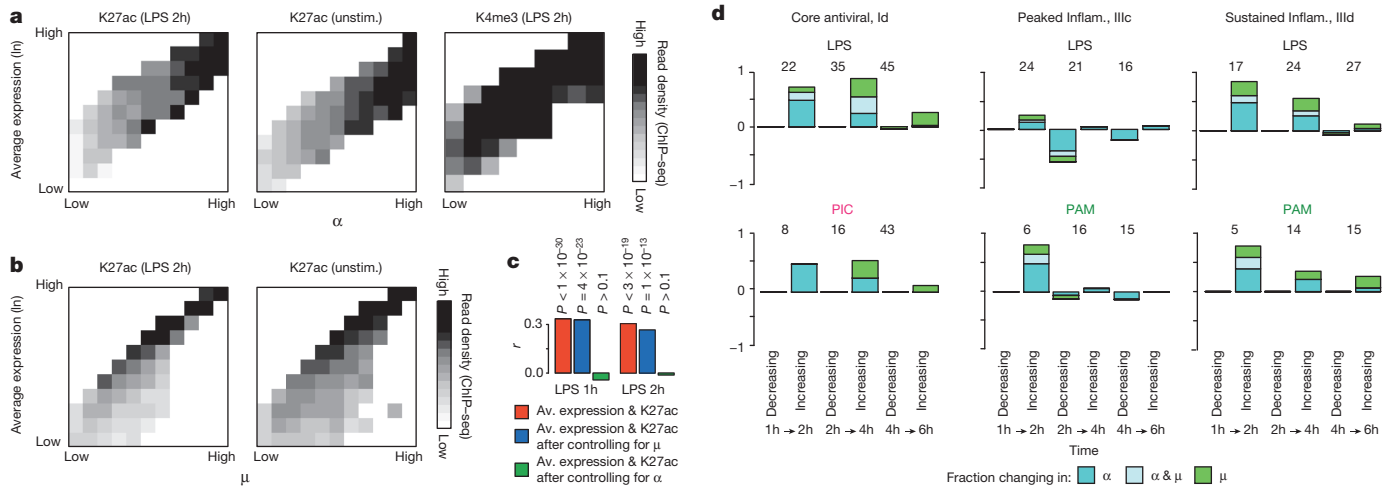


Figure 3 | Dynamic changes in variation during stimulation. **a, b,** The relationship between expression and H3K27ac binding depends on α (**a**), but not on μ (**b**). Plots show average promoter read density (black high; white low; scale bar, bottom) for H3K27ac in LPS 2 h (**a, b**, left) and unstimulated cells (**a**, middle; **b**, right), or H3K4me3 in 2 h LPS (**a**, right) in genes corresponding to each of 10 quantile bins of population expression (y axis) and each of 10 quantile bins of α (x axis) or μ (x axis) (Supplementary Information). **c,** Bar plots showing P values of correlation between average expression levels and K27ac only for immune response genes either as is (red) or when controlling for μ (blue) or α (green). Matching R values for all genes: 0.29 (LPS 1 h, as is),

and unimodal expression by 4 h (Figs 1 and 2). In contrast, α decreased at later time points for peaked inflammatory genes, especially from 2 to 4 h (Fig. 3d, middle; Extended Data Fig. 5f). The temporal patterns in core antiviral gene activation were shared between LPS and PIC. However, unlike in LPS, peaked inflammatory gene expression did not diminish under PAM, and we did not observe statistically significant decreases in α at later time points (Fig. 3d). These coherent shifts suggest that variability reflects regulated immune response phenomena, rather than unconstrained stochastic transcription.

Intercellular determinants of variation

Both differences in intracellular components^{1–4} and changes in the cellular microenvironment^{7,26} can affect heterogeneity. In particular, slow diffusion of cytokines and chemokines could lead to local variation in intercellular signals. As the core antiviral module is enriched for targets of IFN- β , we speculated that upstream variability in IFN- β exposure may drive its heterogeneity (median $\alpha = 0.52$; 30% of genes significantly bimodal, $P < 0.01$, LRT, Extended Data Fig. 9), and thus

0.18 (LPS 1 h, controlling for μ), 0.06 (LPS 1 h, controlling for α), 0.33 (LPS 2 h, as is), 0.23 (LPS 2 h, controlling for μ), 0.08 (LPS 2 h, controlling for α)

d, Dynamic changes in α and μ in each module. Bar plots showing, for each module in select conditions (annotated on top), the fraction of genes (y axis) with a significant change only in α ($P < 0.01$, likelihood ratio test, blue), only in μ ($P < 0.01$, Wilcoxon test, green), or in both (each test independently, light blue), at each transition (x axis). The number of genes over which the proportion is calculated is marked on top of each pair of bars (Supplementary Information, Extended Data Fig. 5f).

profiled cells 2 h after IFN- β stimulation. Supporting our hypothesis, cells stimulated with IFN- β for 2 h exhibited sharply reduced digital variation in the core antiviral module (Fig. 4a, median $\alpha = 0.82$; 7% of genes significantly bimodal).

Precocious expressers of antiviral genes

We next explored the cellular source of interferon in the native LPS response. At 2 h following LPS, *Ifnb1* was bimodally expressed ($P < 10^{-4}$, LRT) and correlated with the expression of the core antiviral module (Extended Data Fig. 9a, d, e). This observation, together with the suppression of digital variation under an IFN- β stimulus, suggested that, in response to LPS, a few cells may first produce (Extended Data Fig. 9d) and secrete a wave of interferon, leading to a gradual coordination of the core antiviral module at later time points via paracrine signalling.

To test this hypothesis, we computed a core antiviral activation score (Supplementary Information) for each cell and compared scores across the LPS time course (Fig. 4b, Extended Data Fig. 9e, f and 10a and Supplementary Information). Although most cells activated the module

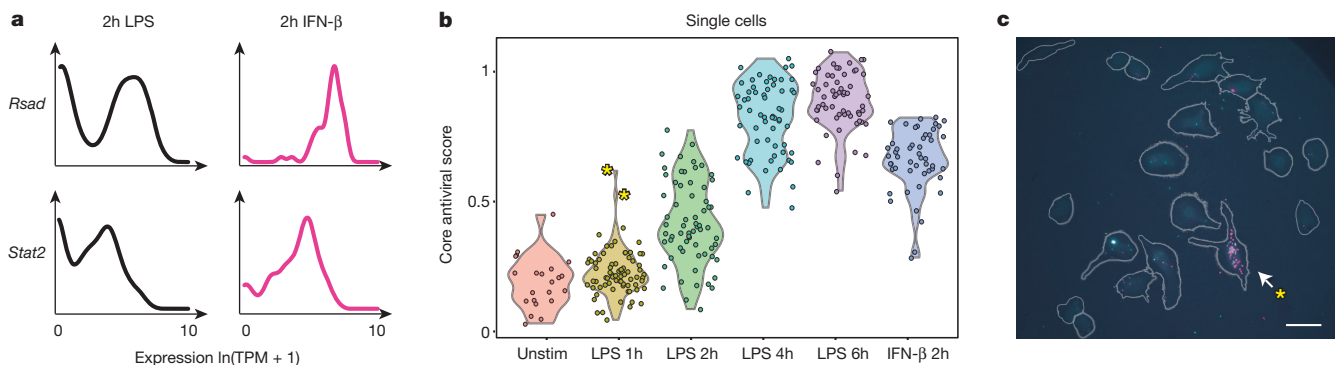


Figure 4 | IFN- β feedback drives heterogeneity in the expression of core antiviral targets. **a,** Single-cell expression distributions for *Rsad* (top) and *Stat2* (bottom) after stimulating with LPS (left, black) or IFN- β (right, magenta) for 2 h. **b,** The core antiviral score (y axis; Supplementary Information, Extended Data Figs 9f and 10a) for each LPS-stimulated cell at each time point

(x axis) and cells simulated for 2 h with IFN- β (on far right). Two precocious cells (yellow asterisk) have unusually high antiviral scores at 1 h LPS. **c,** RNA-FISH confirms the presence of rare precocious responders (arrow; yellow asterisk), positive for both *Ifnb1* (magenta) and *Ifit1* (cyan) 1 h after LPS stimulation. Grey, cell outlines. Scale bar represents 25 μ m.

between 2 h and 4 h, we discovered two cells with strong core antiviral activation at 1 h (Fig. 4b, c, Extended Data Fig. 9f, i, yellow asterisks). We verified the existence and scarcity of these precocious cells 1 h after LPS stimulation by RNA-FISH (Fig. 4c, Supplementary Information); here, appreciable *Ifit1* and *Ifnb1* co-expression was detected in only 0.8% of cells (23 of 2,960, mRNA count ≥ 5 copies, $P = 2 \times 10^{-28}$, proportion test). These precocious cells were indistinguishable from the others except in their expression of the ~ 100 core antiviral genes (Extended Data Fig. 9j, k). We observed similar early responding cells following PIC or PAM stimulation (Extended Data Fig. 9f, h and 10a).

Although these precocious cells are reminiscent of the ‘sentinels’ that have been reported in viral infections and stimulations of fibroblasts^{27,28} (Supplementary Note, Supplementary Information), we note that, in those studies, variable response may be partially due to differences in cells’ ability to sense and respond to the primary stimulus (for example, due to lack of viral sensing or replication). In contrast, all dendritic cells rapidly sense and respond to LPS, as evidenced by the unimodal activation of peaked inflammatory genes at early time points (Extended Data Figs 5b–d, 10a; Fig. 2a, *Tnf*).

Intercellular communication and variation

To examine whether the rare precocious cells were required for coordinating the core antiviral response, we developed an approach to stimulate cells in the absence of cell-to-cell communication. Modifying the standard C_1 workflow, we captured individual unstimulated dendritic cells in a C_1 chip (Supplementary Information), washed in LPS-containing

media, and then immediately sealed each microfluidic chamber to isolate stimulated cells individually for 4 h (on-chip stimulation, Supplementary Information, Fig. 5a). Key experimental conditions, including cell density, were similar between the in-tube and on-chip experiments (Supplementary Information).

In the absence of cell-to-cell communication, core antiviral module genes were bimodally expressed (Fig. 5), with only 8 cells (20%) exhibiting weak activation of the core antiviral module at 4 h (Fig. 5b–d, Extended Data Fig. 9e), probably mimicking the precocious cells observed in-tube at 1 h. This observation suggests an approximate bound for the number of cells capable of autonomously inducing a response by 4 h. Removing cell-to-cell communication also downregulated the expression of maturation markers in all cells and some of the sustained inflammatory genes (Extended Data Fig. 10a), although other key inflammatory genes were unaffected.

Surprisingly, blocking intercellular communication also sharply altered the single-cell expression of peaked inflammatory genes (Fig. 5b–d). Genes encoding key inflammatory cytokines (for example, *Tnf*, *Cxcl1*) switched from bimodal ($\alpha = 0.77, 0.56$, respectively) to unimodal ($\alpha = 1.0, 0.91$; LRT for corresponding α_{MLE} : $P < 10^{-4}$, $P < 10^{-13}$, respectively) expression on-chip (Fig. 5b, c). Indeed, a large portion of the peaked inflammatory genes that were bimodal (LRT $P < 0.01$) after a 4 h LPS stimulation in-tube shifted to unimodal expression on-chip (Extended Data Fig. 10a, b; $P < 0.01$, hypergeometric test), indicating that cell-to-cell signalling is required for dampening the peaked inflammatory program at later time points following LPS. The opposite behaviours

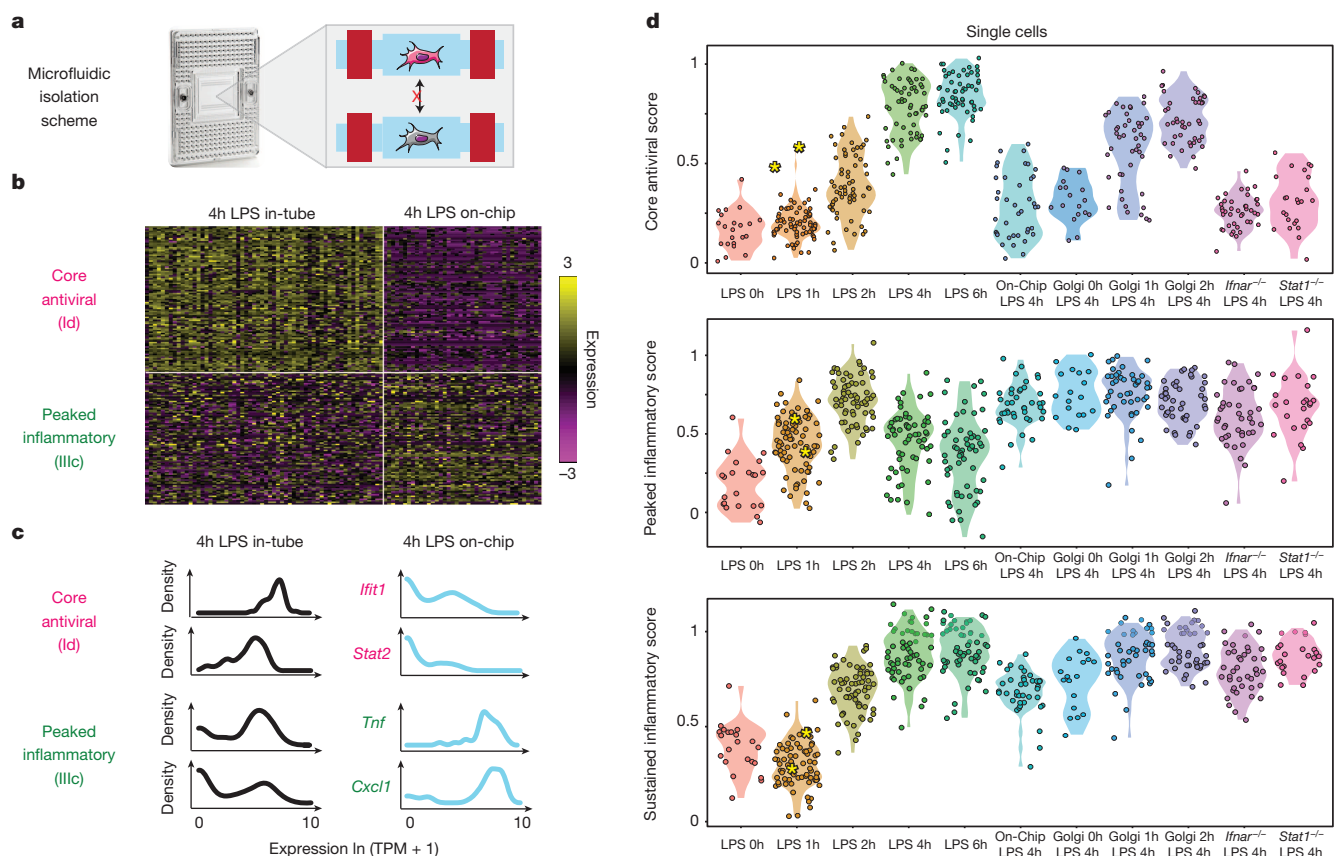


Figure 5 | Microfluidic blocking of cell-to-cell signalling affects response heterogeneity in the core antiviral and peaked inflammatory modules.

a, Experimental blocking of cell-to-cell communication. Left: C_1 chip; right: actuation of microfluidic valves (red bars), following on-chip LPS stimulation, isolates individual cells in sealed chambers, preventing intercellular signalling. **b**, Expression of the genes (rows) in the core antiviral (I_d , top rows) and peaked inflammatory (III_c , bottom rows) modules in single cells (columns) from the in-tube (left) and on-chip (right) stimulations. **c**, Gene expression

distributions for representative genes from the core antiviral (top) and peaked inflammatory (bottom) modules in the in-tube (left, black) or on-chip (right, blue) 4 h LPS stimulation. **d**, Violin plots of, top to bottom, the core antiviral (Supplementary Information, top), peaked inflammatory (middle), and sustained inflammatory (bottom) scores for individual cells from the stimulation conditions listed on the x axis. Yellow asterisks: the two precocious cells from Fig. 4 (Extended Data Fig. 10a).

of the core antiviral and peaked inflammatory modules indicate that intercellular communication can have opposing effects on variation for different gene modules within the same cell.

IFN- β and peaked inflammatory genes

On-chip isolation conflates the effects of different paracrine signals and the loss of cell-to-cell contact. To distinguish these situations, we first profiled dendritic cells from Interferon receptor knockout mice (*Ifnar1*^{-/-}). As expected, and consistent with previous findings¹⁶, antiviral gene expression was undetectable at 4 h in all *Ifnar1*^{-/-} dendritic cells, implying that even the precocious cells require autocrine interferon feedback to activate and sustain their core antiviral responses (Extended Data Fig. 10g). This is further supported by the decoupling of the expression of *Ifnb1* and the core antiviral module in *Ifnar1*^{-/-} dendritic cells stimulated with LPS for 2 h (Extended Data Fig. 9e).

Removal of interferon signalling also strongly affected the peaked inflammatory module: after 4 h of LPS stimulation, *Ifnar1*^{-/-} cells showed a similar increase in the fraction of activated cells as was seen in the on-chip experiment (Fig. 5d, Extended Data Fig. 10a, d, g), suggesting that the absence of interferon signalling, rather than changes in cell-to-cell contact²⁹, was the major driver. Furthermore, dendritic cells lacking *Stat1*, a gene encoding a key transcription factor mediating interferon responses²⁴, also exhibited increased activation and decreased digital variation in peaked inflammatory genes ($P < 0.01$; hypergeometric test; Fig. 5d and Extended Data Fig. 10a, e, g, i). Conversely, the sustained inflammatory module was not appreciably affected by the absence of interferon signalling (Fig. 5d and Extended Data Fig. 10a, g), implying a different mechanism for its downregulation on-chip.

Second paracrine wave for downregulation

Interferon response targets can cross-inhibit inflammatory gene expression either through the direct formation of repressive complexes, for example, the STAT1-inclusive ISGF-3, or by inducing the production of anti-inflammatory cytokines³⁰. The few cells with on-chip antiviral activation exhibited no change in peaked inflammatory gene expression (Fig. 5b). This suggests that the repression of peaked inflammatory genes, unlike antiviral activation, is not directly downstream of IFN- β signalling, but rather may be mediated by a second IFN- β /STAT1-dependent paracrine signal. Peaked induction through two asynchronous paracrine signals is reminiscent of the activation and contraction of keratinocytes following wounding and immune infiltration, respectively³¹.

To test this hypothesis further, we added brefeldin A (GolgiPlug), a secretion inhibitor, either simultaneously with LPS (0 h) or at 1 or 2 h after stimulation, and measured single-cell RNA-seq profiles at 4 h (Fig. 5d, Extended Data Fig. 10a–c). Inhibiting secretion at the time of LPS addition strikingly dampened the antiviral response, similar to the on-chip experiment. However, adding brefeldin A at 2 h did not affect the activation of the core antiviral module and adding it at 1 h had only a modest effect. This indicates that the first hour represents the crucial paracrine window for this response. In contrast, for the peaked inflammatory module, addition at each of the three time points resulted in the module remaining aberrantly activated at 4 h, as on-chip. Collectively, these experiments show that paracrine interferon signalling events before the 1 h time point are crucial for antiviral activation, whereas subsequent, separate signalling is responsible for the desynchronized dampening of peaked inflammatory gene expression (Supplementary Note, Supplementary Information).

Discussion

Here we have analysed how gene expression variation between individual dendritic cells changes with stimulus and time to dissect the regulation of heterogeneity across this immune response. Our statistical analysis reveals that changes in digital (on/off) variation can encode a diversity of temporal response profiles (Fig. 3d, Extended Data Fig. 5f). For example, late-induced core antiviral genes are very weakly expressed early, on average, but are highly expressed in a few precocious cells; the

progressive dampening of peaked inflammatory genes originates, in part, from changes in the fraction of cells detectably expressing these transcripts, rather than a uniform, gradual decrease in their expression in all cells.

Such complex average responses can be generated not only through intricate intracellular circuits in each cell, but also through intercellular communication between cells, as we show for both modules. For example, we uncovered a small number of precocious cells that express *Ifnb1* and core antiviral genes as early as 1 h after LPS stimulation, and through the secretion of IFN- β , help activate core antiviral genes in other cells to coordinate the population response. These cells are indistinguishable from the rest, except in their expression of the core antiviral module (Extended Data Fig. 9j, k), and yet are crucial for an efficient and timely population response (Supplementary Note, Supplementary Information).

IFN- β signalling also dampens a subset of induced inflammatory genes at later time points, and our brefeldin A (GolgiPlug) experiments suggest that a secondary, IFN- β -dependent signal, is involved (Extended Data Fig. 10j, k). This is consistent with a model in which IFN- β secreted by a few cells induces the expression and secretion of secondary anti-inflammatory cytokines from a subset of cells, which, in turn, attenuate the peaked inflammatory responses of their neighbours. Computational analyses, genetic perturbations and recombinant cytokine experiments suggest that IL-10 may be involved in this second wave of negative signalling (Extended Data Fig. 10h, Supplementary Table 4), but further experiments are needed to fully elucidate the mechanism (Supplementary Note, Supplementary Information). One involved component may be the RNA degradation factor ZFP36 (TTP), whose targets are enriched in the peaked inflammatory module³².

The ability of precocious cells to influence others via paracrine signalling may be an efficient strategy for quorum sensing³³, but also may be perilous. If the activation threshold is too low, a few stochastically responding cells could induce an inappropriate immune response. Indeed, this is observed in autoimmune diseases like systemic lupus erythematosus (SLE), in which excess IFN- β production potentiates auto-reactive dendritic cell activation^{34,35}. In contrast, excessively stringent thresholds may limit rapid responses to a viral infection, or the dampening of chronic inflammation (for example, in rheumatoid arthritis or ulcerative colitis^{30,35}). Thus, individual cells probably place tight controls on the regulation of key cytokines, preferring different induction strategies under different stimuli to maximize the balance between responsiveness and control. Indeed, similar population-level *Ifnb1* expression in LPS/PIC (Extended Data Fig. 9c) stems from different underlying phenomena: a substantial fraction of cells express the *Ifnb1* transcript moderately at 2 h LPS ($\alpha = 0.35$, $\mu = 5.1$), whereas just a few cells express *Ifnb1* very highly at 2 h PIC ($\alpha = 0.07$, $\mu = 6.31$; uncorrelated with the cell's activation of the antiviral response^{26,27}; Extended Data Fig. 9e).

Using microfluidics, we achieved the statistical power needed to track transcriptome-wide changes in single-cell expression variation across a variety of conditions, as well as to identify functionally important, rare responses. Microfluidics also allowed us to finely control the stimulation of our cells. Similar and improved techniques will be essential for characterizing other rare sub-populations, such as cancer stem cells, and for studying heterogeneous clinical samples and tissues. Further innovations in massively parallel manipulation and profiling of single cells will continue to improve our understanding of the rich diversity in, and dynamic functional communities that constitute, multicellular populations.

METHODS SUMMARY

Bone-marrow-derived mouse dendritic cells were prepared as previously described¹⁸ and stimulated with pathogenic stimuli for specified time periods. The C₁ Single-Cell Auto Prep System (Fluidigm) was used to perform SMARTer (Clontech) whole transcriptome amplification (WTA)^{15,16,19} on up to 96 individual cells. WTA products were then converted to Illumina sequencing libraries using Nextera XT (Illumina)¹⁵. RNA-seq libraries were also made from 10,000 cells from each parent population (population control). Each sample was sequenced on an Illumina HiSeq 2000 or 2500, and expression estimates (transcripts per million; TPM) for all UCSC-annotated

mouse genes were calculated using RSEM³⁶. Data were further analysed as described in the Supplementary Information. Additional experiments were performed using RNA-FISH (Panomics), on-chip isolated stimulation, knockout mice, secretion blockers (GolgiPlug, BD Biosciences), protein synthesis blockers (cycloheximide, Sigma), and recombinant cytokines. Full Methods and any associated references are provided in the Supplementary Information.

Online Content Any additional Methods, Extended Data display items and Source Data are available in the online version of the paper; references unique to these sections appear only in the online paper.

Received 16 June 2013; accepted 2 May 2014.

Published online 11 June 2014.

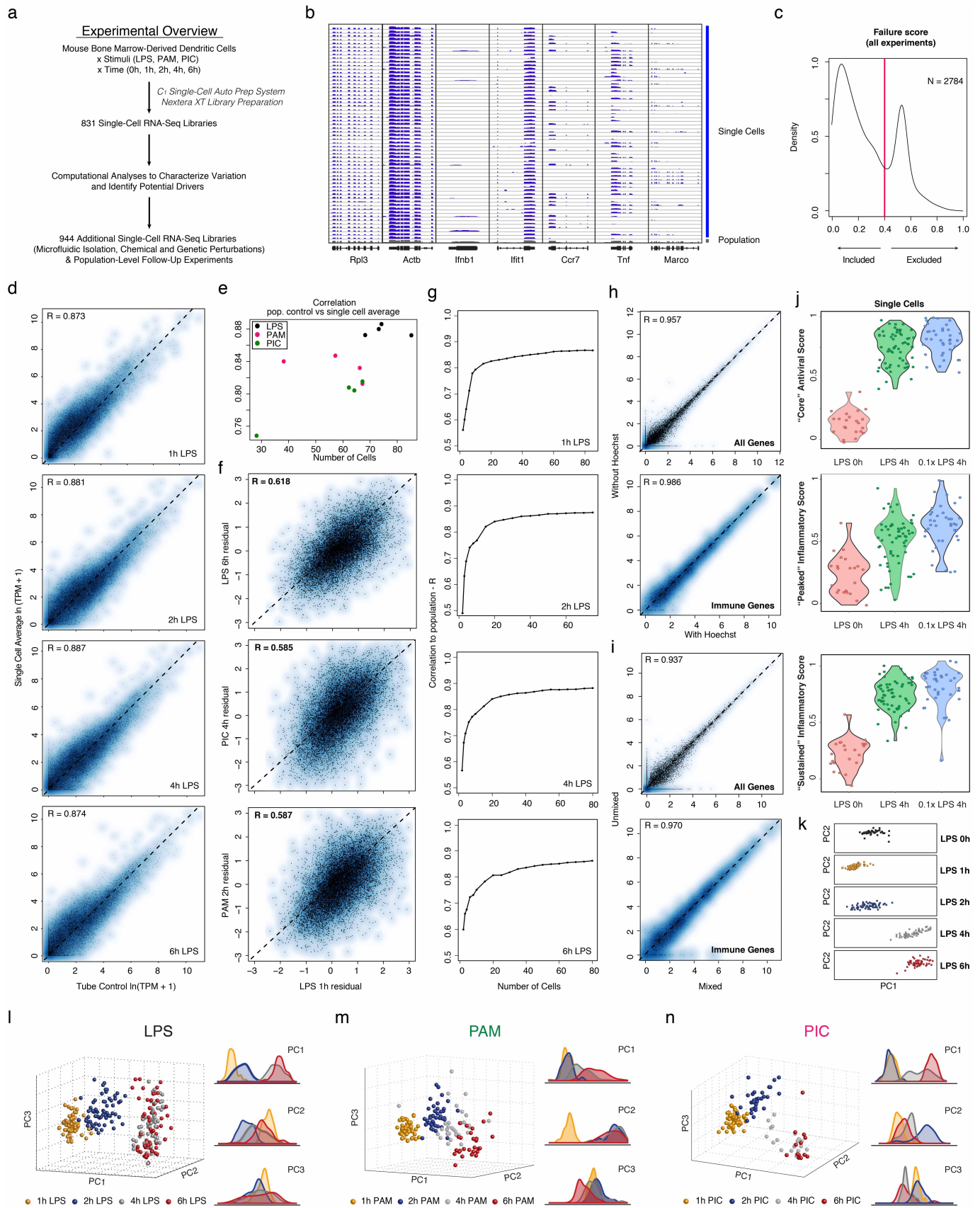
1. Tay, S. *et al.* Single-cell NF- κ B dynamics reveal digital activation and analogue information processing. *Nature* **466**, 267–271 (2010).
2. Raj, A. & Van Oudenaarden, A. Single-molecule approaches to stochastic gene expression. *Ann. Rev. Biophys.* **38**, 255–270 (2009).
3. Slack, M. D., Martinez, E. D., Wu, L. F. & Altschuler, S. J. Characterizing heterogeneous cellular responses to perturbations. *Proc. Natl Acad. Sci. USA* **105**, 19306–19311 (2008).
4. Sharma, S. V. *et al.* A chromatin-mediated reversible drug-tolerant state in cancer cell subpopulations. *Cell* **141**, 69–80 (2010).
5. Spencer, S. L., Gaudet, S., Albeck, J. G., Burke, J. M. & Sorger, P. K. Non-genetic origins of cell-to-cell variability in TRAIL-induced apoptosis. *Nature* **459**, 428–432 (2009).
6. Taniguchi, Y. *et al.* Quantifying *E. coli* proteome and transcriptome with single-molecule sensitivity in single cells. *Science* **329**, 533–538 (2010).
7. Loewer, A. & Lahav, G. We are all individuals: causes and consequences of non-genetic heterogeneity in mammalian cells. *Curr. Opin. Genet. Dev.* **21**, 753–758 (2011).
8. Feinerman, O. *et al.* Single-cell quantification of IL-2 response by effector and regulatory T cells reveals critical plasticity in immune response. *Mol. Syst. Biol.* **6**, 437–453 (2010).
9. Veening, J.-W., Smits, W. K. & Kuipers, O. P. Bistability, epigenetics, and bet-hedging in bacteria. *Ann. Rev. Microbiol.* **62**, 193–210 (2008).
10. Fang, M., Xie, H., Dougan, S. K., Ploegh, H. & Van Oudenaarden, A. Stochastic cytokine expression induces mixed T helper cell states. *PLoS Biol.* **11**, e1001618 (2013).
11. Chalançon, G. *et al.* Interplay between gene expression noise and regulatory network architecture. *Trends Genet.* **28**, 221–232 (2012).
12. Bendall, S. C. *et al.* Single-cell mass cytometry of differential immune and drug responses across a human hematopoietic continuum. *Science* **332**, 687–696 (2011).
13. Hashimshony, T., Wagner, F., Sher, N. & Yanai, I. CEL-Seq: single-cell RNA-Seq by multiplexed linear amplification. *Cell Rep.* **2**, 666–673 (2012).
14. Islam, S. *et al.* Characterization of the single-cell transcriptional landscape by highly multiplex RNA-seq. *Genome Res.* **21**, 1160–1167 (2011).
15. Ramsköld, D. *et al.* Full-length mRNA-Seq from single-cell levels of RNA and individual circulating tumor cells. *Nature Biotechnol.* **30**, 777–782 (2012).
16. Shalek, A. K. *et al.* Single-cell transcriptomics reveals bimodality in expression and splicing in immune cells. *Nature* **498**, 236–240 (2013).
17. Tang, F. *et al.* mRNA-Seq whole-transcriptome analysis of a single cell. *Nature Methods* **6**, 377–382 (2009).
18. Amit, I. *et al.* Unbiased reconstruction of a mammalian transcriptional network mediating pathogen responses. *Science* **326**, 257–263 (2009).
19. Wu, A. R. *et al.* Quantitative assessment of single-cell RNA-sequencing methods. *Nature Methods* **11**, 41–46 (2014).
20. Storey, J. D. & Tibshirani, R. Statistical significance for genomewide studies. *Proc. Natl Acad. Sci. USA* **100**, 9440–9445 (2003).
21. McDavid, A. *et al.* Data exploration, quality control and testing in single-cell qPCR-based gene expression experiments. *Bioinformatics* **29**, 461–467 (2013).
22. Islam, S. *et al.* Highly multiplexed and strand-specific single-cell RNA 5' end sequencing. *Nature Protocols* **7**, 823–828 (2012).
23. Marinov, G. K. *et al.* From single-cell to cell-pool transcriptomes: stochasticity in gene expression and RNA splicing. *Genome Res.* **24**, 496–510 (2014).
24. Garber, M. *et al.* A high-throughput chromatin immunoprecipitation approach reveals principles of dynamic gene regulation in mammals. *Mol. Cell* **47**, 810–822 (2012).
25. Weibrecht, I. *et al.* Visualising individual sequence-specific protein-DNA interactions in situ. *New Biotechnol.* **29**, 589–598 (2012).
26. Lee, T. K. *et al.* A noisy paracrine signal determines the cellular NF κ B response to lipopolysaccharide. *Sci. Signal.* **2**, ra65 (2009).
27. Rand, U. *et al.* Multi-layered stochasticity and paracrine signal propagation shape the type-I interferon response. *Mol. Syst. Biol.* **8**, 584 (2012).
28. Zhao, M., Zhang, J., Phatnani, H., Scheu, S. & Maniatis, T. Stochastic expression of the interferon- β gene. *PLoS Biol.* **10**, e1001249 (2012).
29. Snijder, B. *et al.* Population context determines cell-to-cell variability in endocytosis and virus infection. *Nature* **461**, 520–523 (2009).
30. Benveniste, E. N., Qin, H. & Type, I. Interferons as anti-inflammatory mediators. *Sci. STKE* **416**, pe70 (2007).
31. Freedberg, I. M., Tomic-Canic, M., Komine, M. & Blumenberg, M. Keratins and the keratinocyte activation cycle. *J. Invest. Dermatol.* **116**, 633–640 (2001).
32. Rabani, M. *et al.* Metabolic labeling of RNA uncovers principles of RNA production and degradation dynamics in mammalian cells. *Nature Biotechnol.* **29**, 436–442 (2011).
33. Waters, C. M. & Bassler, B. L. Quorum sensing: cell-to-cell communication in bacteria. *Ann. Rev. Cell Dev. Biol.* **21**, 319–346 (2005).
34. Banchereau, J., Pascual, V. & Type, I. Interferon in systemic lupus erythematosus and other autoimmune diseases. *Immunity* **25**, 383–392 (2006).
35. Hall, J. C. & Rosen, A. Type I interferons: crucial participants in disease amplification in autoimmunity. *Nature Rev. Rheumatol.* **6**, 40–49 (2010).
36. Li, B. & Dewey, C. N. RSEM: accurate transcript quantification from RNA-Seq data with or without a reference genome. *BMC Bioinformatics* **12**, 323 (2011).

Supplementary Information is available in the online version of the paper.

Acknowledgements We thank B. Tilton, T. Rogers and M. Tam for assistance with cell sorting; E. Sheffer, C. Guiducci, D. Thompson, and O. Rozenblatt-Rosen for project management and discussions and the Broad Genomics Platform for sequencing. We thank J. West, R. Lebofsky, A. Leyrat, M. Thu, M. Wong, W. Yorza, D. Toppani, M. Norris and B. Clerkson for contributions to C₁ system development; B. Alvarado, M. Ray and L. Knutson for assistance with C₁ experiments; and M. Unger for discussions. Work was supported by an NIH Postdoctoral Fellowship (1F32HD075541-01, R.S.), an NIH grant (U54 AI057159, N.H.), an NIH New Innovator Award (DP2 OD002230, N.H.), an NIH CEGS (1P50HG006193-01, H.P., N.H., A.R.), NIH Pioneer Awards (5DP1OD003893-03 to H.P., DP1OD003958-01 to A.R.), the Broad Institute (H.P. and A.R.), HHMI (A.R.), the Klarman Cell Observatory at the Broad Institute (A.R.), an ISF-Broad Grant (N.F.), and the ERC (N.F.).

Author Contributions A.R., A.P.M., H.P., A.K.S., R.S. and J.S. conceived and designed the study. A.K.S., J.S., J.J.T., D.G., D.L., P.C., R.S.G., J.T.G., B.F., S.W., J.W., X.W., R.D. and R.R. performed experiments. R.S., A.K.S., S.S. and N.Y. performed computational analyses. R.S., A.K.S., J.S., N.F., H.P., A.P.M. and A.R. wrote the manuscript, with extensive input from all authors.

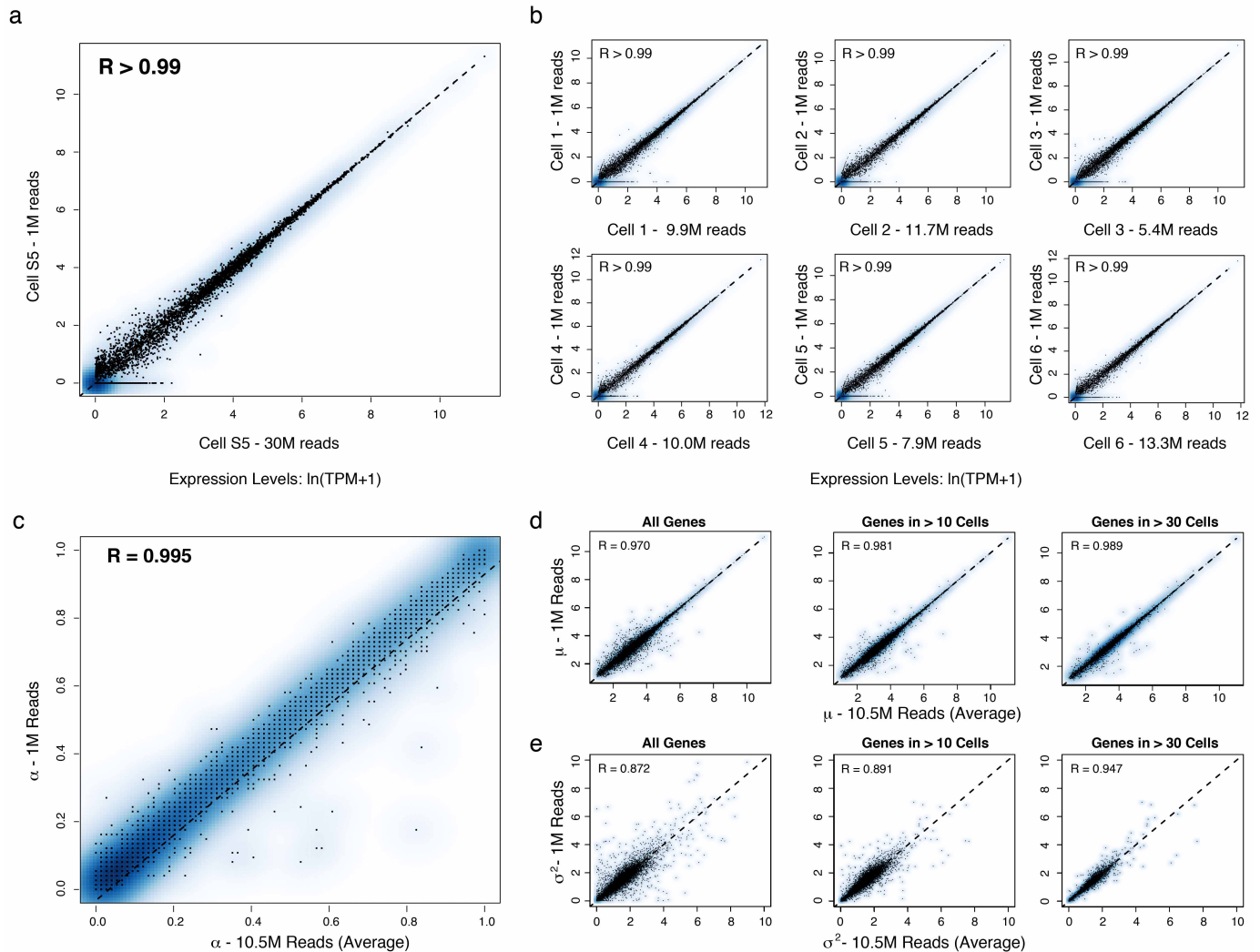
Author Information Data are deposited in GEO under accession number GSE48968. Reprints and permissions information is available at www.nature.com/reprints. The authors declare competing financial interests: details are available in the online version of the paper. Readers are welcome to comment on the online version of the paper. Correspondence and requests for materials should be addressed to R.S. (rahuls@broadinstitute.org), H.P. (Hongkun_Park@harvard.edu) or A.M. (apmay1@gmail.com).



Extended Data Figure 1 | Single-cell RNA-seq of hundreds of dendritic cells.

a, Overview of experimental workflow. **b**, Shown are read densities for seven representative genes (two housekeeping genes (*Rpl3* and *Actb*) and five immune response genes (*Ifnb*, *Ifit1*, *Ccr7*, *Tnf*, *Marco*)) across 60 single cells (blue) and one population control of 10,000 cells (grey; bulk population) after a 4 h LPS treatment. **c**, Distribution of failure scores for all single cells. Single cells with failure scores above 0.4 were discarded (see Supplementary Information). **d–g**, Comparisons of expression estimates for the average single cell and the bulk population. **d**, Scatter plots showing for each gene the relation between the average single-cell expression (*y* axis) and bulk population level expression (*x* axis) for each of four time points following LPS stimulation (1, 2, 4 and 6 h, left to right). **e**, The Pearson correlation coefficients (*y* axis) of each comparison, as in **d**, for each of the time points and stimuli presented in Fig. 1, as a function of the number of cells captured in the respective experiment (*x* axis). **f**, Scatter plots showing the residual (population-level expression minus the single cell average) in a LPS 1 h experiment (*x* axis) versus the residual in each of 3 other experiments (*y* axis, left to right): LPS 6 h, PIC 4 h and PAM 2 h. **g**, The Pearson correlation coefficient (*y* axis) between the bulk population level expression and the single-cell expression average when a different number of sub-sampled cells (*x* axis) is included in the single-cell

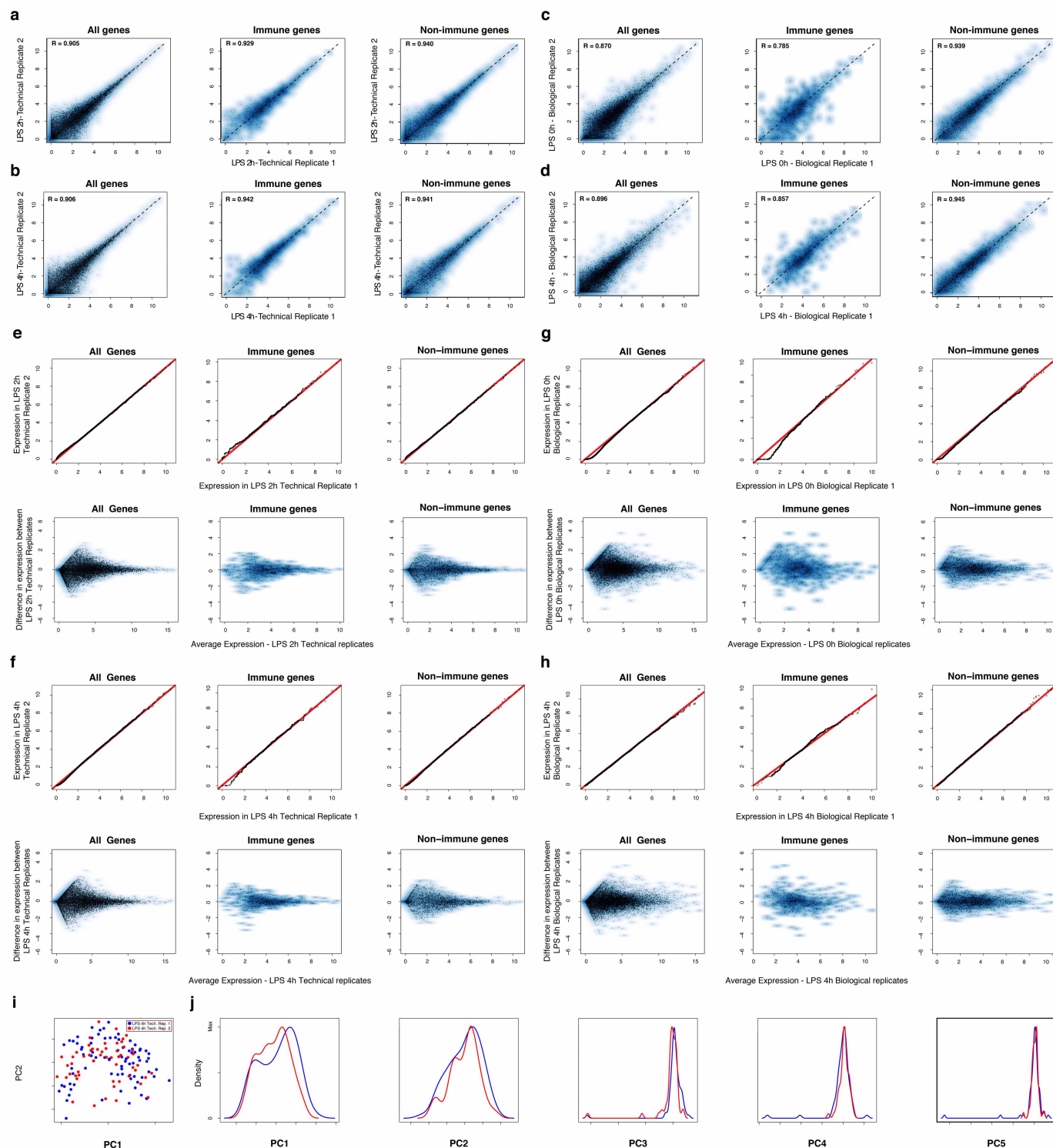
average. **h, i**, Effects of Hoechst dye and periodic mixing on mRNA expression. **h**, Comparable expression levels after 4 h LPS with the addition of small amounts of Hoechst to aid in cell counting (*x* axis) and when no dye is used (*y* axis), when looking at all genes (left) or only immune response genes (right). **i**, Comparable expression levels after 4 h LPS with hourly mixing (*x* axis) or with no mixing (*y* axis), when looking at all genes (left) or only immune response elements (right). **j**, Core antiviral, peaked inflammatory, and sustained inflammatory module activation scores for a $0.1 \times$ LPS stimulation. Shown are violin plots of the scores (*y* axis) for the core antiviral (Supplementary Information, top), peaked inflammatory (Supplementary Information, middle), and sustained inflammatory modules (Supplementary Information, bottom) for each cell in (left to right): LPS 0 h, $1 \times (100 \text{ ng ml}^{-1})$ LPS 4 h, and $0.1 \times (10 \text{ ng ml}^{-1})$ LPS 4 h. **k–n**, PCA of stimulated dendritic cells. **k**, First two principal components (or PCs) from a PCA performed on the LPS stimulation time course. From top to bottom: unstimulated/LPS 0 h, LPS 1 h, LPS 2 h, LPS 4 h, LPS 6 h. **l–n**, PCAs (left) and the distributions of scores (right) for each of the first three PCs for samples collected after stimulation with LPS (**l**), PAM (**m**), or PIC (**n**), for 1 (yellow), 2 (blue), 4 (grey) and 6 (red) hours. A single PCA was performed for all cells in all three time courses.



Extended Data Figure 2 | Effects of shallow read depth on expression estimates. **a, b,** A million reads per cell are sufficient to estimate expression levels. **a,** Scatter plot for a single cell (from Shalek *et al.*¹⁶) showing the relation between expression estimates calculated using 30 M reads (*x* axis) or a sub-sample of 1 M reads (*y* axis). **b,** Scatter plots for six different dendritic cells stimulated for 4 h with LPS. Each plot shows the relation between expression estimates calculated using all reads (*x* axis; number of reads marked on axis label) or a sub-sample of 1 M reads (*y* axis). In all cases, $R > 0.99$. Note that although, in principle, no gene should be estimated as present only in a subsample but not the full data set, this does occur for a very small number of genes (for example, four genes in cell 3), representing a nuanced technical error in RNA-seq estimation. Consider two expressed genes, *A* and *B*, from distinct loci, but with a short stretch of sequence identity. At low sequencing depth, if reads only map to the shared region, estimation tools, such as RSEM³⁶

(used here), can guess erroneously which gene is expressed, such that additional sequencing depth can ‘flip’ the assignment of an uncertain read from gene *A* to gene *B*. These cases are extremely rare, and have a negligible effect.

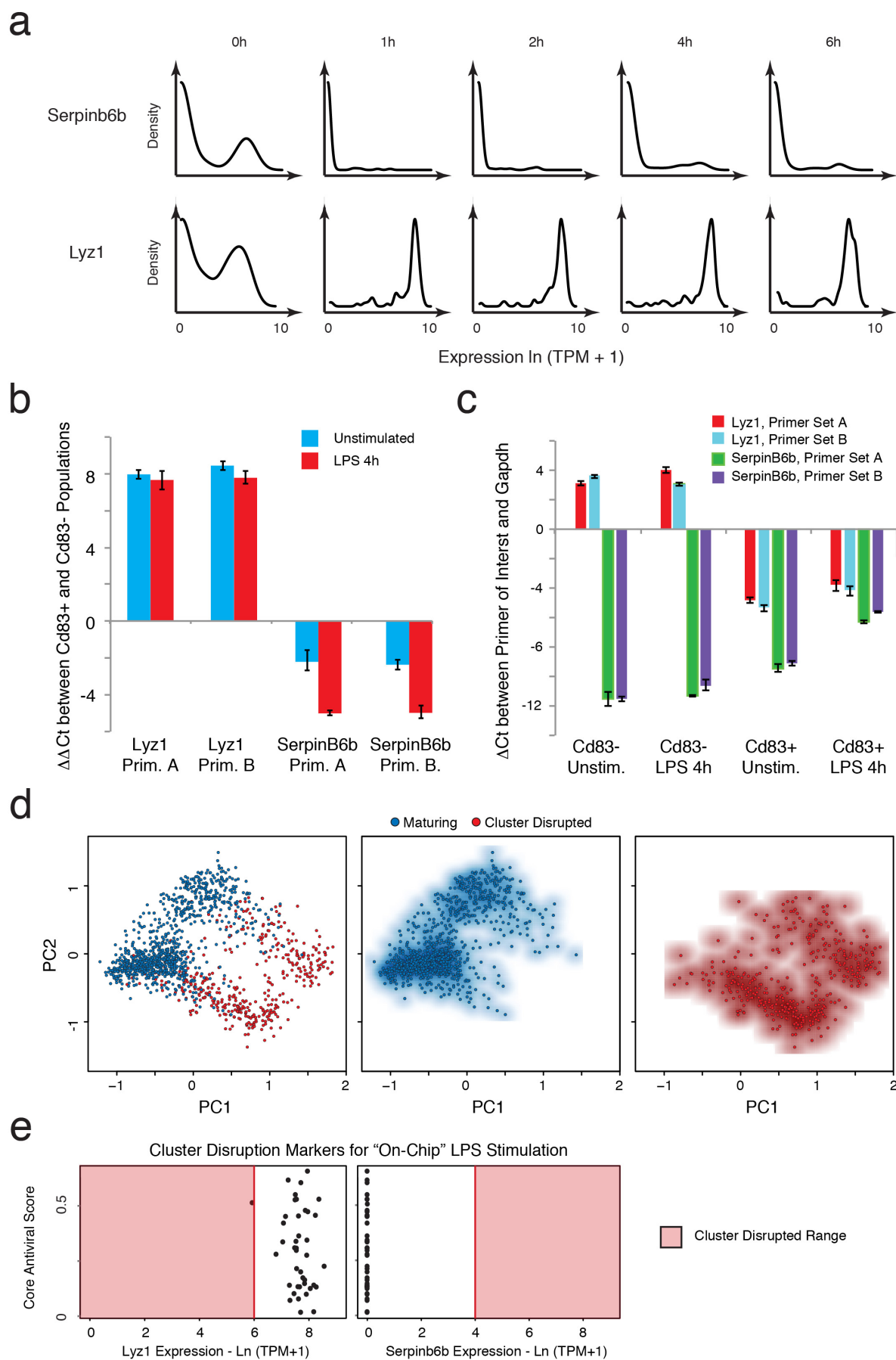
c–e, A million reads per cell are sufficient to estimate μ , σ^2 , and α . Scatter plots showing the relation between α (**c**), μ (**d**), and σ^2 (**e**) values estimated using 10 M reads per cell (on average; *x* axis) or a sub-sample of 1 M reads per cell (*y* axis) from RNA-seq libraries prepared from individual bone-marrow-derived dendritic cells stimulated for 4 h with LPS. **c,** For almost all genes, 1 M reads are sufficient to estimate α . For a very small fraction ($<0.1\%$) of weakly expressed genes, estimates of α are improved with increased sequencing depth. For μ (**d**) and σ^2 (**e**), estimates are plotted for all genes (left), only genes detected in more than 10 cells (middle), or only those genes detected in more than 30 cells (right).



Extended Data Figure 3 | Technical and biological reproducibility.

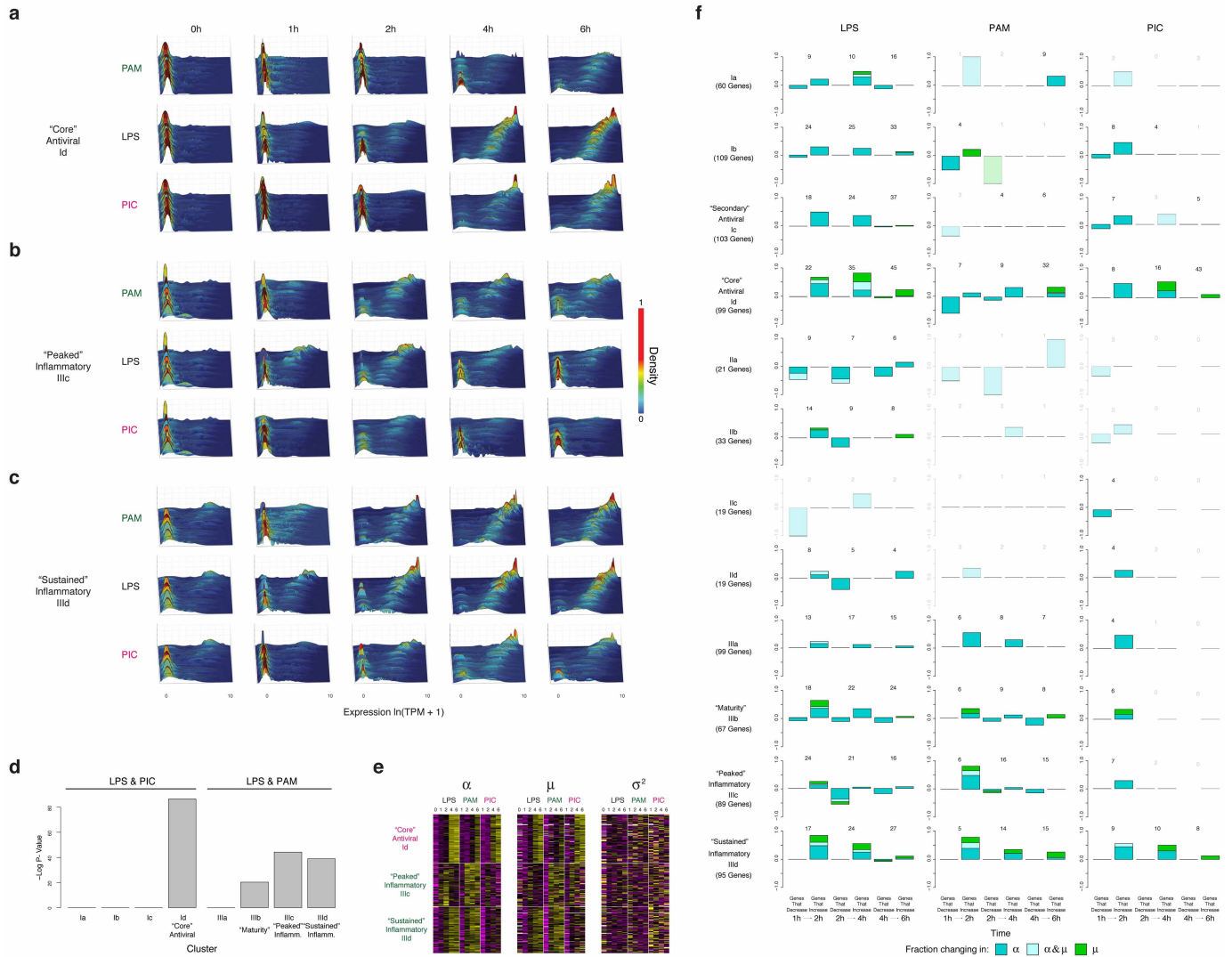
a–d, Scatter plots showing the relationship between the average single-cell expression estimates in either of two technical replicates (LPS 2 h (a), LPS 4 h (b)) or two biological replicates (unstimulated/LPS 0 h (c), LPS 4 h (d)) for all genes (top), immune response genes (middle), or non-immune response genes (bottom). **e, f** QQ plots (top) and MA plots (bottom) showing the similarity in expression estimates for the two LPS 2 h technical replicates (e) or the two LPS 4 h technical replicates (f). Plots are provided across all genes (left), non-immune response genes (middle), or immune response genes (right). **g, h** QQ plots (top) and MA plots (bottom) showing the similarity in expression estimates for all cells (including cluster-disrupted cells) in the two

LPS 0 h/unstimulated biological replicates (g) or the two LPS 4 h biological replicates (h) across either all genes (left), non-immune response genes (middle), or immune response genes (right). Note, that slight variations in the fraction of cluster-disrupted cells and activation state of one of the two 0 h samples results in mild deviations between immune response gene estimates in those biological replicates. **i, j** PCA for the two LPS 4 h technical replicates. **i**, The first two principal components (PC1 and PC2, x and y axis, respectively) of a PCA from the two LPS 4 h stimulation technical replicates (blue: replicate 1; red: replicate 2). **j**, The distributions of scores for cells from each of the two technical replicates on each of the first five PCs (left to right: PC1 to PC5).



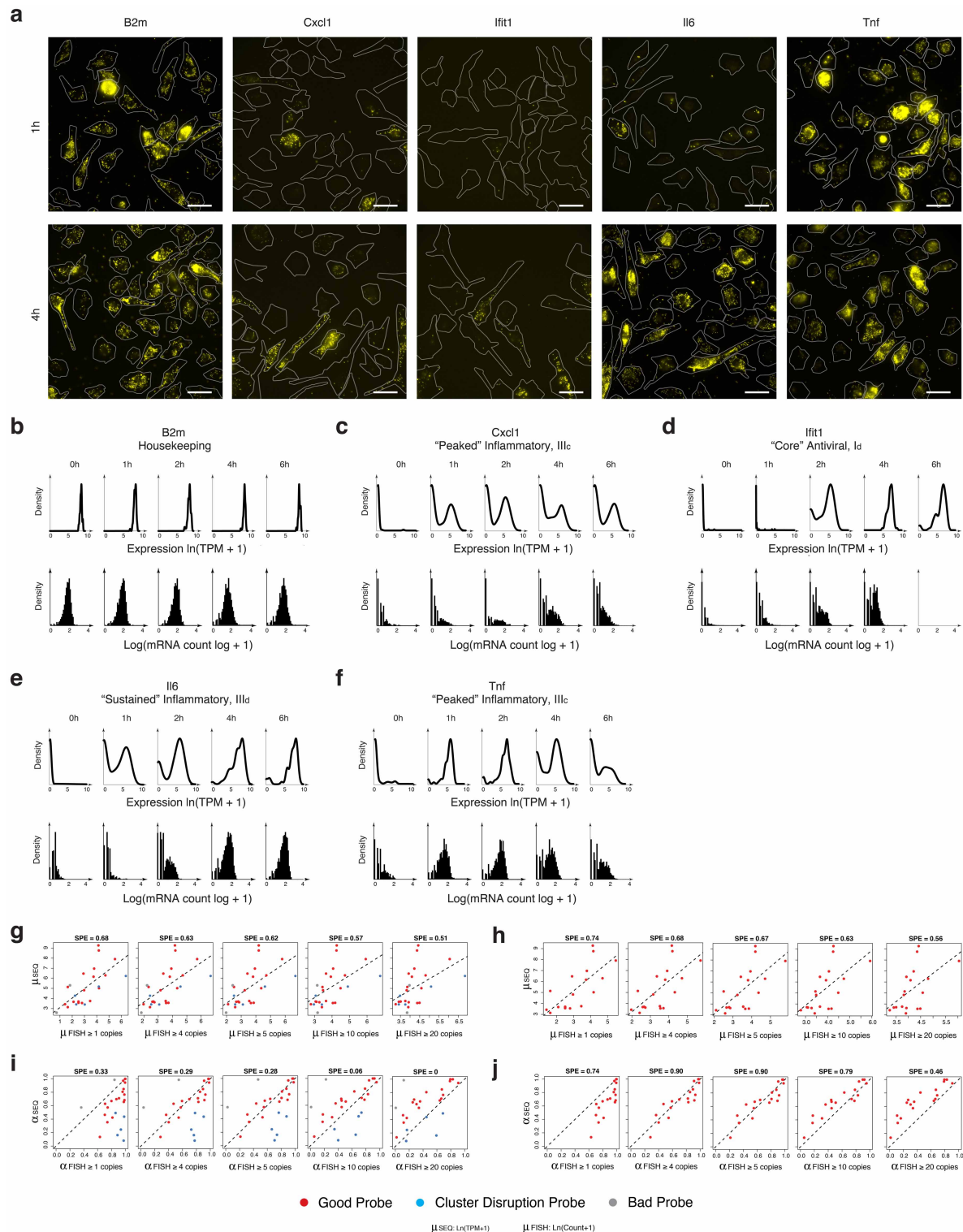
Extended Data Figure 4 | Cluster disruption. **a**, Single-cell expression distributions for *SerpinB6b* (a positive marker of cluster disruption) and *Lyz1* (a negative marker of cluster disruption) at each time point (marked on top) after stimulation with LPS (all cells included, see Supplementary Information). Distributions are scaled to have the same maximum height. **b**, Difference in mRNA expression as measured by qRT-PCR (with a *Gapdh* control) between *Lyz1* or *SerpinB6b* in cells pre-sorted before stimulation on the presence or absence of CD83 expression (CD83⁺ and CD83⁻, respectively), a known cell surface marker of cluster-disrupted cells (see Supplementary Information). Pre-sorted cells were then either unstimulated (blue) or stimulated (red) with LPS for 4 h. **c**, Expression of cluster-disruption markers does not change with

stimulation. qRT-PCR showing the difference between *Gapdh* (control) and *Lyz1* or *SerpinB6b* expression in cells pre-sorted on Cd83 either in the presence or absence of stimulation with LPS. **d**, PCA showing the separation between maturing (blue dots) and cluster-disrupted (red dots) cells. **e**, Expression of cluster disruption markers for cells stimulated with LPS on-chip. For each cell (black dot) stimulated with LPS on-chip, shown are the expression levels (*x* axis) of *SerpinB6b* (cluster disruption cell marker, left) and *Lyz1* (normal maturing cell marker, right) versus its antiviral score (*y* axis). With one exception, the cells are clearly maturing and not cluster-disrupted. Red shading: range of expression in cluster-disrupted cells.



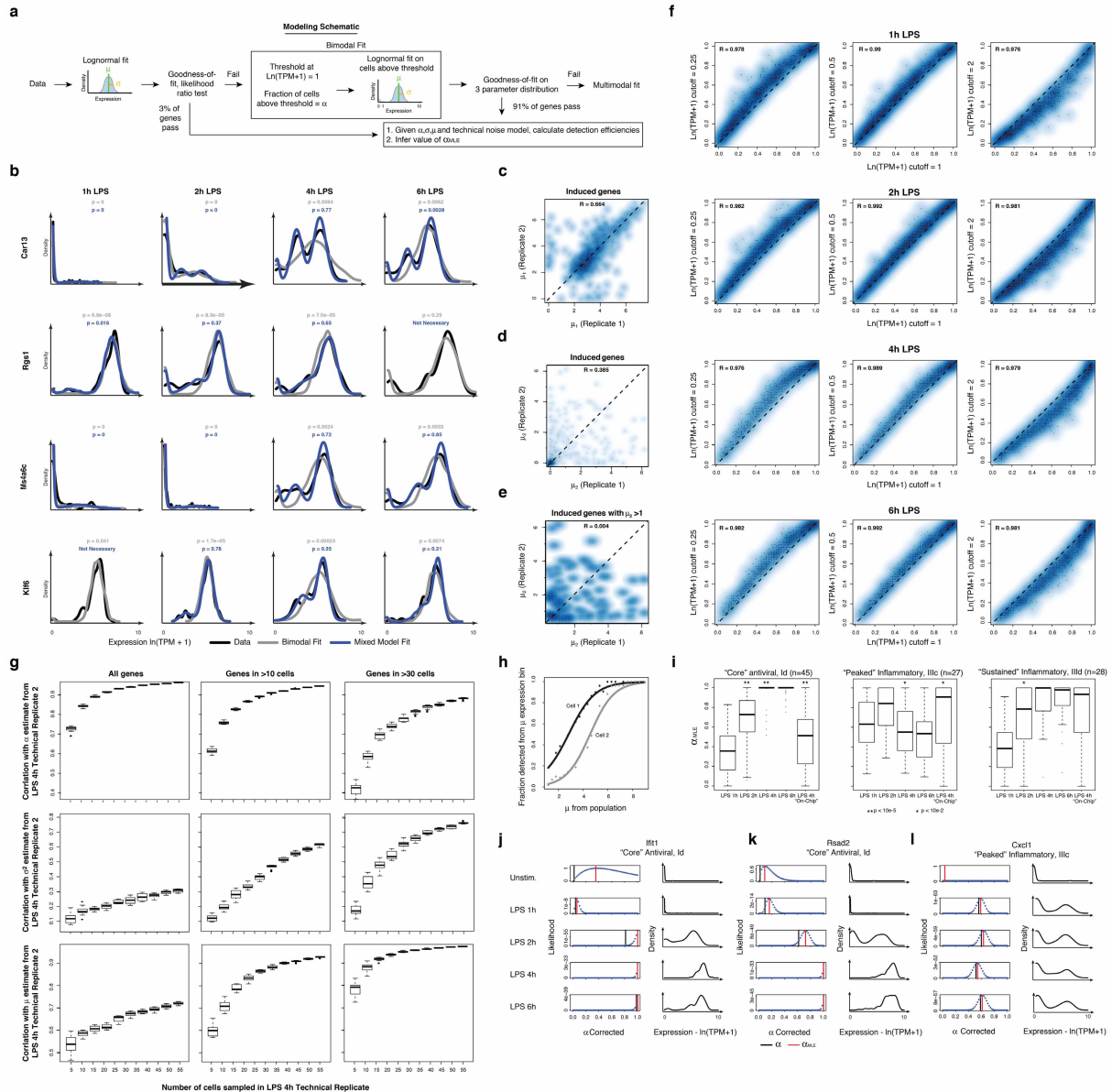
Extended Data Figure 5 | Time-dependent behaviours of single cells from different modules and stimuli. **a–c**, For each of the three key modules: core antiviral, Ia (a), peaked inflammatory, IIIc (b), and sustained inflammatory, IIId (c) shown are wave plots of all of its constituent genes in bone-marrow-derived dendritic cells stimulated with PAM (top), LPS (middle), or PIC (bottom) for 0, 1, 2, 4 and 6 h (left to right). *x* axis: expression level, ln(TPM + 1); *y* axis: genes; *z* axis: single-cell expression density (proportion of cells expressing at that level). Genes are ordered from lowest to highest average expression value at the 4 h LPS time point. **d**, Contributions of each module to measured variation. Significance of the contribution of modules Ia–Id and IIIa–IIId from Fig. 1 to the variation measured throughout the stimulation time course. Shown is the *P* value (Mann–Whitney test) of the tested association between each gene module and the first three PCs, calculated using a statistical resampling method (see Supplementary Information). Only the core antiviral, maturity, and peaked/sustained inflammatory clusters show statistically significant enrichments with the three PCs. **e**, Gene modules show coherent shifts in single-cell expression. Shown are heat maps of scaled

α (left), μ (middle), and σ^2 (right) values (colour bar, bottom) in each time course (LPS, PAM, PIC) for the genes in each of the three key modules (rows, modules marked on left). Heat maps are row-normalized across all three stimuli, with separate scalings for each of the three parameters, to highlight temporal dynamics. Genes are clustered as in Fig. 1. **f**, Dynamic changes in variation during stimulation for each module. For each module (rows) and stimulus (columns), shown are bar plots of the fraction of genes (*y* axis) with a significant change only in α (by a likelihood ratio test, $P < 0.01$, blue), only in μ (Wilcoxon test, $P < 0.01$, green), or in both (each test independently, light blue), at each transition (*x* axis), in different conditions (marked on top), separated by whether they increase or decrease during that transition. In each module and condition, the proportion is calculated out of the genes in the module that are significantly bimodal (by a likelihood ratio test) in at least one time point during the LPS response and are expressed in at least 10 cells in both conditions. Their number is marked on top of each bar; conditions with 3 or fewer genes changing are semi-transparent.



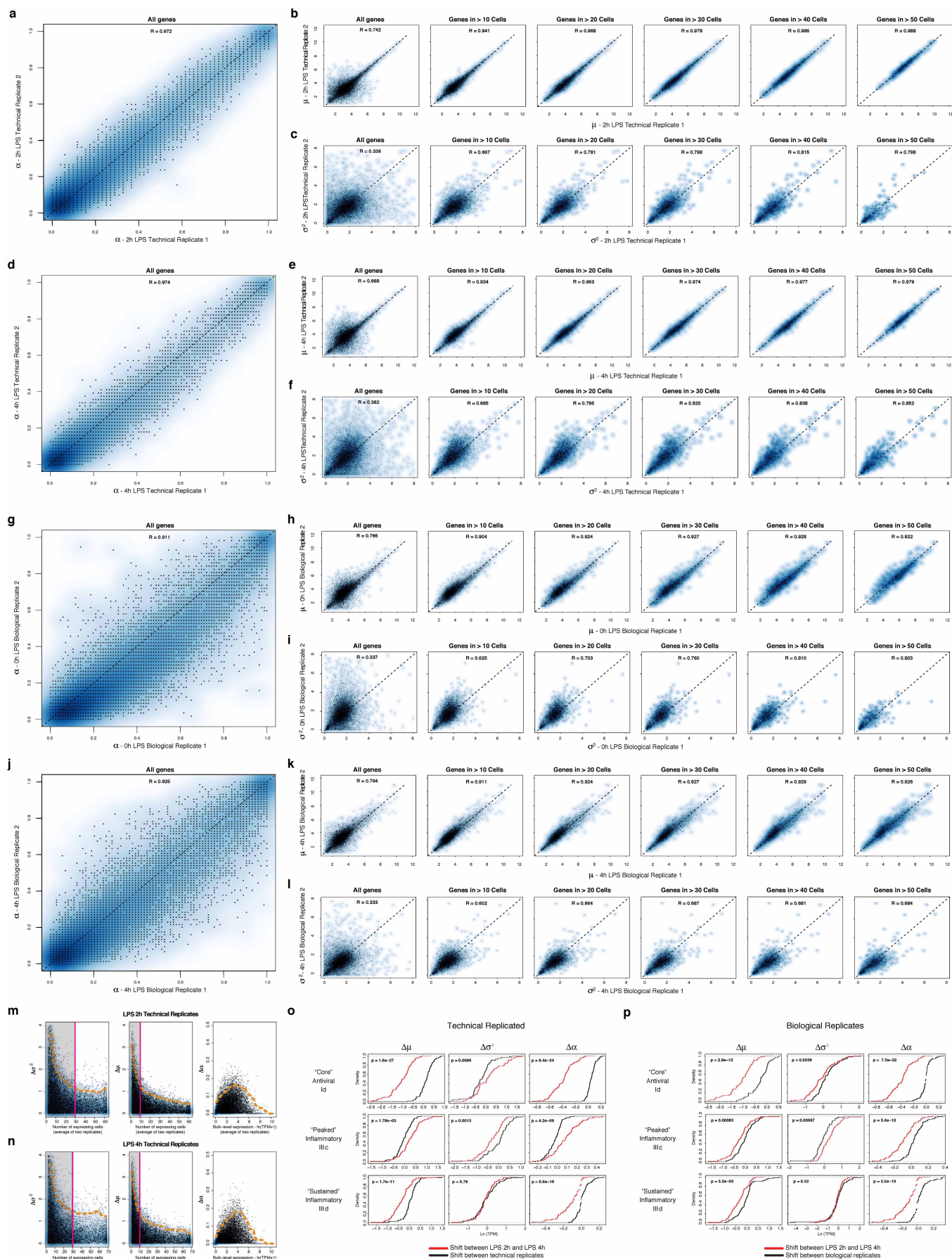
Extended Data Figure 6 | Comparison of single-cell RNA-seq to RNA-FISH. **a–f**, Single-cell mRNA expression distributions by RNA-FISH and single-cell RNA-seq. **a**, Representative images of genes analysed by RNA-FISH at 1 h and 4 h after LPS stimulation. **b–f**, mRNA expression distributions for the housekeeping gene *B2m* (**b**), the peaked inflammatory gene *Cxcl1* (**c**), the core antiviral gene *Ifit1* (**d**), the sustained inflammatory gene *Il6* (**e**), and the peaked inflammatory gene *Tnf* (**f**) measured using either single-cell RNA-seq (top, black curves) or RNA-FISH (black histograms; no smoothing) in either unstimulated cells (LPS 0 h) or cells stimulated with LPS for 1, 2, 4 or 6 h. **g–j**, Determining the detection limit of single-cell RNA-seq by comparison to RNA-FISH. For each of 25 genes, we compared single-cell RNA-seq data (y axis, this study) to RNA-FISH data (x axis, from Shalek *et al.*) based on either

their μ values (**g, h**) or α values (**i, j**), in which for RNA-FISH, expressing cells were defined for μ or α calculation at different thresholds (from left to right: at least 1, 4, 5, 10 or 20 copies per cell). **g, i**, Data from all 25 genes. **h, j**, Data after excluding probes from 5 cluster-disrupted gene markers (blue; *Ccl22*, *Ccr7*, *Irf8*, *SerpinB6b*, *Stat4*), which are less comparable since there are more cluster-disrupted cells in RNA-FISH experiments, and 2 low quality probes (grey; *Pkm2*, *Fus*) that showed very low expression in RNA-FISH, but had high expression in both single cell and population-level RNA-seq experiments. SPE (square-root of percent explained, top) represents the square-root of the total variance in the RNA-seq parameter explained by the RNA-FISH parameter, under the $y = x$ model compared to a constant fit (that is, $y = \bar{y}$).



Extended Data Figure 7 | Fitting gene expression distributions. **a**, Flow chart of model fitting. Shown are the key steps in fitting the 3-parameter model. **b**, Examples of cases where fitting a multimodal distribution is required. Single-cell expression distributions for (top to bottom) *Car13*, *Rgs1*, *Ms4a6c* and *Klf6* at (left to right) 1, 2, 4, and 6 h (marked on top) after stimulation with LPS. Distributions are scaled to have the same maximum height. Data: black lines; Bimodal fits: grey lines; Multimodal fits: blue lines. *P* values (colour-coded) calculated using a goodness-of-fit test (a low *P* value rejects the fit; see Supplementary Information). **c–e**, Reproducibility of gene-specific fitting of the undetected mode, when fitting a mix of two normal distributions to all data points, including those with $\ln(\text{TPM} + 1) < 1$. **c**, **d**, Scatter plot showing the correlation between μ_1 and μ_2 estimates for the two LPS 4 h technical replicates (Supplementary Information), where μ_1 and μ_2 are the two component means (in decreasing order of magnitude) of the two mixed normal distributions. Estimates for μ_2 correlate poorly between technical replicates, particularly when focusing on genes for which μ_2 is greater than 1 (**e**), suggesting that the current data set does not support the use of this additional fit parameter. **f**, Robustness of α estimates to small deviations in the threshold. Scatter plots showing the correlation between α estimates determined when using a cut-off of $\ln(\text{TPM} + 1) = 1$ (*x* axis) versus when using a cut-off of $\ln(\text{TPM} + 1) = 0.25$ (*y* axis, left); 0.5 (*y* axis, middle) or 2 (*y* axis, right) for the LPS time course (top to bottom: 1 h, 2 h, 4 h and 6 h). **g**, Saturation curves for estimates of μ , σ^2 , and α . Box plots depicting the Pearson correlation coefficient between α (top), μ (middle), or σ^2 (bottom) in two LPS 4 h technical replicates, as a function of

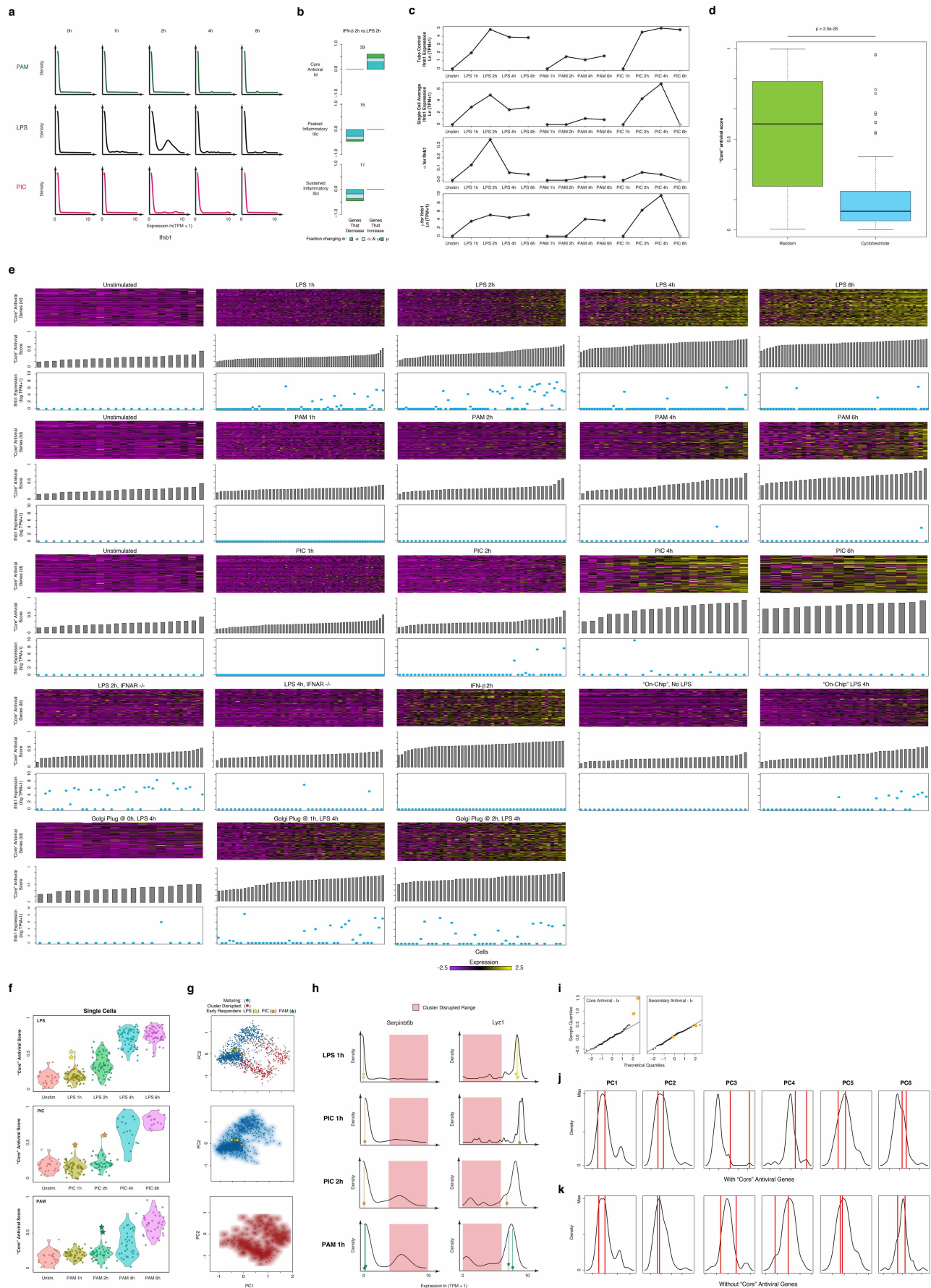
the number of cells randomly drawn from each replicate (full details in Supplementary Information). Plots are shown for all genes (left), as well as those detected in more than 10 (middle) or 30 cells, (right) in both replicates (full data sets). **h**, **i**, Correcting for the relationship between mean expression and average detection. **h**, The probability of detecting a transcript (*y* axis) in a cell as a function of μ (*x* axis). Black, grey curves are two illustrative cells from the LPS 4 h time point. **i**, Differences in α_{MLE} , a stringently-corrected MLE estimate of α (Supplementary Information), across the LPS time course. Shown are the box plots of α_{MLE} values (*y* axis) for bimodally expressed genes (determined by a likelihood ratio test, Supplementary Information) at each time point (1, 2, 4, and 6 h) following LPS stimulation (*x* axis), as well as for the on-chip 4 h LPS stimulation, for each of the core antiviral (left), peaked inflammatory (middle) and sustained inflammatory (right) modules. Stars represent intervals where there is a significant difference in a parameter between two consecutive time points, as determined by a Wilcoxon rank sum test (single star: $P < 10^{-2}$; double star: $P < 10^{-5}$). **j–l**, Estimating an upper bound on α using a likelihood test. For each of three transcripts (*Ifit1* (**j**); *Rgs2* (**k**); and *Cxcl1* (**l**)), shown are their expression distributions (red, left) and the matching likelihood function for a stringent upper estimate of α (blue dots, right), when considering a null model where expression is distributed in a lognormal fashion and any deviations are due to technical detection limits (Supplementary Information). Red vertical line: α_{MLE} ; black vertical line: nominal α . Vertical green bars signify the nominal estimation of α , representing the fraction of cells with detected expression of a transcript.



Extended Data Figure 8 | Reproducibility of estimated μ , σ^2 and α

parameters. **a–f**, Reproducibility of estimated μ , σ^2 and α parameters between technical replicates. Scatter plots showing the relation between the estimated α (**a**), μ (**b**), and σ^2 (**c**) values for the two unstimulated/LPS 0 h technical replicates. For μ (**b**) and σ^2 (**c**), estimates are plotted for all genes (farthest on the left), as well as (left to right) for genes only detected in more than 10, 20, 30, 40 or 50 cells, respectively. **d–f**, show the same plots for the two LPS 4 h technical replicates. **g, h**, Reproducibility of estimated μ , σ^2 and α parameters between biological replicates. Scatter plots showing the relation between the α (**g**), μ (**h**), and σ^2 (**i**) values estimates for the two LPS 2 h biological replicates. For μ (**h**) and σ^2 (**i**), estimates are plotted for all genes (farthest on the left), as well as (left to right) for genes only detected in more than 10, 20, 30, 40 or 50 cells, respectively. **j–l**, show the same plots for the two LPS 4 h biological replicates. **m, n**, Relationship between per-gene errors for μ , σ^2 and α and the number of cells in which the gene's expression is detected, or its bulk expression level. Scatter plots displaying the differences in the σ^2 (left), μ (middle) and

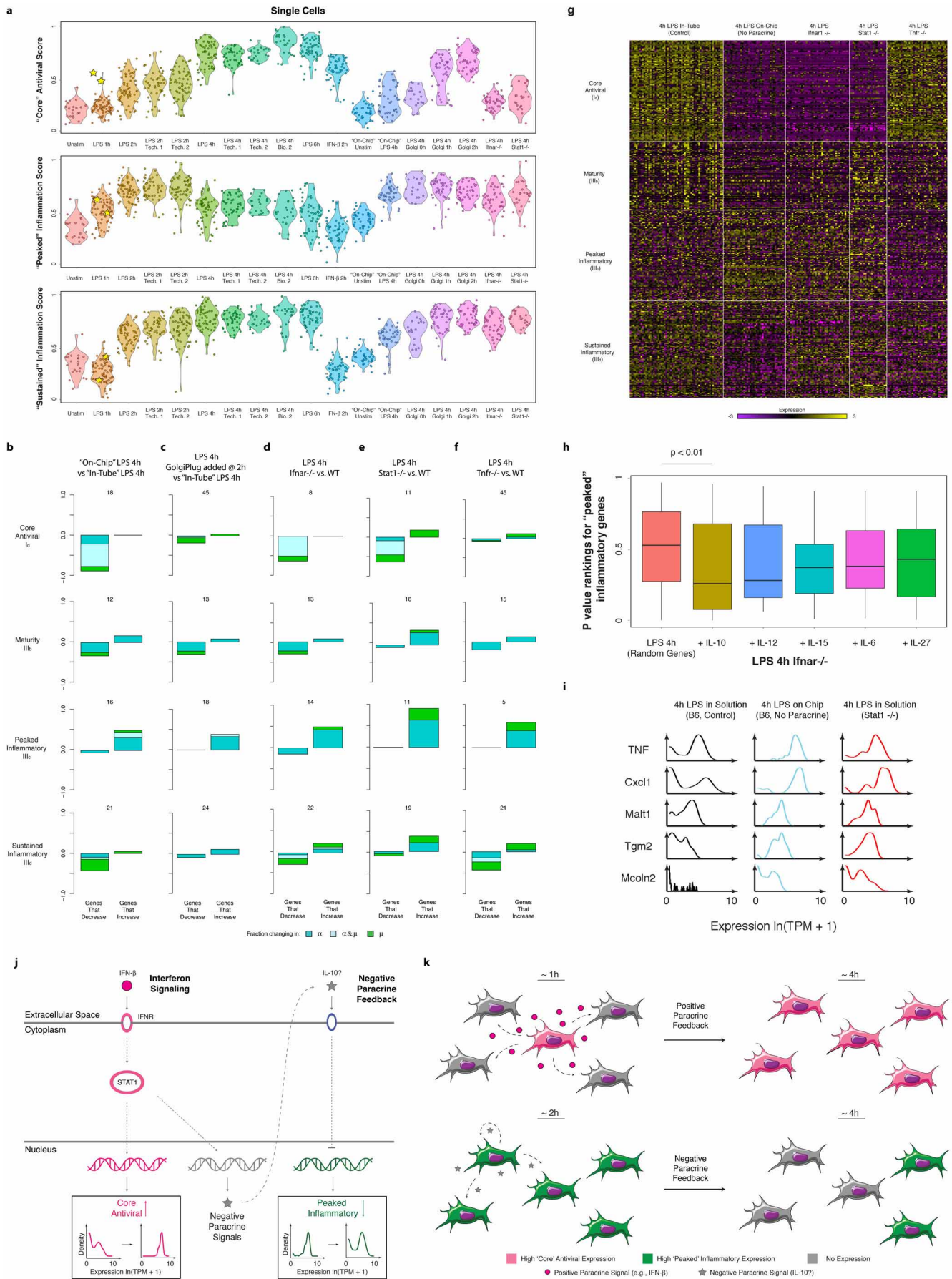
α (right) estimates for each gene between technical replicates for LPS 2 h (**m**) or LPS 4 h (**n**) (y axis) as a function of either the number of cells in which the transcript is detected (x axis, for μ and σ^2), or the transcript's bulk expression level (TPM, x axis, for α). Notably, σ^2 (left) estimates saturate (denoted by a magenta line and shaded box) after ~ 30 detectable events, whereas μ estimates saturate after ~ 10 . Dashed orange line: 95% confidence interval. **o, p**, Changes in μ , σ^2 and α between time points are significant as compared to null models from both technical and biological replicates. Shown are the cumulative distribution functions (CDF) for shifts in μ (left), σ^2 (middle), and α (right) between 2 h and 4 h (red CDF) for the core antiviral (top), peaked inflammatory (middle), and sustained inflammatory (bottom) modules compared to a null model (black CDF) derived from either technical (**o**) or biological (**p**) replicates (Supplementary Information). In the vast majority of cases, the changes between time points are significant, as assessed by a Kolmogorov–Smirnov (KS) test (P value of test in the upper left corner of each plot).



Extended Data Figure 9 | *Ifnb1* expression, production, and precocious cells.

a, b. *Ifnb1* mRNA expression and the effect of IFN- β on variation. **a.** Single-cell expression distributions for the *Ifnb1* transcript at each time point (top) after stimulation with PAM (top, green), LPS (middle, black), or PIC (bottom, magenta). Distributions are produced with the density function in *R* with default parameters, and scaled to have the same maximum density. **b.** For each of three modules defined in Fig. 1 (core antiviral, top; peaked inflammatory, middle; sustained inflammatory, bottom), shown are bar plots of the fraction of genes (*y* axis) with a significant change only in α (by a likelihood ratio test, $P < 0.01$, blue), only in μ (Wilcoxon test, $P < 0.01$, green), or in both (each test independently, light blue) between the 2 h LPS stimulation and the 2 h IFN- β stimulation separated by whether they increase or decrease during that transition. In each module and condition, the proportion is calculated out of the genes in the module that are significantly bimodal (by a likelihood ratio test) in at least time point during the LPS response and are expressed in at least 10 cells in both conditions. Their number is marked on top of each bar. **c, d.** *Ifnb1* mRNA expression patterns and effect of cycloheximide. **c.** From top to bottom, population average *Ifnb1* mRNA expression (top), single-cell average *Ifnb1* mRNA expression (second to top), α (second to bottom) and μ (bottom) estimates for *Ifnb1* for each stimulation condition in Fig. 1. Grey star at 6 h for PIC denotes uncertainty due to the small number of cells captured at that time point. **d.** Shown are box plots of the core antiviral scores (population level, see Supplementary Information) after a 4 h LPS stimulation either where cycloheximide was added at the time of stimulation (right, blue), or during a standard 4 h LPS control (left, green). Core antiviral expression is dramatically decreased by the addition of cycloheximide, suggesting that newly produced protein is needed to initiate the antiviral response. **e.** Relationship between core antiviral gene expression and *Ifnb1* mRNA expression during the LPS, PAM and PIC stimulation time courses and in follow-up experiments. Shown are the expression of core antiviral genes (heat maps: rows, gene; columns, cells) for cells stimulated for 0, 1, 2, 4 or 6 h (left to right) with LPS (top), PAM (middle), or PIC (bottom). Beneath each heat map, grey bars depict the core antiviral score (middle panel, see

Supplementary Information) and blue dots show *Ifnb1* mRNA expression for each cell in every heat map. **f–k.** Identifying the precocious cells. **f.** Core antiviral scores for cells stimulated with LPS, PIC, or PAM. Shown are violin plots of the core antiviral module scores (Supplementary Information, *y* axis) for each cell from time course experiments (from left: 0, 1, 2, 4 and 6 h) of dendritic cells stimulated with LPS (top), PIC (middle) or PAM (bottom). Two precocious cells (yellow stars, top panel) have unusually high antiviral scores at 1 h LPS (yellow stars, top); similarly precocious cells can be seen in PIC at 1 h and 2 h (orange stars, middle) or in PAM at 2 h (turquoise stars, bottom). **g.** Precocious cells in all three responses are typical maturing cells. PCA showing the separation between maturing (blue dots) and cluster-disrupted (red dots) cells (top), as well as only maturing (middle) or only cluster-disrupted (bottom) cells (all as also shown in Extended Data Fig. 4d). The precocious cells from each of the responses are marked as stars (colours as in (f)), and all fall well within the maturing cells. **h.** Precocious cells in all three responses express *Lyz1* and do not express *SerpinB6b*. Shown are mRNA expression distributions for *SerpinB6b* (cluster disruption cell marker, left) and *Lyz1* (normal maturing cell marker, right) in LPS 1 h, PIC 1 h and 2 h, and PAM 1 h (top to bottom). The typical range for expression in cluster-disrupted cells is shaded in red. The precocious cells from each of the responses are marked as stars (colours as in (f)), and all fall well within the maturing cells. **i.** Normal quantile plots of the expression of genes from the core (cluster I_a, left) and secondary (cluster I_c, right) antiviral clusters at 1 h LPS. The two precocious cells (yellow stars) express unusually high levels of core antiviral genes (left) but not of secondary genes (right). **j, k.** The precocious cells are only distinguished by the expression of ~ 100 core antiviral genes. Shown are the distributions of scores for each of the first six PCs (right) for samples collected after stimulation with LPS for 1 h with (j) or without (k) the inclusion of core antiviral genes. Precocious cells (vertical red bars), normally distinguished by the third and fourth principle components (j), become indistinguishable from all other cells if the ~ 100 core antiviral genes are excluded (k) before performing the PCA.



Extended Data Figure 10 | Characterizing the precocious cells. **a**, Core antiviral, peaked inflammatory, and sustained inflammatory module scores during the LPS time course and follow-up experiments. Shown are violin plots of the scores (y axis) for the core antiviral (Supplementary Information, top), peaked inflammatory (Supplementary Information, middle), and sustained inflammatory (Supplementary Information, bottom) modules for cells in each of the experiments (from left to right): LPS 0 h, LPS 1 h, LPS 2 h, LPS 2 h technical replicate 1, LPS 2 h technical replicate 2, LPS 4 h, LPS 4 h technical replicate 1, LPS 4 h technical replicate 2, LPS 4 h biological replicate, LPS 6 h, IFN- β 2 h, on-chip unstimulated, on-chip LPS 4 h, LPS 4 h with GolgiPlug at 0 h, LPS 4 h with GolgiPlug at 1 h, LPS 4 h with GolgiPlug at 2 h, LPS 4 h with *Ifnar*^{-/-} dendritic cells, and LPS 4 h with *Stat1*^{-/-} dendritic cells. Yellow stars: the two precocious cells at 1 h LPS. **b**, Changes in expression and variation during stimulation in the on-chip 4 h LPS stimulation. For genes in the (from top to bottom) core antiviral, maturity, peaked inflammatory and sustained inflammatory modules, shown are bar plots of the fraction of genes (y axis) with a significant change only in α (by a likelihood ratio test, $P < 0.01$, blue), only in μ (Wilcoxon test, $P < 0.01$, green), or in both (each test independently, light blue) between the 4 h on-chip LPS stimulation and the 4 h in-tube LPS stimulation separated by whether they increase or decrease during that transition. In each module and condition, the proportion is calculated out of the genes in the module that are significantly bimodal (by a likelihood ratio test) in at least one time point during the LPS response and are expressed in at least 10 cells in both conditions. Their number is marked on top of each bar. **c–f**, Bar plots, as in **b**, for a 4 h wild-type LPS stimulation (in-tube) and either a 4 h in-tube LPS stimulation where GolgiPlug was added 2 h after LPS (**c**), a 4 h LPS stimulation of *Ifnar*^{-/-} dendritic cells (**d**), a 4 h LPS stimulation of *Stat1*^{-/-} dendritic cells (**e**), or a 4 h LPS Stimulation of *Tnfr*^{-/-} dendritic cells (**f**).

g, Genetic perturbations alter expression and variation in different inflammatory and antiviral modules. Shown is the expression of the genes (rows) in, from top to bottom: the core antiviral (I_d), maturity (III_b), peaked inflammatory (III_c), and sustained inflammatory (III_d) modules in single cells (columns) in, from left to right: the in-tube, on-chip, *Ifnar*^{-/-}, *Stat1*^{-/-}, and *Tnfr*^{-/-} conditions. Yellow/purple colour scale: scaled expression values (z -scores). **h**, Scores of the peaked inflammatory module for *Ifnar*^{-/-} dendritic cells with recombinant cytokines. Shown are box plots of the peaked inflammatory module scores (Supplementary Information, y axis) for three population-level replicates of a 4 h LPS stimulation of *Ifnar*^{-/-} dendritic cells to which a recombinant cytokine (x axis) has been added at 2 h after stimulation. Notably, adding IL-10 significantly reduces the peaked inflammatory module. **i**, *Stat1* knockout affects expression and variation of peaked inflammatory genes. Shown are expression distributions for five peaked inflammatory genes after 4 h of LPS stimulation in each of three conditions: in-tube stimulation of wild-type dendritic cells (control; left), on-chip stimulation of wild-type cells (no cell-to-cell signalling; middle), and a stimulation of dendritic cells from *Stat1*^{-/-} mice (performed in-tube; right). **j**, **k**, Population-level paracrine signalling enhances and coordinates the core antiviral response while dampening and desynchronizing the peaked inflammatory ones. **j**, Gene network model showing how positive IFN- β signalling induces the antiviral response and reduces its heterogeneity, while simultaneously activating negative paracrine feedback, possibly including IL-10, which dampens the peaked inflammatory cluster and increases its heterogeneity. **k**, Cell population model showing how positive and negative paracrine signalling alter antiviral (magenta) and inflammatory (green) gene expression variability across cells. Grey denotes no expression.

The mitochondrial deubiquitinase USP30 opposes parkin-mediated mitophagy

Baris Bingol^{1*}, Joy S. Tea^{1*}, Lilian Phu², Mike Reichelt³, Corey E. Bakalarski⁴, Qinghua Song⁵, Oded Foreman³, Donald S. Kirkpatrick² & Morgan Sheng¹

Cells maintain healthy mitochondria by degrading damaged mitochondria through mitophagy; defective mitophagy is linked to Parkinson's disease. Here we report that USP30, a deubiquitinase localized to mitochondria, antagonizes mitophagy driven by the ubiquitin ligase parkin (also known as PARK2) and protein kinase PINK1, which are encoded by two genes associated with Parkinson's disease. Parkin ubiquitinates and tags damaged mitochondria for clearance. Overexpression of USP30 removes ubiquitin attached by parkin onto damaged mitochondria and blocks parkin's ability to drive mitophagy, whereas reducing USP30 activity enhances mitochondrial degradation in neurons. Global ubiquitination site profiling identified multiple mitochondrial substrates oppositely regulated by parkin and USP30. Knockdown of USP30 rescues the defective mitophagy caused by pathogenic mutations in parkin and improves mitochondrial integrity in parkin- or PINK1-deficient flies. Knockdown of USP30 in dopaminergic neurons protects flies against paraquat toxicity *in vivo*, ameliorating defects in dopamine levels, motor function and organismal survival. Thus USP30 inhibition is potentially beneficial for Parkinson's disease by promoting mitochondrial clearance and quality control.

Mitophagy, a specialized autophagy pathway that mediates the clearance of damaged mitochondria by lysosomes, is important for mitochondrial quality control¹. Defective mitochondria, if left uncleared, can be a source of oxidative stress and compromise the health of the entire mitochondrial network.

Parkinson's disease is characterized prominently, but not solely, by loss of dopaminergic neurons in the substantia nigra. Although the pathogenic mechanisms of Parkinson's disease are unclear, several lines of evidence suggest that mitochondrial dysfunction is central to the disease². Most compellingly, familial Parkinson's disease can be caused by mutations in the ubiquitin ligase parkin and protein kinase PINK1^{3,4}, both of which maintain healthy mitochondria via regulating mitochondrial dynamics and quality control¹. Genetic studies established that PINK1 acts upstream of parkin^{5–7}. PINK1 recruits parkin from the cytoplasm to the surface of damaged mitochondria, leading to parkin-mediated ubiquitination of mitochondrial outer membrane proteins and removal of damaged mitochondria by mitophagy^{8–10}. Parkinson's disease-associated mutations in PINK1 or parkin impair parkin recruitment, mitochondrial ubiquitination, and/or mitophagy^{8,11,12}. In the context of the inherently high mitochondrial oxidative stress in substantia nigra dopamine neurons¹³, loss of parkin-mediated mitophagy could explain the greater susceptibility of substantia nigra neurons to neurodegeneration. Thus, promoting mitophagy and enhancing mitochondrial quality control could benefit dopaminergic neurons. To this end, we performed a screen for deubiquitinase enzymes (DUBs) that function in opposition to parkin and identified USP30, a mitochondria-localized DUB, as an antagonist of parkin-mediated mitophagy.

USP30 antagonizes mitophagy

We screened a Flag-tagged human DUB complementary DNA library in a well-established mitochondrial degradation assay⁸: in cultured cells overexpressing parkin, mitochondria depolarization induced by the

protonophore carbonyl cyanide 3-chlorophenylhydrazone (CCCP) results in loss of mitochondria (measured by immunostaining for mitochondrial outer membrane protein TOM20, also known as TOMM20). CCCP caused a robust disappearance of TOM20 staining in more than 80% of cells transfected with green fluorescent protein (GFP)-conjugated parkin (Fig. 1a). By testing individual cDNAs from a library of about 100 different DUBs, only two DUBs (USP30 and DUBA2; also known as OTUD6A) robustly blocked this loss of TOM20 staining (Fig. 1a). We focused on USP30 because it was reported to be localized in the mitochondrial outer membrane with its enzymatic domain putatively facing the cytoplasm¹⁴. We confirmed specific mitochondrial association of USP30 (Extended Data Fig. 1a–c). Thus, USP30 is in the right subcellular compartment to counteract the action of parkin on mitochondria.

The ability of USP30 overexpression to prevent CCCP-induced mitophagy was further confirmed in dopaminergic SH-SY5Y cells transfected with MYC-parkin (Fig. 1b). In addition to TOM20, USP30 overexpression also blocked the CCCP-induced loss of HSP60 (a mitochondrial matrix protein, also known as HSPD1), indicating that USP30 antagonizes en masse degradation of mitochondria (Fig. 1b–d). A catalytically inactive USP30(C77S) mutant¹⁴ was ineffective at preventing parkin-mediated mitochondrial degradation, indicating that USP30 counteracts mitophagy through deubiquitination (Fig. 1b–d). Consistently, USP30 overexpression reduced accumulation of ubiquitin signal on mitochondria in CCCP-treated GFP-parkin-expressing cells, dependent on USP30 catalytic activity (Extended Data Fig. 2a, b). USP30 co-expressed with parkin also reduced CCCP-induced recruitment of autophagy markers p62 and LC3–GFP^{15–17} to parkin-associated mitochondria (Extended Data Fig. 2c–f). Co-expression of USP30 did not alter parkin expression level or the translocation of parkin to mitochondria (Extended Data Fig. 1d, e; Fig. 1b, e). These data indicate that USP30 functions as a DUB that opposes ubiquitination of mitochondrial proteins by parkin, thereby inhibiting mitophagy.

¹Department of Neuroscience, Genentech, Inc., South San Francisco, California 94080, USA. ²Department of Protein Chemistry, Genentech, Inc., South San Francisco, California 94080, USA. ³Department of Pathology, Genentech, Inc., South San Francisco, California 94080, USA. ⁴Department of Bioinformatics & Computational Biology, Genentech, Inc., South San Francisco, California 94080, USA.

⁵Department of Non-Clinical Biostatistics, Genentech, Inc., South San Francisco, California 94080, USA.

*These authors contributed equally to this work.

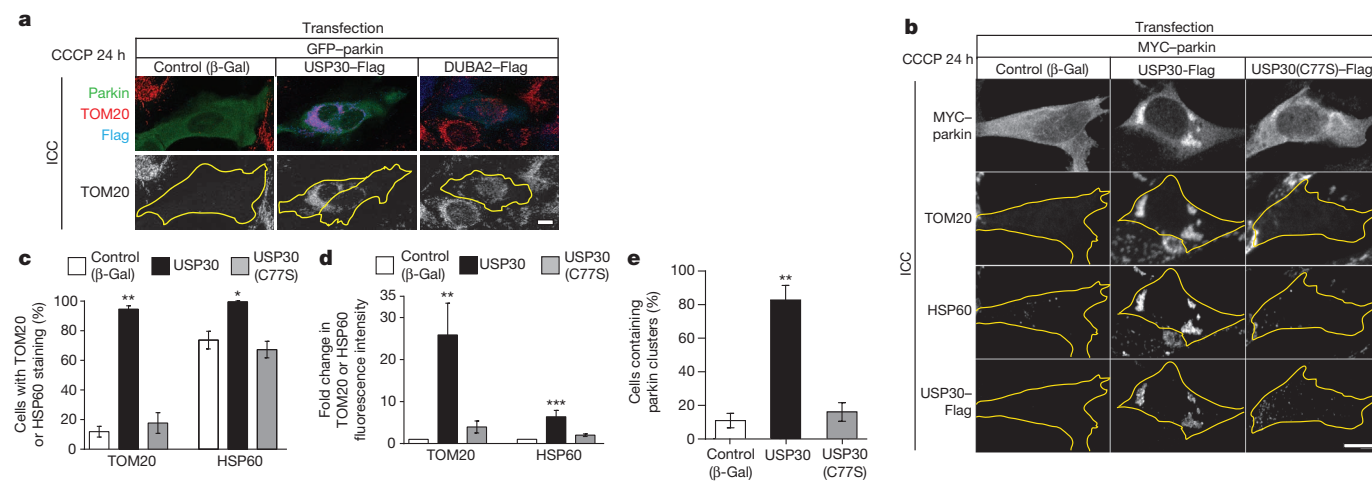


Figure 1 | USP30 antagonizes parkin-mediated mitophagy.

a, b, Immunostaining of HeLa (**a**) or SH-SY5Y (**b**) cells transfected as indicated and treated with CCCP (20 μM, 24 h). Scale bars, 10 μm. **c–e**, Quantification of percent of cells with TOM20 or HSP60 staining (**c**), fold change in TOM20 or

HSP60 immunofluorescence intensity (**d**), and percentage of cells containing parkin clusters (**e**), from **b**. Kruskal–Wallis test. $n = 5–6$ experiments. Error bars, standard error of the mean (s.e.m.).

PINK1, parkin required for mitophagy

To measure mitophagy in neurons, we monitored mt-Keima, a ratio-metric pH-sensitive fluorescent protein that is targeted into the mitochondrial matrix. A low-ratio mt-Keima-derived fluorescence (543 nm/458 nm) reports neutral environment, whereas a high-ratio fluorescence reports acidic pH¹⁸. Thus, mt-Keima enables differential imaging of mitochondria in the cytoplasm and mitochondria in acidic lysosomes. Because mt-Keima is resistant to lysosomal proteases¹⁸, it allows for measurement of cumulative lysosomal delivery of mitochondria over time.

In cultured rat hippocampal neurons, mt-Keima signal accumulated in elongated structures characteristic of mitochondria with low 543 nm/458 nm ratio values (Extended Data Fig. 3a, shown in green), and in multiple round structures throughout the cell body with high ratio (acidic) signal (Extended Data Fig. 3a, red). We confirmed these round mt-Keima-positive structures are most likely to be lysosomes, as previously described (Extended Data Fig. 3b–d)¹⁸. Since almost all of the ‘acidic’ mt-Keima signal was found in neuronal cell bodies, we used the ratio of the area of lysosomal (red) signal/mitochondrial (green) signal within the cell body as a measure of lysosomal delivery of mitochondria (‘mitophagy index’)¹⁸. As quantified by this mitophagy index, the abundance of mt-Keima in lysosomes increased over a time course of days (Extended Data Fig. 3e), indicating ongoing mitophagy in cultured neurons under basal conditions.

In heterologous cells, parkin overexpression can drive mitochondrial degradation upon mitochondrial depolarization; however, it is not yet established whether endogenous parkin and PINK1 are required for mitophagy in either non-neuronal or neuronal cells¹. To examine their roles in neuronal mitophagy, we knocked down parkin or PINK1 in neuronal cultures using small hairpin RNAs (shRNAs) (Extended Data Fig. 3f–i). Compared to control luciferase shRNA, parkin or PINK1 shRNAs (either of two independent sequences) reduced mitochondria delivery to lysosomes (Fig. 2a–d). Consistent with the genetic epistasis in flies^{6,7}, PINK1 overexpression enhanced mitophagy in neurons, an effect that was completely eliminated by parkin knockdown (Extended Data Fig. 3j, k). On the other hand, parkin overexpression by itself had no apparent effect on basal mitophagy, as measured by the mt-Keima assay (Extended Data Fig. 3l, m). Thus, neuronal mitophagy requires both PINK1 and parkin, with PINK1—apparently the limiting factor—acting upstream of parkin.

USP30 antagonizes mitophagy in neurons

Does USP30 suppress mitophagy in neurons? In the mt-Keima assay, USP30 overexpression caused a ~70% reduction in mitophagy index,

indicating that USP30 inhibits lysosomal delivery of mitochondria in neurons (Fig. 2e, f). In contrast, overexpression of enzymatically inactive USP30 (C77S or C77A) induced a robust increase in mitophagy (Fig. 2e, f), probably reflecting a dominant-negative action of catalytically inactive USP30. To test the function of endogenous USP30, we knocked down USP30 using shRNAs (Fig. 2g, h). In neurons, the rat USP30 shRNA induced a modest increase in the area of individual mitochondria in dendrites (Extended Data Fig. 3n, o). More importantly, USP30 knockdown enhanced mitophagy (~60% increase in mitophagy index) (Fig. 2i, j). This effect was ‘rescued’ by co-transfection of shRNA-resistant human USP30 cDNA, indicating that USP30 shRNA was not exerting a non-specific effect (Fig. 2g, i, j). In fact, neurons co-transfected with human USP30 cDNA plus rat USP30 shRNA showed lower levels of lysosomal accumulation of mt-Keima than controls, similar to neurons overexpressing wild-type USP30 by itself (Fig. 2e, f). Moreover, human USP30(C77S) mutant failed to reverse the enhanced mitophagy induced by USP30 shRNA, and actually enhanced mitophagic activity even more than USP30 shRNA (Fig. 2i, j), the latter result suggesting that USP30 knockdown is incomplete. In HEK-293 cells, autophagic flux (as measured by dynamic levels of LC3-II and p62) was inhibited by USP30 overexpression, dependent on enzymatic activity, and enhanced by USP30 knockdown (Extended Data Fig. 4, see Supplementary Results). Together, these results show that endogenous USP30 restrains mitophagy in cells through its DUB activity.

USP30 deubiquitinates mitochondrial proteins

Using mass spectrometry (MS) analysis following immunoaffinity enrichment of ubiquitinated peptides with ubiquitin branch-specific (K-GG) antibodies¹⁹, we identified 41 proteins whose ubiquitination was oppositely regulated by parkin and USP30 (see Supplementary Results, Supplementary Tables 1–3 and Extended Data Fig. 5a). We focused on two such mitochondrial proteins, TOM20 and MIRO1 (also known as RHOT1), that showed large increases in ubiquitination with USP30 knockdown and parkin overexpression. To confirm that USP30 can deubiquitinate these proteins, cell lines stably overexpressing GFP-parkin were transfected with haemagglutinin (HA)-conjugated ubiquitin, and ubiquitinated proteins were immunoprecipitated using anti-HA antibodies. Following mitochondrial depolarization with CCCP, GFP-parkin stable cells showed enhanced ubiquitination of endogenous MIRO1 and TOM20, as measured by immunoblotting for these proteins in the anti-HA immunoprecipitates (Fig. 3a–c). Cotransfection of wild-type USP30, but not DUB-dead USP30(C77S), strongly decreased the amount of ubiquitinated MIRO1 and TOM20 induced by CCCP (Fig. 3a–c). Consistent

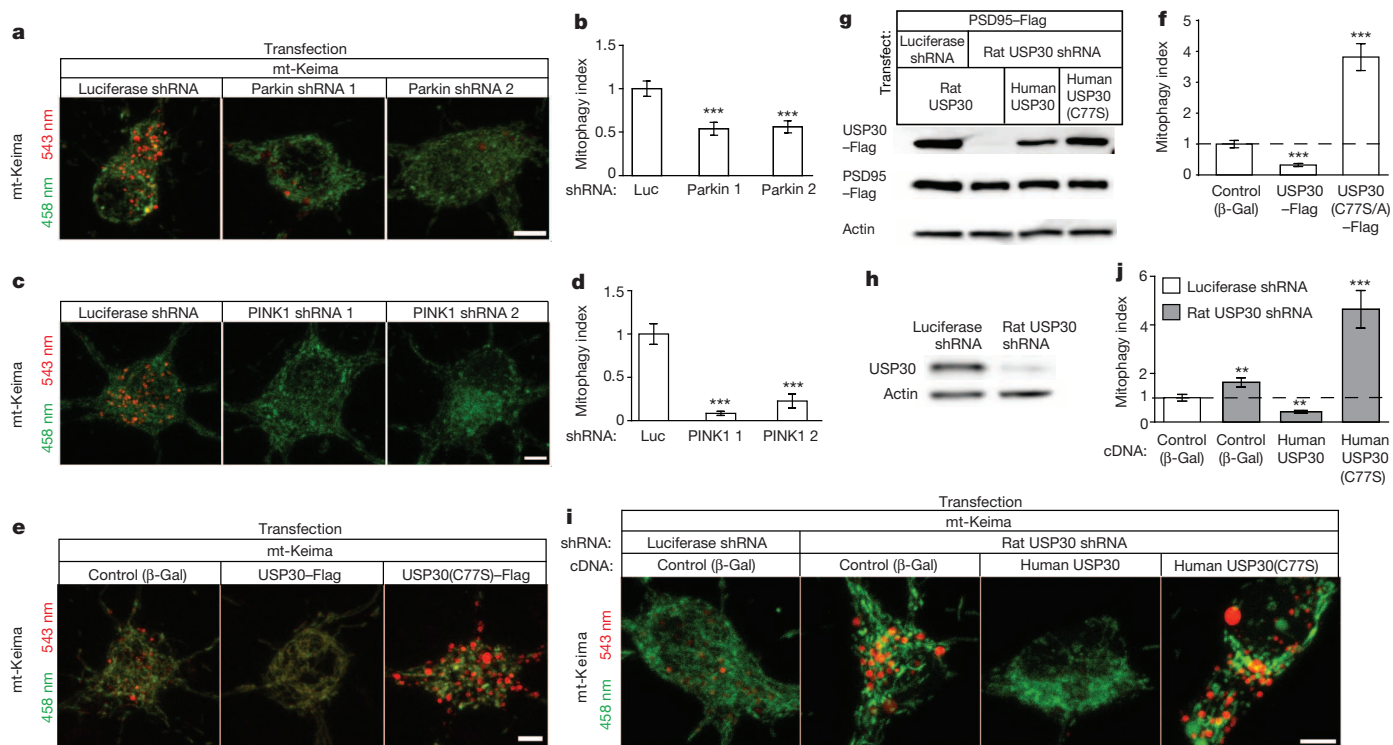


Figure 2 | USP30 antagonizes mitophagy in neurons. **a, c, e, i,** mt-Keima imaging in neurons transfected as indicated. Human USP30 cDNA is insensitive to rat USP30 shRNA in **i**. **b, d, f, j,** Quantification of mitophagy index from **a, c, e, i**. Kruskal–Wallis test. $n = 112$ – 169 (**b**), 54 – 80 (**d**), 80 – 155

(**f**), and 96 – 179 (**j**) cells. $n = 5$ (**b**), 4 (**d**), 8 (**f**), and 7 (**j**) experiments. **g,** Immunoblots of HEK-293 cells transfected as indicated. **h,** Immunoblot of endogenous USP30 in rat hippocampal neurons infected with adeno-associated virus expressing USP30 shRNA. All scale bars, $5 \mu\text{m}$. Error bars, s.e.m.

with a dominant-negative mechanism, USP30(C77S) increased basal TOM20 ubiquitination approximately twofold, and CCCP-induced ubiquitination approximately eightfold (Fig. 3a, c). CCCP did not induce detectable TOM20 or MIRO1 ubiquitination in the parental HEK-293 cell line (lacking GFP-parkin) (Extended Data Fig. 5b). In this cell line, however, overexpression of USP30(C77S) was still able to enhance basal TOM20 ubiquitination and wild-type USP30 to suppress it (Extended Data Fig. 5b). USP30 overexpression in GFP-parkin stable cells significantly reduced CCCP-induced degradation of MIRO1 and TOM20, dependent on USP30 catalytic activity (Extended Data Fig. 5c, d). Taken together, our data indicate that MIRO1 and TOM20 are substrates of USP30, and that USP30 can counteract parkin-mediated ubiquitination and degradation of both MIRO1 and TOM20 following mitochondrial damage. Using the same experimental system (cells overexpressing GFP-parkin and HA-ubiquitin), we tested the function of endogenous USP30 by shRNA knockdown. USP30 knockdown did not affect basal ubiquitination of MIRO1 (in the absence of CCCP) (Fig. 3d). After mitochondrial depolarization, however, and consistent with the MS experiments, USP30 knockdown increased the level of ubiquitinated MIRO1 about 2.5-fold (Fig. 3d, e). Notably, USP30 knockdown increased both basal and CCCP-induced TOM20 ubiquitination, similar to enzymatically inactive USP30 (Fig. 3d, f). The increase in MIRO1 and TOM20 ubiquitination caused by USP30 shRNA was prevented by coexpression of the rat USP30 cDNA (which is insensitive to human USP30 shRNA), indicating the specificity of the RNA interference (RNAi) effect (Extended Data Fig. 5e). These biochemical data corroborate the MS findings that endogenous USP30 acts as a brake on ubiquitination of both MIRO1 and TOM20. Because USP30 knockdown or expression of enzymatically inactive USP30 enhances mitophagy (Fig. 2e–j) and ubiquitination of TOM20 (Fig. 3), and TOM20 degradation accompanies mitophagy (Extended Data Fig. 5c, d), we speculated that TOM20 depletion might trigger mitophagy. In this model, TOM20 overexpression should block mitophagy induced by USP30 knockdown. Instead, we found that overexpression of TOM20—even by itself—led to a robust increase in mitophagy

in the mt-Keima assay (Extended Data Fig. 6c), an effect similar to USP30 knockdown. We therefore proposed that it is the ubiquitination of TOM20, rather than its degradation, that serves as the signal for mitophagy, and that overexpression of TOM20 promotes mitophagy by increasing the pool of substrates available for ubiquitination. Consistent with this hypothesis, overexpression of TOM20-3KR (TOM20(K56R, K61R, K68R) with lysine-to-arginine mutations at three ubiquitination sites regulated by CCCP and USP30) failed to enhance mitophagy (Extended Data Fig. 6a–d). Thus TOM20 is sufficient to drive mitophagy, but this ability depends on its ubiquitination. Moreover, TOM20-3KR blocked the increase in mitophagy induced by USP30(C77S) (Extended Data Fig. 6c, d), implying that the increased mitophagic flux caused by dominant-negative USP30 requires TOM20 ubiquitination. Alternatively, overexpressed TOM20-3KR may oppose USP30(C77S)-induced mitophagy by physically associating with USP30 in a non-catalytic manner. Taken together, these data suggest that ubiquitination of TOM20 can promote mitophagy in neurons, and that inhibition of mitophagy by USP30 can be explained at least in part by TOM20 deubiquitination.

USP30 is a parkin substrate

Since parkin acts on proteins of the outer mitochondrial membrane^{10,20} and since USP30 resides at this location, we wondered whether USP30 is itself a substrate of parkin. Supporting this possibility, we identified USP30-derived ubiquitinated peptides in MS experiments in GFP-parkin cells treated with CCCP (Extended Data Fig. 6e; Supplementary Table 1). We confirmed that parkin can ubiquitinate endogenous USP30 following CCCP treatment (Extended Data Fig. 6f, g). CCCP also induced a significant drop in USP30 levels in GFP-parkin cells (Extended Data Fig. 6h, i). USP30 degradation was inhibited by MG132 and epoxomicin, but not bafilomycin, suggesting that USP30 is degraded by proteasomes (Extended Data Fig. 6j, k). Importantly, parkin with pathogenic G430D or K161N mutations was unable to ubiquitinate or degrade USP30 (Extended Data Fig. 6f–i). These results suggest that parkin ubiquitination

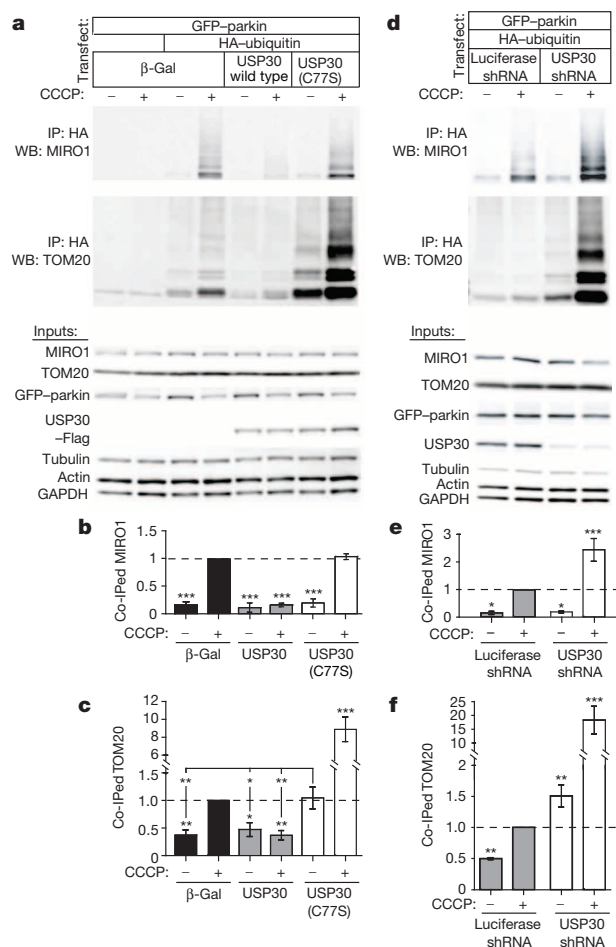


Figure 3 | USP30 and parkin act antagonistically on common substrates. **a, d**, Immunoblotting for MIRO1 and TOM20 in anti-HA immunoprecipitates from GFP-parkin HEK-293 cells transfected as indicated. **b, c**, Quantification of levels of ubiquitinated MIRO1 (**b**) and TOM20 (**c**) from **a**. One-way ANOVA, Bonferroni's test. $n = 6$ (**b**) and 5 (**c**) experiments. **e, f**, Quantification of ubiquitinated MIRO1 (**e**) and TOM20 (**f**) from **d**. One-way ANOVA, Dunnett's test. $n = 4$ (**e**) and 6 (**f**) experiments. Error bars, s.e.m.

and degradation of USP30 might contribute to mitophagy by removing the brake on mitophagy.

USP30 knockdown rescues mitophagy defects

To test whether suppressing USP30 could rescue impaired mitochondrial degradation associated with parkin pathogenic mutations, we focused on two Parkinson's disease-linked parkin mutants, G430D and K161N, which display defects in mitophagy^{8,15}. In SH-SY5Y cells transfected with GFP-parkin(G430D) and treated with CCCP, mitochondria failed to be cleared and instead formed perinuclear clusters in association with the defective parkin protein (Fig. 4a). The same cells doubly transfected with GFP-parkin(G430D) and USP30 siRNA, which led to a knockdown of USP30 protein by ~60% (Extended Data Fig. 7a), showed a ~70% decrease in mitochondria (as measured by total TOM20 or HSP60 immunofluorescence) compared to cells transfected with GFP-parkin(G430D) and control siRNA (Fig. 4a, b). Mitochondrial degradation was not rescued by knockdown of other DUBs (USP6, USP14) (Extended Data Fig. 7b–d). Rescue of mitochondrial degradation was correlated with loss of perinuclear clusters of mutant parkin(G430D) (usually associated with mitochondria) and the appearance of smaller parkin-containing puncta throughout the cytoplasm (Fig. 4a, Extended Data Fig. 7b, c, e). Re-introduction of RNAi-resistant wild-type rat USP30 cDNA, but not the inactive rat USP30(C77S) mutant, prevented the rescue of mitochondrial degradation by USP30 siRNA (Extended

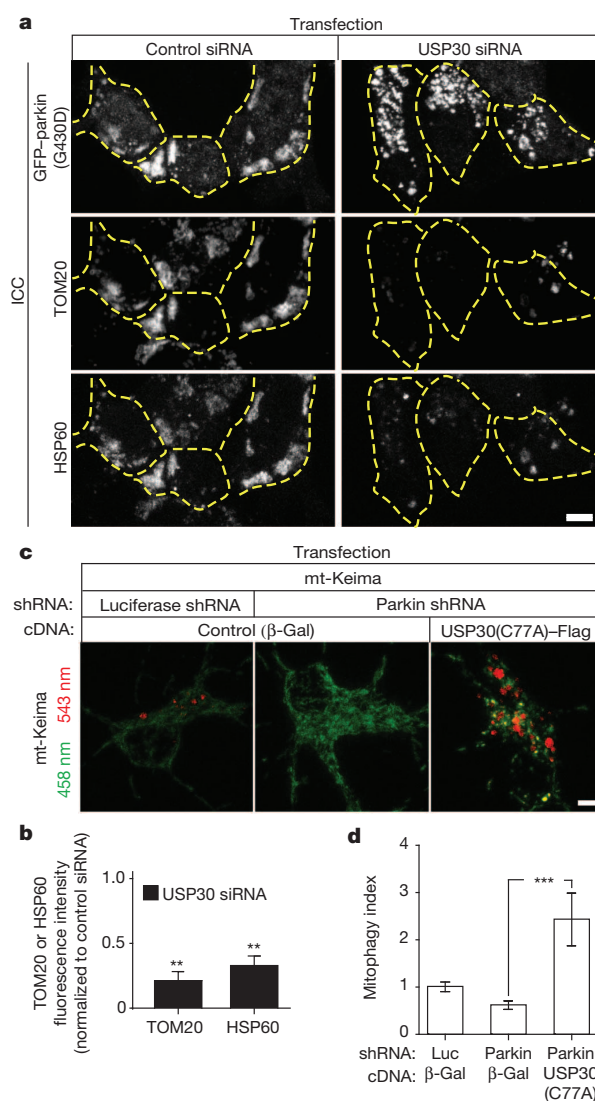


Figure 4 | USP30 knockdown rescues mitophagy defects associated with mutant parkin. **a**, Immunostaining of SH-SY5Y cells expressing GFP-parkin(G430D), transfected with USP30 siRNA and treated with CCCP (20 μ M, 24 h). **b**, Quantification of fold change in TOM20 and HSP60 fluorescence intensity from **a**. Kruskal–Wallis test, $n = 6$ experiments. **c**, mt-Keima imaging in neurons transfected with parkin shRNA and USP30(C77A)-Flag. **d**, Quantification of mitophagy index from **c**. Kruskal–Wallis test, $n = 71$ –77 cells; $n = 3$ experiments. All scale bars, 5 μ m. Error bars, s.e.m.

Data Fig. 7e, f). The mitochondrial degradation defect associated with parkin(K161N) mutant was similarly rescued with USP30 siRNA knockdown (Extended Data Fig. 7g, h). USP30 knockdown also increased levels of p62 and LC3 staining colocalizing with GFP-parkin(K161N) in CCCP-treated cells (Extended Data Fig. 7i–l). In neurons, reduced mitophagy due to parkin or PINK1 knockdown (as measured in the mt-Keima assay) was likewise rescued by dominant-negative USP30(C77A) (Fig. 4c, d; Extended Data Fig. 7m, n). Thus, suppressing the expression or activity of USP30 allows cells to overcome parkin deficiency and restore clearance of damaged mitochondria.

USP30 knockdown protects *in vivo*

What are the functional effects of USP30 knockdown? Reactive oxygen species largely derive from mitochondria, and mitochondria dysfunction may contribute to increased oxidative stress in Parkinson's disease¹. USP30 knockdown in neuronal cultures reduced basal mitochondrial oxidation signal measured by ratiometric imaging with mitochondrial

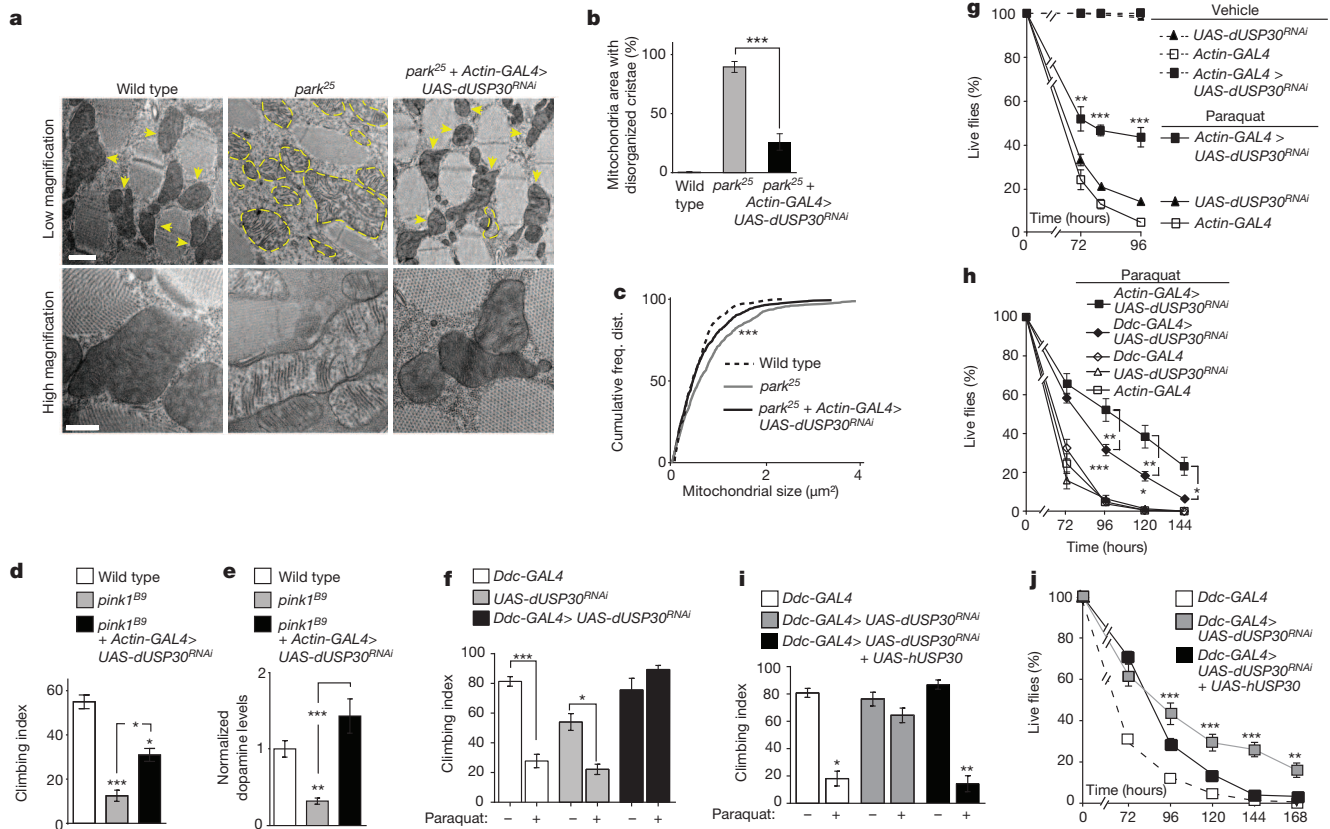


Figure 5 | USP30 knockdown provides protection in vivo. **a**, Transverse sections of *Drosophila* indirect flight muscles of indicated genotypes. Arrowheads, electron-dense mitochondria; dashed lines, 'pale' mitochondria with disorganized cristae. Scale bars, 1 μ m (top), 0.2 μ m (bottom panels). **b**, **c**, Quantification of mitochondrial morphology (**b**) and size distribution (**c**) from **a**. One-way ANOVA, Bonferroni's test (**b**). Kolmogorov-Smirnov test, *park²⁵* versus *park²⁵ + dUSP30 knockdown* (**c**). $n = 3-4$ flies per genotype.

redox potential sensor mito-roGFP¹³ (Extended Data Fig. 8a, b; see Methods), indicating USP30 suppression can ameliorate basal mitochondrial oxidative stress. To test whether knocking down USP30 would provide protection under stress conditions *in vivo*, we used *Drosophila*, a model system for studying Parkinson's disease molecular pathogenesis²¹. To knockdown fly USP30 (CG3016, hereafter called dUSP30), we used the GAL4/UAS system²². We crossed an *Actin-GAL4* driver to a *UAS-dUSP30^{RNAi}* transgenic line, which allows widespread expression of dUSP30 RNAi driven by the actin promoter (referred to as 'dUSP30 knockdown'). Activation of *UAS-dUSP30^{RNAi}* by *Actin-GAL4* led to an approximately 90% reduction of dUSP30 mRNA, compared to the parental lines (Extended Data Fig. 8c). By crossing the 'dUSP30 knockdown' line with *parkin* (*park²⁵*)²³ or *pink1* (*pink1^{B9}*)⁷ mutant flies, we showed that dUSP30 knockdown in these mutant flies largely restored mitochondrial morphology defects (disorganized cristae and enlarged size) in their indirect flight muscles^{7,23} (Fig. 5a-c, Extended Data Fig. 8d-f). dUSP30 knockdown by itself did not affect mitochondrial morphology (Extended Data Fig. 8g). Thus, USP30 suppression can maintain mitochondrial health in the face of parkin or pink1 loss-of-function *in vivo*.

Unlike previous studies²⁴⁻²⁷, we did not observe any dopaminergic neurodegeneration or dopamine depletion in *parkin* mutant *Drosophila* (Extended Data Fig. 9a-g); therefore we could not test the effect of dUSP30 knockdown on these phenotypes. As reported previously⁷, *pink1* mutant flies showed poor performance in a climbing assay and depletion of the neurotransmitter dopamine in their brain (Fig. 5d, e). dUSP30 knockdown driven by *Actin-GAL4* ameliorated the climbing defect and prevented the dopamine depletion (Fig. 5d, e), thus benefitting *pink1* mutant flies in both behavioural and neurochemical terms.

d, e, Effect of dUSP30 knockdown on climbing (**d**) and dopamine levels (**e**) in *pink1^{B9}* flies. Kruskal-Wallis test, $n = 13$ (**d**) and 8 (**e**) experiments. **f-j**, Effect of dUSP30 knockdown, paraquat and human USP30 overexpression on climbing (**f, i**) and survival (**g, h, j**) in wild-type flies. Human USP30 is insensitive to dUSP30-RNAi in **i** and **j**. Kruskal-Wallis test (**f, i**), two-way ANOVA (**g, h, j**), $n = 4-8$ (**f**), 3-8 (**g, h**), 4 (**i**), and 3 (**j**) experiments. Error bars, s.e.m.

To examine the effect of suppressing USP30 in neurons directly relevant to Parkinson's disease, we first used *dopamine decarboxylase* (*Ddc*)-*GAL4*²⁶ to drive *UAS-dUSP30^{RNAi}* specifically in dopamine neurons and other aminergic neurons. As a model of Parkinson's disease, we treated flies with paraquat, a mitochondrial toxin linked to Parkinson's disease^{28,29}. Following treatment with paraquat, the *Ddc-GAL4* and *UAS-dUSP30^{RNAi}* parental fly lines showed reduced climbing performance (Fig. 5f). This behavioural deficit is related to dopamine depletion, as the defect was fully rescued by treatment with L-3,4-dihydroxyphenylalanine (L-DOPA) (Extended Data Fig. 9h). Paraquat treatment caused a 30-60% reduction in dopamine levels in fly heads without altering serotonin levels (Extended Data Fig. 9i, l). Knocking down dUSP30 using *Ddc-GAL4* completely rescued the paraquat-induced climbing impairment (Fig. 5f, Supplementary Video 1). Restoration of climbing function was also observed using a different dopaminergic neuron driver (*Th-GAL4*) or 'whole-body' knockdown of USP30 (*Actin-GAL4*; Extended Data Fig. 9j, k). Strikingly, USP30 knockdown using *Ddc-GAL4* or *Th-GAL4* drivers also prevented paraquat-induced dopamine depletion (Extended Data Fig. 9l, m). We confirmed that the various fly lines ingested similar amounts of paraquat as measured by liquid chromatography-mass spectrometry (see Methods). Paraquat treatment by itself did not cause obvious changes in mitochondrial morphology in fly muscle (Extended Data Fig. 8g) or brain (data not shown). These results show that suppression of USP30 can benefit dopaminergic neurons and motor behaviour in the face of mitochondrial toxicity associated with Parkinson's disease.

We tested the effect of USP30 knockdown on the survival of flies fed with paraquat. Flies expressing dUSP30 RNAi in the whole body lived significantly longer than controls (Fig. 5g). Knockdown of other DUBs

in flies (dUSP47, also known as Ubp64E, or dYOD1, also known as CG4603) did not improve survival; if anything, they exacerbated the rate of death in response to paraquat (Extended Data Fig. 10a–c). Remarkably, USP30 knockdown driven by *Ddc-GAL4* was sufficient to provide significant survival benefit, albeit less than whole-body USP30 knockdown (Fig. 5h). Similar results were obtained using *Th-GAL4* (Extended Data Fig. 10d). As these results rely on only a single dUSP30 RNAi fly line, we confirmed RNAi specificity by introducing RNAi-resistant human USP30 cDNA into flies expressing dUSP30-RNAi (Extended Data Fig. 10e, f). Human USP30 cDNA (driven by either by *Ddc-GAL4* or *Actin-GAL4*) reversed the benefit provided by dUSP30-RNAi in paraquat-treated flies in both the climbing and survival assays (Fig. 5i, j; Extended Data Fig. 10g, h). These results imply that a significant portion of the organismal benefit of USP30 suppression is mediated in dopaminergic neurons, and it further reinforces the idea that USP30 can play a critical role in dopaminergic neuron dysfunction.

Since suppression of USP30 restored mitochondrial integrity in *parkin* and *pink1* mutant flies and functionally protected dopaminergic neurons against the mitochondrial toxin paraquat, our findings provide *in vivo* evidence that inhibition of USP30 might be helpful in diseases caused by mitochondrial damage and dysfunction.

METHODS SUMMARY

Statistical tests and one-way ANOVA post-hoc tests are indicated in figure legends. For multiple comparison analysis, Dunn's and Bonferroni's post-hoc tests were used for all Kruskal–Wallis and two-way ANOVA tests, respectively. *P* values are represented as **P* < 0.05, ***P* < 0.01 and ****P* < 0.001. For details of experimental methods and statistical analysis, see Methods.

Online Content Any additional Methods, Extended Data display items and Source Data are available in the online version of the paper; references unique to these sections appear only in the online paper.

Received 5 August 2013; accepted 28 April 2014.

Published online 4 June 2014.

- Narendra, D. P. & Youle, R. J. Targeting mitochondrial dysfunction: role for PINK1 and Parkin in mitochondrial quality control. *Antioxid. Redox Signal.* **14**, 1929–1938 (2011).
- Hauser, D. N. & Hastings, T. G. Mitochondrial dysfunction and oxidative stress in Parkinson's disease and monogenic parkinsonism. *Neurobiol. Dis.* **51**, 35–42 (2013).
- Kitada, T. *et al.* Mutations in the *parkin* gene cause autosomal recessive juvenile parkinsonism. *Nature* **392**, 605–608 (1998).
- Valente, E. M. *et al.* Hereditary early-onset Parkinson's disease caused by mutations in *PINK1*. *Science* **304**, 1158–1160 (2004).
- Yang, Y. *et al.* Mitochondrial pathology and muscle and dopaminergic neuron degeneration caused by inactivation of *Drosophila* Pink1 is rescued by Parkin. *Proc. Natl Acad. Sci. USA* **103**, 10793–10798 (2006).
- Clark, I. E. *et al.* *Drosophila pink1* is required for mitochondrial function and interacts genetically with *parkin*. *Nature* **441**, 1162–1166 (2006).
- Park, J. *et al.* Mitochondrial dysfunction in *Drosophila PINK1* mutants is complemented by *parkin*. *Nature* **441**, 1157–1161 (2006).
- Narendra, D. P. *et al.* PINK1 is selectively stabilized on impaired mitochondria to activate Parkin. *PLoS Biol.* **8**, e1000298 (2010).
- Narendra, D., Tanaka, A., Suen, D. F. & Youle, R. J. Parkin is recruited selectively to impaired mitochondria and promotes their autophagy. *J. Cell Biol.* **183**, 795–803 (2008).
- Chan, N. C. *et al.* Broad activation of the ubiquitin-proteasome system by Parkin is critical for mitophagy. *Hum. Mol. Genet.* **20**, 1726–1737 (2011).
- Matsuda, N. *et al.* PINK1 stabilized by mitochondrial depolarization recruits Parkin to damaged mitochondria and activates latent Parkin for mitophagy. *J. Cell Biol.* **189**, 211–221 (2010).
- Vives-Bauza, C. *et al.* PINK1-dependent recruitment of Parkin to mitochondria in mitophagy. *Proc. Natl Acad. Sci. USA* **107**, 378–383 (2010).
- Guzman, J. N. *et al.* Oxidant stress evoked by pacemaking in dopaminergic neurons is attenuated by DJ-1. *Nature* **468**, 696–700 (2010).
- Nakamura, N. & Hirose, S. Regulation of mitochondrial morphology by USP30, a deubiquitinating enzyme present in the mitochondrial outer membrane. *Mol. Biol. Cell* **19**, 1903–1911 (2008).
- Geisler, S. *et al.* PINK1/Parkin-mediated mitophagy is dependent on VDAC1 and p62/SQSTM1. *Nature Cell Biol.* **12**, 119–131 (2010).
- Narendra, D., Kane, L. A., Hauser, D. N., Fearnley, I. M. & Youle, R. J. p62/SQSTM1 is required for Parkin-induced mitochondrial clustering but not mitophagy; VDAC1 is dispensable for both. *Autophagy* **6**, 1090–1106 (2010).
- Lee, J.-Y., Nagano, Y., Taylor, J., Lim, K. & Yao, T.-P. Disease-causing mutations in parkin impair mitochondrial ubiquitination, aggregation, and HDAC6-dependent mitophagy. *J. Cell Biol.* **189**, 671–679 (2010).
- Katayama, H., Kogure, T., Mizushima, N., Yoshimori, T. & Miyawaki, A. A sensitive and quantitative technique for detecting autophagic events based on lysosomal delivery. *Chem. Biol.* **18**, 1042–1052 (2011).
- Sarraf, S. A. *et al.* Landscape of the PARKIN-dependent ubiquitylome in response to mitochondrial depolarization. *Nature* **496**, 372–376 (2013).
- Yoshii, S. R., Kishi, C., Ishihara, N. & Mizushima, N. Parkin mediates proteasome-dependent protein degradation and rupture of the outer mitochondrial membrane. *J. Biol. Chem.* **286**, 19630–19640 (2011).
- Guo, M. *Drosophila* as a model to study mitochondrial dysfunction in Parkinson's disease. *Cold Spring Harb. Perspect. Med.* <http://dx.doi.org/10.1101/cshperspecta009944> (2012).
- Brand, A. H. & Perrimon, N. Targeted gene expression as a means of altering cell fates and generating dominant phenotypes. *Development* **118**, 401–415 (1993).
- Greene, J. C. *et al.* Mitochondrial pathology and apoptotic muscle degeneration in *Drosophila parkin* mutants. *Proc. Natl Acad. Sci. USA* **100**, 4078–4083 (2003).
- Whitworth, A. J. *et al.* Increased glutathione S-transferase activity rescues dopaminergic neuron loss in a *Drosophila* model of Parkinson's disease. *Proc. Natl Acad. Sci. USA* **102**, 8024–8029 (2005).
- Wang, C. *et al.* *Drosophila* overexpressing parkin R275W mutant exhibits dopaminergic neuron degeneration and mitochondrial abnormalities. *J. Neurosci.* **27**, 8563–8570 (2007).
- Sang, T. K. *et al.* A *Drosophila* model of mutant human parkin-induced toxicity demonstrates selective loss of dopaminergic neurons and dependence on cellular dopamine. *J. Neurosci.* **27**, 981–992 (2007).
- Cha, G. H. *et al.* Parkin negatively regulates JNK pathway in the dopaminergic neurons of *Drosophila*. *Proc. Natl Acad. Sci. USA* **102**, 10345–10350 (2005).
- Cochemé, H. M. & Murphy, M. P. Complex I is the major site of mitochondrial superoxide production by paraquat. *J. Biol. Chem.* **283**, 1786–1798 (2008).
- Tanner, C. M. *et al.* Rotenone, paraquat, and Parkinson's disease. *Environ. Health Perspect.* **119**, 866–872 (2011).

Supplementary Information is available in the online version of the paper.

Acknowledgements We thank J. Corn and C. Cunningham for discussions. The *park*²⁵ line was a gift of L. Pallanck. PTMscan studies are performed at Genentech under a limited use license from Cell Signaling Technology.

Author Contributions B.B. designed the study and executed and analysed the imaging and biochemistry experiments. J.S.T. executed and analysed the biochemistry and fly experiments. M.R. and O.F. gathered the electron microscopy data. L.P. executed, and C.E.B., Q.S. and D.S.K. analysed the mass spectrometry experiments. B.B. and M.S. wrote the manuscript.

Author Information Reprints and permissions information is available at www.nature.com/reprints. The authors declare competing financial interests: details are available in the online version of the paper. Readers are welcome to comment on the online version of the paper. Correspondence and requests for materials should be addressed to B.B. (bingol.baris@gene.com).

METHODS

DNA construction. For the DUB overexpression screen, a Flag-tagged DUB library consisting of 100 cDNAs was used. For transfection, the following constructs were subcloned into the β -actin promoter-based pCAGGS plasmid: USP30–Flag (rat), USP30–Flag (human), GFP–parkin (human), MYC–parkin (human), Flag–parkin (rat), red fluorescent protein (RFP)–parkin (human), PINK1–GFP (human), TOM20–MYC (human), LC3–GFP (human), HA–ubiquitin, PSD95–Flag, GFP, mito–GFP, and mt–Keima¹⁸. Point mutations were generated using QuikChange II XL (Agilent Technologies) for the following constructs: USP30(C77S)–Flag (rat), USP30(C77A)–Flag (rat), USP30(C77S)–Flag (human), GFP–parkin(K161N) (human), GFP–parkin (G430D) (human). Mito-tagGFP2 (Evrogen) and TOM20-3KR–MYC (Blue Heron) were purchased. β -Gal³⁰ and mito-roGFP³¹ expression plasmids were previously described. Short-hairpin sequences targeting the following regions were cloned into pSuper or pSuper–GFP–neo plasmids: rat PINK1 1 (TCAGGAGATCCAGG CAATT), rat PINK1 2 (CCAGTACCTTGAAGAGCAA), rat parkin 1 (GGAAGT GGTGCTAAGCGA), rat parkin 2 (GAGGAAAAGTCACGAAACA), rat USP30 (CCAGAGCCCTGTTCGGTTT), human USP30 (CCAGAGTCTGTTCGATTT), and firefly luciferase (CGTACGCGGAATACTTCGA).

Antibodies and reagents. The following antibodies were used for immunocytochemistry: rabbit anti-TOM20⁹ (clone no. FL-145; catalogue no. sc11415), mouse anti-TOM20 (clone no. F-10; catalogue no. sc17764), goat anti-HSP60¹⁰ (catalogue no. sc1052) (Santa Cruz Biotechnology); mouse anti-Flag-M2 (catalogue no. F1804), rabbit anti-Flag (catalogue no. F7425), mouse anti-MYC (catalogue no. M4439) (Sigma-Aldrich); chicken anti-GFP (catalogue no. A10262) (Invitrogen); mouse anti-p62³² (catalogue no. BDB610833) (BD Biosciences); rabbit anti-LC3³² (catalogue no. NB100-2220) (Novus Biologicals); and mouse anti-FK2¹¹ (catalogue no. BML-PW8810) (Enzo Life Sciences); mouse anti-LAMP1 (clone no. Ly1C6; catalogue no. ADI-VAM-EN001-D) (StressGen).

The following antibodies were used for immunoblotting: rabbit anti-TOM20⁹ (clone no. FL-145; catalogue no. sc11415), goat anti-HSP60¹⁰ (catalogue no. sc1052) (Santa Cruz Biotechnology); mouse anti-Mfn1³³ (clone no. 3C9; catalogue no. WH0055669M4), HRP-conjugated anti-Flag (catalogue no. A8592), mouse anti-MYC (catalogue no. M4439), rabbit anti-USP30 (catalogue no. HPA016952), rabbit anti-RHOT1 (MIRO1) (catalogue no. HPA010687), rabbit anti-TIMM8a (clone no. 2F11; catalogue no. WH0001678M1) (Sigma-Aldrich); rabbit anti-GFP (catalogue no. A11122), chicken anti-GFP (catalogue no. A10262) (Invitrogen); HRP-conjugated anti-GAPDH (clone no. 14C10; catalogue no. 3683), HRP-conjugated anti- β -actin (clone no. 13E5; catalogue no. 5125), HRP-conjugated anti- β -tubulin (clone no. 9F3; catalogue no. 5346), rabbit anti-VDAC (clone no. D73D12; catalogue no. 4661), mouse anti-parkin (clone no. Prk8; catalogue no. 4211) (Cell Signaling Technology); rabbit anti-Tom70 (catalogue no. 14528-1-AP) (Proteintech Group); mouse anti-ubiquitin¹¹ (clone no. FK2; catalogue no. PW8810) (Enzo Life Sciences); HRP-conjugated anti-HA (clone no. 3F10; catalogue no. 12013819001) (Roche); mouse anti-p62³² (catalogue no. BDB610833) (BD Biosciences); rabbit anti-PINK1 (catalogue no. BC100-494), rabbit anti-LC3³² (catalogue no. NB100-2220) (Novus Bio); and rabbit anti-USP30 (generated by immunizing rabbits with purified human USP30 amino acids 65–517).

Anti-HA affinity matrix beads (Roche Applied Science) were used for immunoprecipitation experiments. Adeno-associated virus type2 (AAV2) particles expressing parkin, PINK1 and USP30 shRNAs were produced by Vector Biolabs, Inc. using the pAAV-BASIC-CAGGFP-WPRE vector containing an H1 promoter and the same shRNA expression cassette as the pSuper vectors.

The following reagents were purchased as indicated: blasticidin S, zeocin, Lipofectamine 2000, Lipofectamine LTX PLUS, LysoTracker Green DND-626 (Invitrogen); PhosSTOP phosphatase inhibitor tablets, cComplete EDTA-free protease inhibitor tablets, DNase I (Roche Applied Science); carbonyl cyanide 3-chlorophenylhydrazone (CCCP), doxycycline, dimethyl sulphoxide, ammonium chloride, rotenone, DTT, aldrithiol, paraquat dichloride, MG132, epoxomicin (Sigma-Aldrich); bafilomycin (Cayman Chemical); L-3,4-dihydroxyphenylalanine (Fluka Analytical); N-ethylmaleimide (Thermo Scientific); and hygromycin (Clontech Laboratories).

Transfection and immunocytochemistry. All heterologous cells were transfected with Lipofectamine 2000 for cDNA expression and Lipofectamine RNAiMAX for siRNA knockdown experiments, according to manufacturer's instructions (Invitrogen). siRNAs were purchased from Dharmacon as siGenome pools (non-Silencing pool 2 was used as control siRNA transfection). Hippocampal cultures were prepared as described previously³⁰ and transfected with Lipofectamine LTX PLUS (Invitrogen) with 1.8 μ g DNA, 1.8 μ l PLUS reagent and 6.3 μ l LTX reagent. Following drug treatments, cells were fixed with 4% paraformaldehyde/4% sucrose in phosphate-buffered saline (PBS, pH 7.4) (Electron Microscopy Sciences). Following permeabilization (0.1% Triton-X in PBS), blocking (2% BSA in PBS) and primary antibody incubation, antibodies were visualized using Alexa dye-conjugated secondary antibodies (Invitrogen). All immunocytochemistry images were acquired with a Leica SP5

laser scanning microscope with a $\times 40/1.25$ oil objective (0.34 μ m per pixel resolution, 1 μ m confocal z-step size).

HEK-293 and SH-SY5Y stable cell line generation. Stably transfected HEK-293 cell lines expressing GFP–parkin (human) wild type, K161N, and G430D were generated by co-transfecting FLP-In 293 cells with a pOG44 Flp-recombinase expression vector (Invitrogen) and a pcDNA5-FRT vector (Invitrogen) expressing the corresponding constructs under a CMV promoter. Cell lines were selected and maintained using 50 μ g ml^{−1} hygromycin selection. Inducible HEK stable cell line expressing GFP–parkin (human) was generated by co-transfecting FLP-In T-Rex 293 cells with pOG44 and a pcDNA5-FRT-TO vector (Invitrogen) expressing GFP–parkin (human). This line was selected and maintained using 50 μ g ml^{−1} hygromycin and 15 μ g ml^{−1} blasticidin. SH-SY5Y stable cells were generated similarly with a Flp-In inducible parental cell line using pcDNA5-FRT-TO and maintained under 75 μ g ml^{−1} hygromycin and 3 μ g ml^{−1} blasticidin. Cell lines were quality controlled by STR analysis and by testing for mycoplasma contamination.

Isolation and identification of ubiquitin modifications by mass spectrometry. To identify parkin substrates, HEK-293 cells stably expressing inducible GFP–parkin (human) were induced using doxycycline (1 μ g ml^{−1}) for 24 h, then treated with 5 μ M CCCP or DMSO vehicle control for 2 h. To determine USP30 substrates, HEK-293 cells were transfected with human USP30 shRNA using Lipofectamine 2000 (Invitrogen) for 6 days, then treated as above.

Immunoaffinity isolation and mass spectrometry methods were used to enrich and identify K-GG peptides from digested protein lysates as previously described^{34,35}. Cell lysates were prepared in lysis buffer (8 M urea, 20 mM HEPES pH 8.0, 1 mM sodium orthovanadate, 2.5 mM sodium pyrophosphate, 1 mM β -glycerophosphate) by brief sonication on ice. Protein samples (60 mg) were reduced at 60 °C for 20 min in 4.1 mM DTT, cooled 10 min on ice, and alkylated with 9.1 mM iodoacetamide for 15 min at room temperature in the dark. Samples were diluted 4 \times using 20 mM HEPES pH 8.0 and digested in 10 μ g ml^{−1} trypsin overnight at room temperature. Following digestion, TFA was added to a final concentration of 1% to acidify the peptides before desalting on a Sep-Pak C₁₈ cartridge (Waters). Peptides were eluted from the cartridge in 40% ACN/0.1% TFA, flash frozen and lyophilized for 48 h. Dry peptides were gently resuspended in 1.4 ml 1 \times IAP buffer (Cell Signaling Technology) and cleared by centrifugation for 5 min at 1,800g. Precoupled anti-KGG beads (Cell Signaling Technology) were washed in 1 \times IAP buffer before contacting the digested peptides.

Immunoaffinity enrichment was performed for 2 h at 4 °C. Beads were washed 2 \times with IAP buffer and 4 \times with water before 2 \times elution of peptides in 0.15% TFA for 10 min each at room temperature. Immunoaffinity enriched peptides were desalted using STAGE-Tips as previously described³⁶.

Liquid chromatography-mass spectrometry (LC-MS) analysis was performed on an LTQ-Orbitrap Velos mass spectrometer operating in data dependent top 15 mode. Peptides were injected onto a 0.1 \times 100-mm Waters 1.7- μ m BEH-130 C18 column using a NanoAcquity UPLC and separated at 1 μ l min^{−1} using a two-stage linear gradient where solvent B ramped first from 2% to 25% over 85 min and then 25% to 40% over 5 min. Peptides eluting from the column were ionized and introduced to the mass spectrometer using an ADVANCE source (Michrom-Bruker). In each duty cycle, one full MS scan collected was at 60,000 resolution in the Orbitrap followed by up to 15 MS/MS scans in the ion trap on monoisotopic, charge state defined precursors ($z > 1$). Ions selected for MS/MS (± 20 p.p.m.) were subjected to dynamic exclusion for 30 s duration.

Mass spectral data were converted to mxml for loading into a relational database. MS/MS spectra were searched using Mascot against a concatenated target-decoy database of tryptic peptides from human proteins (Uniprot) and common contaminants. Precursor ion mass tolerance was set to ± 50 p.p.m. Fixed modification of carbamidomethyl cysteine (+57.0214) and variable modifications of oxidized methionine (+15.9949) and K-GG (+114.0429) were considered. Linear discriminant analysis (LDA) was used to filter peptide spectral matches (PSMs) from each run to 5% false discovery rate (FDR) at the peptide level, and subsequently to a 2% protein level FDR as an aggregate of all runs ($< 0.5\%$ peptide level FDR). Localization scores were generated for each K-GG PSM using a modified version of the AScore algorithm and positions of the modifications localized accordingly as the AScore sequence³⁷. Given that trypsin cannot cut adjacent to ubiquitin modified lysines^{38,39}, PSMs where the AScore sequence reports a -GG modification on the C-terminal lysine are dubious. Possible exceptions to this would be lysines at the C termini of proteins (or *in vivo* truncation products) and PSMs stemming from in source fragmentation of a bona fide K-GG peptide. To establish the most reliable data set for downstream analysis, PSMs where the AScore sequence reported a C-terminal lysine were split into two groups: those with an available internal lysine residue to which the -GG could be alternatively localized, and those which lacked an available lysine. PSMs bearing a C-terminal K-GG but lacking an available lysine were removed from consideration in downstream analyses. For the remaining PSMs, the -GG modification was relocated to the available lysine closest to the C terminus.

Both lists, including the latent hits from the decoy protein sequences, are provided as supplementary tables to permit post hoc analysis.

A modified version of the VistaGrande algorithm, termed XQuant, was used to interrogate the unlabelled peak areas for individual K-GG peptides, guided by direct PSMs or accurate precursor ion and retention time matching (cross quantification). For direct PSMs, quantification of the unlabelled peak area was performed using fixed mass and retention tolerances, as previously described³⁹. To enable cross quantification within XQuant, retention time correlation across pairwise instrument analyses was determined based on high-scoring peptide sequences identified by between one and four PSMs across all analyses within an experiment. Matched retention time pairings were modelled using a linear least squares regression model to yield the retention time correlation equation. In instrument runs where a peptide was not identified by a discrete MS/MS, cross quantification was carried out by seeding the XQuant algorithm with the calculated mass of the precursor ion and its predicted retention time derived from the regression model. While the m/z tolerance was fixed, the retention time tolerance was dynamically adjusted for each pairwise instrument run. In cases where peptides were not confidently identified within a given instrument run but were identified in multiple other runs, multiple cross quantification events were performed to ensure data quality. XQuant results were filtered to a heuristic confidence score of 83 or greater, as previously described³⁹. Full scan peak area measurements arising from multiple quantification events of the same m/z within a single run were grouped together if their peak boundaries in retention time overlapped. From such a group, the peak with the largest total peak area was chosen as its single representative.

To identify candidate substrates of parkin and USP30, graphical analysis and mixed-effect modelling were applied to XQuant data. A mixed-effect model was fit to the AUC data for each protein. 'Treatment' (for example, Control, parkin overexpression/USP30 knockdown, CCCP, Combo) was a categorical fixed effect and 'Peptide' was fit as random effect. False discovery rates (FDR) are calculated based on the P values of each treatment vs Control. Fold-changes and P values of mean AUC from Combo vs Control and Combo vs CCCP were used in preparing 'LiME' plots. The mixed-effect model was fit in R by 'nlme'⁴⁰.

Preparation of cell lysates and immunoprecipitation. For total lysate experiments, cells were lysed after 24 h in SDS sample buffer (Invitrogen) containing sample reducing agent (Invitrogen) and boiled at 95 °C for 5 min. Total lysates were resolved by SDS-PAGE and analysed by immunoblotting. For immunoprecipitation experiments, cells were treated with the indicated concentrations and durations of CCCP at 24 h (overexpression experiments) or 6 days (knockdown experiments) post-transfection. Then, cells were lysed in 0.5% SDS in Tris-buffered saline (137 mM NaCl, 5 mM KCl, 1.5 mM Na₂HPO₄, 25 mM Tris base, 1 mM CaCl₂·2H₂O, 0.5 mM MgCl₂·6H₂O, pH 7.5) and boiled at 70 °C for 10 min. Lysates were then diluted in immunoprecipitation buffer (50 mM HEPES, 150 mM NaCl, 10% glycerol, 1% Triton-X, protease inhibitors (Roche Applied Science), phosphatase inhibitors (Roche Applied Science), DNase I (Roche Applied Science), 2 mM N-ethylmaleimide (Thermo Scientific), pH 7.4), cleared by centrifugation at 31,000g for 10 min, and incubated overnight with anti-HA affinity matrix beads (Roche Applied Science). Inputs and anti-HA immunoprecipitates were resolved by SDS-PAGE and analysed by immunoblotting.

Mitochondria fractionation. Subcellular fractionation was performed using the FOCUS SubCell Kit (G Biosciences) from ~P60 adult male rat forebrain.

Drosophila stocks. The following *Drosophila* lines were obtained for analysis: *Actin5C-GAL4* (Bloomington *Drosophila* Stock Center, 4414), *Ddc-GAL4*^{4,3D} (Bloomington *Drosophila* Stock Center, 7010), *ple-GAL4* (referred to here as *Th-GAL4*, Bloomington *Drosophila* Stock Center, 8848), *UAS-CG3016^{RNAi}* (referred to here as *UAS-dUSP30^{RNAi}*; NIG-Fly Stock Center, 3016R-2), *UAS-CG5486^{RNAi}* (referred to here as *UAS-dUSP47^{RNAi}*; NIG-Fly Stock Center, 5486R-3), *UAS-CG4603^{RNAi}* (referred to here as *UAS-dYOD1^{RNAi}*; NIG-Fly Stock Center, 4603R-2), *pink1^{B9}* (Bloomington *Drosophila* Stock Center, 34749), *park²⁵* (Leo Pallanck, University of Washington), and *park¹* (Bloomington *Drosophila* Stock Center, 34747). For USP30 knockdown experiments, *Actin5C-GAL4* or *Ddc-GAL4* were recombined onto the same chromosome as *UAS-dUSP30^{RNAi}* using standard genetic techniques and were balanced over CyO, y+. For experiments using *Th-GAL4*, flies were generated by crossing *Th-GAL4* with *UAS-dUSP30^{RNAi}* and were not balanced. The X chromosome of flies in *pink1^{B9}* experiments contained w; all other lines used contained y, w. Wild-type controls used were w or y, w, respectively.

UAS-hUSP30 and *UAS-parkin* constructs were generated by PCR amplifying human USP30 or parkin cDNA (Origene), respectively, with primers adding restriction sites EcoRI (5') and NotI (3') and subcloning into pUAST-attB (gift of Konrad Basler). Parkin R275W and Q311X mutations were made using QuikChange II XL (Agilent Technologies). Injections were performed by BestGene, Inc. (Chino Hills, CA) for integration into the 86Fb attP landing site (Bloomington 24749).

Flies were raised on Nutri-Fly 'German Food' Formulation (Genesee, 66-115), prepared per manufacturer's instructions. All flies were raised at 25 °C and crossed

using standard genetic techniques. All experiments were performed using age-matched male flies.

Quantitative RT-PCR. RNA and subsequent cDNA was obtained from five adult male fly heads following manufacturer's instructions (Qiagen RNeasy Plus kit, Applied Biosystems High Capacity cDNA Reverse Transcription kit). Quantitative RT-PCR was performed using an Applied Biosystems ViiA7 Real-Time PCR system using TaqMan Assays Dm01796115_g1 and Dm01796116_g1 (*Drosophila* CG3016 (USP30)), Hs00261902_m1 (human USP30), Dm01795269_g1 (*Drosophila* CG5486 (USP47)), and Dm01840115_s1 (*Drosophila* CG4603 (YOD1)). Dm02134593_g1 (RpII140) was used for normalization.

Transmission electron microscopy of *Drosophila* indirect flight muscles. Adult male thoraxes of indicated ages and genotypes were isolated from the remainder of the body, then longitudinally hemi-sectioned and immediately fixed and processed as previously described²³. Briefly, samples were fixed in modified Karnovsky's fixative (2% paraformaldehyde and 2.5% glutaraldehyde in 0.1 M sodium cacodylate buffer, pH 7.2), post-fixed in 1% aqueous osmium tetroxide, dehydrated through a series of ethanol (50%, 70%, 90%, 95%, 100%) followed by propylene oxide treatments, and embedded in Eponate 12 (Ted Pella, Redding, CA). Ultrathin sections (80 nm) were cut with an Ultracut microtome (Leica), stained with 3.5% aqueous uranyl acetate and 0.2% lead citrate and examined in a JEOL JEM-1400 transmission electron microscope (TEM) at 120 kV. Digital images were captured with a GATAN Ultrascan 1000 CCD camera.

Climbing assays. Flies of indicated ages and genotypes were assayed as below. For paraquat-fed experiments, 1-day old adult males were fed a solution containing 5% sucrose only (in water) or 5% sucrose + 10 mM paraquat (in water) or 5% sucrose + 10 mM paraquat + 1 mM L-3,4-dihydroxyphenylalanine (in water) on saturated Whatman paper. After 48 h of treatment, flies were anesthetized using carbon dioxide and randomly transferred in groups of ten to fresh vials containing only 1% agarose (in water) for a 1-h recovery period from the effects of carbon dioxide. The flies were then transferred into new glass test tubes, gently tapped to the bottom, and scored for their ability to climb. The number of flies climbing 15 cm vertically was recorded at 12 s for *pink1^{B9}* experiments and 30 s for all other experiments; climbing index is calculated as % of flies climbing 15 cm at given time.

Determination of neurotransmitter levels. Flies of indicated ages and genotypes were assayed as below. For paraquat-fed experiments, 1-day old adult males were fed a solution containing 5% sucrose only (in water) or 5% sucrose + 10 mM paraquat (in water) on saturated Whatman paper. After 48 h of treatment, flies were anesthetized using carbon dioxide. Single fly heads were dissected off and immediately placed into 500 µl cold lysis solution on ice. Heads were homogenized using a TissueLyser II (Qiagen) with a 3 mm tungsten carbide bead (Qiagen) at a frequency of 30 Hz for 3 min. Homogenates were spun down and supernatants used in subsequent ELISAs.

For dopamine ELISA, the lysis solution contained 0.01 N hydrochloric acid, 1 mM EDTA, 4 mM sodium metabisulphite. ELISA was performed according to manufacturer's instructions (LDN, BA E-5300). For serotonin ELISA, the lysis solution was provided in the kit as 'Diluent' (LDN, BA E-5900).

Determination of ingested paraquat concentration. 1-day old adult male flies were fed a solution containing 5% sucrose only (in water) or 5% sucrose + 10 mM paraquat (in water) on saturated Whatman paper. After 48 h of treatment, 15 flies were collected per condition and homogenized in 100 µl water. Standard curve samples were generated by spiking appropriate amounts of paraquat to homogenates from untreated flies. Then the samples were vortex mixed, and 200 µl of acetonitrile containing internal standard (Propranolol) was added. The samples were vortexed again and centrifuged at 10,000g for 10 min. 100 µl of supernatants were transferred to a new plate that contained 200 µl of water and analysed by LC-MS/MS to quantify for concentrations of paraquat. The LC-MS/MS consisted of an Agilent 1100 series HPLC system (Santa Clara, CA) and an HTS PAL autosampler from CTC Analytics (Carrboro, NC) coupled with a 4000 Q TRAP MS and TurbolonSpray ion source from Applied Biosystems (Foster City, CA). HPLC separation was performed on a Waters Atlantis dC18 column (3 µm 100 × 2.1 mm) with a Krud Katcher guard column from Phenomenex. Quantitation was carried out using the multiple reaction monitoring (MRM) with transition 185.1 → 165.1 for paraquat and 260.2 → 183.1 for propranolol. The lower and upper limit of the assay is 10 µM and 1000 µM, respectively. The quantification of the assay used a calibration curve which was constructed through plotting the analyte/IS peak area ratio versus the nominal concentration of paraquat with a weighed 1/x² linear regression.

Using this protocol, we confirmed that various fly lines ingested similar amounts of paraquat. (average mass of paraquat per fly: *UAS-dUSP30^{RNAi}*: 3.2 µg, *Actin-GAL4*: 2.7 µg, *Actin-GAL4* > *UAS-dUSP30^{RNAi}*: 2.7 µg)

Dopaminergic neuron degeneration assays. Fly brains were dissected as previously described⁴¹ with the following modifications. Brains were fixed using 4% paraformaldehyde in PBS, primary antibody used was rabbit anti-tyrosine hydroxylase (Pel Freez catalogue no. P40101-0) at 1:100, and secondary antibody used

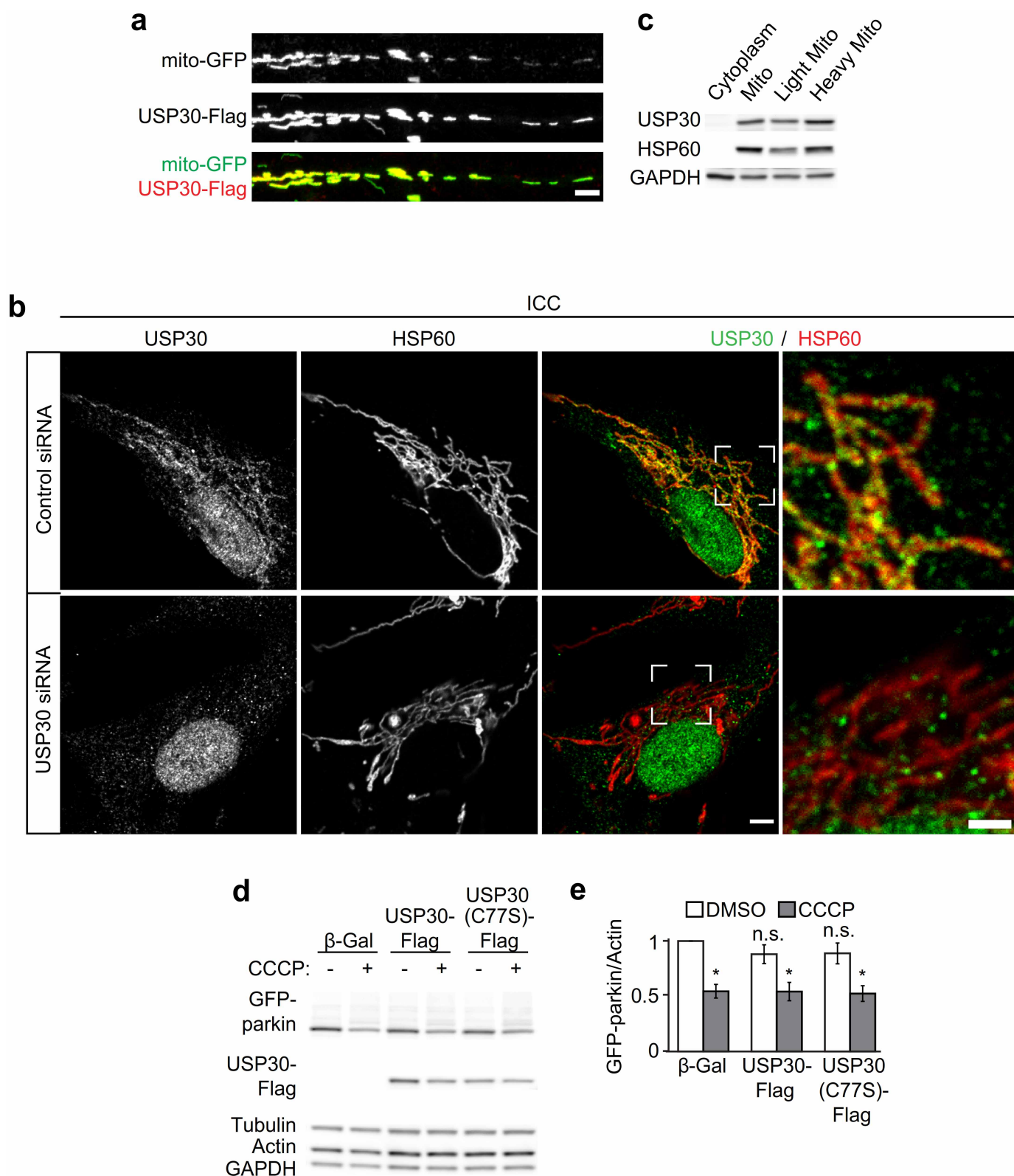
was goat anti-rabbit 488 (Invitrogen) at 1:400. Similar results were obtained using rabbit anti-tyrosine hydroxylase from Millipore (catalogue no. AB152). All images were quantified in a blinded manner. For flies of various *parkin* genotypes, brains were dissected at 20 days of age unless otherwise noted.

Survival assays. Ten adult 1-day old male flies per vial were fed a solution containing 5% sucrose only (in water) or 5% sucrose + 10 mM paraquat (in water) on saturated Whatman paper. The number of live flies was counted at described intervals.

Data collection and statistics. No statistical methods were used to pre-determine sample sizes. Sample sizes were kept similar between experimental groups and replicates of experiments (for example, ~25–30 neurons per well were imaged for mt-Keima experiments from each culture; ~20–50 cells were imaged per well in cell line experiments). All experiments and analysis were done in a blind-manner (blind to the identity of the experimental groups during image acquisition and analysis; blind to the treatment and genotype groups in fly experiments). No data were excluded in the analysis. Culture wells were randomly assigned to plasmid DNAs for transfection in multi-well plates. Imaging fields were randomly chosen during image acquisition. Flies were randomly assigned to treatment groups.

To compute *P* values, Mann–Whitney test, Kruskal–Wallis, and one-way or two-way ANOVA tests were used. Normal distribution was assessed by the Kolmogorov–Smirnov test. Bartlett’s test was used to estimate the variance between the groups that are being compared in one-way ANOVA tests. For multiple comparisons, the following post-hoc tests were used: Dunn’s multiple comparison test (following Kruskal–Wallis non-parametric tests), Dunnett’s multiple comparison test (for comparisons to a single ‘control’ group, following one-way ANOVA tests), Bonferroni’s multiple comparison test (for comparisons between multiple conditions, following one-way or two-way ANOVA tests). *P* values are represented as **P* < 0.05, ***P* < 0.01 and ****P* < 0.001. GraphPad v5 was used for the statistics.

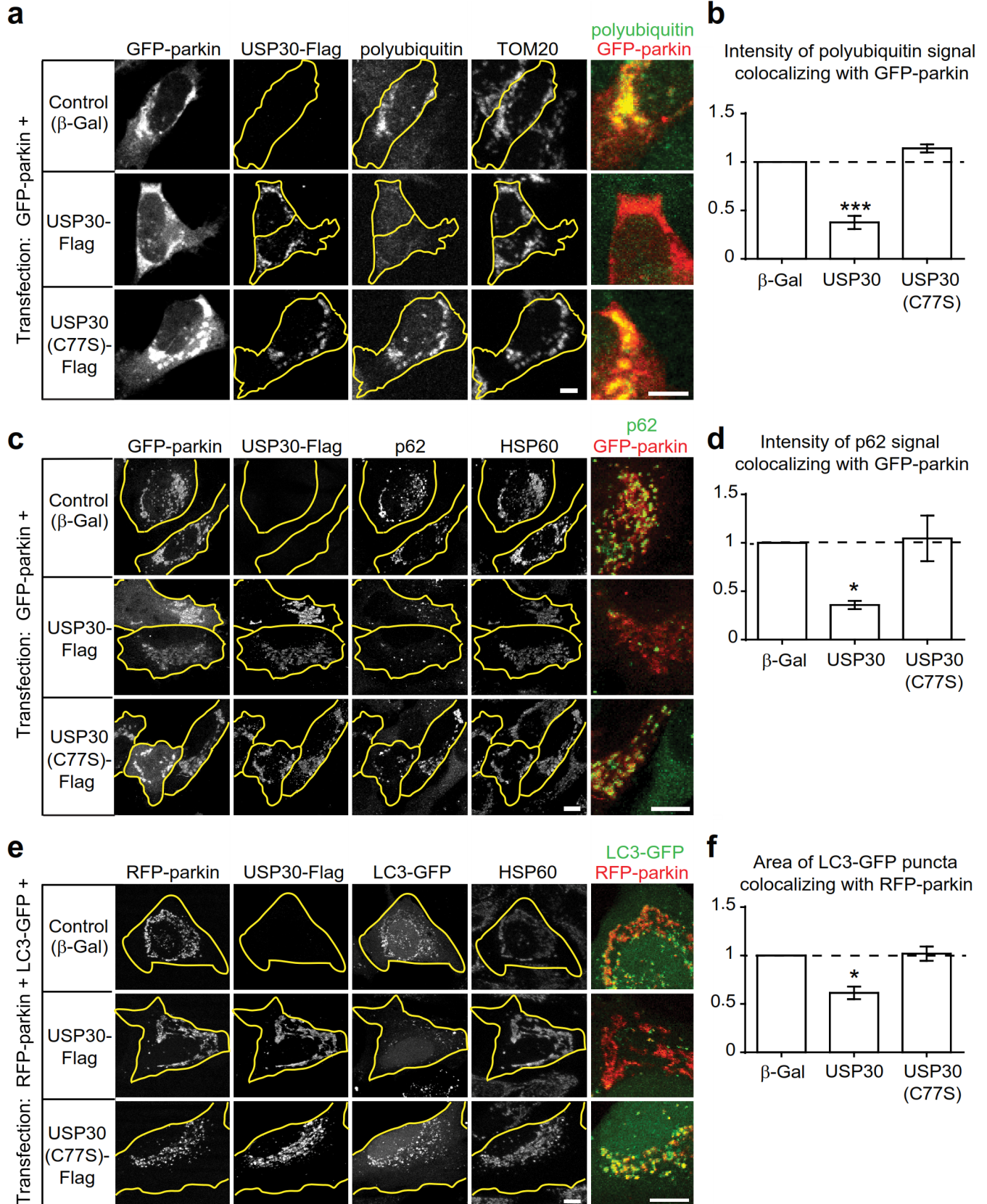
30. Seeburg, D. P. & Sheng, M. Activity-induced Polo-like kinase 2 is required for homeostatic plasticity of hippocampal neurons during epileptiform activity. *J. Neurosci.* **28**, 6583–6591 (2008).
31. Dooley, C. T. *et al.* Imaging dynamic redox changes in mammalian cells with green fluorescent protein indicators. *J. Biol. Chem.* **279**, 22284–22293 (2004).
32. Burchell, V. S. *et al.* The Parkinson’s disease-linked proteins Fbxo7 and Parkin interact to mediate mitophagy. *Nature Neurosci.* **16**, 1257–1265 (2013).
33. Shiba-Fukushima, K. *et al.* PINK1-mediated phosphorylation of the Parkin ubiquitin-like domain primes mitochondrial translocation of Parkin and regulates mitophagy. *Sci. Rep.* **2**, 1002 (2012).
34. Xu, G., Paige, J. S. & Jaffrey, S. R. Global analysis of lysine ubiquitination by ubiquitin remnant immunoaffinity profiling. *Nature Biotechnol.* **28**, 868–873 (2010).
35. Kim, W. *et al.* Systematic and quantitative assessment of the ubiquitin-modified proteome. *Mol. Cell* **44**, 325–340 (2011).
36. Rappsilber, J., Ishihama, Y. & Mann, M. Stop and go extraction tips for matrix-assisted laser desorption/ionization, nanoelectrospray, and LC/MS sample pretreatment in proteomics. *Anal. Chem.* **75**, 663–670 (2003).
37. Beausoleil, S. A., Villen, J., Gerber, S. A., Rush, J. & Gygi, S. P. A probability-based approach for high-throughput protein phosphorylation analysis and site localization. *Nature Biotechnol.* **24**, 1285–1292 (2006).
38. Bustos, D., Bakalarski, C. E., Yang, Y., Peng, J. & Kirkpatrick, D. S. Characterizing ubiquitination sites by peptide based immunoaffinity enrichment. *Mol. Cell. Proteomics* **11**, 1529–1540 (2012).
39. Seyfried, N. T. *et al.* Systematic approach for validating the ubiquitinated proteome. *Anal. Chem.* **80**, 4161–4169 (2008).
40. Pinheiro, J., Bates, D., DebRoy, S., Sarkar, D. & the R Core Team. nlme: linear and nonlinear mixed effects models. R package version 3. (2011).
41. Wu, J. S. & Luo, L. A protocol for dissecting *Drosophila melanogaster* brains for live imaging or immunostaining. *Nature Protocols* **1**, 2110–2115 (2006).



Extended Data Figure 1 | USP30 is a mitochondrial protein.

a, Immunostaining of transfected USP30-Flag (red) and mitochondria-targeted GFP (green) in cultured rat hippocampal neurons. Merge is shown in colour; individual channels in greyscale. Scale bar, 5 μ m. **b**, Immunostaining of SH-SY5Y cells transfected with control or USP30 siRNA. 3 days after transfection, cells were fixed and immunostained for endogenous USP30 and HSP60. USP30 siRNA primarily decreases mitochondrial USP30 antibody staining (scale bar, 5 μ m). Higher magnification images of the boxed regions are

shown in the right panels (scale bar, 2 μ m). **c**, Immunoblots of cytoplasm- and mitochondria-enriched fractions from rat brain with USP30, HSP60 and GAPDH antibodies. **d**, Immunoblots of cell lysates from HEK-293 cells stably expressing GFP-parkin, transfected with the indicated control (β -Gal) and USP30 constructs. 24 h after transfection, cells were treated with CCCP (5 μ M, 2 h) and lysed. **e**, Quantification of immunoblot signal for GFP-parkin from **d**, normalized to actin. * P < 0.05 by Kruskal-Wallis test and Dunn's multiple comparison test. n = 6 experiments. Error bars represent s.e.m.



Extended Data Figure 2 | USP30 counteracts mitochondrial ubiquitination and recruitment of p62 and LC3–GFP in CCCP-treated parkin-expressing cells.

a, Immunostaining of SH-SY5Y cells co-transfected with GFP–parkin and the indicated control (β -Gal) and Flag-tagged USP30 constructs. 24 h after transfection, cells were treated with CCCP (20 μ M, 4 h) and immunostained for GFP, Flag, endogenous TOM20, and polyubiquitin chains (detected with FK2 antibody). Co-localization of GFP–parkin (shown in red) and polyubiquitin (shown in green) is shown in the right panel. Scale bars, 5 μ m. **b**, Quantification of GFP–parkin-associated polyubiquitin staining intensity from **a**, normalized by GFP–parkin area (integrated fluorescence intensity of FK2 staining colocalizing with GFP–parkin/area of GFP–parkin staining). *** $P < 0.001$ by Kruskal–Wallis test and Dunn’s multiple comparison test. $n = 6$ experiments. Error bars represent s.e.m. **c**, Immunostaining of HeLa cells co-transfected with GFP–parkin and the indicated control (β -Gal) and Flag-tagged USP30 constructs. Cells were treated as in **a** and immunostained for GFP, Flag, endogenous p62, and HSP60. Co-localization of GFP–parkin (shown in red)

and p62 (shown in green) is shown in the right panel. Scale bars, 10 μ m.

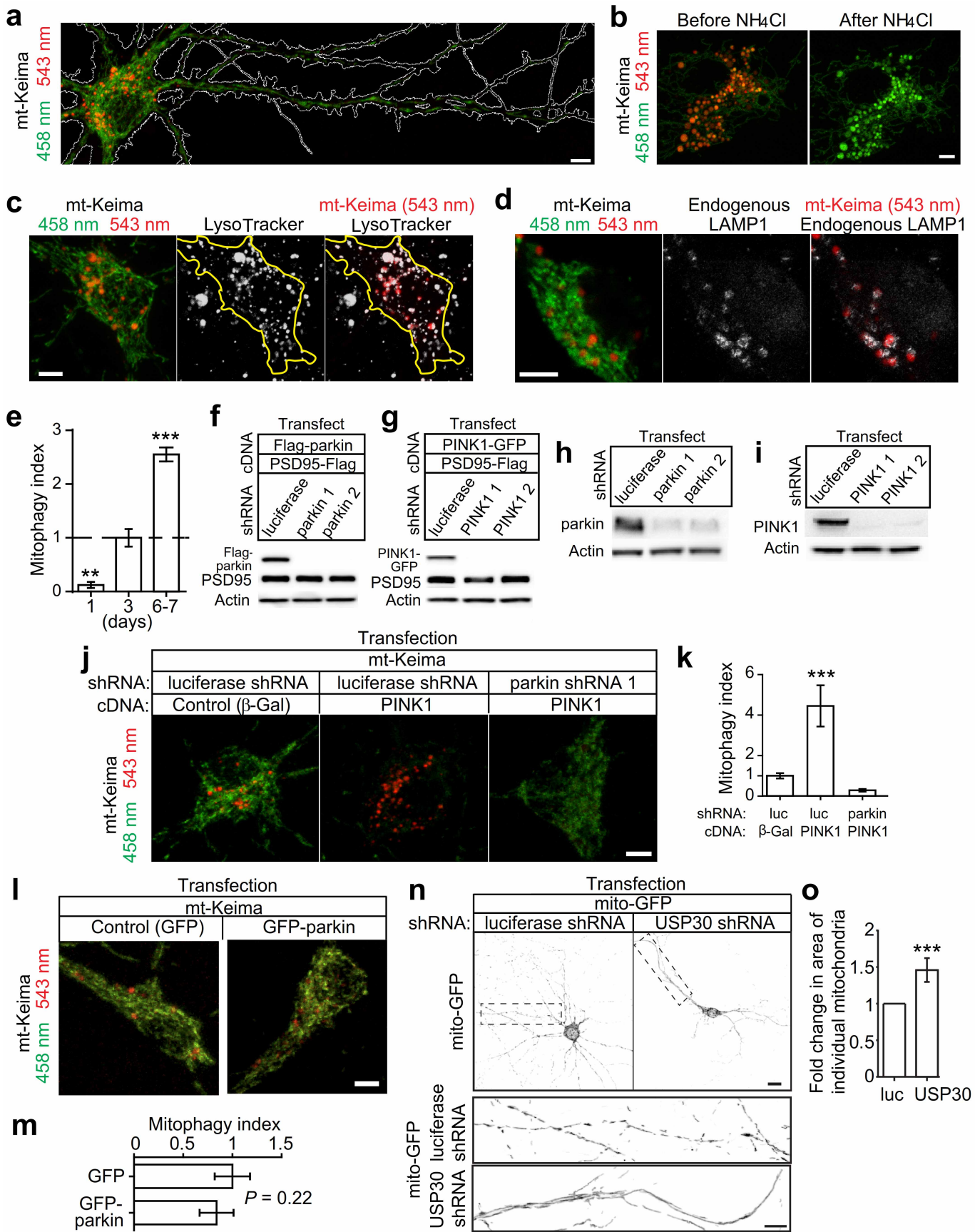
d, Quantification of GFP–parkin-associated p62 staining intensity from **c**, normalized by GFP–parkin area (integrated fluorescence intensity of p62 staining colocalizing with GFP–parkin/area of GFP–parkin staining).

* $P < 0.05$ by Kruskal–Wallis test and Dunn’s multiple comparison test. $n = 5$

experiments. Error bars represent s.e.m. **e**, Immunostaining of HeLa cells co-transfected with RFP–parkin, LC3–GFP and the indicated control (β -Gal) and Flag-tagged USP30 constructs. Cells were treated as in **a** and immunostained for GFP, Flag and endogenous HSP60. Co-localization of

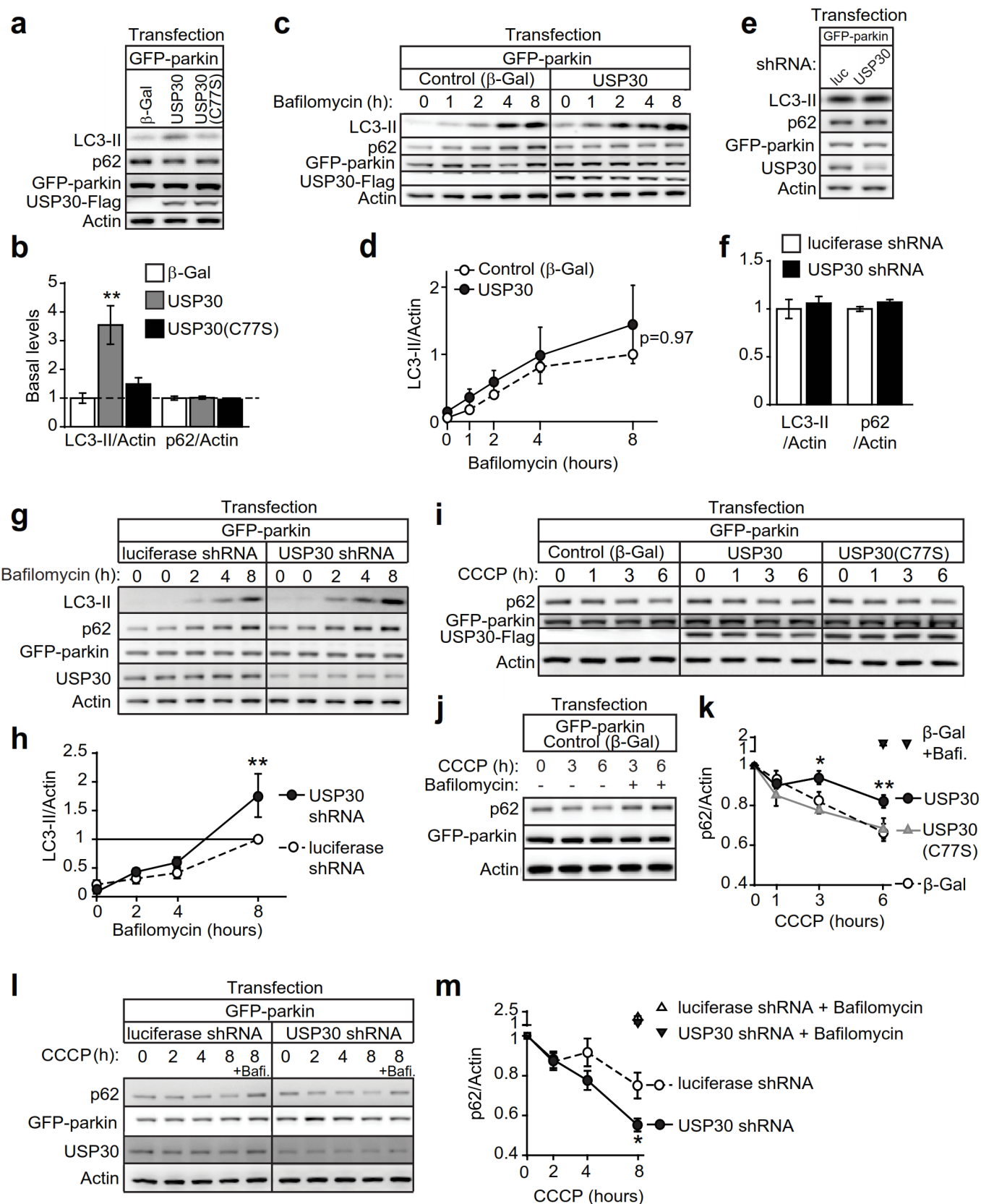
RFP–parkin (shown in red) and LC3–GFP (shown in green) is shown in the right panel. Scale bars, 10 μ m. **f**, Quantification of RFP–parkin-associated LC3–GFP puncta area from **e**, normalized by RFP–parkin area (area of LC3–GFP puncta colocalizing with RFP–parkin/area of RFP–parkin staining). * $P < 0.05$ by Kruskal–Wallis test and Dunn’s multiple comparison test. $n = 5$

experiments. Error bars represent s.e.m.



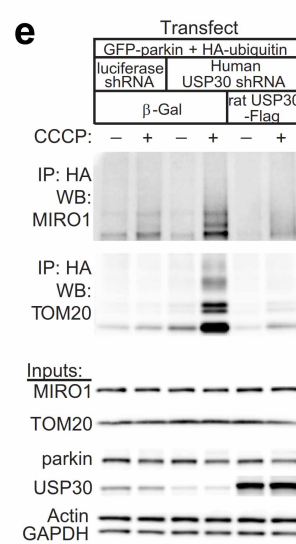
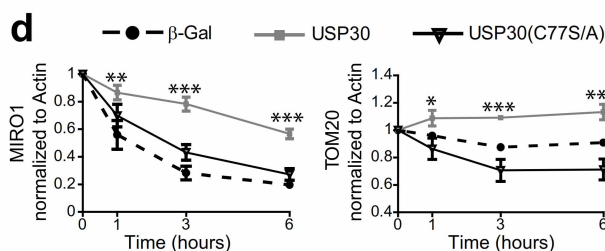
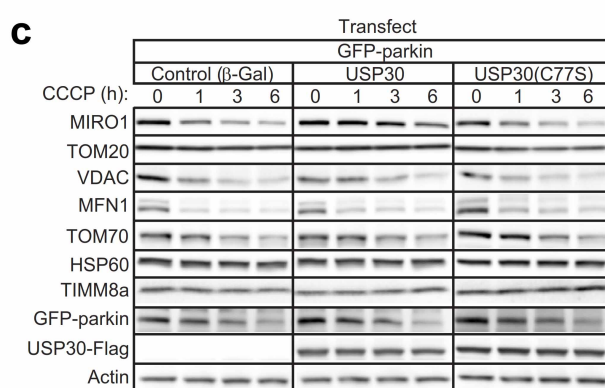
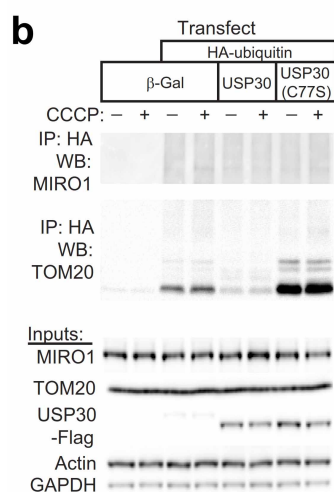
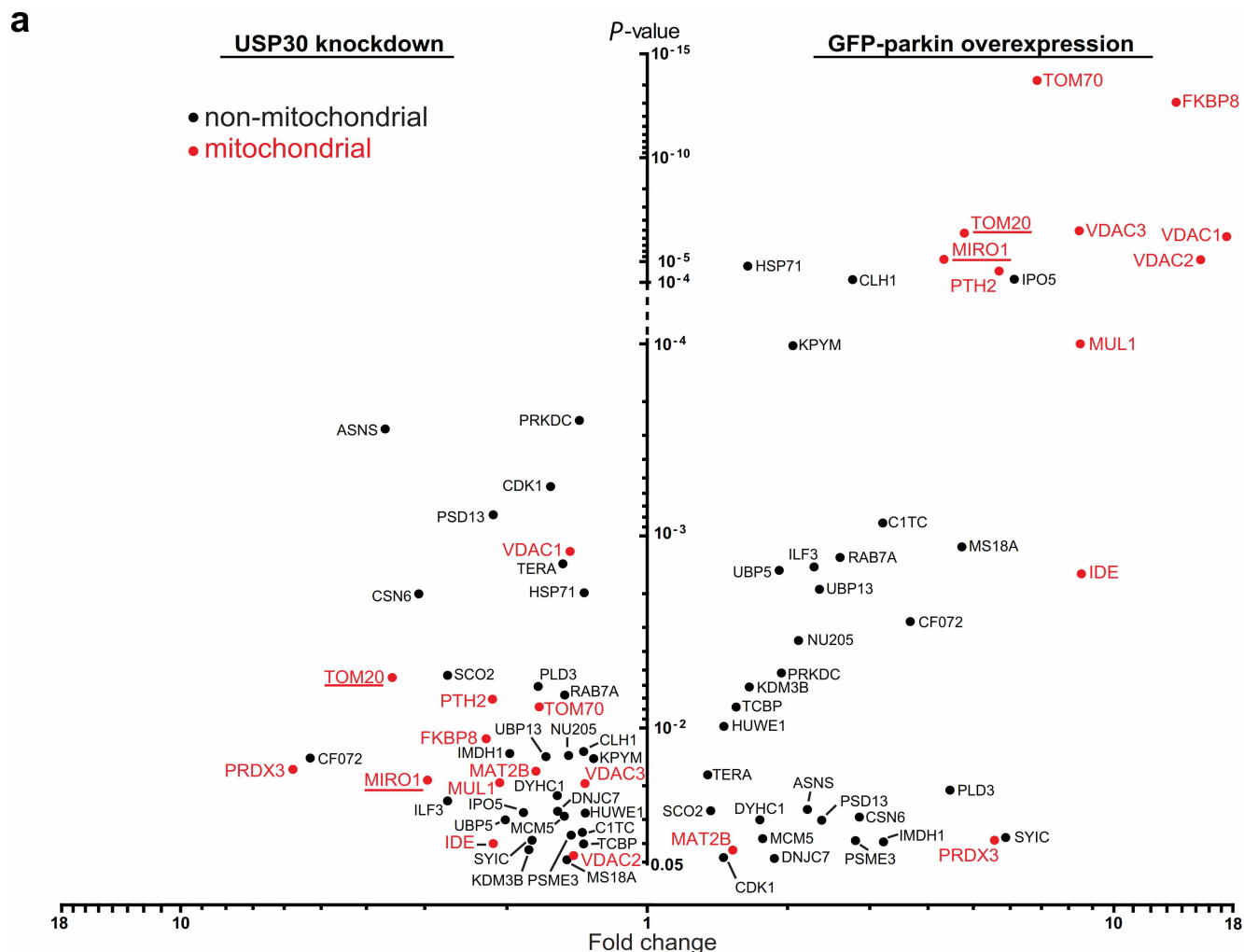
Extended Data Figure 3 | mt-Keima imaging of mitophagy; PINK1 acts upstream of parkin in the mitophagy pathway. **a**, mt-Keima differentially highlights cytoplasmic (green) and lysosomal (red) mitochondria. Cultured hippocampal neurons were transfected with mt-Keima and GFP. Following 2 days of expression, cells were imaged with 458 nm (shown in green) or 543 nm (shown in red) light excitation. GFP signal was used to outline the cell (shown in white). Scale bar, 5 μ m. **b**, mt-Keima imaging in cultured hippocampal neurons before and after NH_4Cl treatment (50 mM, 2 min). mt-Keima signal, collected with 543 nm or 458 nm laser excitation, is shown in red and green, respectively. Neutralizing cells with NH_4Cl completely reversed the high ratio (543 nm/458 nm) signal to low ratio signal specifically in the round structures without affecting the tubular-reticular mitochondrial signal. Scale bar, 5 μ m. **c**, Imaging of mt-Keima and Lysotracker (Lysotracker green DND-26 shown in grey scale) in hippocampal neurons, showing Lysotracker stained the high ratio mt-Keima structures. Scale bar, 5 μ m. **d**, Post hoc immunostaining for endogenous Lamp1 in neurons imaged for mt-Keima signal, showing the colocalization of high-ratio mt-Keima pixels with Lamp1 staining. Immediately following mt-Keima imaging, cells were fixed and stained with anti-Lamp1 antibody (shown in grey scale). Scale bar, 5 μ m. **e**, Quantification of mitophagy index following 1, 3 and 6–7 days of mt-Keima expression in cultured hippocampal neurons. $**P < 0.01$ and $***P < 0.001$ by

Kruskal–Wallis test and Dunn’s multiple comparison test. $n = 29$ –85 cells. $n = 2$ –4 experiments. Error bars represent s.e.m. **f**, **g**, Immunoblots of HEK-293 cell lysates transfected with the indicated cDNA and parkin (**f**) or PINK1 (**g**) shRNA constructs. PSD-95–Flag was co-transfected as a control. Representative blots from three independent experiments are shown. **h**, **i**, Immunoblots of endogenous parkin (**h**) and PINK1 (**i**) in cultured hippocampal neurons infected with adeno-associated virus expressing the indicated shRNAs. Representative blots from two independent experiments are shown. **j**, mt-Keima imaging in neurons transfected with PINK1–GFP and parkin-shRNA 1 (β -Gal and luciferase shRNA as controls). Scale bar, 5 μ m. **k**, Quantification of mitophagy index from **j**. $***P < 0.001$ by Kruskal–Wallis test and Dunn’s multiple comparison test. $n = 55$ –75 cells. $n = 3$ experiments. Error bars represent s.e.m. **l**, mt-Keima imaging in neurons transfected with GFP–parkin or GFP control. Scale bar, 5 μ m. **m**, Quantification of mitophagy index from **l**. ($P = 0.22$ by Mann–Whitney test. $n = 37$ –43 cells. $n = 3$ experiments. Error bars represent s.e.m. **n**, Mitochondria-targeted GFP (mito-GFP) imaging in neurons transfected with luciferase shRNA or USP30 shRNA constructs. Scale bar, 10 μ m. Higher magnification images shown in the bottom panel. Scale bar, 5 μ m. **o**, Quantification of fold change in area of individual dendritic mitochondria from **n**. $***P < 0.001$ by Mann–Whitney test. $n = 9$ experiments. Error bars represent s.e.m.



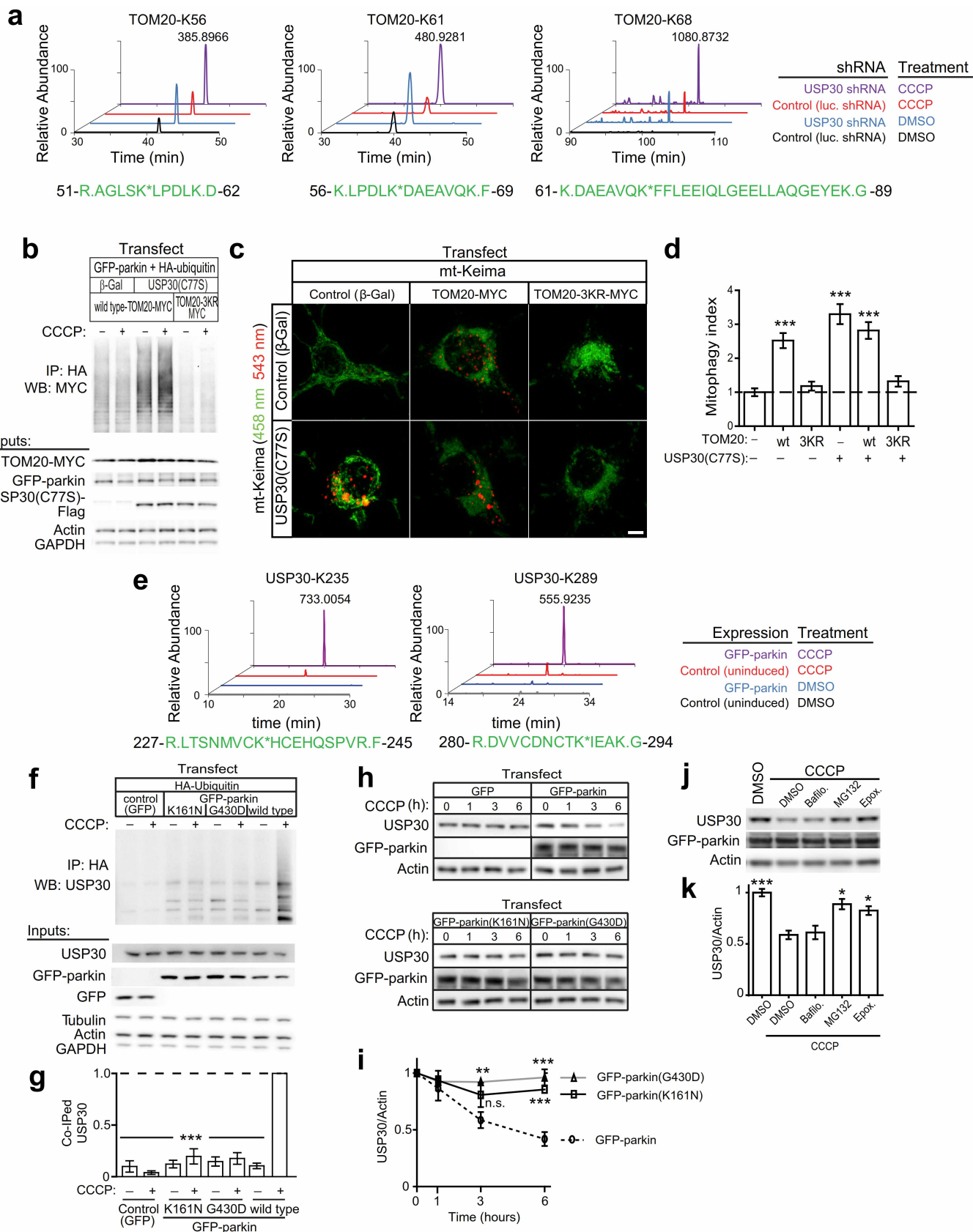
Extended Data Figure 4 | USP30 opposes autophagic flux. **a**, Immunoblots of cell lysates from HEK-293 cells, transfected with GFP-parkin and the indicated control (β -Gal) or USP30 constructs. **b**, Quantification of the LC3-II and p62 immunoblot signal from **a**, normalized to actin. $**P < 0.01$ by Kruskal–Wallis test and Dunn’s multiple comparison test. $n = 6$ experiments. Error bars represent s.e.m. **c**, Immunoblots of cell lysates from HEK-293 cells, transfected with GFP-parkin and β -Gal or USP30 wild type constructs, as indicated. 24 h after transfection, cells were treated with bafilomycin (100 nM, 0–8 h). **d**, Quantification of the LC3-II immunoblot signal from **c**, normalized to actin. $P = 0.97$ by two-way ANOVA and Bonferroni’s multiple comparison test. $n = 5$ experiments. Error bars represent s.e.m. **e**, Immunoblots of cell lysates from HEK-293 cells, transfected with GFP-parkin and control (luciferase) or USP30 shRNA constructs. **f**, Quantification of the LC3-II and p62 immunoblot signal from **e**, normalized to actin. **g**, Immunoblots of cell lysates from HEK-293 cells, transfected with GFP-parkin and control (luciferase) or USP30 shRNA constructs. 6 days after transfection, cells were

treated with bafilomycin (100 nM, 0–8 h). **h**, Quantification of the LC3-II immunoblot signal from **g**, normalized to actin. $**P < 0.01$ by two-way ANOVA and Bonferroni’s multiple comparison test. $n = 4$ experiments. Error bars represent s.e.m. **i**, **j**, Immunoblots of cell lysates from HEK-293 cells, transfected with GFP-parkin and the indicated control (β -Gal) or USP30 constructs. 24 h after transfection, cells were treated with CCCP (20 μ M, 0–6 h). β -Gal transfected cells were also treated with bafilomycin (100 nM, 0–6 h) as a control (shown in **j**). **k**, Quantification of the p62 immunoblot signal from **i**, **j**, normalized to actin. $*P < 0.05$ and $**P < 0.01$ by two-way ANOVA and Bonferroni’s multiple comparison test. $n = 6$ experiments. Error bars represent s.e.m. **l**, Immunoblots of cell lysates from HEK-293 cells, transfected with GFP-parkin and control (luciferase) or USP30 knockdown constructs. 24 h after transfection, cells were treated with CCCP (20 μ M, 0–8 h) and bafilomycin (100 nM), as indicated. **m**, Quantification of the p62 immunoblot signal from **l**, normalized to actin. $*P < 0.05$ by two-way ANOVA and Bonferroni’s multiple comparison test. $n = 6$ experiments. Error bars represent s.e.m.



Extended Data Figure 5 | USP30 deubiquitinates multiple mitochondrial proteins. **a**, Proteins whose ubiquitination is regulated by both USP30 and parkin. Asymmetric ‘volcano plot’ showing the subset of 41 proteins whose ubiquitination significantly increased ($P < 0.05$) by both GFP-parkin overexpression (right side) and USP30 knockdown (left side) in ‘combo’ treatments compared to ‘CCCP-treatment’ alone. ‘Combo’ refers to cells treated with ‘CCCP + GFP-parkin’ or ‘CCCP + USP30-shRNA’. For this subset of proteins, fold-increase in ubiquitination (x -axis) and the P value (y -axis) are reported. Mitochondrial proteins (as identified by the Human MitoCarta database) are shown in red. Fold-changes and P values for all proteins with quantified K-GG peptides are reported in Supplementary Table 1. **b**, Immunoblots of anti-HA-immunoprecipitates for endogenous MIRO1 and TOM20 in parental HEK-293 cell line (that lacks GFP-parkin) transfected with HA-ubiquitin and the indicated Flag-tagged USP30 constructs (β -Gal as control). 24 h after transfection, cells were treated with CCCP (5 μ M, 2 h) and ubiquitinated proteins were immunoprecipitated with anti-HA beads.

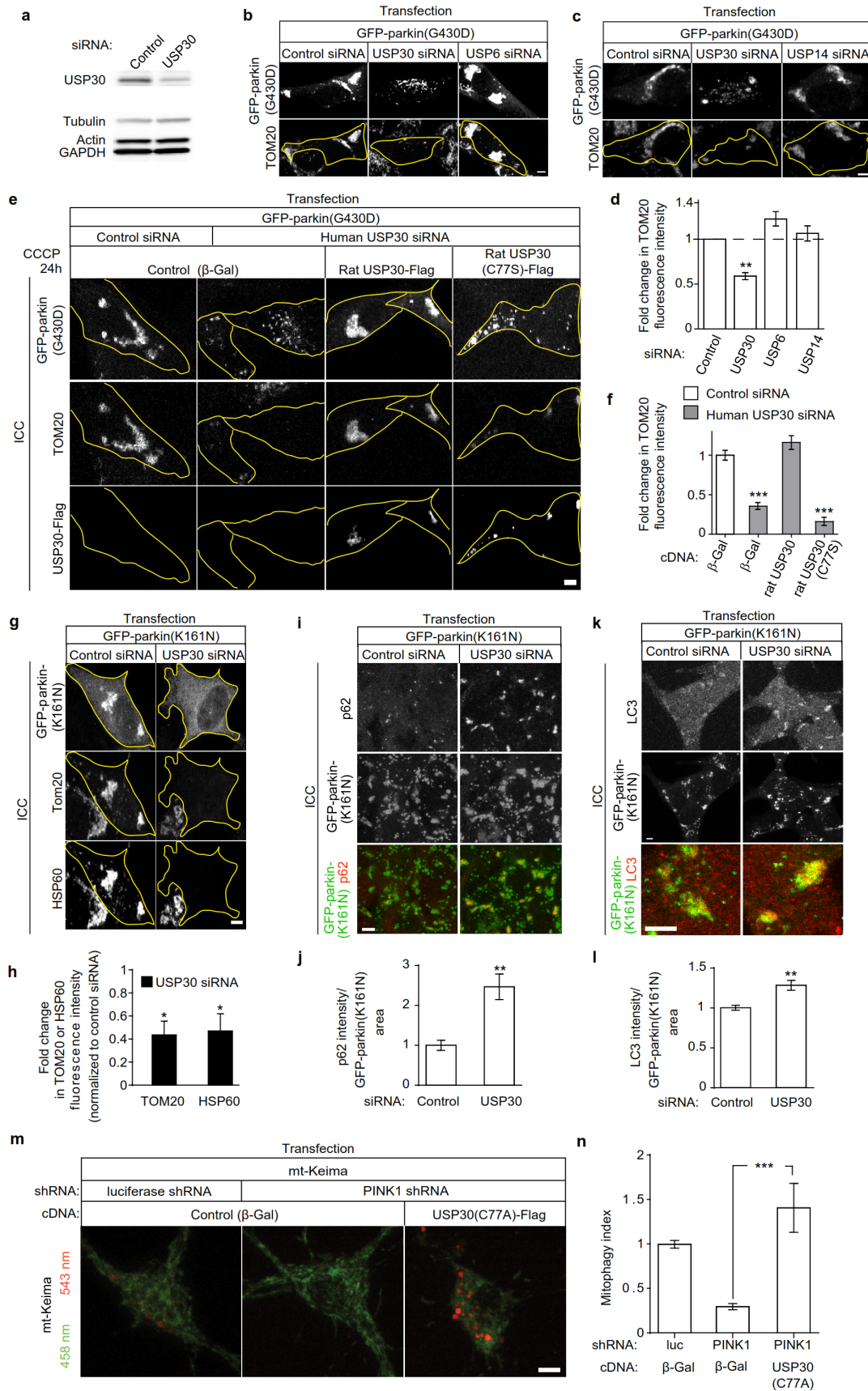
Immunoprecipitates and inputs were blotted with the indicated antibodies. $n = 2$ experiments. **c**, Immunoblots of total lysates of GFP-parkin HEK-293 stable cells that were transfected with the indicated Flag-tagged USP30 constructs, and then treated with CCCP (5 μ M, 0–6 h). **d**, Quantification of MIRO1 and TOM20 immunoblot signals from **c**, normalized to actin. Immunoblot signals for all other proteins (VDAC, Mfn-1, Tom70, HSP60, TIMM8a) did not reach significance. * $P < 0.05$, ** $P < 0.01$, *** $P < 0.001$ compared to β -Gal control, by two-way ANOVA and Bonferroni’s multiple comparison test. $n = 3$ –5 experiments.) **e**, Immunoblots of anti-HA-immunoprecipitates for endogenous MIRO1 and TOM20 with USP30 knockdown. HEK-293 cells stably expressing GFP-parkin were transfected as indicated with HA-ubiquitin, human USP30 shRNA and rat USP30-Flag cDNA that is insensitive to the shRNA (luciferase shRNA and β -Gal as controls). 6 days after transfection, cells were processed as in **b**. $n = 2$ experiments.



Extended Data Figure 6 | TOM20 activates mitophagy through

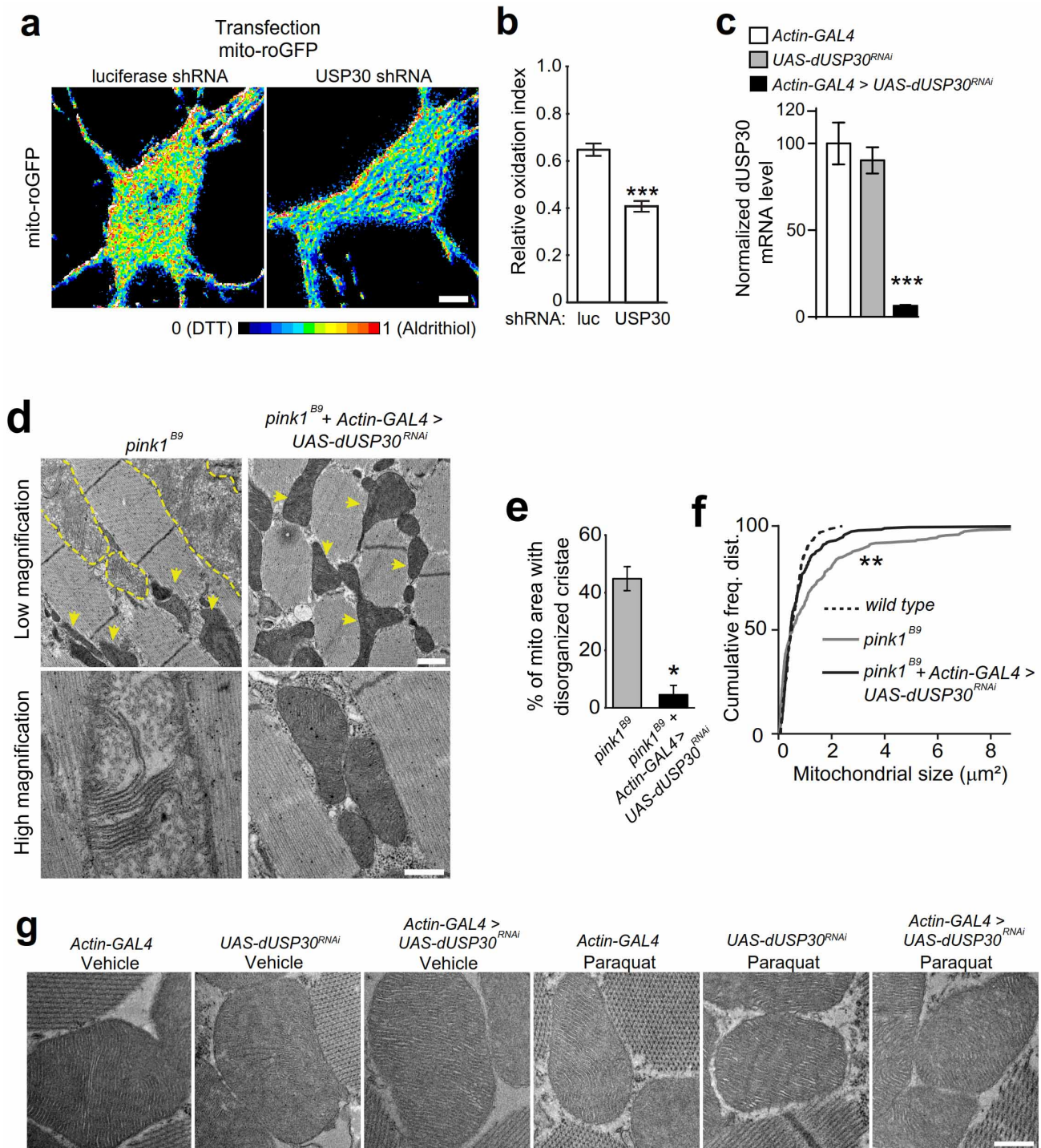
ubiquitination; USP30 is a parkin substrate. **a**, Extracted ion chromatograms corresponding to K-GG peptides identified from TOM20 in the USP30 knockdown mass spectrometry. Relative abundance of each ubiquitinated peptide is shown on the *y*-axis relative to the most abundant analysis, with precursor ion *m/z* indicated above each peak. The sequence of each K-GG peptide is shown below in green. Asterisks denote modified lysine residues. **b**, Immunoblots of HA-ubiquitin precipitates from GFP-parkin HEK-293 cells transfected with the indicated constructs. Following transfection and treatment with CCCP (5 μ M, 2 h), ubiquitinated proteins were immunoprecipitated with anti-HA beads, and precipitates and inputs were blotted with the indicated antibodies. *n* = 3 experiments. **c**, mt-Keima imaging in neurons transfected with the indicated TOM20-MYC and USP30 constructs (β -Gal as control). Scale bar, 5 μ m. **d**, Quantification of mitophagy index from **c**. ****P* < 0.001 by Kruskal-Wallis test and Dunn's multiple comparison test. *n* = 67–80 cells for all groups. *n* = 3 experiments. Error bars represent s.e.m. **e**, Extracted ion chromatograms corresponding to K-GG peptides identified from USP30 in the parkin overexpression mass spectrometry. Similar to **a**. **f**, Immunoblots of anti-HA-immunoprecipitates for endogenous USP30 from cells transfected with wild-type, K161N and G430D GFP-parkin constructs. After 24 h of expression,

cells were treated with CCCP (20 μ M, 2 h) and ubiquitinated proteins were immunoprecipitated with anti-HA beads. Immunoprecipitates and inputs were blotted with the indicated antibodies. **g**, Quantification of immunoblot signal for co-immunoprecipitated USP30 from **f**. Protein levels co-immunoprecipitating with anti-HA beads are normalized to the 'wild-type GFP-parkin + CCCP' group. ****P* < 0.001 by one-way ANOVA and Dunnett's multiple comparison test, compared to 'wild-type GFP-parkin + CCCP'. *n* = 5 experiments. Error bars represent s.e.m. **h**, Immunoblots of lysates prepared from HEK-293 cells transfected with the indicated GFP and GFP-parkin constructs and treated with CCCP (20 μ M, 0–6 h). **i**, Quantification of immunoblot signal for USP30 from **h**, normalized to actin. ***P* < 0.01, ****P* < 0.001 compared to wild-type GFP-parkin, by two-way ANOVA and Bonferroni's multiple comparison test. *n* = 4 experiments. Error bars represent s.e.m. **j**, Immunoblots of lysates prepared from HEK-293 cells transfected with GFP-parkin and treated as indicated (CCCP 20 μ M, 6 h; bafilomycin (100 nM), MG132 (20 μ M), and epoxomicin (2 μ M) were added 15 min before CCCP treatment). **k**, Quantification of immunoblot signal for USP30 from **j**, normalized to actin. **P* < 0.05 and ****P* < 0.001 by one-way ANOVA and Dunnett's multiple comparison test, compared to 'DMSO + CCCP'. *n* = 4 experiments. Error bars represent s.e.m.



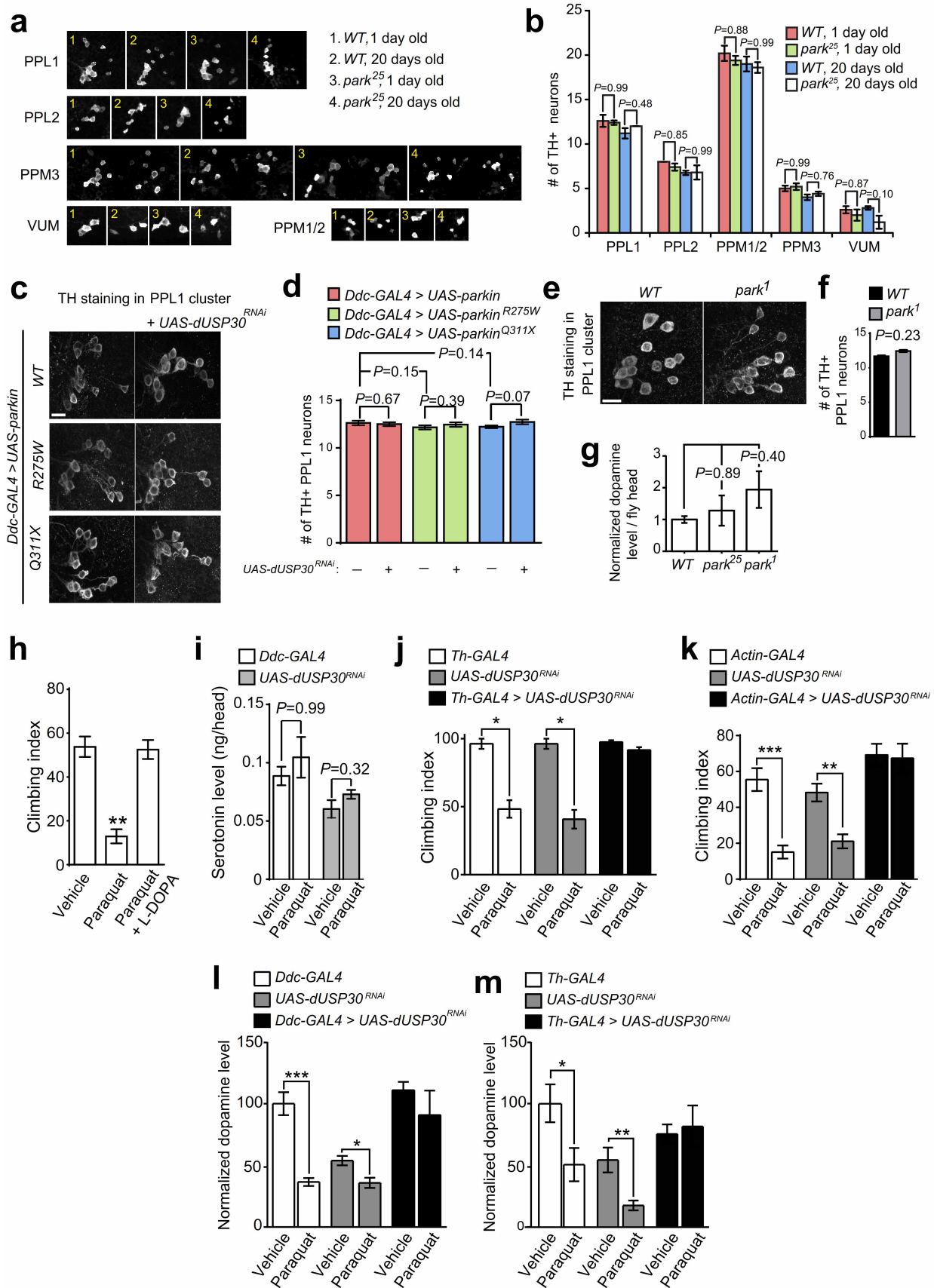
Extended Data Figure 7 | USP30 knockdown rescues mitophagy defects in cells expressing mutant parkin. **a**, Immunoblot for endogenous USP30 in SH-SY5Y cells transfected with USP30 siRNA for 3 days. **b, c**, Immunostaining in SH-SY5Y cells stably expressing GFP-parkin(G430D), transfected with siRNAs against USP30, USP6 or USP14. 3 days after transfection, cells were treated with CCCP (20 μ M, 24 h), then fixed and stained for GFP and endogenous TOM20. Scale bars, 5 μ m. **d**, Quantification of fold change in TOM20 staining intensity from **b** and **c**, normalized to control siRNA. $^{***}P < 0.01$ by Kruskal–Wallis test and Dunn’s multiple comparison test. $n = 3$ experiments. Error bars represent s.e.m. **e**, Immunostaining of SH-SY5Y cells expressing GFP-parkin(G430D), transfected as indicated, and treated with CCCP (20 μ M, 24 h). Rat USP30 cDNA is insensitive to human USP30 siRNA. **f**, Quantification of fold change in TOM20 intensity from **e**. Kruskal–Wallis test, $n = 3$ experiments. **g**, Immunostaining of SH-SY5Y cells expressing GFP-parkin(K161N), and transfected with USP30 siRNA. Following 3 days of knockdown, cells were treated with CCCP (20 μ M, 24 h), then fixed and

stained for GFP and endogenous TOM20 and HSP60. Scale bars, 5 μ m. **h**, Quantification of fold change in TOM20 or HSP60 staining intensity from **g**, normalized to control siRNA. $^{*}P < 0.05$ by Mann–Whitney test, $n = 4$ experiments. Error bars represent s.e.m. **i, k**, Immunostaining of SH-SY5Y cells expressing GFP-parkin(K161N), and transfected with USP30 siRNA. Following 3 days of knockdown, cells were treated with CCCP (20 μ M, 4 h), then fixed and stained for GFP and endogenous p62 (**i**) or LC3 (**k**). Co-localization of GFP-parkin (shown in green) and p62 or LC3 (shown in red) is shown in the lower panel. Scale bars, 5 μ m. **j, l**, Quantification of GFP-parkin(K161N)-associated p62 (**j**) or LC3 (**l**) staining intensity normalized by GFP-parkin(K161N) area, from **i, k**. $^{***}P < 0.01$ by Mann–Whitney test, $n = 9$ –10 experiments. Error bars represent s.e.m. **m**, mt-Keima imaging in neurons transfected with PINK1 shRNA and USP30(C77A)–Flag. Scale bar, 5 μ m. **n**, Quantification of mitophagy index from **m**. Kruskal–Wallis test. $n = 127$ –166 cells. $n = 7$ experiments. Error bars represent s.e.m.



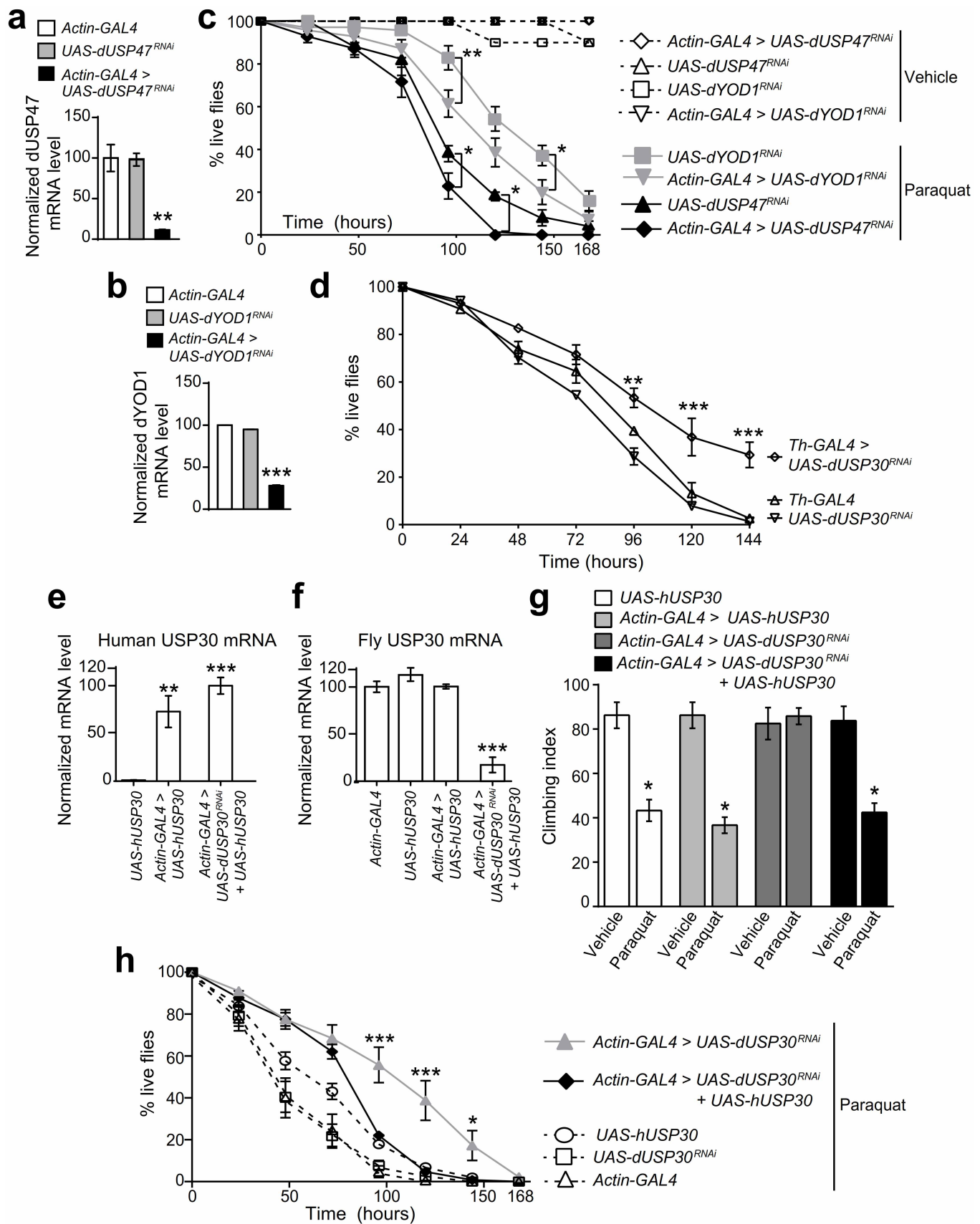
Extended Data Figure 8 | USP30 knockdown decreases oxidative stress in neurons and rescues mitochondrial morphology defects in *PINK1* mutant flies. **a**, Ratiometric mito-roGFP imaging in hippocampal neurons transfected with USP30 shRNA. Following measurement of ratiometric mito-roGFP signal in individual cells, the dynamic range of the probe was calibrated by treating cultures sequentially with DTT (1 mM) to fully reduce the probe, and aldrithiol (100 μM) to fully oxidize the probe¹³. The 'relative oxidation index' is shown in a 'colour scale' from 0 (mito-roGFP ratio after DTT treatment, shown in black) to 1 (mito-roGFP ratio after aldrithiol treatment, shown in red). **b**, Quantification of relative oxidation index from **a**. ****P* < 0.001 by Mann-Whitney test. *n* = 24 cells for luciferase shRNA and 36 cells for USP30 shRNA. *n* = 3 experiments. Error bars represent s.e.m. **c**, Quantitative RT-PCR of dUSP30 mRNA. qRT-PCR in *Actin-GAL4*, *UAS-dUSP30*^{RNAi}, and

Actin-GAL4 > UAS-dUSP30^{RNAi} flies, shown relative to *Actin-GAL4*. dUSP30 mRNA levels were normalized to internal control *Drosophila* Rp1140 mRNA levels. ****P* < 0.001 by one-way ANOVA and Dunnett's multiple comparison test. *n* = 3 experiments. Error bars represent s.e.m. **d**, Transverse sections of *Drosophila* indirect flight muscles of indicated genotypes. Arrowheads, electron-dense mitochondria; dashed lines, 'pale' mitochondria with disorganized cristae. Scale bars, 1 μm (top), 0.2 μm (bottom panels). **e**, **f**, Quantification of mitochondrial morphology (**e**) and size distribution (**f**) from **d**. Mann-Whitney test (**e**). Kolmogorov-Smirnov test, *pink1*^{B9} versus '*pink1*^{B9} + dUSP30 knockdown' (**f**). *n* = 4 flies per genotype. **g**, Transverse sections of indirect flight muscles (IFMs) from vehicle- or paraquat-treated flies of indicated genotypes. Scale bar, 0.5 μm.



Extended Data Figure 9 | Neurodegeneration was not observed in genetic *parkin* fly models; dUSP30 knockdown protects against paraquat-induced climbing and dopamine deficits. **a, c, e**, Representative images of the indicated dopaminergic neuron clusters in flies with indicated genotypes. Scale bars, 10 μ m. **b, d, f**, Blind quantification for panels **a, c, e**. *P* values calculated by Student's *t*-test (**f**) and one-way ANOVA and Bonferroni's multiple comparison test (**b, d**). *n* = 4–5 hemibrains per genotype. Similar results were obtained with additional counts performed for the PPL1 cluster, *n* = 18–40 hemibrains per genotype. Error bars represent s.e.m. **g**, Dopamine levels in fly brains for the indicated genotypes. *n* = 16 flies per genotype. *P* values calculated by one-way ANOVA and Bonferroni's multiple comparison test. **h**, Climbing assay in control flies (*Actin-GAL4*). Flies were treated with vehicle control (5% sucrose) or paraquat (10 mM, 48 h). L-3,4-dihydroxyphenylalanine (1 mM, 48 h) was administered simultaneously with paraquat, as indicated. Graph shows % of flies climbing 15 cm in 30 s. ***P* < 0.01 by Kruskal–Wallis test and Dunn's multiple comparison test. *n* = 6 experiments. Error bars

represent s.e.m. **i**, Serotonin levels per fly head, as assessed by ELISA. Flies were treated with paraquat (10 mM, 48 h) or vehicle control (5% sucrose). *P* values calculated by Kruskal–Wallis test and Dunn's multiple comparison test. *n* = 8 heads, *n* = 2 experiments. Error bars represent s.e.m. **j**, Climbing assay of dUSP30 knockdown flies driven by *Th-GAL4*. Flies were treated with paraquat (10 mM, 48 h) or vehicle control (5% sucrose). Graph shows % of flies climbing 15 cm in 30 s. **P* < 0.05 by Kruskal–Wallis test and Dunn's multiple comparison test. *n* = 4 experiments. Error bars represent s.e.m. **k**, Climbing assay of dUSP30 knockdown flies driven by *Actin-GAL4*. Flies were treated with paraquat (10 mM, 48 h) or vehicle control (5% sucrose). Graph shows % of flies climbing 15 cm in 30 s. ***P* < 0.01 and ****P* < 0.001 by one-way ANOVA and Bonferroni's multiple comparison test. *n* = 6–10 experiments. Error bars represent s.e.m. **l, m**, Normalized dopamine levels per fly head, as assessed by ELISA. Flies of the indicated genotype were treated with paraquat (10 mM, 48 h) or vehicle control (5% sucrose). **P* < 0.05, ***P* < 0.01, and ****P* < 0.001 by Mann–Whitney test. *n* = 8–28 heads. Error bars represent s.e.m.



Extended Data Figure 10 | Knockdown of DUBs dYOD1 or dUSP47 in flies does not provide protection against paraquat; hUSP30 overexpression reverses dUSP30 knockdown benefits. **a, b,** Quantitative RT-PCR measurement of dUSP47 (**a**) and dYOD1 (**b**) mRNA levels in flies of the indicated genotypes, expressed as relative to *Actin-GAL4* genotype. $**P < 0.01$ and $***P < 0.001$ by one-way ANOVA and Dunnett's multiple comparison test. $n = 3$ technical replicates. Error bars represent s.e.m. **c,** Survival curves of flies with dUSP47 or dYOD1 knockdown, treated with vehicle (5% sucrose) or paraquat (10 mM). Graph shows percent of flies alive at indicated times. $*P < 0.05$ and $**P < 0.01$ by two-way ANOVA and Bonferroni's multiple comparison test. $n = 5-7$ experiments. Error bars represent s.e.m. **d,** Survival curves of flies with dUSP30 knockdown driven by *Th-GAL4*, treated with paraquat (10 mM). Graph shows percent of flies alive at indicated times after

feeding with paraquat. $**P < 0.01$ and $***P < 0.001$ by two-way ANOVA and Bonferroni's multiple comparison test. $n = 3$ experiments. Error bars represent s.e.m. **e, f,** Quantitative RT-PCR measurement of *hUSP30* and *dUSP30* mRNA levels in flies of the indicated genotypes. $**P < 0.01$ and $***P < 0.001$ by one-way ANOVA and Dunnett's multiple comparison test. $n = 4$ experiments. Error bars represent s.e.m. **g,** Climbing assay for flies overexpressing hUSP30. Flies of indicated genotypes were fed with vehicle (5% sucrose) or paraquat (10 mM, 48 h); graph shows percent of flies climbing 15 cm in 30 s. $*P < 0.05$ by Kruskal-Wallis test and Dunn's multiple comparison test. $n = 4$ experiments. Error bars represent s.e.m. **h,** Survival assay for flies overexpressing hUSP30. Flies were fed paraquat (10 mM); graph shows % live flies at indicated times. $*P < 0.05$ and $***P < 0.001$ by two-way ANOVA and Bonferroni's multiple comparison test. $n = 4-11$ experiments. Error bars represent s.e.m.

Measurement of the magnetic interaction between two bound electrons of two separate ions

Shlomi Kotler^{1†}, Nitzan Akerman¹, Nir Navon^{1†}, Yinnon Glickman¹ & Roei Ozeri¹

Electrons have an intrinsic, indivisible, magnetic dipole aligned with their internal angular momentum (spin). The magnetic interaction between two electronic spins can therefore impose a change in their orientation. Similar dipolar magnetic interactions exist between other spin systems and have been studied experimentally. Examples include the interaction between an electron and its nucleus and the interaction between several multi-electron spin complexes^{1–5}. The challenge in observing such interactions for two electrons is twofold. First, at the atomic scale, where the coupling is relatively large, it is often dominated by the much larger Coulomb exchange counterpart¹. Second, on scales that are substantially larger than the atomic, the magnetic coupling is very weak and can be well below the ambient magnetic noise. Here we report the measurement of the magnetic interaction between the two ground-state spin-1/2 valence electrons of two ⁸⁸Sr⁺ ions, co-trapped in an electric Paul trap. We varied the ion separation, *d*, between 2.18 and 2.76 micrometres and measured the electrons' weak, millihertz-scale, magnetic interaction as a function of distance, in the presence of magnetic noise that was six orders of magnitude larger than the magnetic fields the electrons apply on each other. The cooperative spin dynamics was kept coherent for 15 seconds, during which spin entanglement was generated, as verified by a negative measured value of -0.16 for the swap entanglement witness. The sensitivity necessary for this measurement was provided by restricting the spin evolution to a decoherence-free subspace that is immune to collective magnetic field noise. Our measurements show a $d^{-3.0(4)}$ distance dependence for the coupling, consistent with the inverse-cube law.

Early during the twentieth century, a number of experiments indicated that the electron is more than just an electrically charged point particle. Introducing the electron spin and its accompanying magnetic moment explained a multitude of experimental observations, such as the fine-structure spectrum of hydrogen, anomalous Zeeman splitting and the famous Stern–Gerlach experiment. Since then, the magnetic field of a single electron has been detected⁶ and its magnetic dipole measured with unprecedented accuracy⁷.

Because a single electron is a tiny magnet, every two electrons should influence each other's magnetic dipole orientation, just like magnets do. However, because electrons are indistinguishable particles, this interaction competes with the Coulomb spin-exchange forces which are dominant on the atomic scale. This can be resolved by increasing the inter-electron separation, *d*. Although the magnetic energy becomes dominant, it also decreases as d^{-3} . Therefore, such an approach can be fruitful only when accompanied by an appropriate increase in the magnetic dipole moment or an improvement in the measurement sensitivity. With recent advances in magnetometry on the scale of tens of nanometres, the magnetic interaction of two nitrogen–vacancy spin-1 defects in diamond has been observed to result in their entanglement⁴, and weak interaction strengths, as low as 60 Hz, have been measured⁵. A comparable magnetic interaction strength was observed between atoms in dipolar quantum gases^{2,3}, where the magnetic dipole of each atom ranged from six to ten times that of the electron.

In this work we used two trapped ⁸⁸Sr⁺ ions, each with a single valence electron and no nuclear spin⁸. These bound electrons inherited

the well-isolated environment of their ions along with a high degree of controllability (Methods Summary). Indeed, ions can be tightly confined and laser-cooled to their mechanical ground state⁹, allowing for the long interrogation times necessary for weak signal measurements. Examples include state-of-the-art detection of electric^{10–12} and magnetic^{13–17} fields, and the detection of gravitational time dilation¹⁸. The relative magnetic dipole correction imposed by using bound rather than free electrons is smaller than 0.0018% (ref. 19), which is well below our reported sensitivity.

We now describe the magnetic dipolar interaction and competing noise. As shown in Fig. 1a, we aligned the external magnetic field along the line connecting the two ions. The spin part of the two-ion Hamiltonian can be written as

$$H = \frac{\hbar}{2} (\omega_{A,1} \sigma_{z,1} + \omega_{A,2} \sigma_{z,2}) + 2\hbar \zeta \sigma_{z,1} \sigma_{z,2} - \hbar \zeta (\sigma_{x,1} \sigma_{x,2} + \sigma_{y,1} \sigma_{y,2}) \quad (1)$$

Here \hbar is the Planck constant divided by 2π ; $\sigma_{j,i}$ is the $j \in \{x, y, z\}$ Pauli spin operator of the *i*th spin; $\omega_{A,i} = g \mu_B B_i / 2\hbar$ is the spin Larmor frequency, where B_i , μ_B and g are the external magnetic field, Bohr magneton and the electron spin gyromagnetic ratio, respectively. The spin–spin interaction strength is $\zeta = \mu_0 (g \mu_B / 2)^2 / 4\pi \hbar d^3$, with μ_0 the vacuum permeability constant. The first term on the right-hand side of equation (1) describes the Zeeman shift of the spins' energy due to the magnetic field. The second and third terms are due to spin–spin interactions. The second term creates a shift in the resonance frequency of one spin that is conditioned on the state of the other, and was recently measured for the case of two nitrogen–vacancy spin-1 defects^{4,5}. The third term results in a collective spin flip in which a spin excitation is exchanged. Owing to conservation of energy, for this term to be on-resonance and effective, the two spins have to be exactly degenerate, that is, B has to be exactly uniform. It is the third term which was at the focus of our experiment.

Ultimately, the ability to measure a weak magnetic spin–spin interaction is limited by collective external magnetic field fluctuations, described by the first term in equation (1). Typical laboratory magnetic field noise amplitudes are of the order of 0.1 μ T, which is equivalent to fluctuations of a few kilohertz in $\omega_{A,i}$ ($i = 1, 2$). These are, however, six orders of magnitude greater than the spin–spin interaction strength.

A state-space solution can remedy the effect of these large magnetic fluctuations. It requires identifying a set of quantum states which are, on the one hand, sensitive to the desired signal, and, on the other hand, invariant under a certain class of noise processes. Previously this approach was used to measure magnetic field gradients^{13,14,16} as well as narrow laser linewidths and the electric quadrupole shift of atomic transitions¹⁰. Here we tailored the states to the magnetic dipolar interaction. The four eigenstates of the Hamiltonian in equation (1) are $|\uparrow\uparrow\rangle$, $|\downarrow\downarrow\rangle$ and the two entangled Bell states $|\Psi_{\pm}\rangle = (|\uparrow\downarrow\rangle \pm |\downarrow\uparrow\rangle) / \sqrt{2}$. The first two eigenstates are twice as susceptible to magnetic field fluctuations than are the single-spin states, whereas the energy splitting between the latter two is $4\hbar\zeta$ and does not depend on B at all (see Fig. 1b for an energy level diagram). By restricting the spin–spin evolution to the decoherence-free subspace

[†]Department of Physics of Complex Systems, Weizmann Institute of Science, Rehovot 76100, Israel. [†]Present addresses: Physical Measurement Laboratory, National Institute of Standards and Technology, Boulder, Colorado 80305, USA (S.K.); Cavendish Laboratory, University of Cambridge, J. J. Thomson Avenue, Cambridge CB30HE, UK (N.N.).

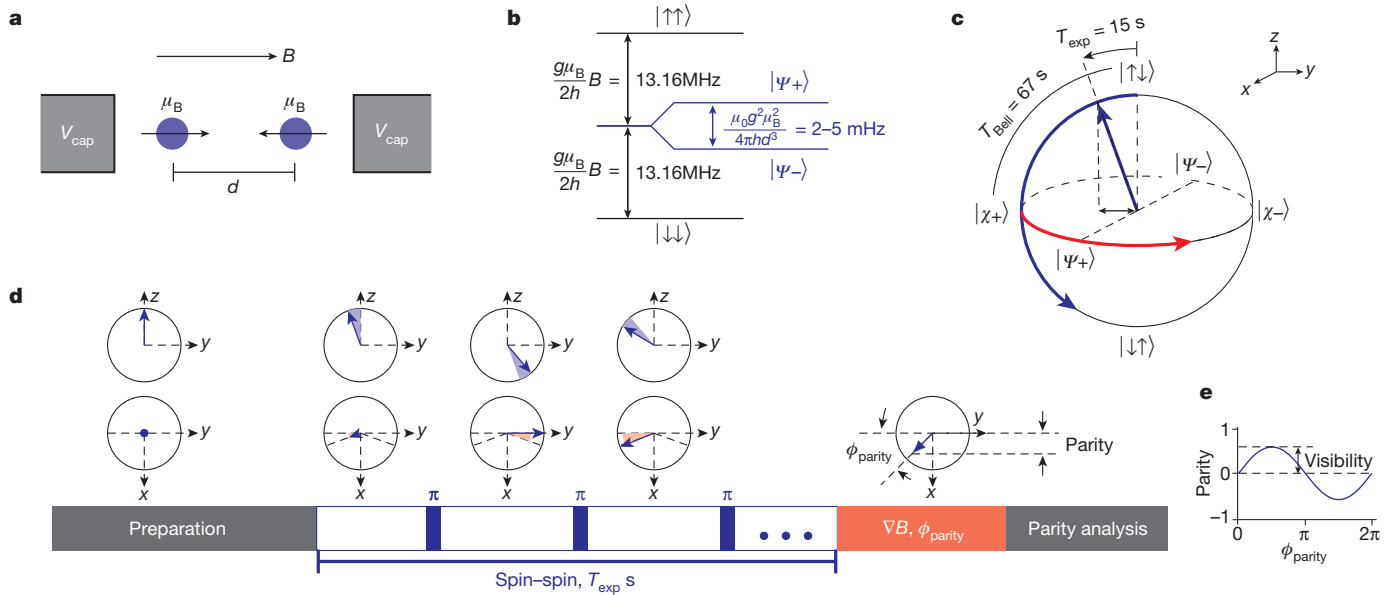


Figure 1 | Experiment overview. **a**, Set-up schematics. Two $^{88}\text{Sr}^+$ ions are trapped in a linear radio-frequency Paul trap (only d.c. electrodes at potential V_{cap} are shown). **b**, Two spins' energy diagram with magnetic interaction eigenvectors $|\Psi_{\pm}\rangle = (|\uparrow\downarrow\rangle \pm |\downarrow\uparrow\rangle)/\sqrt{2}$. **c**, Geometric Bloch representation of the DFS. $|\chi_{\pm}\rangle = (|\uparrow\downarrow\rangle \pm i|\downarrow\uparrow\rangle)/\sqrt{2}$. Spin-spin interaction induces x rotation (blue arc). Magnetic field gradients generate z rotations (red arc). For $d = 2.4 \mu\text{m}$, spin-spin coupling rotates $|\uparrow\downarrow\rangle$ to the fully entangled state $|\chi_{+}\rangle$ after an interaction time $T_{\text{Bell}} = 67 \text{ s}$. Our actual experiment duration was $T_{\text{exp}} = 15 \text{ s}$, corresponding to a 21.6° rotation. This angle is estimated by the parity visibility (black double arrow projection of the Bloch vector on the

equatorial plane). A collective spin flip corresponds to 180° rotation about x . **d**, Experimental sequence. Infinitesimal spin evolution is depicted by the shaded sectors of the z - y and x - y projections of the Bloch sphere. After initialization to $|\uparrow\uparrow\rangle$, spin-spin evolution is interrupted by equidistant collective spin flips, restricting the effect of magnetic field gradients (bottom middle three spheres). The Bloch vector continuously accumulates an angle with respect to z (upper middle three spheres). Finally, a controlled magnetic gradient rotates the Bloch vector about the z axis by ϕ_{parity} radians. The projection of the final Bloch vector on the x axis corresponds to the parity observable. **e**, Parity analysis fringe example (numerical).

(DFS) spanned by $|\Psi_{\pm}\rangle$, it is possible to observe spin-spin interactions without susceptibility to spatially homogeneous magnetic noise.

Spin-spin interaction within the DFS takes a simple form which can be understood in terms of the geometric Bloch sphere representation shown in Fig. 1c. In this subspace, equation (1) takes the form $H_{\text{int}} = 2\hbar\zeta(|\uparrow\downarrow\rangle\langle\downarrow\uparrow| + |\downarrow\uparrow\rangle\langle\uparrow\downarrow|)$. The $|\Psi_{\pm}\rangle$ states are invariant under the interaction (Fig. 1b). All other states undergo rotation (Fig. 1c, solid blue arc) around the direction defined by $|\Psi_{\pm}\rangle$, hereafter referred to as the x direction (Fig. 1c). Starting from the north pole ($|\uparrow\uparrow\rangle$), the system rotates through the fully entangled state $|\chi_{+}\rangle = (|\uparrow\downarrow\rangle + i|\downarrow\uparrow\rangle)/\sqrt{2}$ and towards the south pole ($|\downarrow\downarrow\rangle$).

Even in the DFS, spatial inhomogeneity in the external magnetic field can obscure the spin-spin signal. By observing the energy separation between $|\uparrow\downarrow\rangle$ and $|\downarrow\uparrow\rangle$ and compensating for inhomogeneities with external coils, we were able to reduce the gradients to as low as $\nabla B = 3.57 \times 10^{-7} \text{ T m}^{-1}$ (Supplementary Information). This, however, was still strong enough to lift the degeneracy between $|\uparrow\downarrow\rangle$ and $|\downarrow\uparrow\rangle$ by $\Delta\omega_A = (g\mu_B/2\hbar)(\nabla B)d = 2\pi \times 20 \text{ mHz}$, thus detuning the weak, millihertz, spin-spin coupling from resonance and resulting in the Hamiltonian $H = H_{\text{int}} + (\hbar/2)\Delta\omega_A(|\uparrow\downarrow\rangle\langle\downarrow\uparrow| - |\downarrow\uparrow\rangle\langle\uparrow\downarrow|)$. In geometric terms, starting at the Bloch sphere north pole, the system state is rapidly rotated by the field gradient about the z axis (Fig. 1c, red arc). This counteracts the slower revolution around x imposed by the spin-spin interaction, restricting its effect to a narrow region of solid angle $\sim \pi/400 \text{ sr}$ near the north pole.

Using a train of spin echos, we were able to further reduce these excessive magnetic field inhomogeneities by two orders of magnitude, to a negligible level. During their magnetic spin-spin evolution, the two dipoles were flipped at a rate of $f_0 = 2 \text{ Hz}$. In geometric terms, this corresponds to a train of 180° rotations about the x axis (Fig. 1c). These collective rotations do not change the relative orientation of the spins, leaving the spin-spin interaction invariant (Fig. 1d, upper middle three spheres). The effect of the gradient, however, is averaged to zero because exchanging $|\uparrow\downarrow\rangle$ and $|\downarrow\uparrow\rangle$ is equivalent to constantly switching the sign

of the magnetic field gradient (Fig. 1d, lower middle three spheres). This scheme is an adaptation of the quantum lock-in method¹⁵.

We used parity analysis²⁰ to obtain a physical observable that is first-order sensitive to the interaction strength and the experiment time. The parity observable measures the coherence between $|\uparrow\downarrow\rangle$ and $|\downarrow\uparrow\rangle$. To estimate it, we applied the following experimental sequence (Fig. 1d). The system state was initialized to $|\uparrow\uparrow\rangle$ and then evolved under spin-spin interaction to $|\psi(T)\rangle = \cos(2\zeta T)|\uparrow\uparrow\rangle + i\sin(2\zeta T)|\downarrow\downarrow\rangle$. We then applied a controlled magnetic field gradient, adding a superposition phase ϕ_{parity} to yield $|\psi(T)\rangle = \cos(2\zeta T)|\uparrow\uparrow\rangle + ie^{i\phi_{\text{parity}}}\sin(2\zeta T)|\downarrow\downarrow\rangle$. The expectation value of parity was then estimated as $\langle\text{parity}\rangle = P_{\uparrow\uparrow} + P_{\downarrow\downarrow} - P_1$, where $P_{\uparrow\uparrow}$, $P_{\downarrow\downarrow}$ and $P_1 \equiv P_{\uparrow\downarrow} + P_{\downarrow\uparrow}$ are the probabilities of finding the system in the respective states, measured projectively after performing a collective $\pi/2$ spin rotation (Supplementary Information). In this case, $\langle\text{parity}\rangle = \sin(4\zeta T)\sin(\phi_{\text{parity}})$. The parity visibility, $\sin(4\zeta T)$, is extracted either by scanning ϕ_{parity} (Fig. 1e) or by setting it to $\pi/2$. Geometrically, parity corresponds to the projection of the Bloch vector on the x axis (Fig. 1d, rightmost sphere) and its visibility corresponds to the projection of the Bloch vector on the equatorial plane (Fig. 1c, black double arrow).

Measuring a weak, millihertz-scale, interaction requires an experiment duration of many seconds. Detection fidelity, however, deteriorates at these long times owing to ion motion heating, eventually limiting the experiment duration. As a result, the measured parity visibility reduces by a factor of $\alpha = 1 - 4D(1 - D)$, where D is the average of the $|\uparrow\uparrow\rangle$ and $|\downarrow\downarrow\rangle$ detection fidelities. Figure 2a shows the detection fidelities as a function of time for $|\uparrow\uparrow\rangle$ and $|\downarrow\downarrow\rangle$ at an inter-ion distance of $d = 2.4 \mu\text{m}$. Although our measurement scheme was tailored to be first-order insensitive to heating, its residual effect degraded the detection fidelity from more than 0.95 at $T = 5 \text{ s}$ to as low as 0.88 at $T = 25 \text{ s}$. These measurements are consistent with our measured heating rates, of ~ 10 quanta per second. Asymmetry in the detection scheme accounts for the fidelity of the $|\uparrow\uparrow\rangle$ measurement being better than that of the $|\downarrow\downarrow\rangle$ measurement. Similar detection fidelities are displayed in Fig. 2b as functions of ion separation, for a fixed $T = 15 \text{ s}$ experiment time. As seen, detection

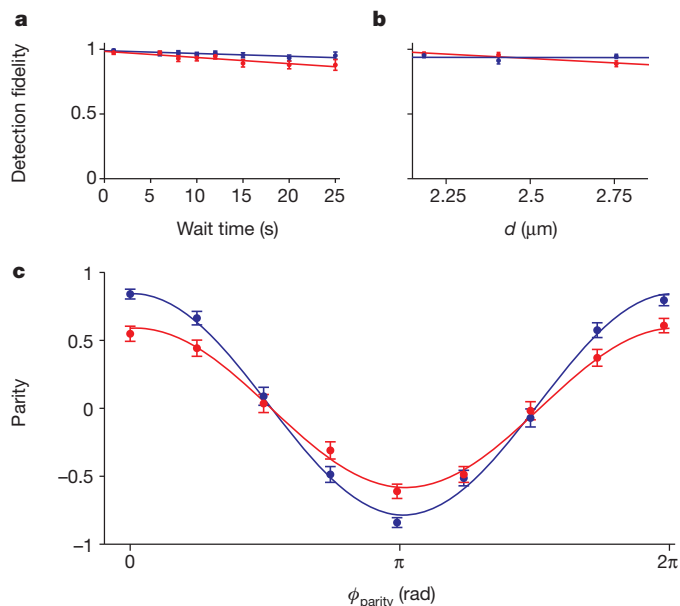


Figure 2 | Characterization of quantum decoherence. **a**, Detection fidelity versus experiment time for $d = 2.4 \mu\text{m}$. The probabilities of measuring $|\uparrow\uparrow\rangle$ and $|\downarrow\downarrow\rangle$ given that the system was initialized to $|\uparrow\uparrow\rangle$ and, respectively, $|\downarrow\downarrow\rangle$ are shown by the red and blue dots. Each point is the average of $N = 119$ projective measurements. Solid lines are linear best fits. During the experiment, collective spin flips are applied at a period of 0.5 s as in the actual spin–spin experiment. Detection fidelities degrade owing to ion motion heating. **b**, Detection fidelity versus d for $T = 15$ s (similar to **a**). The points at $d = 2.18, 2.41, 2.76 \mu\text{m}$ are the averages of $N = 147, 119, 201$ projective measurements, respectively. **c**, Dephasing time estimate. The system is initialized to $|\Psi_+\rangle = (|\uparrow\uparrow\rangle + |\downarrow\downarrow\rangle)/\sqrt{2}$ and then a train of spin flips is applied as in **a** and **b**. Parity analysis is performed after respective wait times of $T = 1$ s and 15 s, shown by the blue and red dots. Each point is the average of $N = 226$ projective measurements. The blue and red lines are best fits to a cosine fringe, yielding respective amplitudes of $0.81(5)$ and $0.59(4)$ and a conservative estimate for the dephasing time of 44 ± 12 s. When factoring out detection efficiency, we observe no statistically significant dephasing. All error bars indicate projection noise.

fidelity increases at lower inter-ion distances, corresponding to higher trap frequencies, where the effect of heating is known to be less pronounced¹¹. A further, minor reduction in α by a factor of >0.98 is due to imperfect initialization. See Supplementary Information for a complete discussion of heating, detection and initialization as well as their effect on α .

We limited our experiment duration to $T = 15$ s, beyond which the decrease in α compromises the increase in signal. Moreover, at the high trap voltages used, longer experiments resulted in a substantial ion loss from the trap owing to ion–crystal instabilities, thereby severely limiting the long averaging required to obtain statistical significance. The optimal 15-s duration chosen was still long enough for dephasing to potentially limit the observation of spin–spin interaction. Here dephasing within the DFS, for example due to residual noise in the magnetic field gradient, averages away the superposition relative phase between $|\uparrow\downarrow\rangle$ and $|\downarrow\uparrow\rangle$. It results in a decreasing parity visibility as a function of time. To characterize this phase coherence, the system was initialized to $|\Psi_+\rangle = (|\uparrow\downarrow\rangle + |\downarrow\uparrow\rangle)/\sqrt{2}$ using a Mølmer–Sørensen entangling gate²¹. This was followed by a wait of duration T while performing spin flips as in the actual spin–spin experiment, and ended with parity analysis. The state $|\Psi_+\rangle$ was chosen because it is invariant under spin–spin coupling, while being sensitive to dephasing. Figure 2c displays the results for $T = 1$ s and $T = 15$ s using blue and red circles, respectively. A best fit to a cosine yields parity amplitudes of $0.81(5)$ ($T = 1$ s) and $0.59(4)$ ($T = 15$ s). A conservative estimate for coherence time, not taking detection fidelity into account, yields 44 ± 12 s. Taking into account the degradation in detection, we cannot observe any statistically significant dephasing after 15 s.

We now turn to describing the main results of this letter. Figure 3 presents the parity measurements for two electronic spins undergoing magnetic dipolar interaction, at an inter-ion distance of $d = 2.4 \mu\text{m}$. A parity oscillation of $\langle\text{parity}\rangle = \pm \alpha \sin(4\xi T) \sin(\phi_{\text{parity}})$ is expected, and will be positive when the initial state is $|\uparrow\downarrow\rangle$ and negative for the initial state $|\downarrow\uparrow\rangle$. Figure 3a shows parity versus ϕ_{parity} for $T = 0.1$ s, which is much shorter than the spin–spin coupling timescale. As expected, no significant parity oscillation amplitude is detected. The $T = 15$ s long-experiment results are shown in Fig. 3b. Here the parity sinusoidal dependence becomes evident. The solid blue and red lines are calculated from theory without any adjustable parameters, showing good agreement with the measured data. Shaded areas represent measurement uncertainties in determining α . The theoretical interaction strength at the $d = 2.4 \mu\text{m}$ distance is $\xi = 2\pi \times 0.93$ mHz, in agreement with a single-parameter best fit of the data to the above theory yielding $\xi = 2\pi \times 0.9(1)$ mHz. With the parity analysis sinusoidal dependence on ϕ_{parity} established, the parity visibility can be measured by fixing $\phi_{\text{parity}} = \pi/2$, acquiring a single point rather than a complete sinusoidal fringe. In Fig. 3c we display visibility versus interaction time (blue circles), which is in agreement with the theoretical curve, visibility $= \alpha \sin(4\xi T)$ (blue line).

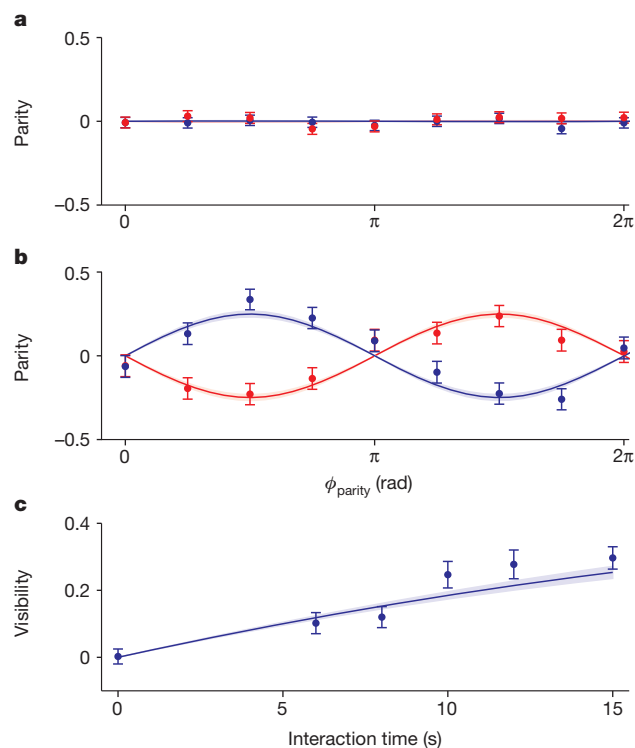


Figure 3 | Coherent oscillations due to magnetic spin–spin interaction for $d = 2.4 \mu\text{m}$. **a**, Parity analysis of a 0.1-s spin–spin experiment. Blue and red dots show parity measurements for the initial states $|\uparrow\downarrow\rangle$ and $|\downarrow\uparrow\rangle$, respectively. Each point is the average of $N = 945$ projective measurements. Solid lines are the spin–spin theory with no adjustable parameters, taking into account the preparation and detection fidelities, characterized in Fig. 2a. **b**, Same as Fig. 3a, for $T = 15$ s. Each point is the average of $N = 236$ projective measurements. Shaded areas are 1-s.d. intervals for the solid line theories, due to the uncertainties in characterizing the preparation and detection fidelities. A best fit to $\alpha \sin(4\xi T) \sin(\phi_{\text{parity}})$ (not shown) yields an estimated coupling constant of $\xi = 2\pi \times 0.9(1)$ mHz, in reasonable agreement with theory ($\xi = 2\pi \times 0.93$ mHz). Here $\alpha = 0.75$ is the visibility degradation factor, extracted from the data shown in Fig. 2a, as explained in the text. **c**, Parity amplitude (visibility) versus spin–spin interaction time, T . The parity observable is measured at $\phi_{\text{parity}} = \pi/2$. The points at $T = 0, 6, 8, 10, 12, 15$ s are the averages of $N = 2,001, 1,000, 1,000, 600, 501, 819$ projective measurements, respectively. Solid line and shaded area are the same as in **a** and **b**. A best fit to $\alpha \sin(4\xi T)$ (not shown) yields $\xi = 2\pi \times 1.1(2)$ mHz. All error bars indicate projection noise.

Although only partial entanglement is generated by spin–spin interaction after 15 s, it can still be observed by measuring a negative expectation value for a properly chosen entanglement witness²². Here we chose the swap operator, defined as $\text{swap} |a, b\rangle = |b, a\rangle$ for any two single spin states $|a\rangle$ and $|b\rangle$. In terms of the two spins' density matrix, $\langle \text{swap} \rangle = P_{\uparrow\uparrow} + P_{\downarrow\downarrow} - \text{visibility}$. Therefore, entanglement is proven by experimentally verifying that²⁰ $P_{\uparrow\uparrow} + P_{\downarrow\downarrow} < \text{visibility}$. We repeat the spin–spin experiment $N = 2,388$ times, for $d = 2.4 \mu\text{m}$, measuring visibility = 0.28(2) and $P_{\uparrow\uparrow} + P_{\downarrow\downarrow} = 0.11(1)$. These conservative estimates, not taking the deterioration in detection fidelity into account, rendered the entanglement witness negative with good statistical significance: $\langle \text{swap} \rangle = -0.16(2)$. Here we assume a projection-noise-limited error in measured probabilities, supported by an Allen deviation analysis. Taking detection fidelity into account, using the calibration shown in Fig. 2a, our maximum-likelihood estimate renders $\langle \text{swap} \rangle = -0.41(4)$. See Supplementary Information for details of the maximum-likelihood estimation and the Allen deviation analysis.

Finally, the spin–spin interaction dependence on inter-electron distance is revealed by repeating the above measurement at different ion separations, d . Figure 4a shows the measured parity visibility (blue circles) versus d , in good agreement with theory (blue line): visibility = $\alpha \sin(4\zeta T)$. Here α is extracted from the data shown in Fig. 2b, and decreases from $\alpha = 0.84$ at $d = 2.18 \mu\text{m}$ to $\alpha = 0.70$ at $d = 2.76 \mu\text{m}$ owing to the larger motion heating rates at lower trap frequencies. The 64% decrease in the visibility is thus a combined effect of the 17% decrease in α and the additional decrease in the spin–spin coupling constant, ζ .

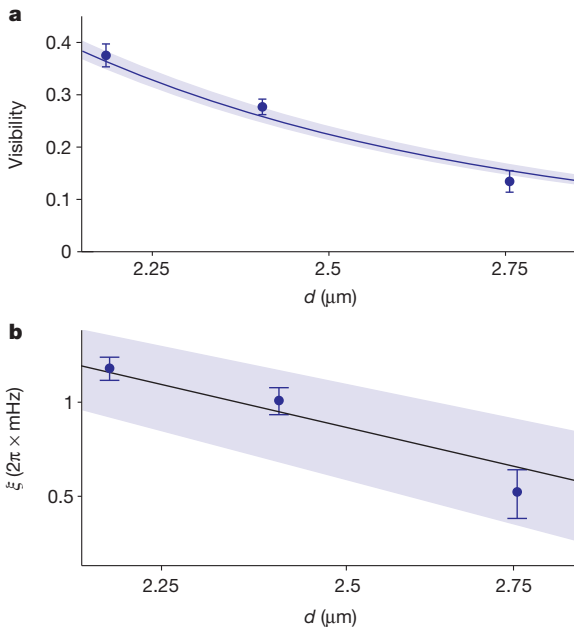


Figure 4 | Magnetic spin–spin interaction as a function of distance. **a**, Parity visibility versus ion separation, d , is shown by the blue dots for a fixed experiment time, $T = 15$ s. The points at $d = 2.18, 2.41, 2.76 \mu\text{m}$ are the averages of $N = 2,306, 4,204, 1,796$ projective measurements, respectively. Error bars indicate projection noise. Solid line is spin–spin theory without adjustable parameters, taking preparation and detection fidelities into account, as characterized in Fig. 2b. Shaded blue area is a 1-s.d. interval for the solid line theory, due to the uncertainties in characterizing the preparation and detection fidelities. **b**, Spin–spin coupling strength ζ versus ion separation (log–log scale). Blue dots are extracted from **a**, using visibility = $\alpha \sin(4\zeta T)$. The visibility degradation factor, α , is extracted from the data in Fig. 2b. Error bars are 1-s.d. estimates due to projection noise in both the measurements and in the extraction of α . The error bar for the $d = 2.75 \mu\text{m}$ point is slightly larger owing to the corresponding decrease in α . Solid black line is spin–spin theory without any adjustable parameters. A linear best fit to $\zeta = \mu_0(g\mu_B/2)^2/4\pi\hbar d^{-n}$ (not shown) yields $n = 3.0(4)$, consistent with the $n = 3$ theoretical exponent. Shaded blue area indicates the $n = 3.0 \pm 0.4$ curves.

We can therefore estimate ζ , using the measured parity visibility, and the independently measured α , as shown in Fig. 4b (blue circles). A best fit to $\zeta = \mu_0(g\mu_B/2)^2/4\pi\hbar d^n$ yields $n = 3.0(4)$, in agreement with the cubic dependence of magnetic spin–spin interactions. Our apparatus allowed for a relatively small variation in d . Shorter distances required operating the trap at voltages higher than 400 V, where trap instabilities limited our integration efforts. Larger inter-ion separations resulted in a diminishing signal-to-noise ratio. Therefore, improving our measurement uncertainty requires a redesign of the ion trap, targeted at high-voltage operation.

Because the measured interaction is very weak, it requires ruling out competing spurious effects. Specifically, the ions' motion in the trap due to heating translates to a magnetic field in the ions' rest frame. Although this cannot lead to spin entanglement, it could contribute to the parity signal. However, because such a field would oscillate at trap frequencies which are all below 5 MHz, it would couple non-resonantly to the spins whose resonant frequency is ~ 13.16 MHz. In Supplementary Information we quantitatively rule out this effect, as well as other possible competing phenomena. These include inter-ion distance fluctuations, quantization axis misalignment, radio-frequency electrode leakage and trap-electrode-generated magnetic field gradients.

We have used a combination of techniques, originally developed for the protection of quantum information, to measure the weak spin–spin magnetic interaction. Future improvements of this experiment may suggest a new platform for the exploration of anomalous spin forces²³ on the micrometre scale. The use of DFSS, which was central to our approach, is not restricted to the specifics of the reported experiment and they could be used in other metrological scenarios^{10,16}. Quantum information processing continues to drive metrology with recent proposals^{24–27} that harness quantum error correction for sensitive measurements.

METHODS SUMMARY

Our apparatus enabled us to place the electronic spins at a controlled distance from one another, as well as to initialize, manipulate and detect their internal spin state with high fidelity. Details of the set-up are found in ref. 8 as well as in the Supplementary Information. Briefly, a Coulomb crystal of two ions was formed in an electrical Paul trap⁹ with Doppler cooling. We used external voltages to push the ions against their Coulomb repulsion (Fig. 1a), thus controlling the inter-ion separation, d . The minimal distance attained was limited by our ability to maintain stable ion crystals without incurring a trap voltage breakdown. The inter-ion distance is the difference between the equilibrium positions of two charged particles trapped in a harmonic trap, $d = (2k_e e^2 / M(2\pi f_{\text{trap}})^2)^{1/3}$, where k_e is Coulomb's constant, e is the electron charge and M is the mass of $^{88}\text{Sr}^+$. The oscillation frequency, f_{trap} , was measured spectroscopically. For $^{88}\text{Sr}^+$, the valence electron spin states are $|\uparrow\rangle = |5s_{1/2}, J = 1/2, M_J = 1/2\rangle$ and $|\downarrow\rangle = |5s_{1/2}, J = 1/2, M_J = -1/2\rangle$. State initialization to $|\uparrow\uparrow\rangle$ was done by optical pumping. We were able to perform all possible collective spin rotations by pulsing a resonant radio-frequency magnetic field and tuning the pulse duration and the radio-frequency field phase. State detection was performed by state-selective fluorescence, distinguishing $|\uparrow\uparrow\rangle$ and $|\downarrow\downarrow\rangle$ from one another and from both $|\uparrow\downarrow\rangle$ and $|\downarrow\uparrow\rangle$, which were indistinguishable²⁸. All these collective operations had typical fidelities of more than 98%. We used inhomogeneities in the ion trap potential to perform differential spin rotations^{29,30}, and were able to generate, for example, $|\uparrow\downarrow\rangle$ with a typical fidelity of more than 98%. Finally, we were able to generate the entangled states $|\Psi_{\pm}\rangle = (|\uparrow\downarrow\rangle \pm |\downarrow\uparrow\rangle)/\sqrt{2}$ using a Molmer–Sørensen entangling gate with a typical fidelity of 95% (ref. 21).

Received 16 December 2013; accepted 15 April 2014.

- Budker, D., Kimball, D. F. & DeMille, D. P. (eds) *Atomic Physics: An Exploration through Problems and Solutions* 1–50 (Oxford Univ. Press, 2004).
- Stuhler, J. *et al.* Observation of dipole-dipole interaction in a degenerate quantum gas. *Phys. Rev. Lett.* **95**, 150406 (2005).
- Lu, M., Burdick, N. Q., Youn, S. H. & Lev, B. L. Strongly dipolar Bose-Einstein condensate of dysprosium. *Phys. Rev. Lett.* **107**, 190401 (2011).
- Dolde, F. *et al.* Room-temperature entanglement between single defect spins in diamond. *Nature Phys.* **9**, 139–143 (2013).
- Grinolds, M. S. *et al.* Nanoscale magnetic imaging of a single electron spin under ambient conditions. *Nature Phys.* **9**, 215–219 (2013).
- Rugar, D., Budakian, R., Mamin, H. & Chui, B. Single spin detection by magnetic resonance force microscopy. *Nature* **430**, 329–332 (2004).
- Hanneke, D., Fogwell, S. & Gabrielse, G. New measurement of the electron magnetic moment and the fine structure constant. *Phys. Rev. Lett.* **100**, 120801 (2008).

8. Akerman, N., Glickman, Y., Kotler, S., Keselman, A. & Ozeri, R. Quantum control of $^{88}\text{Sr}^+$ in a miniature linear Paul trap. *Appl. Phys. B* **107**, 1167–1174 (2012).
9. Wineland, D. *et al.* Experimental issues in coherent quantum-state manipulation of trapped atomic ions. *J. Res. Natl. Inst. Stand. Technol.* **103**, 259–328 (1998).
10. Roos, C. F., Chwalla, M., Kim, K., Riebe, M. & Blatt, R. 'Designer atoms' for quantum metrology. *Nature* **443**, 316–319 (2006).
11. Turchette, Q. A. *et al.* Heating of trapped ions from the quantum ground state. *Phys. Rev. A* **61**, 063418 (2000).
12. Biercuk, M. J., Uys, H., Britton, J. W., VanDevender, A. P. & Bollinger, J. J. Ultrasensitive detection of force and displacement using trapped ions. *Nature Nanotechnol.* **5**, 646–650 (2010).
13. Roos, C. F. *et al.* Bell states of atoms with ultralong lifetimes and their tomographic state analysis. *Phys. Rev. Lett.* **92**, 220402 (2004).
14. Langer, C. *et al.* Long-lived qubit memory using atomic ions. *Phys. Rev. Lett.* **95**, 060502 (2005).
15. Kotler, S., Akerman, N., Glickman, Y., Keselman, A. & Ozeri, R. Single-ion quantum lock-in amplifier. *Nature* **473**, 61–65 (2011).
16. Schmidt-Kaler, F. & Gerritsma, R. Entangled states of trapped ions allow measuring the magnetic field gradient produced by a single atomic spin. *Europhys. Lett.* **99**, 53001 (2012).
17. Kotler, S., Akerman, N., Glickman, Y. & Ozeri, R. Nonlinear single-spin spectrum analyzer. *Phys. Rev. Lett.* **110**, 110503 (2013).
18. Chou, C. W., Hume, D. B., Rosenband, T. & Wineland, D. J. Optical clocks and relativity. *Science* **329**, 1630–1633 (2010).
19. Breit, G. The magnetic moment of the electron. *Nature* **122**, 649 (1928).
20. Sackett, C. A. *et al.* Experimental entanglement of four particles. *Nature* **404**, 256–259 (2000).
21. Navon, N. *et al.* Quantum process tomography of a Mølmer-Sørensen interaction. Preprint at <http://arxiv.org/abs/1309.4502> (2013).
22. Horodecki, M., Horodecki, P. & Horodecki, R. Separability of mixed states: necessary and sufficient conditions. *Phys. Lett. A* **223**, 1–8 (1996).
23. Moody, J. E. & Wilczek, F. New macroscopic forces? *Phys. Rev. D* **30**, 130–138 (1984).
24. Ozeri, R. Heisenberg limited metrology using quantum error-correction codes. Preprint at <http://arxiv.org/abs/1310.3432> (2013).
25. Arrad, G., Vinkler, Y., Aharonov, D. & Retzker, A. Increasing sensing resolution with error correction. *Phys. Rev. Lett.* **112**, 150801 (2014).
26. Kessler, E. M. *et al.* Quantum error correction for metrology. *Phys. Rev. Lett.* **112**, 150802 (2014).
27. Dür, W., Skotiniotis, M., Fröwis, F. & Kraus, B. Improved quantum metrology using quantum error correction. *Phys. Rev. Lett.* **112**, 080801 (2014).
28. Keselman, A., Glickman, Y., Akerman, N., Kotler, S. & Ozeri, R. High-fidelity state detection and tomography of a single-ion Zeeman qubit. *New J. Phys.* **13**, 073027 (2011).
29. Warring, U. *et al.* Individual-ion addressing with microwave field gradients. *Phys. Rev. Lett.* **110**, 173002 (2013).
30. Navon, N. *et al.* Addressing two-level systems variably coupled to an oscillating field. *Phys. Rev. Lett.* **111**, 073001 (2013).

Supplementary Information is available in the online version of the paper.

Acknowledgements We thank J. Avron for discussions on the entanglement witness. We acknowledge support by the Israeli Science Foundation, the Crown Photonics Center, the German-Israeli Science Foundation and M. Kushner Schnur, Mexico.

Author Contributions S.K. designed the scheme for measuring spin–spin coupling. S.K. and N.A. performed the measurements. S.K. analysed the results. S.K., N.A., N.N. and Y.G. developed the techniques necessary to experimentally implement the measurement scheme. S.K. and R.O. wrote the paper. R.O. supervised the work. All authors discussed the results and contributed to the manuscript.

Author Information Reprints and permissions information is available at www.nature.com/reprints. The authors declare no competing financial interests. Readers are welcome to comment on the online version of the paper. Correspondence and requests for materials should be addressed to S.K. (shlomi.kotler@weizmann.ac.il).

Ultrafast X-ray probing of water structure below the homogeneous ice nucleation temperature

J. A. Sellberg^{1,2}, C. Huang³, T. A. McQueen^{1,4}, N. D. Loh⁵, H. Laksmono⁵, D. Schlesinger², R. G. Sierra⁵, D. Nordlund³, C. Y. Hampton⁵, D. Starodub⁵, D. P. DePonte^{6,7}, M. Beye^{1,8}, C. Chen^{1,4}, A. V. Martin⁶, A. Barty⁶, K. T. Wikfeldt², T. M. Weiss³, C. Caronna⁷, J. Feldkamp⁷, L. B. Skinner⁹, M. M. Seibert⁷, M. Messerschmidt⁷, G. J. Williams⁷, S. Boutet⁷, L. G. M. Pettersson², M. J. Bogan⁵ & A. Nilsson^{1,2,3}

Water has a number of anomalous physical properties, and some of these become drastically enhanced on supercooling below the freezing point. Particular interest has focused on thermodynamic response functions that can be described using a normal component and an anomalous component that seems to diverge at about 228 kelvin (refs 1–3). This has prompted debate about conflicting theories^{4–12} that aim to explain many of the anomalous thermodynamic properties of water. One popular theory attributes the divergence to a phase transition between two forms of liquid water occurring in the ‘no man’s land’ that lies below the homogeneous ice nucleation temperature (T_H) at approximately 232 kelvin¹³ and above about 160 kelvin¹⁴, and where rapid ice crystallization has prevented any measurements of the bulk liquid phase. In fact, the reliable determination of the structure of liquid water typically requires temperatures above about 250 kelvin^{2,15}. Water crystallization has been inhibited by using nanoconfinement¹⁶, nanodroplets¹⁷ and association with biomolecules¹⁶ to give liquid samples at temperatures below T_H , but such measurements rely on nanoscopic volumes of water where the interaction with the confining surfaces makes the relevance to bulk water unclear¹⁸. Here we demonstrate that femtosecond X-ray laser pulses can be used to probe the structure of liquid water in micrometre-sized droplets that have been evaporatively cooled^{19–21} below T_H . We find experimental evidence for the existence of metastable bulk liquid water down to temperatures of 227 ± 2 kelvin in the previously largely unexplored no man’s land. We observe a continuous and accelerating increase in structural ordering on supercooling to approximately 229 kelvin, where the number of droplets containing ice crystals increases rapidly. But a few droplets remain liquid for about a millisecond even at this temperature. The hope now is that these observations and our detailed structural data will help identify those theories that best describe and explain the behaviour of water.

Figure 1a sketches our experimental set-up: in vacuum, a liquid jet¹⁹ generates spatially unconfined droplets of supercooled liquid water, the structure of which is then studied using intense, 50-fs, hard-X-ray laser pulses from the Linac Coherent Light Source (LCLS). A Rayleigh jet²⁰ produces a continuous, single-file train of water droplets with a uniform diameter of 34 or 37 μm , and a gas dynamic virtual nozzle²¹ gives trains of smaller droplets with a diameter of 9 or 12 μm . The droplets cool rapidly through evaporation and reach an average temperature that depends primarily on droplet size and travel time through the vacuum (Supplementary Information, section B.3), which we varied systematically by adjusting the distance between the dispenser nozzle and the X-ray pulse interaction region. Scattering patterns (at least 1,800 per data point; Supplementary Information, section A.1.3) were recorded from individual droplets with a single X-ray pulse over the temperature

ranges of 227–252 K and 233–258 K for the droplets generated by gas dynamic virtual nozzle and Rayleigh jet, respectively. Temperature calibrations were performed using the Knudsen theory of evaporative cooling with a typical absolute uncertainty of ± 2 K at the lowest temperatures (Supplementary Information, section B.3.5; Supplementary Tables 5 and 6; and Supplementary Fig. 20); the Knudsen theory was verified through extensive molecular dynamics simulations of droplet cooling (Supplementary Information, section B.2).

Figure 1b shows a typical diffraction pattern of a liquid water droplet with a maximum momentum transfer of $q \approx 3.5 \text{ \AA}^{-1}$ at the corners of the detector. The isotropic water diffraction rings uniquely identify the

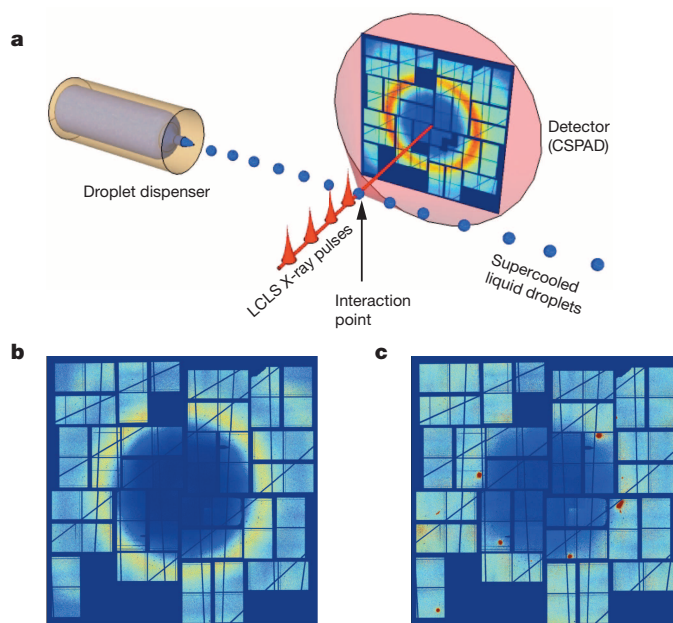


Figure 1 | Coherent X-ray scattering from individual micrometre-sized droplets with a single-shot selection scheme. **a**, A train of droplets (Supplementary Information, section A.1.1) flows in vacuum perpendicular to ~ 50 -fs-long X-ray pulses. A coherent scattering pattern from a water droplet was recorded when a single droplet was positioned in the interaction region at the time of arrival of a single X-ray pulse. CSPAD stands for, Cornell-SLAC pixel array detector. **b**, **c**, Each diffraction pattern is classified (Supplementary Information, section A.1.3) either as a water shot exclusively containing pure liquid scattering characterized by a diffuse water ring (**b**), or as an ice shot characterized by intense and discrete Bragg peaks superposed on the water scattering ring (**c**).

¹SUNCAT Center for Interface Science and Catalysis, SLAC National Accelerator Laboratory, 2575 Sand Hill Road, Menlo Park, California 94025, USA. ²Department of Physics, AlbaNova University Center, Stockholm University, S-106 91 Stockholm, Sweden. ³Stanford Synchrotron Radiation Lightsource, SLAC National Accelerator Laboratory, PO Box 20450, Stanford, California 94309, USA. ⁴Department of Chemistry, Stanford University, Stanford, California 94305, USA. ⁵PULSE Institute, SLAC National Accelerator Laboratory, 2575 Sand Hill Road, Menlo Park, California 94025, USA. ⁶Center for Free-Electron Laser Science, DESY, Notkestrasse 85, 22607 Hamburg, Germany. ⁷Linac Coherent Light Source, SLAC National Accelerator Laboratory, PO Box 20450, Stanford, California 94309, USA. ⁸Institute for Methods and Instrumentation in Synchrotron Radiation Research, Helmholtz-Zentrum Berlin für Materialien und Energie GmbH, Wilhelm-Conrad-Röntgen Campus, Albert-Einstein-Strasse 15, 12489 Berlin, Germany. ⁹Mineral Physics Institute, Stony Brook University, Stony Brook, New York, New York 11794-2100, USA.

liquid. As droplet temperature decreases, broad and bright Bragg peaks from hexagonal ice (Supplementary Information, section A.2.1) are sometimes superposed on the water scattering ring (Fig. 1c). We denote as ‘water shots’ diffraction patterns where we detected only water scattering, and as ‘ice shots’ diffraction patterns containing Bragg peaks. Ice could be detected if the illuminated volume of a droplet contained $>0.05\%$ of ice by mass (Supplementary Information, section A.2.2). For the 12- μm -diameter droplets, the number of ice shots increased drastically as the travel time exceeded ~ 4 ms (Fig. 2). The probing of individual water droplets with single, ultrashort X-ray pulses allowed us to separate water shots from ice shots at each temperature, to give the fraction of droplets containing ice. Even among the droplets that interacted with X-ray pulses approximately 5 ms after exiting the nozzle, with the coldest liquid temperature of 227^{+2}_{-1} K, we found more than 100 water shots that contained water diffraction rings and no ice diffraction peaks out of 3,600 total hits; this is below the onset temperature of ice nucleation (Fig. 2) and inside water’s no man’s land below $T_{\text{H}} \approx 232$ K at ambient pressure¹³.

Structural properties of supercooled water in no-man’s land can be extracted from the X-ray scattering data. The total scattering factor, $S(q)$, for each droplet temperature was obtained by averaging the scattering patterns from the respective water shots and removing the independent atomic scattering (Supplementary Information, section A.3.1). The resulting sequence of temperature-dependent $S(q)$ profiles for liquid water is shown in Fig. 3a, illustrating how the principal maximum of $S(q)$ is split into a peak S_1 , located at $q_1 \approx 2 \text{ \AA}^{-1}$, and a peak S_2 , located at $q_2 \approx 3 \text{ \AA}^{-1}$. The amplitudes of, and separation between, S_1 and S_2 increase with decreasing droplet temperature, indicative of an increase in structural ordering as water is supercooled ever more deeply towards and into no-man’s land. Figure 3b illustrates the shift in the positions of the two peaks with temperature, as obtained from water droplets using the LCLS X-ray laser, and also based on synchrotron radiation data from metastable

liquid water at only slightly supercooled temperatures and from stable liquid water at ambient temperatures; for the latter two data sets, the temperature was measured directly. The continuous changes in the S_1 and S_2 peak positions, without apparent break when moving between the independent X-ray laser and synchrotron radiation data sets, strongly supports the temperature calibration.

At the lowest temperature accessible in the current study, the S_1 and S_2 peak positions approach the corresponding peak positions for tetrahedrally coordinated structures (Fig. 3b), represented by low-density amorphous (LDA) ice as obtained by neutron scattering²² and modelled for clusters of hexagonal ice using kinematic scattering (Supplementary Information, section A.2.3). The rapidly increasing fraction of ice shots on the millisecond timescale below ~ 229 K shows that glassy water, which would be associated with slow dynamics, is not formed at these temperatures (Fig. 2). We note that the continuous change in the positions of the diffraction peaks S_1 and S_2 with temperature resembles the trend of similar diffraction peaks when high-density amorphous ice transforms into LDA ice²³.

The separation between the S_1 and S_2 peaks is very sensitive to the amount and character of tetrahedrally coordinated configurations favoured by water’s directional hydrogen bonds. Water exhibits a peak in the oxygen–oxygen pair-correlation function, $g_{\text{OO}}(r)$, at 4.5 \AA , corresponding to the second-nearest-neighbour distance in tetrahedral coordination, $\sqrt{8/3}a$, where $a \approx 2.8 \text{ \AA}$ is the nearest-neighbour oxygen–oxygen distance in liquid water²⁴. The inset of Fig. 4a shows that increasing temperature reduces the amplitude of the second $g_{\text{OO}}(r)$ peak (henceforth denoted g_2) here obtained from molecular dynamics simulations using the TIP4P/2005 water model (Methods); the same trend has also been observed experimentally for an increase in pressure²⁵ or temperature²⁶. We find that g_2 can be exploited as a good structural parameter to describe the

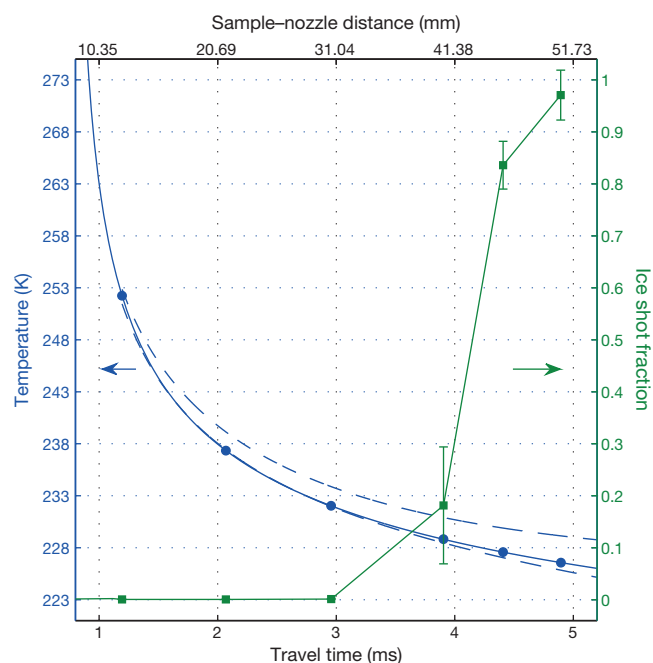


Figure 2 | Time dependence of water crystallization during evaporative cooling. Ice shot fraction (green) and estimated temperature (blue) as functions of travel time in vacuum for droplets of diameter 12 μm and speed 10.35 m s^{-1} . From the ice shot fraction, shown as mean \pm s.d. of two to seven individual recordings, we find the onset of ice nucleation to lie between $232^{+2}_{-0.1}$ and 229^{+2}_{-1} K. The dashed blue lines represent maximum and minimum temperatures from the Knudsen model, which consistently overlap with experimental data sets from SSRL measured at known absolute temperatures (Supplementary Information, sections A.3.2 and B.3.5).

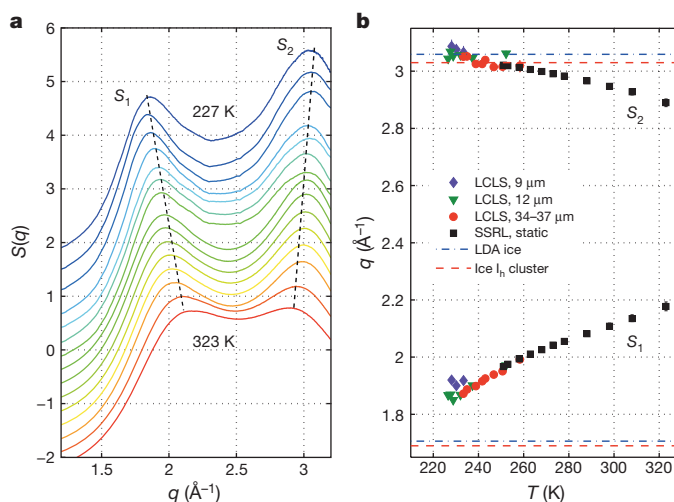


Figure 3 | Temperature dependence of water scattering peaks. **a**, Scattering structure factor, $S(q)$, obtained from single-shot diffraction patterns (Supplementary Information, section A.3.1). Water temperature decreases from bottom to top (SSRL: 323, 298, 273, 268, 263, 258, 253, 251 K; LCLS: 251, 247, 243, 239, 232, 229, 227 K). The data reveal a split of the principal $S(q)$ maximum into two well-separated peaks, S_1 and S_2 (dashed lines). **b**, Temperature dependence of the S_1 and S_2 peak positions, calculated from the maxima of local fifth-order polynomial least-squares fits with error bars estimated by shifting the derivatives of the polynomial fits by $\pm 0.05 \text{ \AA}$ (LCLS) and $\pm 0.15 \text{ \AA}$ (SSRL) (Supplementary Information, section A.3.1). Green triangles are LCLS data from 12- μm -diameter droplets; red circles are LCLS data from 34- and 37- μm -diameter droplets; and black squares are SSRL data from a static liquid sample. Purple diamonds are LCLS data from 9- μm -diameter droplets measured at a separate LCLS run with separate q -calibration (Supplementary Information, section A.1.2). As the temperature decreases in no man’s land, the positions of peaks S_1 and S_2 approach the characteristic values of LDA ice (dash-dot blue lines) as determined from neutron diffraction²² and clusters of hexagonal ice (ice I_{h} ; dashed red lines; Supplementary Information, section A.2.3).

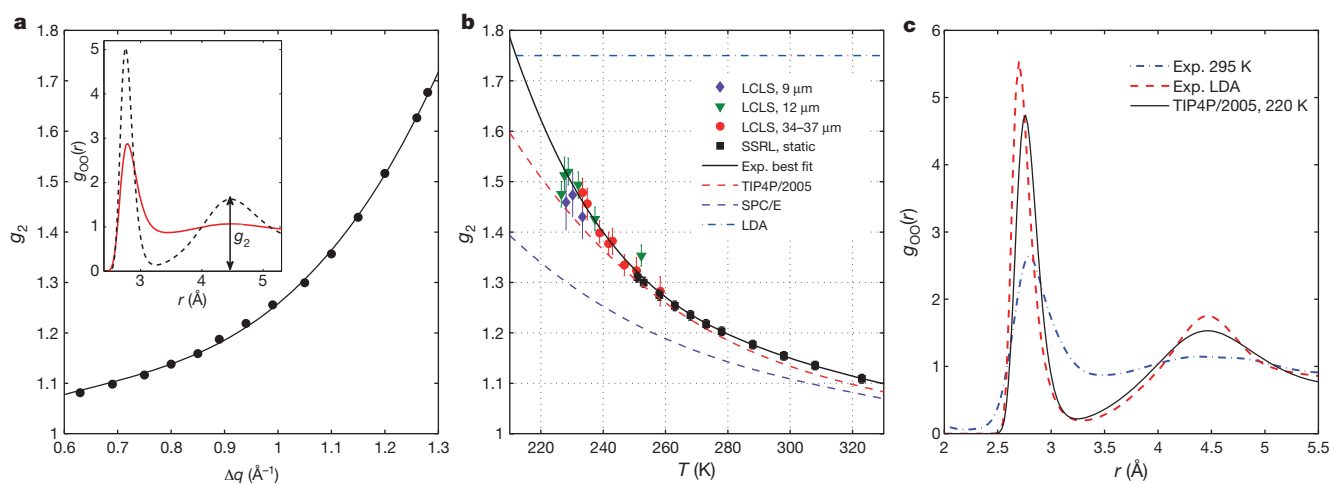


Figure 4 | Temperature dependence of the tetrahedrality of liquid water.

a, Magnitude of the second $g(r)$ peak, g_2 , as a function of the splitting, Δq , between the S_1 and S_2 peaks from TIP4P/2005 molecular dynamics simulations (dots). The inset illustrates g_2 for $g(r)$ at 340 K (red solid line) and 210 K (black dashed line). **b**, Experimental g_2 values, derived from measured Δq values (labels as in Fig. 3b) and the fit to molecular dynamics data shown in **a**, with error bars estimated from the maximum and minimum Δq values allowed by the uncertainty in the S_1 and S_2 peak positions. Also shown is the fourth-order polynomial least-squares fit to the experimental data (black solid line), where the last (that is, low- T) two data points for the 12- μm -diameter droplets

and the last data point for the 9- μm -diameter droplets are ignored owing to high nonlinearity in the detector response, which artificially decreases g_2 (Supplementary Information, section A.3.1). For comparison, the temperature dependences of g_2 for the TIP4P/2005 (red dashed line) and SPC/E (purple dashed line) models are depicted along with the characteristic value of g_2 for LDA ice²² (blue dash-dot line). **c**, The $g(r)$ of TIP4P/2005 water at 220 K (black solid line) bears a striking similarity to LDA ice²² (red dashed line), whereas the measured $g(r)$ of room-temperature water²⁴ (blue dash-dot line) shows significantly less structural correlation.

tetrahedrality of liquid water, as demonstrated by the similar temperature dependences of g_2 and the tetrahedrality, Q , commonly used in molecular dynamics simulations²⁷ (Supplementary Fig. 21). The molecular dynamics simulations furthermore show a clear correlation between g_2 and the splitting, $\Delta q = q_2 - q_1$, between the S_1 and S_2 peaks, where g_2 increases monotonically with Δq (Fig. 4a). We make use of this relationship to extract from the measured Δq data ‘experimental’ g_2 values, which are plotted against temperature in Fig. 4b and compared with g_2 values from molecular dynamics simulations using the TIP4P/2005 and SPC/E water models.

The data in Fig. 4b show that as water is cooled from above its freezing temperature, g_2 and its rate of change increase continuously as would be expected from the accelerated growth of tetrahedral structures in deeply supercooled water. We also note that the best-fit extrapolation of g_2 to low temperatures approaches the limit for LDA ice²² (dash-dot line in Fig. 4b), which is expected to be representative also of crystalline hexagonal ice (Fig. 3b), although g_2 cannot be uniquely defined for a crystalline sample. Furthermore, $g_{\text{OO}}(r)$ for LDA ice and simulated supercooled TIP4P/2005 water at 220 K—with the same g_2 value as the maximum in the experimental data—are very similar, but differ from $g_{\text{OO}}(r)$ for water at ambient conditions (Fig. 4c). The structure of liquid water in no man’s land is therefore distinct from that of water under ambient conditions, exhibiting stronger tetrahedral ordering. The largest g_2 values obtained from the experimental data (Fig. 4b) coincide with the observed onset of ice nucleation at ~ 229 K (Fig. 2), supporting simulations^{10,28} which concluded that the increased abundance and persistence of tetrahedrally coordinated water molecules play a central part as precursor structure for homogeneous ice nucleation.

We still observe a non-negligible number of water shots at the farthest measurement point, reached about 1 ms after the temperature of the corresponding water droplet has dropped to 229^{+2}_{-1} K, where homogeneous nucleation sets in (Fig. 2). This implies that metastable water can transiently exist on the millisecond timescale down to 227^{+2}_{-1} K. We expect that these observations and our data mapping the structural evolution of supercooled liquid water with decreasing temperature (Extended Data Tables 1–4) will enable a quantitative evaluation of different theoretical models that predict this structure in no man’s land and aim to explain water’s anomalous physical properties.

METHODS SUMMARY

Deionized water (PURELAB Ultra Genetic; resistivity 18.2 M Ω cm at 298 K) was measured at the Stanford Synchrotron Radiation Lightsource (SSRL) small-angle X-ray scattering instrument (beam line 4-2) in a static, ~ 5 - μl sample cell with an absolute temperature uncertainty of ± 1 K. The experimental details have been described elsewhere². X-ray scattering experiments on water droplets of diameters 9, 12, 34 and 37 μm were performed using the LCLS coherent X-ray imaging instrument²⁹ on deep supercooling (< 260 K) calibrated according to the Knudsen theory of evaporation (Supplementary Information, section B3). These measurements overlap with those made at SSRL (> 250 K). Molecular dynamics simulations of evaporative cooling of 1–4-nm-radii droplets were performed using the TIP4P/2005 force field to verify the Knudsen theory of evaporation (Supplementary Information, section B2). The single-pulse water scattering patterns at LCLS were recorded with the Cornell-SLAC pixel array detector and corrected for the dark signal, gain variations, the polarization dependence of the X-ray scattering, solid-angle differences and fluctuations in the average photon wavelength between X-ray pulses (Supplementary Information, section A.1.2). More details on the procedure for selecting water shots and sample statistics are given in Supplementary Information, section A.1.3. The total scattering structure factor was obtained from the averaged angularly integrated intensities by removing the atomic form factor contribution (Supplementary Information, section A.3.1). Measurements from both SSRL and LCLS had a scattering momentum transfer range of approximately $0.5 \text{ \AA}^{-1} \leq q \leq 3.5 \text{ \AA}^{-1}$. Large-scale (45,000 molecules) molecular dynamics simulations³⁰ of bulk TIP4P/2005 water and medium-scale (512 molecules) molecular dynamics simulations of SPC/E water were performed for a wide range of temperatures to calculate the total scattering structure factor (Supplementary Information, section C.1.1), including intermolecular oxygen–hydrogen and oxygen–oxygen partial structure factors and the intramolecular oxygen–hydrogen partial structure factor (the hydrogen–hydrogen contribution is negligible), which were used for the calibration of g_2 against Δq (Supplementary Information, section C.1.3).

Online Content Any additional Methods, Extended Data display items and Source Data are available in the online version of the paper; references unique to these sections appear only in the online paper.

Received 26 November 2013; accepted 17 March 2014.

- Speedy, R. J. & Angell, C. A. Isothermal compressibility of supercooled water and evidence for a thermodynamic singularity at -45°C . *J. Chem. Phys.* **65**, 851–858 (1976).
- Huang, C. *et al.* Increasing correlation length in bulk supercooled H_2O , D_2O , and NaCl solution determined from small angle X-ray scattering. *J. Chem. Phys.* **133**, 134504 (2010).

3. Angell, C. A., Sichina, W. J. & Oguni, M. Heat capacity of water at extremes of supercooling and superheating. *J. Phys. Chem.* **86**, 998–1002 (1982).
4. Poole, P. H., Sciortino, F., Essmann, U. & Stanley, H. E. Phase behaviour of metastable water. *Nature* **360**, 324–328 (1992).
5. Sastry, S., Debenedetti, P. G., Sciortino, F. & Stanley, H. E. Singularity-free interpretation of the thermodynamics of supercooled water. *Phys. Rev. E* **53**, 6144–6154 (1996).
6. Angell, C. A. Insights into phases of liquid water from study of its unusual glass-forming properties. *Science* **319**, 582–587 (2008).
7. Limmer, D. T. & Chandler, D. The putative liquid-liquid transition is a liquid-solid transition in atomistic models of water. *J. Chem. Phys.* **135**, 134503 (2011).
8. Palmer, J. C., Car, R. & Debenedetti, P. G. The liquid-liquid transition in supercooled ST2 water: a comparison between umbrella sampling and well-tempered metadynamics. *Faraday Discuss.* **167**, 77–94 (2013).
9. Speedy, R. J. Stability-limit conjecture. An interpretation of the properties of water. *J. Phys. Chem.* **86**, 982–991 (1982).
10. Moore, E. B. & Molinero, V. Structural transformation in supercooled water controls the crystallization rate of ice. *Nature* **479**, 506–508 (2011).
11. Holten, V. & Anisimov, M. A. Entropy-driven liquid-liquid separation in supercooled water. *Sci. Rep.* **2**, 713 (2012).
12. Overduin, S. D. & Patey, G. N. An analysis of fluctuations in supercooled TIP4P/2005 water. *J. Chem. Phys.* **138**, 184502 (2013).
13. Mason, B. J. The supercooling and nucleation of water. *Adv. Phys.* **7**, 221–234 (1958).
14. Smith, R. S. & Kay, B. D. The existence of supercooled liquid water at 150 K. *Nature* **398**, 788–791 (1999).
15. Neufeind, J., Benmore, C. J., Weber, J. K. R. & Paschek, D. More accurate X-ray scattering data of deeply supercooled bulk liquid water. *Mol. Phys.* **109**, 279–288 (2011).
16. Mallamace, F., Corsaro, C., Baglioni, P., Fratini, E. & Chen, S.-H. The dynamical crossover phenomenon in bulk water, confined water and protein hydration water. *J. Phys. Condens. Matter* **24**, 064103 (2012).
17. Manka, A. *et al.* Freezing water in no-man's land. *Phys. Chem. Chem. Phys.* **14**, 4505–4516 (2012).
18. Lvinger, N. E. Water in confinement. *Science* **298**, 1722–1723 (2002).
19. Faubel, M., Schlemmer, S. & Toennies, J. P. A molecular beam study of the evaporation of water from a liquid jet. *Z. Phys. D* **10**, 269–277 (1988).
20. Rayleigh, F. R. S. On the instability of jets. *Proc. Lond. Math. Soc.* **10**, 4–12 (1879).
21. DePonte, D. P. *et al.* Gas dynamic virtual nozzle for generation of microscopic droplet streams. *J. Phys. D Appl. Phys.* **41**, 195505 (2008).
22. Bowron, D. T. *et al.* The local and intermediate range structures of the five amorphous ices at 80 K and ambient pressure: a Faber-Ziman and Bhatia-Thornton analysis. *J. Chem. Phys.* **125**, 194502 (2006).
23. Tulk, C. A. *et al.* Structural studies of several distinct metastable forms of amorphous ice. *Science* **297**, 1320–1323 (2002).
24. Skinner, L. B. *et al.* Benchmark oxygen-oxygen pair-distribution function of ambient water from x-ray diffraction measurements with a wide Q-range. *J. Chem. Phys.* **138**, 074506 (2013).
25. Okhulkov, A. V., Demianets, Y. N. & Gorbaty, Y. E. X-ray scattering in liquid water at pressures of up to 7.7 kbar: test of a fluctuation model. *J. Chem. Phys.* **100**, 1578–1588 (1994).
26. Narten, A. H., Danford, M. D. & Levy, H. A. X-ray diffraction study of liquid water in temperature range 4–200 °C. *Discuss. Faraday Soc.* **43**, 97–107 (1967).
27. Errington, J. R. & Debenedetti, P. G. Relationship between structural order and the anomalies of liquid water. *Nature* **409**, 318–321 (2001).
28. Matsumoto, M., Saito, S. & Ohmine, I. Molecular dynamics simulation of the ice nucleation and growth process leading to water freezing. *Nature* **416**, 409–413 (2002).
29. Boutet, S. & Williams, G. J. The coherent X-ray imaging (CXI) instrument at the Linac Coherent Light Source (LCLS). *New J. Phys.* **12**, 035024 (2010).
30. Wikfeldt, K. T., Huang, C., Nilsson, A. & Pettersson, L. G. M. Enhanced small-angle scattering connected to the Widom line in simulations of supercooled water. *J. Chem. Phys.* **134**, 214506 (2011).

Supplementary Information is available in the online version of the paper.

Acknowledgements We acknowledge the US Department of Energy (DOE) through the SLAC Laboratory Directed Research and Development Program, Office of Basic Energy Sciences through SSRL and LCLS; the AMOS programme within the Chemical Sciences, Geosciences, and Biosciences Division of the Office of Basic Energy Sciences; and the Swedish Research Council for financial support. The molecular dynamics simulations were performed on resources provided by the Swedish National Infrastructure for Computing at the NSC and HPC2N centres. Parts of this research were carried out at LCLS at the SLAC National Accelerator Laboratory. LCLS is an Office of Science User Facility operated for the DOE Office of Science by Stanford University. We also acknowledge the support of the SSRL Structural Molecular Biology group funded by the National Institutes of Health, National Center for Research Resources, Biomedical Technology Grant and the US Department of Energy, Office of Biological and Environmental Research. We wish to thank D. Schafer and M. Hayes for mechanical support; W. Ghonsalves and F. Hoeflich for software support; the SLAC detector group for assistance with the Cornell-SLAC pixel array detector; H. Nakatsutsumi, K. Beyerlein and C. Gati for nozzle support; D. Bowron for providing the data files from ref. 22; J. Spence and C. Stan for discussions; and H. E. Stanley, V. Molinero, C. A. Angell and D. Chandler for critical reading of the manuscript.

Author Contributions A.N., C.H. and M.J.B. had the idea for and designed the experiment; S.B., G.J.W., M.M. and M.M.S. operated the coherent X-ray imaging instrument; M.J.B., D.P.D., T.A.M., J.A.S., C.H., R.G.S., C.Y.H., H.L. and D. Starodub developed, tested and ran the sample delivery system; C.H., T.A.M. and T.M.W. performed the SSRL experiment; J.A.S., T.A.M., H.L., R.G.S., C.H., D.N., M.B., D.P.D., D. Starodub, C.Y.H., C. Chen, L.B.S., M.M.S., M.M., G.J.W., S.B., M.J.B. and A.N. performed the LCLS experiments; A.B., J.A.S., N.D.L., A.V.M., G.J.W. and C. Caronna developed data processing software; J.A.S., C.H., N.D.L., H.L., D.N., A.V.M. and J.F. processed, sorted and analysed data; D. Schlesinger, K.T.W. and L.G.M.P. designed and performed the molecular dynamics simulations; D. Schlesinger, J.A.S., C.H., T.A.M., D. Starodub and L.G.M.P. implemented and simulated the Knudsen theory of evaporation; and A.N., C.H., L.G.M.P., J.A.S., D. Schlesinger and N.D.L. wrote the manuscript with input from all authors.

Author Information Reprints and permissions information is available at www.nature.com/reprints. The authors declare no competing financial interests. Readers are welcome to comment on the online version of the paper. Correspondence and requests for materials should be addressed to J.A.S. (sellberg@slac.stanford.edu) or A.N. (nilsson@slac.stanford.edu).

Extended Data Table 1 | Temperature-dependent S_1 and S_2 peak positions for the 5- μ l static sample

Temperature (K)	q_1 (\AA^{-1})	q_2 (\AA^{-1})
323 \pm 1	2.177 \pm 0.016	2.890 \pm 0.014
308 \pm 1	2.135 \pm 0.013	2.928 \pm 0.011
298 \pm 1	2.108 \pm 0.011	2.947 \pm 0.009
288 \pm 1	2.082 \pm 0.009	2.966 \pm 0.007
278 \pm 1	2.055 \pm 0.007	2.983 \pm 0.006
273 \pm 1	2.042 \pm 0.007	2.991 \pm 0.006
268 \pm 1	2.026 \pm 0.007	2.999 \pm 0.006
263 \pm 1	2.011 \pm 0.006	3.006 \pm 0.005
258 \pm 1	1.994 \pm 0.006	3.013 \pm 0.005
253 \pm 1	1.975 \pm 0.006	3.019 \pm 0.004
251 \pm 1	1.967 \pm 0.005	3.021 \pm 0.004

The temperature-dependent S_1 and S_2 peak positions, respectively q_1 and q_2 , derived from the maxima of local (fifth-order) polynomial least-squares fits for the 5- μ l static sample measured at beamline 4-2 at SSRL in January 2012. The error bars for the temperature correspond to the measurement accuracy (IEC 584-2 standard for K-type thermocouples); the error bars for q_1 and q_2 were estimated by shifting the derivatives of the polynomial fits by $\pm 0.15 \text{ \AA}$ when determining the positions of the maxima (Supplementary Information, section A.3.1).

Extended Data Table 2 | Temperature-dependent S_1 and S_2 peak positions for the 34–37- μm -diameter droplets

Temperature (K)	q_1 (\AA^{-1})	q_2 (\AA^{-1})
258 ⁺⁵ _{−3}	1.992 ± 0.011	3.019 ± 0.021
251 ⁺³ _{−2}	1.950 ± 0.008	3.016 ± 0.014
247 ⁺² _{−1}	1.939 ± 0.008	3.015 ± 0.011
243 ± 2	1.925 ± 0.008	3.039 ± 0.013
242 ± 1	1.915 ± 0.006	3.025 ± 0.011
239 ± 1	1.899 ± 0.006	3.025 ± 0.011
235 ⁺¹ _{−2}	1.887 ± 0.008	3.052 ± 0.013
233 ± 1	1.872 ± 0.007	3.051 ± 0.011

The temperature-dependent S_1 and S_2 peak positions, respectively q_1 and q_2 , derived from the maxima of local (fifth-order) polynomial least-squares fits for the 34–37- μm -diameter droplets measured using the coherent X-ray imaging (CXI) instrument at LCLS in February 2011. The error bars for the temperature were estimated by forcing overlap between experimental data sets using the Knudsen theory of evaporation (Supplementary Information, section B.3.5); the error bars for q_1 and q_2 were estimated by shifting the derivatives of the polynomial fits by ± 0.05 \AA when determining the positions of the maxima (Supplementary Information, section A.3.1).

Extended Data Table 3 | Temperature-dependent S_1 and S_2 peak positions for the 12- μm -diameter droplets

Temperature (K)	q_1 (\AA^{-1})	q_2 (\AA^{-1})
252 ⁺² ₋₁	1.971 ± 0.009	3.062 ± 0.008
237 ⁺² _{-0.2}	1.901 ± 0.006	3.046 ± 0.010
232 ⁺² _{-0.1}	1.868 ± 0.006	3.056 ± 0.010
229 ⁺² ₋₁	1.850 ± 0.005	3.053 ± 0.010
228 ⁺² ₋₁	1.869 ± 0.008	3.068 ± 0.013
227 ⁺² ₋₁	1.867 ± 0.006	3.044 ± 0.010

The temperature-dependent S_1 and S_2 peak positions, respectively q_1 and q_2 , derived from the maxima of local (fifth-order) polynomial least-squares fits for the 12- μm -diameter droplets measured using the CXI instrument at LCLS in February 2011. The error bars for the temperature were estimated by forcing overlap between experimental data sets using the Knudsen theory of evaporation (Supplementary Information, section B.3.5); the error bars for q_1 and q_2 were estimated by shifting the derivatives of the polynomial fits by ± 0.05 \AA when determining the positions of the maxima (Supplementary Information, section A.3.1).

Extended Data Table 4 | Temperature-dependent S_1 and S_2 peak positions for the 9- μm -diameter droplets

Temperature (K)	q_1 (\AA^{-1})	q_2 (\AA^{-1})
233 ⁺² _{−1}	1.918 ± 0.010	3.066 ± 0.022
230 ⁺² _{−1}	1.900 ± 0.009	3.076 ± 0.019
228 ⁺² _{−1}	1.920 ± 0.013	3.087 ± 0.024

The temperature-dependent S_1 and S_2 peak positions, respectively q_1 and q_2 , derived from the maxima of local (fifth-order) polynomial least-squares fits for the 9- μm -diameter droplets measured using the CXI instrument at LCLS in January 2013. The error bars for the temperature were estimated by forcing overlap between experimental data sets using the Knudsen theory of evaporation (Supplementary Information, section B.3.5); the error bars for q_1 and q_2 were estimated by shifting the derivatives of the polynomial fits by ± 0.05 \AA when determining the positions of the maxima (Supplementary Information, section A.3.1).

Metastable liquid–liquid transition in a molecular model of water

Jeremy C. Palmer¹, Fausto Martelli², Yang Liu[†], Roberto Car², Athanassios Z. Panagiotopoulos¹ & Pablo G. Debenedetti¹

Liquid water's isothermal compressibility¹ and isobaric heat capacity², and the magnitude of its thermal expansion coefficient³, increase sharply on cooling below the equilibrium freezing point. Many experimental^{4–8}, theoretical^{9–11} and computational^{12,13} studies have sought to understand the molecular origin and implications of this anomalous behaviour. Of the different theoretical scenarios^{9,14,15} put forward, one posits the existence of a first-order phase transition that involves two forms of liquid water and terminates at a critical point located at deeply supercooled conditions^{9,12}. Some experimental evidence is consistent with this hypothesis^{4,16}, but no definitive proof of a liquid–liquid transition in water has been obtained to date: rapid ice crystallization has so far prevented decisive measurements on deeply supercooled water, although this challenge has been overcome recently¹⁶. Computer simulations are therefore crucial for exploring water's structure and behaviour in this regime, and have shown^{13,17–21} that some water models exhibit liquid–liquid transitions and others do not. However, recent work^{22,23} has argued that the liquid–liquid transition has been mistakenly interpreted, and is in fact a liquid–crystal transition in all atomistic models of water. Here we show, by studying the liquid–liquid transition in the ST2 model of water²⁴ with the use of six advanced sampling methods to compute the free-energy surface, that two metastable liquid phases and a stable crystal phase exist at the same deeply supercooled thermodynamic condition, and that the transition between the two liquids satisfies the thermodynamic criteria of a first-order transition²⁵. We follow the rearrangement of water's coordination shell and topological ring structure along a thermodynamically reversible path from the low-density liquid to cubic ice²⁶. We also show that the system fluctuates freely between the two liquid phases rather than crystallizing. These findings provide unambiguous evidence for a liquid–liquid transition in the ST2 model of water, and point to the separation of time scales between crystallization and relaxation as being crucial for enabling it.

Although several recent investigations using free-energy methods designed specifically to study phase transitions²⁵ have shown that the ST2 model of water undergoes a liquid–liquid transition^{17–19}, other investigations^{22,23} involving seemingly identical simulations using the same model found only a single liquid and a crystalline phase and concluded that what in reality is a crystallization transition had been mistaken for a liquid–liquid transition. Because there are stringent thermodynamic conditions that a first-order transition must satisfy, it is possible, albeit computationally expensive, to definitively verify or falsify the existence of a liquid–liquid transition. To this end we use six state-of-the-art free-energy methods (four of which are documented in Methods) and scaling analysis, and we construct a thermodynamically reversible path between the liquid and crystalline phases of the ST2 model.

Figure 1a, b shows perspective and orthographic projections of the free-energy surface for ST2 water at 228.6 K and 2.4 kbar, as a function of density and an order parameter²⁷, Q_6 , that can distinguish crystalline states from configurations lacking long-range order. It can be seen that two disordered (low- Q_6) phases of different density are in equilibrium (same free energy) with each other, both of them being metastable with respect

to the crystal phase, the latter having much lower free energy. To our knowledge, this is the first time that two metastable liquid phases in equilibrium with each other and a third, stable crystalline phase have been identified in a pure substance at the same temperature and pressure in a computer simulation.

The system-size dependence of the free-energy barrier separating coexisting phases is a stringent test of the presence of a true first-order transition in computer simulations^{22,23,25}. We have calculated the free-energy surface in the low- Q_6 region corresponding to the two liquids for system sizes $N = 192, 300, 400$ and 600 , with Fig. 2a showing that the corresponding barrier heights satisfy the $N^{2/3}$ scaling characteristic of first-order transitions. This scaling is a consequence of the surface free energy increasing as the interface between the liquids grows with system size^{22,23,25}. For the range of system sizes examined, the interface manifests itself through the formation of water clusters with local environments characteristic of each distinct liquid phase. Figure 2b shows an example of this behaviour in a water configuration taken from a simulation performed near the barrier region for $N = 600$. Because non-zero average Q_6 values in an amorphous phase arise solely from fluctuations in finite systems, this quantity must also exhibit a system-size dependence^{22,27}. Figure 2c shows that Q_6 vanishes as $N^{-1/2}$, in agreement with the theoretical expectation^{22,27}, thereby confirming the amorphous character of the low-density liquid (LDL) phase.

Figure 3 shows the free-energy surface computed from standard Monte Carlo (MC) simulations at fixed temperature and pressure, during which each system was sampled for 100 relaxation times without the imposition of any constraint. Over the course of these long simulations, the systems fluctuate between the two coexisting phases enough times so as to allow the calculation of the free-energy surface, which is in excellent agreement with the results shown in Fig. 1b for the low- Q_6 region and also with those obtained from the four other sampling techniques (see Methods and Extended Data Fig. 1). During this time, Q_6 remains invariably in the amorphous region and the systems show no evidence of crystallization. The LDL phase exhibits slow dynamics, and proper scrutiny of a metastable state requires sampling to occur over times that comfortably exceed the system's structural relaxation time, while being significantly shorter than the nucleation time of the stable ice phase. The latter's density is very similar to that of LDL (Fig. 1). Ice nucleation, should it occur, takes place within LDL²⁶, rather than from the high-density liquid (HDL). The inset to Fig. 3 shows the relaxation of fluctuations in density and structural order (Q_6) in LDL. It can be seen that, after an intermediate transient period during which these processes are separated by as much as two orders of magnitude, fluctuations in density and Q_6 decay on very similar time scales. As documented in Methods, this is a general result, but the transient behaviour is sensitive to the particular algorithm used to sample configurations (Extended Data Fig. 2). The results of Fig. 3 confirm that the LDL phase is a properly equilibrated liquid, and that under the conditions investigated here, the characteristic time for nucleation of the stable ice phase is much longer than the structural relaxation time for the LDL phase in the ST2 model of water. The key role of kinetics in stabilizing the liquid–liquid transition is further emphasized by the fact that

¹Department of Chemical and Biological Engineering, Princeton University, Princeton, New Jersey 08544, USA. ²Department of Chemistry, Princeton University, Princeton, New Jersey 08544, USA.

[†]Present address: Air Products and Chemicals Inc., Allentown, Pennsylvania 18195, USA.

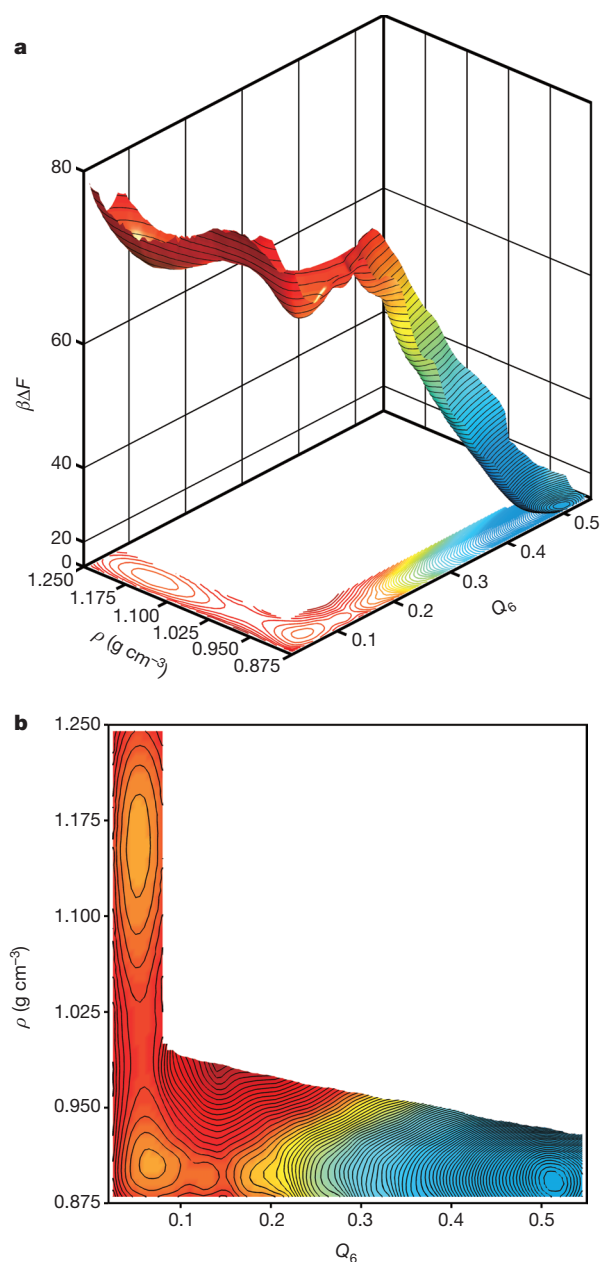


Figure 1 | Thermodynamic equilibrium between metastable liquid polymorphs. **a**, Reversible free-energy surface (F = free energy, $\beta = 1/k_B T$) described by density and the crystalline order parameter, Q_6 , for 192 ST2 water molecules at a point of liquid–liquid coexistence (228.6 K and 2.4 kbar). **b**, An orthographic projection of the free-energy surface shown in **a**. The HDL and LDL basins ($\rho \approx 1.15 \text{ g cm}^{-3}$ and $\rho \approx 0.90 \text{ g cm}^{-3}$, respectively) located at $Q_6 \approx 0.05$ are separated by a $\sim 4k_B T$ free-energy barrier and are metastable with respect to cubic ice ($Q_6 \approx 0.52$, $\rho \approx 0.90 \text{ g cm}^{-3}$) by $\sim 75k_B T$ at this temperature and pressure. The average uncertainty in the free-energy surface is less than $1k_B T$ apart. Contours are $1k_B T$ apart.

the system fluctuates freely between the two liquid basins in unconstrained simulations (Fig. 3) without crystallization, even though the barrier separating the two liquids is comparable to that separating LDL and ice (Fig. 1).

Figures 1 and 3 show that the metastable liquids are not distinguished by Q_6 because of their amorphous nature, suggesting that other order parameters must be used to characterize their structure. The local structure index²⁸ (LSI) is an order parameter that quantifies the extent to which a molecule possesses a tetrahedral environment with well-separated first and second coordination shells. Figure 4 shows the free-energy surface of

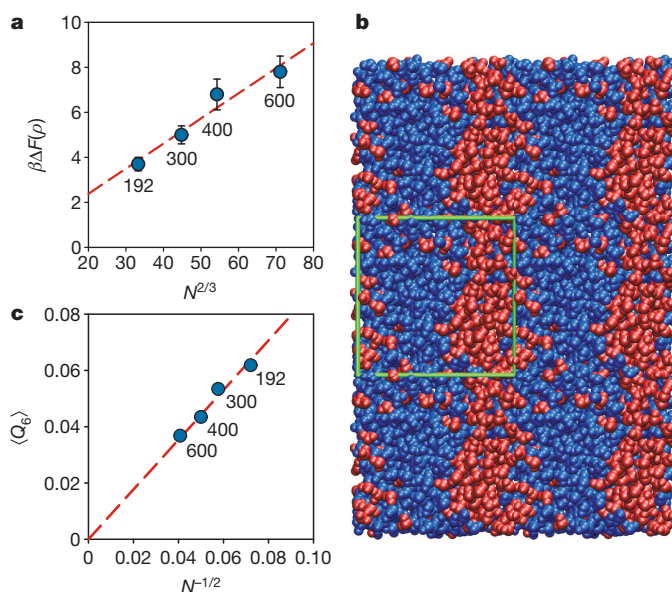


Figure 2 | Finite-size scaling and the liquid–liquid interface. **a**, Free-energy barrier separating the HDL and LDL basins computed at coexistence for systems containing $N = 192, 300, 400$ and 600 ST2 water molecules. The barrier height increases with system size, obeying the $N^{2/3}$ scaling law expected for a first-order phase transition. Error bars were computed using the bootstrap analysis described in Methods. **b**, Large clusters are formed near the barrier region by water molecules with local coordination environments characteristic of HDL and LDL (blue and red molecules, respectively). The local structure index order parameter, I , described in the text and Methods was used to characterize each molecule's local environment, with blue molecules (HDL) having $I \leq 0.12 \text{ \AA}^2$ and red molecules (LDL) having $I > 0.12 \text{ \AA}^2$. The green simulation box containing 600 ST2 water molecules has been replicated across its periodic boundaries to illustrate that the clusters span the length of the unit cell. **c**, The mean value of Q_6 averaged over the LDL basin decreases with system size, scaling as $N^{-1/2}$, and confirming the disordered nature of the liquid. The symbol size is larger than the estimated uncertainty for $\langle Q_6 \rangle$.

ST2 water at 228.6 K and 2.4 kbar for $N = 192$ projected onto the space parameterized by the first moment of the molecular LSI distribution, \bar{I} , and Q_6 . Water molecules within the HDL phase have a disordered coordination structure, resulting in $\bar{I} \approx 0$, because of the presence of interstitial molecules residing between the first and second neighbour shell that disrupt local tetrahedral order. The coordination structure of LDL ($\bar{I} \approx 0.15 \text{ \AA}^2$) is more ordered, with two distinct neighbour shells that give rise to its ice-like density. The LSI parameter also distinguishes the ice phase ($\bar{I} \approx 0.25 \text{ \AA}^2$) with its well-defined coordination structure that exhibits long-range, crystalline order. The inset to Fig. 4 shows that the changes in the coordination structure along the HDL–LDL and LDL–crystal paths are accompanied by large topological rearrangements described by the first moment of the ring size distribution, \bar{R} . The average ring size decreases monotonically along the HDL–LDL path, suggesting a continuous rearrangement process. In contrast, abrupt, non-monotonic behaviour is observed along the transition from LDL to the crystal in the vicinity of the saddle point in the \bar{I} – Q_6 free-energy surface, which is consistent with structural rearrangements that have been observed in ice nucleation trajectories taken from long molecular-dynamics simulations of the TIP4P water model²⁹. We note, however, that the system size examined here, although suitable for accurate free-energy calculations, may be insufficient to provide information about the mechanisms governing the ice nucleation and growth process. Such behaviour should therefore be investigated in future studies using larger systems.

Our free-energy calculations demonstrate that the ST2 model of water exhibits a liquid–liquid phase transition under deeply supercooled conditions. An emerging question is to understand which aspects of intermolecular interactions cause some water models to undergo a liquid–liquid transition with well-separated relaxation and crystallization times, whereas

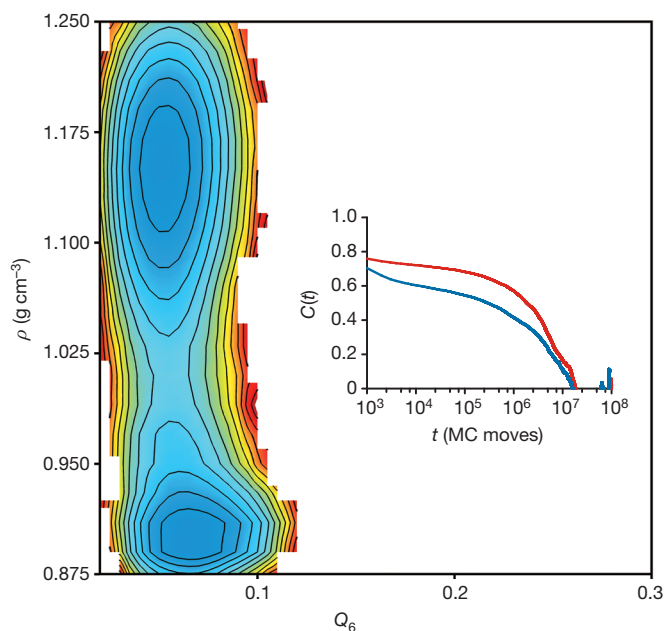


Figure 3 | Free-energy surface from unconstrained simulations. The ρ - Q_6 free-energy surface at 228.6 K and 2.4 kbar computed from 16 unconstrained MC simulations initialized in the low- Q_6 region. Contours are separated by $1k_B T$. Because of the separation of timescales between structural relaxation in the liquid phase and ice nucleation, each simulation was run for more than ~ 100 relaxation times without exhibiting any sign of crystallization. The inset shows autocorrelation functions for density (blue line) and Q_6 (red line) computed from the unconstrained MC simulations performed in the LDL region. Fluctuations in density and structural order (Q_6) decay in tandem on timescales that are relevant to relaxations within the liquid phase, as demonstrated by both order parameters having mean autocorrelation times of $\sim 10^6$ MC moves.

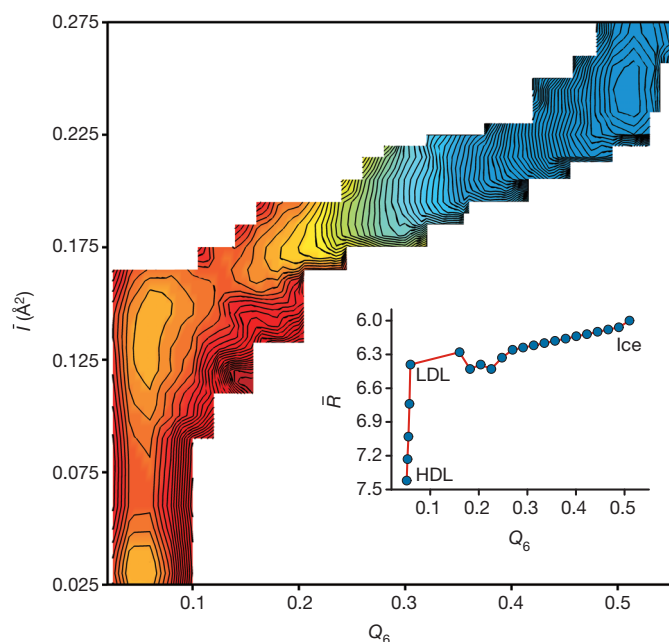


Figure 4 | Structural and topological order in the metastable coexisting liquids and in cubic ice. The free-energy surface at 228.6 and 2.4 kbar described by the first moment of the molecular local structure index distribution, \bar{I} , and the crystalline order parameter, Q_6 . Contours are $1k_B T$ apart. Parameter \bar{I} successfully distinguishes the three phases based on structural order, characterizing the extent to which molecules in each phase possess a tetrahedral environment with well-separated first and second coordination shells. The inset shows that the three phases have distinctive topological features characterized by the first moment of the ring size distribution, \bar{R} .

other models do not show this behaviour. The present results suggest that constraints associated with the breaking and forming of hydrogen bonds, present in ST2 (ref. 24) but not in coarse-grained models¹³, have an important role. Further research using state-of-the-art free-energy methods, such as those employed here, can provide insights into this question and may thereby also improve our understanding of the phase behaviour of real water under deeply supercooled conditions.

METHODS SUMMARY

The reversible free-energy surface described by density, ρ , and the bond-orientational order parameter, Q_6 , was computed for the Ewald-compatible variant of the ST2 water model²⁴ described by Liu *et al.*¹⁷ using MC simulations in the isothermal-isobaric ensemble, augmented with collective, N -particle rotational and translational MC moves and umbrella sampling³⁰. A harmonic umbrella bias potential was used to restrict each MC simulation to a different window in ρ - Q_6 parameter space. Each simulation used to generate Fig. 1 was equilibrated for $\sim 10^4 \tau_{Q_6}$, followed by a production phase of equal or greater duration, where τ_{Q_6} is the integrated autocorrelation time³⁰ for Q_6 in the sampling window. Two-dimensional ρ - Q_6 histograms were generated from uncorrelated samples collected in each umbrella window. The histograms were subsequently combined³⁰ to produce an unbiased estimate of the free energy. Special care was taken to ensure reversibility in the low-density region ($\rho < 0.98 \text{ g cm}^{-3}$), enhancing sampling of degrees of freedom associated with structural order by performing Hamiltonian exchange MC moves³⁰, in which umbrella restraint parameters were swapped between simulations in adjacent windows along Q_6 . Bi-directional sampling was also performed in this region, seeding two separate generations of simulations with initial configurations extracted from a freezing (LDL \rightarrow Ice Ic) or melting (Ice Ic \rightarrow LDL) trajectory. Reversibility was explicitly checked by comparing histograms from each generation of simulations to monitor for hysteresis (path dependence). Saved simulation trajectories were analysed to examine the structural and topological properties of each phase identified in the free-energy surface. The final data sets were subjected to critical scrutiny and were found to be insensitive to the sampling methodology and duration, yielding estimates for the ice Ic-HDL free-energy difference and the HDL-LDL surface tension in harmony with independent simulations and thermodynamic expectations (see Extended Data).

Online Content Any additional Methods, Extended Data display items and Source Data are available in the online version of the paper; references unique to these sections appear only in the online paper.

Received 28 November 2013; accepted 24 April 2014.

- Speedy, R. J. & Angell, C. A. Isothermal compressibility of supercooled water and evidence for a thermodynamic singularity at -45°C . *J. Chem. Phys.* **65**, 851–858 (1976).
- Angell, C. A., Oguni, M. & Sichina, W. J. Heat capacity of water at extremes of supercooling and superheating. *J. Phys. Chem.* **86**, 998–1002 (1982).
- Hare, D. E. & Sorensen, C. M. Densities of supercooled H_2O and D_2O in 25 μm glass capillaries. *J. Chem. Phys.* **84**, 5085–5089 (1986).
- Mishima, O. & Stanley, H. E. Decompression-induced melting of ice IV and the liquid-liquid transition in water. *Nature* **392**, 164–168 (1998).
- Soper, A. K. & Ricci, M. A. Structures of high-density and low-density water. *Phys. Rev. Lett.* **84**, 2881–2884 (2000).
- Winkel, K., Elsaesser, M. S., Mayer, E. & Loerting, T. Water polymorphism: reversibility and (dis)continuity. *J. Chem. Phys.* **128**, 044510 (2008).
- Huang, C. *et al.* The inhomogeneous structure of water at ambient conditions. *Proc. Natl Acad. Sci. USA* **106**, 15214–15218 (2009).
- Clark, G. N. I., Hura, G. L., Teixeira, J., Soper, A. K. & Head-Gordon, T. Small-angle scattering and the structure of ambient liquid water. *Proc. Natl Acad. Sci. USA* **107**, 14003–14007 (2010).
- Poole, P. H., Sciortino, F., Grande, T., Stanley, H. E. & Angell, C. A. Effect of hydrogen-bonds on the thermodynamic behavior of liquid water. *Phys. Rev. Lett.* **73**, 1632–1635 (1994).
- Tanaka, H. Simple view of waterlike anomalies of atomic liquids with directional bonding. *Phys. Rev. B* **66**, 064202 (2002).
- Holten, V. & Anisimov, M. A. Entropy-driven liquid-liquid separation in supercooled water. *Sci. Rep.* **2**, 713 (2012).
- Poole, P. H., Sciortino, F., Essmann, U. & Stanley, H. E. Phase behavior of metastable water. *Nature* **360**, 324–328 (1992).
- Moore, E. B. & Molinero, V. Structural transformation in supercooled water controls the crystallization rate of ice. *Nature* **479**, 506–508 (2011).
- Speedy, R. J. Stability-limit conjecture. An interpretation of the properties of water. *J. Phys. Chem.* **86**, 982–991 (1982).
- Sastry, S., Debenedetti, P. G., Sciortino, F. & Stanley, H. E. Singularity-free interpretation of the thermodynamics of supercooled water. *Phys. Rev. E Stat. Phys. Plasmas Fluids Relat. Interdiscip. Topics* **53**, 6144–6154 (1996).
- Amann-Winkel, K. *et al.* Water's second glass transition. *Proc. Natl Acad. Sci. USA* **110**, 17720–17725 (2013).

17. Liu, Y., Palmer, J. C., Panagiotopoulos, A. Z. & Debenedetti, P. G. Liquid–liquid transition in ST2 water. *J. Chem. Phys.* **137**, 214505 (2012).
18. Poole, P. H., Bowles, R. K., Saika-Voivod, I. & Sciortino, F. Free energy surface of ST2 water near the liquid–liquid phase transition. *J. Chem. Phys.* **138**, 034505 (2013).
19. Palmer, J. C., Car, R. & Debenedetti, P. G. The liquid–liquid transition in supercooled ST2 water: a comparison between umbrella sampling and well-tempered metadynamics. *Faraday Discuss.* **167**, 77–94 (2013).
20. Li, Y. P., Li, J. C. & Wang, F. Liquid–liquid transition in supercooled water suggested by microsecond simulations. *Proc. Natl Acad. Sci. USA* **110**, 12209–12212 (2013).
21. Overduin, S. D. & Patey, G. N. An analysis of fluctuations in supercooled TIP4P/2005 water. *J. Chem. Phys.* **138**, 184502 (2013).
22. Limmer, D. T. & Chandler, D. The putative liquid–liquid transition is a liquid–solid transition in atomistic models of water. *J. Chem. Phys.* **135**, 134503 (2011).
23. Limmer, D. T. & Chandler, D. The putative liquid–liquid transition is a liquid–solid transition in atomistic models of water. II. *J. Chem. Phys.* **138**, 214504 (2013).
24. Stillinger, F. H. & Rahman, A. Improved simulation of liquid water by molecular dynamics. *J. Chem. Phys.* **60**, 1545–1557 (1974).
25. Lee, J. Y. & Kosterlitz, J. M. New numerical method to study phase transitions. *Phys. Rev. Lett.* **65**, 137–140 (1990).
26. Moore, E. B. & Molinero, V. Ice crystallization in water's 'no-man's land'. *J. Chem. Phys.* **132**, 244504 (2010).
27. Steinhardt, P. J., Nelson, D. R. & Ronchetti, M. Bond-orientational order in liquids and glasses. *Phys. Rev. B* **28**, 784–805 (1983).
28. Shiratani, E. & Sasai, M. Molecular scale precursor of the liquid–liquid phase transition of water. *J. Chem. Phys.* **108**, 3264–3276 (1998).
29. Matsumoto, M., Saito, S. & Ohmine, I. Molecular dynamics simulation of the ice nucleation and growth process leading to water freezing. *Nature* **416**, 409–413 (2002).
30. Frenkel, D. & Smit, B. *Understanding Molecular Simulation: From Algorithms to Applications* 2nd edn (Academic, 2002).

Acknowledgements Computations were performed at the Terascale Infrastructure for Groundbreaking Research in Engineering and Science (TIGRESS) facility at Princeton University. P.G.D. acknowledges support from the National Science Foundation (CHE 1213343), A.Z.P. acknowledges support from the US Department of Energy (DE-SC0002128), and R.C. acknowledges support from the US Department of Energy (DE-SC0008626).

Author Contributions J.C.P., R.C., A.Z.P. and P.G.D. planned the study. J.C.P., Y.L. and F.M. performed the simulations and numerical data analysis. J.C.P. and P.G.D. wrote the main paper and methods information. All authors discussed the results and commented on the manuscript at each stage.

Author Information Reprints and permissions information is available at www.nature.com/reprints. The authors declare no competing financial interests. Readers are welcome to comment on the online version of the paper. Correspondence and requests for materials should be addressed to P.G.D. (pdebene@princeton.edu).

METHODS

General sampling protocol. MC simulations in the isothermal-isobaric ensemble employing collective, N -particle smart MC moves³¹ were used to investigate the low-temperature phase behaviour of the ST2 water model²⁴, modified for compatibility with the Ewald treatment for long-range electrostatic interactions^{17,32}. The ρ - Q_6 range relevant to each phase under consideration was explored systematically using windowed umbrella sampling^{30,33}. The parameter space was divided into overlapping windows. Independent MC simulations were performed in each window, restricting sampling to the target region with a harmonic restraint:

$$W(r^N) = \frac{k_p}{2} [\rho(r^N) - \rho^*]^2 + \frac{k_{Q_6}}{2} [Q_6(r^N) - Q_6^*]^2 \quad (1)$$

where r^N is the vector describing the microscopic coordinates of the N -particle system, k_p and k_{Q_6} are spring constants, and parameters ρ^* and Q_6^* specify the window's centre. Values ranging from $5,000k_B T$ to $10,000k_B T$ ($\text{cm}^6 \text{g}^{-2}$) and from $2,000k_B T$ to $6,000k_B T$ for k_p and k_{Q_6} , respectively, proved sufficient to ensure that the simulations sampled in the vicinity of their target window. Technical details regarding the basic MC algorithm, implementation of the ST2 water model, and definition and calculation of Q_6 are described in ref. 19.

Free-energy analysis. Time series data were collected for ρ and Q_6 in each umbrella window during the post-equilibration, production phase of the MC simulations. The data were subsequently re-sampled with an interval equal to the maximum statistical inefficiency in each window, $g \equiv 1 + 2 \times \max(\tau_\rho, \tau_{Q_6})$, where τ_ρ and τ_{Q_6} are the integrated autocorrelation times associated with ρ and Q_6 , respectively. The relaxation times for each observable were typically found to be comparable in magnitude (that is, $\tau_\rho \approx \tau_{Q_6}$), including within sampling windows in the vicinity of the LDL basin. Two-dimensional ρ - Q_6 histograms were generated from the uncorrelated time series data and subsequently combined using the weighted histogram analysis method of Kumar *et al.*³⁴ to produce an unbiased estimate of the free energy, $F(\rho, Q_6) = -k_B T \ln[\varphi(\rho, Q_6)]$, where φ is the microstate probability distribution. Points of liquid-liquid coexistence, where the LDL and HDL basins have equal depths, were located by reweighting in pressure¹⁷:

$$F(\rho, Q_6; p + \Delta p, T) = F(\rho, Q_6; p, T) + \Delta p N / \rho \quad (2)$$

where Δp is the pressure shift. Uncertainties in $F(\rho, Q_6; p + \Delta p, T)$ were estimated from the variance computed from 500 resampled ρ - Q_6 free-energy surfaces generated using the Bayesian bootstrap technique described by Hub *et al.*³⁵. This technique has been shown to provide robust error estimates even in extreme cases where the sampling duration is limited to timescales on the order of the characteristic relaxation time of the biased observable³⁵.

Computing the three-phase diagram. Umbrella sampling MC simulations of 192 ST2 water molecules at 228.6 K and 2.2 kbar were used to compute the reversible free-energy surface in Fig. 1. The high-density region ($\rho \geq 0.98 \text{ g cm}^{-3}$) was sampled by performing independent simulations in 27 density windows in the range $0.98 \text{ g cm}^{-3} \leq \rho^* \leq 1.24 \text{ g cm}^{-3}$ using a spacing of 0.01 g cm^{-3} and $Q_6^* = 0.05$. Simulations in the low-density region ($\rho < 0.98 \text{ g cm}^{-3}$) were carried out in four density windows, namely $\rho^* = 0.91, 0.93, 0.95$ and 0.97 g cm^{-3} . Sampling along Q_6 was enhanced at each of the four target densities using Hamiltonian exchange MC moves³⁶, in which attempts were made to swap parameters k_{Q_6} and Q_6^* between replicas in neighbouring Q_6 windows. Two independent sets of replicas were used for each value of ρ^* in the low-density region. The first set comprised 16 replicas evenly distributed over the range $0.02 \leq Q_6^* \leq 0.17$, and 32 replicas were used in the second group to span the interval $0.16 \leq Q_6^* \leq 0.625$. Exchange attempts were made between even or odd numbered replica pairs with equal probability once every 200 MC moves on average.

Simulations were equilibrated for $\sim 10^4 \tau_{Q_6}$ in each sampling window. Density, Q_6 and the configurational energy were carefully monitored for drift to verify that each simulation had completely equilibrated by the end of this period. Bi-directional sampling between the LDL and ice phase was also performed to serve as an additional check for equilibration in the low-density region. The first generation of simulations was seeded using initial configurations extracted from a trajectory of the LDL freezing into ice Ic, and the second generation was initialized with configurations taken from a melting trajectory. The freezing and melting trajectories were produced by applying a strong umbrella bias to accelerate the phase transition process³⁷. After equilibration, data collection was performed in each window for $\sim 10^4 \tau_{Q_6}$. Histograms generated using data collected from the two generations of simulations in the low-density region were compared to explicitly check for reversibility. The absence of hysteresis confirmed that the simulations were properly equilibrated and sampling the reversible ρ - Q_6 free-energy surface.

Finite-size scaling. Umbrella sampling calculations for $N = 192, 300, 400$ and 600 ST2 water molecules were performed in the low- Q_6 region, using 35 evenly distributed density windows in the range $0.90 \text{ g cm}^{-3} \leq \rho^* \leq 1.24 \text{ g cm}^{-3}$. Simulations in each window were equilibrated for at least $10^2 \tau_{Q_6}$, followed by a production phase of

similar duration. Comparison of the results for $N = 192$ with the more extensive calculations used to generate Fig. 1 provided verification that the sampling duration and explored range of Q_6 were sufficient to accurately reproduce the low- Q_6 portion of the free-energy surface. For each system size considered, the height of the barrier separating the liquids was computed at coexistence from the free energy profile along ρ :

$$F(\rho) = -k_B T \ln \left(\int \exp[-\beta F(\rho, Q_6)] dQ_6 \right) \quad (3)$$

where $\beta = (k_B T)^{-1}$.

Unconstrained sampling. The ρ - Q_6 free-energy surface in Fig. 3 was computed by performing long, unbiased MC simulations of 192 ST2 water molecules at the estimated point of liquid-liquid coexistence (228.6 K and 2.4 kbar). Equilibrated HDL and LDL configurations extracted from umbrella sampling calculations were used to initialize eight independent simulations in the vicinity of each liquid basin. The unbiased simulations were run for two orders of magnitude longer than the integrated Q_6 autocorrelation time in the LDL region. Time series data collected over the duration of each MC simulation were analysed, as described above, to compute free energy.

Analysis of local structure index and topological rings. The LSI²⁸ is an order parameter sensitive to heterogeneity in water's coordination shell capable of distinguishing between molecular configurations characteristic of HDL, LDL and ice. The free-energy surface parameterized by the first moment of the molecular LSI distribution, \bar{I} , and Q_6 was computed from time series data generated by analysing saved trajectories from the long umbrella sampling simulations used to construct Fig. 1. The uncorrelated data were subsequently re-weighted^{38,39} to remove the bias, generating the final estimate of $F(\bar{I}, Q_6)$ shown in Fig. 4. A 0.37-nm cutoff based on the O-O separation distance between neighbouring water molecules was used in the calculation of \bar{I} . Additional details regarding the definition and calculation of \bar{I} may be found in ref. 28. Ring statistics based on King's criteria⁴⁰ were computed from saved trajectories at selected points along the HDL-LDL and LDL-ice paths, applying a 0.35-nm oxygen-based cutoff to determine topological connectivity between adjacent water molecules.

Consistency among sampling methods. To verify that our results withstand critical scrutiny, we have studied the dependence of the free-energy surface on sampling duration and methodology, computing the ρ - Q_6 free-energy surface at 228.6 K and 2.4 kbar using several state-of-the-art computational techniques. Extended Data Table 1 lists the methods we have used, along with τ_ρ and τ_{Q_6} computed in the LDL basin, and the sampling duration in each umbrella window. Four and sixteen identical simulation replicas were used in the well-tempered metadynamics⁴¹ and unconstrained MC calculations, respectively, with each replica being run for the reported duration.

The free-energy surfaces computed using the different sampling methods are shown in Extended Data Fig. 1. In each case we find two coexisting liquids separated by a $\sim 4k_B T$ free-energy barrier, demonstrating that such results are independent of sampling technique. Extended Data Fig. 1 also demonstrates that the results are devoid of non-equilibrium artefacts. Limmer and Chandler²³ have suggested that the LDL basin is such an artefact associated with the sluggish dynamics of ice coarsening, and consequently it was posited that the LDL basin should progressively age as the sampling duration increases, until it eventually vanishes at $\sim 10^2 \tau_{Q_6}$ (ref. 23). In contrast, we do not observe significant changes even when the sampling duration is increased by two orders of magnitude from 10^2 to $10^4 \tau_{Q_6}$. As shown in Extended Data Fig. 1, the techniques that yield such satisfyingly consistent free-energy surfaces include the hybrid MC sampling method⁴² employed by Limmer and Chandler²³. Figure 1 shows that consistent results are obtained even when reversible sampling is performed between the LDL and ice Ic basins. Finally, our results are qualitatively consistent with free-energy calculations employing different variants of the ST2 water model¹⁸, microsecond-long MD trajectories exhibiting abrupt and infrequent transitions between HDL and LDL^{17,43}, and previous finite-size scaling studies⁴³.

Limmer and Chandler²³ have proposed a theory of artificial polymorphism, which posits that a purported separation of timescales between density and structural relaxations (that is, $\tau_{Q_6} \gg \tau_\rho$) gives rise to an illusory LDL basin associated with the coarsening of ice. To scrutinize this prediction, we examined the density and Q_6 autocorrelation functions computed in the LDL region, using the various sampling techniques employed in our study. Extended Data Fig. 2 shows representative autocorrelation functions for three of the sampling techniques. Whereas the density and Q_6 autocorrelation functions exhibit transient behaviour at short times where they are separated by more than one order of magnitude, Extended Data Fig. 2 clearly shows that such short-time behaviour is sensitive to the sampling technique and therefore does not provide a physically meaningful description of the coupling between density and structural relaxations in the system. For each sampling technique, we find that density and Q_6 fluctuations decay in tandem at long times. It is this technique-independent, long-time behaviour that is relevant to sampling the physical properties of the system. Hence, our results demonstrate that Limmer and Chandler's theory²³

can only be justified if the long-time behaviour is completely neglected by defining the relaxation time, for instance, as $C(\tau) = e^{-\tau}$. Although this definition can in general be used to estimate τ , a more careful analysis is required when comparing correlation functions that are decoupled at shorter times but invariably decay together at long times. The physically relevant long-time behaviour may be captured by using a different metric such as the integrated autocorrelation time. Using this definition, we find that $\tau_p \approx \tau_{Q_c}$ for each sampling method listed in Extended Data Table 1. Moreover, by re-sampling our data using an interval equal to the maximum statistical inefficiency in each window, $g \equiv 1 + 2 \times \max(\tau_p, \tau_{Q_c})$, we have excluded the possibility that transient, short-time correlations are embedded in the free-energy surfaces shown in Extended Data Fig. 1 and Figs 1 and 3. We also do not observe significant changes in the free-energy surface shown in Fig. 1 even when the data are re-sampled using an interval of 10^6 g. Consequently, the presence of a LDL basin cannot be attributed to finite-time artefacts associated with transient behaviour occurring on timescales that are orders of magnitude shorter than the sampling interval.

Thermodynamic consistency. The free-energy surface in Fig. 1 shows that the coexisting liquids are metastable with respect to ice Ic at 228.6 K and 2.4 kbar, with the ice phase being lower in free energy by $\sim 75k_B T$ (in extensive units for $N = 192$) or, equivalently, $\Delta G_{\text{Ic-L}} = -742 \text{ J mol}^{-1}$. In contrast, Limmer and Chandler's²³ free energy calculations predict ice Ic–liquid coexistence at a nearby state condition (230 K and 2.6 kbar) for the same variant of the ST2 water model (see the middle column in Fig. 13 of ref. 23). To resolve this significant discrepancy, we have used thermodynamic integration (TI) along with an empirical equation of state (EEOs) parameterized to reproduce the experimental properties of water and ice^{44,45}, to estimate $\Delta G_{\text{Ic-L}}$ under comparable state conditions for water (thus allowing us to subject both our results and those of Limmer and Chandler²³ to thermodynamic scrutiny); and to estimate the melting temperature for the ST2 model at 2.6 kbar (thus allowing us to test the very different predictions for the equilibrium melting temperature of ice Ic at 2.6 kbar in the ST2 model).

Thermodynamic integration was performed using the identity

$$\Delta G_{\text{Ic-L}}(P, T) \equiv \Delta G_{\text{Ih-L}}(P, T) + \Delta G_{\text{Ic-Ih}}(P, T) \quad (4)$$

where subscripts Ic, Ih and L denote ice Ic, ice Ih and the liquid phase, respectively. Two levels of TI were considered for evaluating $\Delta G_{\text{Ih-L}}(P, T)$:

(i) A simple linear extrapolation (LE) using experimental data for the specific volume ($\Delta V_{0,\text{Ih-L}}^m$) and entropy ($\Delta S_{0,\text{Ih-L}}^m$) change upon melting for ice Ih at 1 bar:

$$\Delta G_{\text{Ih-L}}(P, T) = \Delta V_{0,\text{Ih-L}}^m (P - P_{0,\text{Ih}}^m) - \Delta S_{0,\text{Ih-L}}^m (T - T_{0,\text{Ih}}^m), \quad (5)$$

where $P_{0,\text{Ih}}^m = 1 \text{ bar}$ and $T_{0,\text{Ih}}^m$ is the melting temperature at 1 bar.

(ii) The empirical equation of state (EEOs) developed in refs 44, 45, which is applicable over the ranges 0–22 kbar and 175–360 K and accurately describes the phase behaviour of liquid water and several ice polymorphs, including ice Ih.

The difference in free energy between ices Ic and Ih, $\Delta G_{\text{Ic-Ih}}$, was calculated from experimental vapour pressure data for these ice phases⁴⁶ and the enthalpy difference, $\Delta H_{\text{Ic-Ih}}$, measured by calorimetry^{47–50}. The ice phases were assumed to be incompressible, which is justified by the fact that their specific volumes are relatively insensitive to pressure^{44,45}. Because the ST2 water model is over-structured in comparison with real water, it has a melting temperature $T_{0,\text{Ih}}^{\text{m,ST2}} \approx 300 \text{ K}$ for ice Ih at 1 bar (ref. 51), which is significantly higher than $T_{0,\text{Ih}}^m$ for water⁴⁴. Two different approaches were used to account for this behaviour:

(i) A melting temperature of $T_{0,\text{Ih}}^{\text{m,ST2}} = T_{0,\text{Ih}}^m$ was assumed for ice Ih at 1 bar.

(ii) Thermodynamic integration calculations were performed at the same supercooling, $\Delta T^{\text{sc}} \equiv T_{0,\text{Ih}}^m - T$, with respect to the melting temperature of ice Ih at 1 bar.

Our simulations at 228.6 K, for example, were conducted at a supercooling of $\Delta T^{\text{sc}} = 71.4 \text{ K}$ with respect to $T_{0,\text{Ih}}^{\text{m,ST2}}$. In the second approach, the TI was therefore performed from $T_{0,\text{Ih}}^m = 273.15 \text{ K}$ to $T = T_{0,\text{Ih}}^m - \Delta T^{\text{sc}} = 201.75 \text{ K}$ to achieve the same supercooling for real water.

Extended Data Table 2 shows the values of $\Delta G_{\text{Ic-L}}$ predicted by LE and the EEOs for water, along with our $\Delta G_{\text{Ic-L}}$ calculation for the ST2 model at 228.6 K and 2.4 kbar obtained from Fig. 1. Although LE predicts the largest $\Delta G_{\text{Ic-L}}$ due to the assumption of incompressibility, it provides a reasonable order-of-magnitude estimate for this quantity. The more accurate EEOs, which accounts for the changes in the thermodynamic response functions of the liquid as a function of T and P , predicts that $\Delta G_{\text{Ic-L}}$ is smaller by a factor of 2 than the estimate obtained using LE. Because the ice phase produced by freezing LDL contains natural imperfections, the predicted $\Delta G_{\text{Ic-L}}$ for ST2 underestimates the difference in free energy that would be computed using an ideal ice Ic crystal prepared by artificial means. Defects in the crystal may also arise because the number of molecules in our simulations is not commensurate with a cubic supercell of ice Ic. Despite such defects, however, we find that our $\Delta G_{\text{Ic-L}}$ value for the ST2 model is in reasonable agreement with the thermodynamic analysis, regardless of the approach used to compute or to assign the reference temperature in

the equation-of-state calculations. In contrast, Extended Data Table 3 shows that Limmer and Chandler's simulations²³, purportedly for the same ST2 variant and at a nearby state condition (2.2 kbar and 230 K), predict that $\Delta G_{\text{Ic-L}}$ is an order of magnitude smaller than the values calculated by TI using LE and the EEOs. In fact, we find similar disagreement between the TI calculations and the $\Delta G_{\text{Ic-L}}$ values estimated from the free-energy surfaces reported by Limmer and Chandler^{22,23}, even for the other ST2 variants considered in their studies.

Limmer and Chandler²³ observed ice Ic–liquid coexistence (that is, $\Delta G_{\text{Ic-L}}^{\text{ST2}} \approx 0$) at 230 K and 2.6 kbar for the same variant of the ST2 water model examined in our study (see the middle column of Fig. 13 in ref. 23). Reweighting the free-energy surface shown in Fig. 1 in pressure and using the HDL as a reference, we find $\Delta G_{\text{Ic-L}}^{\text{ST2}} \approx -705 \text{ J mol}^{-1}$ at 228.6 K at 2.6 kbar. This value for $\Delta G_{\text{Ic-L}}^{\text{ST2}}$ was used along with LE and the EEOs to predict the melting temperature of ice Ic for the ST2 water model ($T_{\text{Ic}}^{\text{m,ST2}}$), providing an estimate of temperature at which our simulations should be performed to find ice Ic–liquid coexistence at 2.6 kbar. Starting from the initial temperatures (T_1) listed in Extended Data Table 2, the LE and EEOs expressions for $\Delta G_{\text{Ic-L}}$ were integrated at 2.6 kbar to find the temperature, T_2 , satisfying

$$\int_{T_1}^{T_2} \left(\frac{\partial \Delta G_{\text{Ic-L}}}{\partial T} \right)_P dT = \int_{228.6 \text{ K}}^{T_{\text{Ic}}^{\text{m,ST2}}} \left(\frac{\partial \Delta G_{\text{Ic-L}}^{\text{ST2}}}{\partial T} \right)_P dT = 705 \text{ J mol}^{-1} \quad (6)$$

We note that T_1 and T_2 are either defined with respect to ST2's melting temperature for ice Ih at 1 bar (that is, $T_{0,\text{Ih}}^{\text{m,ST2}}$), or the supercooling, ΔT^{sc} , as described above. Thus, $T_{\text{Ic}}^{\text{m,ST2}} \approx T_2$ for calculations performed using $T_{0,\text{Ih}}^m = T_{0,\text{Ih}}^{\text{m,ST2}}$, whereas $T_{\text{Ic}}^{\text{m,ST2}} \approx T_2 + (T_{0,\text{Ih}}^{\text{m,ST2}} - T_{0,\text{Ih}}^m)$ for the latter scenario, where $T_{0,\text{Ih}}^{\text{m,ST2}} - T_{0,\text{Ih}}^m$ is the difference between the melting temperature of ice Ih at 1 bar for the ST2 model and real water.

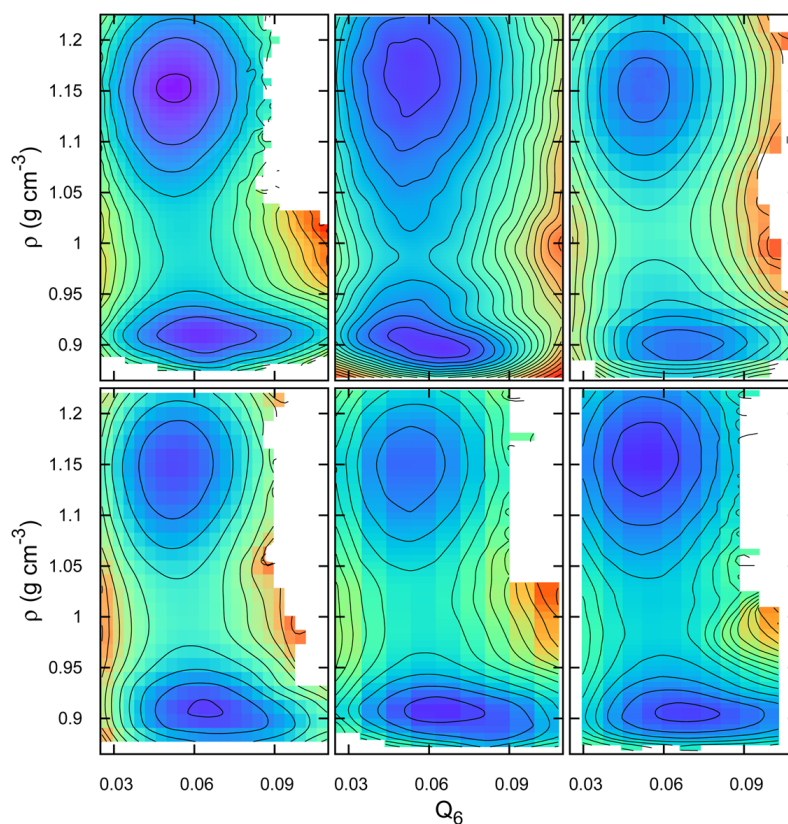
Extended Data Table 4 lists the estimates of $T_{\text{Ic}}^{\text{m,ST2}}$ at 2.6 kbar obtained using the same procedures and reference temperatures as those reported in Extended Data Table 2. The LE predicts $T_{\text{Ic}}^{\text{m,ST2}} \approx 260 \text{ K}$, whereas calculations with the more accurate EEOs estimate $T_{\text{Ic}}^{\text{m,ST2}}$ in the range 272–276 K at 2.6 kbar. To confirm these predictions, we computed $T_{\text{Ic}}^{\text{m,ST2}}$ directly from simulation, using two different techniques. In the first approach, $T_{\text{Ic}}^{\text{m,ST2}}$ was determined using two-phase, ice Ic–liquid (N_{Ic}, T) MC simulations³⁰, imposing a pressure of 2.6 kbar in the direction perpendicular to the ice Ic–liquid interface. Extended Data Fig. 3 shows the time evolution of the crystalline order parameter, Q_6 , for simulations performed at different temperatures near the $T_{\text{Ic}}^{\text{m,ST2}}$ value predicted by the EEOs. Below 270 K, the simulations exhibited a gradual drift towards higher values of Q_6 , indicating that the system was freezing. Similarly, Q_6 decreased for simulations performed above 275 K because of the melting of ice. Our estimate of the melting temperature is therefore the average of these temperatures, $T_{\text{Ic}}^{\text{m,ST2}} \approx 273 \pm 3 \text{ K}$ at 2.6 kbar, which is in excellent agreement with the range 272–276 K predicted using the EEOs. We also computed the ρ – Q_6 free-energy surface at 275 K and 2.2 kbar for $N = 216$ ST2 water molecules using the umbrella sampling procedure described above. Extended Data Fig. 4 shows the resulting ρ – Q_6 free-energy surface after reweighting in pressure using equation (2) to locate the point of ice Ic–liquid coexistence, 275 K and ~ 2.7 kbar. As Extended Data Table 4 shows, this result is in excellent agreement with our thermodynamic calculations using the EEOs and interfacial simulations. Such values are 30–46 K higher than the $T_{\text{Ic}}^{\text{m,ST2}}$ predicted by Limmer and Chandler at the same pressure²³, demonstrating that those free-energy calculations are inconsistent with reasonable thermodynamic expectations based on accurate equations of state for real water and the established physical properties of the ST2 water model.

We have shown that the free-energy surface shown in Fig. 1 is consistent with expectations based on thermodynamic arguments. This is demonstrated by the fact that our estimate of $\Delta G_{\text{Ic-L}}$ for the ST2 model at 228.6 K and 2.4 kbar is in good agreement with calculations performed using the accurate EEOs for water. In addition, we have also demonstrated thermodynamic consistency by using the EEOs along with our $\Delta G_{\text{Ic-L}}^{\text{ST2}}$ value at 228.6 and 2.6 kbar to predict $T_{\text{Ic}}^{\text{m,ST2}} \approx 272$ –276 K. This prediction was verified by performing simulations of the ice Ic–liquid interface and umbrella sampling calculations. Such results demonstrate conclusively that $T_{\text{Ic}}^{\text{m,ST2}}$ at ~ 2.6 kbar is ~ 40 –45 K higher than reported by Limmer and Chandler²³. It therefore seems that their free-energy surface (middle column of Fig. 13 in ref. 23) is distorted to such an extent that the output of their simulations corresponds to an effectively higher temperature. To observe ice Ic–liquid coexistence at 2.6 kbar, as reported by Limmer and Chandler²³, this effective temperature would have to be well above the estimated liquid–liquid critical temperature ($T_c \approx 237 \text{ K}$ for our model³²) for any reasonable variant of the ST2 water model, explaining the absence of a LDL basin in their free-energy surfaces²³. Because the two liquids are only separated by a $\sim 4k_B T$ barrier at 228.6 K and 2.4 kbar, the free-energy surface must be accurately computed to observe the LDL basin. At odds with this requirement, we find a $\sim 70k_B T$ discrepancy between our respective estimates for $\Delta G_{\text{Ic-L}}$ near 228.6 K and 2.6 kbar, which cannot simply be dismissed as non-equilibrium artefacts, as suggested by Limmer and Chandler^{22,23}. Although the precise numerical origin of this discrepancy

is still under investigation, we showed above (see the section on Consistency among sampling methods, and Extended Data Fig. 1) that liquid–liquid coexistence is observed when we perform free-energy calculations using the hybrid MC technique⁴² employed by Limmer and Chandler²³. In our hybrid MC implementation we use the molecular dynamics integrator of Miller *et al.*⁵², whereas Limmer and Chandler²³ employed the constraint algorithm SETTLE⁵³ to simulate rigid ST2 water molecules. Although we have not yet implemented this integrator, Reinhardt *et al.*³⁷ recently observed ‘catastrophic’ divergence from the well-established equation of state for the TIP4P/2005 water model when hybrid MC simulations were performed with SETTLE. A more comprehensive discussion of the different perspectives regarding the liquid–liquid phase transition in ST2 water, computational approaches and related studies has recently been published^{19,54}.

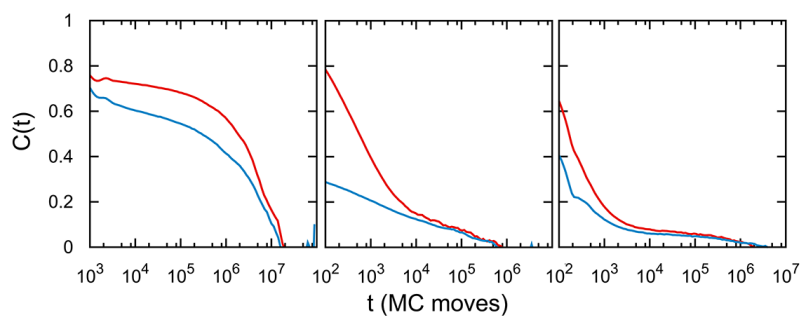
As a final check, we followed the procedure described by Hunter and Reinhardt⁵⁵ to estimate the liquid–liquid surface tension, $\gamma_{\text{L-L}}$, from our finite-size scaling data. We find that $\gamma_{\text{L-L}} \approx 2 \text{ mJ m}^{-2}$, which is comparable to vapour–liquid surface tensions for various water models⁵⁶ at similar reduced temperatures near the vapour–liquid critical point (that is, $\gamma_{\text{V-L}} \approx 5.6\text{--}1.5 \text{ mJ m}^{-2}$ for $T/T_c \approx 0.95\text{--}0.98$), and an order of magnitude smaller than the $\gamma_{\text{Ih-L}} \approx 23 \text{ mJ m}^{-2}$ reported by Handel *et al.*⁵⁷ for the ice Ih–liquid surface tension in TIP4P. Thus, the small value of $\gamma_{\text{L-L}}$ is thermodynamically consistent with our observation that two liquids are forming an interface, not a liquid and a coarsening crystal, and with the fact that our simulations are performed relatively close to the estimated liquid–liquid critical point at a reduced temperature of $T/T_c \approx 0.96$.

31. Rossky, P. J., Doll, J. D. & Friedman, H. L. Brownian dynamics as smart Monte Carlo simulation. *J. Chem. Phys.* **69**, 4628–4633 (1978).
32. Liu, Y., Panagiotopoulos, A. Z. & Debenedetti, P. G. Low-temperature fluid-phase behavior of ST2 water. *J. Chem. Phys.* **131**, 104508 (2009).
33. Torrie, G. M. & Valleau, J. P. Nonphysical sampling distributions in Monte Carlo free-energy estimation: umbrella sampling. *J. Comput. Phys.* **23**, 187–199 (1977).
34. Kumar, S., Bouzida, D., Swendsen, R. H., Kollman, P. A. & Rosenberg, J. M. The weighted histogram analysis method for free-energy calculations on biomolecules. 1. The method. *J. Comput. Chem.* **13**, 1011–1021 (1992).
35. Hub, J. S., de Groot, B. L. & van der Spoel, D. g_wham: a free weighted histogram analysis implementation including robust error and autocorrelation estimates. *J. Chem. Theory Comput.* **6**, 3713–3720 (2010).
36. Sugita, Y. & Okamoto, Y. Replica-exchange molecular dynamics method for protein folding. *Chem. Phys. Lett.* **314**, 141–151 (1999).
37. Reinhardt, A., Doye, J. P. K., Noya, E. G. & Vega, C. Local order parameters for use in driving homogeneous ice nucleation with all-atom models of water. *J. Chem. Phys.* **137**, 194504 (2012).
38. Bonomi, M., Barducci, A. & Parrinello, M. Reconstructing the equilibrium boltzmann distribution from well-tempered metadynamics. *J. Comput. Chem.* **30**, 1615–1621 (2009).
39. Gee, J. & Shell, M. S. Two-dimensional replica exchange approach for peptide-peptide interactions. *J. Chem. Phys.* **134**, 064112 (2011).
40. King, S. V. Ring configurations in a random network model of vitreous silica. *Nature* **213**, 1112–1113 (1967).
41. Barducci, A., Bussi, G. & Parrinello, M. Well-tempered metadynamics: a smoothly converging and tunable free-energy method. *Phys. Rev. Lett.* **100**, 020603 (2008).
42. Duane, S., Kennedy, A. D., Pendleton, B. J. & Roweth, D. Hybrid Monte Carlo. *Phys. Lett. B* **195**, 216–222 (1987).
43. Kesselring, T. A. *et al.* Finite-size scaling investigation of the liquid–liquid critical point in ST2 water and its stability with respect to crystallization. *J. Chem. Phys.* **138**, 244506 (2013).
44. Choukroun, M. & Grasset, O. Thermodynamic model for water and high-pressure ices up to 2.2 GPa and down to the metastable domain. *J. Chem. Phys.* **127**, 124506 (2007).
45. Choukroun, M. & Grasset, O. Thermodynamic data and modeling of the water and ammonia–water phase diagrams up to 2.2 GPa for planetary geophysics. *J. Chem. Phys.* **133**, 144502 (2010).
46. Shilling, J. E. *et al.* Measurements of the vapor pressure of cubic ice and their implications for atmospheric ice clouds. *Geophys. Res. Lett.* **33**, L17801 (2006).
47. Mayer, E. & Hallbrucker, A. Cubic ice from liquid water. *Nature* **325**, 601–602 (1987).
48. Yamamuro, O., Oguni, M., Matsuo, T. & Suga, H. Heat capacity and glass transition of pure and doped cubic ices. *J. Phys. Chem. Solids* **48**, 935–942 (1987).
49. Handa, Y. P., Klug, D. D. & Whalley, E. Difference in energy between cubic and hexagonal ice. *J. Chem. Phys.* **84**, 7009–7010 (1986).
50. Mcmillan, J. A. & Los, S. C. Vitreous ice: irreversible transformations during warm-up. *Nature* **206**, 806–807 (1965).
51. Weber, T. A. & Stillinger, F. H. Pressure melting of ice. *J. Chem. Phys.* **80**, 438–443 (1984).
52. Miller, T. F. *et al.* Symplectic quaternion scheme for biophysical molecular dynamics. *J. Chem. Phys.* **116**, 8649–8659 (2002).
53. Miyamoto, S. & Kollman, P. A. SETTLE: an analytical version of the SHAKE and RATTLE algorithm for rigid water models. *J. Comput. Chem.* **13**, 952–962 (1992).
54. Palmer, J. C. General discussion. *Faraday Discuss.* **167**, 118–127 (2013).
55. Hunter, J. E. & Reinhardt, W. P. Finite-size scaling behavior of the free energy barrier between coexisting phases: determination of the critical temperature and interfacial tension of the Lennard–Jones fluid. *J. Chem. Phys.* **103**, 8627–8637 (1995).
56. Vega, C. & de Miguel, E. Surface tension of the most popular models of water by using the test-area simulation method. *J. Chem. Phys.* **126**, 154707 (2007).
57. Handel, R., Davidchack, R. L., Anwar, J. & Brukhno, A. Direct calculation of solid–liquid interfacial free energy for molecular systems: TIP4P ice–water interface. *Phys. Rev. Lett.* **100**, 036104 (2008).



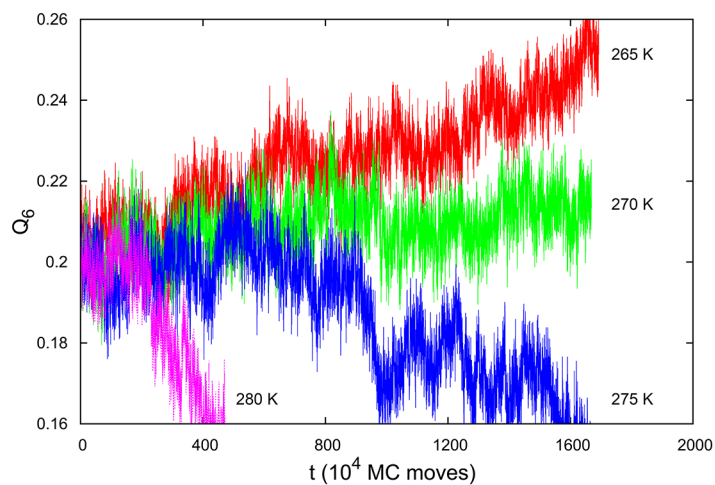
Extended Data Figure 1 | Reversible free-energy surfaces at 228.6 K and 2.4 kbar computed using different sampling techniques. Surfaces on the top row were computed using (from left to right) umbrella sampling MC, well-tempered metadynamics and unconstrained MC; the bottom row shows results

from hybrid MC, parallel tempering MC and Hamiltonian exchange MC simulations. The free-energy barrier separating the liquid basins is $\sim 4k_B T$ for all of the surfaces shown. Contours are $1k_B T$ apart and uncertainties are estimated to be less than $0.5k_B T$.



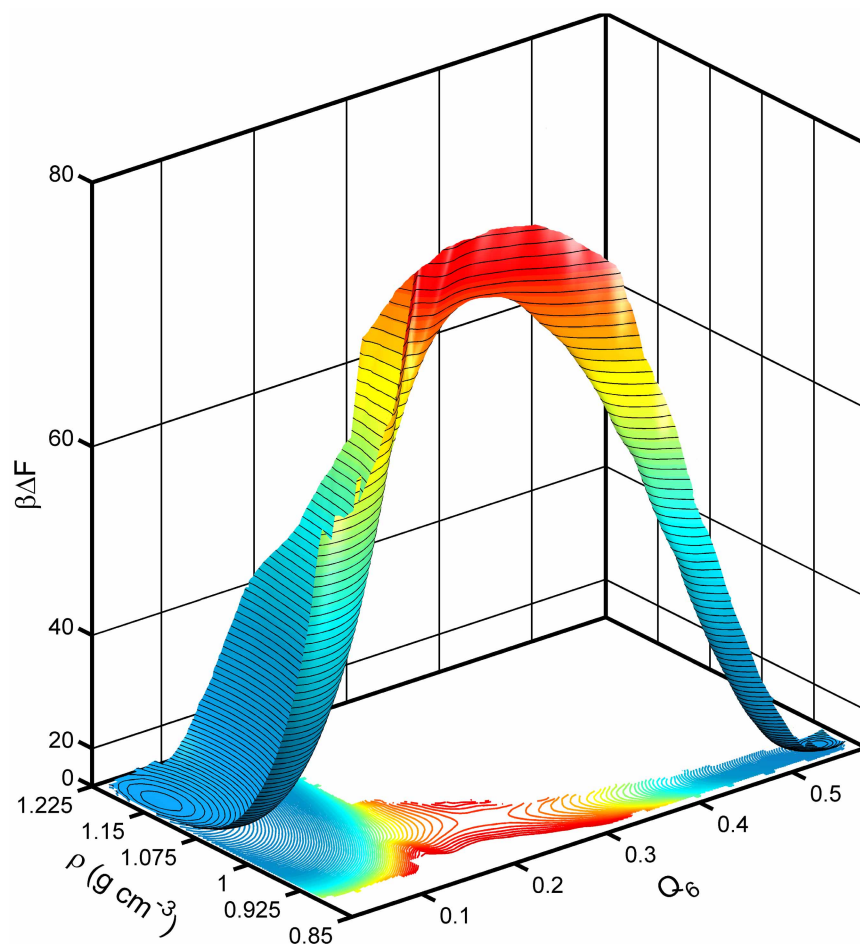
Extended Data Figure 2 | Autocorrelation functions for different sampling techniques. Autocorrelation functions for density (blue) and Q_6 (red) computed in the LDL region using unconstrained MC (left), hybrid MC (centre) and Hamiltonian exchange MC (right). The correlation functions were

calculated by averaging results from at least 12 independent simulations. Density and Q_6 fluctuations decay on very similar timescales, despite exhibiting technique-dependent transient behaviour where these processes may be separated by more than one order of magnitude.



Extended Data Figure 3 | Time evolution of the crystalline order parameter in two-phase MC simulations of the ice Ic–liquid interface at 2.6 kbar. The MC simulations were initiated from configurations containing 512 and 670 ST2 water molecules in the ice Ic and liquid phases, respectively. The x and y dimensions of the simulation cells were fixed in accord with the lattice constant for ice Ic, which was determined at each temperature by performing a separate

calculation for the bulk ice phase, while the z dimension was allowed to fluctuate so as to impose a constant pressure of 2.6 kbar perpendicular to the ice–liquid interface. Drift of Q_6 towards higher or lower values indicates that the system is freezing or melting. The melting temperature of 273 ± 3 K at 2.6 kbar was estimated by averaging the lowest and highest temperatures, respectively, at which melting and freezing were observed.



Extended Data Figure 4 | Reversible free-energy surface at 275 K and 2.7 kbar demonstrating ice Ic–liquid coexistence. The liquid and ice Ic basins have equal depths with respect to the saddle point, indicating that the reported state condition is a point of coexistence. Such results confirm the estimates of

the melting temperature for ice Ic at 2.6 kbar obtained from TI calculations using the EEOS and the two-phase MC simulations of the ice–liquid interface. Contours are $1k_B T$ apart.

Extended Data Table 1 | Sampling methods

Method	τ_ρ , τ_{Q_6} (MC moves)	Sampling duration (τ_{Q_6})
Umbrella sampling MC ^{30,*}	5×10^5 , 5×10^5	10^2
Well-tempered Metadynamics ^{41,*†}	5×10^5 , 5×10^5	10^2
Unconstrained MC [*]	10^6 , 10^6	10^2
Hybrid MC ⁴² + Umbrella Sampling [‡]	10^4 , 10^4	5×10^3
Parallel tempering MC ³⁰ + Umbrella Sampling ^{*,§,}	10^4 , 10^4	$\sim 10^4$
Hamiltonian exchange MC ³⁰ + Umbrella Sampling ^{*,}	10^4 , 10^4	$\sim 10^4$

* Collective, smart MC³¹ moves used.

† Relaxation times estimated from unbiased simulations using the same types of MC moves.

‡ Rigid body integrator of Miller *et al.*⁵²; ~ 10 molecular dynamics integration steps per MC move.

§ Eight replicas spaced between 228.6 and 272 K.

|| Bi-directional sampling performed between the LDL and crystal to ensure reversibility.

State-of-the-art sampling methods used to perform free-energy analysis, along with integrated autocorrelation times for density and the crystalline order parameter Q_6 (τ_ρ and τ_{Q_6} , respectively) computed in the LDL basin at 228.6 K and 2.4 kbar, and the sampling duration in each umbrella sampling window given in terms of τ_{Q_6} .

Extended Data Table 2 | Comparison of ice Ic–liquid free-energy differences obtained from thermodynamic integration and from results presented in the text for the ST2 model

Reference temperature	$\Delta G_{\text{ic-L}}^{\text{LE}}$ (J mol ^{−1})	$\Delta G_{\text{ic-L}}^{\text{EEOS}}$ (J mol ^{−1})	$\Delta G_{\text{ic-L}}^{\text{ST2}}$ (J mol ^{−1})
$T_{0,\text{lh}}^{\text{m}} = T_{0,\text{lh}}^{\text{m, ST2}}$	-1095	-505	-742
$\Delta T^{\text{sc}} = 71.4 \text{ K}$	-1091	-604	-742

Ice Ic–liquid free-energy differences ($\Delta G_{\text{ic-L}}$) predicted by LE and the EEOS for water are in good agreement with the $\Delta G_{\text{ic-L}}$ value calculated for the ST2 model at 228.6 K and 2.4 kbar from the data presented in Fig. 1. The TI calculations using LE and the EEOS were performed using two different reference temperatures (described in Methods) to account for ST2’s over-structured nature in comparison with real water.

Extended Data Table 3 | Comparison of ice Ic–liquid free-energy differences obtained from thermodynamic integration and from results presented by Limmer and Chandler²³ for the ST2 water model

Reference temperature	$\Delta G_{\text{ic-L}}^{\text{LE}}$ (J mol ⁻¹)	$\Delta G_{\text{ic-L}}^{\text{EEOs}}$ (J mol ⁻¹)	$\Delta G_{\text{ic-L}}^{\text{ST2}^*}$ (J mol ⁻¹)
$T_{0,\text{lh}}^{\text{m}} = T_{0,\text{lh}}^{\text{m,ST2}}$	-1077	-537	-66
$\Delta T^{\text{sc}} = 70.0 \text{ K}$	-1087	-636	-66

* Estimated from Fig. 5(b) of ref. 23.

Ice Ic–liquid free-energy differences ($\Delta G_{\text{ic-L}}$) predicted by LE and the EEOs for water are in poor agreement with the $\Delta G_{\text{ic-L}}$ value obtained by Limmer and Chandler²³ for the ST2 model at 230 K and 2.2 kbar. Such disagreement demonstrates that Limmer and Chandler's results do not withstand thermodynamic scrutiny and fail to provide a reasonable description of ST2's phase behaviour. The TI calculations using LE and the EEOs were performed using two different reference temperatures (described in Methods) to account for ST2's over-structured nature in comparison with real water.

Extended Data Table 4 | Estimates of the melting temperature for ice Ic at 2.6 kbar for the ST2 water model

Method	$T_{lc}^{m, ST2}$ (K)
TI (LE, $T_{0, lh}^m = T_{0, lh}^{m, ST2}$)	260
TI (LE, ΔT^{sc})	260
TI (EEOS, $T_{0, lh}^m = T_{0, lh}^{m, ST2}$)	276
TI (EEOS, ΔT^{sc})	272
Interfacial ice Ic-liq. simulation (this work)	273
Umbrella sampling (this work)*	275
Umbrella sampling (Limmer & Chandler ²³)†	230

* Coexistence pressure is 2.7 kbar.
† Estimated from Fig. 13 (middle column) of ref. 23.
Comparison of melting temperature estimates for ice Ic at 2.6 kbar for the ST2 water model calculated using the TI schemes and empirical equations of state for water described in Methods. The estimates of $T_{lc}^{m, ST2}$ obtained from TI using the accurate EEOS of Choukroun and Grasset^{44,45} are in excellent agreement with values computed directly from two-phase MC simulations of the ice Ic–liquid interface and umbrella sampling MC simulations. In contrast, the $T_{lc}^{m, ST2}$ at 2.6 kbar estimated from Limmer and Chandler’s²³ umbrella sampling simulations with the ST2 water model is lower by more than 40 K, demonstrating severe thermodynamic inconsistencies with their free-energy calculations.

Possible control of subduction zone slow-earthquake periodicity by silica enrichment

Pascal Audet¹ & Roland Bürgmann²

Seismic and geodetic observations in subduction zone forearcs indicate that slow earthquakes, including episodic tremor and slip, recur at intervals of less than six months to more than two years^{1,2}. In Cascadia, slow slip is segmented along strike³ and tremor data show a gradation from large, infrequent slip episodes to small, frequent slip events with increasing depth of the plate interface⁴. Observations^{5–7} and models^{8,9} of slow slip and tremor require the presence of near-lithostatic pore-fluid pressures in slow-earthquake source regions; however, direct evidence of factors controlling the variability in recurrence times is elusive. Here we compile seismic data from subduction zone forearcs exhibiting recurring slow earthquakes and show that the average ratio of compressional (P)-wave velocity to shear (S)-wave velocity (v_p/v_s) of the overlying forearc crust ranges between 1.6 and 2.0 and is linearly related to the average recurrence time of slow earthquakes. In northern Cascadia, forearc v_p/v_s values decrease with increasing depth of the plate interface and with decreasing tremor-episode recurrence intervals. Low v_p/v_s values require a large addition of quartz in a mostly mafic forearc environment^{10,11}. We propose that silica enrichment varying from 5 per cent to 15 per cent by volume from slab-derived fluids and upward mineralization in quartz veins¹² can explain the range of observed v_p/v_s values as well as the downdip decrease in v_p/v_s . The solubility of silica depends on temperature¹³, and deposition prevails near the base of the forearc crust¹¹. We further propose that the strong temperature dependence of healing and permeability reduction in silica-rich fault gouge via dissolution–precipitation creep¹⁴ can explain the reduction in tremor recurrence time with progressive silica enrichment. Lower gouge permeability at higher temperatures leads to faster fluid overpressure development and low effective fault-normal stress, and therefore shorter recurrence times. Our results also agree with numerical models of slip stabilization under fault zone dilatancy strengthening¹⁵ caused by decreasing fluid pressure as pore space increases. This implies that temperature-dependent silica deposition, permeability reduction and fluid overpressure development control dilatancy and slow-earthquake behaviour.

Slow earthquakes—comprising slow fault slip, often accompanied by low-frequency tremor (also called episodic tremor and slip, or ETS)—generally recur at regular intervals on the plate interface within the forearc of young and warm subduction zones, downdip of the locked zone^{1,2}. Their association with a dipping layer of extremely low seismic S-wave velocity, interpreted to represent near-lithostatic pore-fluid pressure within subducting oceanic crust, has been established in most locations^{5–7}, thus suggesting a link between fault zone hydrology and the fault–slip behaviour. Factors controlling ETS periodicity are poorly constrained. One possibility involves modulation by periodic external forces including seasonal hydrologic loads and the Earth's 14-month pole tides^{16–18}, but these cannot explain the wide range of observed periods. Segmentation of ETS behaviour in Cascadia correlates qualitatively with the overriding forearc structure and geology³; however, the exact nature of this relation is elusive. In northern Cascadia, tremor observations indicate a systematic decrease in the recurrence time of slow-slip events with increasing depth of the plate interface⁴. Wech

and Creager's⁴ conceptual interpretation of this observation involves a decrease in friction with increasing temperature, resulting in a weaker fault that ruptures more frequently at greater depths.

We compile observations of converted teleseismic waves (or receiver functions) from permanent and temporary broadband stations located in the forearc of circum-Pacific subduction zones where slow earthquakes (slow-slip with or without tremor) are known to occur at regular intervals, including Japan, Cascadia, Mexico, Costa Rica, and New Zealand (Fig. 1a, Extended Data Table 1). At each subduction zone we select stations closest to the inferred slow-earthquake source regions (Extended Data Fig. 1). In Cascadia we consider stations closer to the longer-recurrence ETS events at shallower depths^{4,19}. These data are sensitive to structures with scale lengths of 1–10 km and are dominated by the signature of a dipping, low-velocity layer^{6,19}. The low-velocity zones associated with the slow-earthquake slip areas have very high v_p/v_s values of 2.6 ± 0.3 (1 σ), which have no apparent relationship with the slow-slip recurrence intervals (Fig. 1b). On the other hand, we see a linear and positive relation between the v_p/v_s of the overriding forearc crust and recurrence times of slow earthquakes (Fig. 1c). The forearc v_p/v_s results are in agreement with a number of studies that estimate forearc crust v_p/v_s using different forms of travel time tomography (Fig. 1c; see Methods), which generally show somewhat lower v_p/v_s owing to various forms of data regularization and smoothing.

Following previous studies, we interpret the high v_p/v_s values of the low-velocity layer to represent high, near-lithostatic pore-fluid pressure within subducting upper oceanic crust^{6,7}. Elevated pore-fluid pressures imply that the plate interface represents a low-permeability boundary, presumably caused by mineral precipitation or grain size reduction. The ubiquity of overpressured oceanic crust in slow-earthquake source regions of warm subduction zones suggests that low effective stress on the megathrust is a necessary condition for the occurrence of slow earthquakes. The observed scatter in the low-velocity-zone v_p/v_s values and the absence of a relationship between v_p/v_s and recurrence times may indicate that the measured v_p/v_s values are only a snapshot of more dynamic and possibly fast-changing fluid processes within the oceanic crust. Exploring temporal variations in v_p/v_s may capture such processes, should these be resolvable. The seismic velocities of the overlying forearc crust seem to provide better constraints on the time-integrated effects of fluid flow and accumulation and the associated transport and precipitation of silica¹¹, which apparently correlate with the slow-slip behaviour.

The linear relationship between forearc crust v_p/v_s and the recurrence times of slow earthquakes (Fig. 1c) supports the hypothesis that the structure of the hanging wall of subduction zone forearcs reflects conditions that determine ETS behaviour^{3,20}. We further examine this question by compiling seismic observations of hanging-wall v_p/v_s along a margin-perpendicular profile in northern Cascadia from published data²¹. Values of v_p/v_s progressively decrease from initially high (>1.85) to low (~ 1.65) values with increasing depth (from 20 km to 45 km) to the plate interface, indicating that progressively more overlying crust material with low bulk v_p/v_s is sampled (Fig. 2). Laboratory measurements of v_p/v_s for most crustal rocks at dry conditions fall in the range

¹Department of Earth Sciences, University of Ottawa, Ottawa, Ontario K1N 6N5, Canada. ²Department of Earth and Planetary Science and Berkeley Seismological Laboratory, University of California, Berkeley, California 94720-4767, USA.

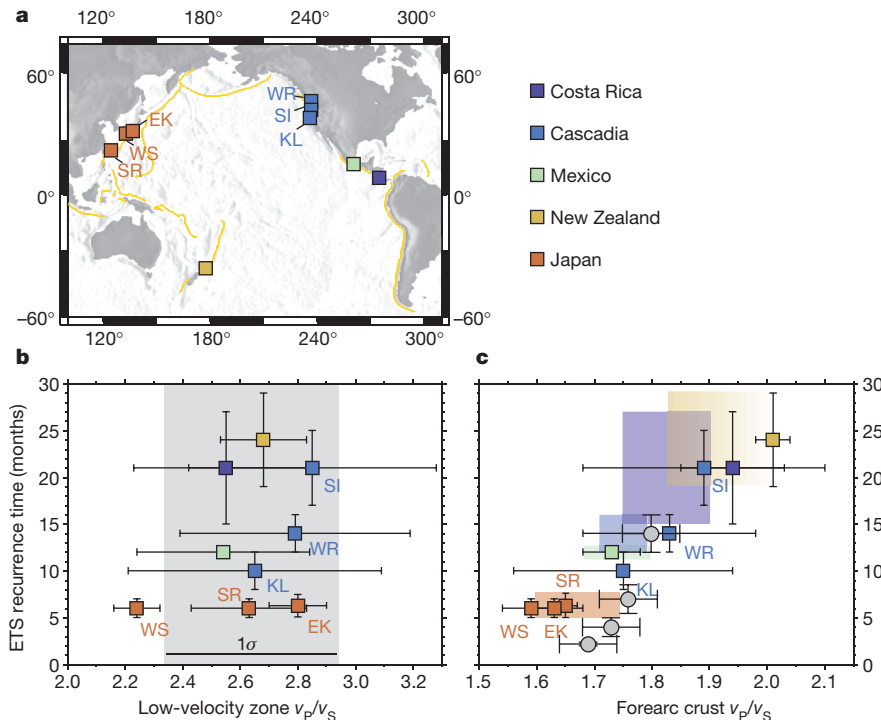


Figure 1 | Subduction zone velocity structure in slow-earthquake source regions. Recurrence times of slow earthquakes (selected regions shown in a; see Methods and Extended Data Table 2 for data sources) compared with v_P/v_S values of a dipping, low-velocity zone interpreted as subducting oceanic crust (b) and overriding forearc crust (c) (Extended Data Table 1 and Fig. 1). Error bars show 1σ uncertainty. High v_P/v_S values of subducting oceanic crust show a large scatter (1σ zone shown in grey) and are uncorrelated with

of 1.7 to 1.85, with higher values found for more mafic compositions¹⁰. These ratios increase further at wet and slightly overpressured conditions²², and the highest v_P/v_S values observed in the updip portion of the Cascadia profile may be explained by the presence of hydrated mafic lithologies and low-grade metamorphic facies. The lowest values require increasing proportions of silica-rich minerals and, in particular, quartz²³, characterized by the lowest velocity ratios ($v_P/v_S = 1.50 \pm 0.03$) determined in the laboratory at ambient temperatures^{10,22}, which decrease further with increasing temperatures up to the α -to- β phase transition (at $>600^\circ\text{C}$) of quartz²⁴.

Quartz-rich rocks are not typically found at those depths in the lower continental crust. Quartz enrichment may be caused by the precipitation of fluid-dissolved silica derived from the progressive dehydration of the downgoing slab. This scenario is supported by seismic¹¹, laboratory¹³ and field evidence¹² that suggest quartz deposition to be progressively more important downdip owing to the temperature dependence of silica solubility in slab-derived fluids¹³. Our data support a massive addition of silica to the deep continental forearc crust, which may locally reach 20% quartz by volume¹¹. Fossil examples of abnormally high concentration of quartz veins include giant mesothermal gold deposits that formed during greenschist facies metamorphism in accretionary complexes²⁵. Although the estimated fluid flux required is about two orders of magnitude greater than fluid production rates estimated from slab dehydration processes in Cascadia²² (see Methods), the availability of silica-saturated fluids from the slab may be greatly enhanced by complete serpentinization of the mantle near the wedge corner²⁶. Silica enrichment as a function of subduction zone age, temperature and plate interface depth can explain the observed pattern of v_P/v_S variations within the overlying crust.

What causes the observed strong correlation between silica enrichment indicated by the forearc v_P/v_S data and decreasing slow-earthquake recurrence times? We postulate that abundant silica-rich fluids from

recurrence times. In c the coefficient of correlation is 0.9 and a two-tailed Student's t -test shows a statistically significant correlation at the 95% level. Also shown in shaded colours are ranges of v_P/v_S estimates from various seismic tomography studies (Extended Data Table 2). Grey circles show along-dip variations in forearc v_P/v_S values²¹ and tremor periodicity for northern Cascadia⁴ (Fig. 2). Labels are SI, Siletzia; WR, Wrangellia; KL, Klamath; SR, Southern Ryukyu; WS, Western Shikoku; and EK, Eastern Kii peninsula.

the slab and increased temperatures accelerate the rate of permeability reduction in the fault zone, which plays a fundamental part in controlling fault strength and stability. At the pressure and temperature

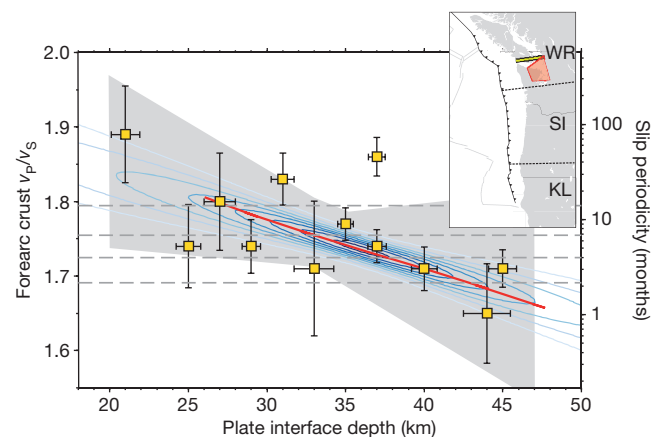


Figure 2 | Down-dip v_P/v_S variations of overlying forearc crust in northern Cascadia. Seismic data (yellow squares; error bars show 1σ uncertainty) are from ref. 21. The linear trend of v_P/v_S as a function of plate interface depth²¹ is used to match the position of the logarithmic decay (solid red line) of slip periodicity along dip⁴. The blue contours show the probability density function at constant intervals (0.01) for the range of linear regressions obtained from bootstrap analysis of the trend, with dark blue being more probable than pale blue. The shaded grey region outlines the range of linear regressions from the bootstrapped samples (see Methods). Horizontal dashed grey lines show v_P/v_S and slip periodicity values extracted at data points that were used to fit the exponential trend of tremor periodicity⁴, plotted in Fig. 1. The inset shows the location of the v_P/v_S profile²¹ (yellow box) and the area used for inferring decay of tremor periodicity⁴ (red shaded area).

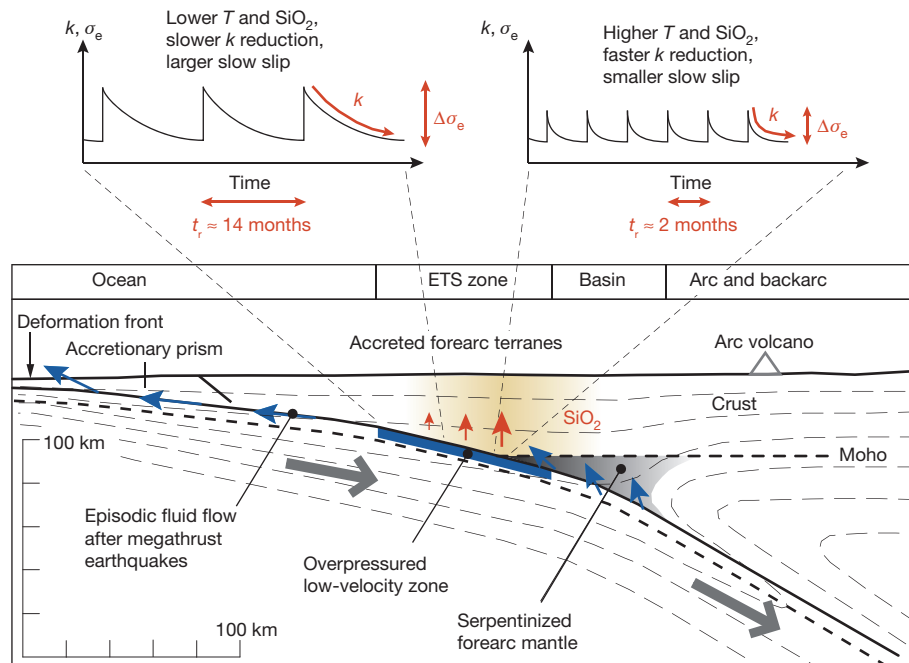


Figure 3 | Conceptual model of silica enrichment controlling slow-earthquake behaviour in northern Cascadia. Progressive silica deposition into quartz minerals and veins due to higher silica solubility with increasing temperature T at depth enriches the overlying forearc crust and decreases v_p/v_s values. Following a slow-slip event, permeability k increases, allowing fluid circulation and a reduction in pore-fluid pressure. Strong

temperature-dependence of permeability reduction in quartz gouge leads to faster re-sealing, overpressure development (shown here as decreasing effective normal stress, σ_e) and thus lower recurrence times t_r with increasing temperature. Thin dashed lines are 200 °C isotherms. Moho, Mohorovičić discontinuity. This figure is modified from ref. 22, with permission.

conditions corresponding to tremor depths, rapid dissolution–precipitation creep processes in a semi-ductile shear zone control permeability reduction in quartz gouge¹⁴. Slow fault slip produces transient permeability increases in fault gouge, followed by resealing^{14,27,28}. Faster healing and reduction in permeability may lead to faster recharge and overpressure development, and thus more rapid reduction in the effective fault-normal stress and more frequent slip events (Fig. 3). Assuming a constant stressing rate along dip, the apparent decrease in slip size with depth depends on stress drop⁹. Our model therefore suggests that stress drop is smaller when permeability reduction and pore-fluid pressure buildup increase more rapidly between slow-slip events. Our model is also consistent with the downdip initiation and updip migration of both large and small slow-slip events⁴, where the updip segment of the plate interface does not always react to a downdip slip pulse because it remains stable at those timescales (that is, fluid overpressure and effective stress have not yet reached the critical threshold for slip). However, it is likely that slip pulses initiating downdip may bring the system to instability when updip conditions are close to critical.

This model can explain the relation between silica enrichment in the forearc crust and slow-earthquake recurrence time as a function of plate interface depth in northern Cascadia (Fig. 3). The control of silica gouge on recurrence time may also be applicable to the global (Fig. 1c) and regional³ observations, if the absolute amount of silica enrichment is a proxy for conditions (temperature, fluids and fault zone mineralogy) that govern creep processes and healing rate in the fault zone. In Cascadia, ETS recurrence-time segmentation correlates with the geology of the forearc crust, where the younger, more mafic (silica-poor) Siletzia terrane has the highest v_p/v_s ratios and longest recurrence times compared with the older, more felsic (silica-rich) forearc terranes to the north and south with shorter recurrence times³. These observations are qualitatively consistent with a control of ETS behaviour by time-integrated and temperature-dependent silica enrichment of the forearc crust.

Numerical simulations of megathrust fault slip suggest that dilatancy strengthening plays an important role in controlling slow-slip behaviour^{9,15}. In areas of strong dilatancy, pore opening is faster than

pore-fluid diffusion during shear, which stabilizes slip and prevents the development of a seismic rupture. In these simulations, dilatancy also modulates the periodicity of slow-slip events, with increasing dilatancy leading to an increase of recurrence time, slip amplitude and duration of slow-slip events¹⁵. These models suggest that an updip increase of dilatancy in the slow-slip zone produces less frequent, slower-slipping ETS in the updip part and more frequent, faster-slipping short-term slip events at greater depths. However, it is not clear through which process changes in forearc v_p/v_s would produce, or be the result of, corresponding changes in dilatancy that lead to the observed linear relation with recurrence time. We speculate that temperature-dependent silica deposition, permeability reduction and overpressure development control dilatancy and thus slow-earthquake behaviour. The lower edge of the episodic slip zone presumably marks a transition to fully ductile flow controlled by dislocation creep, in which fluids act as a weakening factor but pore pressure and dilatancy effects are no longer important.

METHODS SUMMARY

Data used in this study come from several broadband seismic stations located in subduction zone forearcs that exhibit ETS (Extended Data Fig. 1). At each station we compile three-component data with high signal-to-noise ratio (>7.5 dB) on the vertical component from 1990–2011, surface-wave magnitude $M > 5.8$ earthquakes. Seismograms are decomposed into upgoing P- and S-wave modes and are deconvolved using Wiener spectral deconvolution. Receiver functions are filtered at corner frequencies of 0.05 Hz to 0.5 Hz and stacked into 7.5° back-azimuth and 0.002 s km^{-1} slowness bins. We model waveforms using a fast ray-based forward algorithm²⁹. We use a two-layer crustal model with fixed P-wave velocity of 6.5 km s^{-1} composed of continental forearc crust overlying a dipping low-velocity layer representing subducting oceanic crust, underlain by a mantle half-space with fixed P- and S-wave velocities of 8.0 km s^{-1} and 4.5 km s^{-1} , respectively. Strike and dip of the low-velocity layer are taken from global and local slab models³⁰. The misfit is calculated using a normalized correlation scheme and includes both radial and transverse components. Cumulative variance within each receiver function bin is used as an inverse weight in the misfit calculation and the Monte Carlo inversion for model parameters is carried out using a Neighbourhood Algorithm³¹. Results for Cascadia are taken directly from refs 19 and 21. In Costa Rica we extract a subset of data from

the southeastern Nicoya peninsula²⁰. Extended Data Table 1 shows all other measurements for Japan, Mexico and northern New Zealand.

Online Content Any additional Methods, Extended Data display items and Source Data are available in the online version of the paper; references unique to these sections appear only in the online paper.

Received 3 December 2013; accepted 8 April 2014.

- Schwartz, S. Y. & Rokosky, J. M. Slow slip events and seismic tremor at circum-Pacific subduction zones. *Rev. Geophys.* **45**, RG3004 (2007).
- Beroza, G. C. & Ide, S. Slow earthquakes and nonvolcanic tremor. *Annu. Rev. Earth Planet. Sci.* **39**, 271–296 (2011).
- Brudzinski, M. R. & Allen, R. M. Segmentation in episodic tremor and slip all along Cascadia. *Geology* **35**, 907–910 (2007).
- Wech, A. G. & Creager, K. C. A continuum of stress, strength and slip in the Cascadia subduction zone. *Nature Geosci.* **4**, 624–628 (2011).
- Shelly, D. R., Beroza, G. C., Ide, S. & Nakamura, S. Low-frequency earthquakes in Shikoku, Japan, and their relationship to episodic tremor and slip. *Nature* **442**, 188–191 (2006).
- Audet, P., Bostock, M. G., Christensen, N. I. & Peacock, S. M. Seismic evidence for overpressured subducting oceanic crust and megathrust fault sealing. *Nature* **457**, 76–78 (2009).
- Song, T.-R. A. *et al.* Subducting slab ultra-slow velocity layer coincident with silent earthquakes in southern Mexico. *Science* **324**, 502–506 (2009).
- Liu, Y. & Rice, J. R. Spontaneous and triggered aseismic deformation transients in a subduction fault model. *J. Geophys. Res.* **112**, B09404 (2007).
- Segall, P., Rubin, A. M., Bradley, A. M. & Rice, J. R. Dilatant strengthening as a mechanism for slow slip events. *J. Geophys. Res.* **115**, B12305 (2010).
- Christensen, N. I. Poisson's ratio and crustal seismology. *J. Geophys. Res.* **101**, 3139–3156 (1996).
- Ramachandran, K. & Hyndman, R. D. The fate of fluids released from subducting slab in northern Cascadia. *Solid Earth* **3**, 121–129 (2012).
- Breeding, C. M. & Ague, J. J. Slab-derived fluids and quartz-vein formation in an accretionary prism, Otago Schist, New Zealand. *Geology* **30**, 499–502 (2002).
- Manning, C. E. The solubility of quartz in H₂O in the lower crust and upper mantle. *Geochim. Cosmochim. Acta* **58**, 4831–4839 (1994).
- Giger, S. B., Tenthorey, E., Cox, S. F. & Fitz Gerald, J. D. Permeability evolution in quartz gouges under hydrothermal conditions. *J. Geophys. Res.* **112**, B07202 (2007).
- Liu, Y. Numerical simulations on megathrust rupture stabilization under strong dilatancy strengthening in slow slip region. *Geophys. Res. Lett.* **40**, 1311–1316 (2013).
- Shen, Z.-K. *et al.* Pole-tide modulation of slow slip events at circum-Pacific subduction zones. *Bull. Seismol. Soc. Am.* **95**, 2009–2015 (2005).
- Lowry, A. R. Resonant slow fault slip in subduction zones forced by climatic load stress. *Nature* **442**, 802–805 (2006).
- Pollitz, F. F., Wech, A. G., Kao, H. & Bürgmann, R. Annual modulation of non-volcanic tremor in northern Cascadia. *J. Geophys. Res.* **118**, 2445–2459 (2013).
- Hansen, R. T. J., Bostock, M. G. & Christensen, N. I. Nature of the low velocity zone in Cascadia from receiver function waveform inversion. *Earth Planet. Sci. Lett.* **337–338**, 25–38 (2012).
- Audet, P. & Schwartz, S. Y. Hydrologic control of forearc strength and seismicity in the Costa Rican subduction zone. *Nature Geosci.* **6**, 852–855 (2013).
- Audet, P. *et al.* Slab morphology in the Cascadia fore arc and its relation to episodic tremor and slip. *J. Geophys. Res.* **115**, B00A16 (2010).
- Peacock, S. M., Christensen, N. I., Bostock, M. G. & Audet, P. High pore pressures and porosity at 35 km depth in the Cascadia subduction zone. *Geology* **39**, 471–474 (2011).
- Lowry, A. R. & Pérez-Gussinyé, M. The role of crustal quartz in controlling Cordilleran deformation. *Nature* **471**, 353–357 (2011).
- Kern, H. Elastic-wave velocity in crustal and mantle rocks at high pressure and temperature: the role of the high-low quartz transition and of dehydration reactions. *Phys. Earth Planet. Inter.* **29**, 12–23 (1982).
- Sillitoe, R. H. Major gold deposits and belts of the North and South American Cordillera: distribution, tectonomagmatic settings, and metallogenic considerations. *Econ. Geol.* **103**, 663–687 (2008).
- Wada, I., Wang, K., He, J. & Hyndman, R. D. Weakening of the subduction interface and its effects on surface heat flow, slab dehydration, and mantle wedge serpentinization. *J. Geophys. Res.* **113**, B04402 (2008).
- Dempsey, D. E., Rowland, J. V., Zyvoloski, G. A. & Archer, R. A. Modeling the effects of silica deposition and fault rupture on natural geothermal systems. *J. Geophys. Res.* **117**, B05207 (2012).
- Fisher, D. M. & Brantley, S. L. The role of silica redistribution in the evolution of slip instabilities along subduction interfaces: constraints from the Kodiak accretionary complex, Alaska. *J. Struct. Geol.* doi:10.1016/j.jsg.2014.03.010 (in the press).
- Frederiksen, A. W. & Bostock, M. G. Modelling teleseismic waves in dipping, anisotropic structures. *Geophys. J. Int.* **141**, 401–412 (2000).
- Hayes, G. P., Wald, D. J. & Johnson, R. L. Slab1.0: a three-dimensional model of global subduction zone geometries. *J. Geophys. Res.* **117**, B01302 (2012).

Acknowledgements Data used in this study come from the Japan Meteorological Agency, New Zealand National Seismograph Network, and the Tectonic Observatory (Caltech). Funding for this work comes from the Natural Science and Engineering Research Council (Canada) and the Miller Institute for Basic Research in Science (University of California, Berkeley). We thank N. Beeler, A. Rubin and P. Ampuero for discussions and comments.

Author Contributions P.A. performed data processing and inversion. Both P.A. and R.B. contributed to the interpretations and preparation of the final manuscript.

Author Information Reprints and permissions information is available at www.nature.com/reprints. The authors declare no competing financial interests. Readers are welcome to comment on the online version of the paper. Correspondence and requests for materials should be addressed to P.A. (pascal.audet@uottawa.ca).

METHODS

Receiver function analysis. Data used in this study come from several permanent and portable networks of broadband seismic stations located in the forearc of subduction zones that exhibit ETS (Extended Data Fig. 1). At each station we compile all available three-component data with high signal-to-noise ratio (>7.5 dB) on the vertical component from 1990–2011, magnitude $M > 5.8$ earthquakes at teleseismic distances. Seismograms are decomposed into upgoing P- and S-wave modes and are deconvolved using Wiener spectral deconvolution to obtain radial and transverse P-wave receiver functions. Receiver functions are then filtered at corner frequencies of 0.05 Hz to 0.5 Hz and stacked into 7.5° back-azimuth and 0.002 s km^{-1} slowness bins. Coherent signals on the receiver functions represent direct P-to-S conversions and free-surface P-to-S and S-to-S reverberations from velocity contrasts within the underlying column²¹. Each scattered phase displays oppositely polarized pulses that are characteristic of a prominent, dipping low-velocity layer.

Waveform modelling. We model waveforms using a fast ray-based forward algorithm for waves in dipping, anisotropic media²⁹. We use a two-layer crustal model with fixed P-wave velocity of 6.5 km s^{-1} composed of continental forearc crust overlying a dipping low-velocity layer representing subducting oceanic crust, underlain by a mantle half-space with fixed P-wave and S-wave velocities of 8.0 km s^{-1} and 4.5 km s^{-1} , respectively. Parameters that we estimate are the thickness and v_p/v_s of each crustal layer. Our results are only weakly sensitive to variations in the background P-wave velocity structure. Strike and dip of the low-velocity layer are taken from global and local slab models³⁰. The misfit is calculated using a normalized correlation scheme and includes both radial and transverse components. Cumulative variance within each receiver function bin is used as an inverse weight in the misfit calculation and the Monte Carlo inversion for model parameters is carried out using a Neighbourhood Algorithm³¹. Results for Cascadia are taken directly from refs 19 and 21. In Costa Rica we extract a subset of data from the southeastern Nicoya peninsula, where large slow slip occurs²⁰. Extended Data Table 1 shows all other measurements for Japan, Mexico and northern New Zealand.

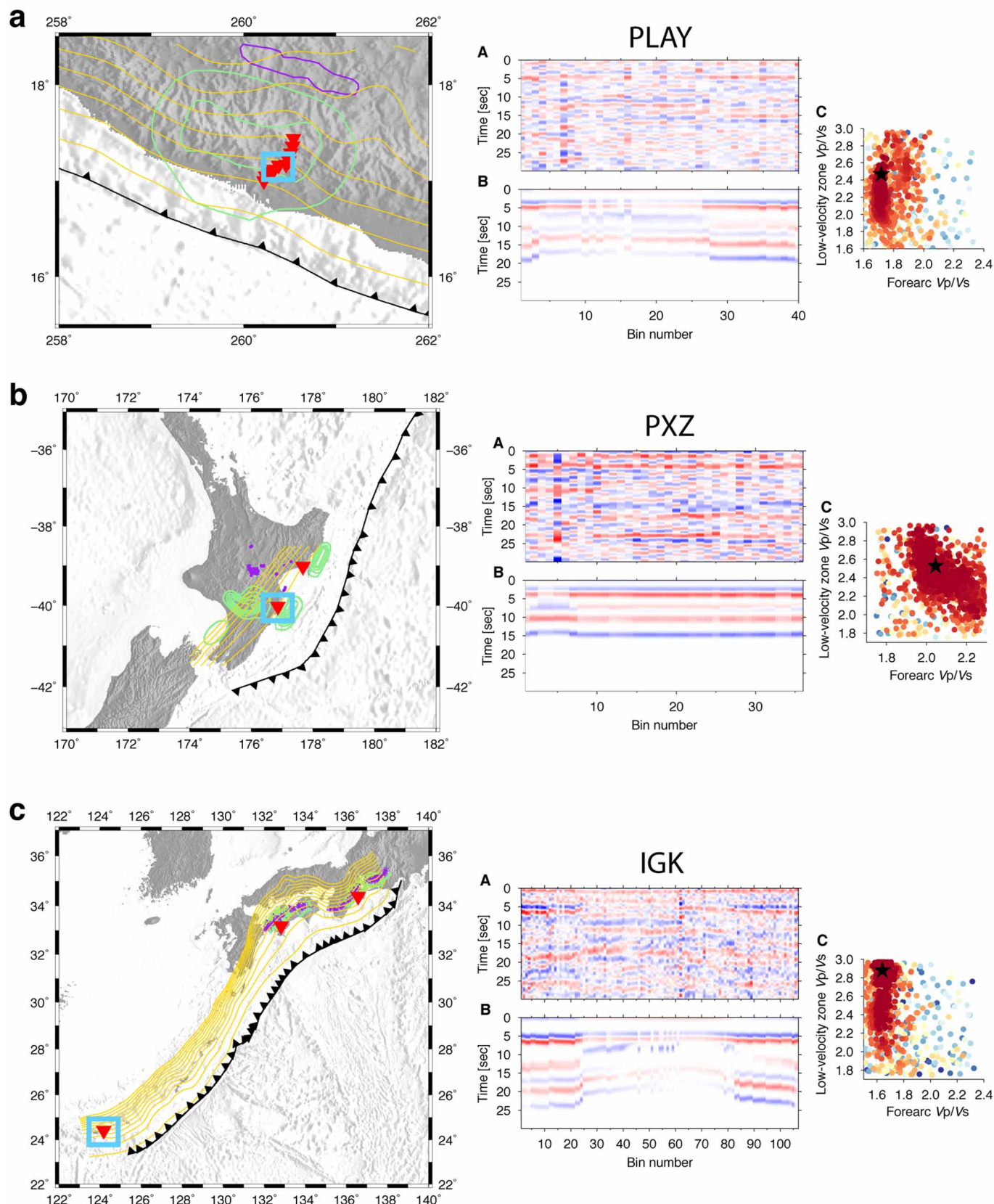
Fluid flux from quartz deposition. Our data suggest a massive addition of silica to the deep continental forearc crust, possibly reaching 20% quartz by volume locally¹¹. Considering the time-integrated flux of $4.5 \times 10^6 \text{ m}^3$ of fluids per m^2 of rock needed to precipitate quartz by regionally flowing fluids from an average local-equilibrium silica-solubility gradient at 350°C – 450°C and 6–8 kbar (ref. 12), a 20% silica enrichment requires a steady-state fluid flux of about 20 mm yr^{-1} over the 40 million years of Cascadia subduction¹¹. This flux is about two orders of magnitude higher than fluid production rates estimated from slab dehydration processes²². However, the local fluid production at the base of the crust near the mantle wedge corner may be greatly increased because complete retrograde serpentinization occurs early owing to the small wedge volume²⁴. Silica-rich fluids are thus no longer consumed

by further serpentinization, which may significantly increase fluid fluxes near the bottom of the forearc crust.

Bootstrap analysis. We performed a bootstrap analysis of the trend between forearc v_p/v_s and plate interface depth. For this analysis we extracted 10,000 random sets of samples (with replacement) from the original data and calculated both the coefficient of correlation ρ and the coefficient of determination r^2 from a linear regression of each set. Median values are 0.8 and 0.6 for ρ and r^2 , respectively, indicating a reasonably good fit. Finally, we determined the probability density function of the bootstrapped regression lines as a function of plate interface depth. The result is a two-dimensional map of the probability density function based on the data, shown in Fig. 2 as contours of constant probability density function values (0.01). The range of regression lines is also plotted in Fig. 2.

Data sources. In Fig. 1 we compare v_p/v_s estimates with recurrence times of slow earthquakes for five different subduction zones. These include Cascadia, Costa Rica, Mexico, southwest Japan (Nankai, Ryukyu) and Hikurangi, New Zealand. Data sources for the recurrence times are listed in Extended Data Table 2. We note that Vergnolle *et al.*³⁶ suggest that only the largest ETS at Guerrero recurring every four years are well documented. We also compile v_p/v_s estimates from various forms of seismic tomography models for each subduction zone (Extended Data Table 2).

- Frederiksen, A. W., Folsom, H. & Zandt, G. Neighbourhood inversion of teleseismic Ps conversions for anisotropy and layer dip. *Geophys. J. Int.* **155**, 200–212 (2003).
- Wallace, L. M. & Beavan, J. Diverse slow slip behaviour at the Hikurangi subduction margin, New Zealand. *J. Geophys. Res.* **115**, B12402 (2010).
- Heki, K. & Kataoka, T. On the biannually repeating slow-slip events at the Ryukyu Trench, southwestern Japan. *J. Geophys. Res.* **113**, B11402 (2008).
- Jiang, Y. *et al.* Slow slip events in Costa Rica detected by continuous GPS observations, 2002–2011. *Geochim. Geophys. Geosyst.* **13**, Q04006 (2012).
- Obara, K. Characteristics and interactions between non-volcanic tremor and related slow earthquakes in the Nankai subduction zone, southwest Japan. *J. Geodyn.* **52**, 229–248 (2011).
- Vergnolle, M. *et al.* Slow slip events in Mexico revised from the processing of 11 year GPS observations. *J. Geophys. Res.* **115**, B08403 (2010).
- DeShon, H. R. *et al.* Seismogenic zone structure beneath the Nicoya Peninsula, Costa Rica, from 3D local earthquake P- and S- wave tomography. *Geophys. J. Int.* **164**, 109–124 (2006).
- Reyners, M., Eberhart-Phillips, D., Stuart, G. & Nishimura, Y. Imaging subduction from the trench to 300 km depth beneath the central North Island, New Zealand, with Vp and Vp/Vs. *Geophys. J. Int.* **165**, 565–583 (2006).
- Matsubara, M., Obara, K. & Kasahara, K. High Vp/Vs zone accompanying non-volcanic tremors and slow slip events beneath southwestern Japan. *Tectonophysics* **472**, 6–17 (2009).
- Huesca-Perez, E. & Husker, A. Shallow travel-time tomography below southern Mexico. *Geophys. J. Int.* **51**, 281–291 (2012).
- Ansell, J. H. & Bannister, S. C. Shallow morphology of the subducted Pacific plate along the Hikurangi margin. *Phys. Earth Planet. Inter.* **93**, 3–20 (1996).



Extended Data Figure 1 | Examples of receiver functions and inversion results for each subduction zone. In a–c the slab contours from refs 30 and 41 are in yellow, contours of slow-slip patches from ref. 2 are in light green, contours and epicentres of tremors from ref. 2 are in purple, and station locations used in this study are shown as inverted red triangles. For a subset of stations (PLAY, PXZ and IGK, identified by the blue squares on the maps) we

show the observed (top, A) and modelled (bottom, B) radial receiver functions ordered by back-azimuth and, for each back-azimuth, by slowness of the incoming P wave. c, A slice through model misfits, with warm colours indicating low values, showing the v_p/v_s of forearc crust versus the v_p/v_s of the low-velocity zone. The star shows the minimum value of the misfit plot (best-fitting value).

Extended Data Table 1 | v_P/v_S results from the inversion of receiver function data

	Station	Longitude	Latitude	Forearc V_P/V_S	Low-velocity zone V_P/V_S
Mexico	PLAY	-99.67	17.12	1.78 ± 0.05	2.5 ± 0.6
	XALT	-99.71	17.10	1.70 ± 0.01	2.7 ± 0.2
	XOLA	-99.62	17.16	1.69 ± 0.01	2.1 ± 0.3
	TICO	-99.54	17.17	1.66 ± 0.02	2.7 ± 0.9
	CARR	-99.51	17.21	1.71 ± 0.01	2.5 ± 0.4
	RIVI	-99.49	17.29	1.74 ± 0.01	2.8 ± 0.7
	ACAH	-99.47	17.36	1.69 ± 0.01	2.1 ± 0.8
	MAZA	-99.46	17.44	1.77 ± 0.01	2.9 ± 0.6
SW Japan	TSA	132.82	33.18	1.59 ± 0.02	2.2 ± 0.8
	WTR	136.58	34.37	1.62 ± 0.05	2.6 ± 0.2
	IGK	124.18	24.41	1.64 ± 0.01	2.8 ± 0.9
Hikurangi	PXZ	176.86	-40.03	1.98 ± 0.06	2.8 ± 0.5
	KNZ	177.67	-39.02	2.02 ± 0.03	2.5 ± 0.7

SW, Southwest.

Extended Data Table 2 | Data sources for ETS recurrence times and seismic velocity models

Subduction Zone	ETS recurrence time	Forearc crust Vp/Vs
Cascadia	Brudzinski & Allen ³	Ramachandran & Hyndman ¹¹
Costa Rica	Jiang et al. ³⁴	DeShon et al. ³⁷
Central Mexico	Lowry ¹⁷	Huesca-Perez & Husker ⁴⁰
Southwest Japan	Heki & Kataoka ³³ ; Obara ³⁵	Matsubara, Obara & Kasahara ³⁹
Hikurangi	Wallace & Beavan ³²	Reyners et al. ³⁸

Data are from refs 3, 11, 17, 32, 33, 34, 35, 37, 38, 39 and 40.

mTORC1 controls the adaptive transition of quiescent stem cells from G_0 to G_{Alert}

Joseph T. Rodgers^{1,2}, Katherine Y. King³, Jamie O. Brett^{1,2}, Melinda J. Cromie^{1,2}, Gregory W. Charville^{1,2}, Katie K. Maguire^{1,2}, Christopher Brunson^{1,2}, Namrata Mastey^{1,2}, Ling Liu^{1,2}, Chang-Ru Tsai³, Margaret A. Goodell³ & Thomas A. Rando^{1,2,4}

A unique property of many adult stem cells is their ability to exist in a non-cycling, quiescent state¹. Although quiescence serves an essential role in preserving stem cell function until the stem cell is needed in tissue homeostasis or repair, defects in quiescence can lead to an impairment in tissue function². The extent to which stem cells can regulate quiescence is unknown. Here we show that the stem cell quiescent state is composed of two distinct functional phases, G_0 and an 'alert' phase we term G_{Alert} . Stem cells actively and reversibly transition between these phases in response to injury-induced systemic signals. Using genetic mouse models specific to muscle stem cells (or satellite cells), we show that mTORC1 activity is necessary and sufficient for the transition of satellite cells from G_0 into G_{Alert} and that signalling through the HGF receptor cMet is also necessary. We also identify G_0 -to- G_{Alert} transitions in several populations of quiescent stem cells. Quiescent stem cells that transition into G_{Alert} possess enhanced tissue regenerative function. We propose that the transition of quiescent stem cells into G_{Alert} functions as an 'alerting' mechanism, an adaptive response that positions stem cells to respond rapidly under conditions of injury and stress, priming them for cell cycle entry.

Adult stem cells have been presumed to exist in one of two states: (1) the quiescent state in which the cell is not actively cycling and (2) the activated state where the cell has committed to or is in the cell cycle^{3,4}. In contrast to the cell cycle, which can be sub-divided into distinct phases, quiescence is not as well characterized. Emerging data suggest that stem cells can regulate quiescent functional properties^{5,6}. Studying the regulation of the transition of satellite cells (SCs) from the quiescent to the activated state, we made a curious observation—SCs in a muscle contralateral to the muscle in which we induced an injury (contralateral satellite cells, CSCs) responded to that distant injury and had cycling properties that were different from those in a non-injured animal (quiescent satellite cells, QSCs) and from the injured tissue (activated satellite cells, ASCs) (Fig. 1a). Using the *Pax7*^{CreER} driver and *Rosa26*^{EYFP} lineage tracer to specifically label SCs^{7,8} (Extended Data Fig. 1a), we found that these CSCs showed markedly increased, but overall still low, propensity to cycle when compared to QSCs, as measured by BrdU (5-bromodeoxyuridine) incorporation *in vivo* (Fig. 1b). Upon isolation and culturing *ex vivo*, CSCs displayed accelerated cell cycle entry as measured by EdU incorporation and time required to complete the first cell division compared to QSCs (Fig. 1c, d). Subsequent cell divisions of progeny of CSCs and QSCs occurred at similar rates to those of ASCs (Extended Data Fig. 1b). This functional response was not limited to SCs in muscle groups directly contralateral to the injury or to the agent of muscle injury (Extended Data Fig. 1c–e).

One of the most obvious changes in ASCs is a dramatic increase in cell size relative to QSCs (Fig. 2a). We found that CSCs displayed a very slight, but significant, increase in cell size relative to QSCs (Fig. 2a, b and Extended Data Fig. 2a, b). Similarly, we also observed that CSCs had stronger EYFP intensity from the *Rosa26*^{EYFP} reporter, elevated levels of pyronin Y staining, and increased incorporation of the ribonucleotide

EU compared to QSCs (Extended Data Fig. 2c–e), which suggests increased transcriptional activity. Principle component analysis (PCA) of the transcriptional profiles of QSCs, CSCs and ASCs showed that CSCs fall between QSCs and ASCs along the first component axis (PC1) (Fig. 2c). Transcriptionally, CSCs were highly correlated with both QSCs and ASCs, more strongly than QSCs and ASCs were correlated (Fig. 2c), which also

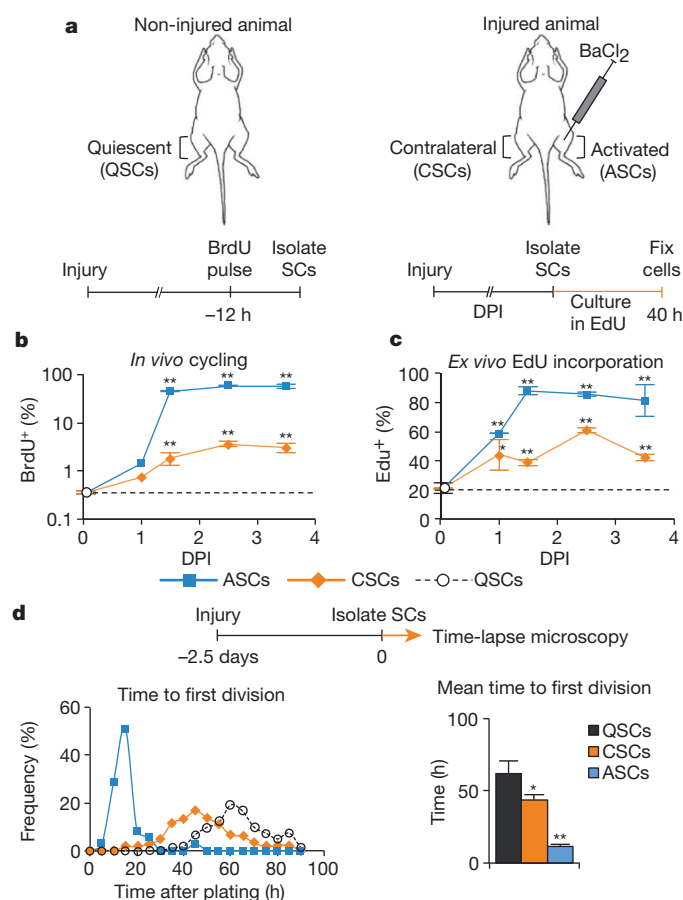


Figure 1 | Satellite cells distant from the site of injury have different cell cycle kinetics than quiescent and activated satellite cells. **a**, Schematic representation of the location of QSCs, CSCs and ASCs in relation to muscle injury. **b**, CSCs have greater propensity to cycle *in vivo* than do QSCs ($n \geq 3$; significance is versus QSCs). **c**, A higher percentage of CSCs incorporate EdU (5-ethynyl-2'-deoxyuridine) after 40 h than QSCs. Data from a representative experiment are presented ($n \geq 2$; significance is versus QSCs). **d**, CSCs require less time to complete the first division ($n = 3$). Details on data presentation and sample size can be found in the Methods Summary and full Methods sections. DPI, days post-injury.

¹Paul F. Glenn Laboratories for the Biology of Aging, Stanford University School of Medicine, Stanford, California 94305, USA. ²Department of Neurology and Neurological Sciences, Stanford University School of Medicine, Stanford, California 94305, USA. ³Department of Pediatrics and Program in Developmental Biology, Baylor College of Medicine, Houston, Texas 77030, USA. ⁴Neurology Service and Rehabilitation Research and Development Center of Excellence, Veterans Affairs Palo Alto Health Care System, Palo Alto, California 94304, USA.

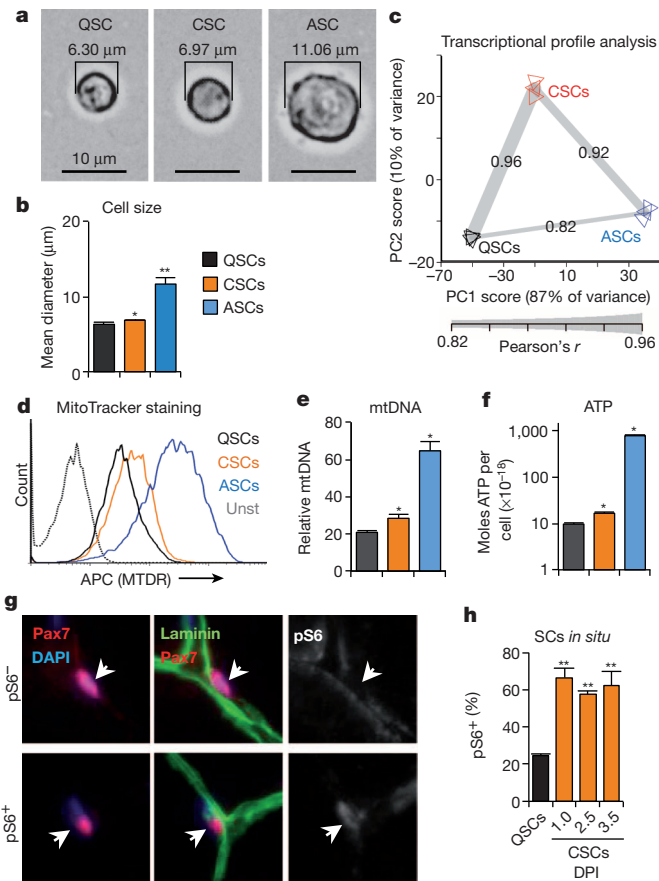


Figure 2 | Satellite cells that are distant from an injury become 'alert'. **a**, Representative images of QSCs, CSCs and ASCs immediately after isolation. **b**, CSCs are larger than QSCs ($n = 3$). **c**, CSCs have a transcriptional profile that is intermediate between QSCs and ASCs (along PC1) as shown by PCA and Pearson's r values ($n = 3$). **d**, Increased mitochondrial activity in CSCs compared to QSCs (representative FACS plot, $n = 4$). Unst, unstained. **e**, CSCs have increased mtDNA content relative to QSCs ($n \geq 3$), measured by qRT-PCR and normalized to genomic DNA (gDNA). **f**, CSCs have more intracellular ATP than QSCs ($n = 4$). **g**, Immunofluorescence immunohistochemistry (IF-IHC) staining of tibialis anterior (TA) muscle showing representative pS6⁻ and pS6⁺ SCs. **h**, Quantification of IF-IHC staining for pS6 in SCs ($n \geq 3$; significance is versus non-injured).

suggests that CSCs are intermediate between QSCs and ASCs. However, detailed immunocytochemistry analysis immediately after isolation showed that CSCs are phenotypically more similar to QSCs (Extended Data Fig. 2f–i). To test if CSCs represent a population of stem cells or a population of committed progenitor cells, we performed transplantation and pulse-chase experiments and found no difference in the engraftment efficiency and capacity for self-renewal between CSCs and QSCs (Extended Data Fig. 2j, k). Together, these data suggest that CSCs are similar to, but distinct from, QSCs and possess the stem cell characteristics of QSCs.

To gain further insight into what distinguishes CSCs from QSCs, we analysed the molecular pathways enriched in genes induced in the CSC transcriptome relative to the QSC expression profile. We found that two annotation groups were significantly enriched in genes upregulated in CSCs relative to QSCs: cell cycle and mitochondrial metabolism (Extended Data Fig. 3a). To further investigate mitochondrial metabolism in CSCs, we performed MitoTracker Deep Red staining and measured mtDNA content and found that, relative to QSCs, CSCs displayed evidence of elevated mitochondrial activity (Fig. 2d, e). Consistent with these findings, and keeping with the increase in cell size, we also found that CSCs have increased levels of cellular ATP (Fig. 2f and Extended Data Fig. 3b–d).

Collectively these data describe a set of properties that distinguishes CSCs from QSCs and ASCs: kinetics of cell cycle entry, propensity to cycle, cell size, transcriptional activity and mitochondrial metabolism. Importantly, CSCs, like QSCs, are still quiescent in that, as a population, almost all CSCs are not actively cycling. Because the injury-induced phenotype of CSCs is intermediate between QSCs and ASCs, we refer to CSCs as 'alert' SCs and the set of properties that distinguishes these cells as the 'alert' phenotype. The characteristics of this alert phenotype described above have a common thread in that they have all been previously linked, in other systems, to the mTORC1 signalling pathway (reviewed in ref. 9). For example, we observed induction of phospho-S6 (pS6), a surrogate of mTORC1 activity, in alert SCs (Fig. 2g, h and Extended Data Fig. 3e–g). Furthermore, we found that by sorting SCs for properties of the alert state (Extended Data Fig. 3h), we enriched for a population of pS6⁺ SCs that also possessed the other attributes of the alert state (elevated propensity to cycle and reduced time to first division) (Extended Data Fig. 3i–m). Together these data show that there is a strong correlation between activation of mTORC1 signalling and the alert phenotype in SCs.

To test if any aspects of the alert response were directly regulated by mTORC1 signalling, we used the *Pax7*^{CreER} driver to specifically ablate *TSC1*, an inhibitor of mTORC1 signalling, in SCs. As a genetic model of mTORC1 activation¹⁰, *TSC1* knockout (KO) QSCs displayed induction of mTORC1 activity (Extended Data Fig. 4a, b). *TSC1* KO QSCs also displayed all aspects of the alert phenotype in an otherwise non-injury context: increased propensity to cycle, accelerated cell cycle entry, increased MitoTracker Deep Red staining and increased cell size (Fig. 3a–c and Extended Data Fig. 4c). To test whether the alert response requires mTORC1, we used a conditional allele of Raptor (*Rptor*)¹¹, an essential component of the mTORC1 signalling complex, with the *Pax7*^{CreER} driver to specifically ablate *Rptor* expression and suppress mTORC1 signalling in SCs (Extended Data Figs 4b and 5a–c). Overall, we found that *Rptor* KO SCs contralateral to a muscle injury were completely unresponsive to the injury and did not manifest any of the injury-induced

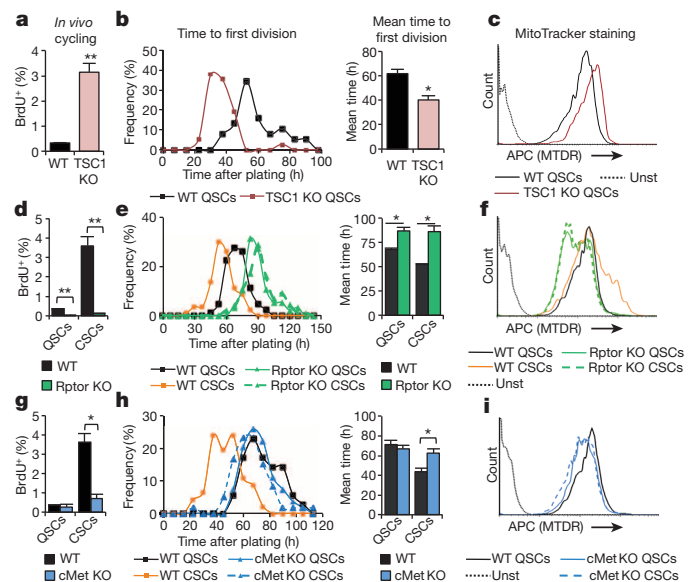


Figure 3 | Activation of mTORC1 is necessary and sufficient for the alert phenotype. **a–c**, *TSC1* KO QSCs display characteristics of alert SCs: increased propensity to cycle *in vivo* (**a**, $n \geq 6$); reduced time to first division (**b**, $n = 3$); increased mitochondrial activity (**c**, representative FACS plot $n = 3$). **d–f**, *Rptor* KO suppresses induction of the alert state. *Rptor* KO CSCs show no differences in: propensity to cycle *in vivo* (**d**, $n \geq 6$); time to first division (**e**, $n = 3$); and mitochondrial activity (**f**, representative FACS plot, $n = 3$). **g–i**, *cMet* KO CSCs show no injury-induced regulation of: propensity to cycle *in vivo* (**g**, $n \geq 4$); time to first division (**h**, $n \geq 3$); and mitochondrial activity (**i**, representative FACS plot, $n = 3$).

changes that alert wild-type CSCs display (Fig. 3d–f and Extended Data Fig 5d, e). These data combined show that mTORC1 signalling in SCs is necessary and sufficient for the alert response.

Next, we focused on the signals upstream of mTORC1 which initiate the alert response and which are regulated by injury. Latent hepatocyte growth factor (HGF) is found in the extracellular matrix of many tissues; upon injury it is processed into an active form by serum proteases^{12,13}. Active HGF can regulate mTORC1 via PI3K–Akt signalling¹⁴. Furthermore HGF is known to influence SC behaviour^{15,16}. To test if HGF signalling has a role in the alert response, we used conditional ablation of the HGF receptor, *cMet*, to suppress HGF signalling in SCs¹⁷. Ablation of *cMet* in SCs completely blocked the activation of mTORC1 signalling, as measured by pS6 staining, in cultured SCs and *in vivo* in CSCs following injury (Extended Data Figs 4b and 5f, g). Consistent with our hypothesis that mTORC1 activation is required for the alert response in SCs, *cMet* KO CSCs did not exhibit any functional response to injury (Fig. 3g–i and Extended Data Fig. 5h). Collectively, these data suggest that signalling downstream of *cMet* is critical for the induction of the alert response in SCs.

Following tissue repair after injury, activity of the HGF activation cascade gradually subsides¹². We found the frequency of pS6⁺ CSCs following a distant injury declined to a level similar to that of non-injured animals 28 days post-injury (DPI) (Extended Data Fig. 6a). We also found that at 28 DPI the propensity to cycle and cell cycle entry kinetics of CSCs returned to those of QSCs (Extended Data Fig. 6b, c). Furthermore, the transcriptional profile of CSCs 28 DPI had returned to that of QSCs (Extended Data Fig. 6d). These data indicate that the alert state is reversible and that the functional and transcriptional changes in alert CSCs that occur downstream of mTORC1 revert to the properties of QSCs when mTORC1 activity subsides.

To gain further understanding of the molecular pathways underlying the functional transition into the alert state, we analysed the transcriptional profiles from the SC-specific genetic models described above. We found that induction of genes involved in mitochondrial metabolism strongly correlated with the ability to transition into the alert state.

Wild-type CSCs and TSC1 KO QSCs show induction and Rptor KO and *cMet* KO CSCs do not (Extended Data Figs 3a and 7a–e). These data suggest that regulation of mitochondrial metabolism is a crucial aspect of stem cell quiescence.

The function of SCs in response to injury is to proliferate, differentiate and form new muscle tissue^{18,19}. As such, we tested whether the functional changes of CSCs affected their differentiation and muscle regenerative abilities. Following isolation and *ex vivo* culturing, CSCs displayed enhanced kinetics of differentiation as measured by expression of myogenin (MyoG) and cell fusion (Fig. 4a, b and Extended Data Fig. 8a). To translate these observations *in vivo*, we assessed the ability of CSCs to participate in muscle regeneration. Three days before injury of the left tibialis anterior (TA) muscle, we performed an ‘alerting’ injury to the right limb to transition SCs in the left TA into the alert state (Fig. 4c). We found that animals that received an ‘alerting’ injury displayed strikingly enhanced muscle regeneration at all time points following injury when compared to the normal muscle regenerative process (Fig. 4d, e). These data show that the functional properties of alert SCs translate into enhanced muscle regenerative ability in response to injury.

The markedly enhanced muscle regenerative function of CSCs prompted us to investigate other conditions which may induce the alert state in SCs. We found that SCs adopted functional aspects of the alert response to bone injuries and to minor skin wounds (Extended Data Fig. 8b, c), injuries for which the role of SCs is not apparent. These data suggest that SCs can adopt the alert state in response to multiple types of injuries and may be a general response of SCs to injury. Therefore, we tested if other populations of quiescent stem cells could similarly adopt properties of the alert state. We found that fibro-adipogenic progenitors (FAPs), a resident mesenchymal stem cell population in skeletal muscle^{20,21}, responded in a similar way as SCs. CFAPs (FAPs in muscles of a limb contralateral to the site of muscle injury) displayed an induction of mTORC1 signalling, accelerated cell cycle entry, increased propensity to cycle and increased cell size when compared to quiescent FAPs from non-injured animals (QFAPs) (Fig. 4f–h and Extended Data Fig. 9a–c). Additionally, we found that long-term haematopoietic stem cells (LT-HSCs) displayed

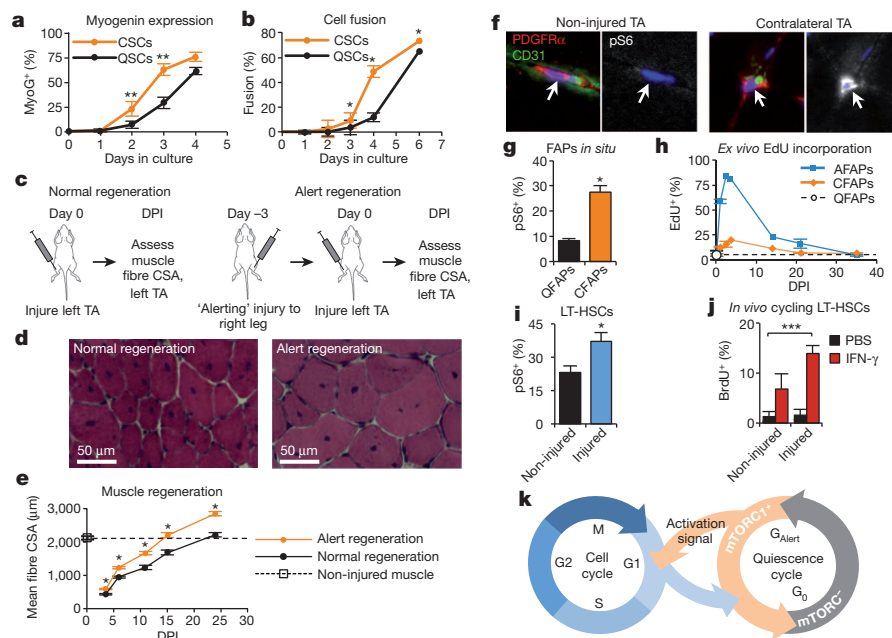


Figure 4 | Stem cells in the alert state have enhanced functional properties. **a, b**, CSCs have enhanced kinetics of myogenic differentiation *ex vivo*. They rapidly express and become MyoG⁺ (**a**) and fuse (**b**, $n = 3$; significance is versus QSCs at same time point). **c**, Schematic depiction of ‘alert’ regeneration experimental design. CSA, cross-sectional area. **d, e**, A prior ‘alerting’ injury enhances the progress of muscle regeneration. Representative histological section (**d**) and quantification of nascent, centrally nucleated muscle fibre CSA

(**e**, $n \geq 3$). **f–h**, FAPs adopt characteristics of the alert state: higher frequency of pS6⁺ FAPs in muscles contralateral to injury (**f**, representative IF-IHC staining); quantification of pS6 staining (**g**, $n = 4$); and accelerated kinetics of cell cycle entry (**h**, $n \geq 2$). **i, j**, LT-HSCs display characteristics of the alert state in response to muscle injury: increased frequency of pS6 staining (**i**, $n \geq 4$) and enhanced activation cycle response to IFN-γ (**j**, $n \geq 3$; *** $P < 0.001$). **k**, Model depicting quiescence cycle of G₀ and G_{Alert} phases.

activation of mTORC1 signalling in response to muscle injury (Fig. 4i and Extended Data Fig. 9d). To test if mTORC1 activation in LT-HSCs caused increased functional potential, as it does in SCs, we then administered interferon- γ (IFN- γ), to the animals to stimulate LT-HSC activation²². Similar to the effect of an 'alerting' injury on muscle regeneration, LT-HSCs primed by muscle injury were more sensitive to IFN- γ and had a more robust response (Fig. 4j). Notably, and similar to what we demonstrated in SCs, the induction of mTORC1 in HSCs increases their mitochondrial activity^{23,24}, which is consistent with a transition into the alert state. Collectively, these data indicate that activation of mTORC1 signalling in quiescent stem cells alters their properties, endowing them with enhanced functional potential, an alerting mechanism that prepares the cell for potential activation.

As it relates to stem cell biology, the data we present here demonstrate that stem cells undergo dynamic transitions between functional phases in the quiescent state. We propose a model in which G_{Alert} and G_0 are phases within quiescence and form a quiescence cycle (Fig. 4k). Although it has been suggested that not all quiescent cells are functionally equivalent^{25,26}, the *in vivo* relevance and the molecular mechanisms regulating functionally distinct states had not previously been elucidated. We propose that mTORC1 activity is a distinguishing aspect of at least two distinct phases within quiescence. Here we demonstrate how these phases of stem cell quiescence *in vivo* are regulated in the context of physiological conditions by mTORC1 (and, for SCs, by cMet). Most importantly, our data indicate that the ability to transition between G_0 and G_{Alert} is critical to the positioning of stem cell populations to be able to respond rapidly in tissue homeostasis and repair while maintaining a pool of deeply quiescent, reserve stem cells. This represents a newly identified form of cellular memory, an adaptive response akin to that in neuronal or immune cells, in which prior experience influences future responses.

METHODS SUMMARY

Unless stated otherwise, in the figure legend, all graphical data are presented as mean \pm s.e.m., except for histograms, and significance was calculated using two-tailed unpaired Student's *t*-tests: * $P < 0.05$, ** $P < 0.01$. When sample size (*n* values) are reported as a range, exact sample size values can be found in the Methods section. Time to first division experiments are presented as a representative histogram plotting data from individual cells and, on the right, as a bar graph depicting the quantitative analysis of the mean time to first division in replicate experiments.

Online Content Any additional Methods, Extended Data display items and Source Data are available in the online version of the paper; references unique to these sections appear only in the online paper.

Received 15 January; accepted 13 March 2014.

Published online 25 May 2014.

- Cheung, T. H. & Rando, T. A. Molecular regulation of stem cell quiescence. *Nature Rev. Mol. Cell Biol.* **14**, 329–340 (2013).
- Rossi, L. *et al.* Less is more: unveiling the functional core of hematopoietic stem cells through knockout mice. *Cell Stem Cell* **11**, 302–317 (2012).
- Li, L. & Clevers, H. Coexistence of quiescent and active adult stem cells in mammals. *Science* **327**, 542–545 (2010).
- Wilson, A. *et al.* Hematopoietic stem cells reversibly switch from dormancy to self-renewal during homeostasis and repair. *Cell* **135**, 1118–1129 (2008).
- Chakkalakal, J. V., Jones, K. M., Basson, M. A. & Brack, A. S. The aged niche disrupts muscle stem cell quiescence. *Nature* **490**, 355–360 (2012).
- Cheung, T. H. *et al.* Maintenance of muscle stem-cell quiescence by microRNA-489. *Nature* **482**, 524–528 (2012).
- Nishijo, K. *et al.* Biomarker system for studying muscle, stem cells, and cancer *in vivo*. *FASEB J.* **23**, 2681–2690 (2009).
- Seale, P. *et al.* Pax7 is required for the specification of myogenic satellite cells. *Cell* **102**, 777–786 (2000).

- Laplanche, M. & Sabatini, D. M. mTOR signaling in growth control and disease. *Cell* **149**, 274–293 (2012).
- Kwiatkowski, D. J. *et al.* A mouse model of TSC1 reveals sex-dependent lethality from liver hemangiomas, and up-regulation of p70S6 kinase activity in Tsc1 null cells. *Hum. Mol. Genet.* **11**, 525–534 (2002).
- Sengupta, S., Peterson, T. R., Laplanche, M., Oh, S. & Sabatini, D. M. mTORC1 controls fasting-induced ketogenesis and its modulation by ageing. *Nature* **468**, 1100–1104 (2010).
- Miyazawa, K. Hepatocyte growth factor activator (HGFA): a serine protease that links tissue injury to activation of hepatocyte growth factor. *FEBS J.* **277**, 2208–2214 (2010).
- Nakamura, T. & Mizuno, S. The discovery of hepatocyte growth factor (HGF) and its significance for cell biology, life sciences and clinical medicine. *Proc. Jpn. Acad., Ser. B, Phys. Biol. Sci.* **86**, 588–610 (2010).
- Trusolino, L., Bertotti, A. & Comoglio, P. M. MET signalling: principles and functions in development, organ regeneration and cancer. *Nature Rev. Mol. Cell Biol.* **11**, 834–848 (2010).
- Yamada, M. *et al.* High concentrations of HGF inhibit skeletal muscle satellite cell proliferation *in vitro* by inducing expression of myostatin: a possible mechanism for reestablishing satellite cell quiescence *in vivo*. *Am. J. Physiol. Cell Physiol.* **298**, C465–C476 (2010).
- Tatsumi, R., Anderson, J. E., Nevoret, C. J., Halevy, O. & Allen, R. E. HGF/SF is present in normal adult skeletal muscle and is capable of activating satellite cells. *Dev. Biol.* **194**, 114–128 (1998).
- Huh, C. G. *et al.* Hepatocyte growth factor/c-met signaling pathway is required for efficient liver regeneration and repair. *Proc. Natl Acad. Sci. USA* **101**, 4477–4482 (2004).
- Brack, A. S. & Rando, T. A. Tissue-specific stem cells: lessons from the skeletal muscle satellite cell. *Cell Stem Cell* **10**, 504–514 (2012).
- Chargé, S. B. & Rudnicki, M. A. Cellular and molecular regulation of muscle regeneration. *Physiol. Rev.* **84**, 209–238 (2004).
- Joe, A. W. *et al.* Muscle injury activates resident fibro/adipogenic progenitors that facilitate myogenesis. *Nature Cell Biol.* **12**, 153–163 (2010).
- Uezumi, A., Fukada, S., Yamamoto, N., Takeda, S. & Tsuchida, K. Mesenchymal progenitors distinct from satellite cells contribute to ectopic fat cell formation in skeletal muscle. *Nature Cell Biol.* **12**, 143–152 (2010).
- Baldrige, M. T., King, K. Y., Boles, N. C., Weksberg, D. C. & Goodell, M. A. Quiescent haematopoietic stem cells are activated by IFN- γ in response to chronic infection. *Nature* **465**, 793–797 (2010).
- Chen, C. *et al.* TSC–mTOR maintains quiescence and function of hematopoietic stem cells by repressing mitochondrial biogenesis and reactive oxygen species. *J. Exp. Med.* **205**, 2397–2408 (2008).
- Gan, B. *et al.* mTORC1-dependent and -independent regulation of stem cell renewal, differentiation, and mobilization. *Proc. Natl Acad. Sci. USA* **105**, 19384–19389 (2008).
- Pardee, A. B. G1 events and regulation of cell proliferation. *Science* **246**, 603–608 (1989).
- Soprano, K. J. WI-38 cell long-term quiescence model system: a valuable tool to study molecular events that regulate growth. *J. Cell. Biochem.* **54**, 405–414 (1994).
- Liu, L. *et al.* Chromatin modifications as determinants of muscle stem cell quiescence and chronological aging. *Cell Rep.* **4**, 189–204 (2013).

Supplementary Information is available in the online version of the paper.

Acknowledgements We would like to thank members of the Rando laboratory for discussions critical to the preparation of this manuscript, especially T. Cheung and S. Biressi. We thank L. Rott for providing assistance with FACS. This work was supported by The Glenn Foundation for Medical Research, by a grant from the Department of Veterans Affairs to T.A.R., and grants from the National Institutes of Health to J.T.R. (K99 AG041764), K.Y.K. (K08 HL098898), M.A.G. (R01 DK092883) and to T.A.R. (P01 AG036695, R01 AG23806 and R01 AR062185).

Author Contributions J.T.R. conceived and designed most of the experiments reported. T.A.R. provided guidance throughout. J.T.R., C.B. and N.M. performed experiments and collected data. J.T.R., J.O.B. and L.L. analysed the microarray data. J.T.R. and K.K.M. conceived and performed bioluminescence experiments. J.T.R. and M.J.C. designed primed regeneration experiments. J.T.R. and G.W.C. performed and analysed transplant experiments. K.Y.K., C.-R.T. and M.A.G. conceived, performed and analysed data from the experiments in HSCs. J.T.R. and T.A.R. analysed data and wrote the manuscript.

Author Information Array data is deposited in GEO (accession numbers GSE55490 and GSE47177), as previously published (ref. 27) and as Supplementary Data Set 1. Reprints and permissions information is available at www.nature.com/reprints. The authors declare no competing financial interests. Readers are welcome to comment on the online version of the paper. Correspondence and requests for materials should be addressed to T.A.R. (rando@stanford.edu).

METHODS

Mice. *TSC1^{fl}*, *Raptor^{fl}*, *cMet^{fl}*, *Rosa26^{EYFP}* and NSG mice were obtained from the Jackson Laboratory. *Pax7^{CreER}* mice were provided by Dr. Charles Keller (OHSU). All experiments were performed with 12–16-week-old male C57BL/6 mice, except in experiments with conditional cMet KO, and associated controls, which were in a mixed background of C57BL/6 and FVB. Animals were genotyped by PCR of tail DNA, except in Extended Data Fig. 5c which was performed using isolated SCs and FAPs, primer sequences available upon request. The genotypes of experimental KO and associated control animals are as follows: TSC1 KO (*TSC1^{fl/fl}*; *Pax7^{CreER/+}*; *Rosa26^{EYFP/+}*) and wild type (*TSC1^{+/+}*; *Pax7^{CreER/+}*; *Rosa26^{EYFP/+}*), Raptor KO (*Raptor^{fl/fl}*; *Pax7^{CreER/+}*; *Rosa26^{EYFP/+}*) and wild type (*Raptor^{+/+}*; *Pax7^{CreER/+}*; *Rosa26^{EYFP/+}*), cMet KO (*cMet^{fl/fl}*; *Pax7^{CreER/+}*; *Rosa26^{EYFP/+}*) and WT (*cMet^{+/+}*; *Pax7^{CreER/+}*; *Rosa26^{EYFP/+}*). Tamoxifen (TMX) (Sigma) was prepared in a mixture of corn oil and 7% ethanol and administered in 5 doses of 50 mg every 2–3 days by intraperitoneal (i.p.) injection. TMX injections were initiated on 6–8-week-old mice, and experimental mice were used 2–4 weeks after TMX administration. In pulse labelling experiments, 10 mg of BrdU were injected i.p. 12 h before mice were euthanized. In continuous labelling experiments, BrdU (0.8 mg ml⁻¹) was administered in the drinking water with 1% sucrose for the indicated period. Mice were housed and maintained in the Veterinary Medical Unit at Veterans Affairs Palo Alto Health Care Systems. Animal protocols were approved by the Administrative Panel on Laboratory Animal Care of VA Palo Alto Health Care System.

Injury models. BaCl₂ was used as the agent for muscle injury unless stated otherwise. Briefly, mice were anaesthetized with isoflurane, and the lower hindlimb was shaved and skin was sterilized. A total of 70 µl of 1.2% BaCl₂ (w/v H₂O) was injected into and along the length of the tibialis anterior (TA) and gastrocnemius (Gas) muscles. Mice were given analgesic and antibiotics and allowed to recover. Muscle crush injuries were performed by opening the skin and fascia over the TA muscle, injuring the muscle with a hemostat along the length of the TA, and closing the skin with sutures. Skin injuries were performed by using scissors to make a 2 cm incision on the abdomen without injuring the peritoneum and closing the incision with wound clips. In all experiments, control, non-injured animals were subject to a mock injury: animals were anaesthetized and administered analgesic and antibiotics.

Muscle regeneration. Alert regeneration experiments were performed as depicted in Fig. 4c, by injuring the TA and Gas muscle in the right hindlimb on day -3 followed by injuring the TA muscle in the left hindlimb on day 0. Control, normal regeneration animals were anaesthetized and given antibiotics and analgesics on day -3. On day 0, normal regeneration animals were subject to identical injuries as alert regeneration animals. At indicated DPI, animals were euthanized, the left TAs extracted, and prepared for histological analysis by freezing in liquid nitrogen cooled isopentane. TA muscles extracted 3.5 and 5 DPI were sectioned and subject to IF-IHC staining with eMHC and laminin antibodies to identify nascent muscle fibres. TA muscles extracted 11, 15, and 24 DPI were sectioned and subject to haematoxylin and eosin (H&E) staining to identify centrally nucleated fibres. The cross-sectional area (CSA) was of nascent fibres in posterior portion of the TA muscle approximately halfway along the proximal–distal axis was performed using AxioVision software (Zeiss).

Cell isolation and FACS purification. Satellite cell isolation was performed as previously described⁶. Briefly, following death, hindlimb skeletal muscles were removed, minced and digested in collagenase and dispase. Satellite cells were purified by gating mononuclear EYFP⁺ cells using a BD FACSAria II or III. As depicted in Fig. 1a, QSCs were isolated from TA and Gas muscle of non-injured animals, ASCs were isolated from injured TA and Gas muscles, and CSCs isolated from TA and Gas contralateral to the injury.

FAPs were purified from muscles isolated and digested as in the SC isolation protocol. Following digestion, FAPs were stained and purified as a population of CD31⁻/CD45⁻ and Sca-1⁺ mononuclear cells, using the following antibodies: CD31-APC (clone MEC 13.3; BD Bioscience), CD45-APC (clone 30-F11; BD Bioscience), Sca1 PacBlue (clone D7; BioLegend).

All FACS comparisons (size, MitoTracker, EYFP, EU, pS6) are from isolations performed on the same day and analysed on the same FACS instrument (BD FACSAria II or III). All FACS plots are representative experiments with similar results in at least 3 independent experiments.

Analysis of HSCs. For mTOR analysis, lin⁻ (lineage markers: B220, CD4, CD8, CD11b, Ly6G, Ter119) cKit⁺ Sca1⁺ CD150⁺ cells were obtained from bone marrow 24 h after injury or mock injury and stained with phospho-mTOR or phospho-S6 antibodies.

For IFN-γ experiments, animals were subjected to muscle injury or mock injury as described above. After 24 h, HSC division was induced with IFN-γ (100 ng per mouse) or PBS by intravenous injection, and 4 mg BrdU was injected i.p. After an additional 24 h, the mice were euthanized and BrdU incorporation was measured in HSCs (Lin⁻ Sca1⁺ cKit⁺ CD150⁺ CD48⁻ EPCR⁺) (BrdU FlowKit; BD Bioscience).

Satellite cell transplantation. Donor EYFP⁺ SCs were FACS purified from *Pax7^{CreER/+}*; *Rosa26^{EYFP/+}* mice, 2.5 DPI (CSCs) or from non-injured animals (QSCs). Donor SCs were counted, washed with PBS and resuspended in PBS with 0.1% BSA at a concentration of 5 × 10⁴ cells in 20 µl. The TA muscle of the host, 12-week-old male NSG mice, was prepared by BaCl₂ injury two days before transplantation. The transplantation was performed by anaesthetizing the host mice, exposing the TA muscle by opening the skin and fascia, and slowly injecting 20 µl of the donor cell solution into the TA using a 50 µl Hamilton syringe. Each host mouse received transplantation of QSCs into the right TA and CSCs into the left TA. After injection, the skin over the TA was closed by sutures, the mice were administered analgesic and antibiotics and were allowed to recover. Two weeks after transplantation, SC engraftment was measured by FACS of EYFP⁺ SCs from the TA muscle of donor mice.

Mitotracker staining. Prior to FACS analysis, 200 nM MitoTracker Deep Red (Invitrogen) was added to muscle digests and incubated for 1 h at 37 °C, with gentle shaking. Digests were washed once and MitoTracker staining was visualized on a BD FACSAria II or III in the APC channel.

Cell culture. SCs and FAPs were cultured on ECM (Sigma) coated poly-D-lysine 8-well chamber slides (BD), 15,000 cells were plated per well and cultured overnight in Hams F10 medium (Cellgro) with 10% fetal bovine serum (Gibco), the next day the medium was switched to Hams F10 with 10% horse serum (Gibco), and cells were cultured in this medium until fixation by PFA. In EdU incorporation experiments, 0.05 mM EdU (Invitrogen) was added to the culture medium and replenished every 12 h until cells were fixed. SCs were fixed 40 h after plating and FAPs were fixed 48 h after plating. For *in vivo* BrdU pulse labelling experiments, cells were isolated, plated and fixed 2 h after isolation.

Time-lapse microscopy. To perform time-lapse microscopy analysis, 10,000 SCs were plated onto ECM coated 8-well chamber slides and allowed to adhere for several hours to slides. After the cells adhered the medium was changed to Hams F10 with 10% HS and the slides were transferred to an environmentally controlled Zeiss Axiophot 200M equipped Axiocam. Time-lapse data acquisition and visualization was made using AxioVision software and images were captured every 15 min. The time required to complete the first division after plating was recorded only for cells that stayed within the acquisition field. Representative data from time-lapse experiments are displayed as histograms, bar graphs of time to first division display quantification of replicate experiments (mean ± s.e.m.).

ATP measurement. SC ATP levels were measured using the ATP Bioluminescence Assay Kit CLS II (Roche) according to the manufacturer's instructions. Briefly, 20,000 SCs were counted with a haemocytometer immediately after isolation, pelleted, and boiled in 100 mM Tris, 4 mM EDTA, pH 7.4 for 2 min. After boiling, the debris was pelleted and supernatant was used for analysis.

Immunostaining. Immunofluorescence immunohistochemistry (IF-IHC) was performed on muscle tissue that was mounted with tragacanth gum and snap frozen in isopentane cooled in liquid nitrogen immediately after dissection. The 8-µm sections were fixed in 4% PFA for 5 min and blocked in donkey serum before staining. Pax7 and eMHC staining was performed with the M.O.M. kit (Vector) according to the manufacturer's instructions. pS6 staining was performed following Pax7 staining by incubating the sections in a solution of PBS, 0.3% Triton X-100, 10% donkey serum and rabbit anti-pS6 antibodies at a dilution of 1:100, overnight. Secondary detection of pS6 was performed with donkey anti-rabbit Alexa 647 antibodies (Invitrogen) at a dilution of 1:500.

Immunocytochemistry (ICC) staining was performed on PFA fixed cells that had been cultured on chamber slides. EdU incorporation was visualized by Click-iT (Invitrogen) according to the manufacturer's instructions. For BrdU analysis, cells were fixed with 70% ethanol and treated with 2N HCl for 20 min before staining with BrdU antibodies. Image capture, analysis and quantification were performed using Velocity software.

All displayed immunostaining images are representative of at least 3 independent experiments.

Western blotting. Western blot analysis was performed on whole cell extracts of 1 × 10⁵ SCs that were counted, washed and lysed in sample buffer immediately after FACS purification. Lysates were subject to SDS-PAGE, transferred to PVDF membrane, and probed with indicated antibodies. Between antibody probing, the PVDF membrane was stripped using Restore Western Blotting Stripping Solution (Pierce).

Bioluminescence. Photo-emission was measured using 10,000 (CD31⁻, CD45⁻, Sca-1⁻, VCAM⁺) SCs purified by FACS from non-injured or 2.5 DPI *Pax7^{CreER/+}*; *Rosa26^{LuSeAP/+}* mice. SCs were allowed to adhere to ECM-coated 6-well plates for 1 h before addition of luminal and imaging with an IVIS imager.

mtDNA quantification. Total DNA was isolated from 10,000 SCs immediately after FACS isolation using QIAamp DNA micro kit (Qiagen) according to the manufacturer's instructions. mtDNA was quantified by qRT-PCR using primers amplifying the Cytochrome B region on mtDNA (forward primer: 5'-CATTAT

TATCGCGGCCCTA-3', reverse primer: 5'-TGTTGGGTTGTTTGATCCTG-3') relative to the β -globin region on gDNA (forward primer: 5'-GAAGCGATTCTA GGAGCAG-3', reverse primer: 5'-GGAGCAGCGATTCTGAGTAGA-3').

Cell size measurements

FACS. Throughout the dissection, digestion, and processing of muscle tissue (described above), preparations were maintained at 37 °C. Immediately upon completion of the isolation protocol, mononuclear EYFP⁺ cells were analysed in the forward scatter channel (FSC) by FACS to assess cell size. Data are presented as representative histograms.

Microscopy. Immediately after isolation, QSCs, 2.5 DPI CSCs, and 2.5 DPI ASCs were plated on 8-well chamber slides and allowed to adhere for 30 min at 37 °C, after which the media was aspirated, chambers removed and a coverslip applied. Bright field images of the slides were acquired using an Axioskop 2 with a $\times 40$ objective lens. The analysis of cell diameter was performed using AxioVision software (Zeiss).

Antibodies. Antibodies used in this study were: anti-Pax7 (#pax7) and anti-eMHC (#F1.652) from DSHB; phospho-S235/6 S6 (#4858 and #4857) and phospho-S2448 mTOR (#2971) from Cell Signaling; rabbit anti-GFP (#A11122) from Invitrogen; chicken anti-GFP (#ab15580), rat anti-laminin (#ab11576) and anti-Raptor (#ab40768) from AbCam; anti-PDGFR α (#AF1062) from R&D Systems; anti-Myogenin (#566358) and anti-MyoD (#554130) from BD; anti-BrdU (#OBD0030G) from Serotec; actin (#A3854) from Sigma. For HSCs: lineage antibodies: anti-B220 (#515-0452-82), anti-CD4 (#515-0042-82), anti-CD8 (#515-0081-82), anti-Mac1 (#515-0112-82), anti-Gr1 (#15-5931-82), anti-Ter119 (#515-5921-82); anti-Ly6A (Sca1) (#25-5981-81); anti-CD117 (cKit) (#747-1171-82), anti-CD150 (#12-1502-82), anti-CD48 (#17-0481-82), anti-EPCR (#17-2012-80) from eBiosciences.

Transcriptional profiling and pre-processing. For each sample, total RNA was isolated by TRIzol (Invitrogen) extraction followed by RNeasy Plus Micro Kit (Qiagen) from ~400,000 SCs pooled from ≥ 4 mice. Hybridization to GeneChip Mouse Gene 1.0 ST Affymetrix arrays was performed by the Stanford Protein and Nucleic Acid Facility. Raw data files are available at the NCBI GEO database (accession numbers GSE55490 and GSE47177).

Intensities were pre-processed using the Expression Console (Affymetrix) for RMA, and probe-sets that cross-hybridized, mapped to multiple transcripts or showed poor signal (intensity of <6.5) in all arrays were excluded. Processed array data are available as Supplementary Data Set 1. Arrays were batch-corrected using ComBat²⁸, and technical replicates were averaged. Probe sets lacking gene symbol annotation were excluded, and for transcripts covered by multiple probe sets, the most informative probe set with average intensity in the top two-thirds of sets for a transcript was selected^{29,30}.

Transcriptional profile analysis. All analyses were performed on mean-centred \log_2 -transformed expression levels.

For gene annotation analysis, the background gene set was all genes after pre-processing (15,343 genes). For each comparison between conditions, to ensure biological importance and reproducibility, the foreground gene set was selected as the smallest of the following: the gene set with 10% FDR by rank products analysis^{31,32}, all genes with at least 1.5-fold directional change between conditions, or the top 1,100 genes ranked by directional fold change. Enrichment analysis and redundancy grouping of KEGG pathways³³ was performed using GeneTerm Linker³⁴ with corrected P value <0.05 , minimum genes per term 4 and minimum silhouette 0.5.

K -medians clustering with the k -means++ seeding algorithm and Manhattan distance was performed on KEGG pathway oxidative phosphorylation genes (ID mmu00190) with $k = 3$. The partition with the smallest sum of intracluster distances was chosen. This partition was validated as being the most tightly clustered (best average sample shadow (0.38) and silhouette (0.61)), robust against different seeds (highest frequency as optimal partition (0.47)), and robust against noise (highest average frequency of reproduced cluster pairs during random projections to lower dimensions (0.80))³⁵.

Statistics. Unless stated otherwise, significance was calculated using two-tailed unpaired Student's t -tests. Differences were considered statistically significant at the $P < 0.05$ level.

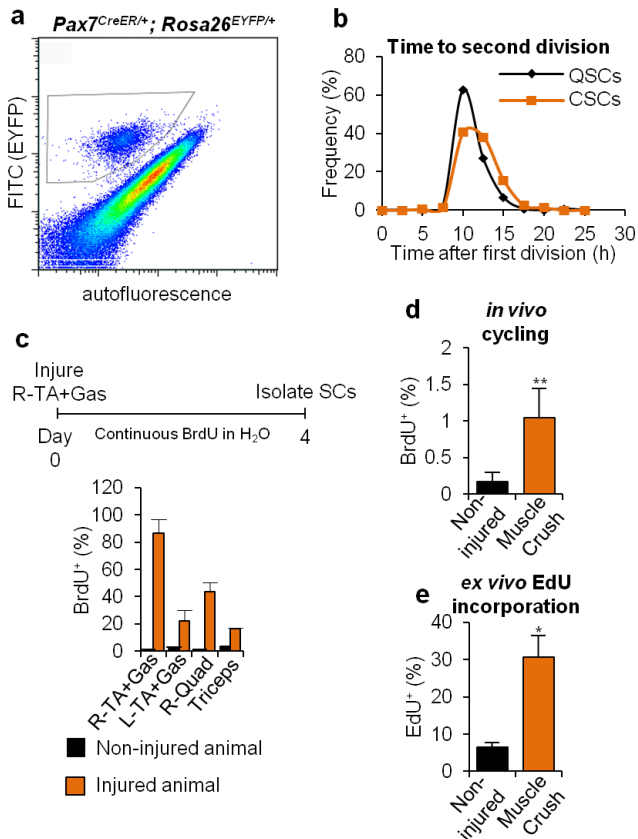
General methods. Unless stated otherwise, sample size (n values) are reported as biological replicates of mice and/or SC isolations from separate mice performed on different days. In figure legends where sample size is reported as a range, the exact sample size values are reported below:

Fig. 1b: QSCs ($n = 13$), CSCs (1.5 DPI, $n = 3$; 2.5 DPI, $n = 7$; 3.5 DPI, $n = 5$), ASCs (1.5 DPI, $n = 3$; 2.5 DPI, $n = 5$; 3.5 DPI, $n = 5$). Fig. 1c: QSCs ($n = 11$), CSCs (1 DPI, $n = 2$; 1.5 DPI, $n = 2$; 2.5 DPI, $n = 2$; 3.5 DPI, $n = 2$), ASCs (1 DPI, $n = 2$; 1.5 DPI, $n = 2$; 2.5 DPI, $n = 2$; 3.5 DPI, $n = 2$). Fig. 2e: QSCs ($n = 4$), CSCs ($n = 3$), ASCs ($n = 3$). Fig. 2f: QSCs ($n = 5$), CSCs ($n = 4$), ASCs ($n = 3$). Fig. 2h: QSCs ($n = 7$), CSCs (1 DPI, $n = 3$; 2.5 DPI, $n = 3$; 3.5 DPI, $n = 4$). Fig. 3a: wild-type QSCs ($n = 11$), TSC1 KO QSCs ($n = 6$). Fig. 3d: wild-type QSCs ($n = 11$), WT CSCs ($n = 7$), Raptor KO CSCs ($n = 6$). Fig. 3g: wild-type QSCs ($n = 11$), WT CSCs ($n = 7$), cMet KO QSCs ($n = 4$), cMet KO CSCs ($n = 5$). Figure 4e: Normal regeneration (3.5 DPI, $n = 6$; 6 DPI, $n = 5$; 11 DPI, $n = 3$; 15 DPI, $n = 3$; 24 DPI, $n = 4$), Alert regeneration (3.5 DPI, $n = 5$; 6 DPI, $n = 5$; 11 DPI, $n = 3$; 15 DPI, $n = 3$; 24 DPI, $n = 4$). Figure 4h: QFAPs ($n = 6$), CFAPs (each point, $n = 2$), AFAPs (each point, $n = 2$). Figure 4i: non-injured ($n = 4$), injured ($n = 5$). Figure 4j: non-injured + PBS ($n = 4$), non-injured plus IFN- γ ($n = 3$), injured plus PBS ($n = 3$), injured plus IFN- γ ($n = 4$).

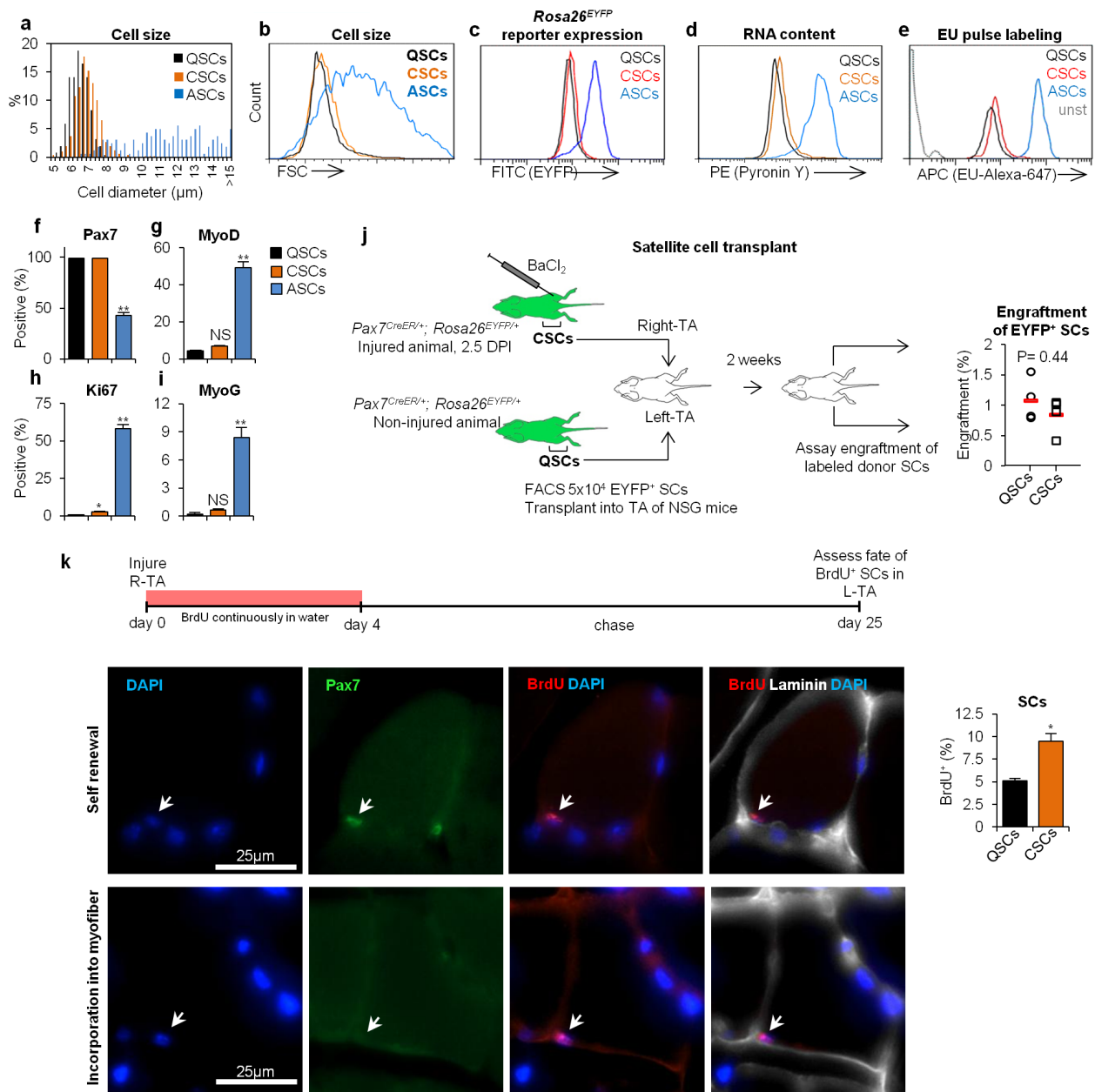
Extended Data Fig. 1c: non-injured ($n = 2$), injured (R-TA, $n = 3$; L-TA, $n = 3$; R-Quad, $n = 2$, triceps, $n = 2$). Extended Data Fig. 3i: ($n = 4$), Extended Data Fig. 3j: ($n = 6$), Extended Data Fig. 3k: ($n = 3$), Extended Data Fig. 3l: ($n = 5$), Extended Data Fig. 3m: ($n = 6$). Extended Data Fig. 5g: wild-type QSCs ($n = 6$), wild-type CSCs ($n = 4$), cMet KO QSCs ($n = 3$), cMet KO CSCs ($n = 6$). Extended Data Fig. 6a: non-injured ($n = 6$), 2.5 DPI ($n = 3$), 7 DPI ($n = 5$), 14 DPI ($n = 3$), 28 DPI ($n = 3$). Extended Data Fig. 6a: QSCs ($n = 13$), CSCs (1.5 DPI, $n = 3$; 2.5 DPI, $n = 7$; 3.5 DPI, $n = 5$; 7 DPI, $n = 2$; 14 DPI, $n = 3$; 21 DPI, $n = 2$; 35 DPI, $n = 2$), ASCs (1.5 DPI, $n = 3$; 2.5 DPI, $n = 5$; 3.5 DPI, $n = 5$; 7 DPI, $n = 2$; 14 DPI, $n = 3$; 21 DPI, $n = 2$; 35 DPI, $n = 2$). Extended Data Fig. 6c: QSCs ($n = 11$), CSCs (2.5 DPI, $n = 2$; 7 DPI, $n = 2$; 14 DPI, $n = 2$; 21 DPI, $n = 2$; 28 DPI, $n = 2$; 35 DPI, $n = 6$), ASCs (2.5 DPI, $n = 2$; 7 DPI, $n = 2$; 14 DPI, $n = 2$; 21 DPI, $n = 2$; 28 DPI, $n = 2$; 35 DPI, $n = 4$). Extended Data Fig. 9c: QFAPs ($n = 6$), CSCs (each point, $n = 2$), ASCs (each point, $n = 2$). Extended Data Fig. 9d: non-injured ($n = 4$), injured ($n = 5$).

In most cases, the data presented were compiled over the course of 2 years, as mice with the appropriate genotype became available. Therefore the magnitude of the effect and variability in the measurements were primary factors in determining sample size and replication of data. Although samples were not explicitly randomized or blinded, mouse identification numbers were used as sample identifiers and thus the genotypes and experimental conditions of each mouse/sample were not readily known or available to the experimenters during sample processing and data collection. The only criteria used to exclude samples involved the health of the animals, such as visible wounds from fighting. In these cases, the animals were handled in accordance with approved IACUC guidelines.

28. Johnson, W. E., Li, C. & Rabinovic, A. Adjusting batch effects in microarray expression data using empirical Bayes methods. *Biostatistics* **8**, 118–127 (2007).
29. Mieczkowski, J., Tyburczy, M. E., Dabrowski, M. & Pokarowski, P. Probe set filtering increases correlation between Affymetrix GeneChip and qRT-PCR expression measurements. *BMC Bioinformatics* **11**, 104 (2010).
30. Miller, J. A. *et al.* Strategies for aggregating gene expression data: the collapseRows R function. *BMC Bioinformatics* **12**, 322 (2011).
31. Breitling, R., Armengaud, P., Amtmann, A. & Herzyk, P. Rank products: a simple, yet powerful, new method to detect differentially regulated genes in replicated microarray experiments. *FEBS Lett.* **573**, 83–92 (2004).
32. Hong, F. *et al.* RankProd: a bioconductor package for detecting differentially expressed genes in meta-analysis. *Bioinformatics* **22**, 2825–2827 (2006).
33. Kanehisa, M., Goto, S., Sato, Y., Furumichi, M. & Tanabe, M. KEGG for integration and interpretation of large-scale molecular data sets. *Nucleic Acids Res.* **40**, D109–D114 (2012).
34. Fontanillo, C., Nogales-Cadenas, R., Pascual-Montano, A. & De las Rivas, J. Functional analysis beyond enrichment: non-redundant reciprocal linkage of genes and biological terms. *PLoS ONE* **6**, e24289 (2011).
35. Valentini, G. Clusterv: a tool for assessing the reliability of clusters discovered in DNA microarray data. *Bioinformatics* **22**, 369–370 (2006).

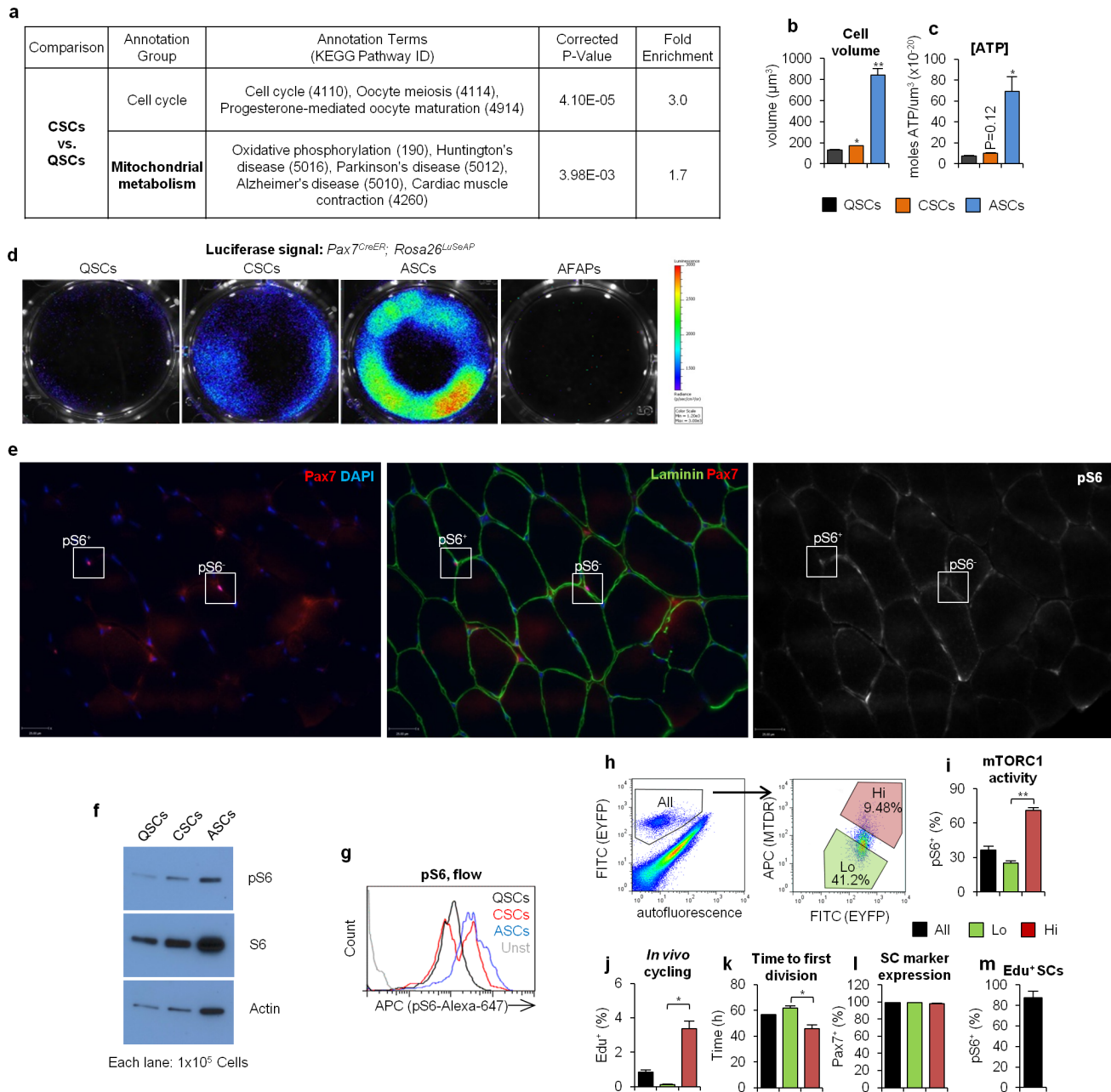


Extended Data Figure 1 | SCs distant from the site of an injury display a functional response to the injury. **a**, Representative FACS plot from isolation of EYFP⁺ SCs from 10-week-old *Pax7^{CreER/+}; Rosa26^{EYFP/+}* mice 3 weeks following TMX treatment. Mononuclear cells from muscle digests were gated in FITC and Pac-Blue (autofluorescence) channels to separate EYFP⁺ SCs. EYFP⁺ SCs were usually 2–4% of all events from muscle digestions. **b**, Progeny of CSCs and QSCs take comparable times to complete the second cell division. Analysis of the time required to complete the second division (QSCs 10.2 ± 2 h, $n = 148$ cells; CSCs 10.9 ± 2 h, $n = 155$), following the first cell cycle (Fig. 1d), shows that accelerated cell cycle kinetics of CSCs is limited to the first division. **c**, SCs throughout the body increase in propensity to cycle in response to injury. In injured animals, SCs isolated from indicated muscle groups show higher frequency of BrdU incorporation when compared to SCs from the same muscle groups from non-injured mice ($n \geq 2$ animals). **d**, Muscle crush injuries increase the *in vivo* cycling propensity of CSCs. Twelve hours after BrdU pulse labelling, SCs isolated from TA and Gast muscles contralateral to muscle crush injury show elevated BrdU labelling frequency versus SCs from those muscles from non-injured mice (mean \pm s.e.m.; non-injured, $n = 5$ animals; muscle crush, $n = 3$; $**P < 0.01$). **e**, SCs contralateral to a muscle crush injury have increased cell cycle entry kinetics. 2.5 DPI SCs contralateral to a muscle crush injury incorporate EdU more rapidly than QSCs when cultured *ex vivo* for 40 h (mean \pm s.e.m., $n = 3$ animals, $*P < 0.05$).



Extended Data Figure 2 | CSCs are distinct from QSCs but retain stem cell characteristics. **a**, CSCs are slightly larger than QSCs and much smaller than ASCs. Immediately after isolation, analysis of cell diameters of QSCs, 2.5 DPI CSCs and 2.5 DPI ASCs, measured by phase contrast microscopy, shows that CSCs have a distribution that is shifted to the right compared to QSCs (histographic representation of data displayed in Fig. 2a, b). **b**, CSCs are larger than QSCs as measured by the FSC parameter by FACS (representative FACS plot, similar results observed in 4 independent experiments). **c**, CSCs have elevated intensity of an EYFP reporter. FACS analysis of EYFP intensity in the FITC channel shows that 2.5 DPI CSCs display a slight shift in EYFP distribution relative to QSCs, suggesting increased expression of this reporter from the *Rosa26* locus (representative FACS plot, similar results observed in 4 independent experiments). **d**, CSCs show elevated levels of pyronin Y staining, suggesting an increased RNA content relative to QSCs, but substantially less than ASCs (representative FACS plot, similar results observed in 4 independent experiments). **e**, CSCs increase global transcriptional activity compared with QSCs. FACS analysis of EU incorporation, following pulse labelling by i.p. injection, shows that 2.5 DPI CSCs have higher levels of EU nucleotide incorporation than QSCs, whereas ASCs show markedly elevated incorporation. **f–i**, Immunocytochemical (ICC) staining of QSCs, 2.5 DPI CSCs and 2.5 DPI ASCs immediately after isolation shows that CSCs are highly similar to QSCs in expression of the QSC marker Pax7 (**f**), as well as markers of

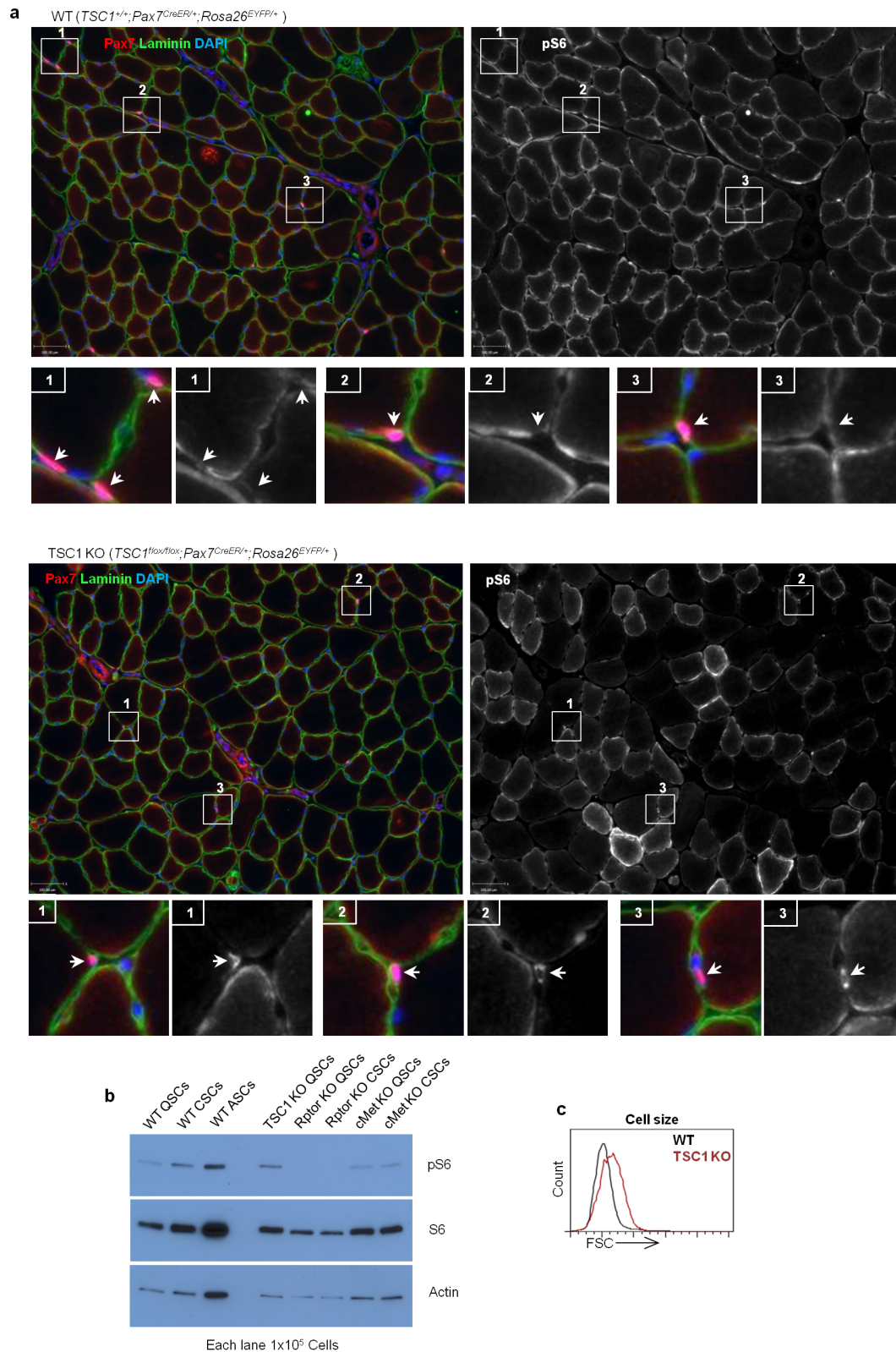
SC activation, MyoD (**g**) and Ki67 (**h**), and myogenic differentiation, MyoG (**i**) (mean \pm s.e.m.; $n = 4$ animals; $*P < 0.05$, $**P < 0.01$). **j**, CSCs have comparable ability to engraft as QSCs. EYFP⁺ QSCs and 2.5 DPI CSCs were isolated from donor mice (*Pax7^{CreER/+}; Rosa26^{EYFP/+}*). A total of 5×10^4 EYFP⁺ QSCs were transplanted into the left TAs and 5×10^4 EYFP⁺ CSCs were transplanted into the right TAs of host NSG mice. Two weeks after transplantation, EYFP⁺ SCs were isolated from TA muscles of host mice and SC engraftment efficiency was measured as the number of EYFP⁺ SCs that were recovered as a percentage of the number of donor SCs that were transplanted ($n = 4$, red line indicates mean). For both donor cell populations, greater than 95% of SCs recovered were found to be Pax7⁺ as measured by ICC (data not shown). **k**, CSCs that incorporate BrdU self-renew. Following injury to one TA muscle, mice were administered BrdU continuously for 4 days followed by 21 days of chase (as shown in the diagram). IF-IHC analysis of the TA contralateral to the injury revealed BrdU⁺ Pax7⁺ cells in the satellite cell position beneath the basal lamina. An example of such a cell is illustrated here (top row of images). On the right is quantification of BrdU⁺ SCs after 21 days of chase by ICC after FACS isolation, showing that CSCs have self-renewal capacity similar to QSCs (mean \pm s.e.m., $n = 3$ animals, $*P < 0.05$). Below is an example of a BrdU⁺ myonucleus in the contralateral TA after 21 days of chase, suggesting that CSCs can also fuse with the adjacent fibre following proliferation.



Extended Data Figure 3 | CSCs have elevated mitochondrial and mTORC1 activity.

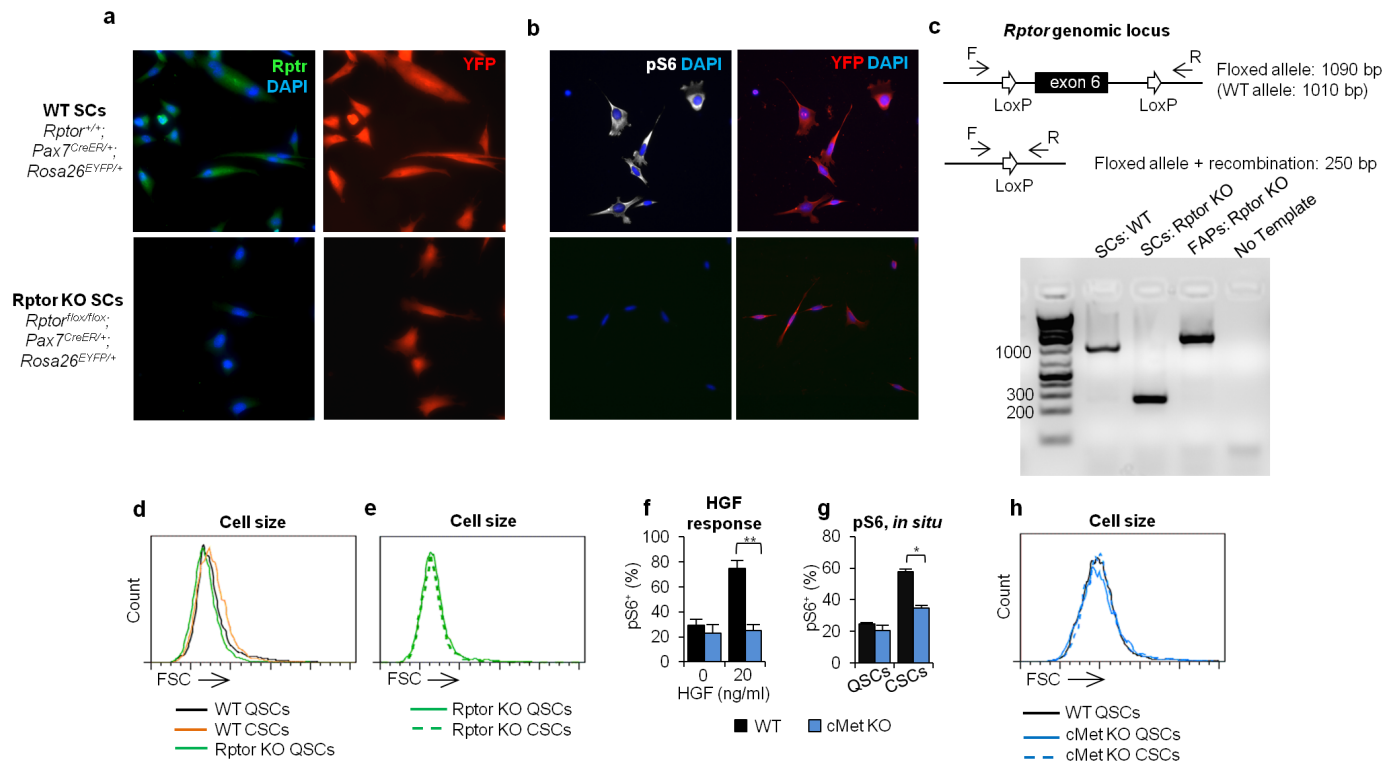
a, Induction of genes involved in the cell cycle and mitochondrial metabolism in CSCs. Pathway analysis of genes that were induced in CSCs versus QSCs showed enrichment of genes involved in the cell cycle and mitochondrial metabolism. Redundant KEGG pathways that contain overlapping genes were assembled into annotation groups (details of array and enrichment analysis are found in the Methods section). **b**, CSCs have slightly increased cell volume compared to QSCs. Cell volume was calculated from cell size measurements (Fig. 2b) (mean \pm s.e.m., $n = 4$ animals, $*P < 0.05$, $**P < 0.01$ compared to QSCs). **c**, CSCs have a slightly greater intracellular ATP concentration than QSCs (mean \pm s.e.m., $n = 4$ animals, $*P < 0.05$ compared to QSCs). **d**, Increase in photo emission from CSCs expressing luciferase reporter (LuSeAP). Immediately after isolation and plating, bioluminescence imaging of 1×10^4 Pax7^{CreER/+}; Rosa26^{LuSeAP/+} SCs shows that 2.5 DPI CSCs have greater luminescence than QSCs, ASCs have substantially elevated luminescence. Activated fibro-adipogenic progenitors (AFAPs) were isolated from the same injured muscle as ASCs and plated as a negative control for LuSeAP expression. Light emission from luciferase is dependent on the amounts of luciferase enzyme, ATP and luciferin. Increased ATP and increased expression from the Rosa26 locus in CSCs (Fig. 2j and Extended Data Fig. 2c) could both contribute to increased luminescence. Data

presented are from a representative experiment with similar results observed in two independent experiments. **e**, Low magnification image of IF-IHC staining of TA muscle. Boxed areas are of the representative pS6⁻ and pS6⁺ SCs that are shown in Fig. 2g. **f**, CSCs have increased levels of pS6 as shown by western blot analysis of whole-cell extracts from 1×10^5 cells of each population collected immediately after isolation. **g**, CSCs show a bimodal distribution of pS6 staining at 1 DPI, with peaks corresponding to the signal in pS6⁻ QSCs and pS6⁺ ASCs when analysed by FACS (representative FACS plot, similar results observed in 3 independent experiments). **h**, Sorting SCs for properties of the alert state (that is, high levels of MitoTracker Deep Red (MTDR) staining and YFP expression) enriches for SCs that display the other properties of alert SCs: elevated mTORC1 activity, reduced time to first division and increased propensity to cycle. Representative gating of MTDR^{Hi};EYFP^{Hi} SCs (Hi) and MTDR^{Lo};EYFP^{Lo} SCs (Lo). **i–m**, Sorting of Hi SCs reveals a sub-population of QSCs that displays characteristics of the alert state. Hi SC cells have increased mTORC1 activity (**i**), an increased propensity to cycle *in vivo* as measured by incorporation of EdU nucleotide 12 h after pulse labelling (**j**), and an accelerated time to first division (**k**). Both Hi and Lo SCs stain positive for the SC marker, Pax7 (**l**). 12 h after an *in vivo* EdU pulse, most SCs that incorporate nucleotide (quantified in **j**) stain positive for pS6 (**m**). Panels **i–m** are displayed as mean \pm s.e.m., $n \geq 3$ animals, $*P < 0.05$, $**P < 0.01$.



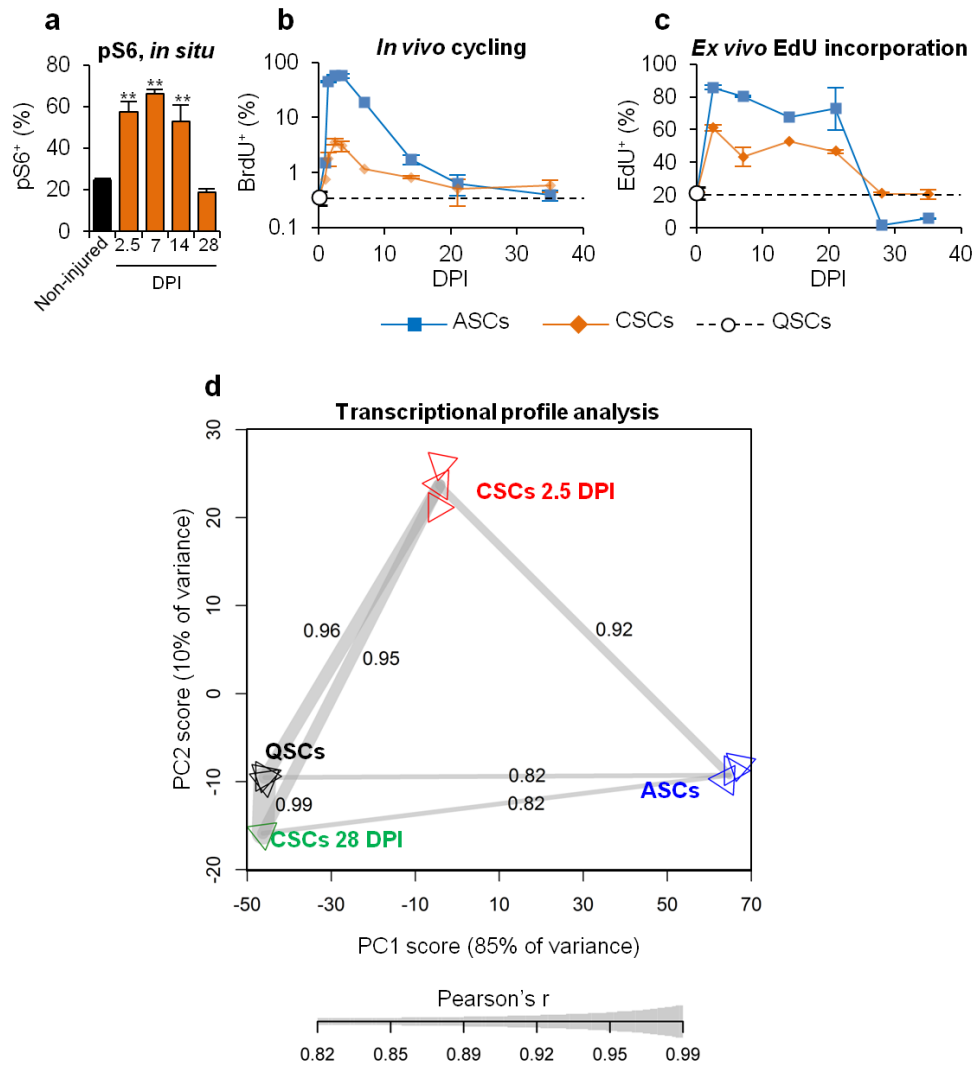
Extended Data Figure 4 | TSC1 KO SCs show induction of pS6 and increased cell size. **a**, TSC1 KO increases SC pS6 levels. IF-IHC staining shows no pS6 staining of SCs in wild-type TA muscle and strong staining of SCs in TSC1 KO TA (representative images of low-magnification muscle section, numbered boxed regions are shown in high magnification below). **b**, Levels of pS6 in SC-specific KO models. TSC1 KO SCs show induction of pS6 when compared to wild-type QSCs, whereas Raptor KO QSCs and CSCs show no detectable pS6. cMet KO QSCs show comparable levels of pS6 as wild-type

QSCs. However, unlike wild-type CSCs, cMet KO CSCs show no induction of pS6. Displayed is western blotting analysis of whole cell extracts from 1×10^5 cells per each population/genetic model collected immediately after isolation. The first three lanes (WT: QSCs, CSCs and ASCs) are the same as Extended Data Fig. 3f and are redisplayed for the purpose of comparison. **c**, TSC1 KO SCs are larger than wild-type SCs (representative FACS plot, similar results observed in 4 independent experiments).



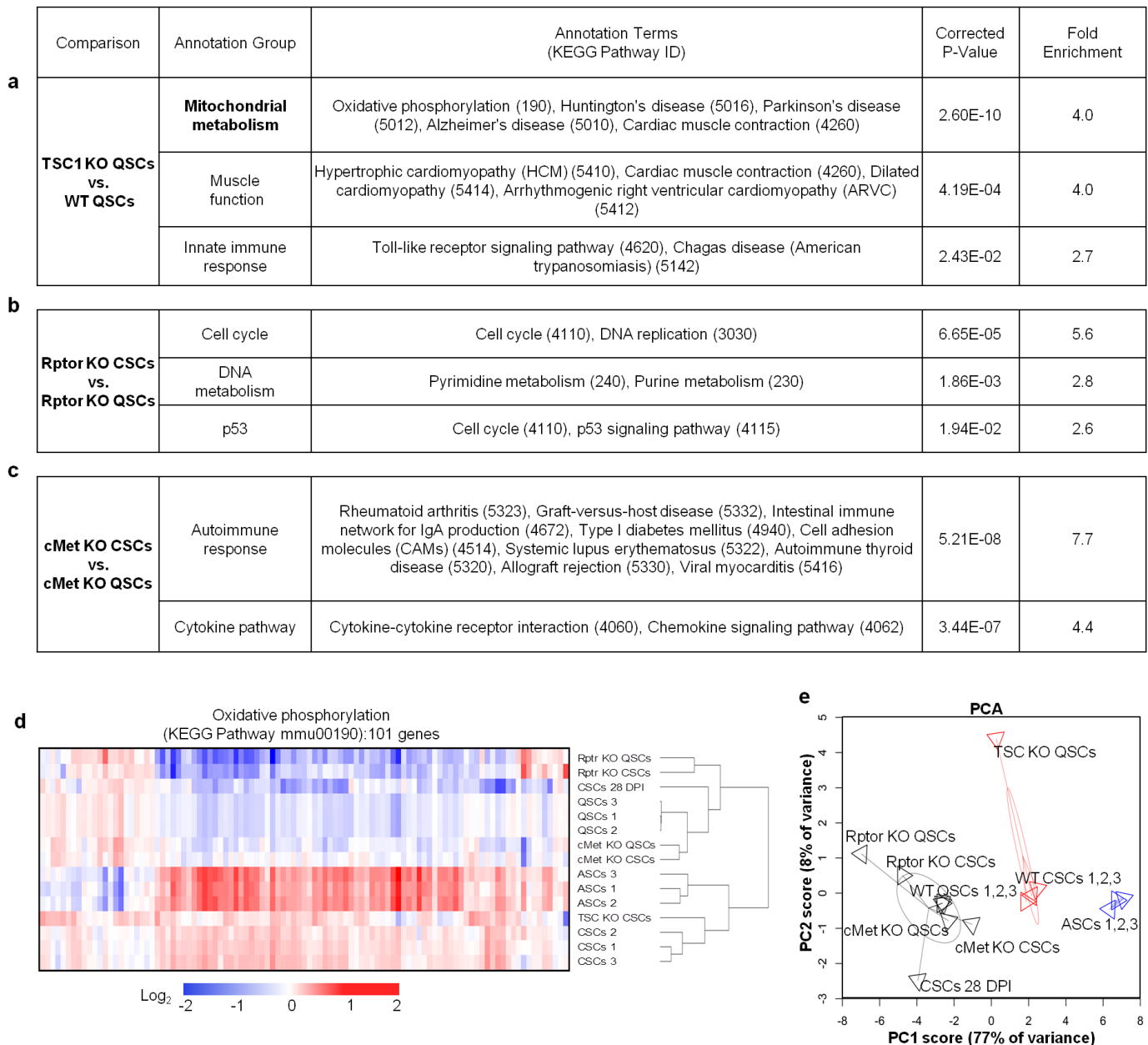
Extended Data Figure 5 | Rptor and cMet KO SCs contralateral to injury display no 'alerting' response. **a**, Depletion of Rptor protein in Rptor KO SCs. ICC staining of EYFP⁺ SCs cultured for 40 h after isolation shows that Rptor protein is undetectable in Rptor KO SCs but clearly detectable in wild-type SCs. **b**, Absence of pS6 in Rptor KO SCs. ICC staining shows that after 40 h in culture, EYFP⁺ wild-type SCs stain strongly pS6⁺ whereas EYFP⁺ Rptor KO SCs do not exhibit any detectable pS6 signal. **c**, PCR verification of *Rptor* exon 6 excision in Rptor KO SCs. Using primers flanking the floxed exon 6 of the *Rptor* genomic locus, PCR analysis of genomic DNA from SCs isolated from a Rptor conditional KO animal (*Rptor*^{flx/flx}; *Pax7*^{CreER/+}; *Rosa26*^{EYFP/+}) shows efficient recombination of the floxed allele, whereas analysis of genomic DNA from SCs from a wild-type animal (*Rptor*^{+/+}; *Pax7*^{CreER/+}; *Rosa26*^{EYFP/+}) and FAPs from a Rptor conditional KO animal does not show recombination. **d**, FACS analysis reveals that Rptor KO SCs are slightly smaller and display a slight leftward shift in FSC distribution relative to wild-type SCs. **e**, Rptor KO

SCs do not enlarge in response to contralateral injury. 2.5 DPI, Rptor KO CSCs show a nearly identical FSC distribution to that of Rptor KO QSCs and do not increase in size in response to contralateral injury as do wild-type CSCs (**d**). **a–e**, Representative data, similar results observed in at least 3 independent experiments. **f**, cMet is required for phosphorylation of S6 by HGF. In culture, wild-type SCs show a robust increase in the frequency of pS6⁺ SCs in response to a 1 h stimulation with HGF whereas cMet KO SCs show no change in pS6 staining frequency (mean \pm s.e.m., $n = 4$, $**P < 0.01$). **g**, cMet KO prevents induction of pS6 in SCs contralateral to injury as measured by IF-IHC (mean \pm s.e.m.; $n \geq 3$ animals, ≥ 50 Pax7⁺ SCs analysed from each animal; $*P < 0.05$). **h**, cMet KO CSCs do not change in size. FACS analysis shows that cMet KO and wild-type QSCs have similar FSC distributions and that this distribution is not altered in cMet KO SCs contralateral to an injury (a representative FACS plot is shown; similar results were observed in 3 independent experiments).



Extended Data Figure 6 | The functional properties of alert CSCs revert back to the QSC state 28 DPI. **a**, Frequency of pS6⁺ CSCs returns to non-injured levels 28 DPI. Quantification of the percentage of pS6⁺ SCs by IF-IHC shows that immediately following injury, most CSCs (orange bars) become pS6⁺. The frequency of pS6⁺ CSCs decreases to levels observed in non-injured animals (black bar) by 28 DPI (mean \pm s.e.m., $n \geq 3$ animals, > 50 Pax7⁺ SCs analysed from each animal, ** $P < 0.01$ versus non-injured). **b**, The propensity of CSCs to cycle returns to the level of QSCs several weeks after injury. At various times after injury, mice were given an i.p. injection of BrdU. SCs were isolated 12 h later from the injured muscles (ASCs) or from the contralateral muscles (CSCs). The frequency of BrdU incorporation returned to

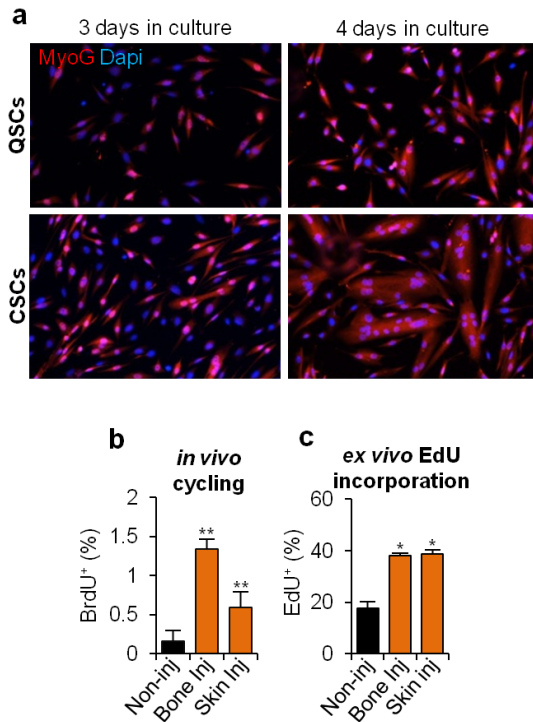
QSC levels (dashed line) by approximately 21 days after injury for both ASCs and CSCs (mean \pm s.e.m.; $n \geq 3$ animals). **c**, Cell cycle entry kinetics of CSCs returns to the level of QSCs several weeks after injury. At various times after injury, SCs or their progeny were isolated from the injured muscles (ASCs) or from the contralateral muscles (CSCs) and cultured *in vitro* for 40 h in the presence of EdU. The frequency of EdU incorporation returned to QSC levels (dashed line) by several weeks after injury for both ASCs and CSCs (mean \pm s.e.m., $n \geq 2$ animals). **d**, CSCs isolated 28 DPI have a transcriptional profile very similar to QSCs as shown by PCA and Pearson's *r* value. Transcriptome analysis was performed as in Fig. 2c, with the addition of data from CSCs 28 DPI.



Extended Data Figure 7 | The ability to adopt the alert state strongly correlates with expression of genes involved in mitochondrial metabolism.

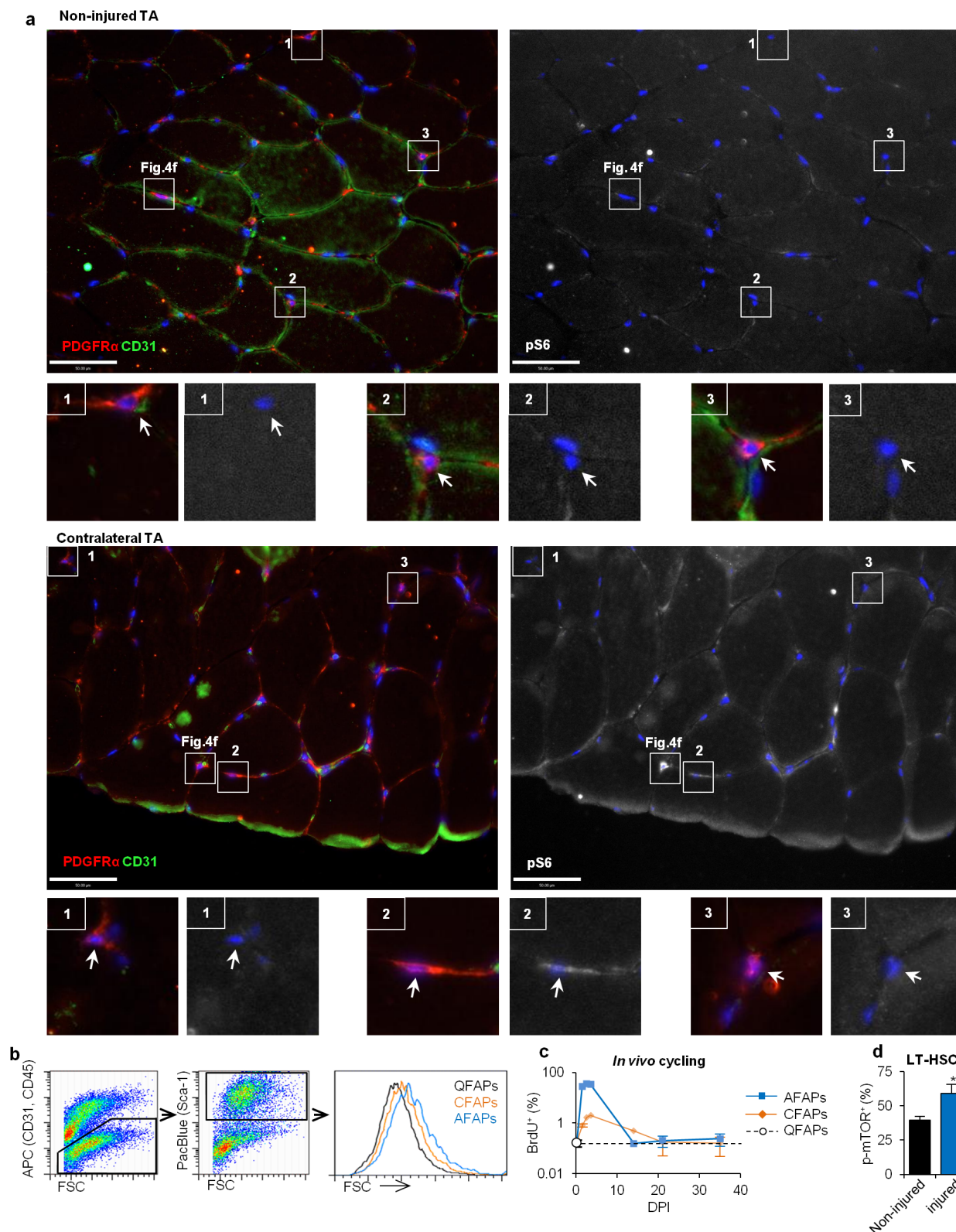
a, Pathway analysis (as performed in Extended Data Fig. 3a) of the genes induced in TSC1 KO QSCs compared to wild-type QSCs shows that genes involved in mitochondrial metabolism are significantly enriched. **b**, **c**, Pathway analyses of the genes induced in Rptor KO CSCs compared to Rptor KO QSCs (**b**) and cMet KO CSCs compared to cMet KO QSCs (**c**) show that genes involved in mitochondrial metabolism are not enriched. **d**, Expression of genes involved in oxidative phosphorylation (KEGG ID mmu00190) is coupled with the alert state. Heat map of the expression of genes in the oxidative phosphorylation pathway shows that models of the alert state (CSCs and TSC1 KO QSCs) have elevated expression of these genes and that models of non-alert SCs (QSCs, Rptor KO SCs and cMet KO SCs) have low expression of these

genes. Hierarchical clustering (Euclidean distance, complete linkage) shows that models of the alert state (CSCs and TSC1 KO SCs) cluster together and that models of non-alert SCs (QSCs, Rptor KO SCs and cMet KO SCs) form another cluster. **e**, Centroid-based clustering using oxidative phosphorylation genes (KEGG ID mmu00190) shows that grouping SCs into three clusters reveals an 'alert' cluster (wild-type CSCs and TSC1 KO QSCs), a 'non-alert' cluster (QSCs, CSCs 28 DPI, Rptor KO QSCs and CSCs and cMet KO QSCs and CSCs), and an 'activated' cluster (ASCs). Ellipses of dispersion show standard deviation (radius) and mean (centre) for each cluster using the first two components from PCA. Combined, these data show that induction of genes involved in mitochondrial metabolism strongly and consistently correlates with ability to adopt the alert state: wild-type CSCs and TSC1 KO QSCs are alert, and Rptor KO and cMet KO CSCs are not alert.



Extended Data Figure 8 | SCs enter the alert state in response to many types of injuries. **a**, Cultures of CSCs differentiate more quickly than do cultures of QSCs (representative ICC staining of MyoG, data quantified in Fig. 4a, b).

b, SCs enter the alert state in response to injuries to non-muscle tissue. SCs contralateral to a tibial fracture (bone inj) and SCs in an animal that received a skin wound on the abdomen (skin inj) increase in propensity to cycle *in vivo* (mean \pm s.e.m.; non-injured, $n = 5$ animals; bone injured, $n = 2$; skin injured, $n = 6$; ** $P < 0.01$ versus non-injured). **c**, SCs increase cycle cell entry kinetics in response to non-muscle injuries. SCs contralateral to a tibial fracture injury and SCs from mice that received a skin injury have increased frequency of EdU incorporation when cultured for 40 h *ex vivo* compared to SCs from non-injured animals (mean \pm s.e.m.; $n = 3$ animals; * $P < 0.05$ versus non-injured).



Extended Data Figure 9 | FAPs and LT-HSCs adopt an alert state in response to muscle injury. **a**, Increased frequency of pS6⁺ FAPs contralateral to muscle injury. Representative IF-IHC staining of TA muscle from a non-injured animal (top) or contralateral to injury (bottom) shows that the frequency of pS6⁺ (PDGFR α ⁺;CD31⁻) FAPs is increased in contralateral muscle (data are quantified in Fig. 4g). Labelled boxes indicate regions for which higher magnification is displayed. **b**, CFAPs increase in size. FACS analysis shows that 2.5 DPI CFAPs increase in FSC distribution compared to QFAPs; AFAPs show a greater increase in size (a representative FACS plot is

shown, similar results were observed in 3 independent experiments). **c**, CFAPs increase in propensity to cycle. Twelve hours following an i.p. injection of BrdU, CFAPs isolated at indicated DPIs have an elevated frequency of BrdU incorporation compared to QFAPs (0 DPI). **d**, Muscle injury increases the frequency of phospho-mTOR⁺ (pmTOR) LT-HSCs. FACS analysis of pmTOR in Lineage⁻, Sca-1⁺, cKit⁺, CD150⁺ HSCs isolated from bone marrow 1 DPI showed that LT-HSCs induce mTORC1 signalling in response to muscle injury (mean \pm s.e.m.; $n \geq 4$; * $P < 0.05$).

The metabolite α -ketoglutarate extends lifespan by inhibiting ATP synthase and TOR

Randall M. Chin¹, Xudong Fu², Melody Y. Pai^{1*}, Laurent Vergnes^{3*}, Heejun Hwang^{2*}, Gang Deng⁴, Simon Diep², Brett Lomenick², Vijaykumar S. Meli⁵, Gabriela C. Monsalve⁵, Eileen Hu², Stephen A. Whelan⁶, Jennifer X. Wang⁷, Gwanghyun Jung², Gregory M. Solis⁸, Farbod Fazlollahi⁹, Chitrada Kaweeteerawat¹⁰, Austin Quach², Mahta Nili¹¹, Abby S. Krall², Hilary A. Godwin¹⁰, Helena R. Chang⁶, Kym F. Faull⁹, Feng Guo⁵, Meisheng Jiang², Sunia A. Trauger⁷, Alan Saghatelian¹², Daniel Braas^{2,13}, Heather R. Christofk^{2,13}, Catherine F. Clarke^{1,4}, Michael A. Teitell^{1,11}, Michael Petrascheck⁸, Karen Reue^{1,3}, Michael E. Jung^{1,4}, Alison R. Frand⁵ & Jing Huang^{1,2}

Metabolism and ageing are intimately linked. Compared with *ad libitum* feeding, dietary restriction consistently extends lifespan and delays age-related diseases in evolutionarily diverse organisms^{1,2}. Similar conditions of nutrient limitation and genetic or pharmacological perturbations of nutrient or energy metabolism also have longevity benefits^{3,4}. Recently, several metabolites have been identified that modulate ageing^{5,6}; however, the molecular mechanisms underlying this are largely undefined. Here we show that α -ketoglutarate (α -KG), a tricarboxylic acid cycle intermediate, extends the lifespan of adult *Caenorhabditis elegans*. ATP synthase subunit β is identified as a novel binding protein of α -KG using a small-molecule target identification strategy termed drug affinity responsive target stability (DARTS)⁷. The ATP synthase, also known as complex V of the mitochondrial electron transport chain, is the main cellular energy-generating machinery and is highly conserved throughout evolution^{8,9}. Although complete loss of mitochondrial function is detrimental, partial suppression of the electron transport chain has been shown to extend *C. elegans* lifespan^{10–13}. We show that α -KG inhibits ATP synthase and, similar to ATP synthase knockdown, inhibition by α -KG leads to reduced ATP content, decreased oxygen consumption, and increased autophagy in both *C. elegans* and mammalian cells. We provide evidence that the lifespan increase by α -KG requires ATP synthase subunit β and is dependent on target of rapamycin (TOR) downstream. Endogenous α -KG levels are increased on starvation and α -KG does not extend the lifespan of dietary-restricted animals, indicating that α -KG is a key metabolite that mediates longevity by dietary restriction. Our analyses uncover new molecular links between a common metabolite, a universal cellular energy generator and dietary restriction in the regulation of organismal lifespan, thus suggesting new strategies for the prevention and treatment of ageing and age-related diseases.

To gain insight into the regulation of ageing by endogenous small molecules, we screened normal metabolites and aberrant disease-associated metabolites for their effects on adult lifespan using the *C. elegans* model. We discovered that the tricarboxylic acid (TCA) cycle intermediate α -KG (but not isocitrate or citrate) delays ageing and extends the lifespan of *C. elegans* by ~50% (Fig. 1a and Extended Data Fig. 1a). In the cell, α -KG (or 2-oxoglutarate; Fig. 1b) is produced from isocitrate by oxidative decarboxylation catalysed by isocitrate dehydrogenase (IDH). α -KG can also be produced anaplerotically from glutamate by oxidative

deamination using glutamate dehydrogenase, and as a product of pyridoxal phosphate-dependent transamination reactions in which glutamate is a common amino donor. α -KG extended the lifespan of wild-type N2 worms in a concentration-dependent manner, with 8 mM α -KG producing the maximal lifespan extension (Fig. 1c); 8 mM was the concentration used in all subsequent *C. elegans* experiments. There is a ~50% increase in α -KG concentration in worms on 8 mM α -KG plates compared with those on vehicle plates (Extended Data Fig. 1b), or ~160 μ M versus ~110 μ M assuming homogenous distribution (Methods). α -KG not only extends lifespan, but also delays age-related phenotypes, such as the decline in rapid, coordinated body movement (Supplementary Videos 1 and 2). α -KG supplementation in the adult stage is sufficient for longevity (Extended Data Fig. 1c).

The dilution or killing of the *C. elegans* bacterial food source has been shown to extend worm lifespan¹⁴, but the lifespan increase by α -KG is not due to altered bacterial proliferation or metabolism (Fig. 1d, e and Extended Data Fig. 1d). Animals also did not view α -KG-treated food as less favourable (Extended Data Fig. 1e, f), and there was no significant change in food intake, pharyngeal pumping, foraging behaviour, body size or brood size in the presence of α -KG (Extended Data Fig. 1e–h; data not shown).

In the cell, α -KG is decarboxylated to succinyl-CoA and CO₂ by α -KG dehydrogenase (encoded by *ogdh-1*), a key control point in the TCA cycle. Increasing α -KG levels by *ogdh-1* RNA interference (RNAi) (Extended Data Fig. 1b) also extends worm lifespan (Fig. 1f and Supplementary Notes), consistent with a direct effect of α -KG on longevity independent of bacterial food.

To investigate the molecular mechanism(s) of longevity by α -KG, we took advantage of an unbiased biochemical approach, DARTS⁷. As we proposed that key target(s) of α -KG are likely to be conserved and ubiquitously expressed, we used a human cell line (Jurkat) that is easy to culture as the protein source for DARTS (Fig. 2a). Mass spectrometry identified ATP5B, the β subunit of the catalytic core of the ATP synthase, among the most abundant and enriched proteins present in the α -KG-treated sample (Extended Data Table 1); the homologous α subunit ATP5A was also enriched but to a lesser extent. The interaction between α -KG and ATP5B was verified using additional cell lines (Fig. 2b; data not shown), and corroborated for the *C. elegans* orthologue ATP-2 (Extended Data Fig. 2a).

α -KG inhibits the activity of complex V, but not complex IV, from bovine heart mitochondria (Fig. 2c and Extended Data Fig. 2b; data not

¹Molecular Biology Institute, University of California Los Angeles, Los Angeles, California 90095, USA. ²Department of Molecular and Medical Pharmacology, University of California Los Angeles, Los Angeles, California 90095, USA. ³Department of Human Genetics, University of California Los Angeles, Los Angeles, California 90095, USA. ⁴Department of Chemistry and Biochemistry, University of California Los Angeles, Los Angeles, California 90095, USA. ⁵Department of Biological Chemistry, University of California Los Angeles, Los Angeles, California 90095, USA. ⁶Department of Surgery, University of California Los Angeles, Los Angeles, California 90095, USA. ⁷Small Molecule Mass Spectrometry Facility, FAS Division of Science, Harvard University, Cambridge, Massachusetts 02138, USA. ⁸Department of Chemical Physiology, The Scripps Research Institute, La Jolla, California 92037, USA. ⁹Pasaron Mass Spectrometry Laboratory, Department of Psychiatry and Biobehavioral Sciences and Semel Institute for Neuroscience and Human Behavior, University of California Los Angeles, Los Angeles, California 90095, USA. ¹⁰Department of Environmental Health Sciences, University of California Los Angeles, Los Angeles, California 90095, USA. ¹¹Department of Pathology and Laboratory Medicine, University of California Los Angeles, Los Angeles, California 90095, USA. ¹²Department of Chemistry and Chemical Biology, Harvard University, Cambridge, Massachusetts 02138, USA. ¹³UCLA Metabolomics Center, University of California Los Angeles, Los Angeles, California 90095, USA.

*These authors contributed equally to this work.

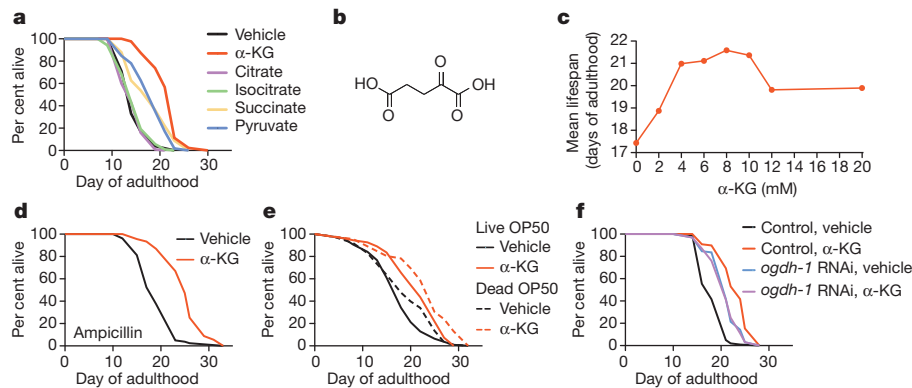


Figure 1 | α -KG extends the adult lifespan of *C. elegans*. **a**, α -KG extends the lifespan of adult worms in the metabolite longevity screen. All metabolites were given at a concentration of 8 mM. **b**, Structure of α -KG. **c**, Dose-response curve of the α -KG effect on longevity. **d**, **e**, α -KG extends the lifespan of worms fed bacteria that have been ampicillin arrested, mean lifespan (days of adulthood) with vehicle treatment (m_{veh}) = 19.4 (n = 80 animals tested),

$m_{\alpha-KG}$ = 25.1 (n = 91), P < 0.0001 (log-rank test) (**d**); or γ -irradiation-killed, m_{veh} = 19.0 (n = 88), $m_{\alpha-KG}$ = 23.0 (n = 46), P < 0.0001 (log-rank test) (**e**). OP50, *E. coli* OP50 strain. **f**, α -KG does not further extend the lifespan of *ogdh-1* RNAi worms, m_{veh} = 21.2 (n = 98), $m_{\alpha-KG}$ = 21.1 (n = 100), P = 0.65 (log-rank test).

shown). This inhibition is also readily detected in live mammalian cells (Fig. 2d; data not shown) and in live nematodes (Fig. 2e), as evidenced by reduced ATP levels. Concomitantly, oxygen consumption rates are lowered (Fig. 2f, g), similar to with *atp-2* knockdown (Extended Data Fig. 2c). Specific inhibition of complex V—but not the other electron transport chain (ETC) complexes—by α -KG is further confirmed by respiratory control analysis¹⁵ (Fig. 2h and Extended Data Fig. 2d–h). To understand the mechanism of inhibition by α -KG, we studied the enzyme inhibition kinetics of ATP synthase. α -KG (released from octyl

α -KG) decreases both the effective velocity of the enzyme-catalysed reaction at an infinite concentration of the substrate (V_{max}) and the Michaelis constant (K_m) of ATP synthase, indicative of uncompetitive inhibition (Fig. 2i and Supplementary Notes).

To determine the significance of ATP-2 to the longevity by α -KG, we measured the lifespan of *atp-2* RNAi adults given α -KG. As reported previously¹³, *atp-2* RNAi animals live longer than control RNAi animals (Fig. 3a). However, their lifespan is not further extended by α -KG (Fig. 3a), indicating that ATP-2 is required for the longevity benefit of

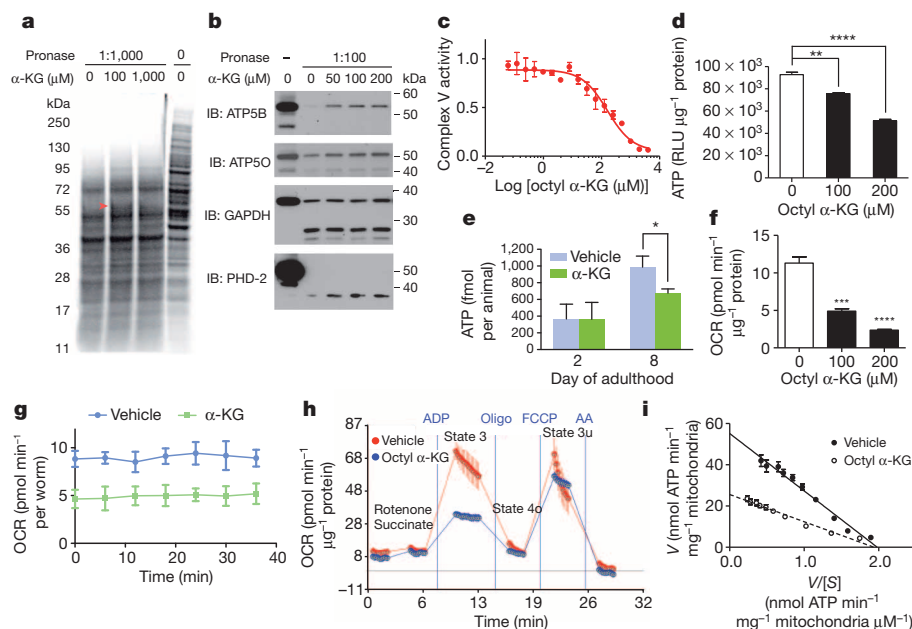


Figure 2 | α -KG binds and inhibits ATP synthase. **a**, DARTS identifies ATP5B as an α -KG-binding protein. Red arrowhead, protected band. **b**, DARTS confirms α -KG binding specifically to ATP5B. IB, immunoblot. **c**, Inhibition of ATP synthase by α -KG (released from octyl α -KG; Supplementary Notes). This inhibition was reversible (data not shown). **d**, **e**, Reduced ATP levels in octyl α -KG-treated normal human fibroblasts ($**P$ = 0.0016, $****P$ < 0.0001; by *t*-test, two-tailed, two-sample unequal variance) (**d**) and α -KG-treated worms (day 2, P = 0.969; day 8, $*P$ = 0.012; by *t*-test, two-tailed, two-sample unequal variance) (**e**). RLU, relative luminescence units. **f**, **g**, Decreased oxygen consumption rate (OCR) in octyl α -KG-treated cells ($***P$ = 0.0004, $****P$ < 0.0001; by *t*-test, two-tailed, two-sample unequal variance) (**f**) and α -KG-treated worms (P < 0.0001; by *t*-test, two-tailed, two-sample unequal variance) (**g**). **h**, α -KG, released from

octyl α -KG (800 μ M), decreases state 3, but not state 4o or 3u (P = 0.997), respiration in mitochondria isolated from mouse liver. The respiratory control ratio is decreased in the octyl α -KG- (3.1 ± 0.6) versus vehicle-treated mitochondria (5.2 ± 1.0) ($*P$ = 0.015; by *t*-test, two-tailed, two-sample unequal variance). Oligo, oligomycin; FCCP, carbonyl cyanide-4-(trifluoromethoxy)phenylhydrazone; AA, antimycin A. **i**, Eadie-Hofstee plot of steady-state inhibition kinetics of ATP synthase by α -KG (produced by *in situ* hydrolysis of octyl α -KG). $[S]$ is the substrate (ADP) concentration, and V is the initial velocity of ATP synthesis in the presence of 200 μ M octanol (vehicle control) or octyl α -KG. α -KG (produced from octyl α -KG) decreases the apparent V_{max} (53.9 to 26.7) and K_m (25.9 to 15.4), by nonlinear regression least-squares fit. **c**–**i**, Results were replicated in two independent experiments. Mean \pm standard deviation (s.d.) is plotted in all cases.

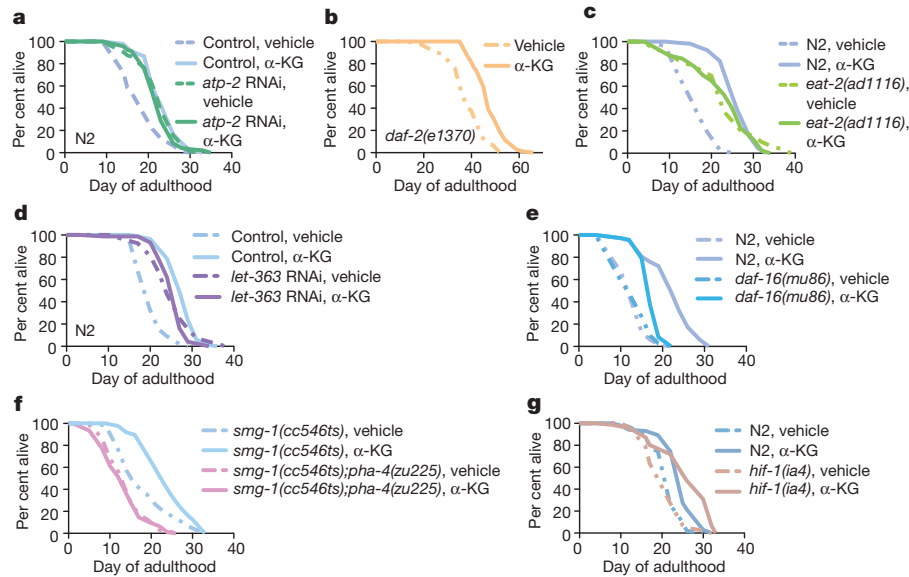


Figure 3 | α -KG longevity is mediated through ATP synthase and the dietary restriction/TOR axis. **a–g**, Effect of α -KG on the lifespan of mutant or RNAi worms. **a**, *atp-2* RNAi, $m_{veh} = 22.8$ ($n = 97$), $m_{\alpha-KG} = 22.5$ ($n = 94$), $P = 0.35$; or RNAi control, $m_{veh} = 18.6$ ($n = 94$), $m_{\alpha-KG} = 23.4$ ($n = 91$), $P < 0.0001$. **b**, *daf-2(e1370)*, $m_{veh} = 38.0$ ($n = 72$), $m_{\alpha-KG} = 47.6$ ($n = 69$), $P < 0.0001$. **c**, *eat-2(ad1116)*, $m_{veh} = 22.8$ ($n = 59$), $m_{\alpha-KG} = 22.9$ ($n = 40$), $P = 0.79$. **d**, *let-363* RNAi, $m_{veh} = 25.1$ ($n = 96$), $m_{\alpha-KG} = 25.7$ ($n = 74$), $P = 0.95$; or *gfp* RNAi control, $m_{veh} = 20.2$ ($n = 99$), $m_{\alpha-KG} = 27.7$ ($n = 81$),

$P < 0.0001$. **e**, *daf-16(mu86)*, $m_{veh} = 13.4$ ($n = 71$), $m_{\alpha-KG} = 17.4$ ($n = 72$), $P < 0.0001$; or N2, $m_{veh} = 13.2$ ($n = 100$), $m_{\alpha-KG} = 22.3$ ($n = 104$), $P < 0.0001$. **f**, *pha-4(zu225)*, $m_{veh} = 14.2$ ($n = 94$), $m_{\alpha-KG} = 13.5$ ($n = 109$), $P = 0.55$. **g**, *hif-1(ia4)*, $m_{veh} = 20.5$ ($n = 85$), $m_{\alpha-KG} = 26.0$ ($n = 71$), $P < 0.0001$; or N2, $m_{veh} = 21.5$ ($n = 101$), $m_{\alpha-KG} = 24.6$ ($n = 102$), $P < 0.0001$. *P* values were determined by the log-rank test. Number of independent experiments: RNAi control (6), *atp-2* (2), *let-363* (3), N2 (5), *daf-2* (2), *eat-2* (2), *pha-4* (2), *daf-16* (2), *hif-1* (5).

α -KG. This requirement is specific because, in contrast, the lifespan of the even longer-lived insulin/IGF-1 receptor *daf-2(e1370)* mutant worms³ is further increased by α -KG (Fig. 3b). Remarkably, oligomycin, an inhibitor of ATP synthase, also extends the lifespan of adult worms (Extended Data Fig. 3a). Together, the direct binding of ATP-2 by α -KG, the related enzymatic inhibition, reduction in ATP levels and oxygen consumption, lifespan analysis, and other similarities (see also Supplementary Notes, Extended Data Fig. 4) to *atp-2* knockdown or oligomycin treatment demonstrate that α -KG probably extends lifespan primarily by targeting ATP-2.

The lower ATP content in α -KG-treated animals suggests that increased longevity by α -KG may involve a state similar to that induced by dietary restriction. Consistent with this idea, we found that α -KG does not extend the lifespan of *eat-2(ad1116)* animals (Fig. 3c), which is a model of dietary restriction with impaired pharyngeal pumping and therefore reduced food intake¹⁶. The longevity of *eat-2* mutants requires TOR (encoded by the *C. elegans* orthologue *let-363*)¹⁷, an important mediator of the effects of dietary restriction on longevity¹⁸. Likewise, α -KG fails to increase the lifespan of *let-363* RNAi animals (Fig. 3d). The AMP-activated protein kinase (AMPK) is another conserved major sensor of cellular energy status¹⁹. Both AMPK (*C. elegans* orthologue *aak-2*) and the FoxO transcription factor DAF-16 mediate dietary-restriction-induced longevity in *C. elegans* fed diluted bacteria²⁰, but neither is required for lifespan extension in the *eat-2* model^{16,20}. We found that in *aak-2* (Extended Data Fig. 5a) and *daf-16* (Fig. 3e) mutants the longevity effect of α -KG is smaller than in N2 animals ($P < 0.0001$), suggesting that α -KG longevity partially depends on AMPK and FoxO; nonetheless, lifespan is significantly increased by α -KG in *aak-2* (24.3%, $P < 0.0001$) and *daf-16* (29.5%, $P < 0.0001$) mutant or RNAi animals (Fig. 3e and Extended Data Fig. 5a, b; data not shown), indicating an AMPK- and FoxO-independent effect of α -KG in increasing longevity.

The inability of α -KG to extend further the lifespan of *let-363* RNAi animals suggests that α -KG treatment and TOR inactivation extend lifespan either through the same pathway (with α -KG acting on or upstream of TOR), or through independent mechanisms or parallel pathways that converge on a downstream effector. The first model predicts that the

TOR pathway will be less active upon α -KG treatment, whereas if the latter model were true then TOR would be unaffected by α -KG treatment. In support of the first model, we found that TOR pathway activity is decreased in human cells treated with octyl α -KG (Fig. 4a and Extended Data Fig. 6a, b). However, α -KG does not interact with TOR directly (Extended Data Fig. 6d, e). Consistent with the involvement of TOR in α -KG longevity, the FoxA transcription factor PHA-4, which is required to extend adult lifespan in response to reduced TOR signalling²¹ and for dietary-restriction-induced longevity in *C. elegans*²², is likewise required for α -KG-induced longevity (Fig. 3f). Moreover, autophagy, which is activated both by TOR inhibition^{18,23} and by dietary restriction²⁴, is markedly increased in worms treated with α -KG (or *ogdh-1* RNAi) and in *atp-2* RNAi animals (Fig. 4b, c, Extended Data Figs 6c, 7 and Supplementary Notes), as indicated by the prevalence of green fluorescent protein GFP::LGG-1 puncta (Methods). Autophagy was also induced in mammalian cells treated with octyl α -KG (Extended Data Fig. 6f). Furthermore, α -KG does not result in significantly more autophagy in either *atp-2* RNAi or *let-363* RNAi worms (Fig. 4b, c). The data provide further evidence that α -KG decreases TOR pathway activity through the inhibition of ATP synthase. Similarly, autophagy is induced by oligomycin, and oligomycin does not augment autophagy in *let-363* RNAi worms (Extended Data Fig. 3b, c).

α -KG is not only a metabolite, but also a co-substrate for a large family of dioxygenases²⁵. The hypoxia inducible factor (HIF-1) is modified by one of these enzymes, the prolyl 4-hydroxylase (PHD) EGL-9, and thereafter degraded by the von Hippel–Lindau (VHL) protein^{26,27}. α -KG extends the lifespan of animals with loss-of-function mutations in *hif-1*, *egl-9* and *vhl-1* (Fig. 3g and Extended Data Fig. 5c), suggesting that this pathway does not play a major part in lifespan extension by α -KG. However, it is prudent to acknowledge that the formal possibility of other α -KG-binding targets having an additional role in the extension of lifespan by α -KG cannot be eliminated at this time.

We show that ageing in *C. elegans* is delayed by α -KG supplementation in adult animals. This longevity effect is probably mediated by ATP synthase, which we identified as a direct target of α -KG, and TOR, a major effector of dietary restriction. Identification of new protein targets

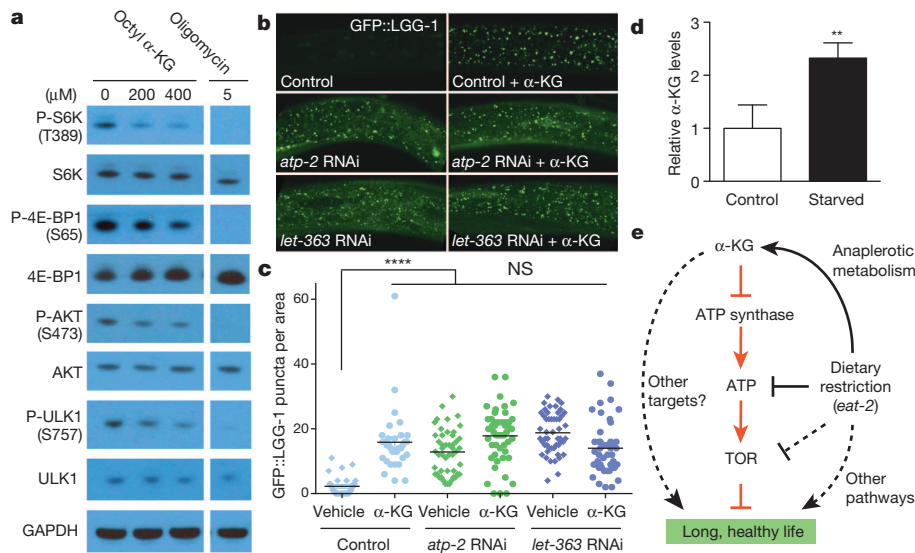


Figure 4 | Inhibition of ATP synthase by α -KG causes a conserved decrease in TOR pathway activity. **a**, Decreased phosphorylation of mammalian TOR substrates in U87 cells treated with octyl α -KG or oligomycin. Similar results were obtained in HEK-293 cells, normal human fibroblasts and mouse embryonic fibroblasts (data not shown). P, phospho. **b**, Increased autophagy in animals treated with α -KG or RNAi for *atp-2* or *let-363*. Photographs were

taken at $\times 100$ magnification. **c**, GFP::LGG-1 puncta quantified using ImageJ (Methods). Data show results of 2–3 independent experiments. Bars indicate the mean. **** $P < 0.0001$; NS, not significant (*t*-test, two-tailed, two-sample unequal variance). **d**, α -KG levels are increased in starved worms. ** $P < 0.01$ (*t*-test, two-tailed, two-sample unequal variance). Mean \pm s.d. is plotted. **e**, Model of α -KG-mediated longevity.

of α -KG illustrates that regulatory networks acted upon by metabolites are probably more complex than appreciated at present, and that DARTS is a useful method for discovering new protein targets and regulatory functions of metabolites. Our findings demonstrate a novel mechanism for extending lifespan that is mediated by the regulation of cellular energy metabolism by a key metabolite. Such moderation of ATP synthesis by metabolite(s) has probably evolved to ensure energy efficiency by the organism in response to nutrient availability. We suggest that this system may be exploited to confer a dietary-restriction-like state that favours maintenance over growth, and thereby delays ageing and prevents age-related diseases. In fact, the TOR pathway is often hyperactivated in human cancer; inhibition of TOR function by α -KG in normal human cells suggests an exciting role for α -KG as an endogenous tumour suppressor metabolite. Interestingly, physiological increases in α -KG levels have been reported in starved yeast and bacteria²⁸, in the liver of starved pigeons²⁹, and in humans after physical exercise³⁰. The biochemical basis for this increase of α -KG is explained by starvation-based anaplerotic gluconeogenesis, which activates glutamate-linked transaminases in the liver to provide carbon derived from amino acid catabolism. Consistent with this idea, α -KG levels are elevated in starved *C. elegans* (Fig. 4d). These findings suggest a model in which α -KG is a key metabolite mediating lifespan extension by starvation/dietary restriction (Fig. 4e).

Longevity molecules that delay ageing and extend lifespan have long been a dream of humanity. Endogenous metabolites such as α -KG that can alter *C. elegans* lifespan suggest that an internal mechanism may exist that is accessible to intervention; whether this can translate into manipulating the ageing process in humans remains to be seen.

METHODS SUMMARY

Lifespan analysis. All lifespan assays were conducted at 20 °C on solid nematode growth media (NGM) and were replicated in at least two independent experiments. *P* values were determined by the log-rank (Mantel–Cox) test; survival curves were generated using GraphPad Prism. All lifespan data are available in Extended Data Table 2.

DARTS. Human Jurkat cell lysates were incubated with α -KG and digested using Pronase. Proteins protected from proteolysis by α -KG binding were analysed by liquid chromatography–tandem mass spectrometry (LC–MS/MS) as described previously⁷, and identified by searching against the human Swissprot database (release 57.15) using Mascot with all peptides meeting a significance threshold of $P < 0.05$.

Online Content Any additional Methods, Extended Data display items and Source Data are available in the online version of the paper; references unique to these sections appear only in the online paper.

Received 3 October 2012; accepted 17 March 2014.

Published online 14 May 2014.

- Colman, R. J. *et al.* Caloric restriction delays disease onset and mortality in rhesus monkeys. *Science* **325**, 201–204 (2009).
- Mattison, J. A. *et al.* Impact of caloric restriction on health and survival in rhesus monkeys from the NIA study. *Nature* **489**, 318–321 (2012).
- Kenyon, C. J. The genetics of ageing. *Nature* **464**, 504–512 (2010).
- Harrison, D. E. *et al.* Rapamycin fed late in life extends lifespan in genetically heterogeneous mice. *Nature* **460**, 392–395 (2009).
- Williams, D. S., Cash, A., Hamadani, L. & Diemer, T. Oxaloacetate supplementation increases lifespan in *Caenorhabditis elegans* through an AMPK/FOXO-dependent pathway. *Aging Cell* **8**, 765–768 (2009).
- Lucanic, M. *et al.* N-acylethanolamine signalling mediates the effect of diet on lifespan in *Caenorhabditis elegans*. *Nature* **473**, 226–229 (2011).
- Lomenick, B. *et al.* Target identification using drug affinity responsive target stability (DARTS). *Proc. Natl Acad. Sci. USA* **106**, 21984–21989 (2009).
- Abrahams, J. P., Leslie, A. G., Lutter, R. & Walker, J. E. Structure at 2.8 Å resolution of F1-ATPase from bovine heart mitochondria. *Nature* **370**, 621–628 (1994).
- Boyer, P. D. The ATP synthase—a splendid molecular machine. *Annu. Rev. Biochem.* **66**, 717–749 (1997).
- Tsang, W. Y., Sayles, L. C., Grad, L. I., Pilgrim, D. B. & Lemire, B. D. Mitochondrial respiratory chain deficiency in *Caenorhabditis elegans* results in developmental arrest and increased life span. *J. Biol. Chem.* **276**, 32240–32246 (2001).
- Dillin, A. *et al.* Rates of behavior and aging specified by mitochondrial function during development. *Science* **298**, 2398–2401 (2002).
- Lee, S. S. *et al.* A systematic RNAi screen identifies a critical role for mitochondria in *C. elegans* longevity. *Nature Genet.* **33**, 40–48 (2002).
- Curran, S. P. & Ruvkun, G. Lifespan regulation by evolutionarily conserved genes essential for viability. *PLoS Genet.* **3**, e56 (2007).
- Gems, D. & Riddle, D. L. Genetic, behavioral and environmental determinants of male longevity in *Caenorhabditis elegans*. *Genetics* **154**, 1597–1610 (2000).
- Brand, M. D. & Nicholls, D. G. Assessing mitochondrial dysfunction in cells. *Biochem. J.* **435**, 297–312 (2011).
- Lakowski, B. & Hekimi, S. The genetics of caloric restriction in *Caenorhabditis elegans*. *Proc. Natl Acad. Sci. USA* **95**, 13091–13096 (1998).
- Hansen, M. *et al.* Lifespan extension by conditions that inhibit translation in *Caenorhabditis elegans*. *Aging Cell* **6**, 95–110 (2007).
- Stanfel, M. N., Shamieh, L. S., Kaeblerlein, M. & Kennedy, B. K. The TOR pathway comes of age. *Biochim. Biophys. Acta* **1790**, 1067–1074 (2009).
- Hardie, D. G., Scott, J. W., Pan, D. A. & Hudson, E. R. Management of cellular energy by the AMP-activated protein kinase system. *FEBS Lett.* **546**, 113–120 (2003).

20. Greer, E. L. & Brunet, A. Different dietary restriction regimens extend lifespan by both independent and overlapping genetic pathways in *C. elegans*. *Aging Cell* **8**, 113–127 (2009).
21. Sheaffer, K. L., Updike, D. L. & Mango, S. E. The target of rapamycin pathway antagonizes *pha-4/FoxA* to control development and aging. *Curr. Biol.* **18**, 1355–1364 (2008).
22. Panowski, S. H., Wolff, S., Aguilaniu, H., Durieux, J. & Dillin, A. PHA-4/Foxa mediates diet-restriction-induced longevity of *C. elegans*. *Nature* **447**, 550–555 (2007).
23. Wullschlegel, S., Loewith, R. & Hall, M. N. TOR signaling in growth and metabolism. *Cell* **124**, 471–484 (2006).
24. Meléndez, A. *et al.* Autophagy genes are essential for dauer development and life-span extension in *C. elegans*. *Science* **301**, 1387–1391 (2003).
25. Loenarz, C. & Schofield, C. J. Expanding chemical biology of 2-oxoglutarate oxygenases. *Nature Chem. Biol.* **4**, 152–156 (2008).
26. Epstein, A. C. *et al.* *C. elegans* EGL-9 and mammalian homologs define a family of dioxygenases that regulate HIF by prolyl hydroxylation. *Cell* **107**, 43–54 (2001).
27. Zhang, Y., Shao, Z., Zhai, Z., Shen, C. & Powell-Coffman, J. A. The HIF-1 hypoxia-inducible factor modulates lifespan in *C. elegans*. *PLoS ONE* **4**, e6348 (2009).
28. Brauer, M. J. *et al.* Conservation of the metabolomic response to starvation across two divergent microbes. *Proc. Natl Acad. Sci. USA* **103**, 19302–19307 (2006).
29. Kaminsky, Y. G., Kosenko, E. A. & Kondrashova, M. N. Metabolites of citric acid cycle, carbohydrate and phosphorus metabolism, and related reactions, redox and phosphorylating states of hepatic tissue, liver mitochondria and cytosol of the pigeon, under normal feeding and natural nocturnal fasting conditions. *Comp. Biochem. Physiol. B* **73**, 957–963 (1982).
30. Bruhnara, L. *et al.* Metabolomics approach for analyzing the effects of exercise in subjects with type 1 diabetes mellitus. *PLoS ONE* **7**, e40600 (2012).

Supplementary Information is available in the online version of the paper.

Acknowledgements We thank S. Lee, M. Hansen, B. Lemire, A. van der Blik, S. Clarke, T. K. Blackwell, R. Johnson, J. E. Walker, A. G. W. Leslie, K. N. Houk, B. Martin, J. Lusis, J. Gober, Y. Wang and H. Sun for advice and discussions. J. Avruch for the *let-363* RNAi vector; J. Powell-Coffman for strains and advice; and K. Yan for technical assistance. Worm strains were provided by the *Caenorhabditis* Genetics Center, which is funded by the National Institutes of Health (NIH) Office of Research Infrastructure Programs (P40 OD010440). We thank the NIH for traineeship support of R.M.C. (T32 GM007104), M.Y.P. (T32 GM007185), B.L. (T32 GM008496) and M.N. (T32 CA009120). X.F. is a recipient of the China Scholarship Council Scholarship. G.C.M. was supported by Ford Foundation and National Science Foundation Graduate Research Fellowships.

Author Contributions Lifespan assays were performed by R.M.C., M.P. and E.H.; DARTS-mass spectrometry by S.D. and B.L.; DARTS-western blots by M.Y.P., H.H. and R.M.C.; mammalian cell experiments by X.F. and H.H.; mitochondrial respiration study design and analyses by L.V. and K.R.; enzyme kinetics and analyses by R.M.C. and J.H.; confocal microscopy by V.S.M., G.C.M. and A.R.F.; ultra-high-performance liquid chromatography-electrospray ionization-tandem mass spectrometry (UHPLC-ESI/MS/MS) by J.X.W. and S.A.T.; compound syntheses by G.D. and M.E.J.; other analyses by H.H., X.F., M.Y.P., D.B., R.M.C., E.H., G.J., G.M.S., C.K. and A.Q. S.A.W., F.F., M.N., A.S.K., H.A.G., H.R. Chang, K.F.F., F.G., M.J., S.A.T., A.S., D.B., H.R. Christofk, C.F.C., M.A.T., M.E.J., L.V., K.R., A.R.F. and M.P. provided guidance, specialized reagents and expertise. J.H. conceived the study. R.M.C. and J.H. wrote the paper. R.M.C., X.F. and J.H. analysed data. All authors discussed the results, commented on the studies and contributed to aspects of preparing the manuscript.

Author Information Reprints and permissions information is available at www.nature.com/reprints. The authors declare no competing financial interests. Readers are welcome to comment on the online version of the paper. Correspondence and requests for materials should be addressed to J.H. (jinghuang@mednet.ucla.edu).

METHODS

Nematode strains and maintenance. *C. elegans* strains were maintained using standard methods³¹. The following strains were used (strain, genotype): Bristol N2, wild type; DA1116, *eat-2(ad1116)II*; CB1370, *daf-2(e1370)III*; CF1038, *daf-16(mu86)I*; PD8120, *smg-1(cc546ts)I*; SM190, *smg-1(cc546ts)I*; *pha-4(zu225)V*; RB754, *aak-2(ok524)X*; ZG31, *hif-1(ia4)V*; ZG596, *hif-1(ia7)V*; JT307, *egl-9(sa307)V*; CB5602, *vhl-1(ok161)X*; DA2123, *adls2122[lgg-1::GFP + rol-6(su1006)]*. They were all obtained from the *Caenorhabditis* Genetics Center (CGC).

RNAi in *C. elegans*. RNAi in *C. elegans* was accomplished by feeding worms HT115 (DE3) bacteria expressing target-gene double-stranded RNA (dsRNA) from the pL4440 vector³². dsRNA production was induced overnight on plates containing 1 mM isopropyl- β -D-thiogalactoside (IPTG). All RNAi feeding clones were obtained from the *C. elegans* ORF-RNAi Library (Thermo Scientific/Open Biosystems) unless otherwise stated. The *C. elegans* TOR (*let-363*) RNAi clone³³ was obtained from Joseph Avruch (MGH/Harvard). Efficient knockdown was confirmed by western blotting of the corresponding protein or by qRT-PCR of the mRNA. The primer sequences used for qRT-PCR are as follows. *atp-2* forward: TGACAACATTTTC CGTTTCACC; *atp-2* reverse: AAATAGCCTGGACGGATGTGAT; *let-363* forward: GATCCGAGACAAGATGAACGTG; *let-363* reverse: ACAATTGGAAAC CCAACCAATC; *ogdh-1* forward: TGATTTGGACCGAGAATTCCTT; *ogdh-1* reverse: GGATCAGACGTTTGAACAGCAC.

We validated the RNAi knockdown of both *ogdh-1* and *atp-2* by quantitative RT-PCR and also of *atp-2* by western blotting. Transcripts of *ogdh-1* were reduced by 85%, and transcripts and protein levels of *atp-2* were reduced by 52% and 83%, respectively, in larvae that were cultivated on bacteria that expressed the corresponding dsRNAs. In addition, RNAi of *atp-2* in this study was associated with delayed post-embryonic development and larval arrest, consistent with the phenotypes of *atp-2(ua2)* animals. Analysis by qRT-PCR indicated a modest but significant decrease by 26% in transcripts of *let-363* in larvae undergoing RNAi; moreover, molecular markers for autophagy were induced in these animals, and the lifespan of adults was extended, consistent with partial inactivation of the kinase.

In lifespan experiments, we used RNAi to inactivate *atp-2*, *ogdh-1* and *let-363* in mature animals in the presence or absence of exogenous α -KG. The concentration of α -KG used in these experiments (8 mM) was empirically determined to be most beneficial for wild-type animals (Fig. 1c). This approach enabled us to evaluate the contribution of essential proteins and pathways to the longevity conferred by supplementary α -KG. Specifically, we were able to substantially but not fully inactivate *atp-2* in adult animals that had completed embryonic and larval development. As described earlier, supplementation with 8 mM α -KG did not further extend (and in fact, on one occasion, even decreased) the lifespan of *atp-2* RNAi animals (Extended Data Table 2), indicating that *atp-2* is required for α -KG to promote longevity. On the other hand, a complete inactivation of *atp-2* would be lethal, and thereby mask the benefit of ATP synthase inhibition by α -KG.

Lifespan analysis. Lifespan assays were conducted at 20 °C on solid nematode growth media (NGM) using standard protocols and were replicated in at least two independent experiments. *C. elegans* were synchronized by performing either a timed egg lay³⁴ or an egg preparation (lysing ~100 gravid worms in 70 μ l M9 buffer³¹, 25 μ l bleach (10% sodium hypochlorite solution) and 5 μ l 10 N NaOH). Young adult animals were picked onto NGM assay plates containing 1.5% dimethyl sulfoxide (DMSO; Sigma, D8418), 49.5 μ M 5-fluoro-2'-deoxyuridine³⁴ (FUDR; Sigma, F0503), and α -KG (Sigma, K1128) or vehicle control (H₂O). FUDR was included to prevent progeny production. Media containing α -KG were adjusted to pH 6.0 (that is, the same pH as the control plates) by the addition of NaOH. All compounds were mixed into the NGM media after autoclaving and before solidification of the media. Assay plates were seeded with OP50 (or a designated RNAi feeding clone, see later). Worms were moved to new assay plates every 4 days (to ensure sufficient food was present at all times and to reduce the risk of mould contamination). To assess the survival of the worms, the animals were prodded with a platinum wire every 2–3 days, and those that failed to respond were scored as dead. For analysis concerning mutant strains, the corresponding parent strain was used as a control in the same experiment.

For lifespan experiments involving RNAi, the plates also contained 1 mM IPTG (Acros, CAS 367-93-1) and 50 μ g ml⁻¹ ampicillin (Fisher, BP1760-25). RNAi was accomplished by feeding N2 worms HT115(DE3) bacteria expressing target-gene dsRNA from pL4440 (ref. 32); control RNAi was done in parallel for every experiment by feeding N2 worms HT115(DE3) bacteria expressing either GFP dsRNA or empty vector (which gave identical lifespan results).

Lifespan experiments with oligomycin (Cell Signaling, 9996) were performed as described for α -KG (that is, NGM plates with 1.5% DMSO and 49.5 μ M FUDR; N2 worms; OP50 bacteria).

For lifespan experiments concerning *smg-1(cc546ts);pha-4(zu225)* and *smg-1(cc546ts)*^{22,35}, from egg to L4 stage the strains were grown at 24 °C, which inactivates the *smg-1* temperature-sensitive allele, preventing mRNA surveillance-mediated degradation of the *pha-4(zu225)* mRNA, which contains a premature stop codon,

and thus produces a truncated but fully functional PHA-4 transcription factor³⁵. Then at the L4 stage the temperature was shifted to 20 °C, which restores *smg-1* function and thereby results in the degradation of *pha-4(zu225)* mRNA. Treatment with α -KG began at the L4 stage.

All lifespan data are available in Extended Data Table 2, including sample sizes. The sample size was chosen on the basis of standards done in the field in published manuscripts. No statistical method was used to predetermine the sample size. Animals were assigned randomly to the experimental groups. Worms that ruptured, bagged (that is, exhibited internal progeny hatching), or crawled off the plates were censored. Lifespan data were analysed using GraphPad Prism; *P* values were calculated using the log-rank (Mantel–Cox) test.

Statistical analyses. All experiments were repeated at least two times with identical or similar results. Data represent biological replicates. Appropriate statistical tests were used for every figure. Data meet the assumptions of the statistical tests described for each figure. Mean \pm s.d. is plotted in all figures unless stated otherwise.

Food preference assay. Protocol adapted from Abada *et al.*³⁶. A 10 cm NGM plate was seeded with two spots of OP50 as shown in Extended Data Fig. 1e. After letting the OP50 lawns dry over 2 days at room temperature, vehicle (H₂O) or α -KG (8 mM) was added to the top of the lawn and allowed to dry over 2 days at room temperature. Approximately 50–100 synchronized adult day 1 worms were placed onto the centre of the plate and their preference for either bacterial lawn was recorded after 3 h at room temperature.

Target identification using DARTS. For unbiased target identification (Fig. 2a), human Jurkat cells were lysed using M-PER (Thermo Scientific, 78501) with the addition of protease inhibitors (Roche, 11836153001) and phosphatase inhibitors³⁷. TNC buffer (50 mM Tris-HCl pH 8.0, 50 mM NaCl, 10 mM CaCl₂) was added to the lysate and protein concentration was then determined using the BCA Protein Assay kit (Pierce, 23227). Cell lysates were incubated with either vehicle (H₂O) or α -KG for 1 h on ice followed by an additional 20 min at room temperature. Digestion was performed using Pronase (Roche, 10165921001) at room temperature for 30 min and stopped using excess protease inhibitors with immediate transfer to ice. The resulting digests were separated by SDS–PAGE and visualized using SYPRO Ruby Protein Gel Stain (Invitrogen, S12000). The band with increased staining from the α -KG lane (corresponding to potential protein targets that are protected from proteolysis by the binding of α -KG) and the matching area of the control lane were excised, in-gel trypsin digested, and subjected to liquid chromatography–tandem mass spectrometry (LC-MS/MS) analysis as described previously^{7,38}. Mass spectrometry results were searched against the human Swissprot database (release 57.15) using Mascot version 2.3.0, with all peptides meeting a significance threshold of *P* < 0.05.

For target verification by DARTS with western blotting (Fig. 2b), HeLa cells were lysed in M-PER buffer (Thermo Scientific, 78501) with the addition of protease inhibitors (Roche, 11836153001) and phosphatase inhibitors (50 mM NaF, 10 mM β -glycerophosphate, 5 mM sodium pyrophosphate, 2 mM Na₃VO₄). Chilled TNC buffer (50 mM Tris-HCl pH 8.0, 50 mM NaCl, 10 mM CaCl₂) was added to the protein lysate, and protein concentration of the lysate was measured by the BCA Protein Assay kit (Pierce, 23227). The protein lysate was then incubated with vehicle control (H₂O) or varying concentrations of α -KG for 3 h at room temperature with shaking at 600 r.p.m. in an Eppendorf Thermomixer. Pronase (Roche, 10165921001) digestions were performed for 20 min at room temperature, and stopped by adding SDS loading buffer and immediately heating at 70 °C for 10 min. Samples were subjected to SDS–PAGE on 4–12% Bis-Tris gradient gel (Invitrogen, NP0322BOX) and western blotted for ATP synthase subunits ATP5B (Sigma, AV48185), ATP5O (Abcam, ab91400) and ATP5A (Abcam, ab110273). Binding between α -KG and PHD-2 (encoded by *EGLN1*) (Cell Signaling, 4835), for which α -KG is a co-substrate³⁹, was confirmed by DARTS. GAPDH (Ambion, AM4300) was used as a negative control.

For DARTS using *C. elegans* (Extended Data Fig. 2a), wild-type animals of various ages were grown on NGM/OP50 plates, washed four times with M9 buffer, and immediately placed in the –80 °C freezer. Animals were lysed in HEPES buffer (40 mM HEPES pH 8.0, 120 mM NaCl, 10% glycerol, 0.5% Triton X-100, 10 mM β -glycerophosphate, 50 mM NaF, 0.2 mM Na₃VO₄, protease inhibitors (Roche, 11836153001)) using Lysing Matrix C tubes (MP Biomedicals, 6912-100) and the FastPrep-24 (MP Biomedicals) high-speed bench-top homogenizer in the 4 °C room (disrupt worms for 20 s at 6.5 m s⁻¹, rest on ice for 1 min; repeat twice). Lysed animals were centrifuged at 14,000 r.p.m. for 10 min at 4 °C to pellet worm debris, and supernatant was collected for DARTS. Protein concentration was determined by BCA Protein Assay kit (Pierce, 23223). A worm lysate concentration of 1.13 μ g μ l⁻¹ was used for the DARTS experiment. All steps were performed on ice or at 4 °C to help prevent premature protein degradation. TNC buffer (50 mM Tris-HCl pH 8.0, 50 mM NaCl, 10 mM CaCl₂) was added to the worm lysates. Worm lysates were incubated with vehicle control (H₂O) or α -KG for 1 h on ice and then 50 min at room temperature. Pronase (Roche, 10165921001) digestions were performed for

30 min at room temperature and stopped by adding SDS loading buffer and heating at 70 °C for 10 min. Samples were then subjected to SDS-PAGE on NuPAGE Novex 4–12% Bis-Tris gradient gels (Invitrogen, NP0322BOX), and western blotting was carried out with an antibody against ATP5B (Sigma, AV48185) that also recognizes ATP-2.

Complex V activity assay. Complex V activity was assayed using the MitoTox OXPHOS Complex V Activity Kit (Abcam, ab109907). Vehicle (H₂O) or α -KG was mixed with the enzyme before the addition of phospholipids. In experiments using octyl α -KG, vehicle (1% DMSO) or octyl α -KG was added with the phospholipids. Relative complex V activity was compared to vehicle. Oligomycin (Sigma, O4876) was used as a positive control for the assay.

Isolation of mitochondria from mouse liver. Animal studies were performed under approved University of California, Los Angeles animal research protocols. Mitochondria from 3-month-old C57BL/6 mice were isolated as described⁴⁰. Briefly, livers were extracted, minced at 4 °C in MSHE plus BSA (70 mM sucrose, 210 mM mannitol, 5 mM HEPES, 1 mM EGTA, and 0.5% fatty acid free BSA, pH 7.2), and rinsed several times to remove blood. All subsequent steps were performed on ice or at 4 °C. The tissue was disrupted in ten volumes of MSHE plus BSA with a glass Dounce homogenizer (5–6 strokes) and the homogenate was centrifuged at 800g for 10 min to remove tissue debris and nuclei. The supernatant was decanted through a cell strainer and centrifuged at 8,000g for 10 min. The dark mitochondrial pellet was resuspended in MSHE plus BSA and re-centrifuged at 8,000g for 10 min. The final mitochondrial pellets were used for various assays as described later.

Submitochondrial particle ATPase assay. ATP hydrolysis by ATP synthase was measured using submitochondrial particles (see ref. 41 and references therein). Mitochondria were isolated from mouse liver as described earlier. The final mitochondrial pellet was resuspended in buffer A (250 mM sucrose, 10 mM Tris-HCl, 1 mM ATP, 5 mM MgCl₂ and 0.1 mM EGTA, pH 7.4) at 10 μ g μ l⁻¹, subjected to sonication on ice (Fisher Scientific Model 550 Sonic Dismembrator; medium power, alternating between 10 s intervals of sonication and resting on ice for a total of 60 s of sonication), and then centrifuged at 18,000g for 10 min at 4 °C. The supernatant was collected and centrifuged at 100,000g for 45 min at 4 °C. The final pellet (submitochondrial particles) was resuspended in buffer B (250 mM sucrose, 10 mM Tris-HCl and 0.02 mM EGTA, pH 7.4).

The SMP ATPase activity was assayed using the Complex V Activity Buffer as described earlier. The production of ADP is coupled to the oxidation of NADH to NAD⁺ through pyruvate kinase and lactate dehydrogenase. The addition of α -KG (up to 10 mM) did not affect the activity of pyruvate kinase or lactate dehydrogenase when external ADP was added. The absorbance decrease of NADH at 340 nm correlates to ATPase activity. Submitochondrial particles (2.18 ng μ l⁻¹) were incubated with vehicle or α -KG for 90 min at room temperature before the addition of activity buffer, and then the absorbance decrease of NADH at 340 nm was measured every 1 min for 1 h. Oligomycin (Cell signaling, 9996) was used as a positive control for the assay.

Assay for ATP levels. Normal human diploid fibroblast WI-38 (ATCC, CCL-75) cells were seeded in 96-well plates at 2×10^5 cells per well. Cells were treated with either DMSO (vehicle control) or octyl α -KG at varying concentrations for 2 h in triplicate. ATP levels were measured using the CellTiter-Glo luminescent ATP assay (Promega, G7572); luminescence was read using Analyst HT (Molecular Devices). In parallel, identically treated cells were lysed in M-PER (Thermo Scientific, 78501) to obtain protein concentration by BCA Protein Assay kit (Pierce, 23223). ATP levels were normalized to protein content. Statistical analysis was performed using GraphPad Prism (unpaired *t*-test).

The assay for ATP levels in *C. elegans* was carried out as follows. Synchronized day 1 adult wild-type *C. elegans* were placed on NGM plates containing either vehicle or 8 mM α -KG. On day 2 and 8 of adulthood, 9 replicates and 4 replicates, respectively, of about 100 worms were collected from α -KG or vehicle control plates, washed 4 times in M9 buffer, and frozen in -80 °C. Animals were lysed using Lysing Matrix C tubes (MP Biomedicals, 6912-100) and the FastPrep-24 (MP Biomedicals) high-speed bench-top homogenizer (disrupt worms for 20 s at 6.5 m s⁻¹, rest on ice for 1 min; repeat twice). Lysed animals were centrifuged at 14,000 r.p.m. for 10 min at 4 °C to pellet worm debris, and supernatant was saved for ATP quantification using the Kinase-Glo Luminescent Kinase Assay Platform (Promega, V6713) according to the manufacturer's instructions. The assay was performed in white opaque 96-well tissue culture plates (Falcon, 353296), and luminescence was measured using Analyst HT (Molecular Devices). ATP levels were normalized to the number of worms. Statistical analysis was performed using Microsoft Excel (*t*-test, two-tailed, two-sample unequal variance).

Measurement of oxygen consumption rates. Oxygen consumption rate (OCR) measurements were made using a Seahorse XF-24 analyser (Seahorse Bioscience)⁴². Cells were seeded in Seahorse XF-24 cell culture microplates at 50,000 cells per well in DMEM media supplemented with 10% FBS and 10 mM glucose, and incubated at 37 °C and 5% CO₂ overnight. Treatment with octyl α -KG or DMSO (vehicle control)

was for 1 h. Cells were washed in unbuffered DMEM medium (pH 7.4, 10 mM glucose) just before measurement, and maintained in this buffer with indicated concentrations of octyl α -KG. OCR was measured three times under basal conditions and normalized to protein concentration per well. Statistical analysis was performed using GraphPad Prism.

Measurement of OCR in living *C. elegans* was carried out as follows. The protocol was adapted from those previously described^{43,44}. Wild-type day 1 adult N2 worms were placed on NGM plates containing 8 mM α -KG or H₂O (vehicle control) seeded with OP50 or HT115 *E. coli*. OCR was assessed on day 2 of adulthood. On day 2 of adulthood, worms were collected and washed four times with M9 to rid the samples of bacteria (we further verified that α -KG does not affect oxygen consumption of the bacteria—therefore, even if there were any leftover bacteria after the washes, the changes in OCR observed would still be worm specific), and then the animals were seeded in quadruplicates in Seahorse XF-24 cell culture microplates (Seahorse Bioscience, V7-PS) in 200 μ l M9 at ~200 worms per well. Oxygen consumption rates were measured seven times under basal conditions and normalized to the number of worms counted per well. The experiment was repeated twice. Statistical analysis was performed using Microsoft Excel (*t*-test, two-tailed, two-sample unequal variance).

Measurement of mitochondrial respiratory control ratio. Mitochondrial respiratory control ratio (RCR) was analysed using isolated mouse liver mitochondria (see ref. 15 and references therein). Mitochondria were isolated from mouse liver as described earlier. The final mitochondrial pellet was resuspended in 30 μ l of MAS buffer (70 mM sucrose, 220 mM mannitol, 10 mM KH₂PO₄, 5 mM MgCl₂, 2 mM HEPES, 1 mM EGTA, and 0.2% fatty acid free BSA, pH 7.2).

Isolated mitochondrial respiration was measured by running coupling and electron flow assays as described⁴⁰. For the coupling assay, 20 μ g of mitochondria in complete MAS buffer (MAS buffer supplemented with 10 mM succinate and 2 μ M rotenone) were seeded into a XF24 Seahorse plate by centrifugation at 2,000g for 20 min at 4 °C. Just before the assay, the mitochondria were supplemented with complete MAS buffer for a total of 500 μ l (with 1% DMSO or octyl α -KG), and warmed at 37 °C for 30 min before starting the OCR measurements. Mitochondrial respiration begins in a coupled state 2; state 3 is initiated by 2 mM ADP; state 4o (oligomycin insensitive, that is, complex V independent) is induced by 2.5 μ M oligomycin; and state 3u (FCCP-uncoupled maximal respiratory capacity) by 4 μ M FCCP. Finally, 1.5 μ g ml⁻¹ antimycin A was injected at the end of the assay. The state 3/state 4o ratio gives the RCR.

For the electron flow assay, the MAS buffer was supplemented with 10 mM sodium pyruvate (complex I substrate), 2 mM malate (complex II inhibitor) and 4 μ M FCCP, and the mitochondria are seeded the same way as described for the coupling assay. After basal readings, the sequential injections were as follows: 2 μ M rotenone (complex I inhibitor), 10 mM succinate (complex II substrate), 4 μ M antimycin A (complex III inhibitor) and 10 mM/100 μ M ascorbate/tetramethylphenylenediamine (complex IV substrate).

ATP synthase enzyme inhibition kinetics. ATP synthesis enzyme inhibition kinetic analysis was performed using isolated mitochondria. Mitochondria were isolated from mouse liver as described earlier. The final mitochondrial pellet was resuspended in MAS buffer supplemented with 5 mM sodium ascorbate (Sigma, A7631) and 5 mM TMPD (Sigma, T7394).

The reaction was carried out in MAS buffer containing 5 mM sodium ascorbate, 5 mM TMPD, luciferase reagent (Roche, 11699695001), octanol or octyl α -KG, variable amounts of ADP (Sigma, A2754), and 3.75 ng μ l⁻¹ mitochondria. ATP synthesis was monitored by the increase in luminescence over time by a luminometer (Analyst HT, Molecular Devices). ATP-synthase-independent ATP formation, derived from the oligomycin-insensitive luminescence, was subtracted as background. The initial velocity of ATP synthesis was calculated from the slope of the first 3 min of the reaction, before the velocity begins to decrease. Enzyme inhibition kinetics was analysed by nonlinear regression least-squares fit using GraphPad Prism.

Assay for mammalian TOR pathway activity. Mammalian (m)TOR pathway activity in cells treated with octyl α -KG or oligomycin was determined by the levels of phosphorylation of known mTOR substrates, including S6K (T389), 4E-BP1 (S65), AKT (S473) and ULK1 (S757)^{45–49}. Specific antibodies used: phospho (P)-S6K T389 (Cell Signaling, 9234), S6K (Cell Signaling, 9202S), P-4E-BP1 S65 (Cell Signaling, 9451S), 4E-BP1 (Cell Signaling, 9452S), P-AKT S473 (Cell Signaling, 4060S), AKT (Cell Signaling, 4691S), P-ULK1 S757 (Cell Signaling, 6888), ULK1 (Cell Signaling, 4773S) and GAPDH (Santa Cruz Biotechnology, 25778).

Assay for autophagy. DA2123 animals carrying an integrated GFP::LGG-1 translocation fusion gene^{50–52}, were used to quantify levels of autophagy. To obtain a synchronized population of DA2123, we performed an egg preparation of gravid adults (by lysing ~100 gravid worms in 70 μ l M9 buffer, 25 μ l bleach and 5 μ l 10 N NaOH) and allowed the eggs to hatch overnight in M9, causing starvation-induced L1 diapause. L1 larvae were deposited onto NGM treatment plates containing vehicle,

8 mM α -KG or 40 μ M oligomycin, and seeded with either *E. coli* OP50, HT115(DE3) with an empty vector, or HT115(DE3)-expressing dsRNAs targeting *atp-2*, *let-363* or *ogdh-1* as indicated. When the majority of animals in a given sample first reached the mid-L3 stage, individual L3 larvae were mounted onto microscope slides and anaesthetized with 1.6 mM levamisole (Sigma, 31742). Nematodes were observed using an Axiovert 200M Zeiss confocal microscope with a LSM5 Pascal laser, and images were captured using the LSM Image Examiner (Zeiss). For each specimen, GFP::LGG-1 puncta (autophagosomes) in the epidermis, including the lateral seam cells and Hyp7, were counted in three separate regions of $140.97 \mu\text{m}^2$ using 'analyze particles' in ImageJ⁵³. Measurements were made blind to both the genotype and supplement. Statistical analysis was performed using Microsoft Excel (*t*-test, two-tailed, two-sample unequal variance).

The assay for autophagy in mammalian cells was carried out as follows. HEK-293 cells were seeded in 6-well plates at 2.5×10^5 cells per well in DMEM media supplemented with 10% FBS and 10 mM glucose, and incubated overnight before treatment with either octanol (vehicle control) or octyl α -KG for 72 h. Cells were lysed in M-PER buffer with protease and phosphatase inhibitors. Lysates were subjected to SDS-PAGE on a 4–12% Bis-Tris gradient gel with MES running buffer and western blotted for LC3 (Novus, NB100-2220). LC3 is the mammalian homologue of worm LGG-1, and conversion of the soluble LC3-I to the lipidated LC3-II is activated in autophagy, for example, upon starvation⁵⁴.

Pharyngeal pumping rates of *C. elegans* treated with 8 mM α -KG. The pharyngeal pumping rates of 20 wild-type N2 worms per condition were assessed. Pharyngeal contractions were recorded for 1 min using a Zeiss M2 BioDiscovery microscope and an attached Sony NDR-XR500V video camera at 12-fold optical zoom. The resulting videos were played back at $0.3\times$ speed using MPlayerX and pharyngeal pumps were counted. Statistical analysis was performed using Microsoft Excel (*t*-test, two-tailed, two-sample unequal variance).

Assay for α -KG levels in *C. elegans*. Synchronized adult worms were collected from plates with vehicle (H_2O) or 8 mM α -KG, washed three times with M9 buffer, and flash frozen. Worms were lysed in M9 using Lysing Matrix C tubes (MP Biomedicals, 6912-100) and the FastPrep-24 (MP Biomedicals) high-speed bench-top homogenizer in the 4°C room (disrupt worms for 20 s at 6.5 m s^{-1} , rest on ice for 1 min; repeat three times). Lysed animals were centrifuged at 14,000 r.p.m. for 10 min at 4°C to pellet worm debris, and the supernatant was saved. The protein concentration of the supernatant was determined by the BCA Protein Assay kit (Pierce, 23223); there was no difference in protein level per worm in α -KG-treated and vehicle-treated animals (data not shown). α -KG content was assessed as described previously⁵⁵ with modifications. Worm lysates were incubated at 37°C in 100 mM KH_2PO_4 (pH 7.2), 10 mM NH_4Cl , 5 mM MgCl_2 and 0.3 mM NADH for 10 min. Glutamate dehydrogenase (Sigma, G2501) was then added to reach a final concentration of $1.83 \text{ units ml}^{-1}$. Under these conditions, glutamate dehydrogenase uses α -KG and NADH to make glutamate. The absorbance decrease was monitored at 340 nm. The intracellular level of α -KG was determined from the absorbance decrease in NADH. The approximate molarity of α -KG present inside the animals was estimated using average protein content ($\sim 245 \text{ ng}$ per worm, from BCA assay) and volume ($\sim 3 \text{ nl}$ for adult worms 1.1 mm in length and $60 \mu\text{m}$ in diameter (<http://www.wormatlas.org/hermaphrodite/introduction/Introframeset.html>)).

For quantitative analysis of α -KG in worms using ultra-high-performance liquid chromatography-electrospray ionization-tandem mass spectrometry (UHPLC-ESI/MS/MS), synchronized day 1 adult worms were placed on vehicle plates with or without bacteria for 24 h, and then collected and lysed in the same manner as described earlier. α -KG analysis by LC/MS/MS was carried out on an Agilent 1290 Infinity UHPLC system and 6460 Triple Quadrupole mass spectrometer (Agilent Technologies) using an electrospray ionization (ESI) source with Agilent Jet Stream technology. Data were acquired with Agilent MassHunter Data Acquisition software version B.06.00, and processed for precursor and product ions selection with MassHunter Qualitative Analysis software version B.06.00 and for calibration and quantification with MassHunter Quantitative Analysis for QQQ software version B.06.00.

For UHPLC, 3 μl calibration standards and samples were injected onto the UHPLC system including a G4220A binary pump with a built-in vacuum degasser and a thermostatted G4226A high performance autosampler. An ACQUITY UPLC BEH Amide analytical column ($2.1 \times 50 \text{ mm}$, $1.7 \mu\text{m}$) and a VanGuard BEH Amide Pre-column ($2.1 \times 5 \text{ mm}$, $1.7 \mu\text{m}$) from Waters Corporation were used at the flow rate of 0.6 ml min^{-1} using 50/50/0.04 acetonitrile/water/ammonium hydroxide with 10 mM ammonium acetate as mobile phase A and 95/5/0.04 acetonitrile/water/ammonium hydroxide with 10 mM ammonium acetate as mobile phase B. The column was maintained at room temperature. The following gradient was applied: 0–0.41 min: 100% B isocratic; 0.41–5.30 min: 100–30% B; 5.30–5.35 min: 30–0% B; 5.35–7.35 min: 0% B isocratic; 7.35–7.55 min: 0–100% B; 7.55–9.55 min: 100% B isocratic.

For the MS detection, the ESI mass spectra data were recorded on a negative ionization mode by MRM. MRM transitions of α -KG and its $\text{ISTD } ^{13}\text{C}_4$ - α -KG (Cambridge Isotope Laboratories) were determined using a 1 min 37% B isocratic UHPLC method through the column at a flow rate of 0.6 ml min^{-1} . The precursor ion of $[\text{M}-\text{H}]^-$ and the product ion of $[\text{M}-\text{CO}_2-\text{H}]^-$ were observed to have the highest signal-to-noise ratios. The precursor and product ions are respectively 145.0 and 100.9 for α -KG, and 149.0 and 104.9 for $\text{ISTD } ^{13}\text{C}_4$ - α -KG. Nitrogen was used as the drying, sheath and collision gas. All the source and analyser parameters were optimized using Agilent MassHunter Source and iFunnel Optimizer and Optimizer software, respectively. The source parameters are as follows: drying gas temperature 120°C , drying gas flow 13 l min^{-1} , nebulizer pressure 55 psi, sheath gas temperature 400°C , sheath gas flow 12 l min^{-1} , capillary voltage 2,000 V, and nozzle voltage 0 V. The analyser parameters are as follows: fragmentor voltage 55 V, collision energy 2 V and cell accelerator voltage 1 V. The UHPLC eluents before 1 min and after 5.3 min were diverted to waste.

Membrane-permeable esters of α -KG. Octyl α -KG, a commonly used membrane-permeable ester of α -KG^{55–58}, was used to deliver α -KG across lipid membranes in experiments using cells and mitochondria. Upon hydrolysis by cellular esterases, octyl α -KG yields α -KG and the by-product octanol. We showed that, whereas octanol control has no effect (Extended Data Fig. 2e, f and Extended Data Fig. 6a), α -KG alone can bind and inhibit ATP synthase (Fig. 2a, b and Extended Data Fig. 2a, b; data not shown), decrease ATP and OCR (Fig. 2e, g), induce autophagy (Fig. 4b) and increase *C. elegans* lifespan (Figs 1, 3, Extended Data Figs 1, 5 and Extended Data Table 2). The existence and activity of esterases in our mitochondrial and cell culture experiments have been confirmed using calcein AM (C1430, Molecular Probes), an esterase substrate that fluoresces upon hydrolysis, and also by mass spectrometry (data not shown). The hydrolysis by esterases explains why distinct esters of α -KG, such as 1-octyl α -KG, 5-octyl α -KG, and dimethyl α -KG, have similar effects to α -KG (Extended Data Fig. 2g, h and Extended Data Table 2).

Synthesis of octyl α -KG. Synthesis of 1-octyl α -KG has been previously described⁵⁹. Briefly, 1-octanol (0.95 ml, 6.0 mmol), DMAP (37 mg, 0.3 mmol) and DCC (0.743 g, 3.6 mmol) were added to a solution of 1-cyclobutene-1-carboxylic acid (0.295 g, 3.0 mmol) in dry CH_2Cl_2 (6.0 ml) at 0°C . After it had been stirred for 1 h, the solution was allowed to warm to room temperature and stirred for another 8 h. The precipitate was filtered and washed with ethyl acetate ($3 \times 100 \text{ ml}$). The combined organic phases were washed with water and brine, and dried over anhydrous Na_2SO_4 . Flash column chromatography on silica gel eluting with 80/1 hexane/ethyl acetate gave octyl cyclobut-1-enecarboxylate as a clear oil (0.604 g, 96%). To a -78°C solution of this oil (0.211 g, 1.0 mmol) in CH_2Cl_2 (10 ml) was bubbled O_3/O_2 until the solution turned blue. The residual ozone was discharged by bubbling with O_2 and the reaction was warmed to room temperature and stirred for another 1 h. Dimethyl sulphide (Me_2S , 0.11 ml, 1.5 mmol) was added to the mixture and it was stirred for another 2 h. The CH_2Cl_2 was removed *in vacuo* and the crude product was dissolved in a solution of 2-methyl-2-butene (0.8 ml) in *t*-BuOH (3.0 ml). To this was added dropwise a solution containing sodium chlorite (0.147 g, 1.3 mmol) and sodium dihydrogen phosphate monohydrate (0.179 g, 1.3 mmol) in H_2O (1.0 ml). The mixture was stirred at room temperature overnight, and then extracted with ethyl acetate ($3 \times 50 \text{ ml}$). The combined organic phases were washed with water and brine, and dried over anhydrous Na_2SO_4 . Flash column chromatography on silica gel eluting with 5/1 hexane/ethyl acetate gave octyl α -KG, which became a pale solid when stored in the refrigerator (0.216 g, 84%).

Synthesis of 5-octyl L-glutamate. L-Glutamic acid (0.147 g, 1.0 mmol) and anhydrous sodium sulphate (0.1 g) was dissolved in octanol (2.0 ml), and then tetrafluoroboric acid-dimethyl ether complex (0.17 ml) was added. The suspended mixture was stirred at 21°C overnight. Anhydrous THF (5 ml) was added to the mixture and it was filtered through a thick pad of activated charcoal. Anhydrous triethylamine (0.4 ml) was added to the clear filtrate to obtain a milky white slurry. Upon trituration with ethyl acetate (10 ml), the monoester monoacid precipitated. The precipitate was collected, washed with additional ethyl acetate ($2 \times 5 \text{ ml}$), and dried *in vacuo* to give the desired product, 5-octyl L-glutamate (0.249 g, 96%) as a white solid. ^1H NMR (500 MHz, acetic acid- d_4): δ 4.12 (dd, $J = 6.6, 6.6 \text{ Hz}$, 1H), 4.11 (t, $J = 6.8 \text{ Hz}$, 2H), 2.64 (m, 2H), 2.26 (m, 2H), 1.64 (m, 2H), 1.30 (m, 10H), 0.89 (t, $J = 7.0 \text{ Hz}$, 3H). ^{13}C NMR (125 MHz, acetic acid- d_4): δ 175.0, 174.3, 66.3, 55.0, 32.7, 30.9, 30.11, 30.08, 29.3, 26.7, 26.3, 23.4, 14.4.

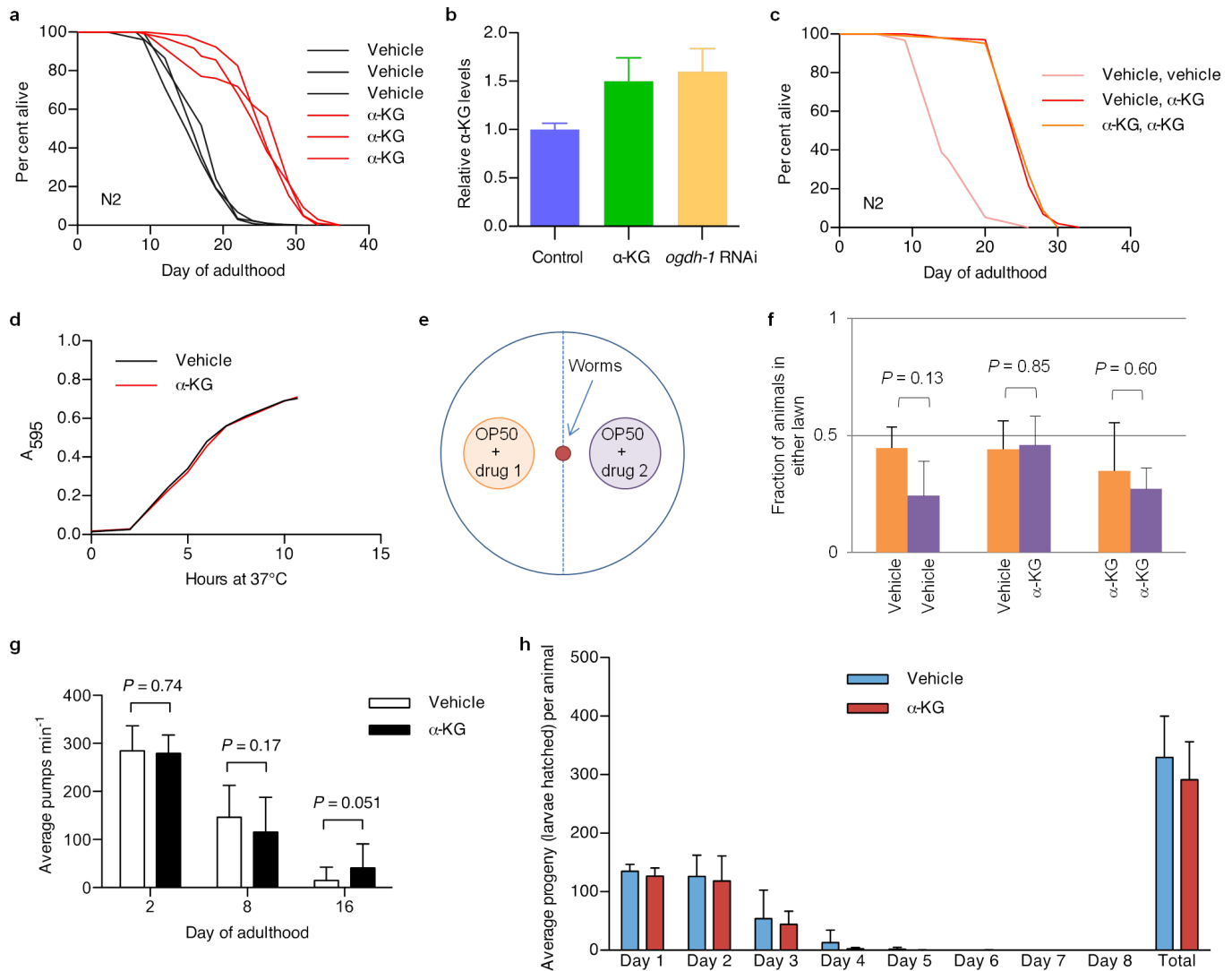
Synthesis of 5-octyl D-glutamate. The synthesis of the opposite enantiomer, that is, 5-octyl D-glutamate, was carried out by the exact same procedure starting with D-glutamic acid. The spectroscopic data was identical to that of the enantiomeric compound.

Synthesis of 5-octyl α -KG. 1-Benzyl 5-octyl 2-oxopentanedioate was obtained as follows. To a solution of 5-octyl L-glutamate (0.249 g) in H_2O (6.0 ml) and acetic acid (2.0 ml) cooled to 0°C was added slowly a solution of aqueous sodium nitrite (0.207 g, 3.0 mmol in 4 ml H_2O). The reaction mixture was allowed to warm slowly to room temperature and was stirred overnight. The mixture was concentrated.

The resulting residue was dissolved in DMF (10 ml) and NaHCO₃ (0.42 g, 5.0 mmol) and benzyl bromide (0.242 ml, 2.0 mmol) were added to the mixture. The mixture was stirred at 21 °C overnight and then extracted with ethyl acetate (3 × 30 ml). The combined organic phase was washed with water and brine and dried over anhydrous MgSO₄. Flash column chromatography on silica gel eluting with 7/1 hexanes/ethyl acetate gave the mixed diester 1-benzyl 5-octyl (S)-2-hydroxypentanedioate as a colourless oil. To this oil, dissolved in dichloromethane (10.0 ml), were added NaHCO₃ (0.42 g, 5.0 mmol) and Dess–Martin periodinane (0.509 g, 1.2 mmol), and the mixture was stirred at room temperature for 1 h and then extracted with ethyl acetate (3 × 30 ml). The combined organic phase was washed with water and brine and dried over anhydrous MgSO₄. Flash column chromatography on silica gel eluting with 5/1 hexanes/ethyl acetate gave the desired 1-benzyl 5-octyl 2-oxopentanedioate (0.22 g, 66%) as a white solid. ¹H NMR (500 MHz, CDCl₃): δ 7.38 (m, 5H), 5.27 (s, 2H), 4.05 (t, J = 6.5 Hz, 2H), 3.14 (t, J = 6.5 Hz, 2H), 2.64 (t, J = 6.5 Hz, 2H), 1.59 (m, 2H), 1.28 (m, 10H), 0.87 (t, J = 7.0 Hz, 3H). ¹³C NMR (125 MHz, CDCl₃): δ 192.2, 171.9, 160.1, 134.3, 128.7, 128.6, 128.5, 67.9, 65.0, 34.2, 31.7, 29.07, 29.05, 28.4, 27.5, 25.7, 22.5, 14.0.

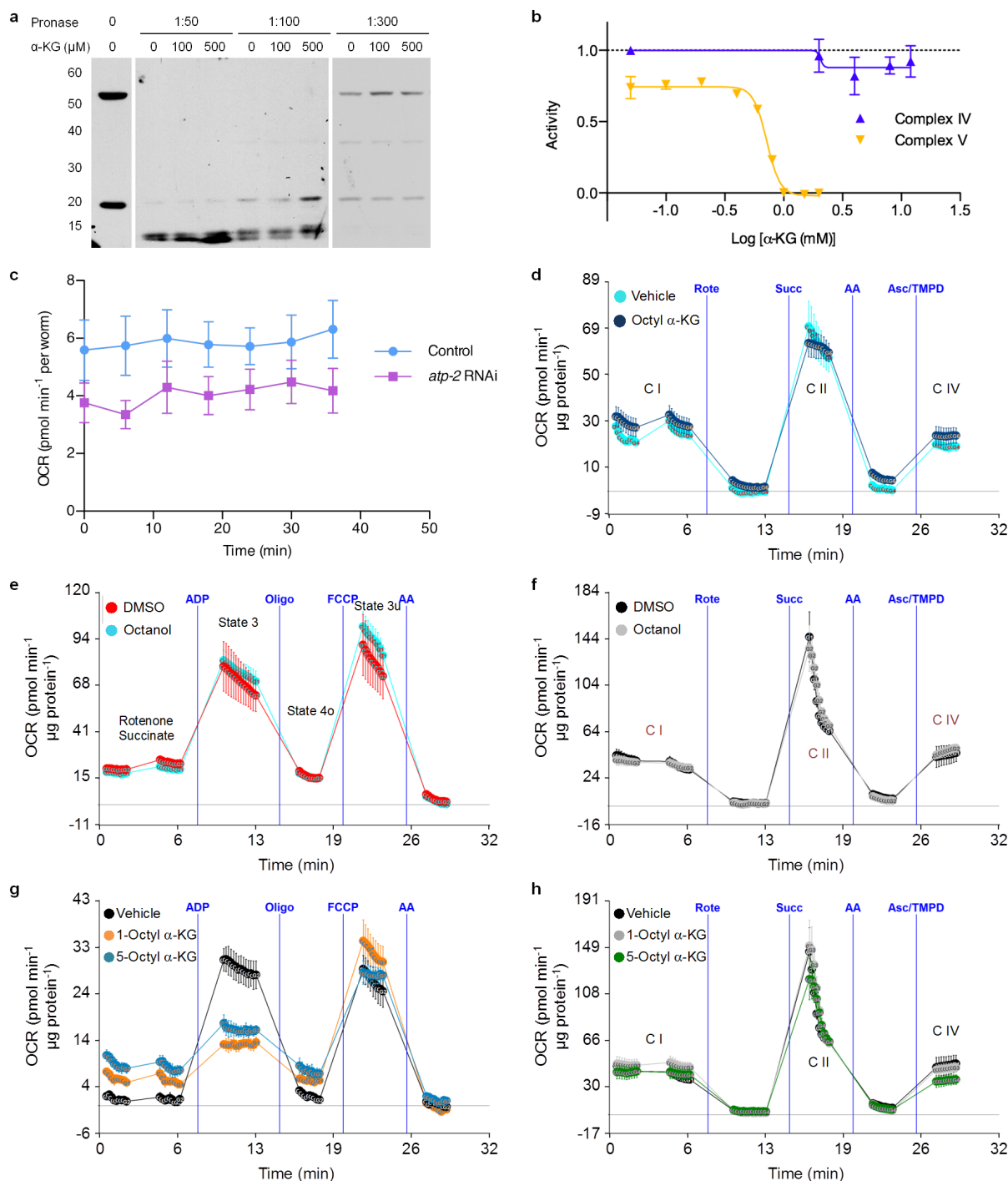
5-Octyl α-KG (5-(octyloxy)-2,5-dioxopentanoic acid) was obtained as follows. To a solution of 1-benzyl 5-octyl 2-oxopentanedioate (0.12 g, 0.344 mmol) in ethyl acetate (15 ml) was added 5% Pd/C (80 mg). Over the mixture was passed a stream of argon and then the argon was replaced with hydrogen gas and the mixture was stirred vigorously for 15 min. The mixture was filtered through a thick pad of Celite to give the desired product 5-octyl α-KG (0.088 g, 99%) as white solid. ¹H NMR (500 MHz, CDCl₃): δ 8.16 (br s, 1H), 4.06 (t, J = 6.5 Hz, 2H), 3.18 (t, J = 6.5 Hz, 2H), 2.69 (t, J = 6.0 Hz, 2H), 1.59 (m, 2H), 1.26 (m, 10H), 0.85 (t, J = 7.0 Hz, 3H). ¹³C NMR (125 MHz, CDCl₃): δ 193.8, 172.7, 160.5, 65.5, 33.0, 31.7, 29.08, 29.06, 28.4, 27.8, 25.8, 22.5, 14.0.

31. Brenner, S. The genetics of *Caenorhabditis elegans*. *Genetics* **77**, 71–94 (1974).
32. Timmons, L. & Fire, A. Specific interference by ingested dsRNA. *Nature* **395**, 854 (1998).
33. Long, X. *et al.* TOR deficiency in *C. elegans* causes developmental arrest and intestinal atrophy by inhibition of mRNA translation. *Curr. Biol.* **12**, 1448–1461 (2002).
34. Sutphin, G. L. & Kaeblerlein, M. Measuring *Caenorhabditis elegans* life span on solid media. *J. Vis. Exp.* **27**, 1152 (2009).
35. Gaudet, J. & Mango, S. E. Regulation of organogenesis by the *Caenorhabditis elegans* FoxA protein PHA-4. *Science* **295**, 821–825 (2002).
36. Abada, E. A. *et al.* *C. elegans* behavior of preference choice on bacterial food. *Mol. Cells* **28**, 209–213 (2009).
37. Lomenick, B., Jung, G., Wohlschlegel, J. A. & Huang, J. Target identification using drug affinity responsive target stability (DARTS). *Curr. Protoc. Chem. Biol.* **3**, 163–180 (2011).
38. Lomenick, B., Olsen, R. W. & Huang, J. Identification of direct protein targets of small molecules. *ACS Chem. Biol.* **6**, 34–46 (2011).
39. Stubbs, C. J. *et al.* Application of a proteolysis/mass spectrometry method for investigating the effects of inhibitors on hydroxylase structure. *J. Med. Chem.* **52**, 2799–2805 (2009).
40. Rogers, G. W. *et al.* High throughput microplate respiratory measurements using minimal quantities of isolated mitochondria. *PLoS ONE* **6**, e21746 (2011).
41. Alberts, B. *Molecular Biology of the Cell* 3rd edn (Garland, 1994).
42. Wu, M. *et al.* Multiparameter metabolic analysis reveals a close link between attenuated mitochondrial bioenergetic function and enhanced glycolysis dependency in human tumor cells. *Am. J. Physiol. Cell Physiol.* **292**, C125–C136 (2007).
43. Yamamoto, H. *et al.* NCoR1 is a conserved physiological modulator of muscle mass and oxidative function. *Cell* **147**, 827–839 (2011).
44. Pathare, P. P., Lin, A., Bornfeldt, K. E., Taubert, S. & Van Gilst, M. R. Coordinate regulation of lipid metabolism by novel nuclear receptor partnerships. *PLoS Genet.* **8**, e1002645 (2012).
45. Pullen, N. & Thomas, G. The modular phosphorylation and activation of p70s6k. *FEBS Lett.* **410**, 78–82 (1997).
46. Burnett, P. E., Barrow, R. K., Cohen, N. A., Snyder, S. H. & Sabatini, D. M. RAFT1 phosphorylation of the translational regulators p70 S6 kinase and 4E-BP1. *Proc. Natl Acad. Sci. USA* **95**, 1432–1437 (1998).
47. Gingras, A. C. *et al.* Hierarchical phosphorylation of the translation inhibitor 4E-BP1. *Genes Dev.* **15**, 2852–2864 (2001).
48. Sarbassov, D. D., Guertin, D. A., Ali, S. M. & Sabatini, D. M. Phosphorylation and regulation of Akt/PKB by the rictor-mTOR complex. *Science* **307**, 1098–1101 (2005).
49. Kim, J., Kundu, M., Viollet, B. & Guan, K. L. AMPK and mTOR regulate autophagy through direct phosphorylation of Ulk1. *Nature Cell Biol.* **13**, 132–141 (2011).
50. Kang, C., You, Y. J. & Avery, L. Dual roles of autophagy in the survival of *Caenorhabditis elegans* during starvation. *Genes Dev.* **21**, 2161–2171 (2007).
51. Hansen, M. *et al.* A role for autophagy in the extension of lifespan by dietary restriction in *C. elegans*. *PLoS Genet.* **4**, e24 (2008).
52. Alberti, A., Michelet, X., Djeddi, A. & Legouis, R. The autophagosomal protein LGG-2 acts synergistically with LGG-1 in dauer formation and longevity in *C. elegans*. *Autophagy* **6**, 622–633 (2010).
53. Schneider, C. A., Rasband, W. S. & Eliceiri, K. W. NIH Image to ImageJ: 25 years of image analysis. *Nature Methods* **9**, 671–675 (2012).
54. Kabeya, Y. *et al.* LC3, a mammalian homologue of yeast Apg8p, is localized in autophagosome membranes after processing. *EMBO J.* **19**, 5720–5728 (2000).
55. MacKenzie, E. D. *et al.* Cell-permeating α-ketoglutarate derivatives alleviate pseudohypoxia in succinate dehydrogenase-deficient cells. *Mol. Cell. Biol.* **27**, 3282–3289 (2007).
56. Zhao, S. *et al.* Glioma-derived mutations in IDH1 dominantly inhibit IDH1 catalytic activity and induce HIF-1α. *Science* **324**, 261–265 (2009).
57. Xu, W. *et al.* Oncometabolite 2-hydroxyglutarate is a competitive inhibitor of α-ketoglutarate-dependent dioxygenases. *Cancer Cell* **19**, 17–30 (2011).
58. Jin, G. *et al.* Disruption of wild-type IDH1 suppresses D-2-hydroxyglutarate production in IDH1-mutated gliomas. *Cancer Res.* **73**, 496–501 (2013).
59. Jung, M. E. & Deng, G. Synthesis of the 1-monoester of 2-ketoalkanedioic acids, for example, octyl α-ketoglutarate. *J. Org. Chem.* **77**, 11002–11005 (2012).



Extended Data Figure 1 | Supplementation with α -KG extends *C. elegans* adult lifespan but does not change the growth rate of bacteria, or food intake, pharyngeal pumping rate or brood size of the worms. **a**, Robust lifespan extension in adult *C. elegans* by α -KG. 8 mM α -KG increased the mean lifespan of *N2* by an average of 47.3% in three independent experiments ($P < 0.0001$ for every experiment, by log-rank test). Experiment 1, mean lifespan (days of adulthood) with vehicle treatment (m_{veh}) = 18.9 ($n = 87$ animals tested), $m_{\alpha-KG}$ = 25.8 ($n = 96$); experiment 2, m_{veh} = 17.5 ($n = 119$), $m_{\alpha-KG}$ = 25.4 ($n = 97$); experiment 3, m_{veh} = 16.3 ($n = 100$), $m_{\alpha-KG}$ = 26.1 ($n = 104$). **b**, Worms supplemented with 8 mM α -KG and worms with RNAi knockdown of α -KGDH (encoded by *ogdh-1*) have increased α -KG levels. Young adult worms were placed on treatment plates seeded with control HT115 *E. coli* or HT115-expressing *ogdh-1* dsRNA, and α -KG content was assayed after 24 h (see Methods). **c**, α -KG treatment beginning at the egg stage and that beginning in adulthood produced identical lifespan increases. Light red, treatment with vehicle control throughout larval and adult stages ($m = 15.6$, $n = 95$); dark red, treatment with vehicle during larval stages and with 8 mM α -KG at adulthood ($m = 26.3$, $n = 102$), $P < 0.0001$ (log-rank test); orange, treatment with 8 mM α -KG throughout larval and adult stages ($m = 26.3$, $n = 102$), $P < 0.0001$ (log-rank test). **d**, α -KG does not alter the

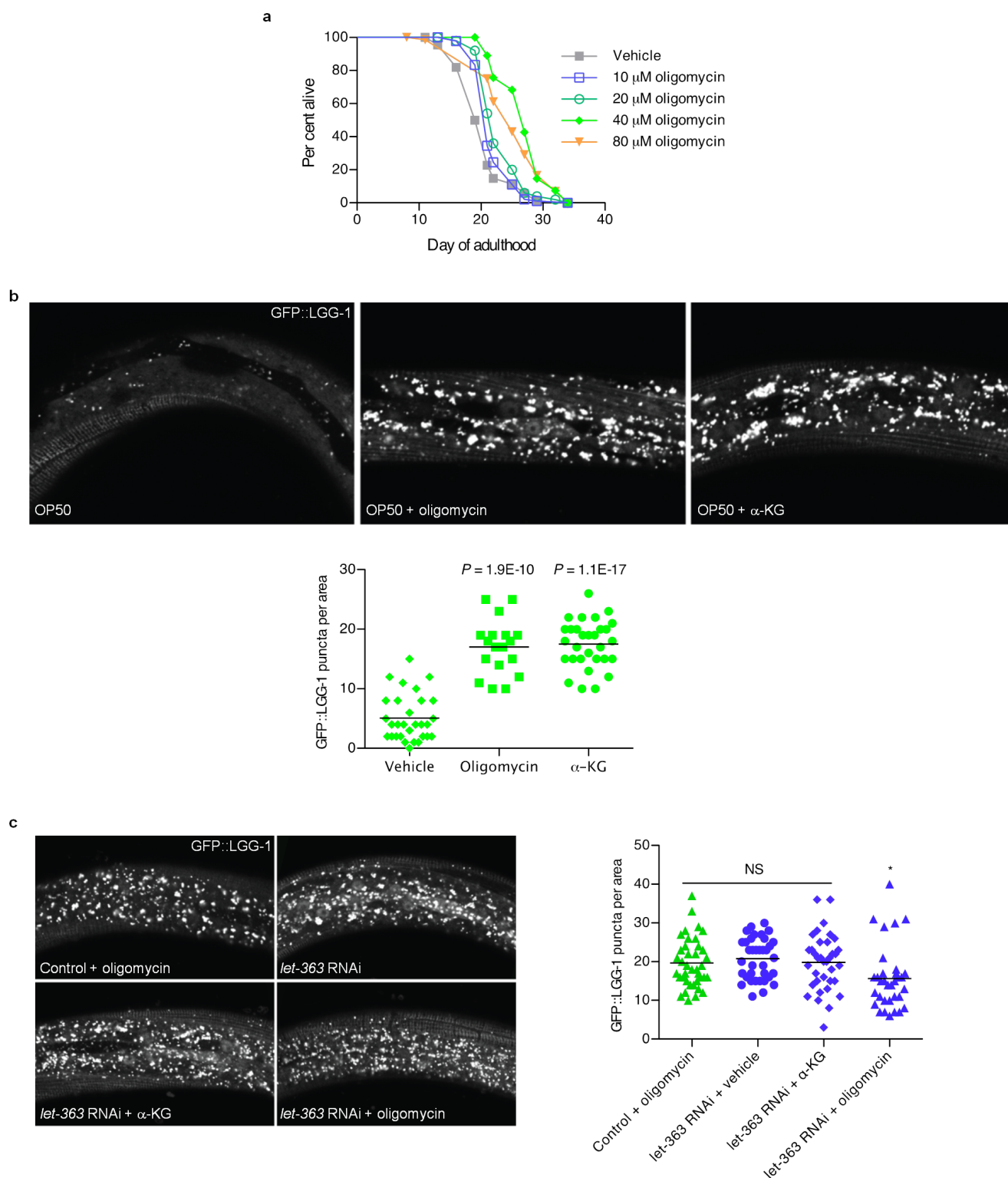
growth rate of the OP50 *E. coli*, which is the standard laboratory food source for nematodes. α -KG (8 mM) or vehicle (H_2O) was added to standard LB media and the pH was adjusted to 6.6 by the addition of NaOH. Bacterial cells from the same overnight OP50 culture were added to the LB \pm α -KG mixture at a 1:40 dilution, and then placed in the 37 °C incubator shaker at 300 r.p.m. The absorbance at 595 nm was read at 1 h time intervals to generate the growth curve. **e**, Schematic representation of food preference assay. **f**, *N2* worms show no preference between OP50 *E. coli* food treated with vehicle or α -KG ($P = 0.85$, by *t*-test, two-tailed, two-sample unequal variance), nor preference between identically treated OP50 *E. coli*. **g**, Pharyngeal pumping rate of *C. elegans* on 8 mM α -KG is not significantly altered (by *t*-test, two-tailed, two-sample unequal variance). **h**, Brood size of *C. elegans* treated with 8 mM α -KG. Brood size analysis was conducted at 20 °C. Ten L4 wild-type worms were each singly placed onto an NGM plate containing vehicle or 8 mM α -KG. Worms were transferred one per plate onto a new plate every day, and the eggs laid were allowed to hatch and develop on the previous plate. Hatchlings were counted as a vacuum was used to remove them from the plate. Animals on 8 mM α -KG showed no significant difference in brood size compared with animals on vehicle plates ($P = 0.223$, by *t*-test, two-tailed, two-sample unequal variance). Mean \pm s.d. is plotted in all cases.



Extended Data Figure 2 | α -KG binds to the β subunit of ATP synthase and inhibits the activity of complex V but not the other ETC complexes.

a, Western blot showing protection of the ATP-2 protein from Pronase digestion upon α -KG binding in the DARTS assay. The antibody for human ATP5B (Sigma, AV48185) recognizes the epitope₁₄₄IMNVIGEPIDERGPIKT KQFAPIHAEAEPEFMEMSVEQELVTGIKVVDLL₁₉₃ that has 90% identity to the *C. elegans* ATP-2. The lower molecular weight band near 20 kDa is a proteolytic fragment of the full-length protein corresponding to the domain directly bound by α -KG. **b**, α -KG does not affect complex IV activity. Complex IV activity was assayed using the MitoTox OXPHOS Complex IV Activity Kit (Abcam, ab109906). Relative complex IV activity was compared to vehicle (H₂O) controls. Potassium cyanide (Sigma, 60178) was used as a positive control for the assay. Complex V activity was assayed using the MitoTox Complex V OXPHOS Activity Microplate Assay (Abcam, ab109907). **c**, *atp-2* RNAi worms have lower oxygen consumption compared to control (*gfp* in RNAi vector), $P < 0.0001$ (t -test, two-tailed, two-sample unequal variance) for

the entire time series (two independent experiments); similar to α -KG-treated worms shown in Fig. 2g. **d**, α -KG does not affect the electron flow through the ETC. Oxygen consumption rate (OCR) from isolated mouse liver mitochondria at basal (pyruvate and malate as complex I substrate and complex II inhibitor, respectively, in the presence of FCCP) and in response to sequential injection of rotenone (Rote; complex I inhibitor), succinate (Succ; complex II substrate), antimycin A (AA; complex III inhibitor), ascorbate/tetramethylphenylenediamine (Asc/TMPD; cytochrome *c* (complex IV) substrate). No difference in complex I (C I), complex II (C II) or complex IV (C IV) respiration was observed after 30 min treatment with 800 μ M octyl α -KG, whereas complex V was inhibited (see Fig. 2h) by the same treatment (two independent experiments). **e**, **f**, No significant difference in coupling (**e**) or electron flow (**f**) was observed with either octanol or DMSO vehicle control. **g**, **h**, Treatment with 1-octyl α -KG or 5-octyl α -KG gave identical results in coupling (**g**) or electron flow (**h**) assays. Mean \pm s.d. is plotted in all cases.

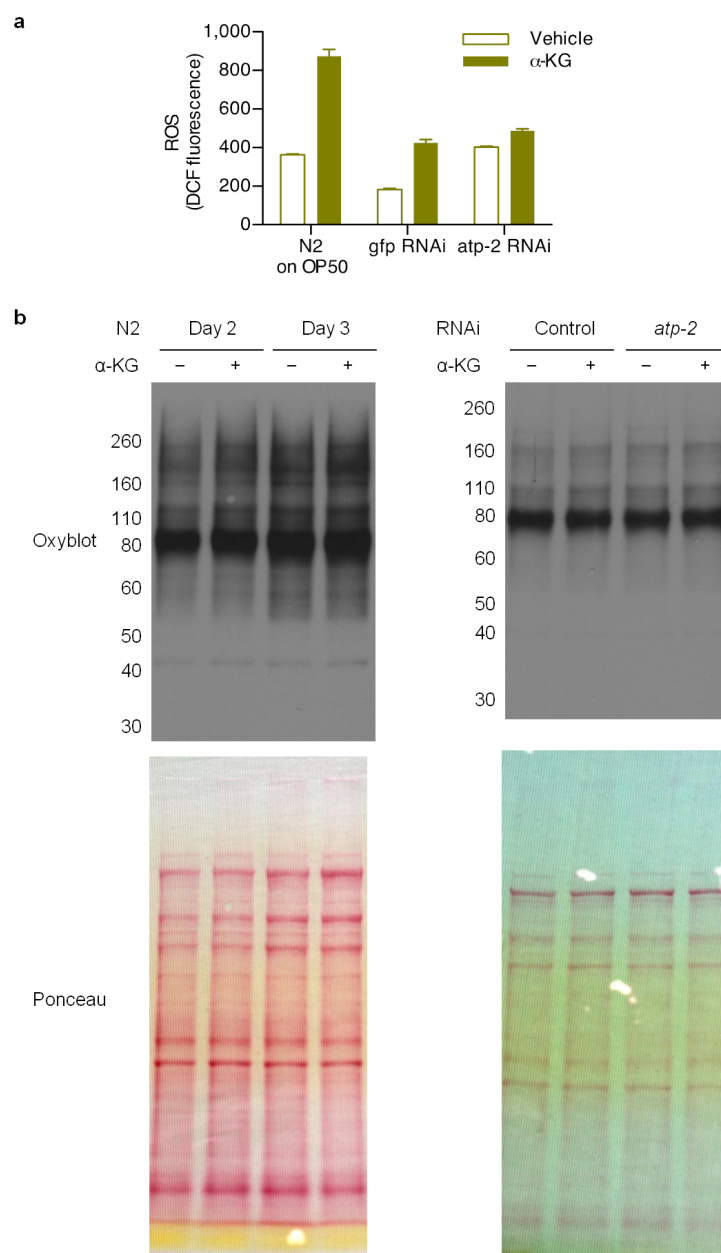


Extended Data Figure 3 | Treatment with oligomycin extends *C. elegans* lifespan and enhances autophagy in a manner dependent on *let-363*.

a, Oligomycin extends the lifespan of adult *C. elegans* in a concentration-dependent manner. Treatment with oligomycin began at the young adult stage. 40 μ M oligomycin increased the mean lifespan of N2 worms by 32.3% ($P < 0.0001$, by log-rank test); see Extended Data Table 2 for details.

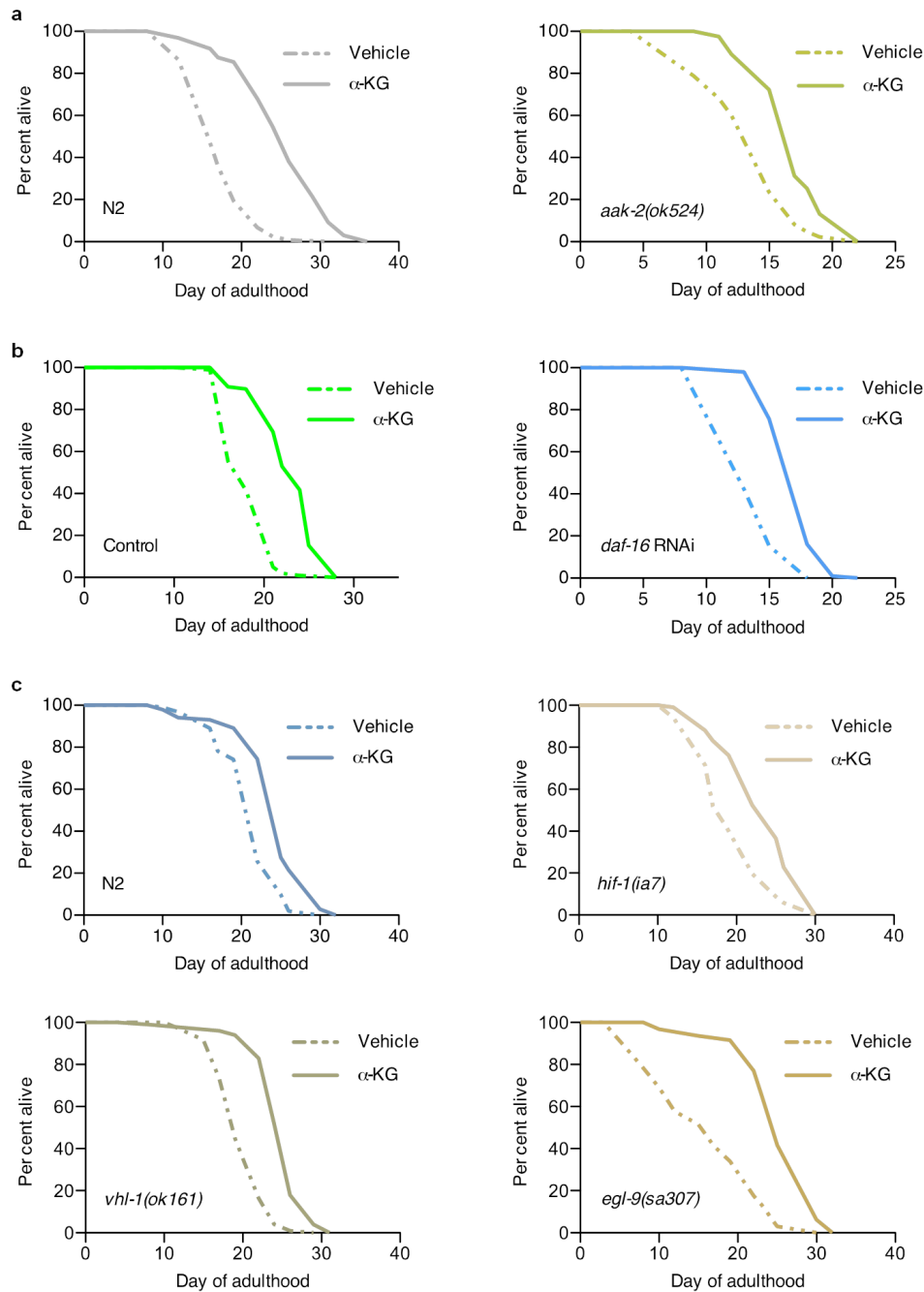
b, Confocal images of GFP::LGG-1 puncta in L3 epidermis of *C. elegans* with vehicle, oligomycin (40 μ M) or α -KG (8 mM), and number of GFP::LGG-1-containing puncta quantified using ImageJ. Bars indicate the mean.

Autophagy in *C. elegans* treated with oligomycin or α -KG is significantly higher than in vehicle-treated control animals (t -test, two-tailed, two-sample unequal variance). **c**, There is no significant difference (NS) between control worms treated with oligomycin and *let-363* RNAi worms treated with vehicle, nor between vehicle- and α -KG-treated *let-363* RNAi worms, consistent with independent experiments in Fig. 4b, c; also, oligomycin does not augment autophagy in *let-363* RNAi worms (if anything, there may be a small decrease, as indicated by an asterisk); by t -test, two-tailed, two-sample unequal variance. Bars indicate the mean. Photographs were taken at $\times 100$ magnification.



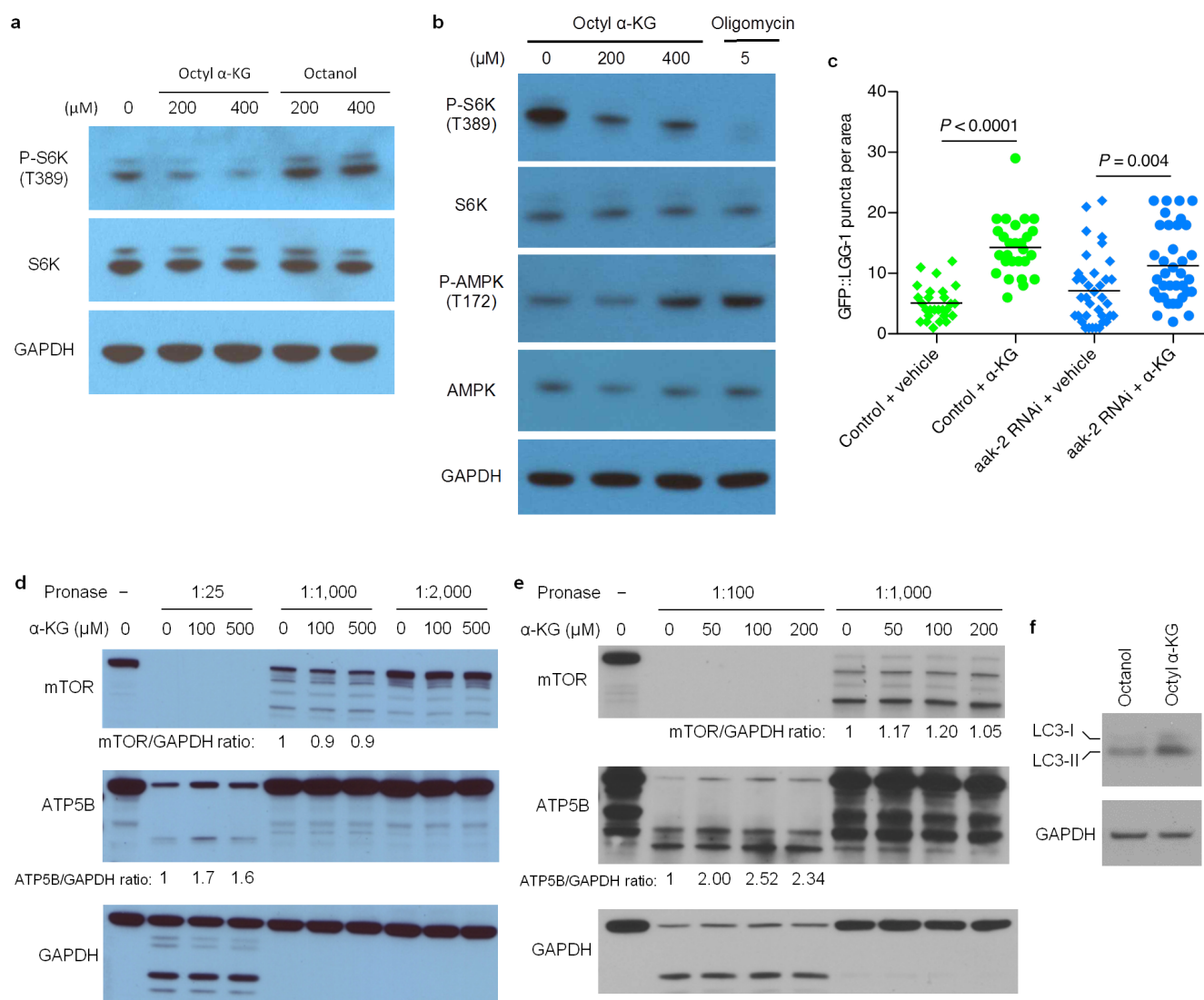
Extended Data Figure 4 | Analyses of oxidative stress in worms treated with α -KG or *atp-2* RNAi. **a**, The *atp-2* RNAi worms have higher levels of 2',7'-dichlorofluorescein (DCF) fluorescence than *gfp* control worms ($P < 0.0001$, by *t*-test, two-tailed, two-sample unequal variance). Supplementation with α -KG also leads to higher DCF fluorescence, in both HT115- (for RNAi) and OP50-fed worms ($P = 0.0007$ and $P = 0.0012$, respectively). Reactive oxygen species (ROS) levels were measured using 2',7'-dichlorodihydrofluorescein diacetate (H_2DCF -DA). As whole worm lysates were used, total cellular oxidative stress was measured here. H_2DCF -DA (Molecular Probes, D399) was dissolved in ethanol to a stock concentration of 1.5 mg ml^{-1} . Fresh stock was prepared every time before use. For measuring ROS in worm lysates, a working concentration of H_2DCF -DA at 30 ng ml^{-1} was hydrolysed by 0.1 M NaOH at room temperature for 30 min to generate 2',7'-dichlorodihydrofluorescein (DCFH) before mixing with whole worm lysates in a black 96-well plate (Greiner Bio-One). Oxidation of DCFH by ROS yields the highly fluorescent DCF. DCF fluorescence was read at excitation/emission of 485/530 nm using SpectraMax MS (Molecular Devices). H_2O_2 was

used as positive control (data not shown). To prepare the worm lysates, synchronized young adult animals were cultivated on plates containing vehicle or 8 mM α -KG and OP50 or HT115 *E. coli* for 1 day, and then collected and lysed as described in Methods. Mean \pm s.d. is plotted. **b**, There was no significant change in protein oxidation upon α -KG treatment or *atp-2* RNAi. Oxidized protein levels were determined by OxyBlot. Synchronized young adult N2 animals were placed onto plates containing vehicle or 8 mM α -KG, and seeded with OP50 or HT115 bacteria that expressed control or *atp-2* dsRNA. Adult day 2 and day 3 worms were collected and washed four times with M9 buffer, and then stored at -80°C for at least 24 h. Laemmli buffer (Biorad, 161-0737) was added to every sample and animals were lysed by alternate boil/freeze cycles. Lysed animals were centrifuged at 14,000 r.p.m. for 10 min at 4°C to pellet worm debris, and supernatant was collected for OxyBlot analysis. Protein concentration of samples was determined by the 660 nm Protein Assay (Thermo Scientific, 1861426) and normalized for all samples. Carbonylation of proteins in each sample was detected using the OxyBlot Protein Oxidation Detection Kit (Millipore, S7150).



Extended Data Figure 5 | Lifespan extension by α -KG in the absence of *aak-2*, *daf-16*, *hif-1*, *vhl-1* or *egl-9*. **a**, Lifespans of α -KG-supplemented N2 worms, $m_{veh} = 17.5$ ($n = 119$), $m_{\alpha-KG} = 25.4$ ($n = 97$), $P < 0.0001$; or *aak-2(ok524)* mutants, $m_{veh} = 13.7$ ($n = 85$), $m_{\alpha-KG} = 17.1$ ($n = 83$), $P < 0.0001$. **b**, N2 worms fed *gfp* RNAi control, $m_{veh} = 18.5$ ($n = 101$), $m_{\alpha-KG} = 23.1$ ($n = 98$), $P < 0.0001$; or *daf-16* RNAi, $m_{veh} = 14.3$ ($n = 99$), $m_{\alpha-KG} = 17.6$ ($n = 99$), $P < 0.0001$. **c**, N2 worms, $m_{veh} = 21.5$ ($n = 101$), $m_{\alpha-KG} = 24.6$ ($n = 102$), $P < 0.0001$; *hif-1(ia7)* mutants, $m_{veh} = 19.6$ ($n = 102$), $m_{\alpha-KG} = 23.6$ ($n = 101$), $P < 0.0001$; *vhl-1(ok161)* mutants, $m_{veh} = 20.0$

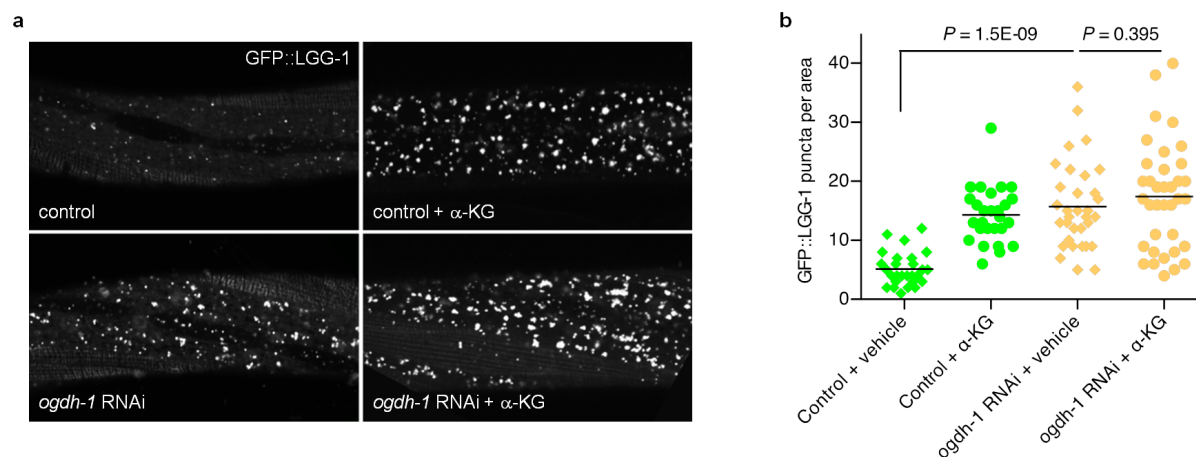
($n = 98$), $m_{\alpha-KG} = 24.9$ ($n = 100$), $P < 0.0001$; or *egl-9(sa307)* mutants, $m_{veh} = 16.2$ ($n = 97$), $m_{\alpha-KG} = 25.6$ ($n = 96$), $P < 0.0001$. P values were determined by the log-rank test. Number of independent experiments: N2 (8), *hif-1* (5), *vhl-1* (1) and *egl-9* (2); see Extended Data Table 2 for details. Two different *hif-1* mutant alleles²⁷ have been used: *ia4* (shown in Fig. 3g) is a deletion over several introns and exons; *ia7* (shown here) is an early stop codon, causing a truncated protein. Both alleles have the same effect on lifespan²⁷. We tested both alleles for α -KG longevity and obtained the same results.



Extended Data Figure 6 | α -KG decreases TOR pathway activity but does not directly interact with TOR.

a, Phosphorylation of S6K (T389) was decreased in U87 cells treated with octyl α -KG, but not in cells treated with octanol control. The same results were obtained using HEK-293 and MEF cells. **b**, Phosphorylation of AMPK (T172) is upregulated in WI-38 cells upon complex V inhibition by α -KG, consistent with decreased ATP content in α -KG-treated cells and animals. However, this activation of AMPK appears to require more severe complex V inhibition than the inactivation of mammalian TOR, as either oligomycin or a higher concentration of octyl α -KG was required for increasing phospho (P)-AMPK whereas concentrations of octyl α -KG comparable to those that decreased cellular ATP content (Fig. 2d) or oxygen consumption (Fig. 2f) were also sufficient for decreasing P-S6K. The same results were obtained using U87 cells. Samples were subjected to SDS-PAGE on 4–12% Bis-Tris gradient gel (Invitrogen, NP0322BOX) and western blotted with specific antibodies against P-AMPK T172 (Cell Signaling, 2535S) and AMPK (Cell Signaling, 2603S). **c**, α -KG still induces autophagy in *aak-2* RNAi worms; $^{**}P < 0.01$ (*t*-test, two-tailed, two-sample unequal variance). The number of GFP::LGG-1 containing puncta was quantified using ImageJ. Bars indicate the mean. **d**, **e**, α -KG does not bind to TOR directly as determined by DARTS. HEK-293 (**d**) or HeLa (**e**) cells were lysed in M-PER buffer (Thermo Scientific, 78501) with the addition of protease inhibitors

(Roche, 11836153001) and phosphatase inhibitors (50 mM NaF, 10 mM β -glycerophosphate, 5 mM sodium pyrophosphate, 2 mM Na_3VO_4). Protein concentration of the lysate was measured by BCA Protein Assay kit (Pierce, 23227). Chilled TNC buffer (50 mM Tris-HCl pH 8.0, 50 mM NaCl, 10 mM CaCl_2) was added to the protein lysate, and the protein lysate was then incubated with vehicle control (DMSO) or varying concentrations of α -KG for 1 h (**d**) or 3 h (**e**) at room temperature. Pronase (Roche, 10165921001) digestions were performed for 20 min at room temperature, and stopped by adding SDS loading buffer and immediately heating at 95 °C for 5 min (**d**) or 70 °C for 10 min (**e**). Samples were subjected to SDS-PAGE on 4–12% Bis-Tris gradient gel (Invitrogen, NP0322BOX) and western blotted with specific antibodies against ATP5B (Santa Cruz, sc58618), mammalian TOR (Cell Signaling, 2972) or GAPDH (Ambion, AM4300). ImageJ was used to quantify the mammalian TOR/GAPDH and ATP5B/GAPDH ratios. Susceptibility of the mammalian TOR protein to Pronase digestion is unchanged in the presence of α -KG, whereas, as expected, Pronase resistance in the presence of α -KG is increased for ATP5B, which we identified as a new binding target of α -KG. **f**, Increased autophagy in HEK-293 cells treated with octyl α -KG was confirmed by western blot analysis of MAP1 LC3 (Novus, NB100-2220), consistent with decreased phosphorylation of the autophagy-initiating kinase ULK1 (Fig. 4a).



Extended Data Figure 7 | Autophagy is enhanced in *C. elegans* treated with *ogdh-1* RNAi. **a**, Confocal images of GFP::LGG-1 puncta in the epidermis of mid-L3 stage, control or *ogdh-1* knockdown *C. elegans* treated with vehicle or α -KG (8 mM). **b**, Number of GFP::LGG-1 puncta quantified using ImageJ.

Bars indicate the mean. *ogdh-1* RNAi worms have significantly higher autophagy levels, and α -KG does not significantly augment autophagy in *ogdh-1* RNAi worms (*t*-test, two-tailed, two-sample unequal variance). Photographs were taken at $\times 100$ magnification.

Extended Data Table 1 | Enriched proteins in the α -KG DARTS sample

Protein Symbol	Protein Name	Score	Control sample		α -KG sample		Enrichment
			Spectra	Peptides	Spectra	Peptides	
ATP5B	ATP synthase subunit beta	4088	23	9	121	15	5.3
HSPD1	60 kDa heat shock protein	2352	31	11	138	29	4.5
PKM2	Pyruvate kinase isozymes M1/M2	2203			56	7	
LCP1	Plastin-2	1865	14	8	76	13	5.4
ATP5A1	ATP synthase subunit alpha	1616	41	9	61	12	1.5
SHMT2	Serine hydroxymethyltransferase	1060	7	5	33	10	4.7
HSP90AA1	Heat shock protein HSP 90-alpha	952	29	8	44	8	1.5
EEF2	Elongation factor 2	943	4	2	37	9	9.3
DDX5	Probable ATP-dependent RNA helicase DDX5	652	7	3	33	10	4.7
HSPA8	Heat shock cognate 71 kDa protein	615	4	2	35	10	8.8

Only showing those proteins with at least 15 spectra in α -KG sample and enriched at least 1.5 fold.

Extended Data Table 2 | Summary of lifespan data

Strain	<i>m</i> (mean lifespan, days)		% difference	<i>P</i> -value	<i>n</i> (number of animals)	
	Vehicle	α -KG			Vehicle	α -KG
<i>N2</i>	18.9	25.8	36.3	< 0.0001	87	96
<i>N2</i>	17.5	25.4	45.6	< 0.0001	119	97
<i>N2</i>	16.3	26.1	60.2	< 0.0001	100	104
<i>eat-2(ad1116)</i>	22.8	22.9	0.5	0.79	59	40
<i>daf-16(mu86)</i>	16.3	18.8	15.1	< 0.0001	106	105
<i>eat-2(ad1116)</i>	21.1	24.0	13.4	0.23	39	59
<i>daf-2(e1370)</i>	38.0	47.6	25.1	< 0.0001	72	69
<i>N2</i>	13.2	22.3	69.8	< 0.0001	100	104
<i>daf-16(mu86)</i>	13.4	17.4	29.5	< 0.0001	71	72
<i>daf-16 RNAi</i>	14.3	17.6	22.9	< 0.0001	99	99
<i>N2</i>	16.1	19.1	19.3	0.0003	97	96
<i>daf-2(e1370)</i>	38.3	43.9	14.6	< 0.0001	109	101
<i>aak-2(ok524)</i>	13.7	17.1	24.3	< 0.0001	85	83
<i>aak-2(ok524)</i>	16.4	17.5	6.7	< 0.0001	97	97
<i>aak-2 RNAi</i>	16.2	19.9	23.3	< 0.0001	93	92
<i>N2</i>	15.6	26.3	68.8	< 0.0001	95	102
<i>N2</i>	15.6	26.3	68.5	< 0.0001	95	102
<i>egl-9(sa307)</i>	16.2	25.6	58.6	< 0.0001	97	96
<i>egl-9(sa307)</i>	19.5	27.3	40.3	< 0.0001	95	101
<i>N2</i>	14.7	21.6	46.9	< 0.0001	100	88
<i>N2</i>	14.0	20.7	47.9	< 0.0001	112	114
<i>N2</i>	21.5	24.6	14.6	< 0.0001	101	102
<i>hif-1(ia4)</i>	20.5	26.0	26.5	< 0.0001	85	71
<i>hif-1(ia7)</i>	19.6	23.6	20.4	< 0.0001	102	101
<i>hif-1(ia4)</i>	21.5	24.7	14.7	< 0.0001	88	87
<i>N2</i>	16.7	23.4	39.7	< 0.0001	104	103
<i>N2</i>	15.8	22.2	40.5	< 0.0001	104	94
<i>N2</i>	18.4	24.6	33.4	< 0.0001	99	89
<i>vhl-1(ok161)</i>	20.0	25.0	24.9	< 0.0001	98	100
<i>hif-1(ia7)</i>	12.4	17.3	38.9	< 0.0001	97	90
<i>hif-1(ia7)</i>	17.9	23.7	32.0	< 0.0001	58	55
<i>N2</i>	16.8	22.4	32.7	< 0.0001	104	101
<i>N2</i>	15.7	21.6	37.6	< 0.0001	85	99
<i>smg-1(cc546ts)</i>	18.4	23.8	29.5	< 0.0001	110	87
<i>smg-1(cc546ts);pha-4(zu225)</i>	14.2	13.5	-4.9	0.5482	94	109
<i>smg-1(cc546ts);pha-4(zu225)</i>	17.6	15.2	-14.0	0.0877	28	34
<i>N2</i>	13.6	20.7	51.8	< 0.0001	103	104
<i>smg-1(cc546ts)</i>	16.2	23.0	42.2	< 0.0001	114	121
<i>smg-1(cc546ts);pha-4(zu225)</i>	13.8	15.2	10.2	0.254	45	45
EV RNAi control	18.6	23.4	26.1	< 0.0001	94	91
<i>atp-2 RNAi</i>	22.8	22.5	-1.3	0.3471	97	94
EV RNAi control	18.8	22.7	20.6	< 0.0001	97	94
gfp RNAi control	18.5	23.1	25.3	< 0.0001	101	98
<i>ogdh-1 RNAi</i>	21.2	21.1	-0.7	0.65	98	100
<i>let-363 RNAi</i>	22.1	23.6	6.8	0.02	94	95
gfp RNAi control	20.2	27.7	37.4	< 0.0001	99	81
<i>let-363 RNAi</i>	25.1	25.7	2.1	0.9511	96	74
EV RNAi control	22.8	27.2	21.6	< 0.0001	70	72
<i>let-363 RNAi</i>	27.4	27.2	-0.8	0.7239	64	80
EV RNAi control	19.7	24.3	23.8	< 0.0001	93	84
<i>atp-2 RNAi</i>	25.3	23.4	-7.4	< 0.0001	87	63

Strain	<i>m</i>		% difference	<i>P</i> -value	<i>n</i>		[Oligomycin]
	Vehicle	Oligomycin			Vehicle	Oligomycin	
<i>N2</i>		25.5	25.2	< 0.0001		72	80 μ M
<i>N2</i>	20.4	27.0	32.3	< 0.0001	88	82	40 μ M
<i>N2</i>		23.1	13.2	0.0005		50	20 μ M
<i>N2</i>		22.0	7.9	0.0106		90	10 μ M

Strain	<i>m</i>		% difference	<i>P</i> -value	<i>n</i>		Treatment
	Vehicle	Treatment			Vehicle	Treatment	
<i>N2</i>	14.5	16.9	16.8	0.0005	73	71	Octyl α -KG (500 μ M)
<i>N2</i>	14.5	17.0	16.8	< 0.0001	73	60	α -KG
<i>N2</i>	14.0	18.8	33.9	< 0.0001	112	114	Dimethyl α -KG
<i>N2</i>	14.0	20.7	47.8	< 0.0001	112	114	α -KG
<i>N2</i>	15.7	21.6	37.6	< 0.0001	85	99	Disodium α -KG

Strain	<i>m</i>		% difference	<i>P</i> -value	<i>n</i>		Food source
	Vehicle	α -KG			Vehicle	α -KG	
<i>N2</i>	17.4	21.2	21.6	0.0001	108	55	Live OP50
<i>N2</i>	19.0	23.0	21.0	0.0003	88	46	Dead OP50 (γ -irradiated)

PTEN action in leukaemia dictated by the tissue microenvironment

Cornelius Miething^{1,2,†}, Claudio Scuoppo², Benedikt Bosbach¹, Iris Appelman^{1,2}, Joy Nakitandwe³, Jing Ma³, Gang Wu³, Laura Lintault^{2,4}, Martina Auer⁵, Prem K. Premisrur², Julie Teruya-Feldstein¹, James Hicks², Helene Benveniste⁶, Michael R. Speicher⁵, James R. Downing³ & Scott W. Lowe^{1,2,4}

PTEN encodes a lipid phosphatase that is underexpressed in many cancers owing to deletions, mutations or gene silencing^{1–3}. *PTEN* dephosphorylates phosphatidylinositol (3,4,5)-triphosphate, thereby opposing the activity of class I phosphatidylinositol 3-kinases that mediate growth- and survival-factor signalling through phosphatidylinositol 3-kinase effectors such as AKT and mTOR². To determine whether continued *PTEN* inactivation is required to maintain malignancy, here we generate an RNA interference-based transgenic mouse model that allows tetracycline-dependent regulation of *PTEN* in a time- and tissue-specific manner. Postnatal *Pten* knockdown in the haematopoietic compartment produced highly disseminated T-cell acute lymphoblastic leukaemia. Notably, reactivation of *PTEN* mainly reduced T-cell leukaemia dissemination but had little effect on tumour load in haematopoietic organs. Leukaemia infiltration into the intestine was dependent on CCR9 G-protein-coupled receptor signalling, which was amplified by *PTEN* loss. Our results suggest that in the absence of *PTEN*, G-protein-coupled receptors may have an unanticipated role in driving tumour growth and invasion in an unsupportive environment. They further reveal that the role of *PTEN* loss in tumour maintenance is not invariant and can be influenced by the tissue microenvironment, thereby producing a form of intratumoural heterogeneity that is independent of cancer genotype.

Stable RNA interference using short-hairpin RNAs (shRNAs) provides a powerful approach for studying tumour suppressor gene activity *in vitro* and *in vivo*^{4–6}. To explore the role of *PTEN* loss in tumour maintenance, we developed shRNA transgenic mouse lines targeting *Pten* using miR-30-based shRNAs expressed from an inducible tetracycline-responsive element promoter⁶ (Fig. 1a and Extended Data Fig. 1). Murine embryonic fibroblasts (MEFs) obtained from embryonic day (E)13.5 embryos of *shPten*;R26-rtTA2 double-transgenic mice displayed reversible knockdown of *Pten* upon doxycycline (Dox) addition and withdrawal, which correlated with increased AKT phosphorylation following insulin stimulation (Fig. 1b and Extended Data Fig. 1c). As expected^{7,8}, Dox-treated mice expressing *shPten* in multiple tissues developed several tumour types including T-cell malignancies (Extended Data Fig. 1e–i).

Owing to the high frequency of T-cell disease in the *shPten* mice and the frequent inactivation of *PTEN* in human T-cell acute lymphoblastic leukaemia (T-ALL)⁹, we focused on the effects of *PTEN* suppression and reactivation in the lymphoid compartment. We crossed mice transgenic for an shRNA against luciferase (*shLuc*) and *shPten* mice to a *Vav-tTA* transgenic line, which expresses a 'Tet-off' Tet transactivator in early B and T cells¹⁰ and drives shRNA expression in a manner that is silenced upon Dox addition (Extended Data Fig. 2 and data not shown). The *Vav-tTA*; *shPten* mice displayed thymic hyperplasia (Extended Data Fig. 2a–d) and, by 16 weeks, a subset deteriorated and had to be euthanized (Fig. 1c), whereas control animals remained healthy ($P < 0.001$). Diseased mice showed massive enhanced green fluorescent protein

(eGFP)-positive tumours that consisted of Thy1.2⁺ CD4⁺ CD8⁺ double-positive T cells filling the thoracic cavity and infiltrating spleen, lymph nodes as well as extrahematopoietic organs like the liver, kidney and intestine (Fig. 1d, Extended Data Figs 2e, f and 3a, and data not shown). *shPten*-expressing tumours demonstrated marked *Pten* knockdown and increased AKT phosphorylation comparable to *Pten*-null T-cell malignancies (Fig. 1e, see ref. 11).

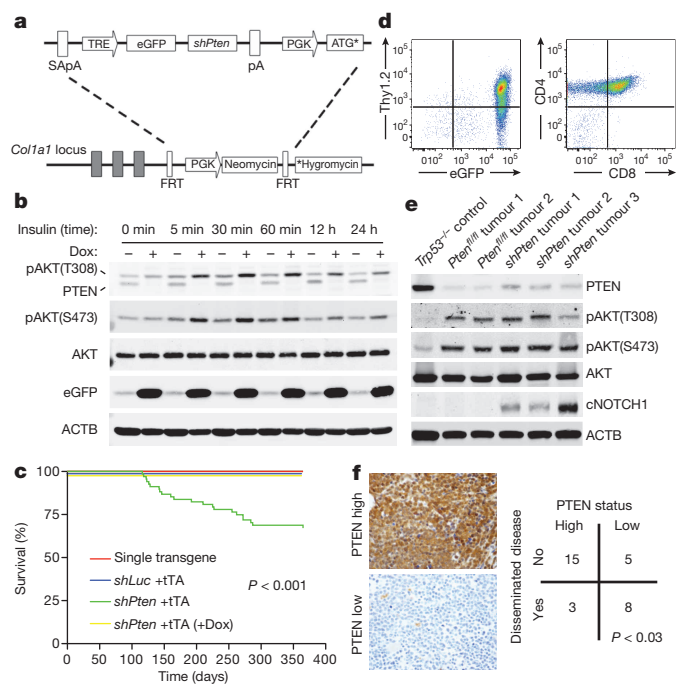


Figure 1 | *Pten* shRNA transgenic mice develop disseminated CD4⁺ CD8⁺ double-positive T-cell leukaemia. **a**, Outline of the targeting construct and the embryonic stem (ES) cell-targeting strategy. FRT, FLP recognition target; pA, polyadenylation site; PGK, phosphoglycerate kinase promoter; SA, splice acceptor site; TRE, tetracycline-responsive element promoter. ATG* denotes truncated ATG sequence; *Hygromycin denotes ATG-less hygromycin resistance gene. **b**, Immunoblot (western blot) analysis of MEFs from *shPten*;R26-rtTA2 transgenic mice ± Dox for 5 days at indicated time points after stimulation with 100 nM insulin. **c**, Overall survival of *Vav-tTA*; *shPten* mice (n = 49) and controls (n = 98, $P < 0.001$ by log-rank). **d**, Flow cytometric analysis of a representative primary *Vav-tTA*; *shPten* tumour for eGFP, Thy1.2, CD4 and CD8 (n = 10). **e**, Western blot analysis of T-cell tumours from *Trp53*^{-/-}, *Pten*^{fl/fl}, *Lck-cre* and *Vav-tTA*; *shPten* mice for the indicated proteins. **f**, PTEN IHC of bone marrow samples of 31 human patients with T-ALL categorized as PTEN high (top left) or low/negative (bottom left). Association of PTEN expression with status for disseminated disease was calculated using a contingency table (Fisher's exact test).

¹Memorial Sloan Kettering Cancer Center, New York, New York 10065, USA. ²Cold Spring Harbor Laboratory, Cold Spring Harbor, New York 11724, USA. ³Department of Pathology, St. Jude Children's Research Hospital, Memphis, Tennessee 38105, USA. ⁴Howard Hughes Medical Institute, New York, New York 10065, USA. ⁵Institute of Human Genetics, Medical University of Graz, A-8010 Graz, Austria. ⁶Departments of Anesthesiology and Radiology, Stony Brook University, Stony Brook, New York 11794, USA. [†]Present address: Department of Medicine I, Medical Center – University of Freiburg, 79106 Freiburg, Germany.

Human T-ALLs with *PTEN* loss often overexpress *MYC* and can harbour *NOTCH1* and *CDKN2A* mutations¹². Analysis of murine *shPten*-expressing tumours by spectral karyotyping, comparative genomic hybridization (CGH) and sequencing of the gene encoding the T-cell receptor β -chain showed that most primary tumours were clonal and harboured the same recurrent translocations between the *Tcra* locus and *Myc* observed in a *Pten* knockout model and a small subset of human T-ALL (Extended Data Figs 3b, c and 4a, and data not shown)^{13,14}. One *shPten* T-ALL showed a *Cdkn2a* deletion by CGH and six out of eight tumours analysed showed activating mutations in the Notch1 PEST domain (Fig. 1e and Extended Data Figs 3c, d and 4b). Gene set enrichment analysis (GSEA) of gene expression profiles obtained from *shPten* leukaemia demonstrated enrichment for a human *PTEN*-mutated T-ALL signature, and profiles from human *PTEN*-mutated T-ALLs were enriched for a murine *shPten* signature (Extended Data Fig. 5a, b). Thus, although all the T-cell leukaemias were initiated by a *Pten* shRNA, they acquire molecular features reminiscent of the human disease^{12,13,15}.

The leukaemia arising in *shPten* mice was highly malignant, and rapidly produced disease when transplanted into recipient mice (Extended Data Fig. 6a). Of note, because the *Vav-tTA;shPten* transgenic mice were of a mixed genetic background, *Rag1*^{-/-} recipients were used to avoid graft rejection. These recipients succumbed to a highly disseminated form of T-ALL consisting of CD4⁺ CD8⁺ double-positive cells that rapidly took over the haematopoietic organs, accumulated to high levels in the peripheral blood, and spread to the liver, kidney and intestine (Fig. 2d and Extended Data Fig. 6b). Notably, decreased PTEN levels were associated with disease dissemination and lower survival in T-ALL patients (Fig. 1f and Extended Data Fig. 6c), and were also linked with intestinal infiltration in patients with peripheral T-cell lymphoma (Extended Data Fig. 6d, e). The association between PTEN loss and disease dissemination in murine and human T-cell malignancies underscores the relevance of the model to human disease.

We reasoned that the transplanted leukaemias described above would be ideal for our experiments as they are highly malignant such that individual primary isolates can be studied for their response to different perturbations in multiple secondary recipients. Recipients were monitored for disease development by weekly analysis of peripheral blood for the presence of eGFP⁺ (*shPten*-expressing) cells. Upon disease manifestation, a cohort of mice was given Dox to silence the shRNA and reactivate PTEN. Notably, Dox treatment almost tripled the survival time of mice harbouring *Vav-tTA;shPten* leukaemia (Fig. 2a; $P < 0.0001$) but had no effect on mice harbouring *Pten*^{-/-} leukaemia (Extended Data Fig. 6f). Immunoblotting of leukaemic cells collected from mice indicated that the system worked as expected: hence, Dox addition led to upregulation of *Pten* messenger RNA (Extended Data Fig. 7a–c and data not shown), silenced eGFP and re-established PTEN to endogenous levels (Fig. 2b and Extended Data Fig. 7d). Therefore, PTEN reactivation had a marked anticancer effect but was by no means curative.

Leukaemia-bearing mice showed magnetic resonance imaging (MRI) signals in multiple haematopoietic compartments, the liver and intestine (Extended Data Fig. 6h, i and data not shown). Although PTEN reactivation had no overt effect on tumour growth in the lymph nodes or spleen, it visibly decreased tumour infiltration into intestine and liver (Fig. 2c and Extended Data Fig. 6g–i). These findings were corroborated by immunohistochemistry (IHC) and flow cytometric quantification of CD4⁺ leukaemic cells (Fig. 2e, f). Notably, Dox treatment had a minimal impact on the proliferation or apoptosis of leukaemic cells residing in the lymph nodes and spleen, but triggered apoptosis in leukaemic cells that had disseminated into the intestine (Fig. 2g and Extended Data Fig. 7e–g). Thus, the impact of PTEN expression on disease progression is dictated by the anatomical location of the leukaemic cell.

We next assessed the phosphorylation state of key phosphatidylinositol 3-kinase (PI3K) effectors in tissue sections by IHC and pathway functionality by positron emission tomography (PET) of ¹⁸F-fluorodeoxyglucose (FDG) uptake into leukaemia cells¹⁶. The heterogeneous responses

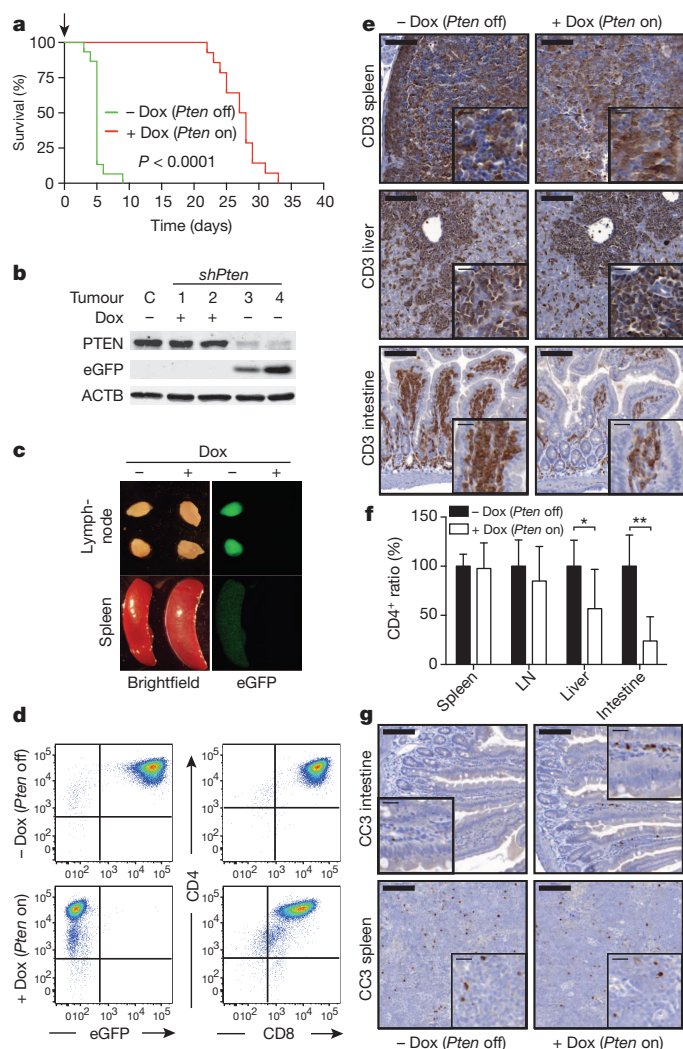


Figure 2 | The impact of PTEN reactivation on leukaemia viability is influenced by anatomical site. **a**, Overall survival of *Rag1*^{-/-} mice transplanted with 1×10^5 cells from *Vav-tTA;shPten* (*shPten*) tumours and treated with Dox (*Pten* on; $n = 14$), or untreated controls (*Pten* off; $n = 15$), $P < 0.0001$ by log-rank test. **b**, Western blot analysis of splenic tumour cells from control, untreated, and mice treated with Dox for 5 days. **c**, Brightfield and eGFP images of lymph nodes and spleen from an untreated mouse (*Pten* off) and mouse treated with Dox for 5 days (*Pten* on) ($n = 10$). **d**, Flow cytometric analysis of CD4, eGFP and CD8 expression in tumour cells from the peripheral blood of mice \pm Dox for 5 days ($n = 10$). **e**, IHC analysis for CD3 expression in the spleen, liver and small intestine from *shPten* T-ALL transplanted mice \pm Dox for 5 days ($n = 3$ per group). Scale bars, 100 μ m, 20 μ m in insets. **f**, Relative tumour infiltration in the indicated organs of transplanted *Rag1*^{-/-} mice off ($n = 7$) and on ($n = 7$) Dox, quantified by flow cytometric analysis of CD4⁺ cells; * $P < 0.05$, ** $P < 0.01$ by Student's *t*-test (\pm s.d.). **g**, IHC staining for cleaved caspase 3 (CC3) in the spleen and intestine from mice 10 days after transplant with *shPten* T-ALL either left untreated or treated with Dox for 36 h. Representative sections from one of three mice per cohort are shown. Scale bars, 100 μ m, 20 μ m in insets.

correlated with the ability of PTEN to effectively suppress aberrant PI3K signalling: whereas S6 and AKT phosphorylation were reduced in disseminated leukaemic cells obtained from the intestine, it persisted in the leukaemic cells collected from the spleen of the same animal (Fig. 3a and Extended Data Fig. 8). Similarly, mice displayed a marked reduction in FDG signal stemming from the liver and intestine within 2 days of PTEN reactivation, an effect that could not simply be accounted for by loss of leukaemia burden (Fig. 3b, c). Conversely, the FDG signal emanating from the spleen and bone marrow remained strong (Fig. 3b, d and Supplementary Videos 1 and 2). The divergent responses to PTEN

activation in a clonal leukaemia suggest that the control of the PI3K pathway can be markedly affected by microenvironmental factors.

Surprisingly, untreated NCr nude mice transplanted with the same number of *shPten* tumour cells survived as long as *Rag1*^{-/-} recipient mice treated with Dox, and did not show a survival advantage following Dox addition (Fig. 4a). The untreated NCr recipients displayed vastly reduced intestinal dissemination of leukaemic cells compared to normal and thymectomized *Rag1*^{-/-} recipients (Fig. 4b and Extended Data Fig. 9a, b, g, h), whereas spleen and lymph nodes were strongly affected (Fig. 4c and Extended Data Fig. 9c, d). Apparently, genetic differences between *Rag1*^{-/-} and NCr mice contribute to variation in disease aggressiveness and the response to PTEN reactivation.

Whereas *Rag1*^{-/-} mice are defective in immunoglobulin and T-cell receptor gene rearrangement, NCr mice have mutations in *Foxn1*, a gene that controls terminal differentiation of epithelial cells in the thymus and other organs¹⁷. Among other changes, NCr mice show decreased

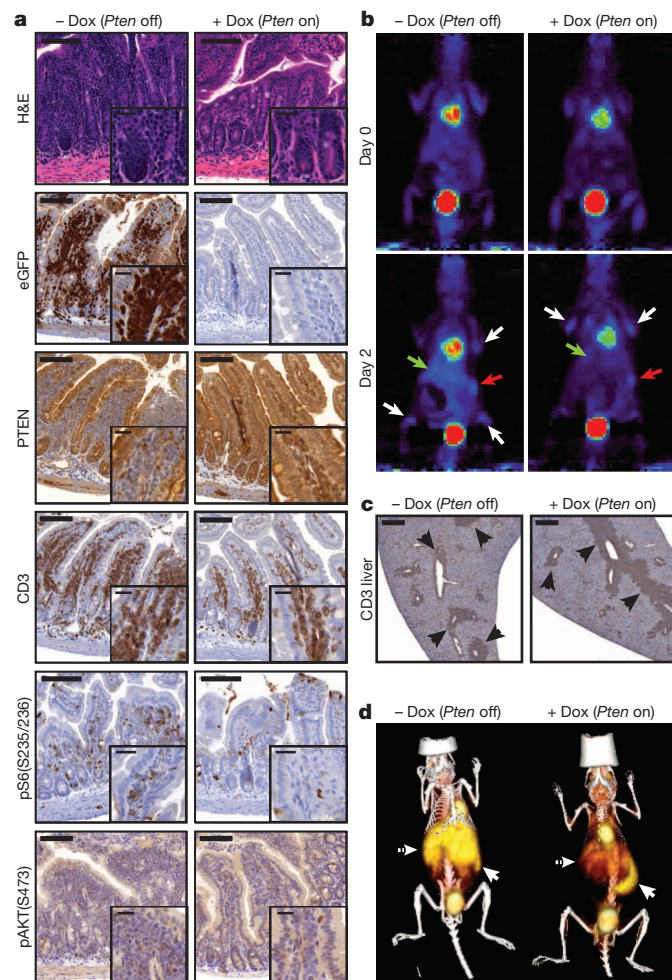


Figure 3 | Tissue-dependent effects of PTEN reactivation on PI3K signalling. **a**, Small intestinal sections from *shPten* T-ALL transplanted mice \pm Dox were stained with haematoxylin and eosin (H&E) or by IHC for the indicated proteins. Representative sections from one of three mice per cohort are shown. Scale bars, 100 μ m, 20 μ m in insets. **b**, Serial ¹⁸F-FDG PET analysis of *shPten* T-ALL transplanted mice before and 2 days after beginning of Dox treatment. White arrows, bone marrow; red arrow, spleen; green arrow, liver/intestine. Representative images from two out of 12 analysed mice are shown. **c**, CD3 IHC staining of *shPten* tumour infiltrations in the liver of mice \pm Dox 4 days after treatment initiation ($n = 3$ per group). Arrows highlight CD3⁺ tumour infiltrates. Scale bars, 500 μ m. **d**, ¹⁸F-FDG PET/CT analysis of *shPten* T-ALL transplanted mice \pm Dox 4 days after beginning of Dox treatment. Full arrow, spleen; dashed arrow, liver/intestine. Representative images from two out of six analysed mice are shown.

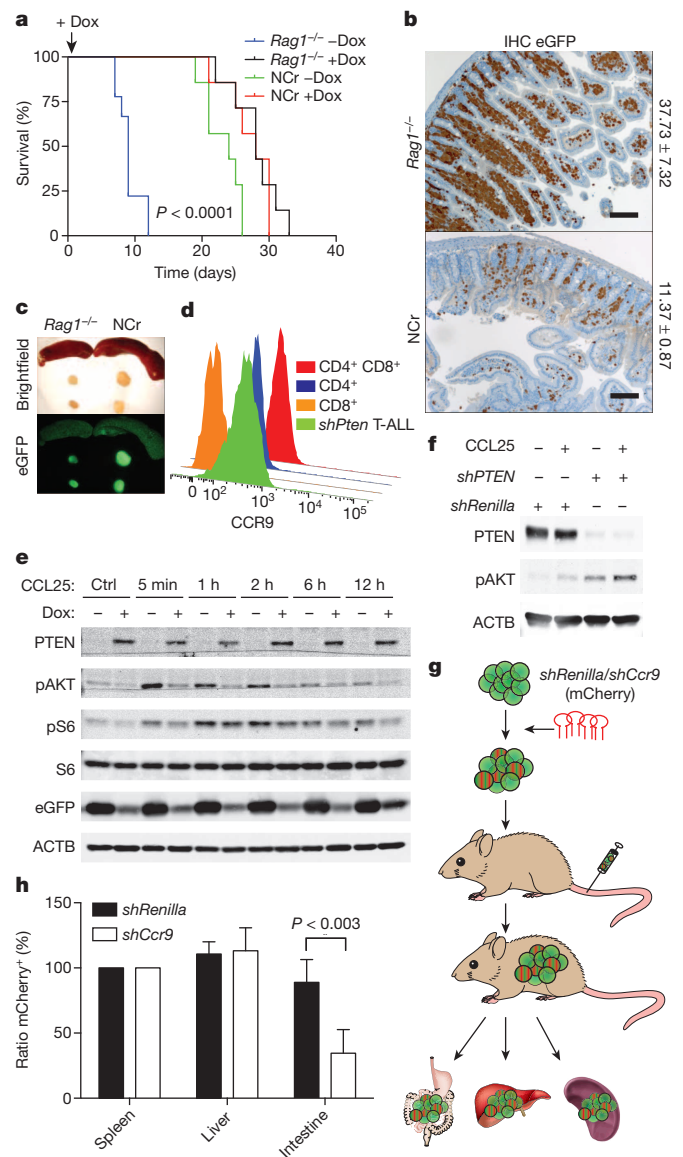


Figure 4 | CCL25-CCR9 chemokine signalling contributes to leukaemia dissemination. **a**, Overall survival of *Rag1*^{-/-} mice ($-$ Dox, $n = 9$; $+$ Dox, $n = 7$) and NCr mice ($-$ Dox, $n = 7$; $+$ Dox, $n = 7$) transplanted with 1×10^5 *shPten* leukaemia cells. Survival of *Rag1*^{-/-} ($-$ Dox) versus NCr ($-$ Dox) mice; $P < 0.0001$ by log-rank test. **b**, IHC staining for eGFP in intestinal sections from *Rag1*^{-/-} and NCr mice transplanted with *shPten* leukaemia ($n = 3$ per cohort). Scale bars, 100 μ m. Numbers show mean fraction (\pm s.d.) of infiltrating eGFP⁺ tumour cells of total viable cells as determined by flow cytometry ($P < 0.03$, Student's t -test). **c**, Representative images of lymph nodes and spleens from transplanted *Rag1*^{-/-} and NCr mice ($n = 7$). **d**, CCR9 receptor expression on *shPten* leukaemia cells, normal CD4⁺ CD8⁺ double-positive and CD4 or CD8 single-positive thymic T cells measured by flow cytometry ($n = 3$ per group). **e**, Western blot analysis of indicated proteins in *shPten* leukaemic cells \pm Dox after stimulation with 500 ng ml⁻¹ CCL25 for the indicated time. **f**, Western blot of indicated proteins in human T-ALL cells infected with either *shRenilla* control or *shPTEN.1522* and \pm stimulation with CCL25 for 15 min. pS6 and pAKT in **e** and **f** denote pS6(S235/236) and pAKT(S473). **g**, Outline of competition experiment of untransduced versus *shCcr9-mCherry*- or control *shRenilla-mCherry*-transduced eGFP⁺ *shPten* tumour cells. **h**, Normalized ratio of mCherry⁺/eGFP⁺ cells over all eGFP⁺ cells isolated from spleen, liver and intestine of five mice per cohort from two independent transplantations (\pm s.d.). Cells were analysed by flow cytometry and normalized to the mCherry/eGFP ratio in the spleen to account for differences in transduction rate.

expression of *Ccl25* (refs 18, 19), which encodes a chemokine that is mainly expressed by epithelial cells in the thymus and small intestine and acts as an important chemoattractant for T cells in the gut^{20,21}. CCL25 acts through CCR9, a G-protein-coupled receptor that can signal through the PI3K pathway and is expressed on a subset of developing thymocytes^{22,23}. Signalling through a related receptor, CCR7, is important for leukaemia dissemination into the central nervous system²⁴; moreover, the CCL25/CCR9 network is required for T-cell dissemination during inflammatory bowel disease, which can be countered by CCR9 antagonists currently in clinical trials^{25,26}. CCL25 levels were decreased in the intestine of NCr mice (Extended Data Fig. 9e, f), whereas CCR9 was highly expressed on the *shPten* leukaemia cells (Fig. 4d). Notably, CCR9 expression was not affected by PTEN reactivation as determined by fluorescence-activated cell sorting and RNA-seq analysis (Extended Data Fig. 9i and data not shown).

To test whether PTEN influences T-ALL homing and survival in the intestine by modulating CCL25 signalling, *shPten* T-cell leukaemia isolates were treated with CCL25 (\pm Dox to modulate PTEN), and cell signalling and motility was assessed in short-term culture. Whereas CCL25 stimulation had little impact on PI3K signalling in the presence of PTEN, *Pten* knockdown sensitized cells to CCL25-induced AKT phosphorylation and, to a lesser extent, S6 phosphorylation (Fig. 4e). Similar results were obtained with two human T-ALL lines transduced with either *shPTEN* or a control shRNA (Fig. 4f and Extended Data Fig. 9j). CCL25 addition also increased migration of murine *shPten* T-ALL cells in a transwell assay, and the effect was largely abrogated by PTEN reactivation (Extended Data Fig. 9k).

Dual-colour *in vivo* competition experiments were performed to assess the contribution of CCR9 signalling to T-ALL dissemination (Fig. 4g). After identifying shRNAs efficient at knocking down *Ccr9* (Extended Data Fig. 10a, b), eGFP⁺ *shPten* leukaemic cells were transduced with either *shCcr9* or *shRenilla* control shRNAs co-expressing the mCherry red fluorescent protein (Fig. 4g and Extended Data Fig. 10d). Upon transplantation and subsequent disease development, mice were euthanized and the fraction of eGFP/mCherry⁺ cells versus all eGFP⁺ cells was determined in various organs (Fig. 4g, h). *shCcr9*-expressing T-ALL cells showed significantly decreased abundance in the intestine but not the spleen or liver (Fig. 4h and Extended Data Fig. 10c, d). Mice transplanted with *shPten* leukaemic cells were also treated with a small molecule inhibitor for CCR9 that is in clinical trials for the treatment of inflammatory bowel disease²⁶. Although the effects on survival were modest, leukaemia dissemination was reduced in the intestine, whereas cells in the spleen and liver were unaffected (Extended Data Fig. 10e–h and data not shown). Hence, in the intestine, PTEN suppression promotes leukaemic cell dissemination and maintenance by modulating CCL25–CCR9 signalling.

In human cancers, *PTEN* deletions often coincide with tumour expansion, metastasis and a generally worse prognosis^{9,27,28}, results confirmed and extended for T-cell disease in this report. Using a powerful new mouse model enabling reversible suppression of endogenous PTEN expression, we show that PTEN loss can promote tumour cell survival at distant sites by amplifying weak environmental cues that enable tumour cells to survive in an otherwise non-supportive microenvironment. Accordingly, the promiscuous yet passive ability of PTEN to attenuate PI3K signalling² may be influenced by the nature and intensity of phosphatidylinositol (3,4,5)-triphosphate-generating signals in different microenvironments, and targeting such tissue-specific signals might present a valid strategy to treat cancer spread. Still, the requirement for PTEN loss in tumour maintenance is not absolute and can be influenced by genetic context^{29,30} and, as shown here, the tumour microenvironment. These observations paint a more complex picture of how PTEN inactivation drives tumour maintenance, and reveal an interplay between tumour and microenvironment that would not be predicted from studies on cultured cells. Nonetheless, this interplay produces a form of intra-tumoral heterogeneity that is independent of genotype but can affect disease progression and perhaps the clinical response to molecularly targeted therapies.

METHODS SUMMARY

ES cell targeting and generation of *Pten* shRNA transgenic mice. KH2 ES cells expressing the reverse transactivator (rtTA2) from the *Rosa26* promoter were electroporated with *Pten* shRNAs cloned into a recombination-mediated cassette exchange vector (cTGM) targeting the *Colla1* locus⁶, and correctly targeted and functional ES cell clones were identified and used to generate live mice by tetraploid embryo complementation. The number of each shRNA is used as index and refers to the position of the first nucleotide of the shRNA guide strand relative to the refseq cDNA sequence. MEFs were generated from 13.5-day-old embryos according to standard protocols. Mice were bred to *CMV-rtTA*, *CAGGS-rtTA* and *Vav-rtTA* transactivator lines to generate heterozygous (for example, *shPten*^{+/−}; *CMV-rtTA*^{+/−}) double-transgenic mice using standard breeding techniques. To induce shRNA expression, *Pten* and firefly luciferase (*Luc*) or Renilla luciferase (*Renilla*) shRNA mice bred to *CMV-rtTA* or *CAGGS-rtTA* mice were put on food containing 625 mg kg^{−1} Dox (Harlan Teklad) immediately after weaning. Dox food was also used to shut off shRNA expression in *Vav-rtTA* transgenic animals at different time points. All mouse experiments were performed in accordance with institutional and national guidelines and regulations and were approved by the Institution Animal Care and Use Committee (IACUC no. 06-02-97-17 (Cold Spring Harbour Laboratory) and no. 11-06-017 (Memorial Sloan Kettering Cancer Center)).

Online Content Any additional Methods, Extended Data display items and Source Data are available in the online version of the paper; references unique to these sections appear only in the online paper.

Received 4 April 2013; accepted 10 March 2014.

Published online 4 May 2014.

- Li, J. *et al.* PTEN, a putative protein tyrosine phosphatase gene mutated in human brain, breast, and prostate cancer. *Science* **275**, 1943–1947 (1997).
- Engelman, J. A., Luo, J. & Cantley, L. C. The evolution of phosphatidylinositol 3-kinases as regulators of growth and metabolism. *Nature Rev. Genet.* **7**, 606–619 (2006).
- Salmena, L., Carracedo, A. & Pandolfi, P. P. Tenets of PTEN tumor suppression. *Cell* **133**, 403–414 (2008).
- Dickins, R. A. *et al.* Probing tumor phenotypes using stable and regulated synthetic microRNA precursors. *Nature Genet.* **37**, 1289–1295 (2005).
- Dickins, R. A. *et al.* Tissue-specific and reversible RNA interference in transgenic mice. *Nature Genet.* **39**, 914–921 (2007).
- Premisrirt, P. K. *et al.* A rapid and scalable system for studying gene function in mice using conditional RNA interference. *Cell* **145**, 145–158 (2011).
- Di Cristofano, A., Pesce, B., Cordon-Cardo, C. & Pandolfi, P. P. Pten is essential for embryonic development and tumour suppression. *Nature Genet.* **19**, 348–355 (1998).
- Stambolic, V. *et al.* High incidence of breast and endometrial neoplasia resembling human Cowden syndrome in *pten*^{+/−} mice. *Cancer Res.* **60**, 3605–3611 (2000).
- Gutierrez, A. *et al.* High frequency of PTEN, PI3K, and AKT abnormalities in T-cell acute lymphoblastic leukemia. *Blood* **114**, 647–650 (2009).
- Kim, W. I., Wiesner, S. M. & Largaespada, D. A. Vav promoter-tTA conditional transgene expression system for hematopoietic cells drives high level expression in developing B and T cells. *Exp. Hematol.* **35**, 1231–1239 (2007).
- Suzuki, A. *et al.* T cell-specific loss of Pten leads to defects in central and peripheral tolerance. *Immunity* **14**, 523–534 (2001).
- Aifantis, I., Raetz, E. & Buonamici, S. Molecular pathogenesis of T-cell leukaemia and lymphoma. *Nature Rev. Immunol.* **8**, 380–390 (2008).
- Guo, W. *et al.* Multi-genetic events collaboratively contribute to *Pten*-null leukaemia stem-cell formation. *Nature* **453**, 529–533 (2008).
- Erikson, J. *et al.* Deregulation of c-myc by translocation of the alpha-locus of the T-cell receptor in T-cell leukemias. *Science* **232**, 884–886 (1986).
- Zhang, J. *et al.* The genetic basis of early T-cell precursor acute lymphoblastic leukaemia. *Nature* **481**, 157–163 (2012).
- Engelman, J. A. *et al.* Effective use of PI3K and MEK inhibitors to treat mutant Kras G12D and PIK3CA H1047R murine lung cancers. *Nature Med.* **14**, 1351–1356 (2008).
- Nehls, M. *et al.* Two genetically separable steps in the differentiation of thymic epithelium. *Science* **272**, 886–889 (1996).
- Bleul, C. C. & Boehm, T. Chemokines define distinct microenvironments in the developing thymus. *Eur. J. Immunol.* **30**, 3371–3379 (2000).
- Nowell, C. S. *et al.* Foxn1 regulates lineage progression in cortical and medullary thymic epithelial cells but is dispensable for medullary sublineage divergence. *PLoS Genet.* **7**, e1002348 (2011).
- Wurbel, M. A. *et al.* The chemokine TECK is expressed by thymic and intestinal epithelial cells and attracts double- and single-positive thymocytes expressing the TECK receptor CCR9. *Eur. J. Immunol.* **30**, 262–271 (2000).
- Campbell, D. J. & Butcher, E. C. Intestinal attraction: CCL25 functions in effector lymphocyte recruitment to the small intestine. *J. Clin. Invest.* **110**, 1079–1081 (2002).
- Youn, B. S., Kim, C. H., Smith, F. O. & Broxmeyer, H. E. TECK, an efficacious chemoattractant for human thymocytes, uses GPR-9–6/CCR9 as a specific receptor. *Blood* **94**, 2533–2536 (1999).
- Uehara, S., Grinberg, A., Farber, J. M. & Love, P. E. A role for CCR9 in T lymphocyte development and migration. *J. Immunol.* **168**, 2811–2819 (2002).

24. Buonamici, S. *et al.* CCR7 signalling as an essential regulator of CNS infiltration in T-cell leukaemia. *Nature* **459**, 1000–1004 (2009).
25. Walters, M. J. *et al.* Characterization of CCX282-B, an orally bioavailable antagonist of the CCR9 chemokine receptor, for treatment of inflammatory bowel disease. *J. Pharmacol. Exp. Ther.* **335**, 61–69 (2010).
26. Eksteen, B. & Adams, D. H. GSK-1605786, a selective small-molecule antagonist of the CCR9 chemokine receptor for the treatment of Crohn's disease. *IDrugs* **13**, 472–781 (2010).
27. Hollander, M. C., Blumenthal, G. M. & Dennis, P. A. PTEN loss in the continuum of common cancers, rare syndromes and mouse models. *Nature Rev. Cancer* **11**, 289–301 (2011).
28. Jotta, P. Y. *et al.* Negative prognostic impact of *PTEN* mutation in pediatric T-cell acute lymphoblastic leukemia. *Leukemia* **24**, 239–242 (2010).
29. Muellner, M. K. *et al.* A chemical-genetic screen reveals a mechanism of resistance to PI3K inhibitors in cancer. *Nature Chem. Biol.* **7**, 787–793 (2011).
30. Ilic, N., Utermark, T., Widlund, H. R. & Roberts, T. M. PI3K-targeted therapy can be evaded by gene amplification along the MYC-eukaryotic translation initiation factor 4E (eIF4E) axis. *Proc. Natl Acad. Sci. USA* **108**, E699–E708 (2011).

Supplementary Information is available in the online version of the paper.

Acknowledgements We are grateful to J. Cappellani, D. Grace, J. Simon and M. Taylor for technical assistance, S.-Y. Kim for performing tetraploid embryo complementation, J. Cheng for RNA-seq analysis, M. Riggs for CGH array analysis, M. Lupu and C. Le for MRI imaging, V. Longo and P. Zanzonico for PET analysis, J. Pichardo for data management, L. Lopez and A. Giri for tissue microarray construction, M. Saborowski for help with IHC staining, A. Roselló-Díez and M. Asher for expertise in antibody staining characterization and C. Sherr for constructive comments and editorial advice. We thank J. Jaen, M. Penfold and M. Walters from ChemoCentryx for providing the CCR9 small molecule inhibitor. C.M. was supported by a fellowship from the DFG (Mi1210/1-1). I.A.

received support by a fellowship from the Deutsche Krebshilfe (DKH no. 109902). C.S. was supported by the Angel Foundation with a Curt Engelhorn fellowship. This work was also supported by a program project grant from the National Cancer Institute, a Leukemia and Lymphoma Society Specialized Center of Research, and philanthropic funds from the Don Monti Foundation. S.W.L. is supported by the Geoffrey Beene Foundation and is an investigator at the Howard Hughes Medical Institute.

Author Contributions C.M. and S.W.L. designed the study. C.M., C.S., P.K.P. and L.L. performed shRNA design and testing, targeting vector construction and E.S. cell targeting. C.M., B.B., I.A., C.S. and L.L. performed mouse breeding, transplantation experiments and analysed data. C.M. and I.A. performed *in vitro* migration assays and analysed data. C.M. and H.B. ran the mouse MRI experiments and analysed data. C.M. and B.B. performed the ¹⁸F-FDG-PET experiments and analysed data. J.H. performed CGH analysis, and J.H. and C.M. analysed data. J.T.-F. performed the histopathological analysis of mouse and human tumours, and J.T.-F. and C.M. analysed data. B.B. and C.M. performed paraffin embedding, sectioning and IHC staining of mouse tissues and analysed data. C.M. performed flow cytometry, immunoblotting and analysed data. J.N. performed the RNA-seq sample processing and J.N., J.M., J.R.D., C.S. and C.M. analysed data. C.S. ran the GSEA analysis and comparison with human expression data. M.A. and M.R.S. performed the SKY analysis of mouse tumours, and M.A., M.R.S. and C.M. analysed data. S.W.L. supervised the project. C.M., C.S., B.B. and S.W.L. wrote the paper. All authors reviewed the manuscript.

Author Information Data sets from RNA-seq analysis were deposited at the Sequence Read Archive (SRA) at the European Nucleotide Archive under the accession number PRJEB5498. Reprints and permissions information is available at www.nature.com/reprints. The authors declare no competing financial interests. Readers are welcome to comment on the online version of the paper. Correspondence and requests for materials should be addressed to S.W.L. (lowes@mskcc.org).

METHODS

Constructs and shRNAs. To identify potent shRNAs targeting murine and human *Pten*, various 97-bp oligonucleotides predicted from sensor-based and other shRNA design algorithms (Extended Data Fig. 4c and data not shown)^{31,32} were XhoI-EcoRI cloned into the miR-30 cassette of the MLP vector and tested as described previously (Extended Data Fig. 1a)³³. The two most efficient murine *Pten* shRNAs (*Pten.1522* and *Pten.2049*, numbers refer to the position of the first nucleotide of the shRNA guide strand relative to the refseq cDNA sequence) were cloned into a recombination-mediated cassette exchange (RCME) vector (cTGM) targeting the *Col1a1* locus (see Fig. 1a)^{6,34}. For knockdown of human *PTEN*, the *Pten.1522* shRNA, which showed complete overlap with the human *PTEN* sequence, was used. For knockdown of murine *Ccr9*, multiple shRNAs were designed, cloned and tested as described above. The two most efficient shRNAs, *shCcr9.904* (97-mer: 5'-TGCT GTTGACAGTGAGCGCAAGGATAAGAATGCCAAGCTATAGTGAAGCCA CAGATGTATAGCTTGGCATTCTTATCCTTATGCCTACTGCCTCGGA-3') and *shCcr9.2357* (97-mer: 5'-TGCTGTTGACAGTGAGCGCCCCAACAGTTT ACAACCTTTATAGTGAAGCCA CAGATGTATAAAGTTGTAAACTGTTG GGATGCCTACTGCCTCGGA-3'), were cloned into a LMN-cherry vector (MSCV-miR30-pgk-NeoR-IRES-mCherry) for dual-colour competition assays (see below).

ES cell targeting and generation of transgenic mice. Two potent shRNAs against murine *Pten* were cloned into a cassette that links eGFP and shRNA expression downstream of *TRE*, and targeted into a defined locus downstream of the collagen, type I, alpha 1 (*Col1a1*) gene in KH2 ES cells expressing the reverse transactivator (rtTA2) from the *Rosa26* promoter³⁵ by RMCE (Fig. 1a and Extended Data Fig. 1a)^{6,34}. Southern blotting showed correct transgene insertion, and Dox-inducible knockdown of endogenous *PTEN* was confirmed by western blot analysis (Extended Data Fig. 1b).

Germline transgenic mice were generated by tetraploid embryo complementation. MEFs were generated from 13.5-day-old embryos according to standard protocols. Since both shRNAs caused a similar degree of *Pten* knockdown and PI3K pathway activation and equally promoted tumorigenesis in *in vivo* transplantation experiments (Extended Data Fig. 1c, d and data not shown), we focused subsequent analysis on a single (*shPten.1522*) transgenic line.

Mice were bred to *CMV-rtTA*, *CAGGS-rtTA* and *Vav-tTA* transactivator lines^{6,10,35} to generate compound heterozygous or homozygous (for example, *shPten*^{+/-}; *CMV-rtTA*^{+/-} or *shPten*^{+/-}; *Vav-tTA*^{+/-}) double-transgenic mice using standard breeding techniques. To induce shRNA expression, *Pten* and firefly luciferase (*Luc*) or Renilla luciferase (*Renilla*) shRNA mice bred to *CMV-rtTA* or *CAGGS-rtTA* mice were put on food containing 625 mg kg⁻¹ Dox (Harlan Teklad) immediately after weaning. As predicted from knockout mice^{7,36}, most double-transgenic mice harbouring the inducible *shPten* allele together with the broadly expressing *CMV-rtTA* or the *CAGGS-rtTA3* transactivator strains^{6,35} developed tumours within 12 months of Dox addition (Extended Data Fig. 2; data not shown). Dox food was also used to shut off shRNA expression in *Vav-tTA* transgenic animals at different time points. For the *Vav-tTA*; *shPten* mice survival studies, a number of *Vav-tTA*⁺; *shPten*⁺ mice (*n* = 49) and controls (*Vav-tTA*⁺; *shLuc*⁺ (*n* = 20), *Vav-tTA*⁺; *shPten*⁻ (*n* = 68), *Vav-tTA*⁺; *shPten*⁺ + Dox (*n* = 10)) were generated and analysed. No difference in phenotype was observed between heterozygous (*shPten*^{+/-}; *Vav-tTA*^{+/-}) and homozygous (*shPten*^{+/-}; *Vav-tTA*^{+/-}) mice. All mouse experiments were performed in accordance with institutional and national guidelines and regulations and were approved by the Institution Animal Care and Use Committee (IACUC no. 06-02-97-17 (Cold Spring Harbour Laboratory) and no. 11-06-017 (Memorial Sloan Kettering Cancer Center)).

Statistics and reagents. For all murine survival studies, a group size of at least five animals per condition was chosen, which allowed the detection of twofold differences in survival with a power of 0.89, assuming a two-sided test with a significance threshold α of 0.05 and a standard deviation of less than 50% of the mean. For the primary animals, all mice with the correct genotype were included in the analysis. For the transplantation experiments, all mice receiving similar amounts of transplanted cells as determined by flow cytometric and/or whole-body immunofluorescent evaluation 5–10 days after transplant were included in the analysis. For the reactivation and treatment experiments, animals were assigned into different groups by random picking from the non-selected transplanted group of mice 5–10 days after transplant. Blinding of animals in the reactivation/inhibitor treatment studies was not feasible, because of requirements by the local animal housing facility to mark cages if containing special food/treatment.

Appropriate statistical tests were applied as indicated, including non-parametric tests for experiments where sample size was too small to assess normal distribution. All *t*-tests and derivatives were two-sided. For all tests, variation was calculated as standard deviation and included in the graphs as error bars. To investigate whether *PTEN* expression has an impact on tumour dissemination in human T-ALL, we performed IHC staining for *PTEN* on bone marrow sections from 31 patients with newly diagnosed T-ALL, for which clinical data on disease dissemination was available.

Owing to the relatively low number of patient specimens and because the variables were nonlinear, we analysed the data in a contingency table using Fisher's exact test. We also re-analysed the contingency table using Berger's test, with similar results³⁷. For probing an association between *PTEN* expression status and intestinal infiltration in human T-cell lymphoma patients, the same statistical tests were applied.

All antibodies used for western blot analysis were purchased from Cell Signaling Technology unless otherwise specified, including the antibodies against *PTEN* (cat no. 9188), pAKT(S473, cat no. 4060), pAKT(T308, cat no. 2965), AKT (cat no. 4691), S6 (cat no. 2317), pS6(S235/236, cat no. 4858), cleaved Notch1 (cat no. 4147). For intracellular flow cytometric analysis of pS6(S235/236) directly, Pacific-Blue fluorescence-coupled antibodies were purchased from Cell Signaling (cat no. 8520).

Antibodies for flow cytometry were purchased from BioLegend unless otherwise specified. Mouse antibodies included CD3 (clone 145-2C11), CD4 (clone GK1.5), CD8 (clone 53-6.7), Thy1.2 (clone 30-H12), CD45 (clone 30-F11), CCR9 (clone 9B1), CD11b (clone M1-70), Gr-1 (clone RB6-8C5), CD44 (clone IM7), CD25 (clone PC61).

Human T-ALL cell lines HBP-ALL and TALL1 were a kind gift from I. Aifantis. All cell lines were tested for absence of mycoplasma and authenticated by flow cytometry and western blotting.

Transplantation experiments. For transplantation, single-cell suspensions were generated from primary tumours and 1×10^5 cells were injected into sublethally (450 rad) irradiated recipient female *Rag1*^{-/-} (on a C57B6 background, cat no. 2216) or NCr nude mice (on an inbred albino background, cat no. 2019) via tail vein injection. All mice used as transplant recipients were purchased from Jackson Laboratory. Mice were monitored by serial flow cytometric analysis of the peripheral blood. Once eGFP⁺ cells reached >5% of total leukocytes, cohorts of mice were started on Dox containing food as indicated.

Analysis of human T-ALL and PTCL patient samples. For the analysis of survival of *PTEN* normal versus *PTEN* altered patients with T-ALL, published genomic and mRNA expression data on patients with T-ALL was used (accession number GSE28703)¹⁵. *PTEN* altered (*n* = 20) included patients with *PTEN* deletion, mutation, underexpression (<0.8 sigma after *z* scoring) and any combination of such alterations, and *PTEN* normal (*n* = 62) included all other patients with available data. For IHC analysis, samples from patients with T-ALL were analysed as individual bone marrow biopsies. For the T-cell lymphoma samples, tissue microarrays were constructed as previously published³⁸ using a fully automated Beecher Instrument, ATA-27. The study cohort comprised 84 patients with T-cell lymphomas and 31 patients with T-ALL. The T-cell lymphomas could be subdivided into enteropathy-associated T-cell lymphoma (4) and peripheral T-cell lymphoma involving bowel or gastrointestinal tract (7), T/NK cell lymphoma (4), angioimmunoblastic T-cell lymphoma (9), anaplastic large cell lymphoma (14), and peripheral T-cell lymphoma with non bowel or gastrointestinal tract involvement (46). All samples were consecutively ascertained at the Memorial Sloan-Kettering Cancer Center (MSKCC) between 2001 and 2012. Use of tissue samples were approved with an Institutional Review Board Waiver and the Human Bio-specimen Utilization Committee. All biopsies were evaluated at MSKCC, and the histological diagnosis was based on H&E staining. The *PTEN* antibody (rabbit monoclonal antibody from Cell Signaling, 138G6, no. 9559) was used at a 1:30 dilution. IHC analysis was performed on the Ventana Discovery XT automated platform according to the manufacturer's instructions. Results were scored as 0, 1, 2 for *PTEN* with 0 = no staining of tumour cells, with endothelial cell- and macrophage-positive; 1 = weak staining of tumour cells, compared to endothelial cell- and macrophage-positive; 2 = strong staining of tumour cells, compared to endothelial cell- and macrophage-positive. Representative images were taken using the Olympus BX41 model, DP20 camera, at $\times 60$ objective.

MRI. The mice were anesthetized with 2–3% isoflurane delivered in O₂ and allowed to breathe spontaneously during the imaging study. The mice were positioned supine in a custom-made acrylic cradle fitted with a snout mask for continuous delivery of anaesthesia. Non-invasive, MRI-compatible monitors (pulse-oximetry, respiratory rate and rectal temperature probe, SA Instruments) were positioned for continuous monitoring of vital signs while the animal underwent MRI imaging. During imaging, body temperature was kept strictly within 36.5–37.5 °C using a computer-assisted air heating system (SA Instruments). All imaging was performed on a 9.4T/20 MRI instrument interfaced to a Bruker Advance console and controlled by Paravision 5.0 software (Bruker Biospin). A volume radiofrequency coil (diameter 11.2 mm) used in transmit and receive mode were used for all imaging acquisitions. Following localizer anatomical scout scans, a 2D multi-slice T2-weighted RARE sequence along the coronal slice direction with fat suppression was obtained with the following parameters: TR = 12,500 ms, TE = 40 ms, RARE factor = 8, NA = 8, FOV = 6.0 \times 6.0 cm² (256 \times 256), yielding an in-plane resolution of 0.234 \times 0.234 mm², slice thickness = 0.9 mm total scanning time = 10 min 40 s.

¹⁸F-FDG-PET analysis. For PET analysis, mice were fasted for 6 h before intravenous injection of 0.5 mCi ¹⁸F-FDG. Mice were kept for 1 h under isoflurane anaesthesia and subsequently imaged on a Focus 120 microPET (Siemens) or in

some cases an Inveon MicroPET/CT (Siemens). Image normalization and analysis was performed using the ASI Pro MicroPET analysis software and the Inveon Workplace software package (Siemens Medical Solutions).

CGH. CGH experiments were performed using standard Agilent 244k mouse whole genome arrays, and hybridizations were carried out according to the manufacturer's recommendations. Data processing, normalization and segmentation were carried out as described³⁹.

Multiplex-FISH (M-FISH)/spectral karyotyping analysis. Cells were cultured in RPMI-1640 with L-glutamine (PAA) supplemented with 10% FBS, 1% penicillin-streptomycin, 50 μ M mercaptoethanol, 50 U ml⁻¹ human interleukin 2 and 5 μ g ml⁻¹ concanavalin A for 48–72 h at 37 °C and 5% CO₂. To prepare metaphases, colcemid at a final concentration of 0.1 μ g ml⁻¹ was added to the cells for 120 min. Spinning at 300g for 8 min was followed by hypotonic treatment in pre-warmed 0.075 M KCl for 20 min at 37 °C. Cells were fixed in cold ethanol/acetic acid (3:1) and air-dried slides were prepared.

The M-FISH hybridization was performed with a panel of mouse M-FISH probes (21 \times Mouse mFISH probe kit, MetaSystems) according to the manufacturer's instructions. In brief, the probes were denatured at 75 °C for 5 min, and pre-annealed at 37 °C for 30 min. Slides were incubated in 0.1 \times SSC for 1 min, denatured in 0.07N NaOH at room temperature for 1 min, quenched in 0.1 \times SSC at 4 °C and 2 \times SSC at 4 °C for 1 min each, dehydrated in an ethanol series and air dried. M-FISH probe was applied onto the slides and hybridization was performed for 48 h in a humidified chamber at 37 °C. Following hybridization, the slides were washed in 0.4 \times SSC at 72 °C for 2 min, followed by a wash in 2 \times SSC, 0.05% Tween20 at room temperature for 2 min. Counterstaining was performed using DAPI (4',6-diamidino-2-phenylindole) and mounted with phenylenediamine.

Slides were visualized using a Leica DMRXA-RF8 epifluorescence microscope equipped with special filter blocks (Chroma Technology). For image acquisition, a Sensys CCD camera (Photometrics) with a Kodak KAF 1400 chip was used. Both the camera and microscope were controlled with Leica Q-FISH software (Leica Microsystems Imaging Solutions). Images were analysed using the Leica MCK-Software package (Leica Microsystems Imaging Solutions).

Western blotting, flow cytometry and antibodies. Western blotting was performed according to standard protocols. In brief, tissues were either snap frozen in liquid nitrogen and homogenized, or dissociated into single cells using 100 μ m nylon mesh (CellStrainer, BD Falcon). Protein was extracted using standard protein lysis buffer (20 mM Tris (pH 7.5), 150 mM NaCl, 1 mM EDTA, 1 mM EGTA, 1% Triton, 2.5 mM sodium pyrophosphate, 1 mM β -glycerophosphate, 1 mM Na₃VO₄) supplemented with a protease inhibitor cocktail (Complete Roche Diagnostics) and quantified using a Bradford Protein Assay (Bio-Rad). Proteins were separated on a polyacrylamide gel (ProteinIII, Bio-Rad) and transferred to a PVDF membrane (Immobilon-F, Millipore). Protein bands were resolved using fluorochrome-conjugated secondary antibodies on an Odyssey scanner (Licor). All western blot experiments were replicated at least twice.

For the analysis of pAkt and pS6 induction after CCL25 stimulation, *shPten* T-ALL cells derived from spleen tissues of tumour-bearing *shPten* mice and adapted to cell culture were either left untreated or treated with Dox for 4 days to reactivate PTEN, starved overnight at 0.5% FBS and then treated with CCL25 for the indicated time points. For the CCL25 stimulation assay of the human T-ALL cell lines HBP-ALL and TALL1, the cells were infected with a retroviral vector coexpressing a *shPTEN*. 1522 or *Renilla* control shRNA and a puromycin-resistance cassette linked to GFP. After selection with puromycin for 5 days, the cells were starved overnight at 0.1% FBS and then treated with CCL25 for 15 min before collecting for immunoblot analysis.

For flow cytometric analysis (FACS), single-cell suspensions were brought to a concentration of 1×10^6 cells per ml in FACS-buffer (PBS, pH 7.4, 1% BSA) and stained with the indicated antibodies as per the manufacturer's protocol. After washing, cells were measured on a Guava easyCyte (Millipore) or LSRII (Becton Dickinson) FACS machine. Cell sorting was performed on a Becton Dickinson FACSAria II machine. For intracellular pS6 measurement, cells were fixed with 2% paraformaldehyde and permeabilized with methanol before staining for pS6 as previously described⁴⁰.

CCL25 expression. For quantification of CCL25 chemokine levels in the intestine of *Rag1*^{-/-} and Ncr nude mice, parts of the jejunum and ileum were dissected from euthanized animals, cleaned in phosphate-buffered saline (pH 7.4), and snap frozen in liquid nitrogen. Tissues were homogenized in T-PER Tissue Protein Extraction Buffer (Pierce Biotechnology) supplemented with a protease inhibitor cocktail (Complete Roche Diagnostics) to prevent degradation of proteins during and after homogenization. Protein extracts were centrifuged at 20,000 r.c.f., supernatants were collected, and total protein content was assayed using the Bradford Protein Assay (Bio-Rad). Tissue homogenates were analysed for CCL25 protein levels by a 3-step sandwich enzyme-linked immunosorbent assay as per the manufacturer's instructions (R&D Systems).

Transwell migration assay. For transwell migration assays, 5×10^5 cells with or without Dox treatment were starved in RPMI containing 1% serum for 12h overnight and the next day 3×10^5 viable cells were plated in 200 μ l in the upper part of a 24-well Boyden chamber insert with a membrane pore size of 8 μ m (Greiner Bio-One). The lower part of the chamber was filled with 600 μ l medium containing 500 ng ml⁻¹ recombinant CCL25 (R&D Systems). Following a 4 h incubation at 37 °C and 7.5% CO₂, migrating cells in the lower chamber were counted using a Guava easyCyte cell counter (Millipore). Transwell migration experiments were run in triplicate for each condition on two independent tumour isolates.

Histology and IHC. Organ samples were fixed in fresh 4% paraformaldehyde at 4 °C overnight and further subjected to routine histological procedures for embedding in paraffin. 5- μ m sections of the samples from at least three different animals per group were placed on microscopic slides next to one another to enable cross-comparison within a slide after H&E staining or IHC staining with the antibodies indicated. Antibodies used were GFP (D5.1) XP, PTEN (D4.3), p-AKT (S473) (D9E), p-ribosomal protein S6 (S235/236) (D57.2.2E), cleaved caspase 3 (Asp175) (all: Cell Signaling Technologies), Ki67 (VP-K451, Vector Laboratories) and CD3 (A0452) (DAKO). Stained slides were scanned with a Panoramic Scan 250 Flash or MIDI system and images acquired using Panoramic Viewer 1.15.2 (both: 3DHistech). Additional images were taken on a Zeiss Axio Imager.Z2 system.

shCcr9 hairpin design and competition experiments. shRNAs targeting *Ccr9* were generated as previously described³³ and cloned into a retroviral vector coexpressing mCherry (LMN-C³⁸). Knockdown of *Ccr9* was quantified in a murine T-ALL cell line by flow cytometry using an Alexa 647-conjugated antibody against murine CCR9 (clone 9B1, eBiosciences). The two most efficient shRNAs, *shCcr9.904* (97-mer: 5'-TGCTGTTGACAGTGAGCGCAAGGATAAGAATGCCAAGCTATAGCTGAAGC CACAGATGTATAGCTTGGCATTCTTATCCTTATGCCTACTG CCTCGGA-3') and *shCcr9.2357* (97-mer: 5'-TGCTGTTGACAGTGAGCGCCC CAACAGTTTACAACCTTTAT AGTGAAGCCACAGATGTATAAAGGTTGTAACTGTTGGGATGCCTACTGCTCGGA-3'), were used for subsequent assays. For the infection of tumour cells, eGFP⁺ *shPten* T-ALL cells were grown on OP9-DL1 feeders in the presence of 10 ng ml⁻¹ mIL7 in Optimem Glutamax medium (Gibco/Life Technologies) and infected with either *shCcr9* or *shRenilla* control shRNAs. Approximately 0.75×10^6 infected *shPten* cells (20–30% mCherry⁺) were transplanted into recipient *Rag1*^{-/-} mice irradiated with 450 rad, and monitored for disease development. Diseased mice were euthanized, and spleen, bone marrow, liver, lung, small intestine and kidney tissues were collected and minced to generate single-cell suspensions for flow cytometric measurement of eGFP- and mCherry-positive cell fractions. Relative mCherry fractions from different organs were determined by normalizing to the spleen fraction as 100%.

CCR9 inhibitor treatment. The CCR9 inhibitor CCX8037 was kindly provided by Chemocentryx^{25,41}. For cell culture treatment, different concentrations of CCX8037 were used as indicated. For *in vivo* experiments, mice were treated with 30 mg kg⁻¹ inhibitor or vehicle (HPMC 1%) administered via subcutaneous injection every 12 h (CCX8037).

Clonality analysis of murine shPten tumours. Clonality analysis by PCR amplification and sequencing of murine TCR β sequences was performed as previously described⁴². In brief, clonality was assayed at V-DJ and D-J rearrangements in a mixture of 20 family-specific upstream primers located within V β gene segments, consensus primers located 5' of D β 1 and D β 2 gene segments and consensus downstream primers located 3' of J β 1 and J β 2 gene segments. PCR products were analysed by direct Sanger sequencing.

Profiling of Notch1 mutations by Sanger sequencing. *Vav-tTA;shPten* tumours were analysed for *Notch1* hotspot mutations located in Exon 26, 27 and 34 by Sanger sequencing as described previously⁴³, including one new oligonucleotide primer pair: Ex34B-f: 5'-GCCAGTACAACCCACTACGG-3'; Ex34B-r: 5'-CCTGAAGCACTGGAA-AGGAC-3'.

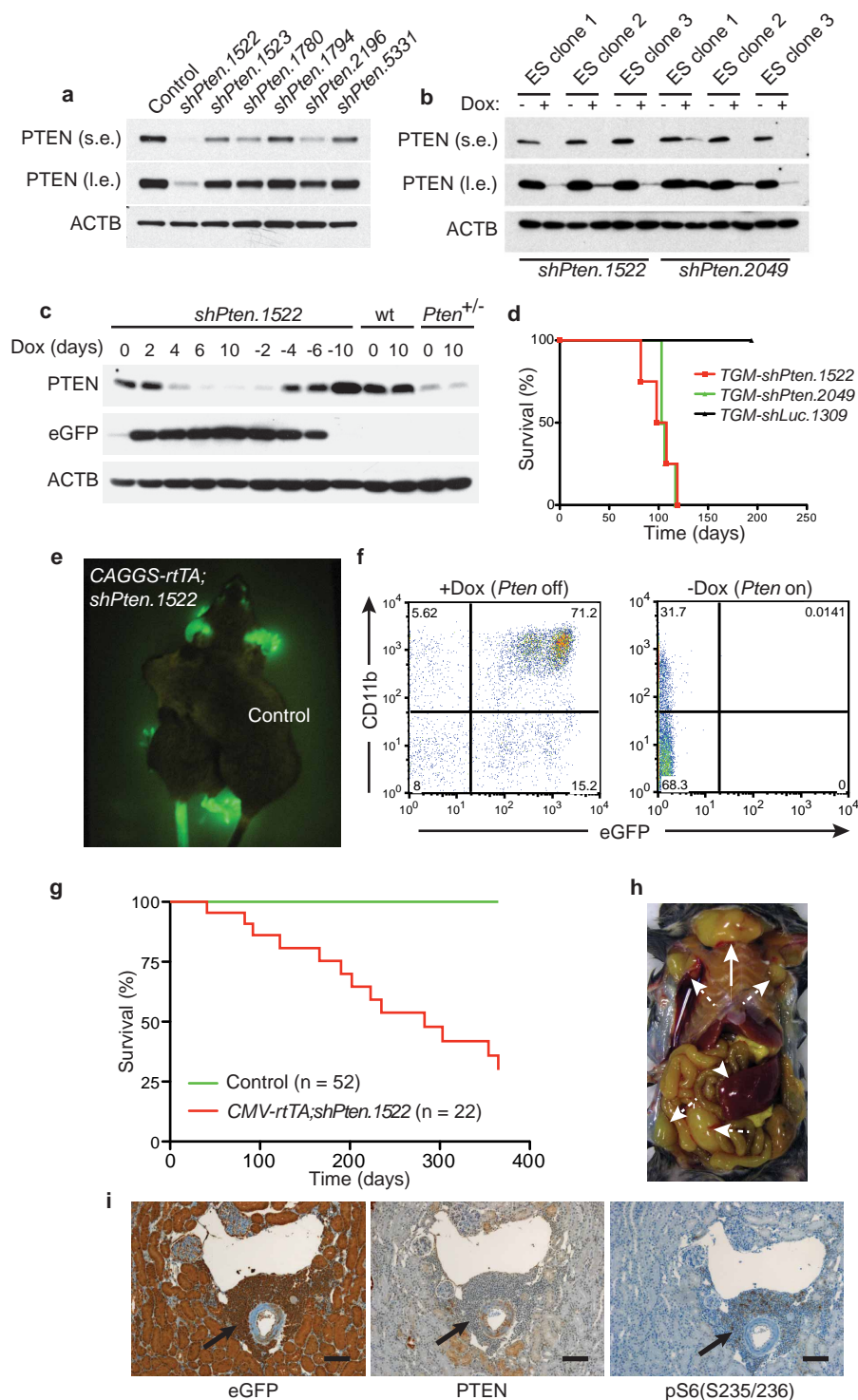
RNA-seq data generation and bioinformatic analysis. Total RNA was extracted from *shPten* leukaemic cells on/off Dox purified by sorting for CD4 expression with magnetic beads using Trizol (Invitrogen). RNA quality and quantity were assessed using Agilent RNA 6000 Nano Chip (Agilent Technologies) and Qubit 2.0 fluorometer (Life Technologies), respectively. RNA-seq libraries were prepared from 1 μ g of total RNA per sample using the TruSeq RNA Sample Preparation Kit v2 (Illumina) following the standard protocol with slight modification (10 PCR cycles). RNA-seq library quality and quantity were assessed using the Agilent DNA 1000 Chip and Kappa Library qPCR kit (Kappa Biosystems). Libraries were clustered on an Illumina cBot and sequenced on the HiSeq2000 (2 \times 100-bp reads) using Illumina chemistry (Illumina).

The RNA-seq paired-end reads were mapped to the mouse mm9 genome and its corresponding transcript sequences using an in-house mapping and quality assessment pipeline¹⁵. Transcript expression levels were estimated as fragments per kilobase of transcript per million mapped reads (FPKM) and gene FPKMs were computed by summing the transcript FPKMs for each gene using the Cuffdiff2 program⁴⁴.

We called a gene 'expressed' in a given sample if it had a FPKM value ≥ 0.5 based on the distribution of FPKM gene expression levels and excluded genes that were not expressed in any sample from the final gene expression data matrix for downstream analysis. Differentially expressed genes were identified using LIMMA⁴⁵ and false discovery rate was estimated by Benjamini–Hochberg method⁴⁶. GSEA^{47,48} and the Database for Annotation, Visualization and Integrated Discovery (DAVID v6.7)⁴⁹ were used to assess pathway enrichment. All mouse RNA-seq data sets are submitted to the European Nucleotide Archive (ENA) and can be accessed under the accession number PRJEB5498 at <http://www.ebi.ac.uk/ena/data/view/PRJEB5498>.

GSEA. To test for mouse *shPten* signature enrichment in PTEN-disrupted human T-ALL, we established a *shPten*-dependent signature using the 100 most upregulated genes in *shPten* T-ALL samples (untreated, $n = 3$) against PTEN-restored samples (Dox-treated, $n = 4$) samples. Publicly available human T-ALL gene expression profiles (GSE28703, $n = 47$) were processed using RMA (quantile normalization) and supervised for PTEN status (PTEN disrupted including PTEN deletion, mutation or both, $n = 10$; PTEN wild-type, $n = 37$) according to the published sample genetic features annotation¹⁵. Statistical significance of GSEA results was assessed using 1,000 sample permutations. For enrichment of human PTEN T-ALL signature in mouse *shPten* T-ALL (Dox-off) profiles against PTEN-restored (Dox-on) profiles, a human PTEN-disrupted signature was generated by including the 100 most upregulated genes in PTEN-disrupted versus PTEN-wild type T-ALL samples. Mouse genes were ranked by supervising untreated to Dox-treated *shPten* T-ALL. Statistical significance of human PTEN-disrupted signature enrichment was assessed using 1,000 gene set permutations.

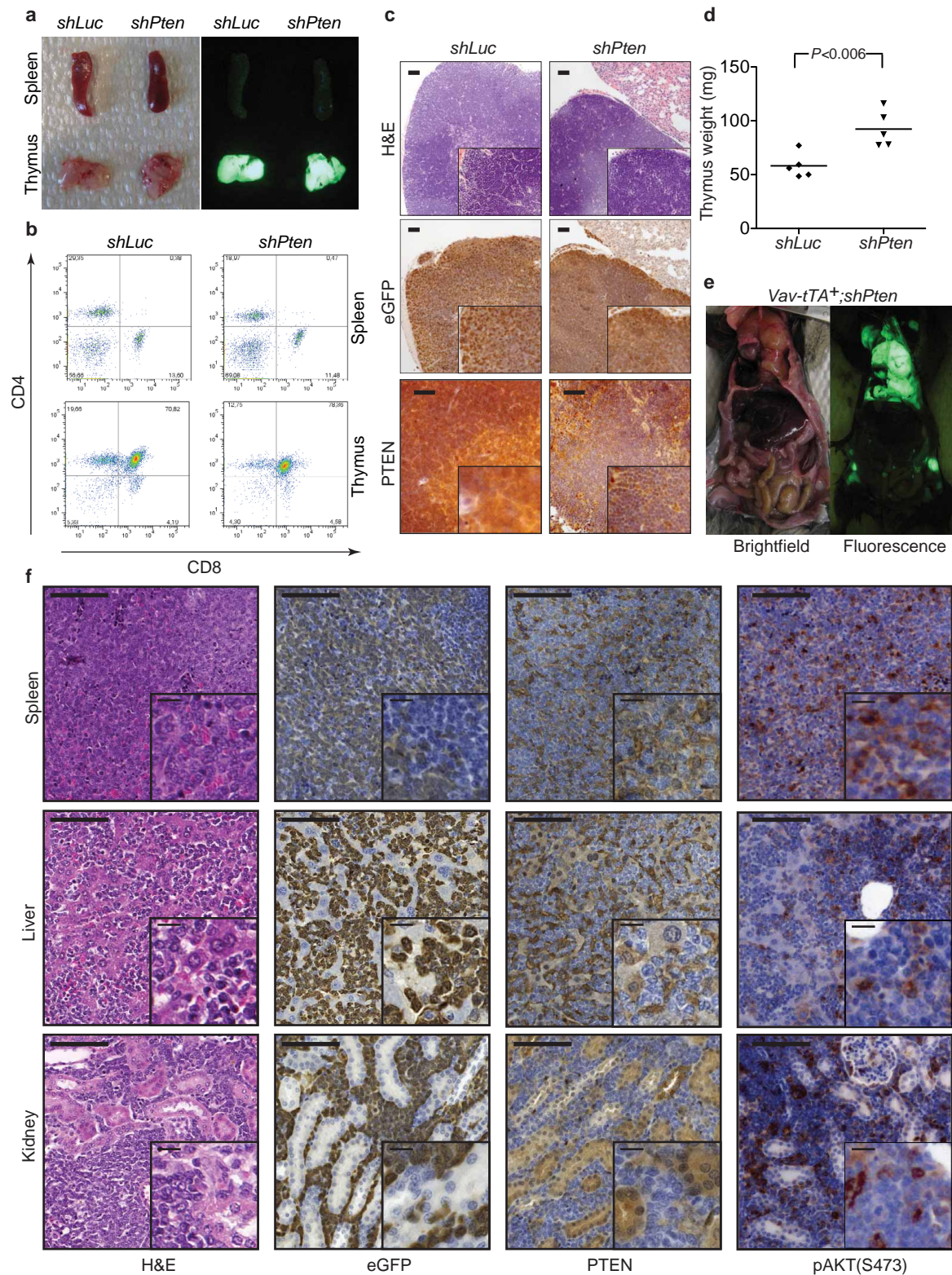
31. Huesken, D. *et al.* Design of a genome-wide siRNA library using an artificial neural network. *Nature Biotechnol.* **23**, 995–1001 (2005).
32. Fellmann, C. *et al.* Functional identification of optimized RNAi triggers using a massively parallel sensor assay. *Mol. Cell* **41**, 733–746 (2011).
33. Dow, L. E. *et al.* A pipeline for the generation of shRNA transgenic mice. *Nature Protocols* **7**, 374–393 (2012).
34. Beard, C., Hochedlinger, K., Plath, K., Wutz, A. & Jaenisch, R. Efficient method to generate single-copy transgenic mice by site-specific integration in embryonic stem cells. *Genesis* **44**, 23–28 (2006).
35. Kistner, A. *et al.* Doxycycline-mediated quantitative and tissue-specific control of gene expression in transgenic mice. *Proc. Natl Acad. Sci. USA* **93**, 10933–10938 (1996).
36. Suzuki, A. *et al.* High cancer susceptibility and embryonic lethality associated with mutation of the *PTEN* tumor suppressor gene in mice. *Curr. Biol.* **8**, 1169–1178 (1998).
37. Berger, R. L. & Boos, D. D. P-values maximized over a confidence set for the nuisance parameter. *J. Am. Stat. Assoc.* **89**, 1012–1016 (1994).
38. Scuoppo, C. *et al.* A tumour suppressor network relying on the polyamine–hypusine axis. *Nature* **487**, 244–248 (2012).
39. Lakshmi, B. *et al.* Mouse genomic representational oligonucleotide microarray analysis: detection of copy number variations in normal and tumor specimens. *Proc. Natl Acad. Sci. USA* **103**, 11234–11239 (2006).
40. Zhao, Z. *et al.* p53 loss promotes acute myeloid leukemia by enabling aberrant self-renewal. *Genes Dev.* **24**, 1389–1402 (2010).
41. Tubo, N. J. *et al.* A systemically-administered small molecule antagonist of CCR9 acts as a tissue-selective inhibitor of lymphocyte trafficking. *PLoS ONE* **7**, e50498 (2012).
42. Gärtner, F. *et al.* Immature thymocytes employ distinct signaling pathways for allelic exclusion versus differentiation and expansion. *Immunity* **10**, 537–546 (1999).
43. O'Neil, *et al.* Activating Notch1 mutations in mouse models of T-ALL. *Blood* **107**, 781–785 (2006).
44. Trapnell, C. *et al.* Differential analysis of gene regulation at transcript resolution with RNA-seq. *Nature Biotechnol.* **31**, 46–53 (2013).
45. Smyth, G. K. Linear models and empirical bayes methods for assessing differential expression in microarray experiments. *Stat. Appl. Genet. Mol. Biol.* **3**, Article3 (2004).
46. Hochberg, Y. & Benjamini, Y. More powerful procedures for multiple significance testing. *Stat. Med.* **9**, 811–818 (1990).
47. Subramanian, A. *et al.* Gene set enrichment analysis: a knowledge-based approach for interpreting genome-wide expression profiles. *Proc. Natl Acad. Sci. USA* **102**, 15545–15550 (2005).
48. Subramanian, A., Kuehn, H., Gould, J., Tamayo, P. & Mesirov, J. P. GSEA-P: a desktop application for Gene Set Enrichment Analysis. *Bioinformatics* **23**, 3251–3253 (2007).
49. Huang da, W., Sherman, B. T. & Lempicki, R. A. Systematic and integrative analysis of large gene lists using DAVID bioinformatics resources. *Nature Protocols* **4**, 44–57 (2009).



Extended Data Figure 1 | *Pten* shRNA-transgenic mice enable conditional expression of PTEN and develop tumours after prolonged *Pten* knockdown.

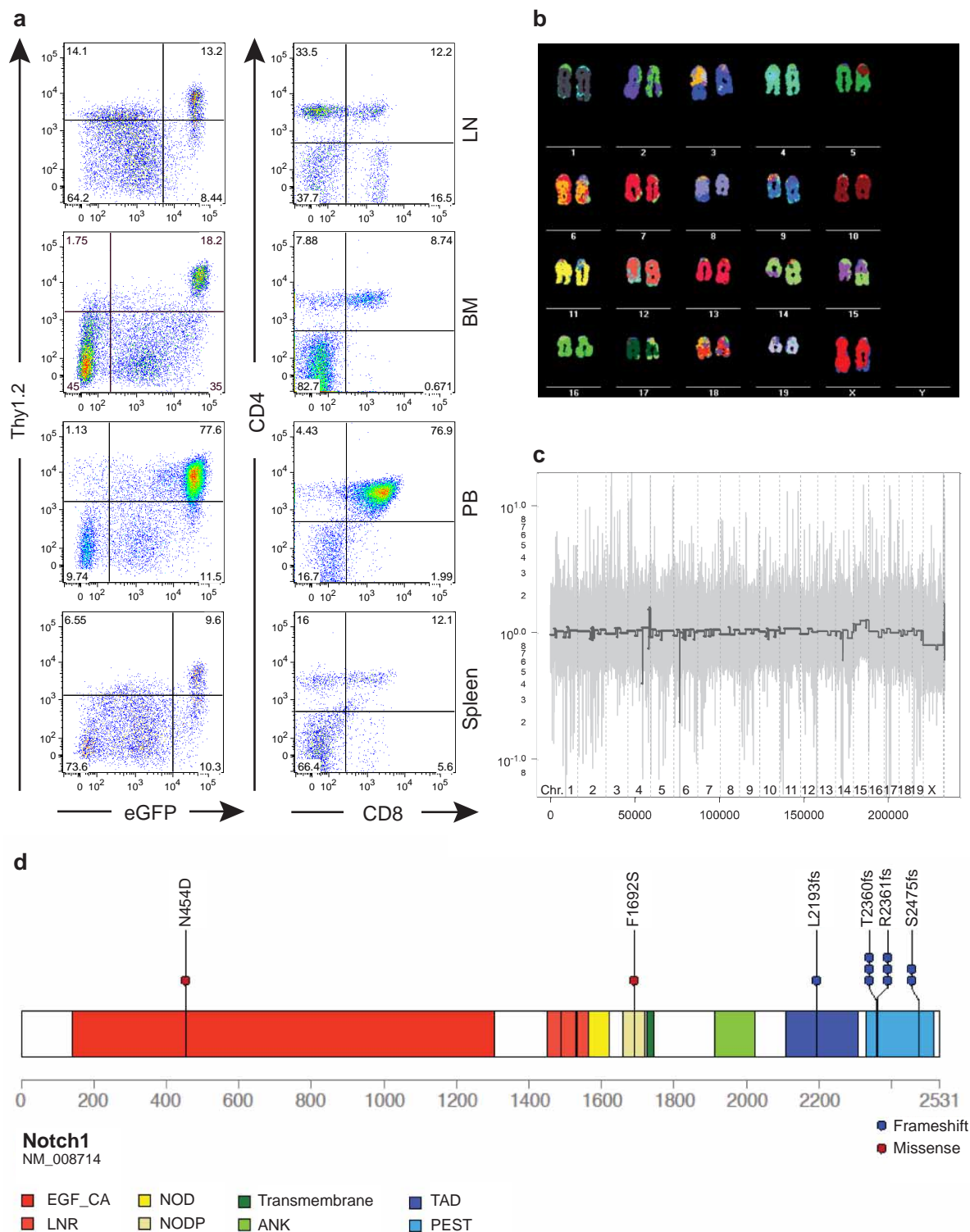
a, Western blot analysis of PTEN protein knockdown in NIH 3T3 cells infected with different *Pten* shRNAs at low multiplicity of infection. l.e., long exposure; s.e., short exposure. **b**, PTEN protein knockdown assessed by western blot in ES cell clones targeted with two different *Pten* shRNAs, either treated with Dox or left untreated. **c**, MEFs from *Rosa26-rtTA;shPten.1522* transgenic mice, wild-type control mice, or *Pten*^{+/-} mice were treated with Dox for the indicated times and analysed for PTEN, GFP and ACTB expression by western blot. **d**, Overall survival of mice receiving bone marrow cells from *tTA*-transgenic mice infected with an inducible TRE-GFP-miR-30 (TGM) retroviral vector expressing *shPten.1522*, *shPten.2049* or control after irradiation with 600 rad. **e**, Fluorescence image of a *CAGGS-rtTA;shPten.1522* mouse on Dox for 5 days

and a *CAGGS-rtTA*-only control mouse. **f**, Flow cytometric analysis of the peripheral blood of a *CAGGS-rtTA;shPten.1522* mouse on Dox and an off Dox control mouse for myeloid (CD11b) and GFP marker expression 10 days after initiating Dox food. **g**, Overall survival curve of *CMV-rtTA;shPten.1522* double-transgenic and control mice (single-transgenic *shPten.1522* or *CMV-rtTA*). Dox treatment for shRNA induction was started after weaning (at ~4 weeks of age). **h**, Situs of a tumour-bearing *CAGGS-rtTA;shPten.1522* double-transgenic mouse. A large thymic tumour (full arrow), as well as enlarged lymph nodes (dashed arrows) and spleen (arrowhead), are visible. **i**, Immunohistochemical staining of kidney sections from a *CAGGS-rtTA;shPten.1522* mouse for the indicated antigens. Arrows highlight a tumour infiltrate around a kidney venule. Scale bars, 100 μ m.



Extended Data Figure 2 | *Vav-tTA;shPten* transgenic mice with targeted *shPten* expression in the haematopoietic lineage display thymic hyperplasia by 6 weeks, and a subset develops thymic tumours infiltrating multiple peripheral organs. **a, Brightfield (left) and fluorescence (right) images of spleen and thymus from *Vav-tTA;shLuc* (control) and *Vav-tTA;shPten* double-transgenic mice at 5 weeks. **b**, Flowcytometry analysis of spleen and thymus single-cell suspensions from *Vav-tTA;shLuc/shPten* mice for CD4/CD8 expression. **c**, IHC analysis of thymic tissue from 6-week-old *Vav-tTA;shLuc* and *Vav-tTA;shPten* mice. Sections were stained with haematoxylin and eosin (H&E), anti-GFP or anti-PTEN antibodies, showing**

heterogeneous GFP staining and correspondingly variable PTEN knockdown. Scale bars, 200 μ m for H&E and GFP, 100 μ m for PTEN. The insets are $\times 2$ magnifications. **d**, Thymus weight of 6-week-old *Vav-tTA;shLuc* and *Vav-tTA;shPten* mice ($n = 5$ for both groups, $P < 0.006$ by t -test). **e**, Brightfield and GFP-fluorescence images of a *Vav-tTA;shPten* mouse with tumours. **f**, IHC staining of spleen, liver and kidney tissues from a *Vav-tTA;shPten* mouse with primary T-cell disease. Sections were stained for H&E, GFP, PTEN and phospho-AKT(S473) as indicated, showing heterogeneous staining owing to variable tumour infiltration. Scale bars, 100 μ m, insets 25 μ m.



Extended Data Figure 3 | Immunophenotype, chromosomal aberrations and *Notch1* mutations observed in murine *shPten* tumours. **a**, Flow cytometric analysis of organ infiltration by primary tumours in *Vav-tTA;shPten.1522* transgenic mice. Single-cell suspensions of indicated tissues were analysed for eGFP, Thy1.2, CD4 and CD8 expression. BM, bone marrow; LN, lymph node; PB, peripheral blood. **b**, Spectral karyotyping analysis of a T-cell tumour arising in *Vav-tTA;shPten.1522* mice, showing a t(14;15) translocation. **c**, CGH analysis of a *Vav-tTA;shPten.1522* leukaemia.

Genomic tumour DNA was analysed on Affymetrix CGH SNP arrays and compared to normal skin tissue. *x* axis indicates genomic coordinate and *y* axis represents $\log_2(\text{tumour/germline})$. **d**, Schematic of the murine NOTCH1 protein generated using protein paint (<http://explore.pediatriccancergenomeproject.org/proteinPainter>), highlighting the different NOTCH1 protein domains and the mutations detected in the murine *shPten* and *Pten*^{-/-} T-ALL tumours.

a

Mouse No.	Karyotype
CM90	40~42, XY, +Y[1], -X[1], +2[8], -8[1], -18[1] [cp10]
CM92	41, XX, +15
CM122	37~41, XX, t(14;15) [6], -X[1], +10[1], -3[1], -8[1], -9[1], -16[1], +4[1], +10[1] [cp11]

b

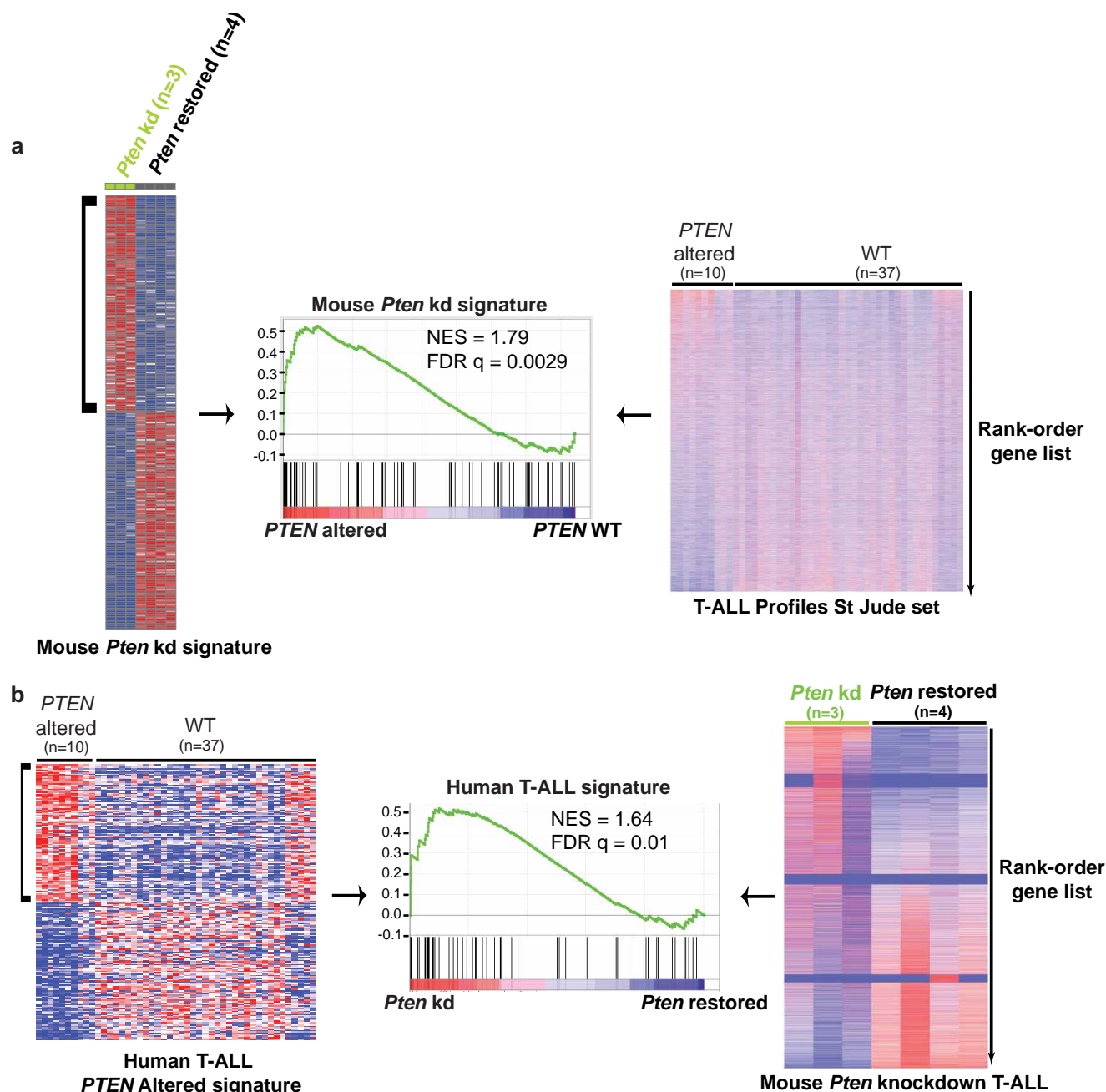
GeneName	Chr	mm9_Pos	Class	AAChange	ProteinGI	mRNA_acc	Sample Name
Notch1	2	26315225	frameshift	S2475fs	224967065	NM_008714	shPten tumor 1 primary
Notch1	2	26315225	frameshift	S2475fs	224967065	NM_008714	shPten tumor 1 secondary
Notch1	2	26335472	missense	N454D	224967065	NM_008714	shPten tumor 2
Notch1	2	26315567	frameshift	T2360fs	224967065	NM_008714	shPten tumor 2
Notch1	2	26315564	frameshift	R2361fs	224967065	NM_008714	shPten tumor 3
Notch1	2	26322049	missense	F1692S	224967065	NM_008714	shPten tumor 3
Notch1	2	26315567	frameshift	T2360fs	224967065	NM_008714	shPten tumor 4
Notch1	2	26315567	frameshift	T2360fs	224967065	NM_008714	shPten tumor 5
Notch1	2	26316068	frameshift	L2193fs	224967065	NM_008714	shPten tumor 6
Notch1	2	26315566	frameshift	R2361fs	224967065	NM_008714	shPten tumor 6
Notch1	2	26315553	deletion	R2361fs	224967065	NM_008714	PTEN-KO tumor

c

<i>Pten</i> shRNA	97-mer oligo
shPten.1967	TGCTGTTGACAGTGAGCG CCCAGATGTTAGTGACAATGAA TAGTGAAGCCACAGAT GTA TTCATTGTCACTAACATCTGGA TGCCTACTGCCTCGGA
shPten.2049	TGCTGTTGACAGTGAGCG AAAGATCAGCATTACAAATTA TAGTGAAGCCACAGAT GTA TAATTTGTGAATGCTGATCTTC TGCCTACTGCCTCGGA
shPten.1766	TGCTGTTGACAGTGAGCG CATCGATAGCATTGCGAGTATA TAGTGAAGCCACAGAT GTA TATACTGCAAATGCTATCGATT TGCCTACTGCCTCGGA
shPten.1522	TGCTGTTGACAGTGAGCG ACCAGCTAAAGGTGAAGATATA TAGTGAAGCCACAGAT GTA TATATCTTCACCTTTAGCTGGC TGCCTACTGCCTCGGA
shPten.1687	TGCTGTTGACAGTGAGCG CTTGGGTAAATACGTTCTTCAT TAGTGAAGCCACAGAT GTA ATGAAGAACGTATTTACCCAAA TGCCTACTGCCTCGGA
shPten.1178	TGCTGTTGACAGTGAGCG ATTCTGTGAAGATCTTGACCAA TAGTGAAGCCACAGAT GTA TTGGTCAAGATCTTCACAGAAG TGCCTACTGCCTCGGA
shPten.1202	TGCTGTTGACAGTGAGCG ACTAAGTGAAGATGACAATCAT TAGTGAAGCCACAGAT GTA ATGATTGTCTCTTCACCTTAGC TGCCTACTGCCTCGGA
shPten.2052	TGCTGTTGACAGTGAGCG AATCAGCATTACAAATTACAA TAGTGAAGCCACAGAT GTA TTGTAATTTGTGAATGCTGATC TGCCTACTGCCTCGGA
shPten.1780	TGCTGTTGACAGTGAGCG ACAGTATAGAGCGTGCAGATAA TAGTGAAGCCACAGAT GTA TTATCTGCACGCTCTATACTGC TGCCTACTGCCTCGGA
shPten.1198	TGCTGTTGACAGTGAGCG CATGGCTAAGTGAAGATGACAA TAGTGAAGCCACAGAT GTA TTGTCATCTTCACCTTAGCCATT TGCCTACTGCCTCGGA
shPten.1523	TGCTGTTGACAGTGAGCG ACAGCTAAAGGTGAAGATATAT TAGTGAAGCCACAGAT GTA ATATATCTTCACCTTTAGCTGG TGCCTACTGCCTCGGA
shPten.1794	TGCTGTTGACAGTGAGCG CGCAGATAATGACAAGGAGTAT TAGTGAAGCCACAGAT GTA AATACTCCTTGTCATTATCTGCA TGCCTACTGCCTCGGA
shPten.2196	TGCTGTTGACAGTGAGCG CCAGATTGCAGTTATAGGAACA TAGTGAAGCCACAGAT GTA TGTTCCTATAACTGCAATCTGA TGCCTACTGCCTCGGA
shPten.5331	TGCTGTTGACAGTGAGCG CAGTGTATAAACTCCACTTAA TAGTGAAGCCACAGAT GTA TTAAGTGGAGTTTATAACACTA TGCCTACTGCCTCGGA

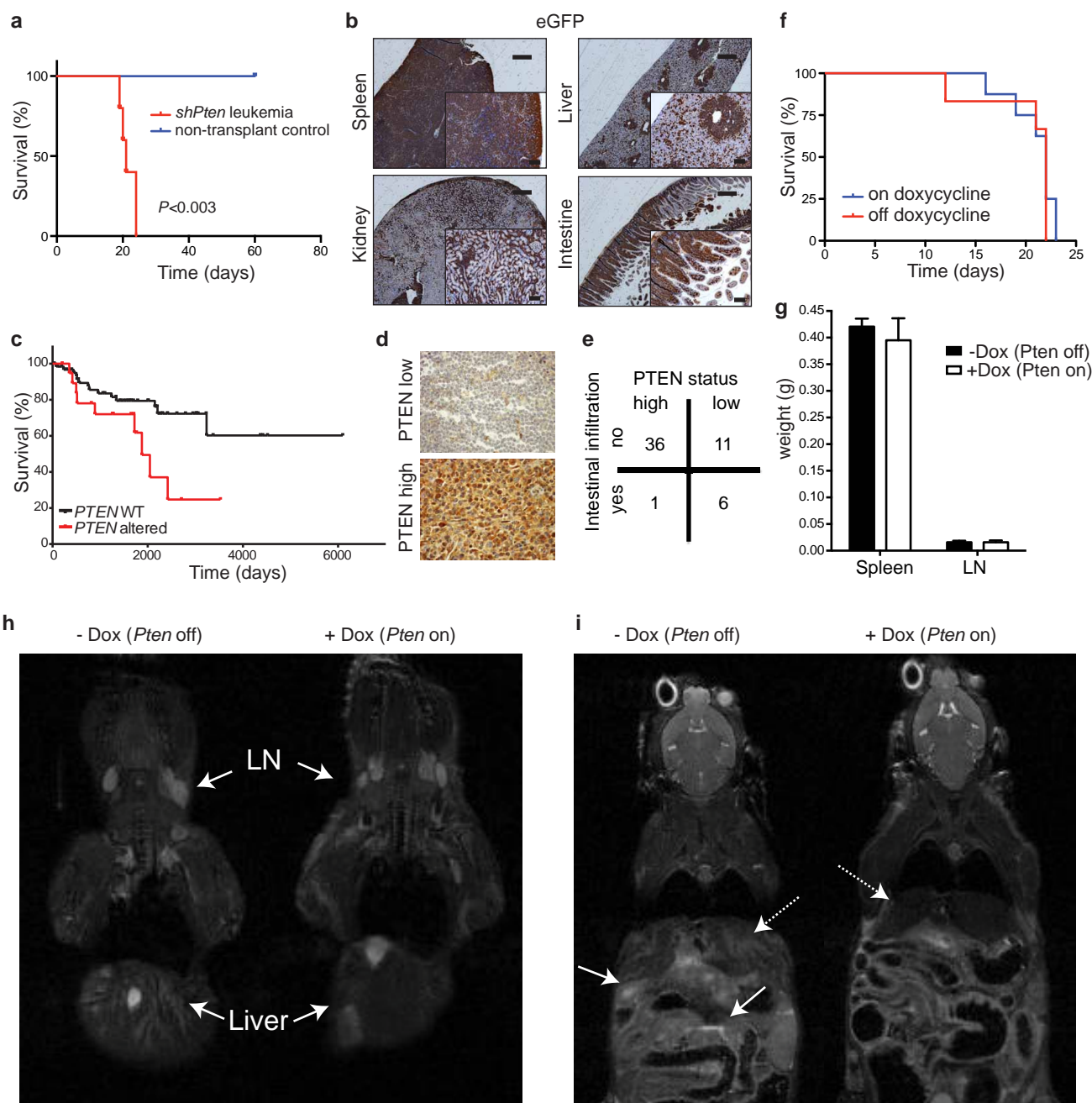
Extended Data Figure 4 | Summary of karyotyping and *Notch1* sequencing of *shPten* T-ALL tumours. **a**, Results from a multiplex FISH analysis of three different primary *shPten*-induced T-ALL tumours. At least ten cells were analysed for each sample, and chromosomal gains, deletions or translocations

are highlighted. **b**, Summary of *Notch1* mutations identified in *shPten* and *Pten* knockout tumours. **c**, Sequence of all shRNAs targeting murine *Pten* that were tested in the study. Sense and guide strand are highlighted in red.



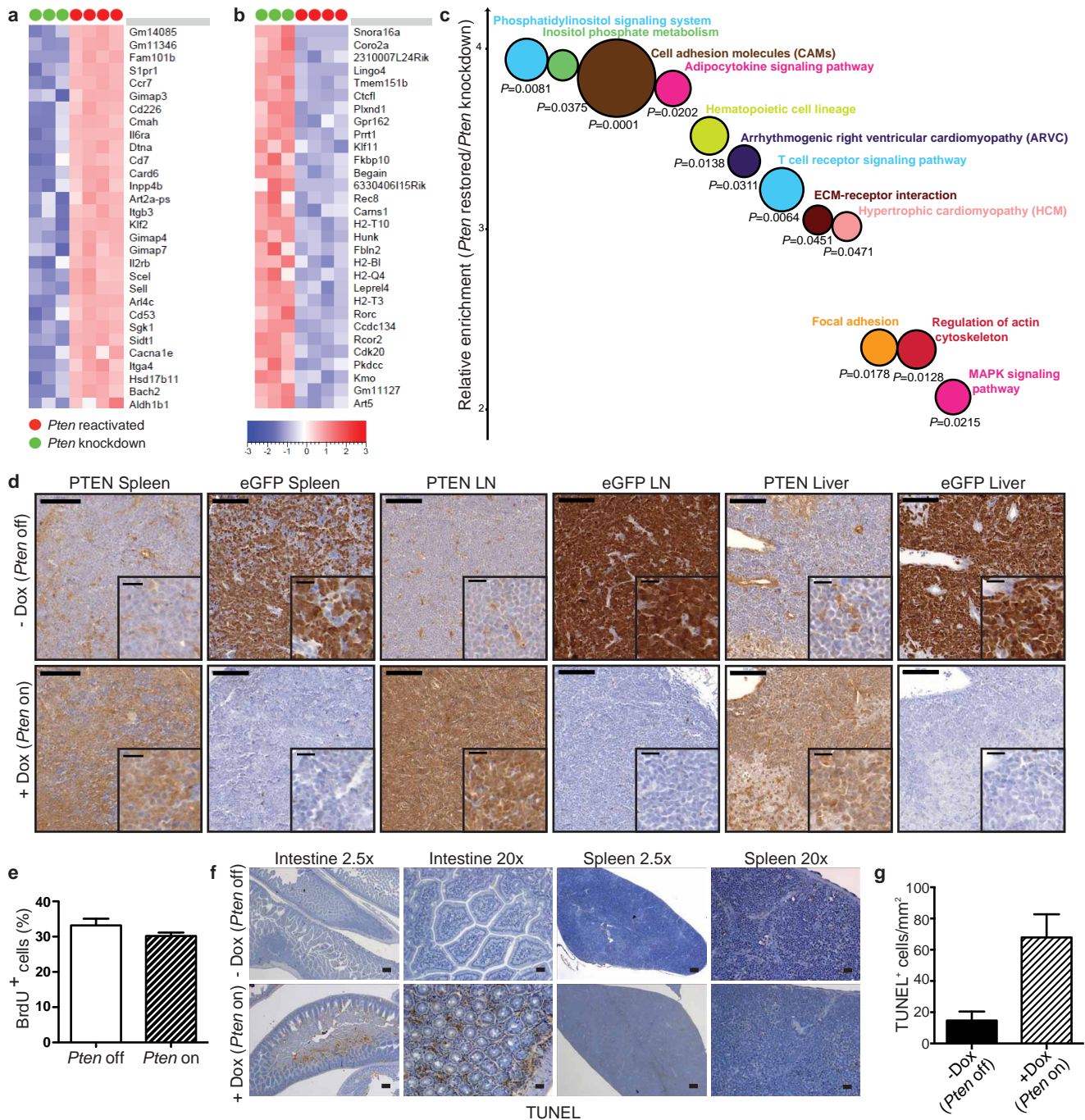
Extended Data Figure 5 | GSEA shows similar gene expression patterns in human and mouse T-ALL lacking *Pten*. **a**, GSEA of a mouse *shPten* signature in *PTEN*-altered human T-ALL was tested after establishing the *shPten*-dependent signature using the 100 most upregulated genes in *shPten* T-ALL samples (untreated, $n = 3$) against *PTEN*-restored samples (Dox-treated, $n = 4$) as determined by RNA-seq analysis (data not shown). Publicly available human T-ALL gene expression profiles (GSE28703, $n = 47$) were processed using RMA (quantile normalization) and supervised for *PTEN* status (*PTEN* altered including *PTEN* deletion, mutation or both, $n = 10$; *PTEN* wild-type

(WT), $n = 37$) according to the published sample annotation¹⁸. Statistical significance of GSEA results was assessed using 1,000 samples permutations. **b**, For enrichment of human *PTEN* T-ALL signature in mouse *shPten* knockdown (kd) T-ALL (Dox-off) profiles against *Pten*-restored (Dox-on) profiles, a human *PTEN*-disrupted signature was generated by including the 100 most upregulated genes in *PTEN*-disrupted versus *PTEN*-wild type T-ALL samples. Mouse genes were ranked by supervising untreated to Dox-treated *shPten* T-ALLs. Statistical significance of human *PTEN*-disrupted signature enrichment was assessed using 1,000 gene set permutations.



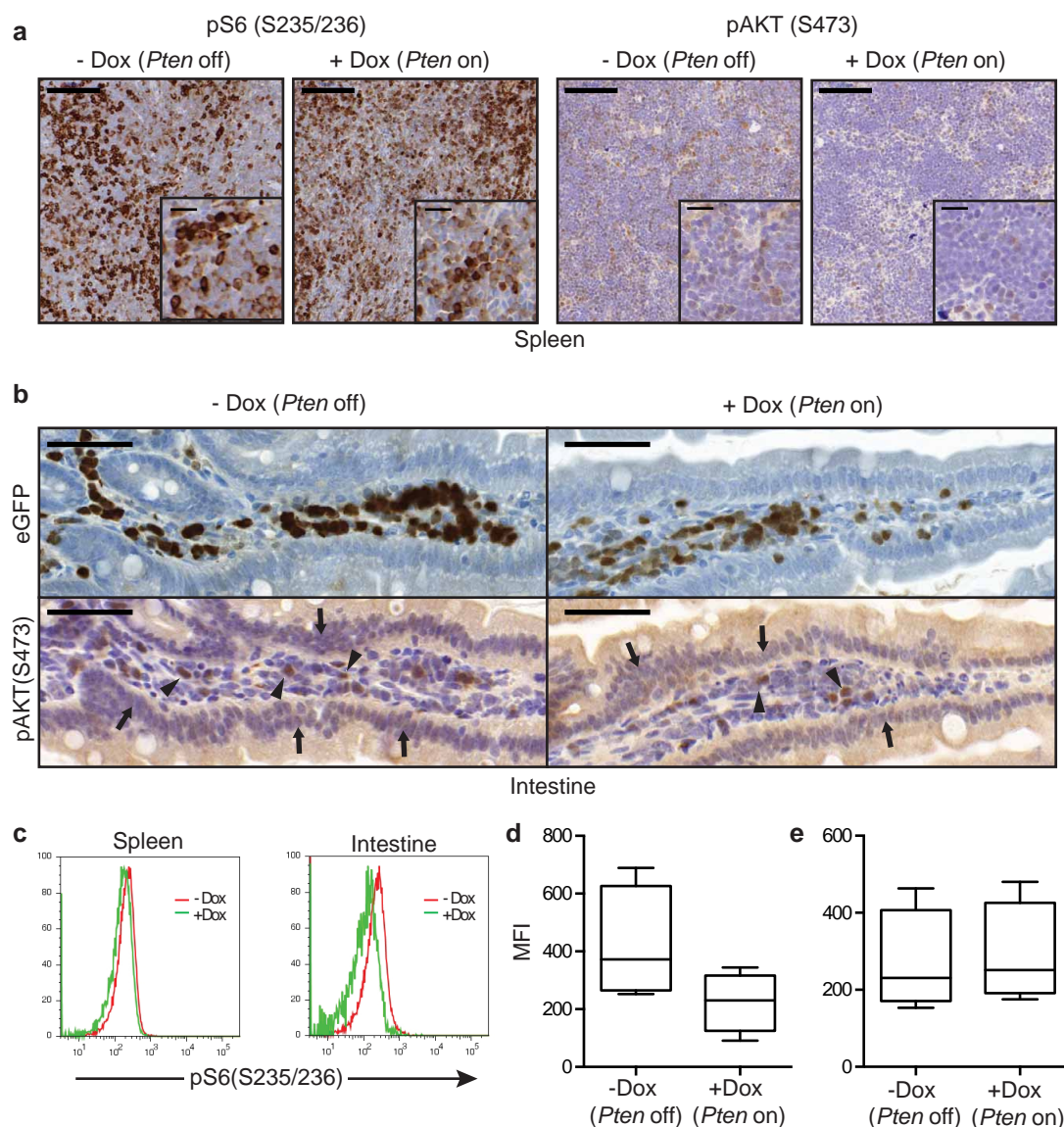
Extended Data Figure 6 | Secondary recipients of *shPten* T-ALL cells display extensive intestinal tumour infiltration similar to a subset of human patients characterized by peripheral T-cell lymphoma and low PTEN expression. **a**, Overall survival of sublethally irradiated *Rag1*^{-/-} mice transplanted with 1×10^5 T-ALL cells from primary *Vav-tTA;shPten.1522* mice compared to untransplanted mice ($n = 5$ for both groups, $P < 0.003$). **b**, IHC staining for eGFP expression in the indicated tissues from secondary T-ALL transplant recipients. Scale bars, 400 μ m, 100 μ m for insets. **c**, Overall survival of PTEN normal (WT) versus PTEN-altered patients with T-ALL analysed from published data on patients with T-ALL¹⁵, $P = 0.02$). PTEN-altered ($n = 20$) includes patients with *PTEN* deletion, mutation, underexpression (<0.8 sigma after z scoring) and any combination of such alterations; PTEN normal ($n = 62$) include all other patients with available data. **d**, PTEN IHC staining of tissue microarrays of tumour sections from

Memorial Sloan Kettering Cancer Center patients with peripheral T-cell lymphomas. Examples of low (top panel) and high (bottom panel) PTEN expression samples are shown. **e**, Contingency table showing a significant association ($P < 0.003$; Fisher's exact test) between low expression of PTEN and intestinal infiltration in PTCL patients. **f**, Overall survival of *Rag1*^{-/-} mice transplanted with T-ALL cells from *Pten*^{fl/fl}; *Lck-cre* mice \pm Dox ($n = 5$ for each group). **g**, Weight of spleen ($n = 4$) and lymph nodes ($n = 8$) in *Rag1*^{-/-} mice transplanted with *Vav-tTA;shPten* leukaemic cells untreated or treated with Dox for 5 days (\pm s.d.). **h**, MRI of *Rag1*^{-/-} mice transplanted with *Vav-tTA;shPten* leukaemic cells untreated or treated with Dox for 5 days, 14 days after transplant. Arrows highlight lymph nodes (LN) and increased signals in the liver. Representative images for one out of three analysed mice per condition are shown. **i**, MRI imaging of the intestine and liver of the same mice as in **h** are shown. Dashed arrows highlight the liver, full arrows the intestine.



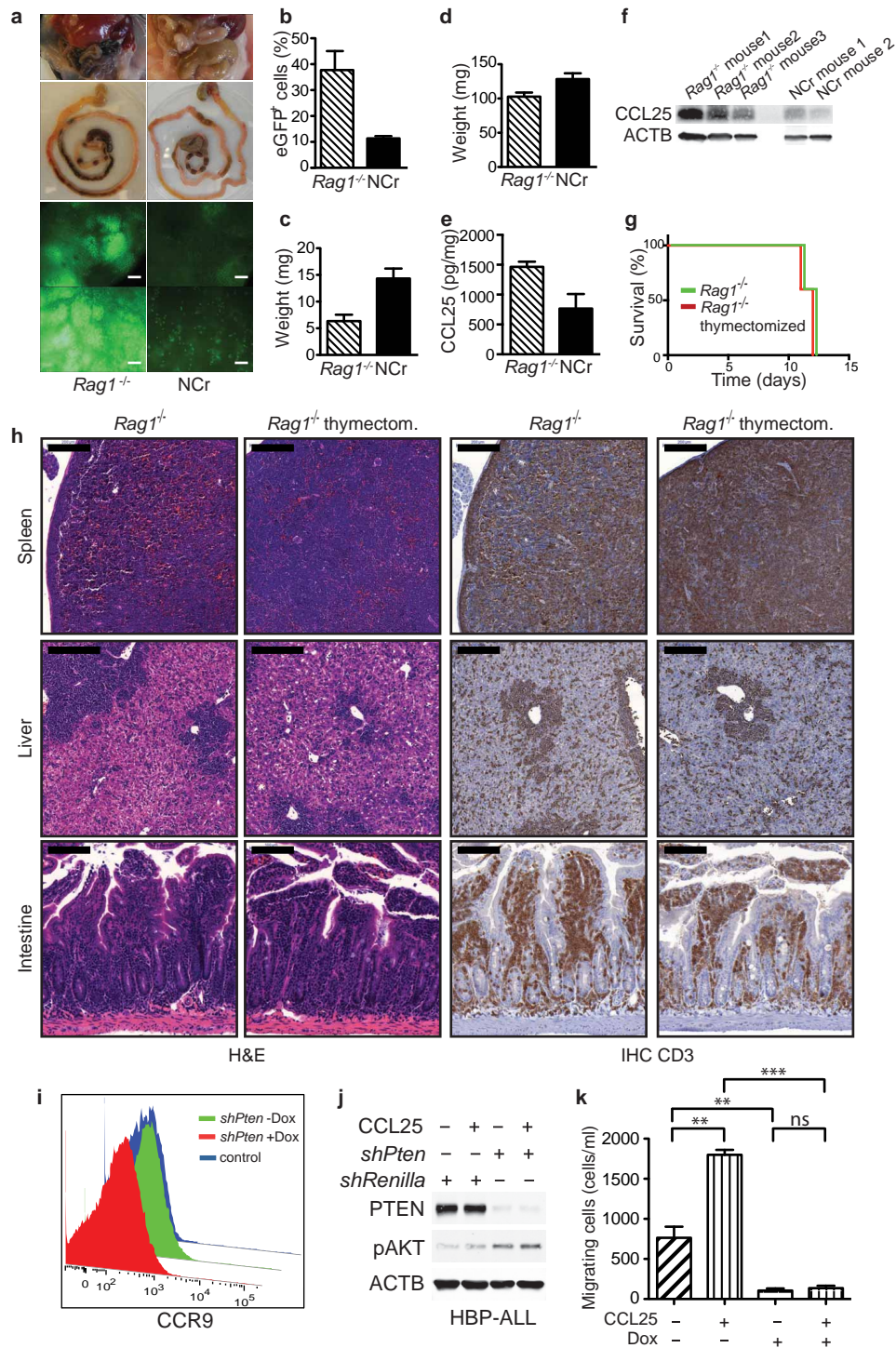
Extended Data Figure 7 | *Pten* reactivation affects multiple pathways and increases apoptosis in tumour cells infiltrating the intestine, but not in the spleen. **a, b,** Heatmap of top 30 upregulated (**a**) and downregulated (**b**) genes after *Pten* reactivation as determined by RNA-seq on CD4-sorted leukaemic samples isolated from the spleen. Three mice with *Pten* knocked down and four mice with reactivated *Pten* were analysed. *Pten* is one of the top 50 upregulated genes after reactivation, but is not included on the list. **c,** Bubblegraph visualization of the most significantly affected pathways as determined by DAVID pathway analysis. *y* axis represents relative pathway enrichment in *Pten* reactivated versus *Pten* knockdown leukaemic cells, and size of the bubble graph is inversely proportional to *P* value. **d,** IHC analysis for expression of GFP and PTEN in spleen, lymph node (LN) and liver from

shPten-tumour-transplanted mice \pm Dox treatment (5 days after start of Dox treatment; $n = 3$ per group). Representative sections are shown. Scale bars, 100 μ m for full images, 20 μ m for insets. **e,** *In vivo* 5-bromodeoxyuridine (BrdU) uptake in leukaemic cells isolated from the lymph nodes of mice transplanted with *Vav-tTA;shPten* primary T-ALL tumours \pm Dox. $n = 3$ for each group (\pm s.d.). **f,** TUNEL staining of spleen and intestinal sections of *Rag1*^{-/-} mice serially transplanted with *Vav-tTA;shPten* leukaemia cells and either left untreated or treated with Dox 24 h before sectioning. Scale bars, 200 μ m ($\times 2.5$) and 50 μ m ($\times 10$). **g,** Quantification of TUNEL-stained sections from the intestinal sections in **f**. TUNEL positive cells from three representative areas of 1 mm² from two different intestine sections were counted for each condition ($P < 0.01$) (\pm s.d.).



Extended Data Figure 8 | AKT and S6 protein phosphorylation is affected by PTEN reactivation in the intestine. **a**, IHC staining for phospho-S6 (pS235/236-S6) and phospho-AKT (pS473AKT) of spleen sections from *Rag1*^{-/-} mice transplanted with *Vav-tTA;shPten* tumour cells from primary mice and either treated with Dox or left untreated 2 days after treatment begin ($n = 3$ per group). Scale bars, 100 μ m, 20 μ m for insets. Representative images are shown. **b**, IHC staining for pS473-AKT (bottom) in the intestine, showing very low pAKT signal in the intestinal epithelial cells independent of Dox treatment status (arrows; bottom left and right panels), conversely strong staining for pAKT was detected in some of the infiltrating tumour cells (arrow heads). The signal was reduced concomitantly with the overall

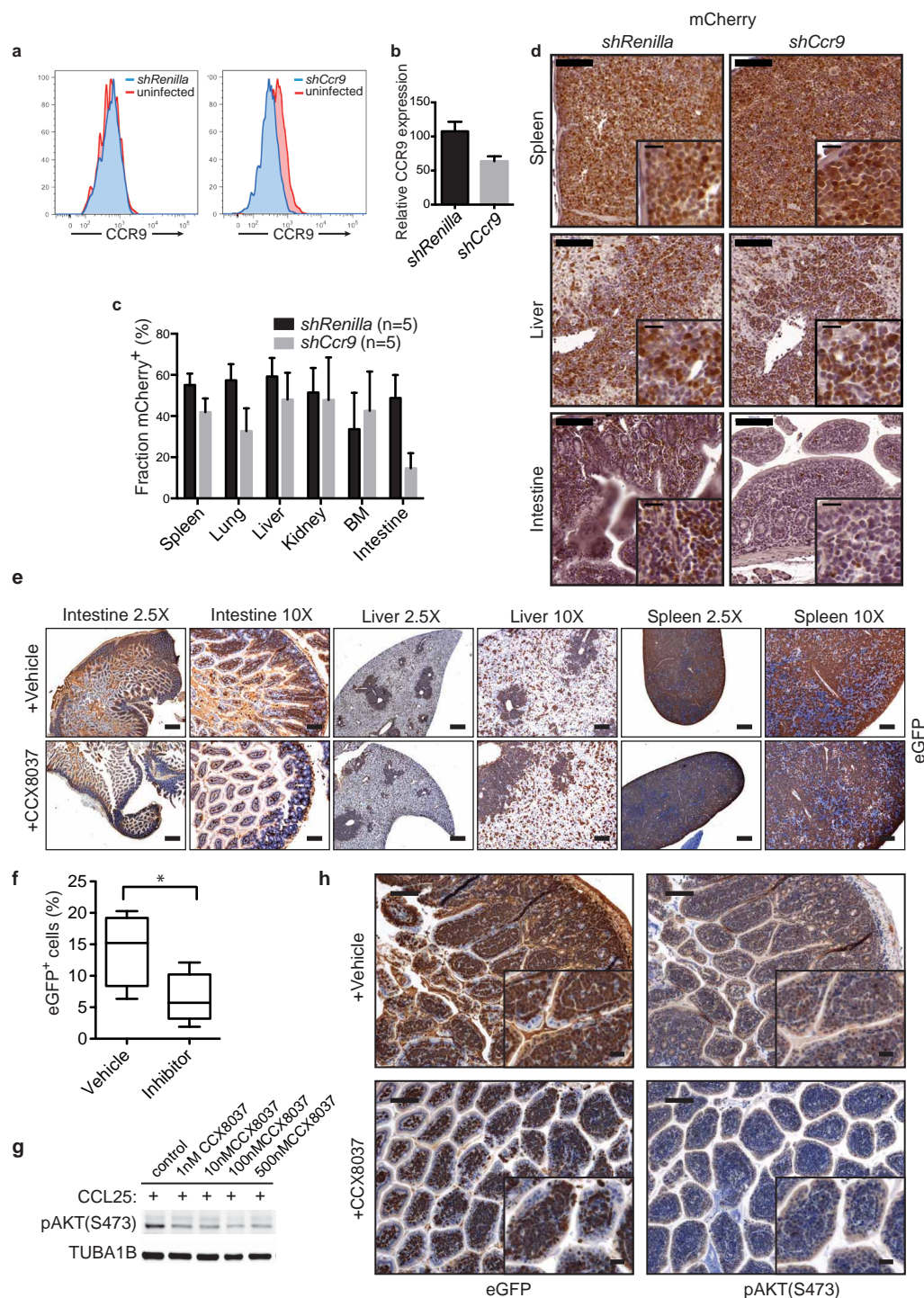
reduction of the *Pten*-shRNA-linked GFP signal (top) after 36 h of Dox treatment (+ Dox; right panels). **c**, Representative histogram of flow cytometric analysis for intracellular pS6 signal in CD4⁺ cells isolated from spleen and intestine of *Rag1*^{-/-} mice transplanted with *shPten* tumour cells and either treated with Dox for 5 days or left untreated. **d**, Flow cytometric quantification of pS6 signal in CD4⁺ cells isolated from the intestine (**d**) and spleens (**e**) of *Rag1*^{-/-} mice transplanted with primary *shPten* tumours and treated \pm Dox for 5 days ($n = 4$ for each condition, $P < 0.04$ for the intestine and not significant for the spleen by paired *t*-test). MFI, mean fluorescent intensity, error bars represent s.d.



Extended Data Figure 9 | NCr mice display a reduced intestinal tumour infiltration, which is not dependent on the absence of the thymus.

a, Brightfield pictures of the intestinal sites of *Rag1*^{-/-} and NCr nude mice serially transplanted with *shPten* tumours (top four panels) and fluorescence images (FI) of cells infiltrating the small intestine in these mice (bottom four panels). Scale bars, 800 μ m (top FI panels) and 100 μ m (bottom FI panels). Pictures were taken on a Nikon SMZ 1000 stereomicroscope. **b**, Quantification of the intestinal infiltration in transplanted *Rag1*^{-/-} or NCr mice by flow cytometry ($P < 0.03$). **c**, **d**, Weight of lymph nodes ($P < 0.01$) (**c**) and spleens ($P = n.s.$) (**d**) in transplanted *Rag1*^{-/-} and NCr mice. **e**, CCL25 expression in the small intestine of *Rag1*^{-/-} and NCr mice measured by ELISA. Error bars in **b–e** show s.d. **f**, Western blot analysis of CCL25 expression in the small intestine of *Rag1*^{-/-} and NCr mice. **g**, Overall survival of *Rag1*^{-/-} and thymectomized *Rag1*^{-/-} mice after transplant with *shPten* T-ALL cells ($n = 5$

per group). **h**, H&E and immunohistochemical analysis of CD3 expression of spleen, liver and intestine from *Rag1*^{-/-} and thymectomized *Rag1*^{-/-} mice transplanted with *shPten* T-ALL cells. Scale bars, 200 μ m for spleen and liver and 100 μ m for intestinal samples. **i**, Flow cytometric measurement of CCR9 expression on *shPten* leukaemia cells either in the absence of Dox (*Pten* knocked down) or Dox-treated (*Pten* reactivated). One representative analysis out of four analysed on/off Dox pairs is shown. A CCR9 negative B-cell line was used as control. **j**, Immunoblot analysis of PTEN, p-AKT(S473) and ACTB expression in human HBP-ALL T-ALL cells infected with either a control shRNA (*shRenilla*) or a shRNA targeting *PTEN*, and either starved or stimulated for 15 min with 500 ng ml⁻¹ CCL25. **k**, *shPten* tumour cell migration across a Boyden chamber in the presence or absence of 1 μ g ml⁻¹ Dox and 500 ng ml⁻¹ CCL25. One representative experiment of two is shown, samples were run in triplicate; ** $P < 0.01$, *** $P < 0.001$ by *t*-test (\pm s.d.).



Extended Data Figure 10 | CCR9 inactivation by shRNA knockdown or by pharmacologic inhibition attenuates intestinal tumour infiltration.

a, CCR9 expression on the surface of *shPten* tumour cells either infected with a control shRNA (*shRenilla*) (left) or with a shRNA targeting *Ccr9* (right) as measured by flow cytometry, compared to uninfected cells, respectively. **b**, Flow cytometry-based quantification of CCR9 suppression in *shCcr9*-infected *shPten* T-ALL cells compared to *shRenilla*-infected cells, *n* = 5 for each cohort (\pm s.d.). **c**, Raw percentage of *shRenilla/shCcr9*-expressing *shPten* T-ALL cells \pm s.d. in different tissue compartments of mice 12 days after transplantation, determined by flow cytometry, *n* = 5 for each cohort. *P* < 0.0005 (intestine). **d**, IHC analysis for mCherry (left, *shRenilla*-mCherry; right, *shCcr9*-mCherry)-expressing cells in tissue sections of mice from **c**. Spleen, liver and intestinal sections of mice transplanted with *shRenilla*- or *shCcr9*-infected T-ALL cells were analysed for mCherry expression. Representative stains from one mouse

out of three analysed mice are shown. Scale bars, 100 μ m, insets 20 μ m. **e**, IHC staining for eGFP expression in representative sections of small intestine, liver and spleen of *Vav-tTA;shPten* tumour-bearing mice treated with vehicle or the CCR9 inhibitor CCX8037 (*n* = 3). Scale bars, 400 μ m ($\times 2.5$) and 100 μ m ($\times 10$). **f**, Flow cytometric quantification of intestinal tumour infiltration in *Rag1*^{-/-} mice transplanted with *Vav-tTA;shPten* leukaemia cells and treated with vehicle (*n* = 4) or a small molecule inhibitor of CCR9 (*n* = 5). **P* < 0.05 by *t*-test (\pm s.d.). **g**, Immunoblot analysis of p-AKT expression 15 min after stimulation of *shPten* leukaemia cells with CCL25 in the absence or presence of indicated concentrations of CCX8037. **h**, IHC analysis of eGFP and p-AKT signal in representative sections of small intestine from *Vav-tTA;shPten* tumour-bearing mice treated with vehicle or the CCR9 inhibitor CCX8037. Scale bars, 100 μ m, 25 μ m for insets.

Inactivation of PI(3)K p110 δ breaks regulatory T-cell-mediated immune tolerance to cancer

Khaled Ali^{1†}, Dalya R. Soond^{2*†}, Roberto Piñeiro^{1*}, Thorsten Hagemann³, Wayne Pearce¹, Ee Lyn Lim², Hicham Bouabe², Cheryl L. Scudamore⁴, Timothy Hancox⁵, Heather Maecker⁶, Lori Friedman⁶, Martin Turner², Klaus Okkenhaug^{2§} & Bart Vanhaesebroeck^{1§}

Inhibitors against the p110 δ isoform of phosphoinositide-3-OH kinase (PI(3)K) have shown remarkable therapeutic efficacy in some human leukaemias^{1,2}. As p110 δ is primarily expressed in leukocytes³, drugs against p110 δ have not been considered for the treatment of solid tumours⁴. Here we report that p110 δ inactivation in mice protects against a broad range of cancers, including non-haematological solid tumours. We demonstrate that p110 δ inactivation in regulatory T cells unleashes CD8⁺ cytotoxic T cells and induces tumour regression. Thus, p110 δ inhibitors can break tumour-induced immune tolerance and should be considered for wider use in oncology.

PI(3)K p110 δ ^{D910A} (δ ^{D910A}) mice, in which endogenous p110 δ kinase is inactive, present specific immune deficiencies^{5,6} but are not predisposed to cancer. To test whether host p110 δ activity affects tumour growth, we inoculated weakly immunogenic syngeneic cancer cell lines into δ ^{D910A} mice. Compared to wild-type mice, δ ^{D910A} mice were more resistant to B16 melanoma, with reduced tumour incidence and almost abrogated lymph node metastasis in those mice that developed tumours (Fig. 1a). Growth of Lewis lung carcinoma (LLC) and EL4 thymoma cells was also suppressed in δ ^{D910A} mice (Fig. 1b, c). Similar observations were made with luciferase-labelled 4T1 breast cancer cells injected into the mammary fat pad. At euthanization, δ ^{D910A} mice showed reduced mass and luciferase activity of the primary 4T1 tumour (Fig. 1d) and lower metastasis (Fig. 1e). In wild-type mice, 4T1 tumours were detected by day 10 and grew progressively until day 30, at which point the mice became moribund (Fig. 1f). In some δ ^{D910A} mice, 4T1 tumours grew initially, but then started to regress from days 15–20 onwards (Fig. 1f). Across ten independent experiments, 97% (71/73) of wild-type mice had an observable cancer mass at the end of study, compared to 65% (43/66) of δ ^{D910A} mice, with a median survival time of 23 and 40 days in wild-type and δ ^{D910A} mice, respectively (Fig. 1g).

Effective tumour immunity is limited by regulatory T cell (T_{reg})-mediated immune suppression⁷. δ ^{D910A} mice show enhanced FOXP3⁺ CD4⁺ T_{reg} in the thymus but impaired subsequent T_{reg} maintenance and functionality in the periphery⁸. δ ^{D910A} T_{reg} also produce less interleukin (IL)-10 and express lower levels of CD38, but show normal expression of most 'T_{reg}-signature' genes, including FOXP3, CD25 (also known as IL2RA), CTLA4 and ICOS^{8,9}. We therefore considered that reduced T_{reg} function in δ ^{D910A} mice might lead to enhanced tumour resistance. FOXP3⁺ CD4⁺ T_{reg} in the draining lymph nodes of 4T1 tumour-bearing δ ^{D910A} mice did not expand as robustly as in wild-type mice (Fig. 2a); however, no consistent differences in T_{reg} expansion were observed in the B16 or EL4 tumour models between naive and tumour-bearing mice of either genotype (not shown). To assess T_{reg} function, we carried out adoptive T_{reg} transfer experiments in EL4 tumour-bearing

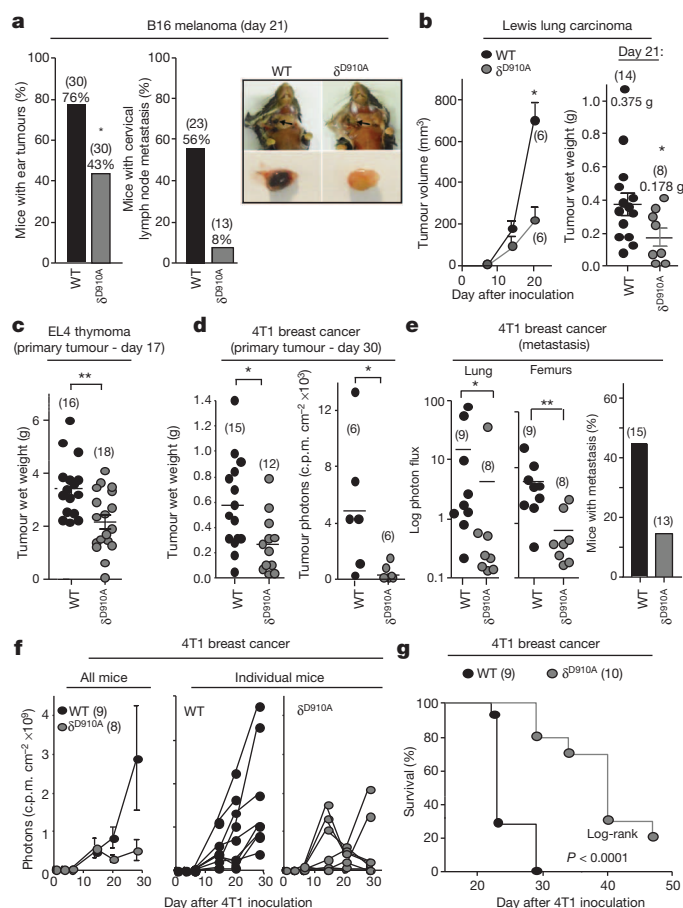


Figure 1 | Impact of genetic inactivation of p110 δ on tumour growth and metastasis. **a**, Percentage of mice with visible B16 ear tumours (left) or lymph nodes metastasis (right). Photographs show B16 metastases in cervical lymph nodes and representative excised lymph nodes. **b–d**, Primary tumour burden of the indicated tumour lines. **e**, 4T1 metastasis as detected by luciferase activity (left and middle) or histology (right), expressed as a percentage of the total number of tumour-bearing animals per group. **f**, Growth of primary 4T1 tumours. **g**, Survival of 4T1 tumour-bearing mice. * $P < 0.05$, ** $P < 0.01$ (non-parametric Mann–Whitney t -test). Numbers in brackets represent number of mice used per experiment. Each dot represents an individual mouse. Shown are the mean \pm standard error of mean (s.e.m.) from at least two independent experiments in which statistical significance was demonstrated.

¹UCL Cancer Institute, Paul O’Gorman Building, University College London, 72 Huntley Street London WC1E 6DD, UK. ²Laboratory of Lymphocyte Signalling and Development, The Babraham Institute, Babraham Research Campus, Cambridge CB22 3AT, UK. ³Centre for Cancer and Inflammation, Barts Cancer Institute, Queen Mary University of London, Charterhouse Square, London EC1M 6BQ, UK. ⁴Mary Lyon Centre, MRC Harwell, Harwell Science and Innovation Campus, Harwell OX11 0RD, UK. ⁵Piramed Pharma, 957 Buckingham Avenue, Slough, Berkshire SL1 4NL, UK. ⁶Cancer Signaling and Translational Oncology, Genentech Inc DNA Way, South San Francisco, California 94080-4990, USA. [†]Present Addresses: Oncology Research, Amgen, 1120 Veterans Boulevard, South San Francisco, California 94080, USA (K.A.); University of Birmingham, School of Infection and Immunity, Centre for Translational Inflammation Research, New Queen Elizabeth Hospital Research Laboratory, Mindelsohn Way, Edgbaston, Birmingham B15 2WB, UK (D.R.S.).

*These authors contributed equally to this work.

§These authors jointly supervised this work.

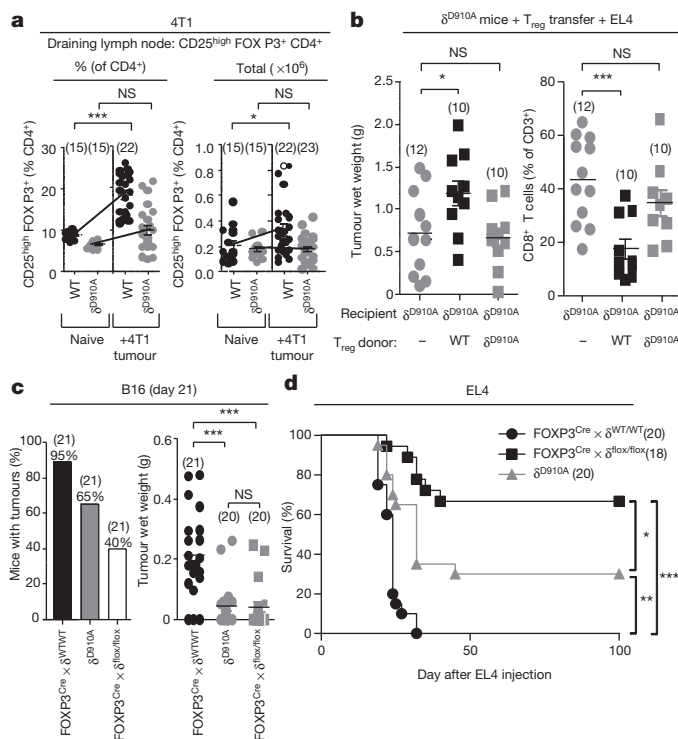


Figure 2 | Inactivation of p110 δ in T_{reg} is sufficient to confer cancer resistance. **a**, Relative and total numbers of T_{reg} in the draining lymph nodes of naive and 4T1 tumour-bearing mice. **b**, Impact of adoptive transfer of T_{reg} into δ^{D910A} mice on EL4 tumour wet weight and tumour-infiltrating CD8⁺ T cells. **c**, Number of mice with visible B16 tumours and B16 tumour weight in mice of the indicated genotype. **d**, Survival of EL4 tumour-bearing mice of the indicated genotype. * $P < 0.05$, ** $P < 0.01$, *** $P < 0.001$ (a–c, non-parametric Mann–Whitney t -test; d, log-rank (Mantel–Cox) test). Numbers in brackets denote the number of mice used per experiment. Each dot represents an individual mouse. Shown are the mean \pm standard error of mean (s.e.m.) from at least two independent experiments in which statistical significance was demonstrated.

mice. Transfer of wild-type T_{reg} into δ^{D910A} mice restored EL4 tumour growth and suppressed the relative abundance of tumour-infiltrating CD8⁺ T cells (Fig. 2b). By contrast, the transfer of the same number of δ^{D910A} T_{reg} into δ^{D910A} mice did not affect EL4 tumour growth (Fig. 2b), indicating a functional defect in δ^{D910A} T_{reg}. FOXP3^{YFP-Cre} × $\delta^{flox/flox}$ mice, in which p110 δ was selectively deleted in T_{reg} (by a Cre transgene expressed from the *Foxp3* locus) did not display spontaneous auto-immune or inflammatory responses (not shown) but showed reduced growth of B16 cells (Fig. 2c) and extended survival time upon inoculation of EL4 cells, to an even greater extent than in δ^{D910A} mice (Fig. 2d). These data demonstrate that p110 δ inactivation in T_{reg} is both necessary and sufficient to confer tumour resistance. However, these data also revealed a potential negative impact of p110 δ inhibition on effector T cells, as FOXP3^{YFP-Cre} × $\delta^{flox/flox}$ mice were more cancer-resistant than δ^{D910A} mice (Fig. 2d). We therefore investigated the effect of p110 δ inactivation on CD4 and CD8 effector T cells in the context of an ongoing tumour response.

Depletion of CD8⁺ T cells but not of CD4⁺ T cells on day 10 after 4T1 inoculation in δ^{D910A} mice eliminated cancer protection (Fig. 3a, b). These data show that CD8⁺ T cells are responsible for restricting tumour growth in δ^{D910A} mice, but do not exclude an accessory role for CD4⁺ T cells. In line with published data⁵, naive wild-type mice had higher relative numbers of activated/memory CD44^{high} CD4⁺ and CD44^{high} CD8⁺ T cells than δ^{D910A} mice (Extended Data Fig. 1a). Upon 4T1 inoculation in wild-type mice, the relative numbers of these cells were either enhanced (tumour-draining lymph nodes) or reduced (blood and spleen), but in δ^{D910A} mice showed a trend towards expansion (Extended Data

Fig. 1a), indicating that δ^{D910A} mice are capable of mounting both CD4⁺ and CD8⁺ T-cell responses against 4T1 tumours. Wild-type and δ^{D910A} splenocytes from tumour-bearing mice, incubated *in vitro* with mitomycin C-treated 4T1 cells, generated equivalent cytotoxic activity against 4T1, with no specific lysis of LLC (Fig. 3c). Compared to wild-type cultures, δ^{D910A} cultures contained similar proportions of CD4 and CD8 T-cell subsets (Extended Data Fig. 1b), with a reduced frequency of activated/memory CD44^{high} CD4⁺ cells (Fig. 3d) and unaffected frequency of CD44^{high} CD8⁺ cells (Fig. 3d). Interestingly, despite this reduced proportion of δ^{D910A} CD44^{high} CD4⁺ cells, the frequency of interferon (IFN)- γ ⁺ CD4⁺ cells in phorbol myristate acetate (PMA)/ionomycin-stimulated cultures of splenocytes from 4T1 tumour-bearing mice was unaffected by p110 δ inactivation (Fig. 3e), with the frequency of IFN- γ ⁺ CD8⁺ cells even enhanced upon p110 δ inactivation (Fig. 3e). Upon inoculation with LLC cells expressing ovalbumin (LLC-OVA), wild-type and δ^{D910A} mice generated similar levels of tumour-infiltrating OVA-specific CD8⁺ T cells (Fig. 3f), showing that systemic *in vivo* inactivation of p110 δ does not impede the development or recruitment of antigen-specific anti-tumour CD8⁺ cells.

To test the intrinsic ability of δ^{D910A} CD8 T cells to eliminate tumours, we crossed δ^{D910A} mice to OT-I transgenic mice, which carry an OVA-specific MHC class I-restricted T-cell receptor transgene. *In vitro*-generated δ^{D910A} OT-I cytotoxic T lymphocytes (CTLs) were less efficient than wild-type OT-I CTLs at EL4-OVA killing (Fig. 3g) and produced lower levels of cytotoxic mediators (Extended Data Fig. 1c). Pharmacological inactivation of p110 δ during the *in vitro* CTL expansion of wild-type OT-I cells partially suppressed CTL function, in a manner indistinguishable from genetic inactivation of p110 δ (Fig. 3g), whereas p110 δ blockade during the killing phase itself did not affect CTL function (Fig. 3g). Despite these *in vitro* defects in δ^{D910A} OT-I CTLs, adoptive transfer of these cells in wild-type mice before challenge with EL4-OVA provided equal cancer protection to inoculation of wild-type OT-I T cells (Fig. 3h), showing that *in vivo* CTL responses can remain competent in the absence of CD8 T-cell-intrinsic p110 δ activity. Taken together, these data indicate that p110 δ inhibition impairs differentiation of CD8 T cells to become fully competent CTLs; however, fully differentiated CTLs do not seem to require p110 δ activity to kill target cells and on balance, in the context of reduced T_{reg} function in δ^{D910A} mice, can mediate effective anti-tumour activity.

CD4 T cells can also contribute to tumour elimination by promoting the activation of macrophages and natural killer cells or by direct lysis of MHC class II⁺ tumour cells¹⁰. Indeed, CD4⁺ T cells with enhanced PI(3)K activity are superior in their capacity to reject tumour growth, probably as a consequence of their increased production of IFN- γ ¹¹. Conversely, δ^{D910A} OT-II CD4 cells were less effective than wild-type OT-II cells in preventing EL4-OVA tumour growth (Fig. 3h), consistent with our previous finding that δ^{D910A} OT-II T cells produce less IFN- γ *in vitro* and *in vivo*^{12,13}. Therefore, in the context of an otherwise normal immune system, δ^{D910A} CD4⁺ cells show inferior anti-tumour immunity. However, the production of IFN- γ by CD4 and CD8 T cells from 4T1 tumour-bearing δ^{D910A} mice, in which T_{reg} are also defective, appeared to be intact (Fig. 3e), suggesting that p110 δ inhibition can affect the balance between regulatory and effector CD4⁺ T cells such that the effector cells prevail in the context of anti-tumour responses.

A salient feature of CD4 and CD8 T cells is the ability to raise a more potent and rapid immune response to subsequent exposure to cognate antigen. Upon surgical removal of 4T1 primary tumours when they had reached 9 mm in diameter and established metastatic foci¹⁴, wild-type mice all succumbed to regrowth of the primary tumour and metastatic disease. By contrast, >50% of post-surgical δ^{D910A} mice showed survival extension beyond 100 days (Fig. 3i), demonstrating that p110 δ inhibition can suppress cancer relapse and presumably metastatic cancer after surgery. δ^{D910A} mice which had remained tumour-free for >200 days after surgery were cancer-resistant upon rechallenge with a higher 4T1 dose (Fig. 3j), suggesting that surgical intervention in δ^{D910A} mice supports the development of an effective memory anti-tumour response.

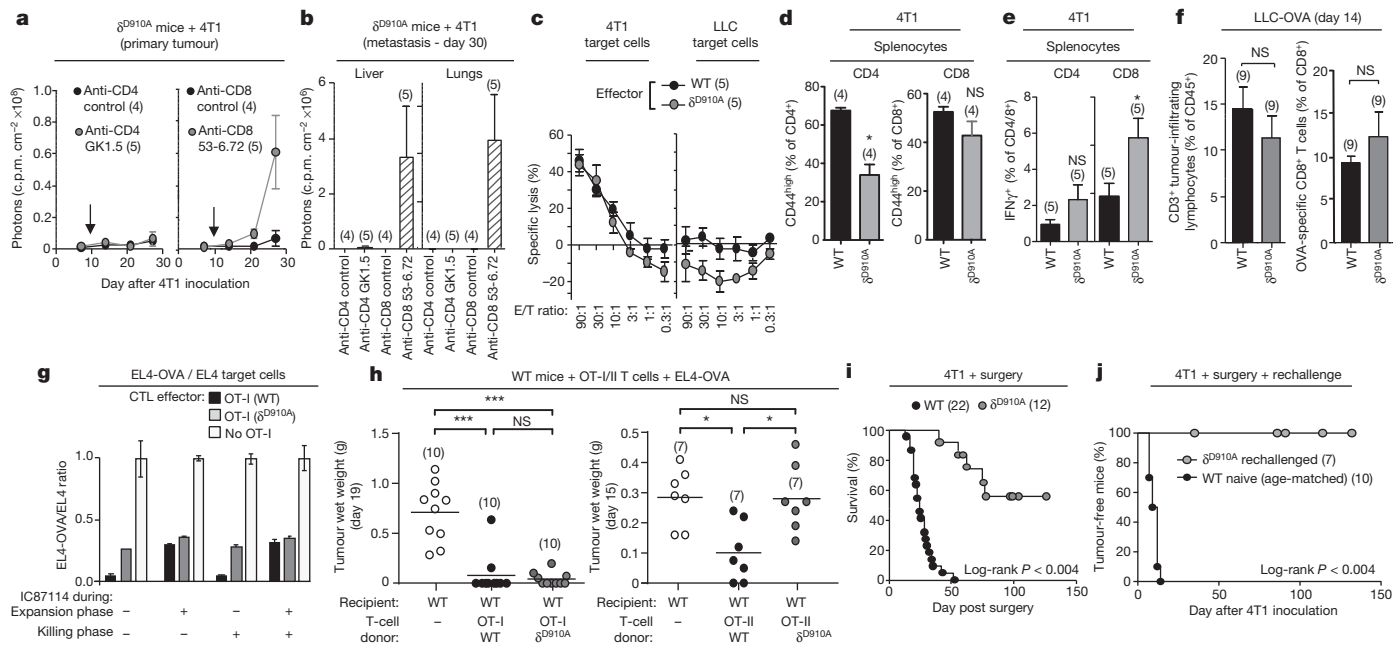


Figure 3 | Impact of p110 δ inactivation on T-cell-mediated anti-tumour immunity. **a**, Growth of 4T1 in δ^{D910A} mice injected with antibodies to CD4 or CD8. Arrow indicates the time of antibody injection. **b**, Metastasis in CD4 or CD8 T-cell-depleted 4T1 tumour-bearing δ^{D910A} mice. **c**, *In vitro* cytotoxic activity of splenocytes, isolated from 4T1 tumour-bearing wild-type and δ^{D910A} mice 21 days after inoculation and cultured for 4 days with mitomycin-treated 4T1 cells. E/T, effector to target (4T1 or LLC) ratio. **d**, Frequency of CD4⁴IFN γ CD4⁺ and CD8⁺ T cells in splenocytes from 4T1 tumour-bearing mice cultured for 5 days with mitomycin-treated 4T1 cells. **e**, Frequency of IFN γ -⁺ T cells after 16 h PMA + ionomycin stimulation of splenocytes from wild-type and δ^{D910A} 4T1 tumour-bearing mice. **f**, Relative levels of tumour-infiltrating CD3⁺ lymphocytes and OVA-specific CD8⁺ T cells in LLC-OVA tumours

in wild-type or δ^{D910A} mice. **g**, *In vitro* cell killing of a 1:1 EL4-OVA:EL4 mix following 24 h incubation with CTL from wild-type or a δ^{D910A} OT-I mice (at an E/T ratio of 10:1), incubated with or without the p110 δ inhibitor IC87114 during the 8-day expansion phase, the 24-h killing phase, or both. Cell killing efficiency is expressed as the ratio of EL4-OVA cells over EL4 cells remaining after incubation with effector cells. **h**, Effect of adoptive transfer in wild-type mice of OT-I CD8⁺ or OT-II CD4⁺ cells on growth of subsequently inoculated EL4-OVA. **i**, Survival of post-surgical 4T1 tumour-bearing mice. **j**, Survival of δ^{D910A} mice that had remained tumour-free >200 days after surgery, and of naive wild-type mice, following injection of 10,000 4T1 cells. Statistics are as described in the legend to Fig. 2.

To assess the potential importance of p110 δ in myeloid cells in cancer, we tested the impact of p110 δ inactivation in *Rag*^{-/-} mice. *Rag*^{-/-} mice, which lack mature B and T cells, showed enhanced primary 4T1 tumour size and metastasis (Fig. 4a) compared to wild-type mice. *Rag*^{-/-} \times δ^{D910A} mice showed a similar 4T1 primary tumour burden to *Rag*^{-/-} mice (Fig. 4a) but had fewer metastatic lesions in lung (Fig. 4a) and liver (not shown), indicating that p110 δ inactivation in a non-B/T-cell lineage delays 4T1 tumour progression but is not sufficient to instigate tumour rejection. We next assessed the impact of p110 δ inactivation on myeloid-derived suppressor cells (MDSCs), a heterogeneous population of bone marrow-derived myeloid cells that co-express the CD11b and Gr1 surface markers and which have a prominent role in immune suppression in cancer^{15,16}. Neutrophils are also CD11b⁺ Gr1⁺ but are thought not to be immune-suppressive¹⁷. Upon inoculation with 4T1 cells, known to be potent MDSC inducers^{16,17}, CD11b⁺ Gr1^{high} cells accumulated in the spleens of both wild-type and δ^{D910A} mice, even before tumours were palpable, and continued to differentially accumulate in both genotypes as tumours grew, correlating with tumour size (Fig. 4b). The Ly6C and Ly6G surface markers, which are both recognized by the Gr1 antibody, have been used to subdivide MDSCs into two CD11b⁺ subpopulations, namely monocytic (M)-MDSCs (Ly6C^{high} Ly6G^{low}) and polymorphonuclear (PMN)-MDSCs (Ly6C^{low} Ly6G^{high})¹⁷. Although neutrophils are difficult to differentiate from PMN-MDSCs, here we designated the neutrophil population as Ly6C^{high} cells with intermediate/high Ly6G expression (Fig. 4c and Extended Data Fig. 2a). PMN-MDSCs, predominant in 4T1 tumour-bearing wild-type mice (Fig. 4c), were substantially reduced in δ^{D910A} mice, correlating with a relative increase in neutrophils in the latter (Fig. 4c). Interestingly, the number of PMN-MDSCs in spleens from 4T1 tumour-bearing mice correlated with the number of T_{regs} (Fig. 4d). Depletion of CD8⁺ cells in 4T1 tumour-bearing

δ^{D910A} mice, which led to enhanced tumour growth (Fig. 3a, b), also led to increased PMN-MDSC numbers and reduced neutrophil numbers (Fig. 4e). It was therefore difficult to ascertain whether the reduced PMN-MDSC numbers in δ^{D910A} mice are a consequence of an intrinsic role for p110 δ in these cells or an indirect consequence of a reduced tumour burden in δ^{D910A} mice (Fig. 4b). In support of the former, wild-type PMN-MDSCs suppressed T-cell proliferation *in vitro*, whereas MDSCs from δ^{D910A} mice with regressing tumours did not (Fig. 4f and Extended Data Fig. 2b). Neutrophils from both genotypes did not suppress T-cell responses (Fig. 4f). Moreover, splenocytes from tumour-bearing δ^{D910A} mice showed reduced *in vitro* production of transforming growth factor- β , vascular endothelial growth factor and IL-6 (Fig. 4g), each of which can contribute to immune suppression and/or tumour growth^{15,16}.

Administration of PI-3065, a small molecule inhibitor with selectivity for p110 δ (Extended Data Fig. 3a, b and Extended Data Table 1), also suppressed 4T1 tumour growth and metastasis, to a similar extent as genetic inactivation of p110 δ , marked by initial tumour progression, followed by tumour regression (Fig. 5a and Extended Data Fig. 3c, d). Of interest, 4T1 cells do not express detectable levels of p110 δ (Extended Data Fig. 3e) and are not growth-inhibited *in vitro* by PI-3065 (Extended Data Fig. 3f). Long-term administration of PI-3065 to mice was well-tolerated and did not induce weight loss (Extended Data Fig. 3g).

We next tested the impact of PI-3065 in the LSL.*Kras*^{G12D/+}; *p53*^{R172H/+}; *Pdx*^{Cre/+} (or KPC) model of pancreatic ductal adenocarcinoma, which expresses endogenous mutant *KRAS*^{G12D} and *p53*^{R172H} in PDX1⁺ pancreatic cells. KPC mice were left to develop palpable disease before treatment with vehicle or PI-3065 was commenced. Under these therapeutic conditions, PI-3065 prolonged survival and reduced the incidence of macroscopic metastases and other disease-associated pathologies (Fig. 5b). The relative abundance of peripheral T_{reg} in lymph nodes after 7 days

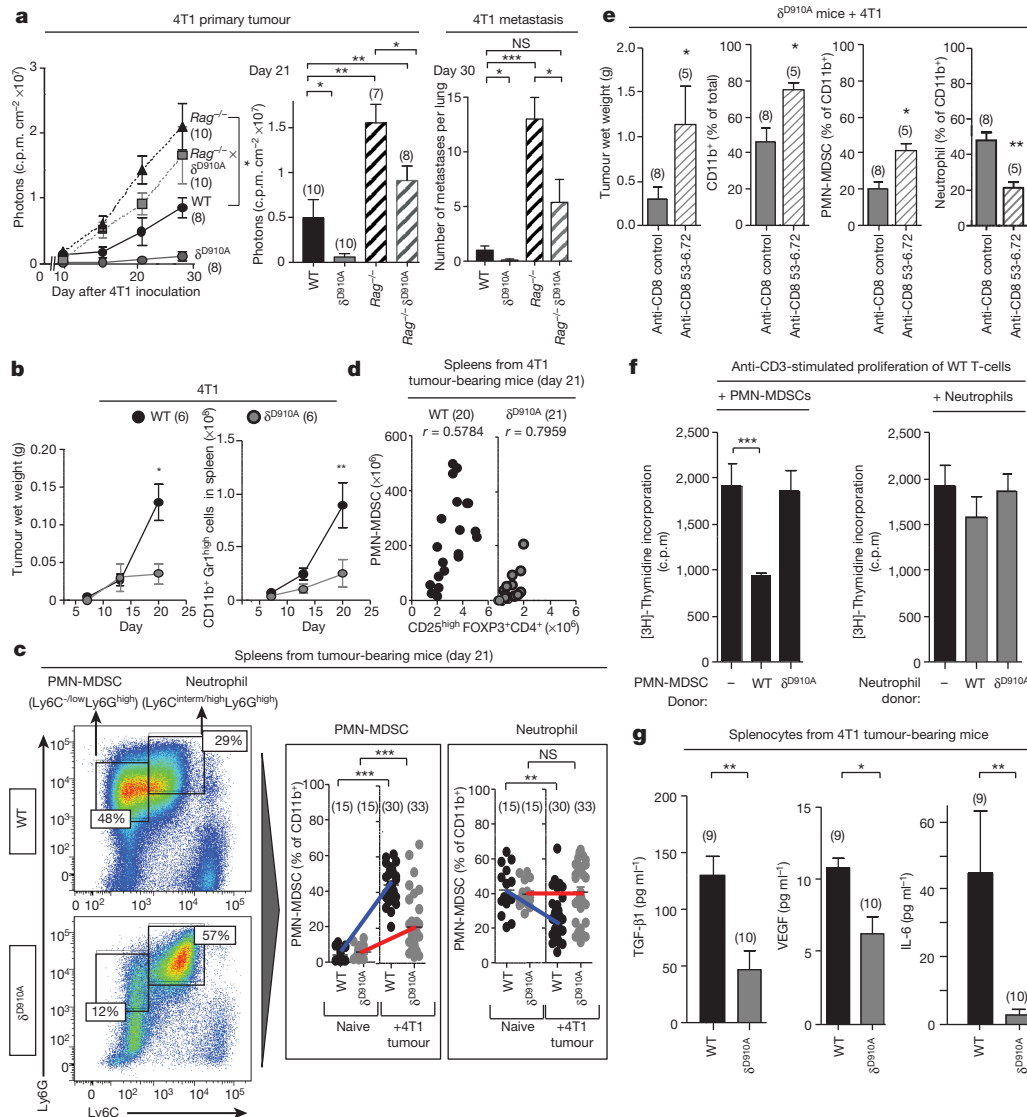


Figure 4 | Impact of p110 δ inactivation on myeloid cells in 4T1 tumour-bearing mice. **a**, 4T1 primary tumour growth and lung metastasis in wild-type, δ^{D910A} , $Rag^{-/-}$ and $Rag^{-/-}/\delta^{D910A}$ mice. **b**, 4T1 tumour growth and total numbers of splenic CD11b⁺Gr1^{high} myeloid cells in wild-type and δ^{D910A} mice. **c**, Gating strategy used to identify myeloid cell subsets and frequency of splenic PMN-MDSCs and neutrophils of naive and 4T1 tumour-bearing wild-type and δ^{D910A} mice. **d**, Spearman correlation between

accumulation of splenic PMN-MDSCs and T_{reg} in wild-type or δ^{D910A} mice. **e**, Impact of depleting CD8⁺ T cells in δ^{D910A} mice on 4T1 tumour burden and presence of splenic myeloid cell populations. **f**, Impact of purified splenic myeloid cells on proliferation of anti-CD3-stimulated wild-type T cells. **g**, Cytokine production by splenocytes from 4T1 tumour-bearing (30 days after inoculation) cells from wild-type or δ^{D910A} mice, individually cultured for 4 days. Statistics are as described in the legend to Fig. 2.

of treatment was reduced (Fig. 5c), correlating with higher levels of CD44^{high} CD8⁺ lymphocytes in the draining lymph nodes (Fig. 5d) and relatively higher levels of infiltrating CD8⁺ T cells in pancreatic lesions 14 days after treatment (Fig. 5e). These data indicate that therapeutic targeting of p110 δ can promote immune-mediated elimination of cancer.

Concerns have been raised about inhibiting p110 δ in cancer as this might impair CTLs and negatively impact on cancer immune surveillance^{4,18}. Our data show that although p110 δ blockade reduces the effectiveness of CTLs, it also overrides T_{reg}- and probably also MDSC-mediated suppression of anti-tumour immune responses, enabling even weakened CTLs to successfully attack tumours. Thus, p110 δ is apparently more essential for regulatory rather than effector T-cell responses against cancer cells. In addition, inhibition of the PI(3)K pathway in CD8 T cells may help maintain them in a stem-cell like state¹⁹ with enhanced potential for generating durable anti-tumour responses. Consistent with this notion, δ^{D910A} mice resisted tumour rechallenge following surgical removal of the first tumour. The p110 δ inhibitor Idelalisib has shown

impressive therapeutic impact in chronic lymphocytic leukaemia (CLL) and non-Hodgkin's lymphoma^{1,2}. In CLL, p110 δ blockade interferes with stroma-derived survival and adhesion signals supporting the tumour cells⁴, but it is unclear if this fully explains the effectiveness of p110 δ inhibition. Our finding that p110 δ inhibition can unlock adaptive anti-tumour responses provides a potential additional mechanism for the efficacy of p110 δ blockade in CLL, and adds to the emerging rationale for targeting PI(3)K in the tumour stroma⁴, to dampen inflammation (p110 γ)²⁰ and angiogenesis (p110 α)²¹.

Tumour-induced immune suppression constitutes an important barrier for effective anti-tumour immunity and immunotherapy in cancer. Our work suggests that p110 δ inhibitors, by disrupting the function of T_{reg} and possibly of MDSCs, have the potential to shift the balance from immune tolerance towards effective anti-tumour immunity. This provides a rationale for p110 δ inhibition both in solid and haematological cancers, possibly as an adjuvant to cancer vaccines, adoptive cell therapy, or other strategies that promote tumour-specific immune responses.

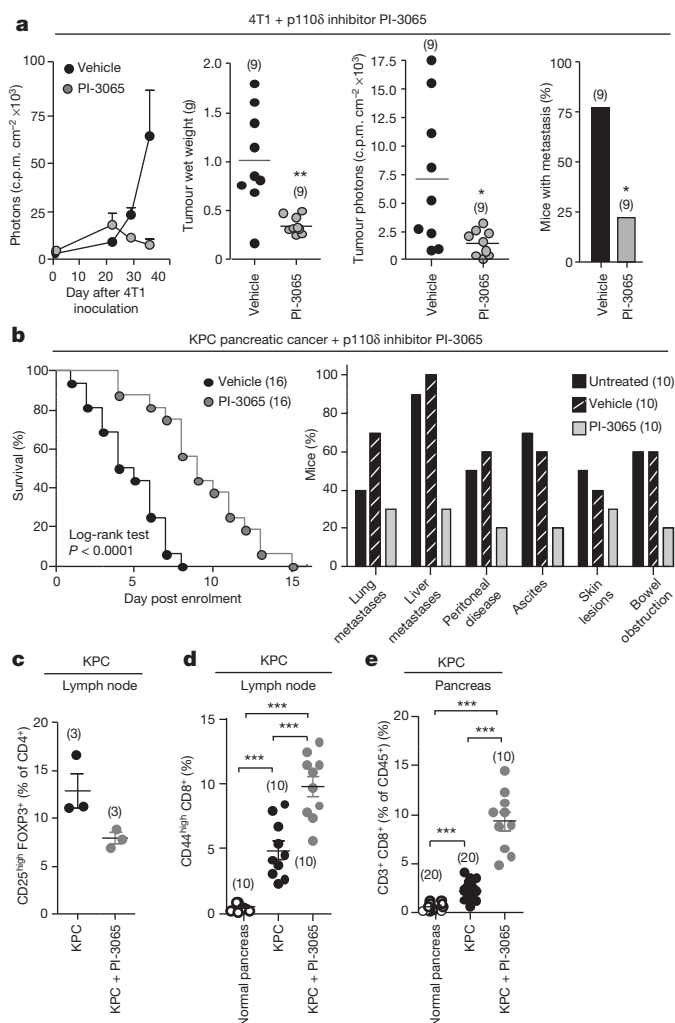


Figure 5 | Impact of pharmacological inactivation of p110δ on tumour growth and T-cell responses. **a**, Mice, dosed with vehicle or PI-3065 (75 mg kg⁻¹, daily) for 36 days and inoculated with 10⁵ 4T1 cells 12 h post first dosing, were assessed for tumour growth by luciferase imaging (first panel), tumour weight (second panel) or luciferase activity in tumours excised 35 days after inoculation (third panel). Incidence of 4T1 metastasis (fourth panel), as detected by haematoxylin and eosin (H&E) staining and histology, expressed as percentage of the total number of tumour-bearing animals per group. **b**, Impact of PI-3065 (75 mg kg⁻¹) on KPC mouse survival (left) and macrometastases and cancer-associated pathology (right). **c**, Proportion of T_{reg} (percentage of CD4⁺) in the draining lymph nodes of KPC mice administered vehicle or PI-3065. **d**, Proportion of CD44^{high} T cells (percentage of CD8⁺) in the draining lymph nodes of KPC mice administered vehicle or PI-3065. **e**, Relative numbers of CD8⁺ T cells (percentage of CD45⁺) in normal pancreas and PDAC lesions of KPC mice treated or not with PI-3065. Statistics are as described in the legend to Fig. 2.

METHODS SUMMARY

All animal procedures were in compliance with institutional animal care and use committee guidelines. Details of procedures and reagents are described in Supplementary Information.

Online Content Any additional Methods, Extended Data display items and Source Data are available in the online version of the paper; references unique to these sections appear only in the online paper.

Received 16 April 2013; accepted 7 May 2014.

Published online 11 June 2014.

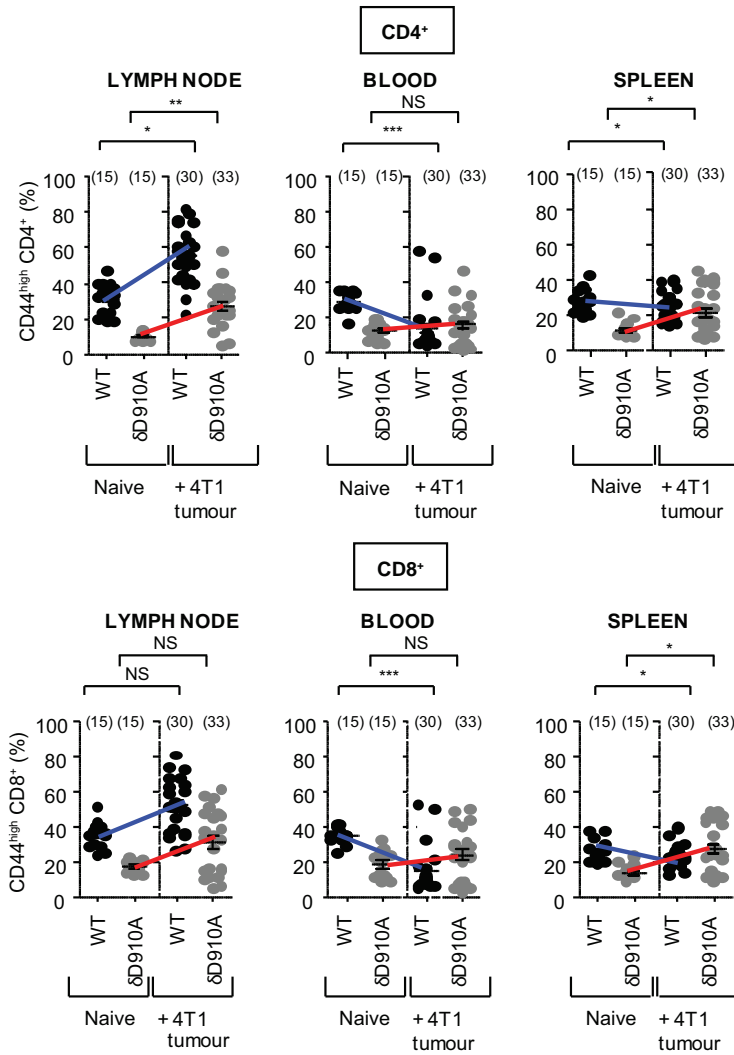
- Furman, R. R. *et al.* Idelalisib and rituximab in relapsed chronic lymphocytic leukemia. *N. Engl. J. Med.* **370**, 997–1007 (2014).
- Gopal, A. K. *et al.* PI3K inhibition by idelalisib in patients with relapsed indolent lymphoma. *N. Engl. J. Med.* **370**, 1008–1018 (2014).
- Vanhaesebroeck, B. *et al.* PI10δ, a novel phosphoinositide 3-kinase in leukocytes. *Proc. Natl Acad. Sci. USA* **94**, 4330–4335 (1997).
- Fruman, D. A. & Rommel, C. PI3K and cancer: lessons, challenges and opportunities. *Nature Rev. Drug Discov.* **13**, 140–156 (2014).
- Okkenhaug, K. *et al.* Impaired B and T cell antigen receptor signaling in p110Δ PI 3-kinase mutant mice. *Science* **297**, 1031–1034 (2002).
- Okkenhaug, K. Signaling by the phosphoinositide 3-kinase family in immune cells. *Annu. Rev. Immunol.* **31**, 675–704 (2013).
- Curiel, T. J. Regulatory T cells and treatment of cancer. *Curr. Opin. Immunol.* **20**, 241–246 (2008).
- Patton, D. T. *et al.* Cutting edge: the phosphoinositide 3-kinase p110δ is critical for the function of CD4⁺ CD25⁺ Foxp3⁺ regulatory T cells. *J. Immunol.* **177**, 6598–6602 (2006).
- Patton, D. T., Wilson, M. D., Rowan, W. C., Soond, D. R. & Okkenhaug, K. The PI3K p110δ regulates expression of CD38 on regulatory T cells. *PLoS ONE* **6**, e17359 (2011).
- Muranski, P. & Restifo, N. P. Adoptive immunotherapy of cancer using CD4⁺ T cells. *Curr. Opin. Immunol.* **21**, 200–208 (2009).
- Soond, D. R. *et al.* Pten loss in CD4 T cells enhances their helper function but does not lead to autoimmunity or lymphoma. *J. Immunol.* **188**, 5935–5943 (2012).
- Okkenhaug, K. *et al.* The p110δ isoform of phosphoinositide 3-kinase controls clonal expansion and differentiation of Th cells. *J. Immunol.* **177**, 5122–5128 (2006).
- Soond, D. R. *et al.* PI3K p110δ regulates T-cell cytokine production during primary and secondary immune responses in mice and humans. *Blood* **115**, 2203–2213 (2010).
- Paluski, B. A., Smyth, M. J. & Ostrand-Rosenberg, S. Interferon-gamma-dependent phagocytic cells are a critical component of innate immunity against metastatic mammary carcinoma. *Cancer Res.* **62**, 4406–4412 (2002).
- Gabrilovich, D. I., Ostrand-Rosenberg, S. & Bronte, V. Coordinated regulation of myeloid cells by tumours. *Nature Rev. Immunol.* **12**, 253–268 (2012).
- Bunt, S. K., Sinha, P., Clements, V. K., Leips, J. & Ostrand-Rosenberg, S. Inflammation induces myeloid-derived suppressor cells that facilitate tumor progression. *J. Immunol.* **176**, 284–290 (2006).
- Youn, J. I., Nagaraj, S., Collazo, M. & Gabrilovich, D. I. Subsets of myeloid-derived suppressor cells in tumor-bearing mice. *J. Immunol.* **181**, 5791–5802 (2008).
- Putz, E. M. *et al.* PI3Kδ is essential for tumor clearance mediated by cytotoxic T lymphocytes. *PLoS ONE* **7**, e40852 (2012).
- Gattinoni, L., Klebanoff, C. A. & Restifo, N. P. Paths to stemness: building the ultimate antitumor T cell. *Nature Rev. Cancer* **12**, 671–684 (2012).
- Schmid, M. C. *et al.* Receptor tyrosine kinases and TLR/IL1Rs unexpectedly activate myeloid cell PI3Kγ, a single convergent point promoting tumor inflammation and progression. *Cancer Cell* **19**, 715–727 (2011).
- Soler, A. *et al.* Inhibition of the p110α isoform of PI 3-kinase stimulates nonfunctional tumor angiogenesis. *J. Exp. Med.* **210**, 1937–1945 (2013).

Supplementary Information is available in the online version of the paper.

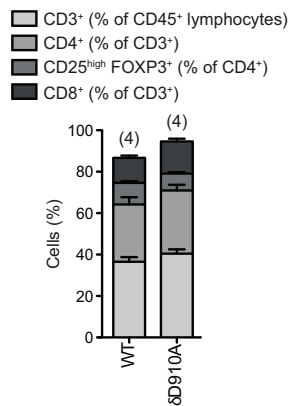
Acknowledgements This research was supported by Cancer Research UK (C23338/A10200; C23338/A15965 to B.V. and C18270/A12888 to T. Hagemann), Biotechnology and Biological Sciences Research Council (BB/E009867/1 to K.O.) and Wellcome Trust (095691/Z/11/Z) (to K.O.). We thank D. Sutherland, J. Nonomiya, J. Lesnick and K. Reif (Genentech) for technical assistance, M. Whitehead, D. Dubuisson, D. Patton, E. Slack, N. Harrington, G. Rosignoli, W. P. Day, A. Brown, P. Depledge, F. Leenders, J. Pang, L. Salphati and X. Zhang for experimental help, D. Fearon and J. Arnold for LLC-OVA cells, and A. Rudensky for FoxP3^{TFP-Cre} mice.

Author Contributions K.A., D.R.S., R.P., E.L.L., H.B. and W.P. performed experiments and data analyses with input from K.O. and B.V. D.R.S. and K.O. generated the FoxP3^{TFP-Cre} × δ^{lox/lox} mice and helped to design, perform and interpret experiments. R.P. and W.P. helped design experiments. T. Hagemann and his team carried out the KPC experiments and performed analysis with help of K.A. M.T. generated the p110δ^{lox/lox} mice. T. Hancox performed chemistry for small molecule inhibitor development. H.M. helped to design and performed *in vivo* pharmacological cancer experiments. L.F. helped design and interpret pharmacological data. C.L.S. performed and interpreted histopathology. K.A., K.O. and B.V. wrote the paper.

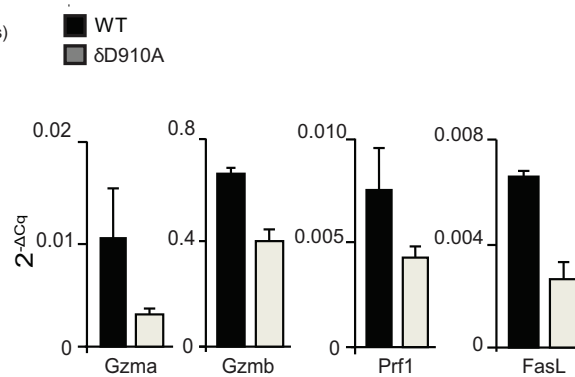
Author Information Reprints and permissions information is available at www.nature.com/reprints. The authors declare competing financial interests: details are available in the online version of the paper. Readers are welcome to comment on the online version of the paper. Correspondence and requests for materials should be addressed to K.A. (khaleida@amgen.com), K.O. (klaus.okkenhaug@babraham.ac.uk) or B.V. (bart.vanh@ucl.ac.uk).

a**b**

4T1
Splenocyte CTL culture (day 5)

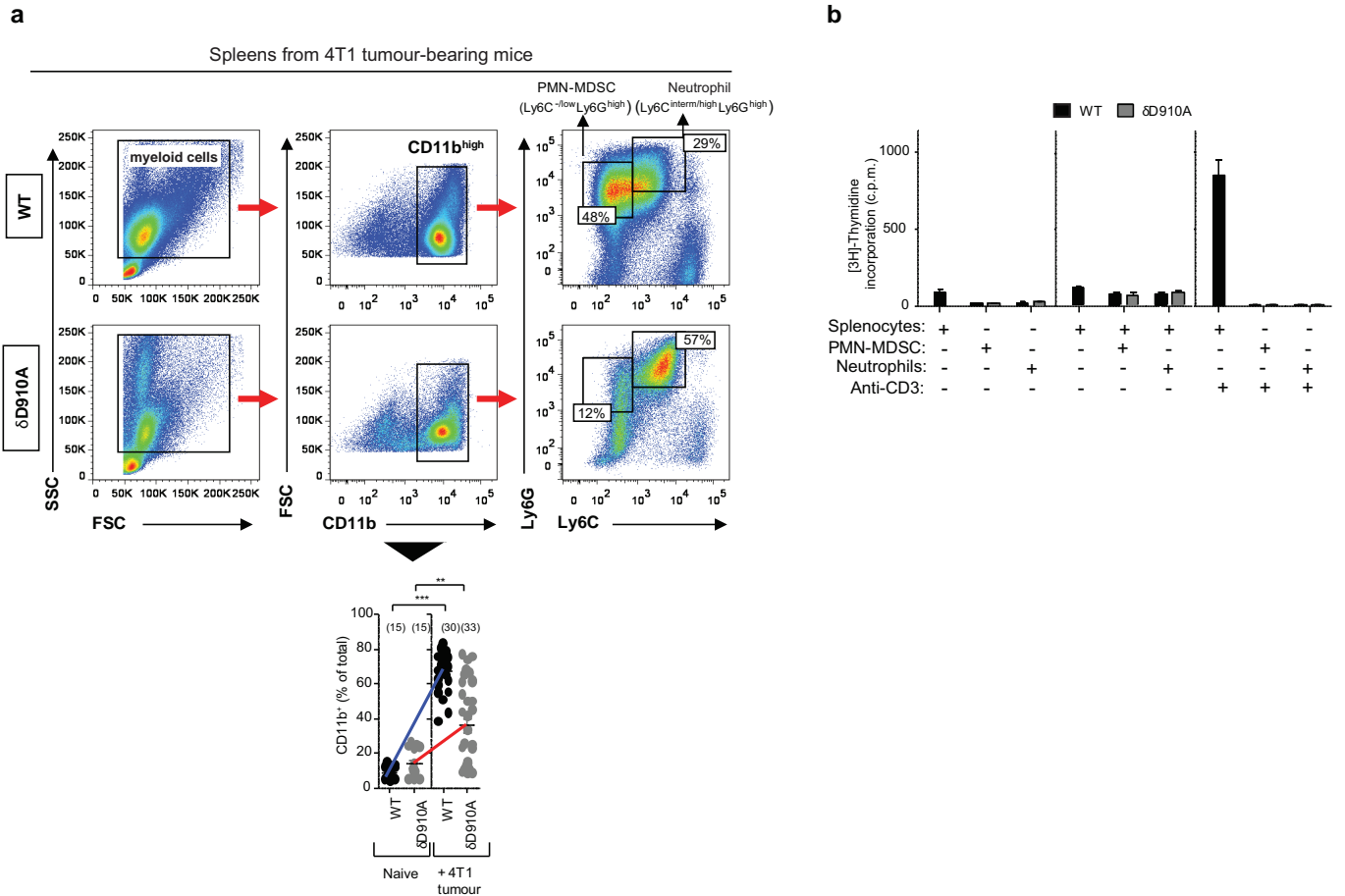
**c**

OT-I CTL



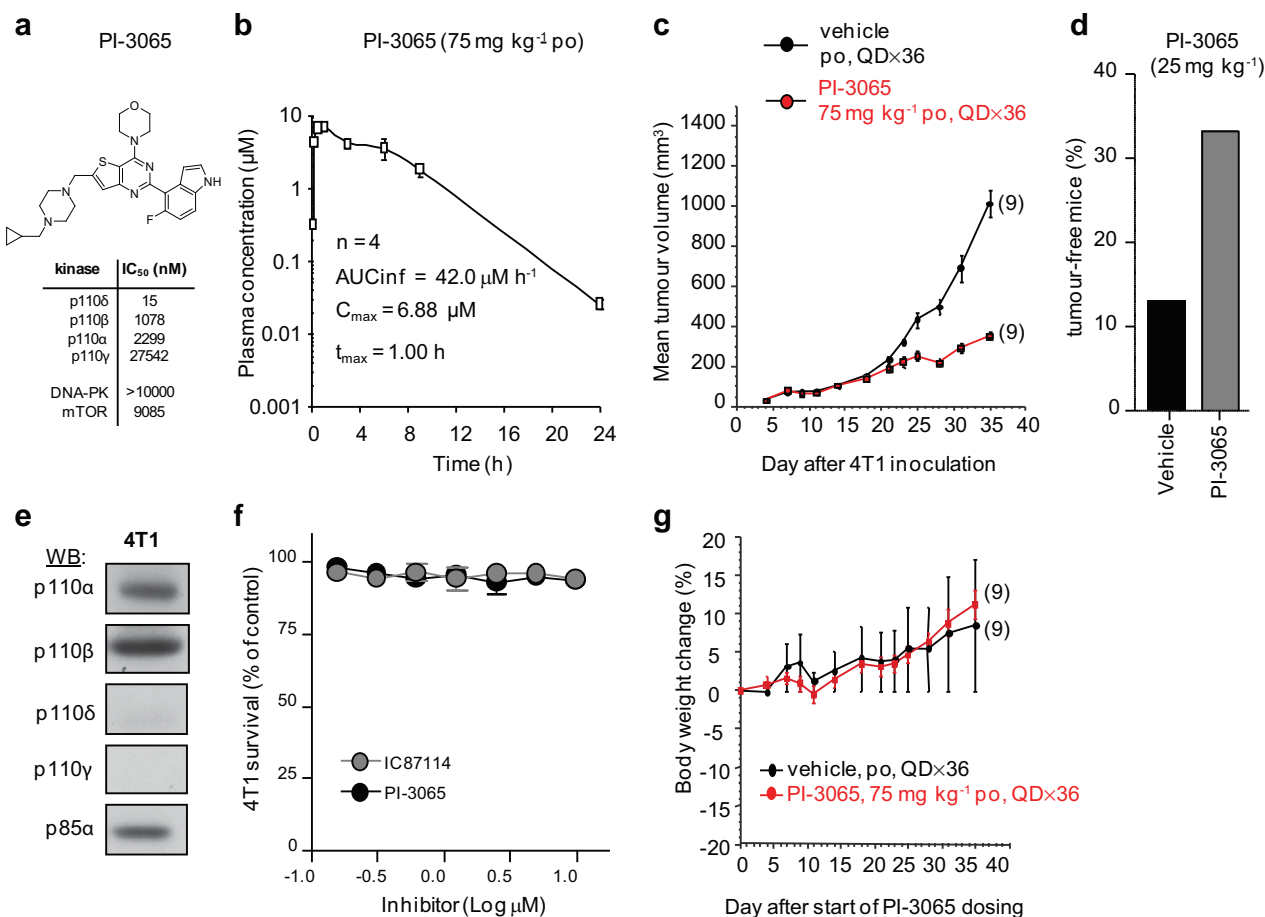
Extended Data Figure 1 | Impact of p110 δ inactivation on CD4 and CD8 T cells in mice with 4T1 or EL4 tumours. **a**, Levels of CD44^{high} CD4⁺ and CD44^{high} CD8⁺ T cells in the indicated immune compartments of naive and 4T1 tumour-bearing on day 26 after inoculation in wild-type or $\delta D910A$ mice. **b**, Distribution of cells on day 5 of culture of splenocytes, isolated from 4T1 tumour-bearing wild-type and $\delta D910A$ mice 21 days after inoculation, in the presence of mitomycin-treated 4T1 cells. **c**, Gene expression in CTLs derived

from splenocytes from wild-type and $\delta D910A$ OT-I mice, cultured in the presence of SIINFEKL OVA peptide and IL-2. Gzma, granzyme A; Gzmb, granzyme B; Prf1, perforin and (FasL or CD95L) Fas ligand. Expression levels are presented relative to $\beta 2$ -microglobulin. * $P < 0.05$, ** $P < 0.01$, *** $P < 0.001$ (non-parametric Mann-Whitney t -test). Numbers in brackets indicate the number of mice used per experiment. Each dot represents an individual mouse.



Extended Data Figure 2 | Impact of p110δ inactivation on myeloid cells in 4T1 tumours. **a**, Gating strategy used to identify myeloid cell subsets. Splenic cells were gated on CD11b^{high} cells followed by Ly6C and Ly6G gating. FSC, forward scatter; SSC, side scatter (top). Frequency of CD11b⁺ cells in the spleen of wild-type and δD910A naïve mice and in 4T1 tumour-bearing mice on day 21 after inoculation (bottom). **b**, [³H]-Thymidine incorporation in co-cultures

of splenocytes and purified myeloid cells, in combinations as indicated, with or without stimulation with anti-CD3 antibodies. Cultures were made using cells derived from individual mice. Error bars represent standard deviation from the mean of biological replicates. **P* < 0.05, ***P* < 0.01 (non-parametric Mann–Whitney *t*-test). Numbers in brackets indicate the number of mice used per experiment. Each dot represents an individual mouse.



Extended Data Figure 3 | Characterization of the p110δ-selective inhibitor PI-3065. **a**, PI-3065 structure and *in vitro* IC₅₀ on selected PI3K family members. No significant activity against 72 protein kinases was observed at ≤ 10 μM in a KinaseProfiler assay (Millipore). **b**, Pharmacokinetic parameters of PI-3065. Mean (± s.d.) plasma concentration profile of PI-3065 following a single oral dose (75 mg kg⁻¹) administered per os (po) to female BALB/c mice. AUC_{inf}, area under the curve, extrapolated to infinity; C_{max}, highest observed plasma concentration; t_{max}, time at which C_{max} occurred, QD, quaque die (every day). **c**, Growth of primary 4T1 tumours, inoculated in the breast fat pad, measured by calipers and expressed as tumour volume. Mice were dosed per os with vehicle or PI-3065 (75 mg kg⁻¹, daily) for 36 days. 10⁵ tumour cells were inoculated 12 h post first dosing. **d**, Percentage of

tumour-free mice upon continuous per os treatment of mice with vehicle or PI-3065 (25 mg kg⁻¹, twice daily) for 37 days, with tumour cells inoculated on day 7 of PI-3065 dosing. 15 mice were used for each genotype. **e**, Class I PI3K isoform expression in 4T1 cells. **f**, Proliferation of 4T1 cells following a 4-h treatment with the indicated p110δ inhibitors, washing and (3-(4,5-dimethylthiazol-2-yl)-5-(3-carboxymethoxy phenyl)-2-(4-sulphophenyl)-2H-tetrazolium salt (MTS) staining after 48 h culture. **g**, Percentage body weight change (from day 0) of 4T1 tumour-bearing mice upon daily per os administration of PI-3065 (75 mg kg⁻¹) or vehicle for 36 consecutive days. *P < 0.05, **P < 0.01 (non-parametric Mann-Whitney *t* test). Numbers in brackets indicate the number of mice used per experiment.

Extended Data Table 1 | Comparison of PI-3065 with Idelalisib (formerly called GS-1101 or CAL-101) and IC87114

Compound	Ki (nM)				IC50 (nM)				anti-IgM stimulated whole blood	anti-IgM-stimulated human R1 B cell lymphoma
	p110 δ	p110 α	p110 β	p110 γ	p110 δ	p110 α	p110 β	p110 γ	CD69 expression IC50 (nM)	pAkt IC50 (nM)
PI-3065	1.5	110	130	940	5	910	600	>10000	38	36
Idelalisib	1.1	270	121	16	2.5	670	260	22	60	41
IC87114	34	>2100	>2100	370	46	>10000	>10000	1300	3500	>7800

Human whole blood was stimulated with anti-IgM followed by FACS for CD69 as described^{22,23}. Human B-cell lymphoma R1-1 cells were pre-incubated for 30 min with vehicle or compound before stimulation with anti-IgM for 1 h at 37 °C, followed by determination of Akt-Ser 473 phosphorylation, as described^{22,23}.

22. Murray, J. M. *et al.* Potent and highly selective benzimidazole inhibitors of PI3-kinase delta. *J. Med. Chem.* **55**, 7686–7695 (2012).

23. Safina, B. S. *et al.* Discovery of novel PI3-kinase δ specific inhibitors for the treatment of rheumatoid arthritis: taming CYP3A4 time-dependent inhibition. *J. Med. Chem.* **55**, 5887–5900 (2012).

CFIm25 links alternative polyadenylation to glioblastoma tumour suppression

Chioniso P. Masamha^{1*}, Zheng Xia^{2*}, Jingxuan Yang³, Todd R. Albrecht¹, Min Li³, Ann-Bin Shyu¹, Wei Li² & Eric J. Wagner¹

The global shortening of messenger RNAs through alternative polyadenylation (APA) that occurs during enhanced cellular proliferation represents an important, yet poorly understood mechanism of regulated gene expression^{1,2}. The 3' untranslated region (UTR) truncation of growth-promoting mRNA transcripts that relieves intrinsic microRNA- and AU-rich-element-mediated repression has been observed to correlate with cellular transformation³; however, the importance to tumorigenicity of RNA 3'-end-processing factors that potentially govern APA is unknown. Here we identify CFIm25 as a broad repressor of proximal poly(A) site usage that, when depleted, increases cell proliferation. Applying a regression model on standard RNA-sequencing data for novel APA events, we identified at least 1,450 genes with shortened 3' UTRs after CFIm25 knockdown, representing 11% of significantly expressed mRNAs in human cells. Marked increases in the expression of several known oncogenes, including cyclin D1, are observed as a consequence of CFIm25 depletion. Importantly, we identified a subset of CFIm25-regulated APA genes with shortened 3' UTRs in glioblastoma tumours that have reduced CFIm25 expression. Downregulation of CFIm25 expression in glioblastoma cells enhances their tumorigenic properties and increases tumour size, whereas CFIm25 overexpression reduces these properties and inhibits tumour growth. These findings identify a pivotal role of CFIm25 in governing APA and reveal a previously unknown connection between CFIm25 and glioblastoma tumorigenicity.

Recently, it has become increasingly clear that mRNA 3'-end formation is subject to dynamic regulation under diverse physiological conditions^{2–5}. Over 50% of human genes have multiple polyadenylation signals, thereby increasing the potential diversity in mRNA transcript length⁶. The formation of mRNA transcripts using these distinct poly(A) sites (PASs) is carried out by APA, with the most common form involving differential use of alternative PASs located within the same terminal exon (reviewed in ref. 7). Processing at the PAS most proximal to the stop codon (pPAS) removes negative regulatory elements that reduce mRNA stability or impair translation efficiency, such as AU-rich elements (AREs)⁸ and microRNA (miRNA) targeting sites^{9,10}. It has been reported that both rapidly proliferating cells^{1,2} and transformed cells^{3,11} preferentially express mRNAs with shortened 3' UTRs. Despite these observations, the mechanisms that control the extensive distal-to-proximal PAS switch observed in proliferative and/or transformed cells, the relationship between cause and effect, and the critical target genes subject to this regulation, are not well characterized.

To measure relative changes in endogenous APA events, we devised a quantitative polymerase chain reaction after reverse transcription (qRT-PCR) assay to monitor the transcript-specific use of the distal PAS (dPAS) while normalizing for total mRNA levels for three test transcripts, cyclin D1 (*CCND1*), *DICER1* and *TIMP2*, known to undergo APA^{3,12}. Using this approach, we readily detected appreciable usage of dPASs for all three genes in HeLa cells (Extended Data Fig. 1). This was somewhat surprising given their highly transformed state, but is consistent with

previous reports that not all transformed cells tested exhibit appreciable 3' UTR shortening^{1,3}. Previous studies implicate multiple members of the cleavage and polyadenylation (CPA) machinery as potentially regulating poly(A) site selection^{12–15}. To test the relative contribution of these factors to the APA of the three test genes, we used systematic RNA interference (RNAi) (Fig. 1a–c). We observed only small changes in the relative use of the dPAS after knockdown of members of the cleavage and polyadenylation specificity factor (CPSF), cleavage stimulation factor (CSTF) and cleavage factor IIm (CFIIm) complexes (Fig. 1d–f). By contrast, we detected significant reduction in dPAS usage after knockdown of the members of the CFIm complex. These results are consistent with a recent report that CFIm68 depletion decreases 3' UTR length¹⁴; however, the most notable PAS switching was found to occur after knockdown of CFIm25. We therefore focused all further analyses on CFIm25.

Traditional methods of global PAS profiling use mRNA partitioning and digestion to sequence poly(A) junctions within messages^{1,16,17}. To identify global targets of CFIm25 with a more streamlined approach requiring less sample manipulation, we performed high-depth ($>3 \times 10^8$ reads) RNA sequencing (RNA-seq) after knocking down CFIm25 in parallel with a control knockdown. We determined that 23% of RNA-seq reads can be uniquely mapped to 3' UTRs of expressed genes leading to approximately 200-fold sequence coverage (Extended Data Fig. 2a, b). We first analysed the three test genes and observed markedly reduced read density within the 3' UTRs in response to CFIm25 depletion (Fig. 2a). These results not only confirm our qRT-PCR findings that HeLa cells robustly use the dPAS for all three test genes under basal conditions but also demonstrate that considerable 3' UTR shortening induced by CFIm25 knockdown is readily visualized by analysing the read density of RNA-seq data.

On the basis of this promising observation, we applied a novel bioinformatics algorithm termed 'dynamic analysis of alternative polyadenylation from RNA-seq' (DaPars; see Methods) for the *de novo* identification of all instances of 3' UTR alterations between control and CFIm25 knockdown cells, regardless of a pre-annotated pPAS within each RefSeq transcript. DaPars uses a linear regression model to identify the exact location of this novel proximal 3' UTR as the optimal fitting point (Fig. 2b, red point) as well as the abundance of both novel and annotated UTRs. The degree of difference of 3' UTR usage between the samples was then quantified as a change in percentage dPAS usage index (Δ PDUI), which is capable of identifying lengthening (positive index) or shortening (negative index) within the 3' UTR. When applied to the 12,273 RefSeq transcripts whose average terminal exon sequence coverage is more than 30-fold, DaPars identified 1,453 transcripts possessing a significant, reproducible shift in 3' UTR usage in response to CFIm25 depletion (Fig. 2c and Extended Data Fig. 2c, d). Notably, among this group of transcripts, 1,450 are shifted to pPAS usage in CFIm25 knockdown cells. We found a significant enrichment of the CFIm25 UGUA binding motif and previously reported CFIm25 iCLIP sequence tags¹⁴ within 3' UTRs that shortened after CFIm25 knockdown relative to transcripts exhibiting no length change (Extended Data Fig. 3).

¹Department of Biochemistry and Molecular Biology, The University of Texas Medical School at Houston, Houston, Texas 77030, USA. ²Division of Biostatistics, Dan L. Duncan Cancer Center and Department of Molecular and Cellular Biology, Baylor College of Medicine, Houston, 77030 Texas, USA. ³The Vivian L. Smith Department of Neurosurgery, The University of Texas Medical School at Houston, Houston, Texas 77030, USA.

*These authors contributed equally to this work.

Figure 1 | CFIm25 depletion leads to consistent and robust 3' UTR shortening of test genes.

a–c, Western blot analysis of HeLa cell lysates treated with control siRNA (Con.) and siRNAs individually targeting each of the CPA machinery and Symplekin (Sym.). In all cases, tubulin (Tub.) was used as a loading control. **d–f**, Quantified results of three biologically independent qRT-PCR experiments on RNA isolated from cells represented in panels **a–c** with the factors presented in the same order as shown in western blots **a–c**. See Methods for quantification details.

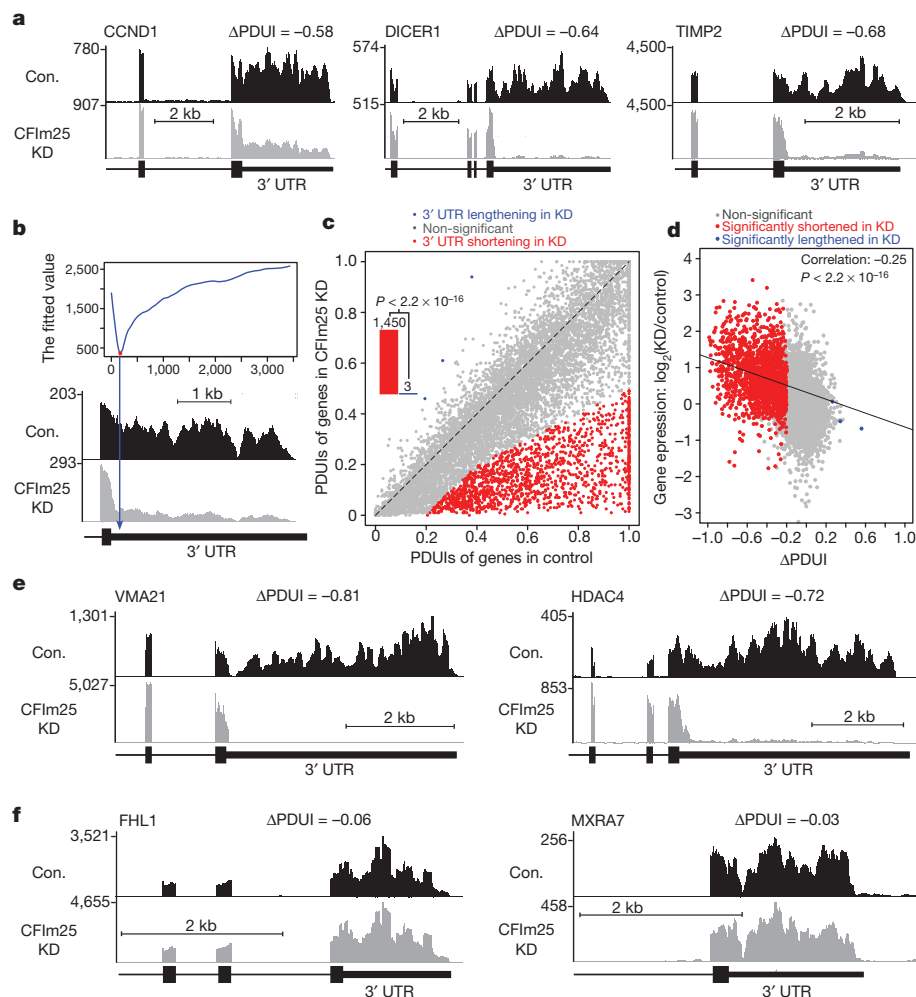
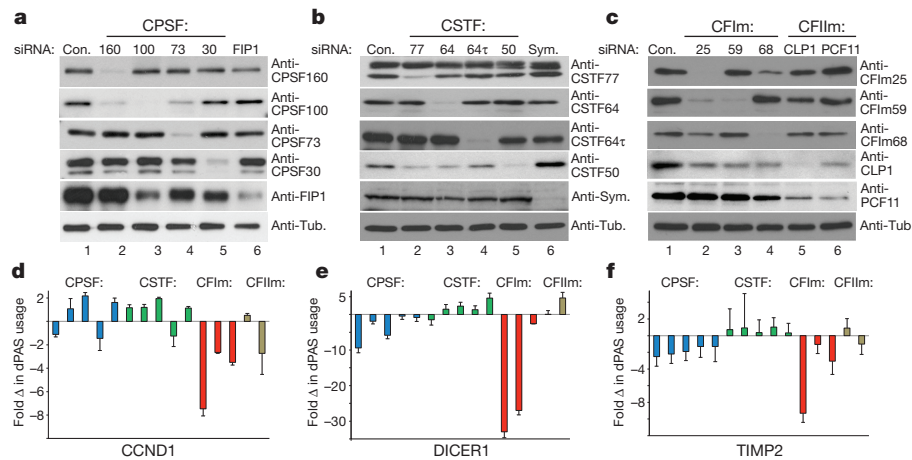


Figure 2 | The DaPars algorithm identifies broad targets of CFIm25 in standard RNA-seq data. **a**, RNA-seq read density for 3' UTR, terminal exon and upstream exon(s) after the control (Con.) siRNA treatment and CFIm25 knockdown (KD) in HeLa cells. Numbers on y-axis indicate RNA-seq read coverage. **b**, Diagram depicts how the differential alternative 3' UTR usage was identified based on DaPars. The y-axis shows the fitting value of the DaPars regression model and the locus with minimum fitting value (red point) is the predicted alternative pPAS for the RNA-seq data (bottom). **c**, Scatterplot of PDUIs in control and CFIm25 knockdown cells where mRNAs significantly shortened ($n = 1,450$) or lengthened ($n = 3$) after CFIm25 knockdown (false discovery rate (FDR) ≤ 0.05 , absolute $\Delta\text{PDUI} \geq 0.2$ and

at least twofold change of PDUIs between CFIm25 knockdown and control cells) are coloured. The shifting towards pPAS is significant ($P < 2.2 \times 10^{-16}$, binomial test). **d**, Correlation between dPAS site usage and gene expression levels of control and CFIm25 knockdown cells. The x-axis shows ΔPDUI ; a negative value indicates that pPAS is prone to be used in CFIm25 knockdown cells. The y-axis shows the logarithm of the expression level of genes from the CFIm25 knockdown relative to the control sample. **e**, Representative RNA-seq density plots along with ΔPDUI values for genes whose 3' UTR is shortened in response to CFIm25 knockdown. Numbers on y-axis indicate RNA-seq read coverage. **f**, Representative RNA-seq density plots along with ΔPDUI values of genes whose 3' UTR is unchanged by CFIm25 knockdown.

Moreover, we determined that 70% of transcripts whose 3' UTR is shortened after CFIm25 knockdown use a pPAS within the first one-third of their 3' UTR. By contrast, only 29% of multi-PAS transcripts that did not alter 3' UTR length in response to CFIm25 have an annotated pPAS in the first third of their 3' UTR. This demonstrates that CFIm25 APA targets are enriched with pPASs positioned close to the stop codon to maximize their degree of 3' UTR shortening. Collectively, these results clearly indicate that the function of CFIm25 is to broadly repress proximal poly(A) site choice, and consequently, the shortening of 3' UTR length is considerable for the majority of CFIm25-regulated transcripts upon its depletion.

One potential consequence of 3' UTR shortening in CFIm25 knockdown is the loss of miRNA-binding sites and/or AREs, resulting in truncated mRNA transcripts that evade negative regulation. Although the correlation between transcript expression change and Δ PDI was modest (Pearson correlation = -0.25), it does reveal that transcripts with shorter 3' UTR in CFIm25 knockdown cells have overall higher expression levels (Fig. 2d). We observed that 64% of transcripts with shortened 3' UTRs exhibited significantly increased steady-state levels, 34% were unchanged, and only 2% were significantly reduced (Extended Data Fig. 4). We have also organized the list of CFIm25-regulated genes with respect to their Δ PDI score, change in relative levels of transcript, and predicted numbers of ARE motifs and miRNA target sites lost after APA (Supplementary Table 1) and observed that gene expression positively correlates with the number of lost ARE motifs and miRNA target sites (Extended Data Fig. 5). Several examples of novel genes whose APA is regulated by CFIm25 are shown in Fig. 2e and it is important to note that not all long 3' UTRs were observed to shorten in response to CFIm25 knockdown, indicating that the CFIm complex regulates many, but not all genes capable of APA (Fig. 2f). Collectively, these data demonstrate the power and ease of the DaPars algorithm to identify APA within standard RNA-seq, and indicate that the major form of CFIm25 regulation is to repress pPAS choice at a global level.

To validate the Δ PDI results, we created qRT-PCR amplicons to monitor dPAS usage of six genes whose 3' UTRs were found to be shortened after CFIm25 knockdown and two that were not altered. Using these amplicons, we analysed RNA isolated from cells effectively depleted of CFIm25 using two independent short interfering RNAs (siRNAs) (Fig. 3a, inset), and observed high congruence between qRT-PCR results and those obtained using RNA-seq and Δ PDI (Fig. 3a, graph). To test formally for the presence of de-repressed protein expression from mRNAs with shortened 3' UTRs, we measured their levels in lysates from knockdown cells (Fig. 3b). We observed considerable increases in protein levels of CFIm25 target genes, including several that have a well-documented role in tumour growth, such as cyclin D1, glutaminase and methyl-CpG-binding protein 2 (MECP2)^{18–22}. It is worth noting that the 3' UTR of each of these genes has been shown to be subject to miRNA-mediated inhibition^{23–25}. Consistent with this observation, we also noted enhanced cellular proliferation in response to knockdown of CFIm25 relative to control knockdown in HeLa cells (Fig. 3c). Finally, to determine whether the 3' UTR is sufficient to elicit translational de-repression of a heterologous protein in response to CFIm25 knockdown, we used reporters with the SMOC1 3' UTR cloned downstream of luciferase or the GAPDH 3' UTR, which was not found to alter its poly(A) site usage. We observed that only the luciferase activity specifically resulting from the luciferase-SMOC1 reporter was increased in response to knockdown of CFIm25 (Fig. 3d), supporting the idea that the increased expression of endogenous SMOC1 protein when CFIm25 is depleted is mediated through its 3' UTR.

The collective observations that CFIm25 depletion leads to broad 3' UTR shortening, enhanced expression of growth promoting genes and increased cell proliferation support the hypothesis that CFIm25 is a novel anti-proliferative gene whose levels may be reduced in human cancers. We focused our analysis on glioblastoma, as recent reports indicate that brain tissue possesses the longest 3' UTRs^{26,27}. We reasoned that tumours derived from these cells might be more sensitive to changes in CFIm25 levels than other cancers. To test this prediction, we downloaded

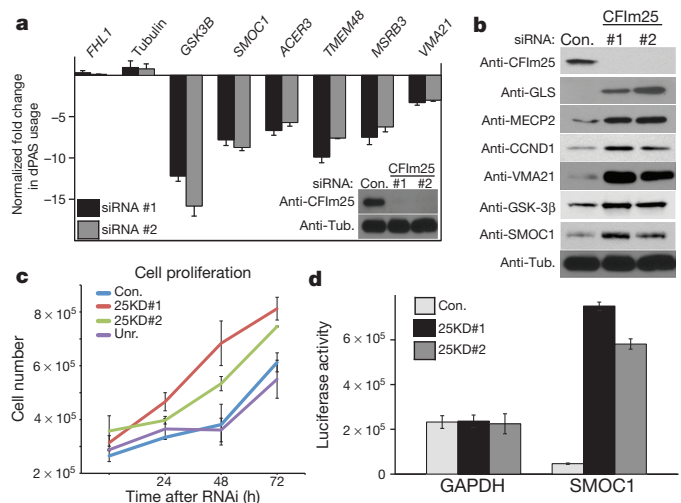


Figure 3 | Increased pPAS usage after CFIm25 depletion results in increased protein translation and enhanced cell proliferation. **a**, qRT-PCR results of select genes shown as fold change in dPAS usage after CFIm25 depletion. Experiments were performed in triplicate with data shown as mean \pm standard deviation from the mean (s.d.). The inset shows western blot analysis demonstrating effective knockdown of CFIm25 using two distinct siRNAs. Tub., tubulin. **b**, Results of western blot analysis of cell lysates after knockdown of CFIm25 using siRNA. **c**, Growth of HeLa cells was measured after RNAi of CFIm25 compared with cells transfected with control siRNA or the siRNA to the CFIm complex subunit PCF11 (Unr.). Results shown are mean \pm standard deviation (s.d.) ($n = 3$). **d**, Graph representing luciferase activity from cells transfected with a luciferase reporter containing the 3' UTR of either GAPDH or of SMOC1 after being transfected with either control or CFIm25 siRNA. Data are the average of three independent experiments and error bars show s.d.

archived patient RNA-seq data from The Cancer Genome Atlas (TCGA), stratified it according to CFIm25 expression, and analysed it using DaPars. Indeed, following the same cut-offs in our HeLa RNA-seq 3' UTR analysis, we identified 60 genes with altered 3' UTRs, with 59 of those experiencing shortening in glioblastoma expressing lower levels of CFIm25 (Fig. 4a and Supplementary Table 2). Among those genes, a significant number of events (24 genes; $P = 2.2 \times 10^{-12}$ by hypergeometric testing) were also shortened in CFIm25 knockdown HeLa cells and this percentage of overlap increased markedly to 86% as the Δ PDI cut-off increased from 0.2 to 0.4 (Extended Data Fig. 6). Two representative examples of genes, FOS-related antigen 2 (*FRA2*; also known as *FOSL2*) and *MECP2*, with shortened 3' UTRs in low CFIm25-expressing glioblastoma tumours is shown in Fig. 4b, demonstrating a compelling similarity between the patient samples and HeLa cells before and after CFIm25 knockdown. Overexpression of either of these genes has been shown to enhance cell proliferation^{18,28}.

To test formally whether altering CFIm25 expression can modulate glioblastoma tumorigenic properties, we screened a panel of glioblastoma cell lines and observed that U251 cells naturally express lower levels of CFIm25 compared with LN229 cells (Fig. 4c). To raise CFIm25 levels in U251 cells, we created cell lines stably expressing either Myc-tagged CFIm25 or green fluorescent protein (GFP) as a control. In parallel, we used RNAi to reduce CFIm25 levels in LN229 cells (Fig. 4c). We observed a significant reduction in anchorage-dependent growth and cellular invasion in U251 cells overexpressing CFIm25 compared with the GFP control, whereas reducing CFIm25 in LN229 cells caused an increase in both of these properties (Extended Data Fig. 7). To determine if the altered *in vitro* properties of glioblastoma cells affected tumour growth kinetics *in vivo*, we used a subcutaneous xenograft model. Increased expression of CFIm25 in U251 cells resulted in a marked reduction in tumour growth and decreased tumour cell proliferation (Fig. 4d and Extended Data Fig. 8). By contrast, depletion of CFIm25 in LN229 cells caused a profound increase in tumour size (Fig. 4e and Extended

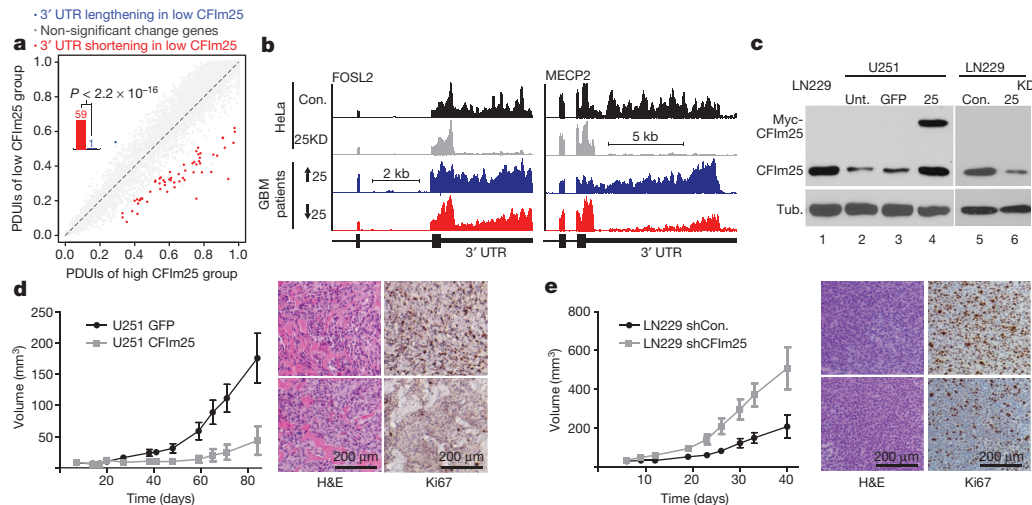


Figure 4 | Altered expression of CFIm25 modulates glioblastoma tumour growth. **a**, The global analysis of 3' UTR changes in glioblastoma (GBM) patient samples with either high or low levels of CFIm25. Scatterplot of PDIUs from both data sets using the same cut-offs as in Fig. 2c. The shifting to pPAS in the low CFIm25 group is significant ($P < 2.2 \times 10^{-16}$; binomial test). **b**, Representative UCSC Genome Browser images of RNA-seq data, demonstrating 3' UTR shortening after CFIm25 knockdown in HeLa cells and in glioblastoma patient samples with high (blue) or low CFIm25 expression (red). KD, knockdown. **c**, Western blot analysis of lysates from two glioblastoma cell lines. Note that the overexpressed Myc-CFIm25 also increases endogenous CFIm25 levels in U251 cells. Tub., tubulin; Unt.,

untreated. **d**, Growth comparison of U251 tumours overexpressing either GFP (control) or CFIm25. Data represent the average of ten mice per group. Right panel shows representative haematoxylin and eosin (H&E) and Ki67 staining of U251 GFP tumours (top) or U251 CFIm25 tumours (bottom). Scale bars, 200 μ m. **e**, Growth comparison of LN229 tumours derived from cells transduced with lentiviruses expressing a scrambled short hairpin RNA (shRNA) (control) or with lentiviruses expressing shRNA targeting CFIm25. Data represent the average of ten mice per group. Right panel shows representative H&E and Ki67 staining of LN229 tumours expressing shRNA targeting CFIm25 (top) or LN229 tumours expressing scrambled shRNA (bottom). Scale bars, 200 μ m.

Data Fig. 9). Collectively, these results uncover a tumour suppressive property of CFIm25 in glioblastoma that is probably mediated through its broad repression of APA-dependent mRNA 3' UTR shortening.

We identified CFIm25 among 15 cleavage and polyadenylation factors as a key factor that broadly regulates APA. Importantly, the data presented here also extend our understanding of APA in regulated gene expression through the demonstration that extensive shortening of 3' UTRs causally leads to enhanced cellular proliferation and tumorigenicity, probably through the upregulation of growth promoting factors, such as cyclin D1. These results indicate the importance of 3' UTR usage in cell growth control and underscore the need for further research into the mechanism and regulation of APA and its potential links to other human diseases.

METHODS SUMMARY

Human cell lines used were cultured using standard techniques. RNAi and western blot experiments were conducted as described previously²⁹. For luciferase experiments, one day after the second siRNA hit, cells were transfected with 3' UTR *Renilla* luciferase plasmids and activity was assayed after 24 h. Total RNA for pRT-PCR was reverse transcribed using MMLV-RT (Invitrogen). qRT-PCR reactions were performed using SYBRGREEN (Fermentas). Duplicate control and CFIm25 knockdown samples were sequenced by HiSeq 2000. RNA-seq reads were aligned (hg19) using TopHat 2.0.10³⁰. All the TCGA glioblastoma RNA-seq BAM files were downloaded from the UCSC Cancer Genomics Hub (<https://cghub.ucsc.edu/>). DaPars was used to identify differential 3' UTR usage from RNA-seq (Z.X. *et al.*, unpublished observations; <https://code.google.com/p/dapars/>). For tumour xenografts, U251 cells were stably transfected with GFP or CFIm25 plasmids. LN229 cells were transfected with lentivirus expressing CFIm25 shRNA. After subcutaneous injection of cell lines into nude mice, glioblastoma tumour size was monitored and tumours were removed and histologically analysed.

Online Content Any additional Methods, Extended Data display items and Source Data are available in the online version of the paper; references unique to these sections appear only in the online paper.

Received 30 January 2013; accepted 13 March 2014.

Published online 11 May 2014.

- Elkon, R. *et al.* E2F mediates enhanced alternative polyadenylation in proliferation. *Genome Biol.* **13**, R59 (2012).

- Sandberg, R., Neilson, J. R., Sarma, A., Sharp, P. A. & Burge, C. B. Proliferating cells express mRNAs with shortened 3' untranslated regions and fewer microRNA target sites. *Science* **320**, 1643–1647 (2008).
- Mayr, C. & Bartel, D. P. Widespread shortening of 3'UTRs by alternative cleavage and polyadenylation activates oncogenes in cancer cells. *Cell* **138**, 673–684 (2009).
- Ji, Z., Lee, J. Y., Pan, Z., Jiang, B. & Tian, B. Progressive lengthening of 3' untranslated regions of mRNAs by alternative polyadenylation during mouse embryonic development. *Proc. Natl Acad. Sci. USA* **106**, 7028–7033 (2009).
- Mangone, M. *et al.* The landscape of *C. elegans* 3'UTRs. *Science* **329**, 432–435 (2010).
- Tian, B., Hu, J., Zhang, H. & Lutz, C. S. A large-scale analysis of mRNA polyadenylation of human and mouse genes. *Nucleic Acids Res.* **33**, 201–212 (2005).
- Di Giammartino, D. C., Nishida, K. & Manley, J. L. Mechanisms and consequences of alternative polyadenylation. *Mol. Cell* **43**, 853–866 (2011).
- Chen, C.-Y. A. & Shyu, A.-B. AU-rich elements: characterization and importance in mRNA degradation. *Trends Biochem. Sci.* **20**, 465–470 (1995).
- Farh, K. K. *et al.* The widespread impact of mammalian MicroRNAs on mRNA repression and evolution. *Science* **310**, 1817–1821 (2005).
- Wu, L. & Belasco, J. G. Let me count the ways: mechanisms of gene regulation by miRNAs and siRNAs. *Mol. Cell* **29**, 1–7 (2008).
- Singh, P. *et al.* Global changes in processing of mRNA 3' untranslated regions characterize clinically distinct cancer subtypes. *Cancer Res.* **69**, 9422–9430 (2009).
- Kubo, T., Wada, T., Yamaguchi, Y., Shimizu, A. & Handa, H. Knock-down of 25 kDa subunit of cleavage factor Im in HeLa cells alters alternative polyadenylation within 3'-UTRs. *Nucleic Acids Res.* **34**, 6264–6271 (2006).
- Yao, C. *et al.* Transcriptome-wide analyses of CstF64–RNA interactions in global regulation of mRNA alternative polyadenylation. *Proc. Natl Acad. Sci. USA* **109**, 18773–18778 (2012).
- Martin, G., Gruber, A. R., Keller, W. & Zavolan, M. Genome-wide analysis of pre-mRNA 3' end processing reveals a decisive role of human cleavage factor I in the regulation of 3'UTR length. *Cell Reports* **1**, 753–763 (2012).
- Thomas, P. E. *et al.* Genome-wide control of polyadenylation site choice by CPSF30 in *Arabidopsis*. *Plant Cell* **24**, 4376–4388 (2012).
- Jan, C. H., Friedman, R. C., Ruby, J. G. & Bartel, D. P. Formation, regulation and evolution of *Caenorhabditis elegans* 3'UTRs. *Nature* **469**, 97–101 (2011).
- Shepard, P. J. *et al.* Complex and dynamic landscape of RNA polyadenylation revealed by PAS-Seq. *RNA* **17**, 761–772 (2011).
- Bernard, D. *et al.* The methyl-CpG-binding protein MECP2 is required for prostate cancer cell growth. *Oncogene* **25**, 1358–1366 (2006).
- Scinski, P. *et al.* Cyclin D1 provides a link between development and oncogenesis in the retina and breast. *Cell* **82**, 621–630 (1995).
- Weinstat-Saslow, D. *et al.* Overexpression of cyclin D1 mRNA distinguishes invasive and *in situ* breast carcinomas from non-malignant lesions. *Nature Med.* **1**, 1257–1260 (1995).

21. Liu, W. *et al.* Reprogramming of proline and glutamine metabolism contributes to the proliferative and metabolic responses regulated by oncogenic transcription factor c-MYC. *Proc. Natl Acad. Sci. USA* **109**, 8983–8988 (2012).
22. Wang, J. B. *et al.* Targeting mitochondrial glutaminase activity inhibits oncogenic transformation. *Cancer Cell* **18**, 207–219 (2010).
23. Klein, M. E. *et al.* Homeostatic regulation of MeCP2 expression by a CREB-induced microRNA. *Nature Neurosci.* **10**, 1513–1514 (2007).
24. Deshpande, A. *et al.* 3'UTR mediated regulation of the cyclin D1 proto-oncogene. *Cell Cycle* **8**, 3592–3600 (2009).
25. Gao, P. *et al.* c-Myc suppression of miR-23a/b enhances mitochondrial glutaminase expression and glutamine metabolism. *Nature* **458**, 762–765 (2009).
26. Miura, P., Shenker, S., Andreu-Agullo, C., Westholm, J. O. & Lai, E. C. Widespread and extensive lengthening of 3' UTRs in the mammalian brain. *Genome Res.* **23**, 812–825 (2013).
27. Ulitsky, I. *et al.* Extensive alternative polyadenylation during zebrafish development. *Genome Res.* **22**, 2054–2066 (2012).
28. Nakayama, T. *et al.* Aberrant expression of Fra-2 promotes CCR4 expression and cell proliferation in adult T-cell leukemia. *Oncogene* **27**, 3221–3232 (2008).
29. Wagner, E. J. & Garcia-Blanco, M. A. RNAi-mediated PTB depletion leads to enhanced exon definition. *Mol. Cell* **10**, 943–949 (2002).
30. Trapnell, C., Pachter, L. & Salzberg, S. L. TopHat: discovering splice junctions with RNA-Seq. *Bioinformatics* **25**, 1105–1111 (2009).

Supplementary Information is available in the online version of the paper.

Acknowledgements We would like to thank members of the E.J.W., A.-B.S. and W.L. laboratories for helpful discussions, P. Carpenter for reviewing the manuscript, and Q. Zhu and T. Shan of LC Sciences for their efforts on the RNA-seq. This work was supported by a CPRIT grant to E.J.W. and A.-B.S. (RP100107), and in part by a Department of Defense grant to E.J.W. (W81XWH-11-1-0304), National Institutes of Health (NIH) grants to A.-B.S. (GM046454) and E.J.W. (CA167752 and CA166274), and an endowment from Houston Endowment (to A.-B.S.). Work in the W.L. laboratory is funded by grants from the Department of Defense (W81XWH-10-1-0501), CPRIT (RP110471-C3) and NIH (R01HG007538). Work in the M.L. laboratory is funded by grants from the Dr Marnie Rose Foundation and the William and Ella Owens Medical Research Foundation. C.P.M. acknowledges a Department of Defense Postdoctoral Visionary Award (W81XWH-12-1-0218).

Author Contributions A.-B.S., W.L. and E.J.W. designed the study. C.P.M., T.R.A. and J.Y. performed the described experiments with conceptual advice from M.L. W.L. and Z.X. conducted bioinformatic analyses and developed the DaPars algorithm. C.P.M., Z.X., W.L., A.-B.S. and E.J.W. wrote the manuscript.

Author Information Raw sequence data has been deposited in the Gene Expression Omnibus under accession number GSE42420. Reprints and permissions information is available at www.nature.com/reprints. The authors declare no competing financial interests. Readers are welcome to comment on the online version of the paper. Correspondence and requests for materials should be addressed to E.J.W. (Eric.J.Wagner@uth.tmc.edu), A.-B.S. (Ann-Bin.Shyu@uth.tmc.edu) or W.L. (WL1@bcm.edu).

METHODS

RNA-seq. We used whole transcriptome RNA-seq to investigate alternative PAS usage in a genome-wide fashion. Two control and two CFIm25 knockdown samples were sequenced by HiSeq 2000 (LC Sciences). Paired-end RNA-seq reads with 101 bp in each end were aligned to the human genome (hg19) using TopHat 2.0.10³⁰. RefSeq gene expressions were quantified by RSEM³¹. A statistical summary of read alignments and average gene expressions can be found in Extended Data Fig. 2. More than 12,000 (~50%) human RefSeq genes can be detected through RNA-seq with expression levels more than 1 fragments per kilobase of transcript sequence per million mapped paired-end reads (FPKM)³². More importantly, the average of 23% of RNA-seq reads can be uniquely mapped to 3' UTRs of expressed genes that renders around 200× coverage on UTRs. All the TCGA glioblastoma RNA-seq BAM files were downloaded from the UCSC Cancer Genomics Hub (CGHub; <https://cghub.ucsc.edu/>).

Analysis of APA from RNA-seq. We used a novel bioinformatics algorithm DaPars (Z.X. *et al.*, unpublished observations; <https://code.google.com/p/dapars/>) for the *de novo* identification of APA from RNA-seq. The observed sequence coverage was represented as a linear combination of novel and annotated 3' UTRs. For each RefSeq transcript with annotated PAS, we used a regression model to infer the end point of alternative novel PAS within this 3' UTR at single nucleotide resolution, by minimizing the deviation between the observed read coverage and the expected read coverage based on a two-PAS model, in both control and CFIm25 knockdown samples simultaneously.

To quantify the relative PAS usage, we defined the percentage of dPAS usage for each sample as PDUI index. The greater the PDUI is, the more the dPAS of a transcript is used and vice versa.

ΔPDUI. We used the following three criteria to detect the most significant shifted 3' UTR events: First, given the expression levels of short and long 3' UTRs in two samples in each condition, we compute the significance of the difference of mean PDUIs using Fisher's exact test, which is further adjusted by Benjamini-Hochberg (BH) procedure to control the FDR at a level of 5%. Second, the absolute difference of mean PDUIs must be no less than 0.2. Third, the absolute log₂ ratio (fold change) of mean PDUIs must be no less than 1. To avoid false positive estimation on low coverage transcripts, we required that there be more than 30-fold coverage on the 3' UTR region of both samples. For genes with multiple annotated PASs, we only kept the one with the greatest absolute ΔPDUI value. Last, we identified 1,453 transcripts possessing a significant shift in 3' UTR usage in response to CFIm25 knockdown, the vast majority of which have shortened 3' UTRs in CFIm25 knockdown.

Bioinformatic analyses of 3' UTR shortening. As miRNA binding sites and other regulatory sequences such as AREs reside in 3' UTRs^{33,34}, APA has an important role in mRNA stability, translation and translocation. Indeed, it has been reported that shorter 3' UTRs produce higher levels of protein³. To elucidate the consequences of 3' UTR shortening, we provided the numbers of lost ARE motifs and miRNA binding sites due to the 3' UTR shortening for the transcripts shifting to proximal 3' UTR usage in CFIm25 knockdown cells (Supplementary Table 1). The ARE is one of the most prominent *cis*-acting regulatory elements found in 3' UTRs to target mRNAs for rapid degradation³⁵. The eight different consensus ARE motifs, including the plain AUUUA pentamer, were retrieved from the ARE site database³⁵. miRNA-mRNA binding information was based on miRNA target prediction database TargetScanHuman version 6.2^{36–38}. To limit the miRNA to high-confidence sites, we required the probability of the preferentially conserved targeting (PCT) score to be more than 0 for all highly conserved miRNA families³⁸.

Differentially expressed gene expression analysis. With two replicates in each group, we used edgeR³⁹ to call differentially expressed genes with FDR < 0.05. To better quantify gene expression with shorter 3' UTRs, we counted reads based on the coding regions of each transcript.

Cell culture and cell counts. All the cell lines used (HeLa, U251 and LN229) were cultured in DMEM supplemented with 10% FBS (+1% penicillin and streptomycin) in a 5% CO₂ incubator at 37 °C. Cell counts were done using a standard hemacytometer.

siRNA and western blot assays. Both siRNA transfection and western blot analysis were performed as previously described²⁹. The siRNA was purchased from Sigma and all the siRNAs used are shown below. After transfection, cells were harvested for mRNA extraction, western blotting or Matrigel assay. To detect 3'-end-processing factors by western blotting, the following primary antibodies from Bethyl Laboratories were used: CPSF160, CPSF100, CPSF73, CPSF30, FIP1, CSTF77, CSTF64t, CSTF50, CFIm68 and CFIm59. Other antibodies used include CFIm25 (PTGlabs), CSTF64 and CFIm PCF11, and Symplekin (Sigma) and CFIm CLP1 (Epitomics). Additional antibodies include VMA21, GLS, ACER3 and GSK-3β (PTGlabs); cyclin D1 (Cell Signaling); and SMOC1 and tubulin (Abcam).

siRNA sequences. We used the following siRNA sequences. CPSF160 si1: 5'-GC UUUAAGAAGGUCCCUCA; si2: 5'-CUUACCACGUGGAGUCUAA; CPSF100 si1: 5'-CUCAACUUCUUGAUCAGAU; si2: 5'-GGAUAGAUGGUGUCUAG

A; CPSF73 si1: 5'-CCAUAUACUGGUCCCUUUA; si2: 5'-GAUAUUGGAAGU UCAGUCA; CPSF30 si1: 5'-GUGCCUAUAUCUGUGAUUU; si2: 5'-CCUAUA UCUGUGAUUUUGAA; FIP1 si1: 5'-CGAAUGGGACUUGAAGUUA; si2: 5'-GA CAAGUACUGCCUCCAGA; CSTF77 si1: 5'-GAAGACUUAUGAACGCCUU; si2: 5'-CACAGAAUCAACCUAUGA; CSTF64 si1: 5'-GGCUUUAGUCCCGG GCAGA; si2: 5'-GGUUAUGGCUUCUGUGAAU; CSTF64t si1: 5'-GUCUUAG AGACACGUGUAA; si2: 5'-CUAAUGUUCUGUGAACCA; CSTF50 si1: 5'-G UCGUAAGUCCGUGCACCA; si2: 5'-CUACUUCUCCGUUUUAUGA; Symplekin si1: 5'-CAGUUAACUCGGGCCUGA; si2: 5'-GAGACAUUGAGUUGCGUCU; CFIm25 si1: 5'-CCUCUUACCAUUUAUACUU; si2: 5'-GCUAUAUACAGUG UAGAAU; CFIm59 si1: 5'-CUCAUCUGUCUGUGUGGAU; si2: 5'-GCAAUU UCCAGCAGUGCCA; CFIm68 si1: 5'-CUGCAAUUUCUUUUAAUUA; si2: 5'-GGAACAAGACGUGAACGAU; CFIm CLP1 si1: 5'-GCUUAUGUCUCAA GGACA; si2: 5'-CAGUUCAGUUGGAGUUGUU; CFIm PCF11 si1: 5'-GUAC CUUAUGGAUUCUUAU; si2: 5'-GUAUCUCACUGCCUUUACU) and the control siRNA used was described elsewhere²⁹.

qRT-PCR. After appropriate transfections, total RNA was extracted using TRIzol Reagent (Life Technologies) using the manufacturer's protocol. For qRT-PCR the mRNA was reverse transcribed using MMLV-RT (Invitrogen) using the manufacturer's protocol to generate cDNA. The qRT-PCR reactions were performed using Stratagene MxPro3000P (Agilent Technologies) and SYBRGREEN (Fermentas). Common primers were designed to target the open reading frame and normalize for total transcript. The distal primers were designed to target sequences just before the dPAS and detect long transcripts that use the dPAS. All primers used are shown below. Data were calculated using a modified version of the 2^{-ΔΔCT} method to show changes in dPAS usage, where CT is the threshold cycle. First, the CT values for the common and distal amplicons were normalized to the levels of 7SK, where ΔCT (common or distal) = CT_{common or distal} - CT_{7SK}. Then ΔΔCT = ΔCT_{distal} - ΔCT_{common} (note that we applied the correction factor for difference in amplification efficiency calculated in Extended Data Fig. 1). To show fold changes normalized to the control siRNA-transfected samples the following equation was used: normalized ΔΔΔCT = ΔΔCT_{average target siRNA} - ΔΔCT_{average of control siRNA}. Then the decrease (-) or increase (+) in dPAS usage was calculated as ±2^{normalized ΔΔΔCT}.

Oligonucleotides used for qRT-PCR. Cyclin D1 common forward, 5'-CTGC CAGGACGATCGAAG; reverse, 5'-AATGCTCCGGAGAGAGGGACT; distal forward, 5'-ATCGAGAGGCCAAAGGCT; reverse, 5'-CGTCTTTTGTGTC TTCTGCTGGA; DICER1 common forward, 5'-CTCATTATGACTTGCTATGT CGCCTTG; reverse, 5'-CACAATCTCATGCTGGTGAGAG; distal forward 5'-TGCTTTCCGAGTCCTAACTATG; reverse, 5'-AATGCCACAGACAAAAAT GACC; TIMP2 common forward, 5'-CAACCCTATCAAGAGGATCCAGAT; reverse, 5'-GATGTCGAGAACTCCTGCTTG; distal forward, 5'-GACATCA GCTGTAATCATTCCTGTG; reverse, 5'-CGATGCCAAATGGAGAGC; FHL1 common forward, 5'-CTGGCACAAGACTGCTTCACTGTG; reverse 5'-GAT TGTCCTTCATAGGCCACCACTGG; distal forward, 5'-GCCAGGGCTGT CATCAACATGGATA; reverse 5'-TGCATTTCAAGTAAGCGGTAGGTGGA; tubulin common forward, 5'-GAAGGCTCATCTCCACTTTGGAAG; reverse, 5'-TGCTAGCAGTGTCTCATGCTCG; distal forward, 5'-GCATCAGTAGCTG AGTGCACCTCTGGT; reverse, 5'-GTAGAGGGTATGAAGGGCAAGAACTCT; VMA21 common forward, 5'-GATAAGGCGGCGCTGAACGCACTGG; reverse, 5'-TGAGCCTTCATCCAGGCCACATACACA; distal forward, 5'-CATCTGC ACAGCACCTTACAGTTTGC; reverse, 5'-GAAATCGAGCACATCCAAATC CTCCC; GSK-3β common forward, 5'-CTGGTCCGAGGAGAACCCATGTT TCG; reverse, 5'-CAGCCAACACAGCCAGCAGACCATAC; distal forward, 5'-GAGCTGAGCCCATGTTGTGTGTAAAC; reverse, 5'-GGTTCACTTCAG CAGGCAGGACAACCTC; SMOC1 common forward, 5'-CTCTGATGGCAGGT CCTACGATCCA; reverse, 5'-GTATGGCACTGCACCTGGGTAAAGGAG; distal forward, 5'-GAGTCTGCAATTGTACTGCGGACTCCA; reverse 5'-CA TGGGATCTGGACTCCCTTCCTCTC; ACER3 common forward, 5'-CAGCT GGACTGGTGGAGGAGAACT; reverse, 5'-GTGGAAGCACCAGGATCCCA TTCCTACC; distal forward, 5'-CTGTTCAAGCTAATACAGCATTTTCT; reverse, 5'-GTGAATAAGCAGACTGAGATTACCTG; TMEM48 common forward, 5'-CATTCATCTCAGCAACTCATGCATCT; reverse 5'-CTGTTAGTACCACT GCAGGGAACCAC; distal forward, 5'-GTGCTGTGTACTAAATACAGGCCA CATAGTG; reverse 5'-CCTGGTTCCAACAGATGGTGTGTAGA; MSRB3 common forward, 5'-CTCTGGGAAGTGCGCAGTCCGGGT; reverse, 5'-GTCCCTT TCTCCTGAGTGACATGG; distal forward, 5'-GCAGGATATGGAGTGCAATG AACTGAG; reverse, 5'-ACAGTAAGAGCTGGATGCAGAGA; 7SK forward, 5'-GACATCTGTACCCCCATTGATC; reverse, 5'-TCTGCAGTCTTGAAGC TTGAC.

Luciferase assays. One day after a second hit with siRNA (as described earlier), HeLa cells were transfected with 0.25 μg of gene-specific 3' UTR *Renilla* luciferase plasmids (SMOC1 and GAPDH from Switchgear Genomics) using Lipofectamine

2000 (Invitrogen). *Renilla* luciferase activity was assayed 24 h after plasmid transfection using Stop and Glo reagent (Promega).

Generation of stable cell lines. LN229 cells were transfected with CFIm25-specific shRNA or control shRNA using polybrene in 6-well plates. Two days after lentiviral transfection cells were transfected with a second hit of lentivirus. Selection was done using $1 \mu\text{g ml}^{-1}$ of puromycin over 2 weeks. U251 cells were transfected with either GFP or CFIm25 expressing pcDNA3 plasmids using Lipofectamine 2000 (Invitrogen) according to the manufacturer's protocol. Selection was performed over 1–2 weeks using 2.5 mg ml^{-1} of G418.

Soft agar assay. Soft agar assays were used to determine anchorage-dependent growth. For the base layer, 1% of UltraPure low melting point agarose (Invitrogen) was mixed 1:1 with $2\times$ DMEM media and plated in 6-well plates giving a 1.5 ml bottom layer of 0.5% agar. Then 3×10^4 cells of LN229 shRNA stably transfected cells were titrated into $2\times$ DMEM and mixed with an equal volume of 0.6% agar to give a 0.3% layer and 1.5 ml was dispensed into each well. The agar was covered with 1 ml of $1\times$ DMEM and incubated in a humidified incubator at 37°C (5% CO_2). Fresh media was added once a week. After 2 weeks, colonies formed were stained with 0.01% crystal violet, photographed and counted. For U251 plasmid transfected cells the same protocol was followed except that a third (0.3%) layer of agar was plated on top of the layer containing the cell suspension.

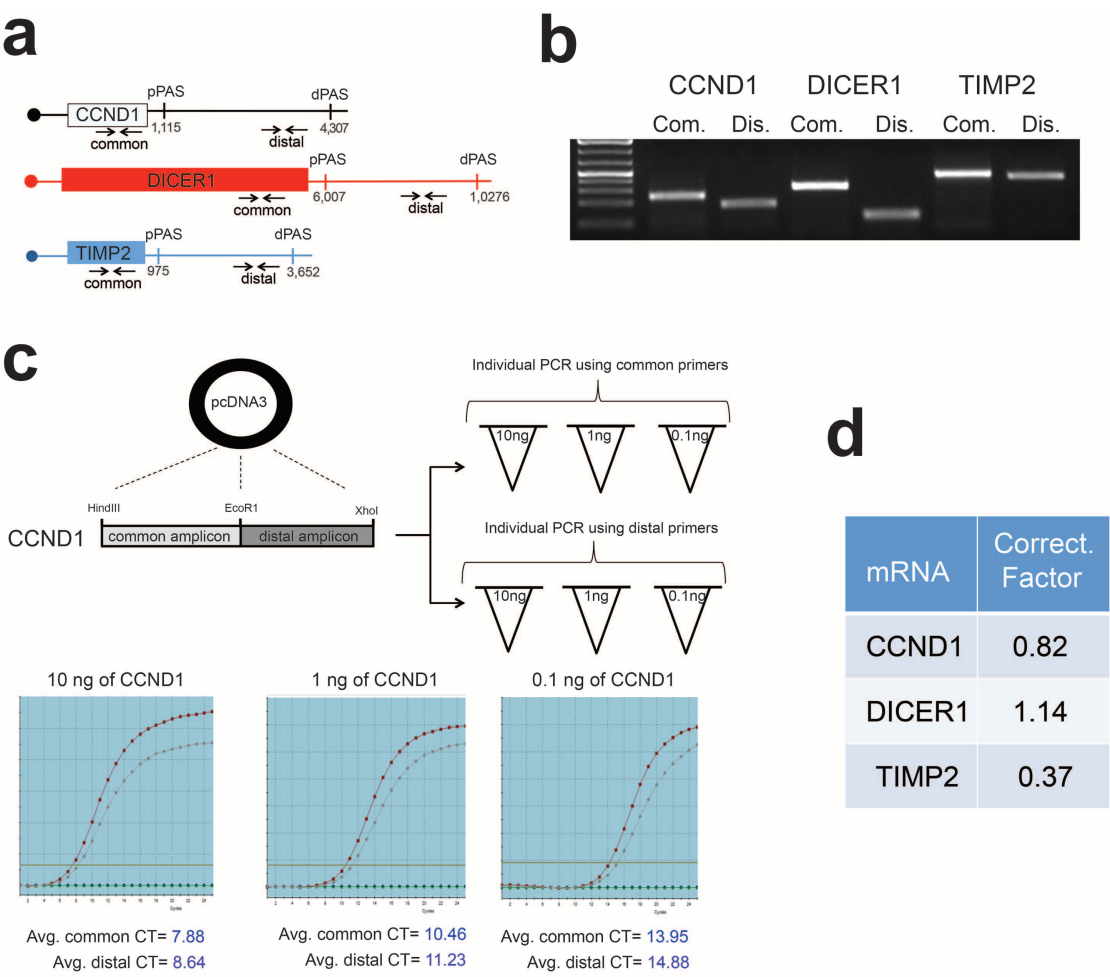
Matrigel invasion assay. The Matrigel invasion assay was performed following the manufacturer's protocol. Briefly, the 6-well BioCoat Matrigel Invasion Chamber (Becton Dickinson) was rehydrated with FBS free DMEM. The Matrigel trans-well inserts were then transferred to 6-well plates containing 10% FBS on the bottom. U251 siRNA-transfected or LN229 shRNA-transfected cells were plated (5×10^5 cells per well) in triplicate wells of the upper chamber in serum-free media. After 24 h, cells were stained with 0.01% crystal violet, and the number of invading cells was counted at $\times 20$ magnification in 10 fields for each well.

Statistical tests. Unless otherwise specified, experiments were done using three biological replicates and data are shown as average \pm s.d., and statistical analysis was done using a two-tailed student *t*-test.

Subcutaneous xenograft tumour model. Hsd:Athymic Nude-Foxn1nu nude mice at age 5–6 weeks were used. For each cell line (LN229 or U251), 20 male nude mice

were randomly assigned into two groups ($n = 10$). Stably transfected LN229 and U251 cells were resuspended in pure culture medium with the concentration of 3×10^7 cells ml^{-1} . One-hundred-microlitre cell suspensions (3×10^6 cells) were inoculated subcutaneously into the lower right flank of the mice using a 27-gauge needle. Tumour diameters are measured with digital callipers, and the tumour volume in mm^3 is calculated by the formula: volume = (width)² \times length/2. The tumour size data were collected and processed blindly. The animal experiments were performed under the Institutional Review Board approved animal protocol AWC-13-115.

31. Ward, A. & Dutton, J. R. Regulation of the Wilms' tumour suppressor (*WT1*) gene by an antisense RNA: a link with genomic imprinting? *J. Pathol.* **185**, 342–344 (1998).
32. Trapnell, C. *et al.* Transcript assembly and quantification by RNA-Seq reveals unannotated transcripts and isoform switching during cell differentiation. *Nature Biotechnol.* **28**, 511–515 (2010).
33. Kaplan, P. J., Mohan, S., Cohen, P., Foster, B. A. & Greenberg, N. M. The insulin-like growth factor axis and prostate cancer: lessons from the transgenic adenocarcinoma of mouse prostate (TRAMP) model. *Cancer Res.* **59**, 2203–2209 (1999).
34. Fabian, M. R., Sonenberg, N. & Filipowicz, W. Regulation of mRNA translation and stability by microRNAs. *Annu. Rev. Biochem.* **79**, 351–379 (2010).
35. Bräulke, T., Dittmer, F., Gotz, W. & von Figura, K. Alteration in pancreatic immunoreactivity of insulin-like growth factor (IGF)-binding protein (IGFBP)-6 and in intracellular degradation of IGFBP-3 in fibroblasts of IGF-II receptor/IGF-II-deficient mice. *Horm. Metab. Res.* **31**, 235–241 (1999).
36. Hu, J. F. *et al.* Lack of reciprocal genomic imprinting of sense and antisense RNA of mouse insulin-like growth factor II receptor in the central nervous system. *Biochem. Biophys. Res. Commun.* **257**, 604–608 (1999).
37. Ellis, M. J. *et al.* Insulin-like growth factors in human breast cancer. *Breast Cancer Res. Treat.* **52**, 175–184 (1998).
38. Friedman, R. C., Farh, K. K.-H., Burge, C. B. & Bartel, D. P. Most mammalian mRNAs are conserved targets of microRNAs. *Genome Res.* **19**, 92–105 (2009).
39. Gómez-Angelats, M., Teeguarden, J. G., Dragan, Y. P. & Pitot, H. C. Mutational analysis of three tumor suppressor genes in two models of rat hepatocarcinogenesis. *Mol. Carcinog.* **25**, 157–163 (1999).



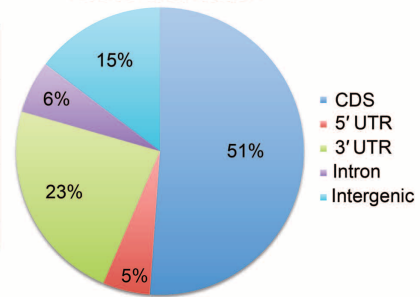
Extended Data Figure 1 | Design and optimization of the qRT-PCR assay to monitor APA of three test genes. **a**, Schematic denotes the relative location of the common and distal primer annealing sites in each test gene and the approximate locations of the annotated proximal and distal poly(A) sites, depicted as pPAS and dPAS, respectively. The numbers demarcate where the 3' UTR starts and ends according to ENSEMBL. **b**, Ethidium-stained agarose gel of RT-PCR products of equal cycle number from the different amplicons using HeLa cell mRNA. **c**, Both the common and distal cyclin D1 amplicons were cloned into the same pcDNA3 plasmid in tandem. Three dilutions of each plasmid were made and amplified individually with each amplicon in

triplicate. The two lines on the graph depict the amplification curve for the common and distal amplicons. The expectation is that identical cycle threshold (CT) values should be attained for each, given that the PCR reactions were conducted using identical amounts of starting material. The average of three individual experiments is shown for each dilution and the average CT deviation of either amplicon at all of the dilutions was calculated as a correction factor. **d**, The experiment shown in **c** was repeated for DICER1 and TIMP2 to determine their respective correction factors, which was then applied to experiments shown in Fig. 1.

a

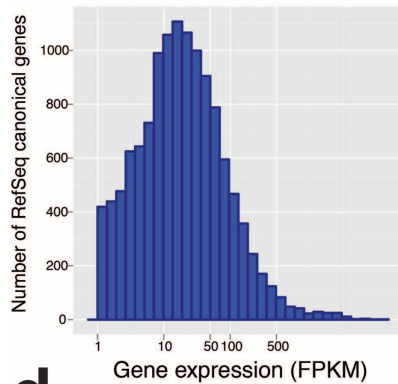
Samples	Con. R1	Con. R2	CFIm25KD R1	CFIm25KD R2
Mapped reads	269,463,902	270,426,980	265,270,708	282,404,060
#CDS	52.4%	47.6%	53.0%	51.5%
#5' UTR	5.2%	5.2%	5.5%	5.4%
#3' UTR	27.0%	23.4%	21.4%	20.3%
#Intron	6.3%	5.8%	6.0%	5.6%
#Intergenic	9.1%	17.9%	14.1%	17.3%
3' UTR average coverage	236	205	184	185

Reads distribution

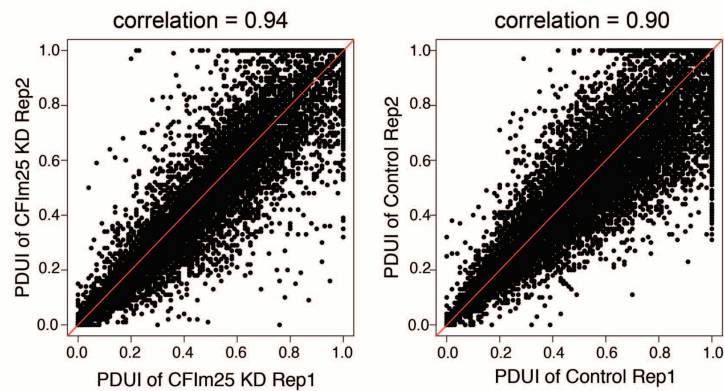


b

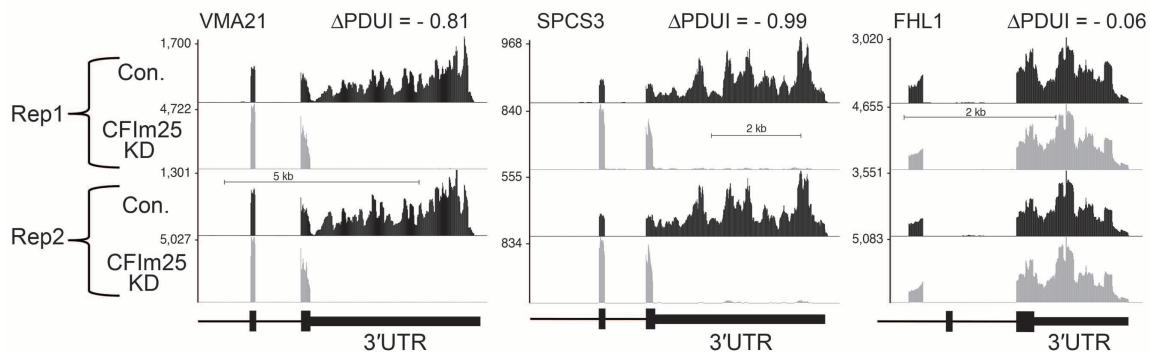
Distribution of genes with FPKM ≥ 1



c



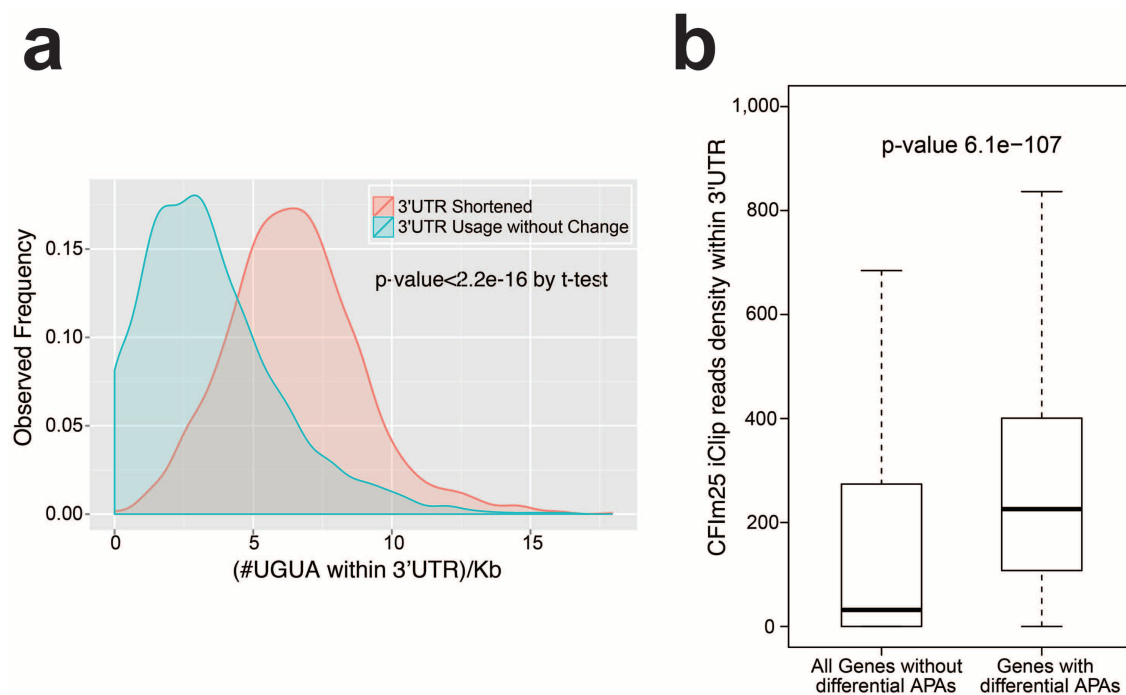
d



Extended Data Figure 2 | Summary of RNA-seq alignment and reproducibility of PDUI and CFIm25-depletion-induced 3' UTR shortening.

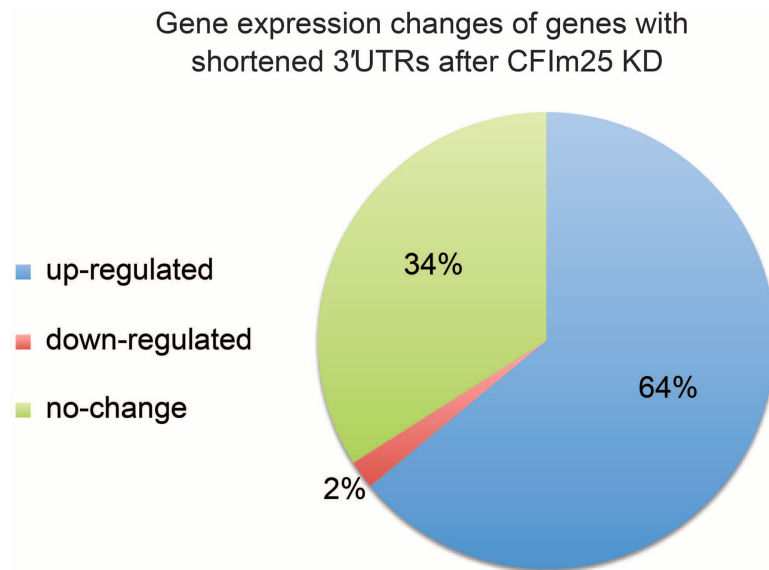
a, RNA-seq read statistics of the four biologically independent experiments where HeLa cells were treated with either control siRNA (Control) or CFIm25 siRNA (CFIm25KD). Pie chart on the right represents genomic distribution of reads that were mapped to human genome hg19. The percentage was calculated by averaging all samples. CDS, coding region. **b**, Histogram of gene expression of RefSeq genes with fragments per kilobase of transcript sequence per million mapped paired-end reads (FPKM) no less than 1.

c, Scatterplot of the two biological replicates for each condition with high Pearson correlation ($r \geq 0.9$) demonstrating a high level of reproducibility between sample PDUI scores. Each dot represents the PDUI of a transcript. **d**, Genome browser screen images from four independent RNA-seq experiments. Each represents an independent biological sample where HeLa cells were transfected with either the control siRNA (Con.) or an siRNA that knocked down CFIm25. Both VMA21 and SPCS3 were found to undergo 3' UTR shortening after CFIm25 knockdown whereas FHL1 was found not to change.



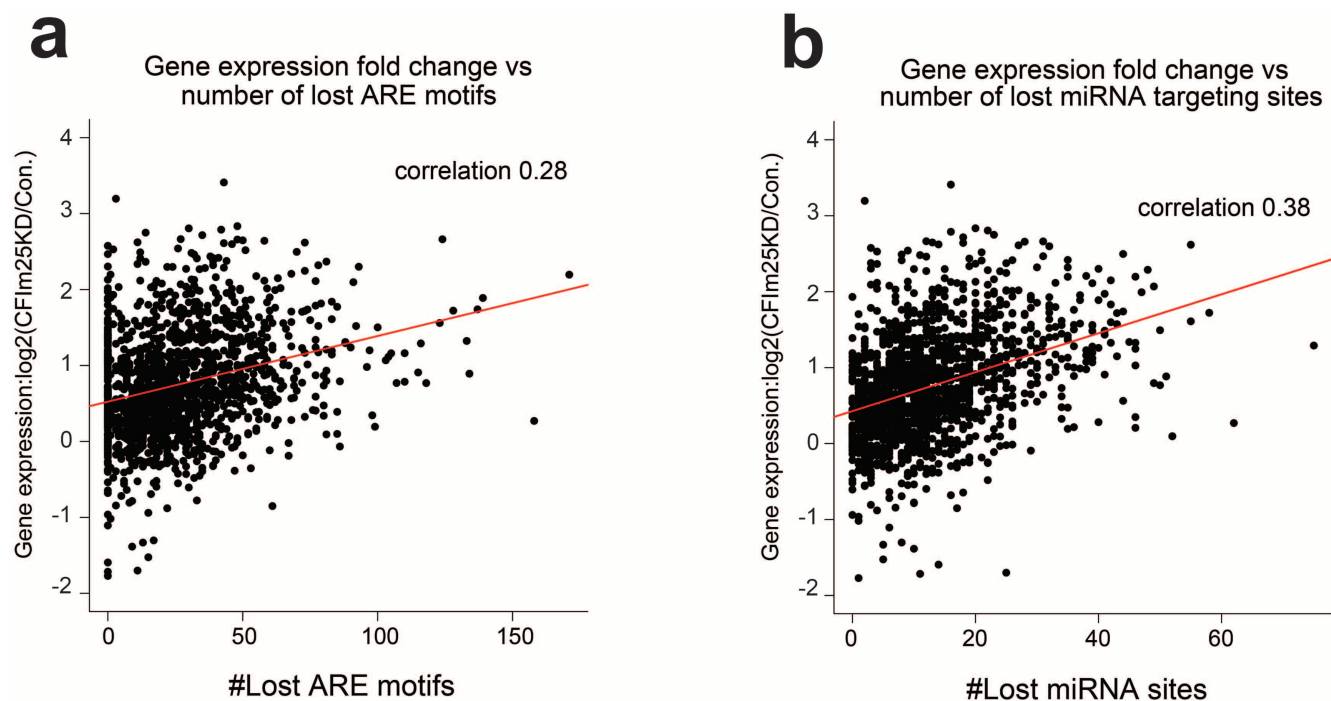
Extended Data Figure 3 | Shortened transcripts have more UGUA CFIm25-binding motifs than unaltered transcripts. **a**, CFIm25 is known to bind to the UGUA motif. The number of UGUA motifs within the 3' UTRs of genes with 3' UTR shortening after CFIm25 knockdown relative to genes with unaltered 3' UTRs was calculated and compared. Here we selected the genes without

3' UTR change according to them having a Δ PDUI value ≤ 0.05 . **b**, iCLIP tags from ref. 14 (Gene Expression Omnibus accession number GSE37398) were superimposed onto data derived from PDUI analysis of CFIm25 knockdown cells. The box plot demonstrates the enrichment of CFIm25 binding within 3' UTRs that are altered after CFIm25 knockdown ($P = 6.1 \times 10^{-107}$, *t*-test).



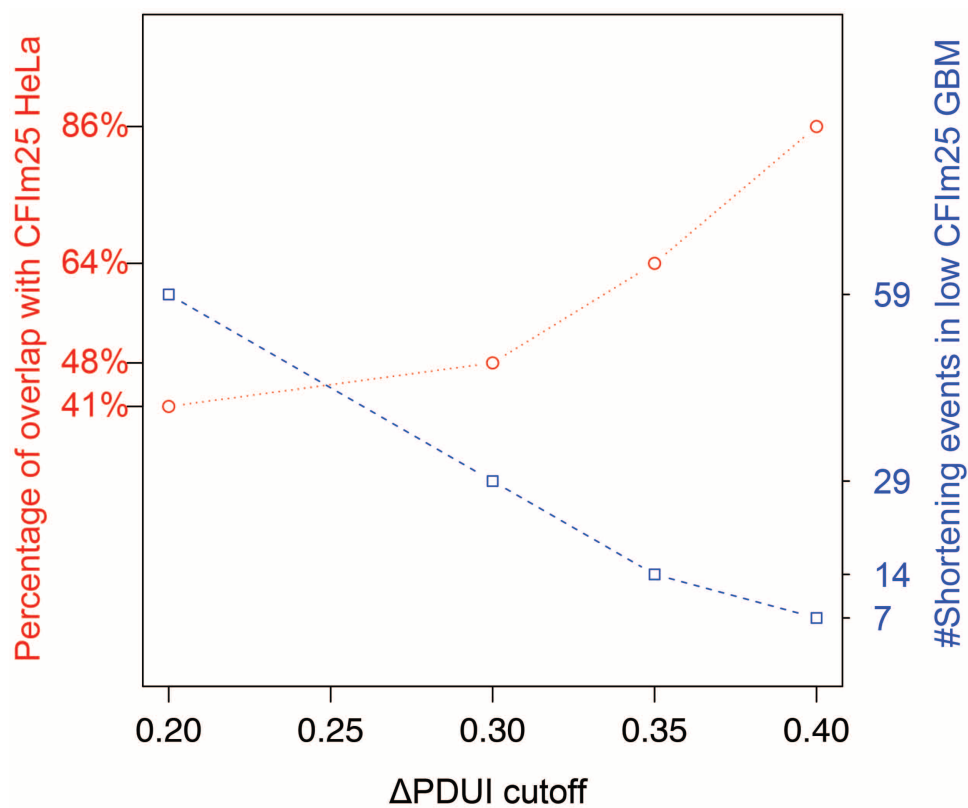
Extended Data Figure 4 | Gene expression changes of genes with shortened 3' UTRs. Pie chart was calculated from the list of 1,450 genes exhibiting shortened 3' UTRs due to CFIm25 knockdown (dn, down). Differentially

expressed gene analysis was performed using edgeR with $FDR \leq 0.05$ (see Methods).

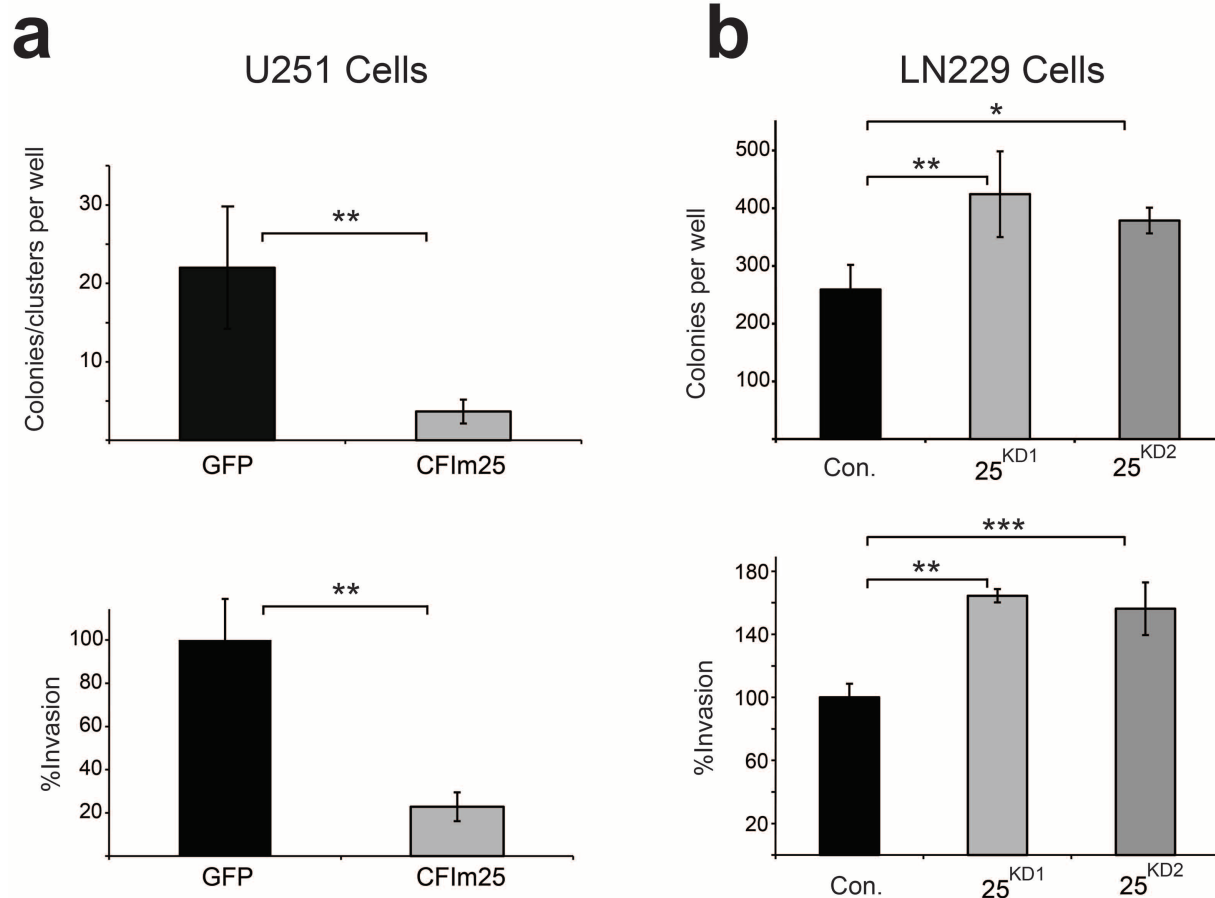


Extended Data Figure 5 | The Pearson correlation between gene expression fold change and the number of lost negative regulatory elements. Left, the number of lost AREs (AU-rich elements) due to 3' UTR shortening was calculated using the ARE database and plotted against change in gene

expression levels after CFIm25 knockdown (KD). Right, similar to the left except the number of lost patented miRNA target sites (Targetscan 6.2) was plotted.

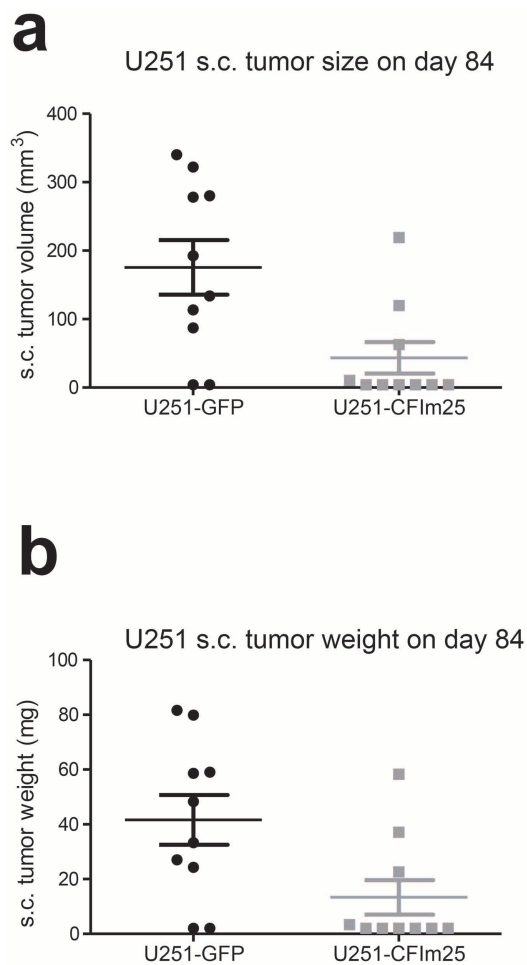


Extended Data Figure 6 | Overlap between shortening events in glioblastoma with low CFIm25 and shortening events in HeLa cells after CFIm25 knockdown. Left, y-axis (red) represents the percentage of shortening events in low CFIm25 glioblastoma that are also shortened in HeLa cells after CFIm25 knockdown. Right, y-axis (blue) shows the number of shortening events in low CFIm25 glioblastoma (GBM) against different ΔPDUI cut-offs.



Extended Data Figure 7 | Overexpression of CFIm25 reduces invasion and colony formation whereas CFIm25 depletion increases invasion and colony formation. **a**, U251 cells were transfected with either GFP or CFIm25. Top left, Cells were replated in soft agar and the number of colonies/clusters formed were determined. Bottom left, Matrigel invasion assay for cells overexpressing CFIm25 or GFP. **b**, Top right, LN229 cells were transfected with either control or two different lentiviral plasmids targeting CFIm25 (KD1 and KD2). Stably

transfected cells were plated on soft agar and the resulting colonies were counted for KD1 and KD2, respectively. Bottom right, LN229 cells were transfected with either control or two different siRNAs (KD1 and KD2) directed against CFIm25 and were replated for a Matrigel invasion assay. All the experiments were done in biological triplicates and shown is the mean \pm s.d. All *P* values were from the two-tailed student *t*-test of the control versus sample. **P* < 0.1, ***P* < 0.01, ****P* < 0.001.

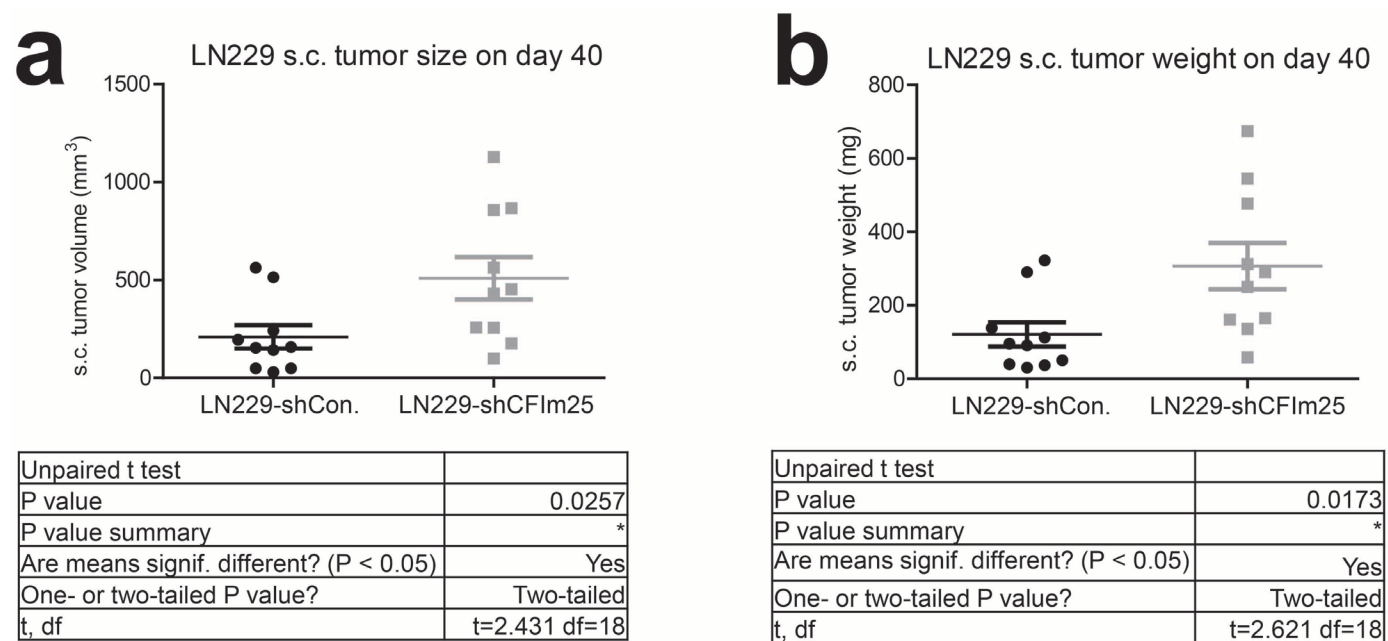


Extended Data Figure 8 | Overexpression of CFIm25 in U251 tumours reduces their size and weight. a, b, U251 subcutaneous (s.c.) xenograft tumours were isolated from nude mice on day 84 after implantation and

Table Analyzed	U251 s.c. tumor size on day 84
Column A	U251-GFP
vs	vs
Column B	U251-CFIm25
Unpaired t test	
P value	0.0102
P value summary	*
Are means signif. different? (P < 0.05)	Yes
One- or two-tailed P value?	Two-tailed
t, df	t=2.869 df=18

Table Analyzed	U251 s.c. tumor weight on day 84
Column A	U251-GFP
vs	vs
Column B	U251-CFIm25
Unpaired t test	
P value	0.0197
P value summary	*
Are means signif. different? (P < 0.05)	Yes
One- or two-tailed P value?	Two-tailed
t, df	t=2.560 df=18

measured for volume (**a**) and weight (**b**) ($n = 10$). U251-GFP indicates control U251 cells expressing GFP and U251-CFIm25 indicates cells transduced with a lentivirus that overexpresses CFIm25.



Extended Data Figure 9 | Reduction in CFIm25 expression levels enhances LN229 tumour size and weight. **a, b,** LN229 subcutaneous (s.c.) xenograft tumours were isolated from nude mice on day 40 after implantation and measured for volume (**a**) and weight (**b**) (*n* = 10). LN229-shCon. indicates control lentiviral transduced cells and LN229-shCFIm25 indicates cells transduced with a lentivirus that expresses shRNA targeting CFIm25.

Persistent gut microbiota immaturity in malnourished Bangladeshi children

Sathish Subramanian¹, Sayeeda Huq², Tanya Yatsunenkov¹, Rashidul Haque², Mustafa Mahfuz², Mohammed A. Alam², Amber Benezra^{1,3}, Joseph DeStefano¹, Martin F. Meier¹, Brian D. Muegge¹, Michael J. Barratt¹, Laura G. VanArendonk¹, Qunyuan Zhang⁴, Michael A. Province⁴, William A. Petri Jr⁵, Tahmeed Ahmed² & Jeffrey I. Gordon¹

Therapeutic food interventions have reduced mortality in children with severe acute malnutrition (SAM), but incomplete restoration of healthy growth remains a major problem^{1,2}. The relationships between the type of nutritional intervention, the gut microbiota, and therapeutic responses are unclear. In the current study, bacterial species whose proportional representation define a healthy gut microbiota as it assembles during the first two postnatal years were identified by applying a machine-learning-based approach to 16S ribosomal RNA data sets generated from monthly faecal samples obtained from birth onwards in a cohort of children living in an urban slum of Dhaka, Bangladesh, who exhibited consistently healthy growth. These age-discriminatory bacterial species were incorporated into a model that computes a 'relative microbiota maturity index' and 'microbiota-for-age Z-score' that compare postnatal assembly (defined here as maturation) of a child's faecal microbiota relative to healthy children of similar chronologic age. The model was applied to twins and triplets (to test for associations of these indices with genetic and environmental factors, including diarrhoea), children with SAM enrolled in a randomized trial of two food interventions, and children with moderate acute malnutrition. Our results indicate that SAM is associated with significant relative microbiota immaturity that is only partially ameliorated following two widely used nutritional interventions. Immaturity is also evident in less severe forms of malnutrition and correlates with anthropometric measurements. Microbiota maturity indices provide a microbial measure of human postnatal development, a way of classifying malnourished states, and a parameter for judging therapeutic efficacy. More prolonged interventions with existing or new therapeutic foods and/or addition of gut microbes may be needed to achieve enduring repair of gut microbiota immaturity in childhood malnutrition and improve clinical outcomes.

Severe acute malnutrition and moderate acute malnutrition (MAM) are typically defined by anthropometric measurements: children are classified as having SAM if their weight-for-height Z-scores (WHZ)³ are below three standard deviations (-3 s.d.) from the median of the World Health Organization (WHO) reference growth standards, whereas those with WHZ between -2 and -3 s.d. are categorized as having MAM. SAM and MAM typically develop between 3 and 24 months after birth⁴. A standardized treatment protocol for SAM and its complications has been developed in Bangladesh¹. The result has been a reduction in mortality rate, although the extent to which this protocol results in long-term restoration of normal growth and development needs to be ascertained through longitudinal studies^{5,6}. There is similar lack of clarity about the long-term efficacy of nutritional interventions for MAM^{7,8}.

Food is a major factor that shapes the proportional representation of organisms present in the gut microbial community (microbiota), and its gene content (microbiome). The microbiota and microbiome in turn have an important role in extracting and metabolizing dietary ingredients^{9–14}. To investigate the hypothesis that healthy postnatal

development (maturation) of the gut microbiota is perturbed in malnutrition¹², we monitored 50 healthy Bangladeshi children monthly during the first 2 years after birth (25 singletons, 11 twin pairs, 1 set of triplets; 996 faecal samples collected monthly; see Methods and Supplementary Tables 1–3). By identifying bacterial taxa that discriminate the microbiota of healthy children at different chronologic ages, we were able to test our hypothesis by studying 6 to 20-month-old children presenting with SAM, just before, during, and after treatment with two very different types of food intervention, as well as children with MAM. The results provide a different perspective about malnutrition; one involving disruption of a microbial facet of our normal human postnatal development.

To characterize gut microbiota maturation across unrelated healthy Bangladeshi children living in separate households, faecal samples were collected at monthly intervals up to 23.4 ± 0.5 months of age in a training set of 12 children who exhibited consistently healthy anthropometric scores (WHZ, -0.32 ± 0.98 (mean \pm s.d.)) 22.7 ± 1.5 faecal samples per child; Supplementary Table 4a). The bacterial component of their faecal microbiota samples was characterized by V4-16S rRNA sequencing (Supplementary Table 5) and assigning the resulting reads to operational taxonomic units (OTUs) sharing $\geq 97\%$ nucleotide sequence identity (see Methods; a 97%-identity OTU is commonly construed as representing a species-level taxon). The relative abundances of 1,222 97%-identity OTUs that passed our filtering criterion¹⁵ were regressed against the chronologic age of each child at the time of faecal sample collection using the Random Forests machine learning algorithm¹⁶. The regression explained 73% of the variance related to chronologic age. The significance of the fit was established by comparing fitted to null models in which age labels of samples were randomly permuted with respect to their 16S rRNA microbiota profiles ($P = 0.0001$, 9,999 permutations). Ranked lists of all bacterial taxa, in order of 'age-discriminatory importance', were determined by considering those taxa, whose relative abundance values when permuted have a larger marginal increase in mean squared error, to be more important (see Methods). Tenfold cross-validation was used to estimate age-discriminatory performance as a function of the number of top-ranking taxa according to their feature importance scores. Minimal improvement in predictive performance was observed when including taxa beyond the top 24 (see Supplementary Table 6 for the top 60). The 24 most age-discriminatory taxa identified by Random Forests are shown in Fig. 1a in rank order of their contribution to the predictive accuracy of the model and were selected as inputs to a sparse 24-taxon model.

To test the extent to which this sparse model could be applied, we applied it, with no further parameter optimization, to additional monthly faecal samples collected from two other healthy groups of children: 13 singletons (WHZ, -0.4 ± 0.8 (mean \pm s.d.)) and 25 children from a birth-cohort study of twins and triplets, (WHZ, -0.5 ± 0.7 (mean \pm s.d.)), all born and raised in Mirpur, Bangladesh (Supplementary Table 4b, c). We

¹Center for Genome Sciences and Systems Biology, Washington University in St. Louis, St. Louis, Missouri 63108, USA. ²Centre for Nutrition and Food Security, International Centre for Diarrhoeal Disease Research, Dhaka 1212, Bangladesh. ³Department of Anthropology, New School for Social Research, New York, New York 10003, USA. ⁴Division of Statistical Genomics, Washington University in St. Louis, St. Louis, Missouri 63108, USA. ⁵Departments of Medicine, Microbiology and Pathology, University of Virginia School of Medicine, Charlottesville, Virginia 22908, USA.

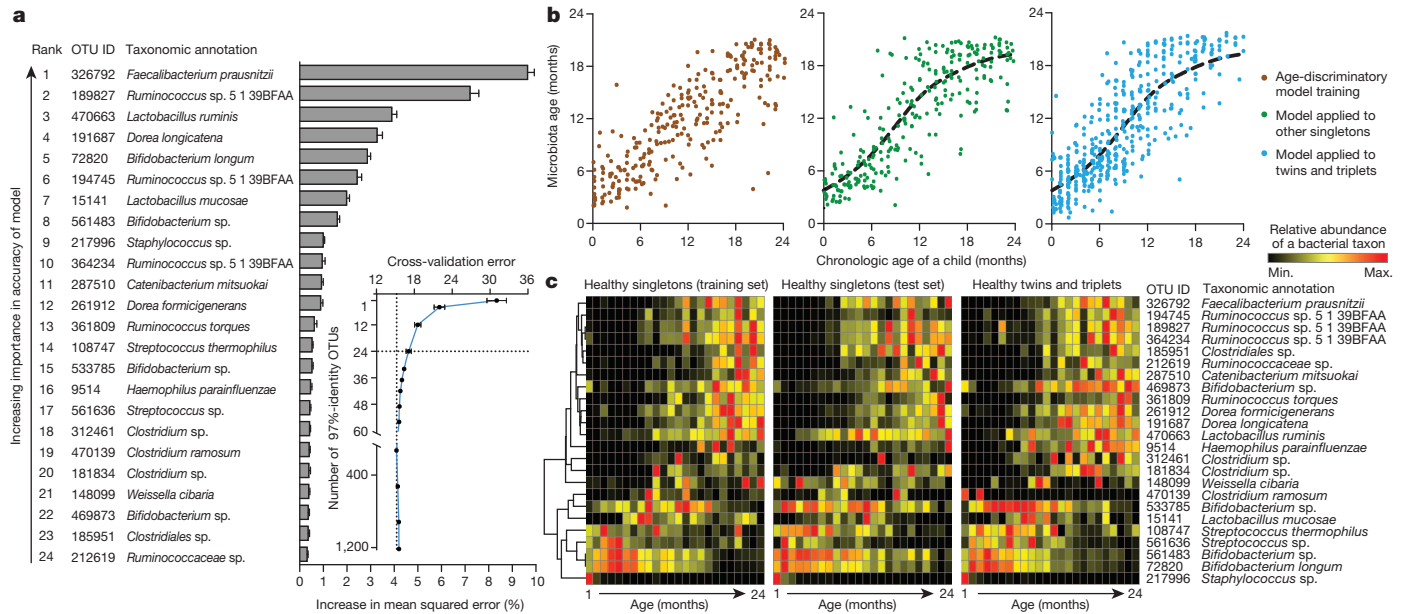


Figure 1 | Bacterial taxonomic biomarkers for defining gut-microbiota maturation in healthy Bangladeshi children during the first 2 years of life. **a**, Twenty-four age-discriminatory bacterial taxa were identified by applying Random Forests regression of their relative abundances in faecal samples against chronologic age in 12 healthy children ($n = 272$ faecal samples). Shown are 97%-identity OTUs with their deepest level of confident taxonomic annotation (also see Supplementary Table 6), ranked in descending order of their importance to the accuracy of the model. Importance was determined based on the percentage increase in mean-squared error of microbiota age prediction when the relative abundance values of each taxon were randomly permuted (mean importance \pm s.d., $n = 100$ replicates). The insert shows tenfold cross-validation error as a function of the number of input 97%-identity OTUs used to regress against the chronologic age of children in the training set, in order of variable importance (blue line). **b**, Microbiota age predictions in

a birth cohort of healthy singletons used to train the 24 bacterial taxa model (brown, each circle represents an individual faecal sample). The trained model was subsequently applied to two sets of healthy children: 13 singletons set aside for model testing (green circles, $n = 276$ faecal samples) and another birth cohort of 25 twins and triplets (blue circles, $n = 448$ faecal samples). The curve is a smoothed spline fit between microbiota age and chronologic age in the validation sets (right two panels of **b**), accounting for the observed sigmoidal relationship (see Methods). **c**, Heatmap of mean relative abundances of the 24 age-predictive bacterial taxa plotted against the chronologic age of healthy singletons used to train the Random Forests model, and correspondingly in the healthy singletons, and twins and triplets used to validate the model (hierarchical clustering performed using the Spearman rank correlation distance metric).

found that the model could be applied to both groups ($r^2 = 0.71$ and 0.68 , respectively), supporting the consistency of the observed taxonomic signature of microbiota maturation across different healthy children living in this geographic locale (Fig. 1b, c).

Two metrics of microbiota maturation were defined by applying the sparse model to the 13 healthy singletons and 25 members of twin pairs and triplets that had been used for model validation. The first metric, relative microbiota maturity, was calculated as follows:

$$\text{relative microbiota maturity} = \text{microbiota age of child}$$

$$- \text{microbiota age of healthy children of similar chronologic age}$$

where microbiota age values for healthy children were interpolated across the first 2 years of life using a spline fit (Fig. 1b). The second metric, microbiota-for-age Z score, was calculated as follows:

$$\text{MAZ} = \frac{(\text{microbiota age} - \text{median microbiota age of healthy children of same chronologic age})}{(\text{s.d. of microbiota age of healthy children of the same chronologic age})}$$

where MAZ is the microbiota-for-age Z-score, and median and s.d. of microbiota age were computed for each month up to 24 months. The MAZ accounts for the variance of predictions of microbiota age as a function of different host age ranges (when considered in discrete monthly bins) (see Extended Data Fig. 1 for the calculation of each metric, and Supplementary Notes for discussion of how this approach defines immaturity as a specific recognizable state rather than as a lack of maturity).

To study the influences of genetic and environmental factors on these microbiota maturation indices, we examined their distribution in healthy Bangladeshi twins and triplets. Monozygotic twins were not significantly more correlated in their maturity profiles compared to dizygotic twins, and within the set of triplets, the two monozygotic siblings were not more

correlated than their fraternal sibling (monozygotic pairs, 0.1 ± 0.5 (Spearman's $Rho \pm$ s.d.); dizygotic pairs, 0.33 ± 0.3 ; in the case of the triplets, values for the monozygotic pair and fraternal sibling were 0.1 ; and 0.24 ± 0.3 , respectively). Maturity was significantly decreased in faecal samples obtained during and 1 month after diarrhoeal episodes ($P < 0.001$ and $P < 0.01$, respectively) but not beyond that period (Extended Data Fig. 2). There was no discernable effect of recent antibiotic usage (1 week before sampling) on relative microbiota maturity, whereas intake of infant formula was associated with significantly higher maturity values (Supplementary Table 7). Family membership explained 29% of the total variance in relative microbiota maturity measurements (log-likelihood ratio = 102.1 , $P < 0.0001$; linear mixed model) (see Supplementary Notes, Supplementary Tables 8 and 9, and Extended Data Fig. 3 for analyses of faecal microbiota variation in mother-infant dyads and fathers).

To investigate the effects of SAM on microbiota maturity, 64 children with SAM who had been admitted to the Nutritional Rehabilitation Unit of the International Centre for Diarrhoeal Disease Research, Bangladesh (ICDDR,B), Dhaka Hospital, were enrolled in a study to investigate the configuration of their faecal microbiota before, during and after treatment with either an imported, internationally used ready-to-use therapeutic food (RUTF; Plumpy'Nut) or a locally produced, lower-cost nutritional food combination (Khichuri-Halwa). Children ranged in age from 6 to 20 months of age at the time of enrollment and were randomly assigned to either of the treatment arms. At enrollment, WHZ averaged -4.2 ± 0.7 (mean \pm s.d.) (see Supplementary Tables 10–12 for patient metadata and Fig. 2a for study design). In the initial 'acute phase' of treatment, infection control was achieved with parenteral administration of ampicillin and gentamicin for 2 and 7 days, respectively, and oral amoxicillin for 5 days (from days 3 to 7 of the antibiotic treatment protocol). Children with SAM were initially stabilized by being fed the milk-based gruel, 'suji',

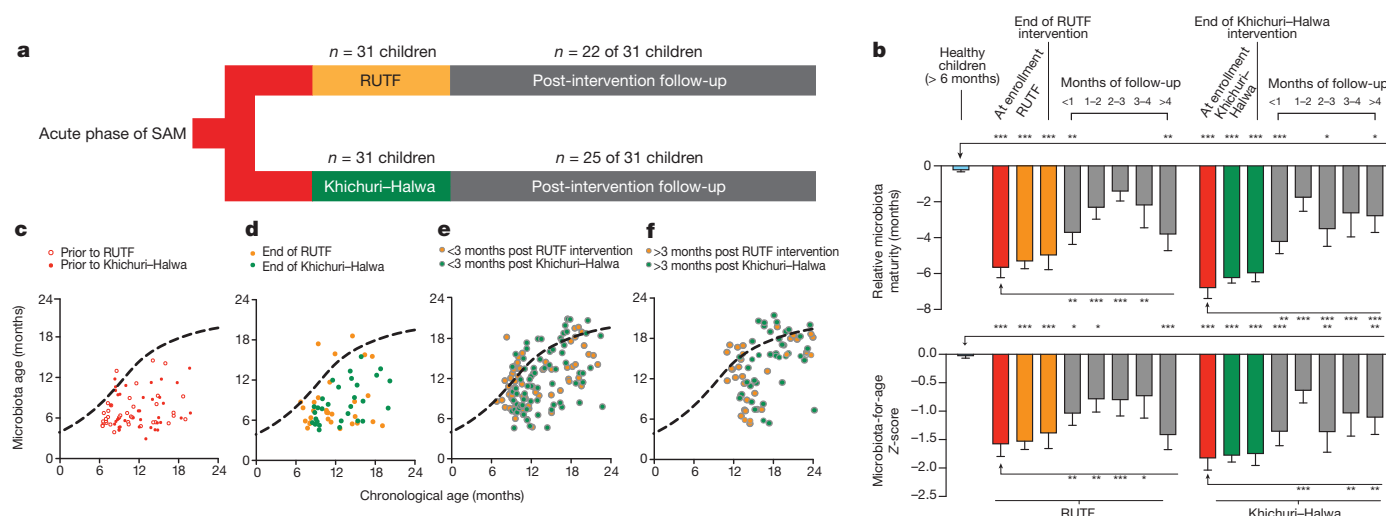


Figure 2 | Persistent immaturity of the gut microbiota in children with SAM. **a**, Design of the randomized interventional trial. **b**, Microbiota maturity defined during various phases of treatment and follow-up in children with SAM. Relative microbiota maturity in the upper portion of the panel is based on the difference between calculated microbiota age (Random Forests-based sparse 24-taxon model) and values calculated in healthy children of similar chronologic age, as interpolated over the first 2 years of life using a spline curve. In the lower portion of the panel, maturity is expressed as a microbiota-for-age Z-score (MAZ). Mean values \pm s.e.m. are plotted. The significance of differences between microbiota indices at various stages of the clinical trial is

indicated relative to healthy controls (arrows above the bars) and versus samples collected at enrollment for each intervention group (arrows below the bars) (post-hoc Dunnett's multiple comparison procedure of linear mixed models; * $P < 0.05$, ** $P < 0.01$, *** $P < 0.001$). Healthy children not used to train the Random Forests model served as healthy controls ($n = 38$). **c–f**, Plot of microbiota age for each child with SAM at enrollment (**c**), at the conclusion of the food intervention phase (**d**), and within (**e**) and beyond (**f**) 3 months of follow-up. The curve shown in each panel was fit using predictions in healthy children: this curve is the same as that replicated across each plot in Fig. 1b.

followed by randomization to either an imported peanut-based RUTF intervention or an intervention with locally produced, rice-and-lentil-based therapeutic foods (Khichuri and Halwa; see Methods and Supplementary Table 13 for compositions of all foods used during nutritional rehabilitation). During this second 'nutritional rehabilitation phase' (1.3 ± 0.7 weeks long) children received $150\text{--}250 \text{ kcal kg}^{-1}$ body weight per day of RUTF or Khichuri-Halwa ($3\text{--}5 \text{ g protein kg}^{-1}$ per day), plus micronutrients including iron. Children were discharged from the hospital after the completion of this second phase; during the 'post-intervention phase', periodic follow-up examinations were performed to monitor health status. Faecal samples were obtained during the acute phase before treatment with Khichuri-Halwa or RUTF, then every 3 days during the nutritional rehabilitation phase, and monthly thereafter during the post-intervention follow-up period.

There was no significant difference in the rate of weight gain between the RUTF and Khichuri-Halwa groups (10.9 ± 4.6 versus $10.4 \pm 5.4 \text{ g kg}^{-1}$ body weight per day (mean \pm s.d.); Student's t -test, $P = 0.7$). The mean WHZ at the completion of nutritional rehabilitation was significantly improved in both treatment groups (-3.1 ± 0.7 (mean \pm s.d.) RUTF, $P < 0.001$; and -2.7 ± 1.6 Khichuri-Halwa, $P < 0.0001$), but not significantly different between groups ($P = 0.15$). During follow-up, WHZ remained significantly lower compared to healthy children (-2.1 ± 1.2 , Khichuri-Halwa; -2.4 ± 0.8 RUTF versus -0.5 ± 1.1 for healthy, $P < 0.0001$; Extended Data Fig. 4a). Children in both treatment arms also remained markedly below normal height and severely underweight throughout the follow-up period (Extended Data Fig. 4b, c).

The Random Forests model derived from healthy children was used to define relative microbiota maturity for children with SAM at the time of enrollment, during treatment, at the end of either nutritional intervention, and during the months of follow-up. The results revealed that compared to healthy children, children with SAM had significant microbiota immaturity at the time that nutritional rehabilitation was initiated and at cessation of treatment (Dunnett's post-hoc test, $P < 0.0001$ for both groups; Fig. 2b). Within 1 month of follow-up, both groups had improved significantly. However, improvement in this metric was short-lived for the RUTF and Khichuri-Halwa groups, with regression to significant immaturity relative to healthy children beyond 4 months after

treatment was stopped (Fig. 2b and Supplementary Table 14). MAZ, like relative microbiota maturity, indicated a transient improvement after RUTF intervention that was not durable beyond 4 months. In the Khichuri-Halwa group, relative microbiota maturity and MAZ improved following treatment, but subsequently regressed, exhibiting significant differences relative to healthy children at 2–3 months, and >4 months after cessation of treatment (Fig. 2b and Supplementary Table 14).

Both food interventions had non-durable effects on other microbiota parameters. The reduced bacterial diversity associated with SAM persisted after Khichuri-Halwa and only transiently improved with RUTF (Extended Data Fig. 5 and Supplementary Table 14). We identified a total of 220 bacterial taxa that were significantly different in their proportional representation in the faecal microbiota of children with SAM compared to healthy children; 165 of these 220 97%-identity OTUs were significantly diminished in the microbiota of children with SAM during the longer term follow-up period in both treatment groups (Extended Data Figs 6 and 7, and Supplementary Table 15).

Although the majority of children in both treatment arms of the SAM study were unable to provide faecal samples before the initiation of antibiotic treatment due to the severity of their illness, a subset of nine children each provided one or two faecal samples ($n = 12$) before administration of parenteral ampicillin and gentamicin, and oral amoxicillin. Microbiota immaturity was manifest at this early time-point before antibiotics in these nine children (relative microbiota maturity: -5.15 ± 0.9 months versus -0.03 ± 0.1 for the 38 reference healthy controls; Mann-Whitney, $P < 0.0001$). Sampling these nine children after treatment with parenteral and oral antibiotics but before initiation of RUTF or Khichuri-Halwa (6 ± 3.6 days after hospital admission) showed that there was no significant effect on microbiota maturity (Wilcoxon matched-pairs rank test, $P = 1$). When pre-antibiotic faecal samples from these nine children were compared to samples collected at the end of all treatment interventions (dietary and antibiotic, 20 ± 9 days after admission), no significant differences in relative microbiota maturity (Wilcoxon, $P = 0.7$), MAZ, bacterial diversity (or WHZ) were found (Extended Data Fig. 8a–d). This is not to say that these interventions were without effects on overall community composition: opposing changes in the relative abundance of Streptococcaceae and Enterobacteriaceae were readily apparent

(Extended Data Fig. 8e, f; note that the Random Forests model classified both the microbiota of children with SAM sampled before and at the conclusion of all treatment interventions as immature, indicating lack of a generic immature state). Although these findings indicate that the relative microbiota immaturity associated with SAM was not solely attributable to the antibiotics used to treat these children, we could not, in cases where children were unable to provide pre-intervention faecal samples, measure the effects of other antibiotics, consumed singly or in various combinations during the acute infection control and nutritional rehabilitation phases, on their metrics of microbiota maturation (see Supplementary Notes and Supplementary Table 16 for further evidence indicating antibiotic use in the follow-up period did not correlate with the persistence of microbiota immaturity in children with SAM).

SAM affects approximately 4% of children in developing countries. MAM is more prevalent, particularly in South Central Asia, where it affects approximately 19% (30 million children)⁷. Epidemiological studies indicate that periods of MAM are associated with progression to SAM, and with stunting which affects >40% of children under the age of five in Bangladesh¹⁷. Therefore, we extended our study to children from the singleton cohort at 18 months of age, when all had transitioned to solid foods ($n = 10$ children with WHZ lower than -2 s.d., the threshold for MAM; 23 children with healthy WHZ; Supplementary Table 17). The relationship between relative microbiota maturity, MAZ and WHZ was significant (Spearman's $Rho = 0.62$ and 0.63 , $P < 0.001$, respectively; Extended Data Fig. 9a, b). Comparing children with MAM to those defined as healthy revealed significantly lower relative microbiota maturity, MAZ and differences in the relative abundances of age-discriminatory taxa in the malnourished group (Extended Data Figs 9d–l and 10a, b). These results suggest that microbiota immaturity may be an additional pathophysiological component of moderately malnourished states.

In conclusion, definition of microbiota maturity using bacterial taxonomic biomarkers that are highly discriminatory for age in healthy children has provided a way to characterize malnourished states, including whether responses to food interventions endure for prolonged periods of time beyond the immediate period of treatment. RUTF and Khichuri-Halwa produced improvements in microbiota maturity indices that were not sustained. Addressing the question of how to achieve durable responses in children with varying degrees of malnutrition may involve extending the period of administration of existing or new types of food interventions⁷. One testable hypothesis is that a population's microbiota conditioned for generations on a diet will respond more favourably to nutrient supplementation based on food groups represented in that diet. Next-generation probiotics using gut-derived taxa may also be required in addition to food-based interventions. The functional roles (niches) of the age-discriminatory taxa identified by our Random Forests model need to be clarified since they themselves may be therapeutic candidates and/or form the basis for low cost field-based diagnostic assessments.

Systematic analyses of microbiota maturation in different healthy and malnourished populations living in different locales, representing different lifestyles and cultural traditions^{11,18}, may yield a taxonomy-based model that is generally applicable to many countries and types of diagnostic and therapeutic assessments. Alternatively, these analyses may demonstrate a need for geographic specificity when constructing such models (and diagnostic tests or therapeutic regimens). Two observations are notable in this regard. First, expansion of our sparse model from 24 to 60 taxa yielded similar results regarding the effects of diarrhoea in healthy individuals, MAM and SAM (and its treatment with RUTF and Khichuri-Halwa) on microbiota maturity (see Supplementary Notes). Second, we applied the model that we used for Bangladeshi children to healthy children in another population at high risk for malnutrition. The results show that the model generalizes ($r^2 = 0.6$) to a cohort of 47 Malawian twins and triplets, aged 0.4–25.1 months, who were concordant for healthy status in a previous study¹¹ (WHZ, -0.23 ± 0.97 (mean \pm s.d.); Supplementary Table 18). Age-discriminatory taxa identified in healthy Bangladeshi children show similar age-dependent changes in their representation in the microbiota of healthy Malawian

children, as assessed by the Spearman rank correlation metric (Extended Data Fig. 10c, d).

The question of whether microbiota immaturity associated with SAM and MAM is maintained during and beyond childhood also underscores the need to determine the physiologic, metabolic and immunologic consequences of this immaturity, and how they might contribute to the associated morbidities and sequelae of malnutrition, including increased risk for diarrhoeal disease, stunting, impaired vaccine responses, and cognitive abnormalities^{2,19}. Our study raises a testable hypothesis: namely, that assessments of microbiota maturation, including in the context of the maternal–infant dyad, will provide a more comprehensive view of normal human development and of developmental disorders, and generate new directions for preventive medicine. Testing this hypothesis will require many additional clinical studies but answers may also arise from analyses of gut microbiota samples that have already been stored from previous studies.

METHODS SUMMARY

All subjects lived in Dhaka, Bangladesh (see Methods and Supplementary Notes for anthropologic assessment of Mirpur, an urban slum in Bangladesh, where most subjects resided). Informed consent was obtained and studies were conducted using protocols approved by the ICDDR,B, Washington University, and University of Virginia institutional review boards (IRBs). Linear mixed models were applied to test hypotheses in repeated measurements of relative abundance of 97%-identity OTUs and maturation metrics in time-series profiling of faecal microbiota²⁰. To account for similarity between observations from repeated sampling of the same individuals and families, we fit random intercepts for each subject in the case of adults and singletons, nested these intercepts within each family in the case of twins and triplets, and included age as a fixed-effect covariate, while testing the significance of associations between the microbiota and specified host and environmental factors. Differences between microbiota maturation metrics in each treatment phase of SAM were compared to values at enrollment in each treatment group, and to healthy children within the same age range (excluding samples from children used to train the Random Forests model), using analysis of variance (ANOVA) of linear mixed models followed by Dunnett's post-hoc comparisons.

Online Content Any additional Methods, Extended Data display items and Source Data are available in the online version of the paper; references unique to these sections appear only in the online paper.

Received 10 October 2013; accepted 29 April 2014.

Published online 4 June 2014.

1. Ahmed, T. *et al.* Mortality in severely malnourished children with diarrhoea and use of a standardised management protocol. *Lancet* **353**, 1919–1922 (1999).
2. Ashraf, H. *et al.* A follow-up experience of 6 months after treatment of children with severe acute malnutrition in Dhaka, Bangladesh. *J. Trop. Pediatr.* **58**, 253–257 (2012).
3. World Health Organization Department of Nutrition for Health and Development. WHO child growth standards growth velocity based on weight, length and head circumference: methods and development. (World Health Organization, 2009).
4. Victora, C. G., de Onis, M., Hallal, P. C., Blössner, M. & Shrimpton, R. Worldwide timing of growth faltering: revisiting implications for interventions. *Pediatrics* **125**, e473–e480 (2010).
5. Ahmed, T. & Begum, B. Badiuzzaman, Ali, M. & Fuchs, G. Management of severe malnutrition and diarrhea. *Indian J. Pediatr.* **68**, 45–51 (2001).
6. Ahmed, T. *et al.* P0580 Use of a standardized protocol based on local diet results in satisfactory rates of weight gain of severely malnourished children undergoing nutritional rehabilitation. *J. Pediatr. Gastroenterol. Nutr.* **39**, S277 (2004).
7. Lazzarini, M., Rubert, L. & Pani, P. Specially formulated foods for treating children with moderate acute malnutrition in low- and middle-income countries. *Cochrane Database Syst. Rev.* CD009584 (2013).
8. Prentice, A. M. *et al.* Critical windows for nutritional interventions against stunting. *Am. J. Clin. Nutr.* **97**, 911–918 (2013).
9. Muegge, B. D. *et al.* Diet drives convergence in gut microbiome functions across mammalian phylogeny and within humans. *Science* **332**, 970–974 (2011).
10. Wu, G. D. *et al.* Linking long-term dietary patterns with gut microbial enterotypes. *Science* **334**, 105–108 (2011).
11. Yatsunenko, T. *et al.* Human gut microbiome viewed across age and geography. *Nature* **486**, 222–227 (2012).
12. Smith, M. I. *et al.* Gut microbiomes of Malawian twin pairs discordant for kwashiorkor. *Science* **339**, 548–554 (2013).
13. David, L. A. *et al.* Diet rapidly and reproducibly alters the human gut microbiome. *Nature* **505**, 559–563 (2014).
14. Tang, W. H. W. *et al.* Intestinal microbial metabolism of phosphatidylcholine and cardiovascular risk. *N. Engl. J. Med.* **368**, 1575–1584 (2013).

15. Faith, J. J. *et al.* The long-term stability of the human gut microbiota. *Science* **341** (2013).
16. Breiman, L. Random Forests. *Mach. Learn.* **45**, 5–32 (2001).
17. Dewey, K. G. *et al.* Infant weight-for-length is positively associated with subsequent linear growth across four different populations. *Matern. Child Nutr.* **1**, 11–20 (2005).
18. Lin, A. *et al.* Distinct distal gut microbiome diversity and composition in healthy children from Bangladesh and the United States. *PLoS ONE* **8**, e53838 (2013).
19. Nahar, B. *et al.* Effects of a community-based approach of food and psychosocial stimulation on growth and development of severely malnourished children in Bangladesh: a randomised trial. *Eur. J. Clin. Nutr.* **66**, 701–709 (2012).
20. Bates, D., Maechler, M. & Bolker, B. lme4: Linear mixed-effects models using Eigen and R syntax. <http://CRAN.R-project.org/package=lme4> (2011).

Supplementary Information is available in the online version of the paper.

Acknowledgements We thank the parents and children from Dhaka, Bangladesh for their participation in this study, J. Hoisington-López and S. Deng for technical assistance, and N. Griffin, A. Kau, N. Dey and J. Faith for suggestions during the course of this work. This work was supported by the Bill & Melinda Gates Foundation. The clinical component of the SAM study was funded by the International Atomic Energy

Agency. The birth cohort study of singletons was supported in part by the NIH (AI043596). S.S. is a member of the Washington University Medical Scientist Training Program. A.B. is the recipient of an SBE Doctoral Dissertation Research Improvement Grant (NSF Award no. SES-1027035).

Author Contributions S.S. and J.I.G. designed the metagenomic study, S.H., T.A., R.H., M.A.A., M.M., W.A.P. Jr designed and implemented the clinical monitoring and sampling for the SAM trial, participated in patient recruitment, sample collection, sample preservation and/or clinical evaluations; S.S. generated the 16S rRNA data with assistance from M.F.M. and B.D.M.; A.B. and J.D. performed the anthropology study; S.S., T.Y., Q.Z., L.G.V., M.J.B., M.A.P. and J.I.G. analysed the data; S.S. and J.I.G. wrote the paper.

Author Information 16S rRNA sequences, generated from faecal samples in raw format prior to post-processing and data analysis, have been deposited at the European Nucleotide Archive (accession number PRJEB5482). Reprints and permissions information is available at www.nature.com/reprints. The authors declare competing financial interests: details are available in the online version of the paper. Readers are welcome to comment on the online version of the paper. Correspondence and requests for materials should be addressed to J.I.G. (jgordon@wustl.edu).

METHODS

Singleton birth cohort. Full details of the design of this now-complete birth cohort study have been described previously²¹. Faecal microbiota samples were profiled from 25 children who had consistently healthy anthropometric measures based on quarterly (every 3 months) measurements (Supplementary Table 1). The WHZ threshold used for 'healthy' (on average above -2 s.d.) was based on median weight and height measurements obtained from age- and gender-matched infants and children by the Multi-Centre Growth Reference study of the World Health Organization³. Clinical parameters, including diarrhoeal episodes and antibiotic consumption associated with each of their faecal samples are provided in Supplementary Table 2.

A second group studied from this singleton cohort consisted of 33 children sampled cross-sectionally at 18 months, including those who were incorporated as healthy reference controls, and those with a WHZ < -2 who were classified with MAM (Supplementary Table 17).

Twins and triplets birth cohort. Mothers with multiple pregnancy, identified by routine clinical and sonographic assessment at the Radda Maternal Child Health and Family Planning (MCH-FP) Clinic in Dhaka, were enrolled in a prospective longitudinal study ($n = 11$ mothers with twins, 1 mother with triplets). The zygosity of twin pairs and triplets was determined using plasma DNA and a panel of 96 polymorphic single-nucleotide polymorphisms (SNPs) (Center for Inherited Disease Research, Johns Hopkins University). Four twin pairs were monozygotic, six were dizygotic, and the set of triplets consisted of a monozygotic pair plus one fraternal sibling (Supplementary Table 1; note that one of the 11 twin pairs could not be tested for zygosity because plasma samples were not available). Information about samples from healthy twins, triplets and their parents, including clinical parameters associated with each faecal sample, is provided in Supplementary Tables 2 and 3.

The three healthy Bangladeshi groups used for model training and validation had the following WHZ scores: -0.32 ± 1 (mean \pm s.d.; 12 singletons randomized to the training set), -0.44 ± 0.8 (13 singletons randomized to one of the two validation sets), and -0.46 ± 0.7 (twins and triplets in the other validation set) (Supplementary Table 4). The average number of diarrhoeal episodes in the singleton training set, the singleton validation set, and the twin and triplet validation set (4, 4.6 and 1.7, respectively) was comparable to values reported in previous surveys of another cohort of 0–2-year-old Bangladeshi children (4.25 per child per year)²².

There were no significant differences in the number of diarrhoeal episodes per year per child and the number of diarrhoeal days per year per child between the singleton training and validation sets (Student's t -test, $P = 0.5$). Moreover, across all training and validation sets, neither of these diarrhoeal parameters correlated with mean age-adjusted Shannon diversity indices (Spearman's Rho, -0.18 and -0.12 , $P = 0.22$ and 0.4 , respectively). The fraction of faecal samples collected from each child where oral antibiotics had been consumed within the prior 7 days was not significantly different between the training and two validation sets (one-way ANOVA, $P = 0.14$; see Supplementary Table 4).

Severe acute malnutrition study. Sixty-four children in the Nutritional Rehabilitation Unit of ICDDR,B, Dhaka Hospital suffering from SAM (defined as having a WHZ less than -3 s.d. and/or bilateral pedal oedema) were enrolled in a randomized interventional trial to compare an imported peanut-based RUTF, Plumpy'Nut (Nutriset Plumpyfield, India) and locally produced Khichuri–Halwa (clinical trial NCT01331044). Initially, children were stabilized by rehydration and feeding 'suji', which contains whole bovine milk powder, rice powder, sugar and soybean oil (approximately 100 kcal kg^{-1} body weight per day, including $1.5 \text{ g protein kg}^{-1}$ per day). Children were then randomized to the Khichuri–Halwa or RUTF groups. Khichuri consists of rice, lentils, green leafy vegetables and soybean oil; Halwa consists of wheat flour (atta), lentils, molasses and soybean oil. Children randomized to the Khichuri–Halwa treatment arm also received milk suji '100' during their nutritional rehabilitation phase (a form of suji with a higher contribution of calories from milk powder compared to suji provided during the acute phase). RUTF is a ready-to-use paste that does not need to be mixed with water; it consists of peanut paste mixed with dried skimmed milk, vitamins and minerals (energy density, 5.4 kcal g^{-1}). Khichuri and Halwa are less energy-dense than RUTF (1.45 kcal g^{-1} and 2.4 kcal g^{-1} , respectively, see Supplementary Table 13 for a list of ingredients for all foods used during nutritional rehabilitation).

The primary outcome measurement, rate of weight gain (g kg^{-1} per day), along with improvement in WHZ after nutritional rehabilitation are reported by child in Supplementary Table 10. Faecal samples were collected before randomization to the RUTF and Khichuri–Halwa treatment arms, every 3 days during nutritional rehabilitation and once a month during the follow-up period (information associated with each faecal sample is provided in Supplementary Table 11).

Anthropologic study. To obtain additional information about household practices in the Mirpur slum of Dhaka, in-depth semi-structured interviews and observations were conducted over the course of 1 month in nine households ($n = 30$ individuals). This survey, approved by the Washington University and ICDDR,B IRBs, involved

three ICDDR,B field research assistants, and three senior scientific staff in the ICDDR,B Centre for Nutrition and Food Security, plus two anthropologists affiliated with Washington University in St. Louis. Parameters that might affect interpretation of metagenomic analyses of gut microbial-community structure were noted, including information about daily food preparation, food storage, personal hygiene and childcare practices.

Characterization of the bacterial component of the gut microbiota by V4-16S rRNA sequencing. Faecal samples were frozen at -20°C within 30 min of their collection and subsequently stored at -80°C before extraction of DNA. DNA was isolated by bead-beating in phenol and chloroform, purified further (QIAquick column), quantified (Qubit) and subjected to polymerase chain reaction (PCR) using primers directed at variable region 4 (V4) of bacterial 16S rRNA genes. Bacterial V4-16S rRNA data sets were generated by multiplex sequencing of amplicons prepared from 1,897 faecal DNA samples ($26,580 \pm 26,312$ (mean \pm s.d.) reads per sample, paired-end 162- or 250-nucleotide reads; Illumina MiSeq platform; Supplementary Table 5). Reads of 250 nucleotides in length were trimmed to 162 nucleotides, then all reads were processed using previously described custom scripts, and overlapped to 253-nucleotide fragments spanning the entire V4 amplicon¹⁵. 'Mock' communities, consisting of mixtures of DNAs isolated from 48 sequenced bacterial members of the human gut microbiota combined in one equivalent and two intentionally varied combinations, were included as internal controls in the Illumina MiSeq runs. Data from the mock communities were used for diversity and precision-sensitivity analyses employing methods described previously^{15,23}.

Reads with $\geq 97\%$ nucleotide sequence identity (97%-identity) across all studies were binned into operational taxonomic units (OTUs) using QIIME (v 1.5.0), and matched to entries in the Greengenes reference database (version 4feb2011)^{24,25}. Reads that did not map to the Greengenes database were clustered *de novo* with UCLUST at 97%-identity and retained in further analysis. A total of 1,222 97%-identity OTUs were found to be present at or above a level of confident detection (0.1% relative abundance) in at least two faecal samples from all studies. Taxonomy was assigned based on the naive Bayesian RDP classifier version 2.4 using 0.8 as the minimum confidence threshold for assigning a level of taxonomic classification to each 97%-identity OTU.

Definition of gut-microbiota maturation in healthy children using Random Forests. Random Forests regression was used to regress relative abundances of OTUs in the time-series profiling of the microbiota of healthy singletons against their chronologic age using default parameters of the R implementation of the algorithm (R package 'randomForest', $n\text{tree} = 10,000$, using default $m\text{try}$ of $p/3$ where p is the number of input 97%-identity OTUs (features))²⁶. The Random Forests algorithm, due to its non-parametric assumptions, was applied and used to detect both linear and nonlinear relationships between OTUs and chronologic age, thereby identifying taxa that discriminate different periods of postnatal life in healthy children. A rarefied OTU table at 2,000 sequences per sample served as input data. Ranked lists of taxa in order of Random Forests reported 'feature importance' were determined over 100 iterations of the algorithm. To estimate the minimal number of top ranking age-discriminatory taxa required for prediction, the *rfcv* function implemented in the 'randomForest' package was applied over 100 iterations. A sparse model consisting of the top 24 taxa was then trained on the training set of 12 healthy singletons (272 faecal samples). Without any further parameter optimization, this model was validated in other healthy children (13 singletons, 25 twins and triplets) and then applied to samples from children with SAM and MAM. A smoothing spline function was fit between microbiota age and chronologic age of the host (at the time of faecal sample collection) for healthy children in the validation sets to which the sparse model was applied.

Alpha diversity comparisons. Estimates of within-sample diversity were made at a rarefaction depth of 2,000 reads per sample. A linear regression was fit between the Shannon diversity index (SDI) and postnatal age in the 50 healthy children using a mixed model (see the additional details regarding statistical methods, below). An estimate of the coefficient for the slope of SDI with age and intercept was extracted, residuals of this regression were defined as a ΔSDI metric, and associations of this metric with clinical parameters were tested in the cohort of healthy twins and triplets. To test for differences in SDI as a function of health status and chronologic age in malnourished children, we compared the distribution of age-adjusted ΔSDIs in children with SAM between treatment phases.

Detection of associations of bacterial taxa with nutritional status and other parameters. Relative abundances of 97%-identity OTUs were used in linear mixed models as response variables to test for associations with clinical metadata as predictors. For each comparison, we restricted our analysis to 97%-identity OTUs and bacterial families whose relative abundance values reached a level of confident detection (0.1%) in a minimum of 1% of samples in each comparison. Pseudocounts of 1 were added to 97%-identity OTUs to account for variable depth of sequencing between samples, and relative abundances were arcsin-square-root-transformed to approximate homoscedasticity when applying linear models. P values of associations

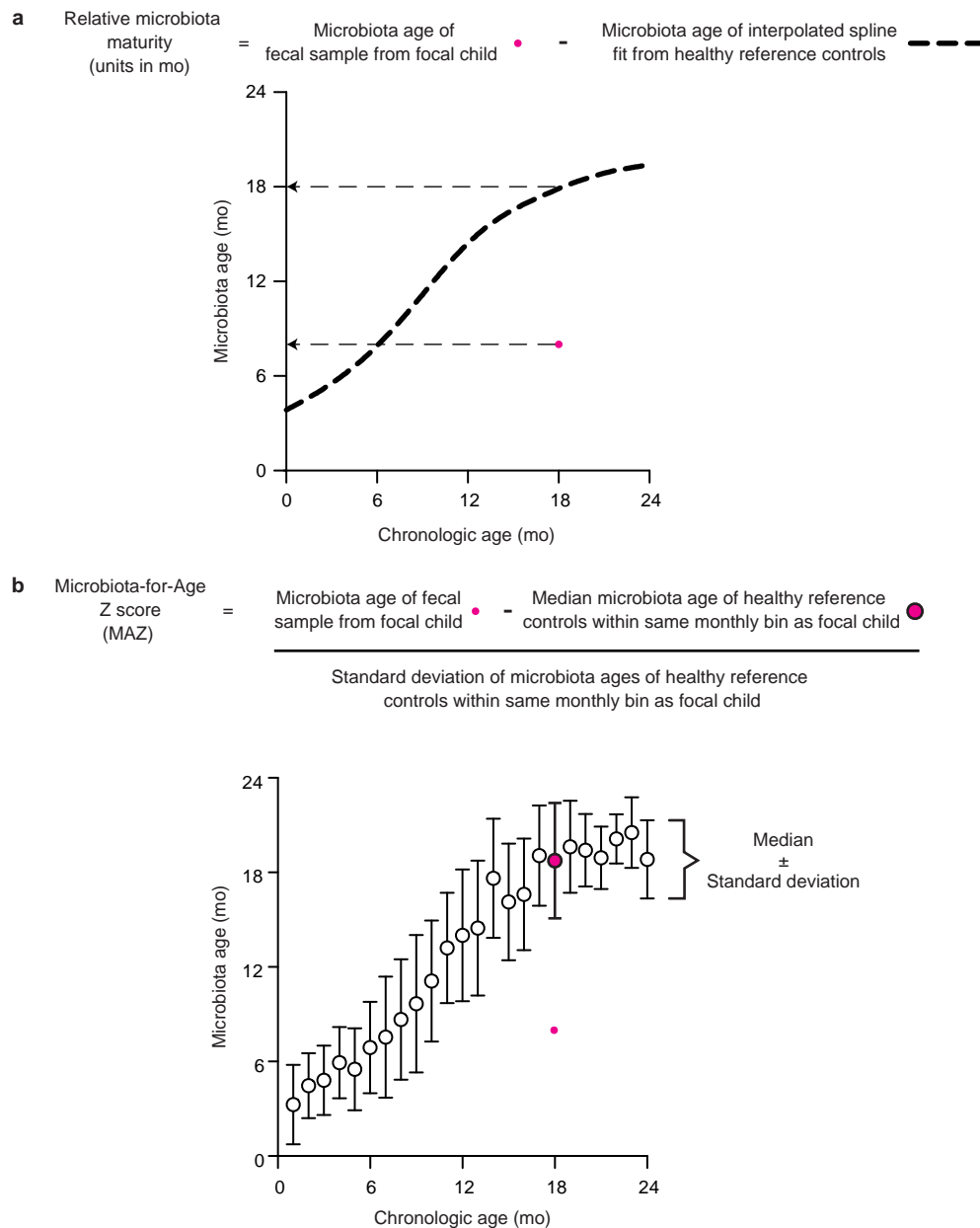
of factors with the relative abundance of bacterial taxa were computed using ANOVA type III (tests of fixed effects), subjected to Benjamini–Hochberg false discovery rate (FDR) correction.

Enteropathogen testing. Clinical microscopy was performed for all faecal samples collected at monthly intervals from the singleton birth cohort and from healthy twins and triplets, and screened for *Entamoeba histolytica*, *Entamoeba dispar*, *Escherichia coli*, *Blastocystis hominis*, *Trichomonas hominis*, *Blastocystis hominis*, Coccidian-like bodies, *Giardia lamblia*, *Ascaris lumbricoides*, *Trichuris Tricuris*, *Ancylostoma duodenale*/*Necator americanus*, *Hymenolepis nana*, *Endolimax nana*, *Iodamoeba butschlii* and *Chilomastix mesnili*. The effects of enteropathogens, detected by microscopy on relative microbiota maturity, MAZ and SDI were included in our analysis of multiple environmental factors in Extended Data Fig. 2 and Supplementary Table 7. In cases in which children presented with SAM plus diarrhoea, faecal samples collected before nutritional rehabilitation were cultured for *Vibrio cholerae*, *Shigella flexneri*, *Shigella boydii*, *Shigella sonnei*, *Salmonella enterica*, *Aeromonas hydrophila* and *Hafnia alvae*. See Supplementary Tables 10 and 19 for results of enteropathogen testing.

Additional details regarding statistical methods. Linear mixed models were applied to test for associations of microbiota metrics (relative microbiota maturity, MAZ and SDI) with genetic and environmental factors in twins and triplets. Log-likelihood ratio tests and *F* tests were used to perform backward elimination of non-significant random and fixed effects²⁷. Relative microbiota maturity, MAZ and SDI were defined at different phases of treatment and at defined periods of follow-up (<1 month, 1–2, 3–4 and >4 months after completion of the RUTF or Khichuri–Halwa

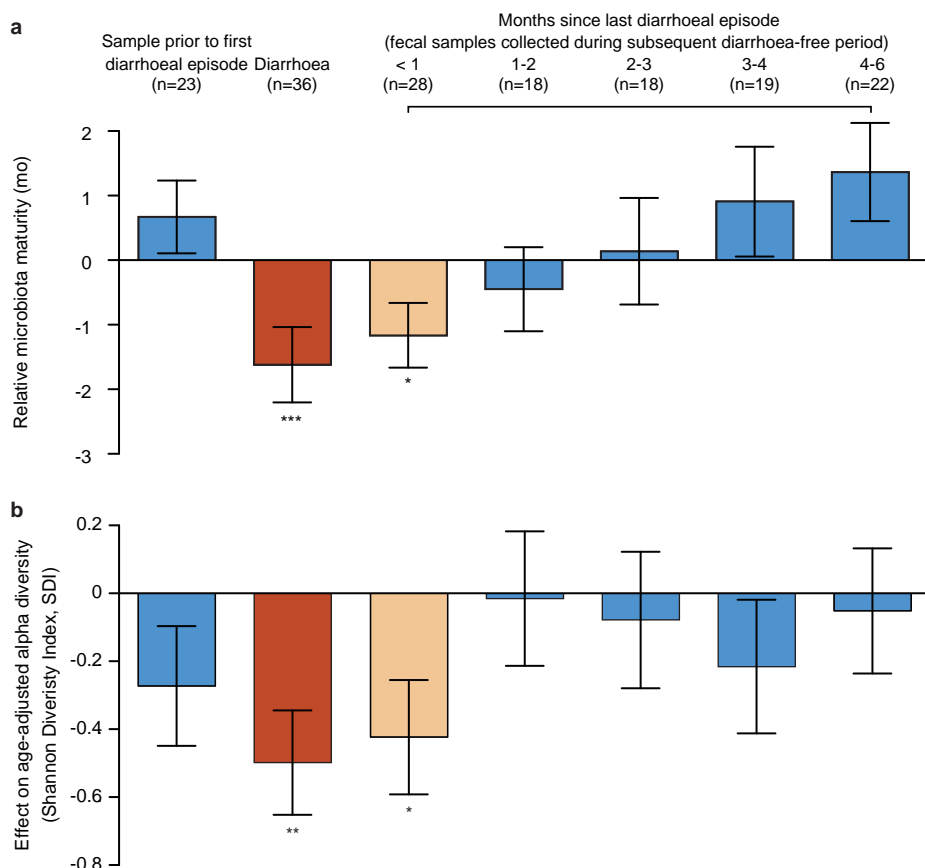
nutritional intervention) in children with SAM relative to healthy children. ‘Treatment phase’ was specified as a categorical multi-level factor in a univariate mixed model with random by-child intercepts. Dunnett’s post-hoc comparison procedure was performed to compare each treatment phase relative to healthy controls and relative to samples collected at enrollment in each food intervention group.

21. Mondal, D. *et al.* Contribution of enteric infection, altered intestinal barrier function, and maternal malnutrition to infant malnutrition in Bangladesh. *Clin. Infect. Dis.* **54**, 185–192 (2012).
22. Pathela, P. *et al.* Diarrheal illness in a cohort of children 0–2 years of age in rural Bangladesh: I. Incidence and risk factors. *Acta Paediatr.* **95**, 430–437 (2006).
23. Bokulich, N. A. *et al.* Quality-filtering vastly improves diversity estimates from Illumina amplicon sequencing. *Nature Meth.* **10**, 57–59 (2013).
24. Caparaso, J. G. *et al.* QIIME allows analysis of high-throughput community sequencing data. *Nature Meth.* **7**, 335–336 (2010).
25. McDonald, D. *et al.* An improved Greengenes taxonomy with explicit ranks for ecological and evolutionary analyses of bacteria and archaea. *ISME J.* **6**, 610–618 (2012).
26. Liaw, A. & Weiner, M. Classification and regression by randomForest. R package version 4.6-7. *R News* **2**, 18–22 (2002).
27. Kuznetsova, A., Brockhoff, P. B. & Christensen, R. H. B. lmerTest: tests for random and fixed effects for linear mixed effect models (lmer objects of lme4 package). <http://CRAN.R-project.org/package=lmerTest> (2013).
28. National Institute of Population Research and Training (NIPORT), Mitra and Associates, and ICF International. Bangladesh Demographic and Health Survey 2011. Dhaka, Bangladesh and Calverton, Maryland, USA: NIPORT, Mitra and Associates, and ICF International (2013).



Extended Data Figure 1 | Illustration of the equations used to calculate 'relative microbiota maturity' and 'microbiota-for-age Z-score'. **a, b,** The procedure to calculate both microbiota maturation metrics are shown for a single faecal sample from a focal child (pink circle) relative to microbiota age values calculated in healthy reference controls. These reference values are

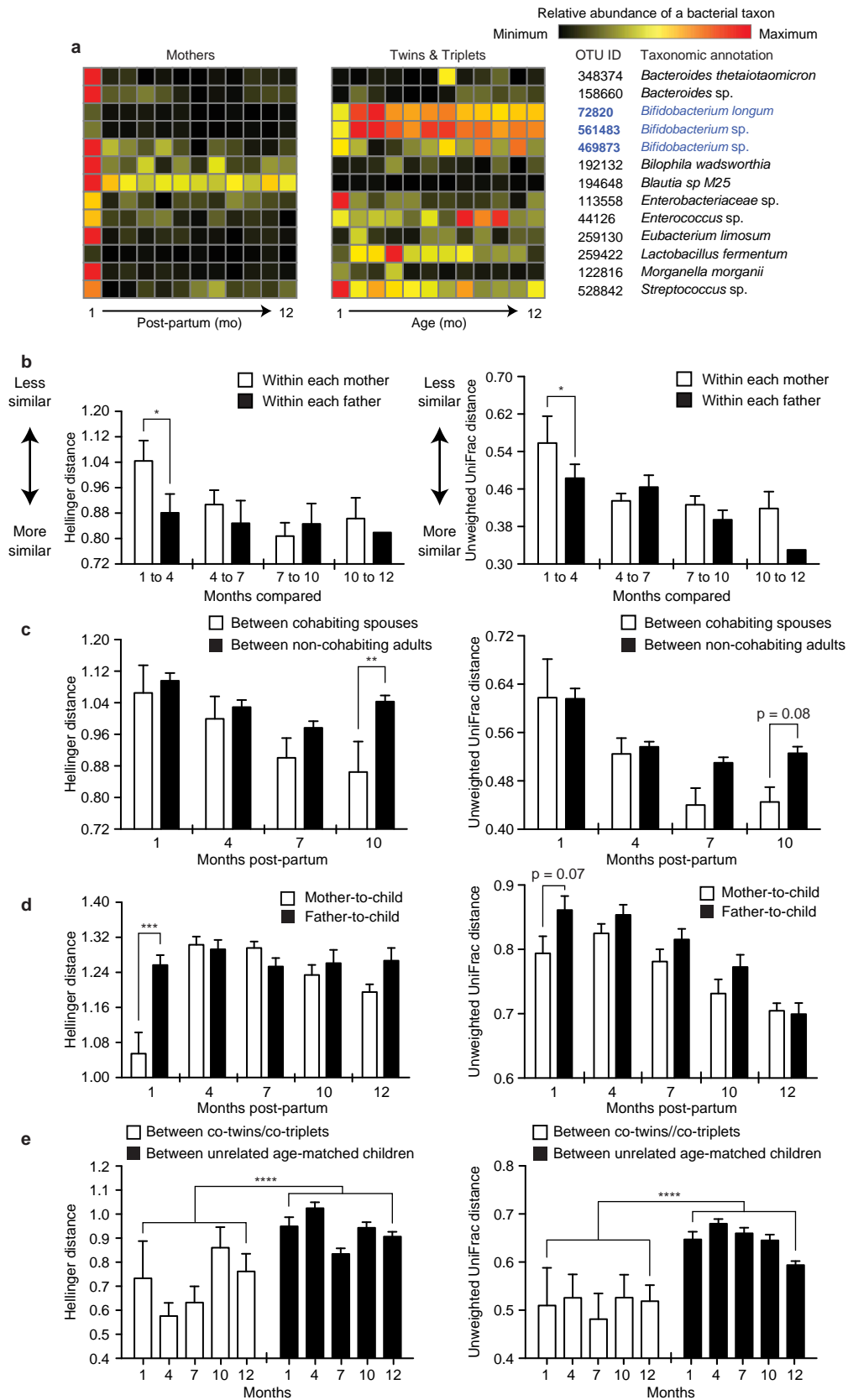
computed in samples collected from children used to validate the Random-Forests-based sparse 24-taxon model and are shown in **a**, as a broken line of the interpolated spline fit and in **b**, as median \pm s.d. values for each monthly chronologic age bin from months 1 to 24.



Extended Data Figure 2 | Transient microbiota immaturity and reduction in diversity associated with diarrhoea in healthy twins and triplets. **a**, The transient effect of diarrhoea in healthy children. Seventeen children from 10 families with healthy twins or triplets had a total of 36 diarrhoeal illnesses where faecal samples were collected. Faecal samples collected in the months immediately before and following diarrhoea in these children were examined in an analysis that included multiple environmental factors in the 'healthy twins and triplets' birth cohort. Linear mixed models of these specified environmental factors indicated that 'diarrhoea', 'month following diarrhoea' and 'presence of formula in diet' have significant effects on relative microbiota

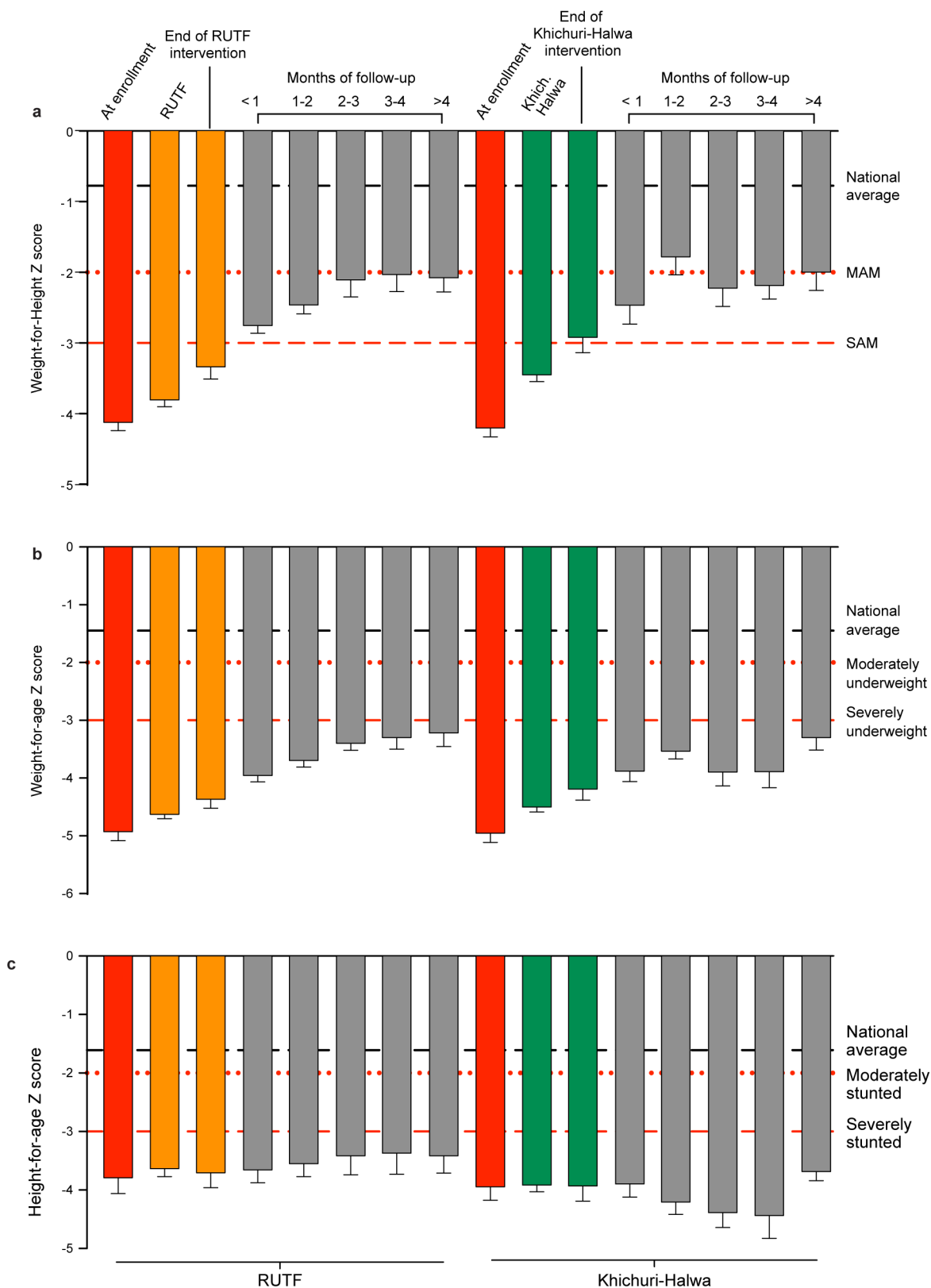
maturity, while accounting for random effects arising from within-family and within-child dependence in measurements of this maturity metric. The factors 'postnatal age', 'presence or absence of solid foods', 'exclusive breastfeeding', 'enteropathogen detected by microscopy', 'antibiotics' as well as 'other periods relative to diarrhoea' had no significant effect. The numbers of faecal samples (*n*) are shown in parenthesis. Mean values \pm s.e.m. are plotted.

* $P < 0.05$, *** $P < 0.001$. See Supplementary Table 7 for the effects of dietary and environmental covariates. **b**, Effect of diarrhoea and recovery on age-adjusted Shannon diversity index (SDI). Mean values of effect on SDI \pm s.e.m. are plotted. * $P < 0.05$, ** $P < 0.01$.



Extended Data Figure 3 | Gut microbiota variation in families with twins and triplets during the first year of life. **a**, Maternal influence. Heatmap of the mean relative abundances of 13 bacterial taxa (97%-identity OTUs) found to be statistically significantly enriched in the first month post-partum in the faecal microbiota of mothers (see column labelled 1) compared to microbiota sampled between the second and twelfth months post-partum (FDR-corrected $P < 0.05$; ANOVA of linear mixed-effects model with random by-mother intercepts). An analogous heatmap of the relative abundance of these taxa in their twin or triplet offspring is shown. Three of these 97%-identity OTUs are members of the top 24 age-discriminatory taxa (blue) and belong to the genus *Bifidobacterium*. **b–e**, comparisons of maternal, paternal and infant microbiota. Mean values \pm s.e.m. of Hellinger and unweighted UniFrac distances between the faecal microbiota of family members sampled over time were computed. Samples obtained at postnatal months 1, 4, 10 and 12 from twins and triplets, mothers and fathers were analysed ($n = 12$ fathers;

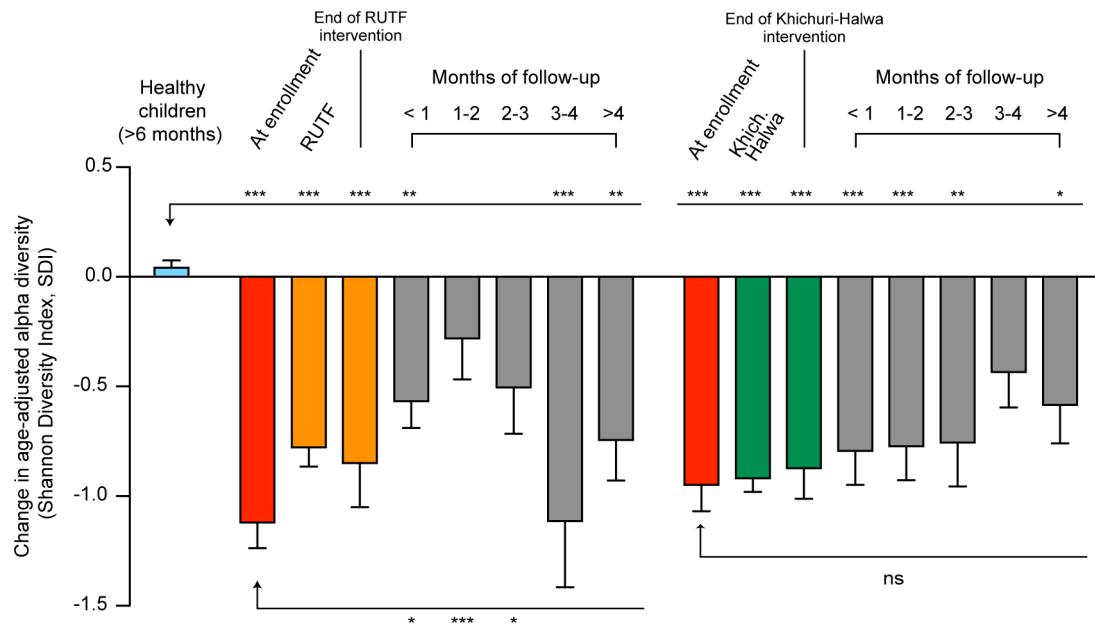
12 mothers; 25 children). **b**, Intrapersonal variation in the bacterial component of the maternal microbiota is greater between the first and fourth months after childbirth than variation in fathers. **c**, Distances between the faecal microbiota of spouses (each mother–father pair) compared to distances between all unrelated adults (male–female pairs). The microbial signature of co-habitation is only evident 10 months following childbirth. **d**, **e**, The degree of similarity between mother and infant during the first postpartum month is significantly greater than the similarity between microbiota of fathers and infants (**d**) while the faecal microbiota of co-twins are significantly more similar to one another than to age-matched unrelated children during the first year of life (**e**). For all distance analyses, Hellinger and unweighted UniFrac distance matrices were permuted 1,000 times between the groups tested. P values represent the fraction of times permuted differences between tested groups were greater than real differences between groups. * $P < 0.05$, ** $P < 0.01$, *** $P < 0.001$.



Extended Data Figure 4 | Anthropometric measures of nutritional status in children with SAM before, during and after both food interventions.

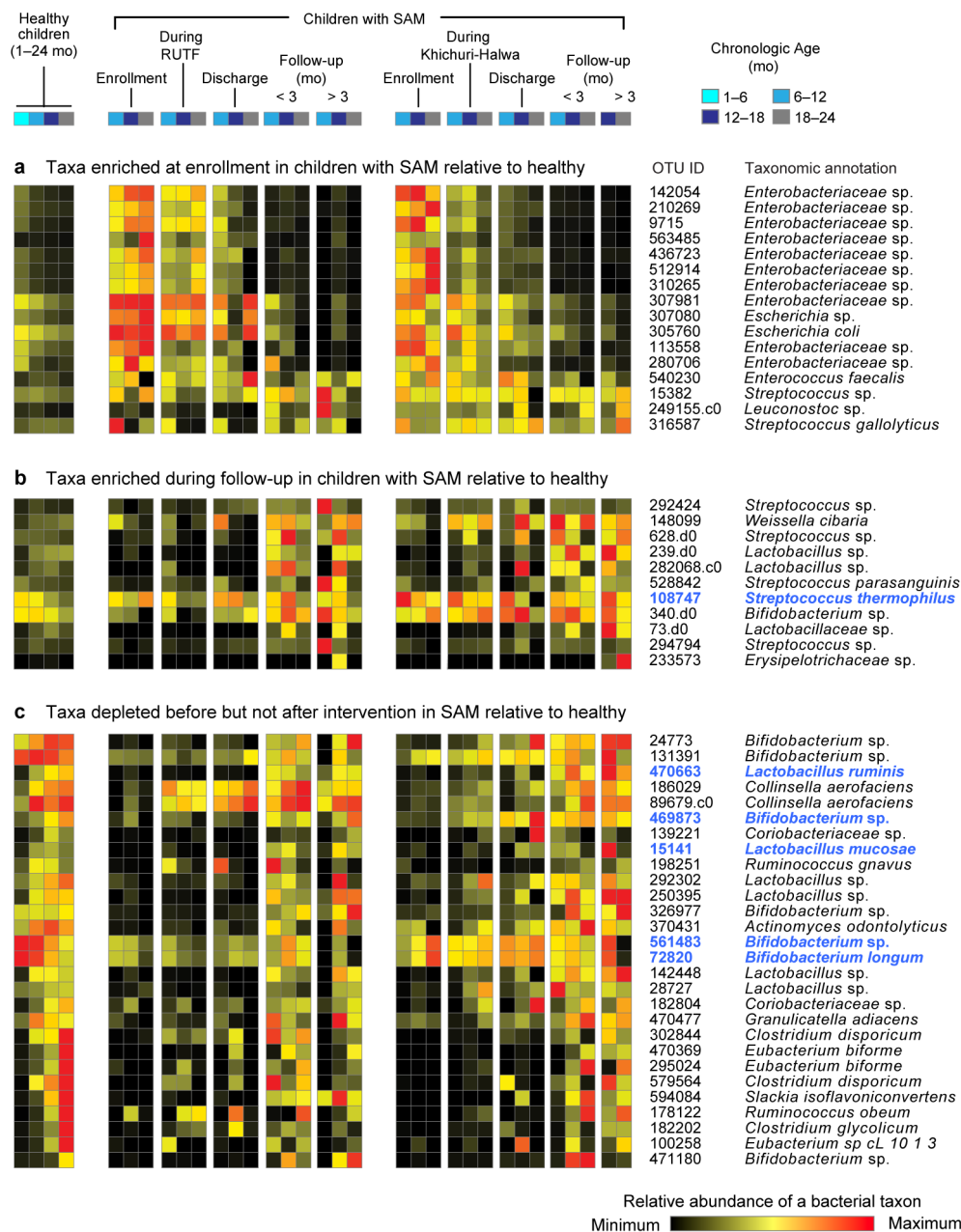
a–c, Weight-for-height Z-scores (WHZ) (**a**) height-for-age Z-scores (HAZ) (**b**) and weight-for-age Z-scores (WAZ) (**c**). Mean values \pm s.e.m. are plotted

and referenced to national average anthropometric values for children surveyed between the ages of 6 and 24 months during the 2011 Bangladeshi Demographic Health Survey (BDHS)²⁸.



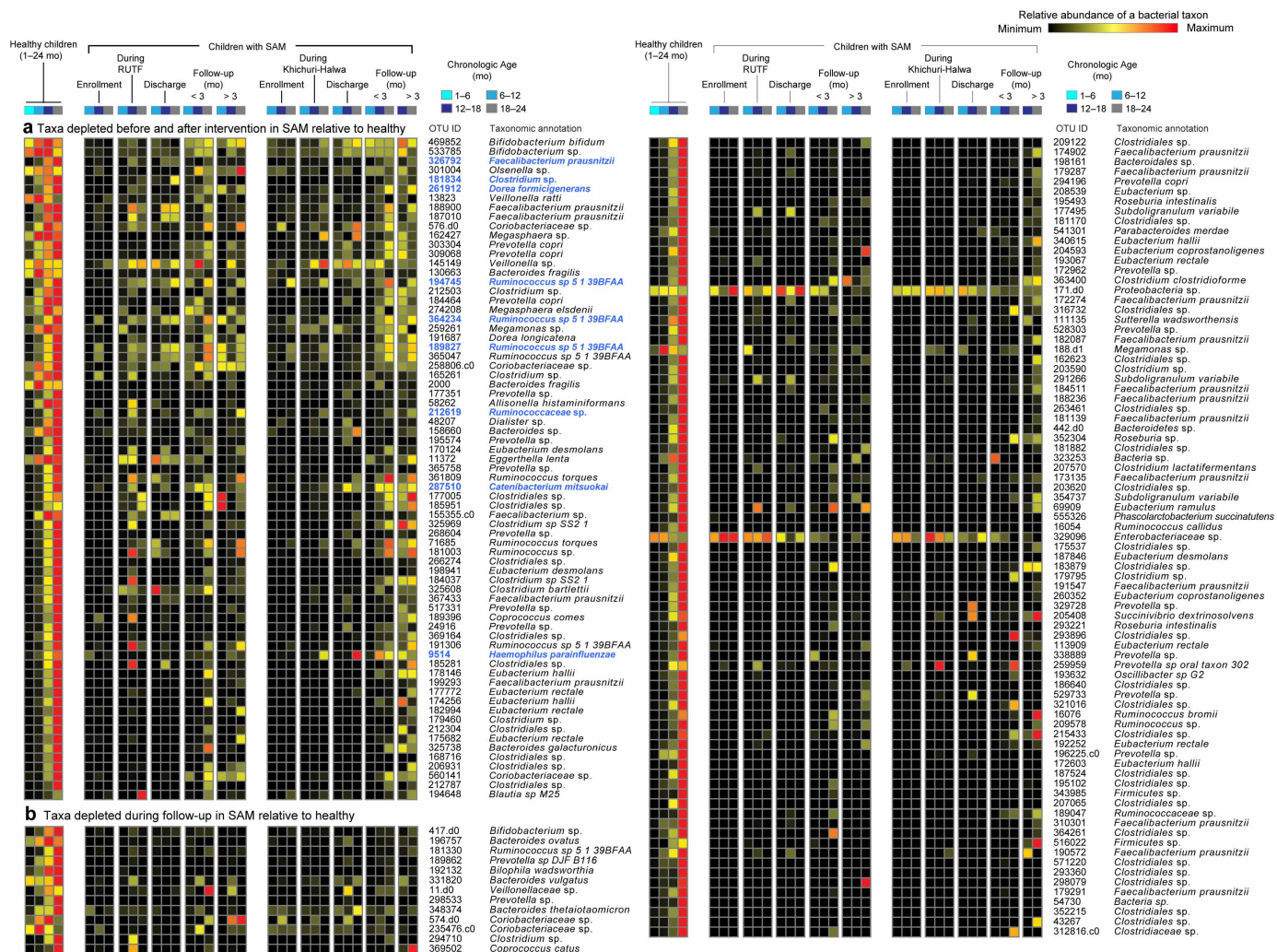
Extended Data Figure 5 | Persistent reduction of diversity in the gut microbiota of children with SAM. Age-adjusted Shannon diversity index for faecal microbiota samples collected from healthy children ($n = 50$), and from children with SAM at various phases of the clinical trial (mean values \pm s.e.m. are plotted). The significance of differences between SDI at

various stages of the clinical trial is indicated relative to healthy controls (above the bars) and versus the time of enrollment before treatment (below the bars). * $P < 0.05$, ** $P < 0.01$, *** $P < 0.001$ (post-hoc Dunnett's multiple comparison procedure of linear mixed models). See Supplementary Table 14.



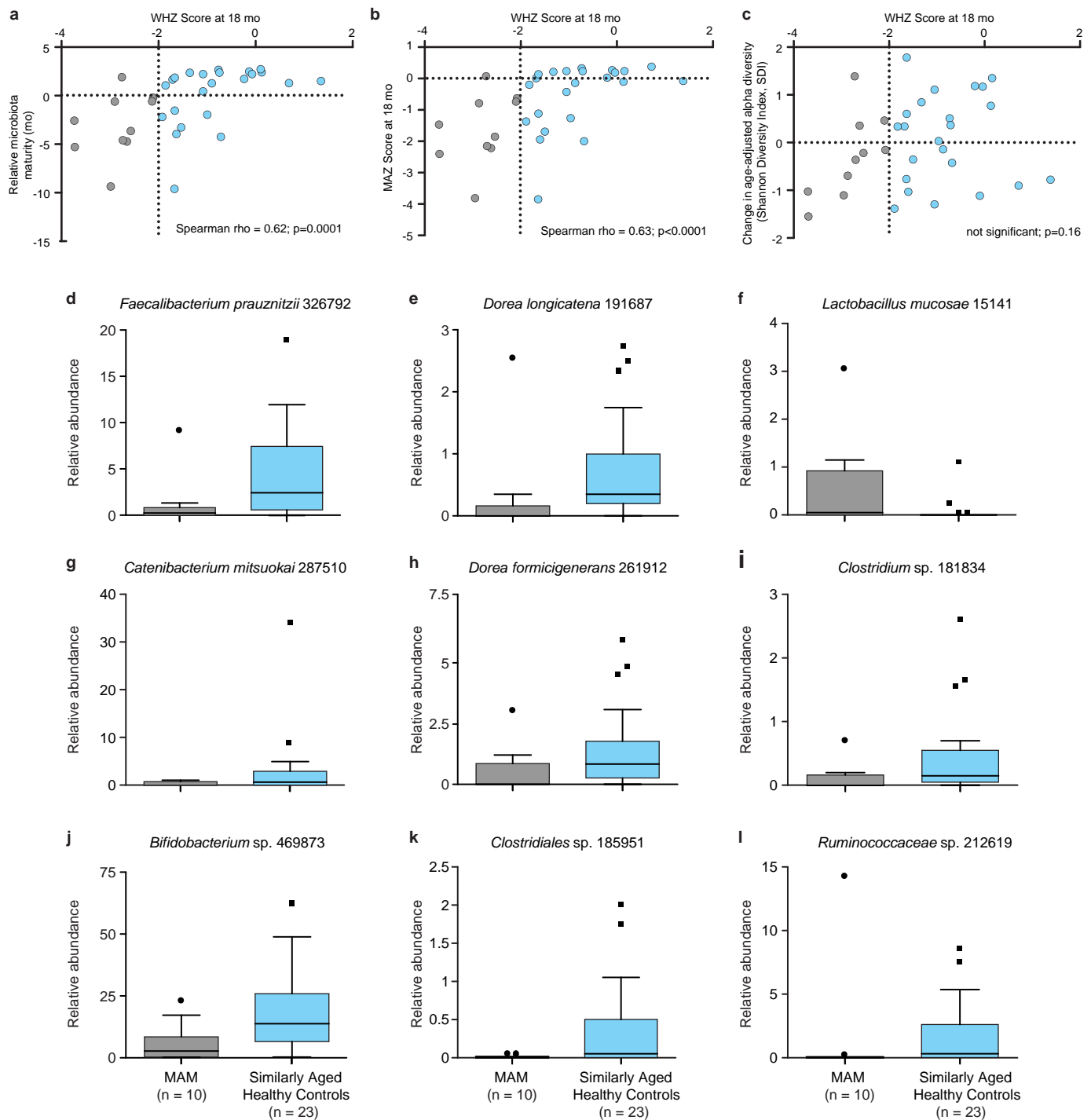
Extended Data Figure 6 | Heatmap of bacterial taxa significantly altered during the acute phase of treatment and nutritional rehabilitation in the microbiota of children with SAM compared to similar-age healthy children. Bacterial taxa (97%-identity OTUs) significantly altered (FDR-corrected $P < 0.05$) in children with SAM are shown (see Supplementary Table 15 for P values and effect size for individual taxa). Three groups of bacterial taxa are

shown: those enriched before the food intervention (a); those enriched during the follow-up phase compared to healthy controls (b); and those that are initially depleted but return to healthy levels (c). Members of the top 24 age-discriminatory taxa are highlighted in blue. Note that there were no children represented in the Khichuri–Halwa arm under the age of 12 months during the ‘follow-up after 3 months’ period.



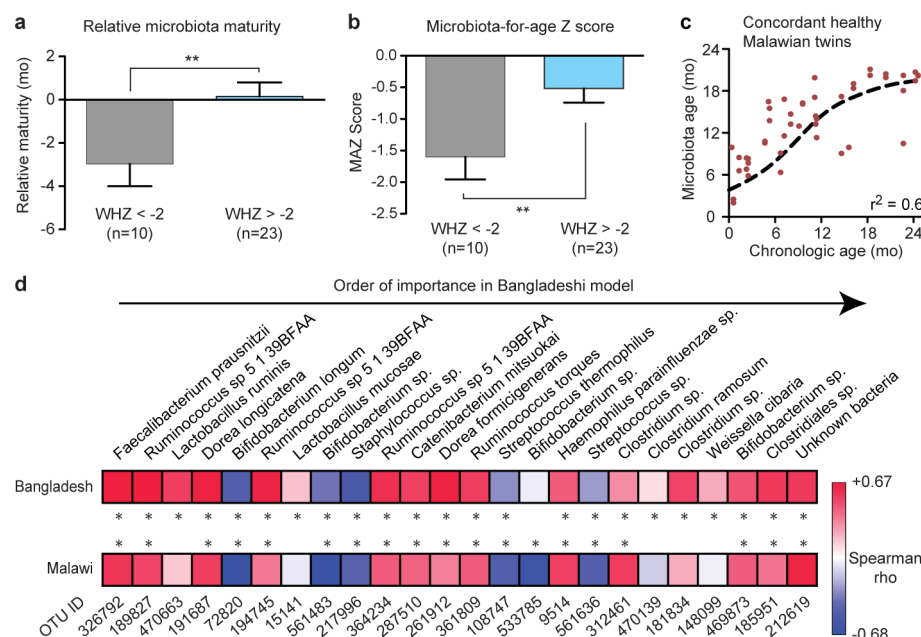
Extended Data Figure 7 | Heatmap of bacterial taxa altered during long-term follow-up in the faecal microbiota of children with SAM compared to similar-age healthy children. a, b, Bacterial taxa (97%-identity OTUs) significantly altered (FDR-corrected $P < 0.05$) in children with SAM are shown (see Supplementary Table 15 for P values and effect sizes for individual taxa).

a, Taxa depleted across all phases of SAM relative to healthy. b, Those depleted during the follow-up phase. Members of the top 24 age-discriminatory taxa are highlighted in blue. Note that there were no children under the age of 12 months represented in the Khichuri–Halwa treatment arm during the ‘follow-up after 3 months’ period.



Extended Data Figure 9 | Relative microbiota maturity and MAZ correlate with WHZ in children with MAM. **a–c**, WHZ are significantly inversely correlated with relative microbiota maturity (**a**) and MAZ (**b**) in a cross-sectional analysis of 33 children at 18 months of age who were above and below the anthropometric threshold for MAM (Spearman's $\rho = 0.62$ and 0.63 , respectively; $***P < 0.001$). In contrast, there is no significant correlation between WHZ and microbiota diversity (**c**). **d–l**, Relative abundances of age-discriminatory 97%-identity OTUs that are inputs to the Random Forests

model that are significantly different in the faecal microbiota of children with MAM compared to age-matched 18-month-old healthy controls (Mann–Whitney U -test, $P < 0.05$). Box plots represent the upper and lower quartiles (boxes), the median (middle horizontal line), and measurements that are beyond 1.5 times the interquartile range (whiskers) and above or below the 75th and 25th percentiles, respectively (points) (Tukey's method, PRISM software v6.0d). Taxa are presented in descending order of their importance to the Random Forests model. See Extended Data Fig. 10a, b.



Extended Data Figure 10 | Cross-sectional assessment of microbiota maturity at 18 months of age in Bangladeshi children with and without MAM, plus extension of the Bangladeshi-based model of microbiota maturity to Malawi. **a, b,** Children with MAM (WHZ lower than -2 s.d.; grey) have significantly lower relative microbiota maturity (**a**) and MAZ (**b**) compared to healthy individuals (blue). Mean values \pm s.e.m. are plotted $**P < 0.01$ (Mann–Whitney U -test). See Extended Data Fig. 9 for correlations of metrics of microbiota maturation with WHZ and box-plots of age-discriminatory taxa whose relative abundances are significantly different in children with MAM relative to healthy reference controls. **c,** Microbiota age predictions resulting from application of the Bangladeshi 24-taxon model to 47

faecal samples (brown circles) obtained from concordant healthy Malawian twins and triplets are plotted versus the chronologic age of the Malawian donor (collection occurred in individuals ranging from 0.4 to 25.1 months old). The results show the Bangladeshi model generalizes to this population, which is also at high risk for malnutrition (each circle represents an individual faecal sample collected during the course of a previous study¹¹). **d,** Spearman rho and significance of rank order correlations between the relative abundances of age-discriminatory taxa, and the chronologic age of all healthy Bangladeshi children described in the present study as well as concordant healthy Malawian twins and triplets. $*P < 0.05$.

Ribosomal oxygenases are structurally conserved from prokaryotes to humans

Rasheduzzaman Chowdhury¹, Rok Sekirnik^{1*}, Nigel C. Brissett^{2*}, Tobias Krojer³, Chia-hua Ho¹, Stanley S. Ng³, Ian J. Clifton¹, Wei Ge¹, Nadia J. Kershaw¹, Gavin C. Fox⁴, Joao R. C. Muniz³, Melanie Vollmar³, Claire Phillips³, Ewa S. Pilka³, Kathryn L. Kavanagh³, Frank von Delft³, Udo Oppermann^{3,5}, Michael A. McDonough¹, Aidan J. Doherty² & Christopher J. Schofield¹

2-Oxoglutarate (2OG)-dependent oxygenases have important roles in the regulation of gene expression via demethylation of *N*-methylated chromatin components^{1,2} and in the hydroxylation of transcription factors³ and splicing factor proteins⁴. Recently, 2OG-dependent oxygenases that catalyse hydroxylation of transfer RNA^{5–7} and ribosomal proteins⁸ have been shown to be important in translation relating to cellular growth, T_H17-cell differentiation and translational accuracy^{9–12}. The finding that ribosomal oxygenases (ROXs) occur in organisms ranging from prokaryotes to humans⁸ raises questions as to their structural and evolutionary relationships. In *Escherichia coli*, YcfD catalyses arginine hydroxylation in the ribosomal protein L16; in humans, MYC-induced nuclear antigen (MINA53; also known as MINA) and nucleolar protein 66 (NO66) catalyse histidine hydroxylation in the ribosomal proteins RPL27A and RPL8, respectively. The functional assignments of ROXs open therapeutic possibilities via either ROX inhibition or targeting of differentially modified ribosomes. Despite differences in the residue and protein selectivities of prokaryotic and eukaryotic ROXs, comparison of the crystal structures of *E. coli* YcfD and *Rhodothermus marinus* YcfD with those of human MINA53 and NO66 reveals highly conserved folds and novel dimerization modes defining a new structural subfamily of 2OG-dependent oxygenases. ROX structures with and without their substrates support their functional assignments as hydroxylases but not demethylases, and reveal how the subfamily has evolved to catalyse the hydroxylation of different residue side chains of ribosomal proteins. Comparison of ROX crystal structures with those of other JmjC-domain-containing hydroxylases, including the hypoxia-inducible factor asparaginyl hydroxylase FIH and histone *N*^e-methyl lysine demethylases, identifies branch points in 2OG-dependent oxygenase evolution and distinguishes between JmjC-containing hydroxylases and demethylases catalysing modifications of translational and transcriptional machinery. The structures reveal that new protein hydroxylation activities can evolve by changing the coordination position from which the iron-bound substrate-oxidizing species reacts. This coordination flexibility has probably contributed to the evolution of the wide range of reactions catalysed by oxygenases.

To investigate the structural basis of catalytic differences within the ROX subfamily of JmjC-domain-containing hydroxylases and their relationship with the JmjC-containing histone *N*^e-methyl lysine demethylases (KDMs, Fig. 1a), we conducted structural analyses on both prokaryotic (initially YcfD from *E. coli* (EcYcfD) and subsequently that from the thermophile *R. marinus* (RmYcfD)) and human ROXs (MINA53_{26–465} and NO66_{183–641}). We used RmYcfD to obtain a YcfD substrate structure. All four ROXs show marked similarities in their folds: the JmjC domain is followed by helical dimerization and carboxy-terminal ‘winged helix’ (WH) domains¹³ (Fig. 1b). The ROX JmjC domains consist of

11–12 β -strands, 8 of which (I–VIII) form a double-stranded β -helix (DSBH), which is stereotypical of 2OG-dependent oxygenases^{14,15} (Fig. 1c and Extended Data Fig. 1).

The dimerization domains have a two-fold symmetry and comprise a bundle of three α -helices (Extended Data Fig. 2); the dimers are stabilized by electrostatic and hydrogen bonding as well as hydrophobic interactions. Consistent with a catalytic role for this domain, dimerization blocking substitutions, EcYcfD(I211R) and MINA53(R313E) decrease activity. Hydrogen-bonding and electrostatic interactions are substantially more important in RmYcfD dimerization than for the other ROXs, consistent with the increased occurrence of electrostatic interactions in thermophiles¹⁶. The ROX C-terminal domains, which are required for activity (Extended Data Fig. 3), are reminiscent of WH domains involved in protein–protein and protein–nucleic-acid interactions¹³; however, their overall negative charge suggests that they may not directly bind nucleic acids. In contrast to ROXs, other JmjC-containing hydroxylases—FIH¹⁷, tRNA yW-synthesizing protein 5 (TYW5)⁶, JmjC-domain-containing protein 4 (JMJD4)⁹, JMJD5 (ref. 18) and JMJD6 (ref. 4)—and KDMs, do not contain a WH domain (Fig. 2). The combined structures led to the proposal that the ROX fold evolved into those of JmjC-containing hydroxylases and KDMs partly via loss of the WH domain, which enabled the C-terminal helical bundle to take on other roles as in KDMs or the dimerization mode as observed in FIH¹⁷.

ROX structures were determined in complex with Mn(II) and 2OG or *N*-oxalylglycine (NOG), replacing Fe(II) and 2OG. As for most 2OG-dependent oxygenases, the metal is octahedrally coordinated by a 2-His-1-carboxylate triad from DSBH β II and β VII^{14,15} (Fig. 3); two coordination sites are occupied by the 2OG/NOG oxalyl group, leaving one for H₂O/O₂ binding (Fig. 4 and Extended Data Fig. 4). With the YcfDs, the NOG C5 carboxylate is positioned to salt bridge with EcYcfD Arg 140 or RmYcfD Arg 148 on DSBH β IV (Extended Data Fig. 4). This arrangement is notable because with other 2OG-dependent oxygenases in which the 2OG C5 carboxylate interacts with an Arg residue, it is located on β VIII^{14,15}. In human ROXs, the 2OG C5-carboxylate-interacting residue is a lysine (MINA53 Lys 194, NO66 Lys 355) from β IV, as in most JmjC-containing hydroxylases and KDMs. These observations suggest that eukaryotic JmjC-containing hydroxylases and KDMs evolved from prokaryotic ROXs.

Initial attempts to obtain substrate complexes by co-crystallization/soaking crystals were unsuccessful. We therefore pursued alternatives, one involving using a thermostable YcfD homologue, which we considered may have a relatively low substrate dissociation constant (*K*_d), enabling complex crystallization. RmYcfD (which has 31% identity with EcYcfD) catalyses L16 fragment (20-residue peptide, amino acids Lys 72–Glu 91) Arg 82 hydroxylation with an approximately sevenfold lower Michaelis constant (*K*_m) than EcYcfD (268 μ M and 1.9 mM, respectively). A RmYcfD–L16_{72–91} structure, obtained by co-crystallization, was solved

¹The Department of Chemistry and Oxford Centre for Integrative Systems Biology, University of Oxford, Mansfield Road, Oxford OX1 3TA, UK. ²Genome Damage and Stability Centre, University of Sussex, Brighton BN1 9RQ, UK. ³Structural Genomics Consortium, University of Oxford, Headington, Oxford OX3 7DQ, UK. ⁴Synchrotron SOLEIL, Saint Aubin, 91192 Gif-sur-Yvette Cedex, France. ⁵NIHR Oxford Biomedical Research Unit, Botnar Research Centre, Oxford OX3 7LD, UK.

*These authors contributed equally to this work.

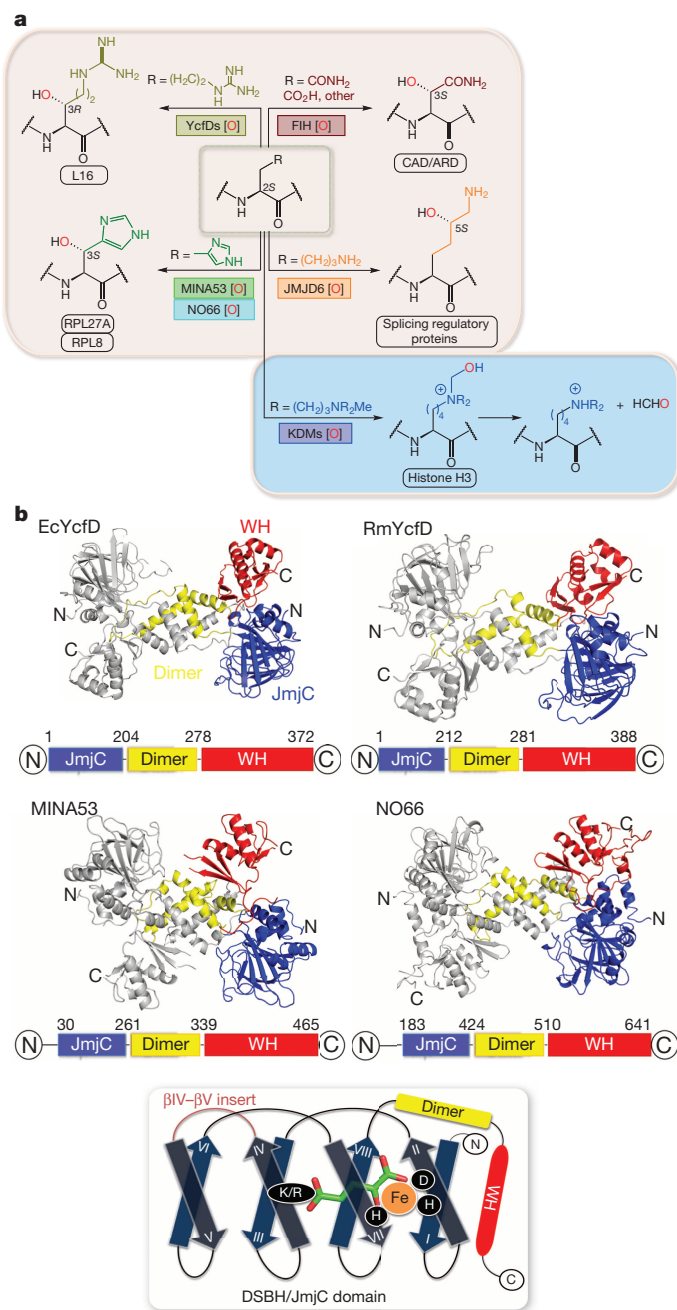


Figure 1 | The overall folds of the ribosomal oxygenases. **a**, Reactions catalysed by ROX and related oxygenases. ARD, ankyrin repeat domain; CAD, C-terminal transactivation domain of HIF- α . **b**, Ribbon representations of EcYcfD, RmYcfD, MINA53 and NO66 homodimers. The monomers contain a JmjC domain with the DSBH core present in all 2OG-dependent oxygenases (blue) followed by dimerization (yellow) and C-terminal WH domains (red). Domain architecture and a schematic representation of the DSBH core β -strands (β I–VIII) that form major (blue, β I, β VIII, β III and β VI) and minor sheets (grey, β II, β VII, β IV and β V) is shown boxed. The insert between β IV and β V (purple) is involved in substrate binding. The three Fe-coordinating residues are on the β II and β VII strands (black circles). 2OG is in green sticks; the 2OG C5-carboxylate-binding residue, Arg (YcfDs) or Lys (human ROXs) from β IV is a black circle.

by molecular replacement using the apo EcYcfD structure (Protein Data Bank (PDB) accession 4CCL). The overall EcYcfD and RmYcfD structures are similar (C α root mean squared deviation (r.m.s.d.) 1.58 Å); L16 residues Lys 77–Lys 85 are visible in the electron density map (Fig. 3c).

For the human ROXs, we used electrospray ionization–mass spectrometry guided disulphide crosslinking^{19,20} to obtain substrate complexes

(Extended Data Fig. 5). Structures were obtained for wild-type NO66–RPL8(G220C) (complex 1), NO66(L299C/C300S)–RPL8(G220C) (complex 2) and NO66(S373C)–RPL8(G214C) (complex 3) pairs. Electron density corresponding to RPL8 residues 215–223 (complex 1), 213–223 (complex 2) and 212–223 (complex 3) was observed at the active site (Fig. 3b and Extended Data Fig. 5). The RPL8 residues (215–219)—including the hydroxylated His 216—adopt near identical conformations (C α r.m.s.d., 0.29–0.36 Å), implying that all three structures represent catalytically functional complexes (Extended Data Fig. 5). In the light of the NO66–RPL8 structures, we identified a MINA53 residue (Tyr 209) suitable for crosslinking: MINA53(Y209C) crystallized in complex with RPL27A(G37C) with electron density observed for RPL27A residues 36–44 (Fig. 3a). Further validation of the functional relevance of the crosslinked structures comes from comparisons with the wild-type RmYcfd–L16 structure and kinetic studies demonstrating activities with most variants (Extended Data Fig. 6).

MINA53 and NO66 bind their RPL27A and RPL8 substrates in a conserved manner ($C\alpha$ r.m.s.d., RPL27A_{38–43}, RPL8_{215–220}; 0.8 Å). Comparison of human ROX and RmYcfD complexes reveals similarities in substrate binding, particularly for the hydroxylated residue and for substrate residues to the amino-terminal side of the hydroxylated residue. In all ROX complexes, substrates bind with the same N/C directionality, as observed for FIH¹⁷ and for one KDM—plant homeodomain finger 8 (PHF8)²¹ (and probably other KDM2/7 subfamily members)—but differing from that for most KDMs (KDM4A²², KDM6B²³ and KDM6A²⁴) (Fig. 2). The substrates bind in shallow channels on the ROX surfaces and form multiple interactions/hydrogen bonds with residues from DSBH β I, β II and β VIII, and the extended β IV– β V loop. Although the N-terminal regions of RPL27A (amino acids 36–39), RPL8 (213–216) and L16 (78–81) bind similarly, the C-terminal regions of RPL27A (40–44) and RPL8 (217–223) form more extensive interactions with human ROXs than does L16 (83–85) with RmYcfD (Fig. 3). Notably, both RPL27A and RPL8 substrates make hydrophobic contacts with the WH domains in MINA53 and NO66 (Extended Data Fig. 3). In addition, MINA53 forms a catalytically important salt-bridge interaction between RPL27A Arg 42 and MINA53 Asp 333 located on the α -helix connecting the dimerization and WH domains (Extended Data Figs 6 and 7).

The general binding mode of the hydroxylated residues is conserved between prokaryotic and human ROXs, that is, they bind in deep pockets and the positions of the hydroxylated β -methylenes nearly superimpose (Fig. 4). There are, however, clear differences in the way human ROXs and RmYcfD bind their target residue side chains (Fig. 3). With human ROXs, the binding of RPL27A His 39/RPL8 His 216 involves a series of hydrogen bonds to backbone amides or side chains of human ROX residues: MINA53 Gln 136/NO66 Arg 297; MINA53 Asn 165/NO66 Asn 326; MINA53 Tyr 167/NO66 Tyr 328; and MINA53 Ser 257/NO66 Ser 421 (Fig. 3a, b). With RmYcfD, the Arg 82 'slots' into a hydrophobic cleft defined by RmYcfD Tyr 137 and Met 120 side chains and hydrogen bonds to RmYcfD Asp 118 and Ser 208 (Fig. 3c). Mutagenesis studies on ROXs support the observed binding modes of the substrate residues (Extended Data Figs 6 and 8).

There are conflicting reports as to the catalytic activities of some JmjC-containing hydroxylases, including NO66, which has been classified as both a hydroxylase⁸ and a KDM²⁵. Comparison of ROXs with KDMs and FIH (Figs 2 and 4a) identifies distinctive structural features characteristic of JmjC-containing hydroxylases and KDMs, in addition to the roles of the WH domains. This is important because it supports the assignment of hydroxylase (but not demethylase) activities for ROXs and other human JmjC-containing hydroxylases; for example, FIH¹⁷ and JMJD6 (ref. 4). In our assays with isolated MINA53 and NO66 we have consistently not observed enzyme-catalysed demethylation under conditions in which JmjC-containing KDMs are active⁸. Although we cannot rule out the possibility that some of the JmjC-containing hydroxylases may have KDM activities under different conditions or in cells, the multiple structures reported here suggest that for this to occur, substantial active-site rearrangements would be required on substrate binding. In

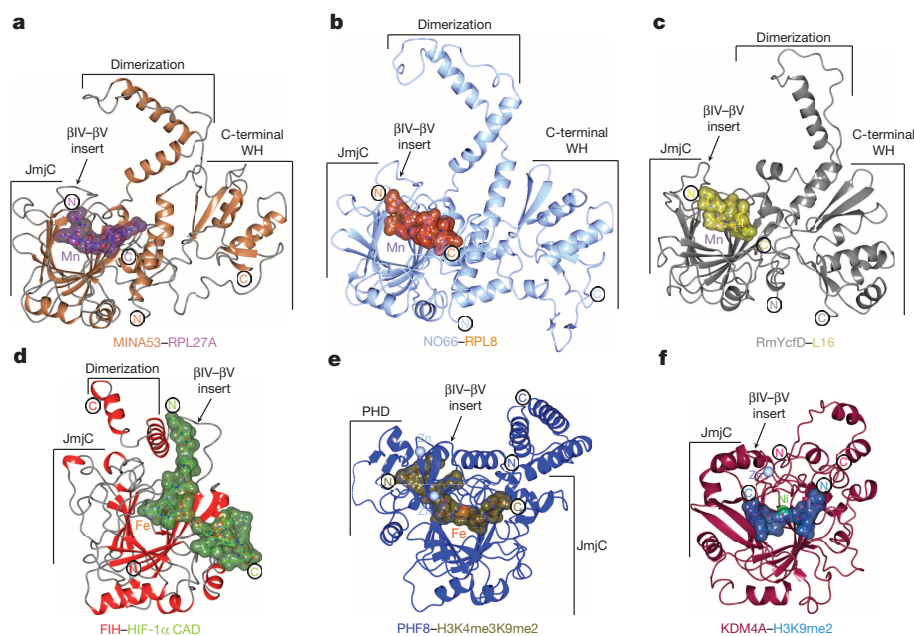


Figure 2 | Comparison of the substrate structures for ROXs and JmjC-containing enzymes. **a–f**, Ribbon representations of ROX and related 2OG-dependent oxygenase-substrate complexes. **a**, MINA53-Mn-2OG-RPL27A_(32–50) (P_{2121} , 2.05 Å). **b**, NO66-Mn-NOG-RPL8_(205–224) (P_{2121} , 2.35 Å). **c**, RmYcfD-Mn-NOG-L16_(72–91) (P_{2121} , 3.0 Å). **d**, FIH-Fe-NOG-HIF-1 α _(786–826) (PDB accession 1H2K). **e**, PHF8-Fe-NOG-H3K4me3K9me2_(2–25) (PDB accession 3KV4). **f**, KDM4A-Ni-NOG-H3K9me2_(7–14) (PDB accession 2OX0). For comparison, the DSBH core of each structure is in a similar orientation. Note the directionality of substrate binding in the JmjC domains. The active-site metals (Fe/surrogate) are colour-coded spheres. Analyses of the structures reveal that the ROX overall folds (**a–c**), oligomerization states and active-site architectures are evolutionarily conserved.

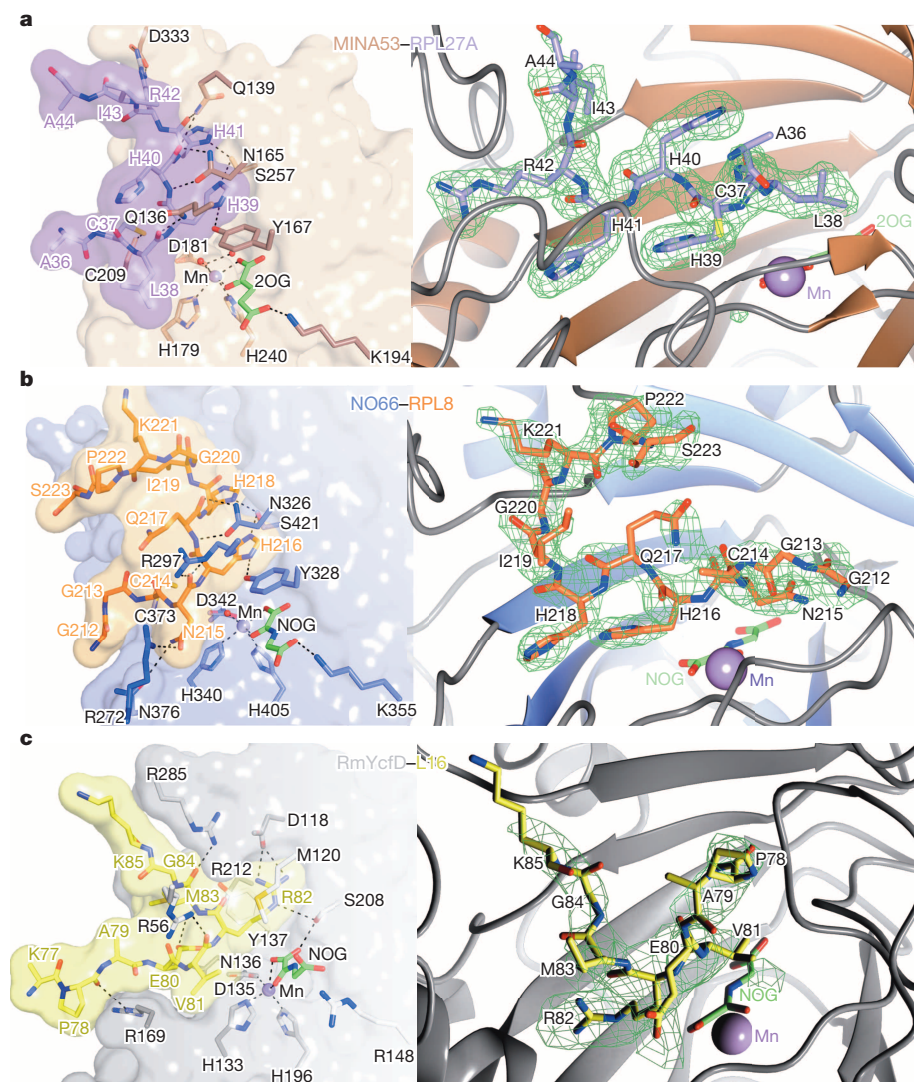


Figure 3 | Features of ROX-substrate binding. **a–c**, Ribbon representations of MINA53 (**a**), NO66 (**b**) and RmYcfD (**c**) monomers showing difference electron density ($F_o - F_c$ omit map) for substrates contoured to 3σ (right panels). Left panels depict active-site surface representations, showing key hydrogen bonds and polar interactions (dotted lines) with substrates. **a**, With MINA53, the RPL27A His 39 imidazole nitrogens form hydrogen bonds with Tyr 167/Ser 257 ($N\delta_{\text{His 39-OH}}\text{Tyr 167}$ 2.9 Å; $N\epsilon_{\text{His 39-O}}\text{'Ser 257}$ 3.1 Å). **b**, In NO66, RPL8 His 216 is similarly bound in a deep pocket; the RPL8 His 216 imidazole nitrogens form hydrogen bonds with Tyr 328/Ser 421 ($N\delta_{\text{His 216-OH}}\text{Tyr 328}$ 3.2 Å; $N\epsilon_{\text{His 216-O}}\text{'Ser 421}$ 2.7 Å) and hydrophobic interactions with Ile 244 that project its pro-S hydrogen towards the metal (metal- $\beta\text{-CH}_2$, 4.4 Å). **a, b**, Although MINA53 (**a**) uses four primary amides—Asn 101, Gln 136, Gln 139 and Asn 165—to interact with RPL27A backbone amides, NO66 (**b**) uses two arginines (272, 297) to hydrogen bond with the RPL8 Asn 215 side chain and RPL8 His 216 backbone. **c**, In the RmYcfD-L16 complex, the L16 Arg 82 binds in a pocket defined by the Tyr 137/Met 120 side chains, which form π -cation and hydrophobic interactions with the L16 Arg 82 side chain. The Arg 82 guanidino group makes electrostatic interactions with the RmYcfD Asp 118 carboxylate (O-NH , 2.8–3.1 Å) and hydrogen bonds to RmYcfD Ser 208 ($N\epsilon_{\text{Arg 82-OH}}\text{'Ser 208}$ 3.5 Å; $N\eta_{\text{Arg 82-CO}}\text{'Ser 208}$ 3.2 Å). Although MINA53 Tyr 167 and NO66 Tyr 328 are not positionally related to RmYcfD Tyr 137, the role of the serine (MINA53 Ser 257, NO66 Ser 421, RmYcfD Ser 208, βVIII) in binding the hydroxylated His/Arg is conserved in ROXs. Substitutions of these residues cause marked loss of activity (see Extended Data Fig. 6).

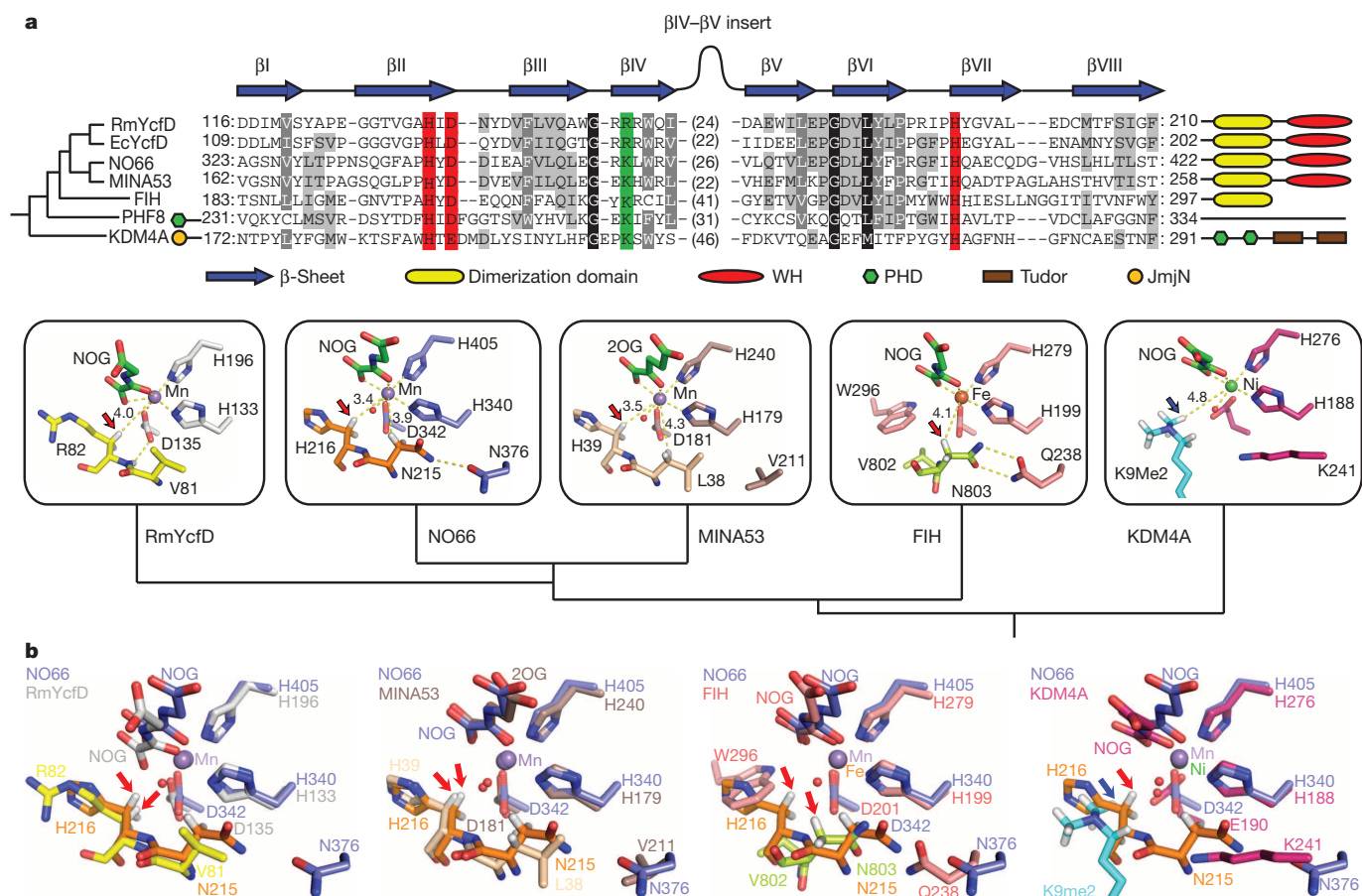


Figure 4 | Proposed sequence of evolution of active-site chemistry of ROXs and related JmjC-containing 2OG-dependent oxygenases. **a**, **b**, The figure compares views from active sites of representative JmjC-containing enzymes and suggests how the ROX fold evolved into JmjC-containing hydroxylases and KDMs. Structurally informed cross-genomic bioinformatic analyses imply that ROXs are the earliest identified JmjC-containing 2OG-dependent oxygenases³⁰; YcfD and NO66 both exist in prokaryotes but only NO66 is identified in eukaryotes. Coupled to the analyses of the active sites, these analyses imply that NO66 and its close relatives are the precursors of MINA53 and other JmjC-containing hydroxylases and KDMs. **a**, Top, structure-based alignment of ROX, FIH, PHF8 and KDM4A with the DSBH core, labelled βI–VIII, the iron-coordinating and the 2OG C5-carboxylate-binding residues are indicated in red and green. Bottom, analyses of active sites suggest conservation of metal/2OG binding in ROX, FIH and KDMs. Note the 2OG

C5-carboxylate-binding residue (usually from βIV in JmjC-containing enzymes) changes from an Arg (in YcfDs) to a Lys (in human ROXs and JmjC-containing hydroxylases/KDMs) (Extended Data Fig. 4). **b**, Overlays of the NO66/RmYcfD, NO66/MINA53, NO66/FIH and NO66/KDM4A active-site views. The hydroxylated β-methylenes nearly superimpose in ROXs, such that the oxidized C–H bonds (red arrows, 3-pro-R in L16 Arg 82 and 3-pro-S in RPL27A His 39 and RPL8 His 216) project towards the metal. The spatial relationship of the hydroxylated C3/Ne-methyl carbon with respect to the metal (and associated reactive oxidizing species) is conserved in ROXs and the demethylases, for example, KDM4A, but not in FIH. Note the different hydroxylation positions, but the similar orientation of the CAD Asn 803 (bound to FIH) (hydroxylated) and RPL8 Asn 215 (bound to NO66) (not hydroxylated).

ROXs and KDM4A–H3K9me2 (PDB accession 2OX0)²² complex structures, the different substrates bind with ‘opposite’ N-to-C directionalities with respect to the catalytic machinery. The histone K9me_n side chain is positioned similarly to the ROX-hydroxylated residue side chains; however, because KDM-catalysed hydroxylations occur at N^ε-methyl lysine-residue termini, their target residues do not penetrate as far into the enzyme active site (Fig. 4a). The ROXs also lack two flexible loops linking α4–βI (amino acids 164–175) and α9–α10 (amino acids 302–317) in KDM4A, which are conserved in KDMs^{21–24} and which form important interactions with the Kme_n side chain, illustrating how the ‘core’ ROX fold has been modified by evolution to accommodate the Kme_n side chain.

Like ROXs, FIH catalyses β-hydroxylation of an Asn residue in its HIF-α transcription factor substrate¹⁷ and of other residues, including histidines in ankyrins²⁶. Superimposition of human ROX and FIH-substrate structures is interesting from catalytic and evolutionary perspectives. Although both FIH and human ROXs catalyse histidine 3S hydroxylation, the positions of their substrate imidazoles is markedly different (Fig. 4 and Extended Data Fig. 9). The positioning of hydroxylated methylenes relative to the metal differs substantially: in the overlaid

structures, the angle between the metal and the Cβ atoms of the RPL27A His 39/RPL8 His 216 (human ROX substrate) and HIF-1α Asn 803 (FIH substrate) is ~50° (Fig. 4 and Extended Data Fig. 9), demonstrating that the reactive oxidizing intermediates (Fe(IV)=O)^{15,27} react from different coordination positions in different oxygenases. Studies with 2OG-dependent halogenases have led to the proposal that iron-bound reactive intermediates abstract a hydrogen from the substrate and deliver a halogen or hydroxyl from different coordination positions to form products²⁸. In contrast, our work implies flexibility in the coordination positions with respect to the hydrogen abstracted in different JmjC-containing hydroxylases from which the ferryl-oxo reacts. Together with other structural considerations, this observation has consequences for the evolution of the JmjC-containing oxygenases.

RPL8 (NO66 substrate) has an Asn at the –1 position relative to the hydroxylated His 216 (YcfD/MINA53 substrates have hydrophobic residues at the analogous positions). The RPL8 Asn 215 methylene is only slightly (0.5 Å) further from the metal than that of RPL8 His 216, revealing the extreme sensitivity of oxygenase catalysis to geometric positioning. There is a notable correlation in the binding of RPL8 Asn 215 and HIF-1α Asn 803 to NO66 and FIH, respectively, even though one residue is

hydroxylated and one is not; the primary amides of both RPL8 Asn 215 and HIF-1 α Asn 803 hydrogen bond with primary amides, that is, NO66 Asn 376 and FIH Gln 239. Collectively these observations reveal that 2OG-dependent oxygenases can evolve new activities not only by 'directly' altering the nature of enzyme–substrate interactions (including by altering the directionality of substrate binding), but also by changing the coordination position from which the ferryl intermediate reacts.

The combined structures reveal that the observed modes of ROX hydroxylations have probably evolved into those of other JmjC-containing hydroxylases and the KDMs, both by altering the coordination position from which the ferryl-oxo reacts and by engineering the depth of substrate penetration. Structurally informed phylogenetic analyses (Extended Data Fig. 10), coupled to the observation that NO66 is more widely distributed than FIH and MINA53, reveal that prokaryotic YcfDs evolved into NO66, which is a branch point leading to the eukaryotic JmjC-containing hydroxylases and demethylases. 2OG-dependent oxygenases are among the most catalytically flexible of all enzyme families. Recent work has revealed that FIH manifests remarkable catalytic promiscuity, including the ability to oxidize Asn and His residues²⁹. Our structural studies reveal that ROXs react with substrates through a different but evolutionarily related binding mode to FIH. The catalytic capabilities of 2OG-dependent oxygenases for protein oxidations thus probably extend beyond those presently identified.

METHODS SUMMARY

Recombinant human MINA53 and NO66 and bacterial EcYcfD and RmYcfD were produced in *E. coli* and purified by metal affinity/cation exchange and size-exclusion chromatography. Assays comprised incubation with Fe(II), 2OG and substrate followed by mass spectrometry and/or 2OG turnover assays. Crystals were grown by vapour diffusion (Supplementary Table 1) and cryo-cooled in liquid nitrogen. Data were collected on Swiss Light Source X10SA, European Synchrotron Radiation Facility BM16 and Diamond Light Source MX beamlines. MINA53 and EcYcfD structures were solved by single-wavelength anomalous diffraction or by single isomorphous replacement with anomalous scattering using SeMet derivatives. The NO66 structure was solved by molecular replacement (MR) using the MINA53 JmjC domain. Phases of the substrate complex structures were solved by MR using apo structures (MINA53 (PDB accession 4BU2), NO66 (PDB accession 4DIQ); Supplementary Tables 2–4).

Online Content Any additional Methods, Extended Data display items and Source Data are available in the online version of the paper; references unique to these sections appear only in the online paper.

Received 30 September 2013; accepted 14 March 2014.

Published online 11 May 2014.

- Klose, R. J. & Zhang, Y. Regulation of histone methylation by demethylination and demethylation. *Nature Rev. Mol. Cell Biol.* **8**, 307–318 (2007).
- Walport, L. J., Hopkinson, R. J. & Schofield, C. J. Mechanisms of human histone and nucleic acid demethylases. *Curr. Opin. Chem. Biol.* **16**, 525–534 (2012).
- Kaelin, W. G. Jr & Ratcliffe, P. J. Oxygen sensing by metazoans: the central role of the HIF hydroxylase pathway. *Mol. Cell* **30**, 393–402 (2008).
- Webby, C. J. et al. Jmjd6 catalyses lysyl-hydroxylation of U2AF65, a protein associated with RNA splicing. *Science* **325**, 90–93 (2009).
- Fu, Y. et al. The AlkB domain of mammalian ABH8 catalyzes hydroxylation of 5-methoxycarbonylmethyluridine at the wobble position of tRNA. *Angew. Chem. Int. Edn Engl.* **49**, 8885–8888 (2010).
- Kato, M. et al. Crystal structure of a novel JmjC-domain-containing protein, TYW5, involved in tRNA modification. *Nucleic Acids Res.* **39**, 1576–1585 (2011).
- van den Born, E. et al. ALKBH8-mediated formation of a novel diastereomeric pair of wobble nucleosides in mammalian tRNA. *Nature Commun.* **2**, 172 (2011).
- Ge, W. et al. Oxygenase-catalyzed ribosome hydroxylation occurs in prokaryotes and humans. *Nature Chem. Biol.* **8**, 960–962 (2012).
- Feng, T. et al. Optimal translational termination requires C4 lysyl hydroxylation of eRF1. *Mol. Cell* **53**, 645–654 (2014).
- Henri, J. et al. Structural and functional insights into *Saccharomyces cerevisiae* Tpa1, a putative prolylhydroxylase influencing translation termination and transcription. *J. Biol. Chem.* **285**, 30767–30778 (2010).
- Loenarz, C. et al. Hydroxylation of the eukaryotic ribosomal decoding center affects translational accuracy. *Proc. Natl Acad. Sci. USA* **111**, 4019–4024 (2014).

- Yosef, N. et al. Dynamic regulatory network controlling T_H17 cell differentiation. *Nature* **496**, 461–468 (2013).
- Teichmann, M., Dumay-Odelot, H. & Fribourg, S. Structural and functional aspects of winged-helix domains at the core of transcription initiation complexes. *Transcription* **3**, 2–7 (2012).
- Hausinger, R. P. Fell/ α -ketoglutarate-dependent hydroxylases and related enzymes. *Crit. Rev. Biochem. Mol. Biol.* **39**, 21–68 (2004).
- Clifton, I. J. et al. Structural studies on 2-oxoglutarate oxygenases and related double-stranded β -helix fold proteins. *J. Inorg. Biochem.* **100**, 644–669 (2006).
- Szilágyi, A. & Zavodszky, P. Structural differences between mesophilic, moderately thermophilic and extremely thermophilic protein subunits: results of a comprehensive survey. *Structure* **8**, 493–504 (2000).
- Elkins, J. M. et al. Structure of factor-inhibiting hypoxia-inducible factor (HIF) reveals mechanism of oxidative modification of HIF-1 α . *J. Biol. Chem.* **278**, 1802–1806 (2003).
- Del Rizzo, P. A., Krishnan, S. & Trievel, R. C. Crystal structure and functional analysis of JMJD5 indicate an alternate specificity and function. *Mol. Cell. Biol.* **32**, 4044–4052 (2012).
- Yang, C. G. et al. Crystal structures of DNA/RNA repair enzymes AlkB and ABH2 bound to dsDNA. *Nature* **452**, 961–965 (2008).
- Woon, E. C. et al. Linking of 2-oxoglutarate and substrate binding sites enables potent and highly selective inhibition of JmjC histone demethylases. *Angew. Chem. Int. Edn Engl.* **51**, 1631–1634 (2012).
- Horton, J. R. et al. Enzymatic and structural insights for substrate specificity of a family of jumoni histone lysine demethylases. *Nature Struct. Mol. Biol.* **17**, 38–43 (2010).
- Ng, S. S. et al. Crystal structures of histone demethylase JMJD2A reveal basis for substrate specificity. *Nature* **448**, 87–91 (2007).
- Kruidenier, L. et al. A selective jumoni H3K27 demethylase inhibitor modulates the proinflammatory macrophage response. *Nature* **488**, 404–408 (2012).
- Sengoku, T. & Yokoyama, S. Structural basis for histone H3 Lys 27 demethylation by UTX/KDM6A. *Genes Dev.* **25**, 2266–2277 (2011).
- Sinha, K. M., Yasuda, H., Coombes, M. M., Dent, S. Y. & de Crombrughe, B. Regulation of the osteoblast-specific transcription factor Osterix by NO66, a Jumoni family histone demethylase. *EMBO J.* **29**, 68–79 (2010).
- Yang, M. et al. Factor-inhibiting hypoxia-inducible factor (FIH) catalyses the post-translational hydroxylation of histidyl residues within ankyrin repeat domains. *FEBS J.* **278**, 1086–1097 (2011).
- Hoffart, L. M., Barr, E. W., Guyer, R. B., Bollinger, J. M. Jr & Krebs, C. Direct spectroscopic detection of a C–H-cleaving high-spin Fe(IV) complex in a prolyl-4-hydroxylase. *Proc. Natl Acad. Sci. USA* **103**, 14738–14743 (2006).
- Wong, S. D. et al. Elucidation of the Fe(IV)=O intermediate in the catalytic cycle of the halogenase SyrB2. *Nature* **499**, 320–323 (2013).
- Yang, M. et al. Substrate selectivity analyses of factor inhibiting hypoxia-inducible factor. *Angew. Chem. Int. Edn Engl.* **52**, 1700–1704 (2013).
- Iyer, L. M., Abhiman, S., de Souza, R. F. & Aravind, L. Origin and evolution of peptide-modifying dioxygenases and identification of the wybutosine hydroxylase/hydroperoxidase. *Nucleic Acids Res.* **38**, 5261–5279 (2010).

Supplementary Information is available in the online version of the paper.

Acknowledgements We thank the Biotechnology and Biological Sciences Research Council, the Wellcome Trust, European Research Council, Medical Research Council, Oxford NIHR Biomedical Research Unit, Cancer Research UK, Arthritis Research UK, Bayer Healthcare, the Rosetree Foundation and the Slovenian Academy of Sciences and Arts (R.S.) for funding. We thank the scientists of beamlines X10SA (Swiss Light Source) and I02, I03, I04, I04-1 (Diamond Light Source) for assistance. The Structural Genomics Consortium is a registered charity (number 1097737) funded by Abbvie, Boehringer Ingelheim, the Canadian Institutes for Health Research, the Canadian Foundation for Innovation, Eli Lilly, Genome Canada, GlaxoSmithKline, the Ontario Ministry of Economic Development and Innovation, Janssen, Novartis Research Foundation, Pfizer, Takeda and the Wellcome Trust.

Author Contributions R.C., R.S., N.C.B., C.-h.H., W.G., N.J.K., C.P., S.S.N. and E.S.P. cloned the constructs and purified proteins; R.C. and R.S. performed assays; R.C., R.S., N.C.B., S.S.N., C.-h.H. and E.S.P. crystallized the protein–ligand/substrate complexes; R.C., N.C.B., T.K., S.S.N., I.J.C., G.C.F., K.L.K., F.v.D. and M.A.M. collected and processed X-ray data; R.C., N.C.B., T.K., J.R.C.M., M.V. and M.A.M. solved and refined complex structures; R.C., R.S., M.A.M. and C.J.S. analysed data; R.C., U.O., A.J.D. and C.J.S. designed the studies; R.C. and C.J.S. wrote the paper with the help of others. See Supplementary Table 5 for further details.

Author Information Atomic coordinates and structure factors for the crystal structures have been deposited in the PDB under accession numbers 2XDV, 4DIQ, 4BU2, 4BXF, 4CCJ, 4CCK, 4CCL, 4CCM, 4CCN, 4CCO, 4LIU, 4LIT, 4LIV, 4CSW and 4CUG. Reprints and permissions information is available at www.nature.com/reprints. The authors declare no competing financial interests. Readers are welcome to comment on the online version of the paper. Correspondence and requests for materials should be addressed to C.J.S. (christopher.schofield@chem.ox.ac.uk) or R.C. (rashaduzzaman.chowdhury@chem.ox.ac.uk).

METHODS

Recombinant protein production and enzyme assays. Complementary DNA sequences encoding N-terminally truncated MINA53 (amino acids 26–465) and NO66 (amino acids 183–641) were PCR amplified from the Mammalian Gene Collection (MGC; accession numbers BC014928 and BC011350, respectively) and cloned into pNIC28-Bsa4 vector. Full-length EcYcfD was cloned into pET-28a(+) vector (Novagen) as previously described⁸. The *RmycD* gene (NCBI gene accession number 8566662) was amplified by PCR from genomic DNA of *R. marinus*, and was cloned into pGEM-T Easy Vector and then into pET-28a(+). Stratagene's QuickChange site-directed mutagenesis kit was used to make all ROX mutations using the above constructs as templates.

Wild-type ROX enzymes/variants were produced as native His₆-tagged proteins in *E. coli* BL21(DE3) as described⁸. For crystallization experiments, selenomethionine (SeMet)-derivatized enzymes, SeMet-MINA53 and SeMet-EcYcfD, were produced in *E. coli* BL21(DE3)-R3-pRARE2 and BL21(DE3) strains, respectively. In general, cells were grown in Le Master media³¹ (alternatively in SelenoMethionine Medium Base plus Nutrient Mix) supplemented with SeMet (40–50 mg ml⁻¹) and kanamycin (30 µg ml⁻¹) at 37 °C (while shaking at 200 r.p.m.) until an optical density at 600 nm (OD_{600 nm}) of 1.2 (SeMet-MINA53) or 0.6 (SeMet-EcYcfD) was reached. Protein expression was then induced with 0.2 mM (SeMet-MINA53) or 1.0 mM (SeMet-EcYcfD) isopropyl-β-D-thiogalactoside (IPTG) and allowed to continue for 18 h at 18 °C. All native/SeMet-derivatized proteins were purified from cell lysates using immobilized Ni²⁺ affinity chromatography with gradient elution using imidazole and/or ion-exchange chromatography. For YcfDs, imidazole was removed by buffer exchange to 50 mM HEPES-Na pH 7.5 using a PD10 desalting column followed by a further purification using Q-Sepharose HP (EcYcfD) or SourceQ 16 (RmYcfD) anion exchange chromatography. For MINA53 and NO66, the His₆ tag was removed by incubation with TEV protease followed by a final-step purification using size-exclusion chromatography in 50 mM HEPES-Na pH 7.5, 500 mM NaCl, 5% (v/v) glycerol, 0.5 mM tris(2-carboxyethyl)phosphine (TCEP). Proteins were concentrated to 10–30 mg ml⁻¹ and were of >95% purity, as determined by SDS-PAGE. All columns were supplied by GE Healthcare. Assays were performed as described⁸.

Crystallization, data collection and processing. Crystals of MINA53, NO66, EcYcfD and RmYcfD complexes were grown as described in Supplementary Table 1. In general, crystals were cryoprotected by transferring to a solution of mother liquor supplemented with 20% (v/v) ethylene glycol (MINA53/NO66) or 25% (v/v) glycerol (YcfDs) before being cryo-cooled in liquid nitrogen.

As described in Supplementary Tables 2–4, data on native and SeMet-derivatized crystals were collected at 100 K using synchrotron radiation at the Swiss Light Source (SLS) beamline X10SA, European Synchrotron Radiation Facility (ESRF) beamline BM16 and Diamond Light Source (DLS) beamlines. The data were processed as outlined in Supplementary Tables 2–4.

Structure solution and refinement

MINA53 structures. SHAKE-AND-BAKE³² was used to identify five Se positions in the SeMet-MINA53–NOG data set (P₄3₂ space group); refinement of heavy atom parameters and phasing was carried out with SHARP³³ using the single isomorphous replacement with anomalous scattering (SIRAS) method with MINA53–NOG (native) as the native and SeMet-MINA53 as the derivative data set (Supplementary Table 2). The electron density map after density modification with SOLOMON³⁴ was of good quality; automated model building with ARP/wARP resulted in a >80% complete model with one MINA53 molecule per asymmetric unit, which corresponds to an unusually high solvent content of ~75%. Refinement was carried out with BUSTER³⁵ and after several cycles of manual rebuilding with COOT³⁶, the model converged to 19.7% *R*_{cryst} and 22.9% *R*_{free}. Atomic coordinates and structure factors for this structure are deposited in the PDB database under the accession number 2XDV.

SeMet-MINA53–2OG structure was solved by using phases from a highly redundant single-wavelength anomalous dispersion (SAD) data set collected around the Se absorption edge. Using Patterson seeding and dual-space direct methods, SHELXD (SHELXCDE pipeline³⁷/CCP4 suite³⁸) located six out of eight possible Se sites. Refinement of substructure solution followed by density modification with SHELXE³⁷ resulted in good-quality initial phases to 2.8 Å resolution. Automated model building with BUCCANEER³⁹ resulted in a model where core regions including the JmjC and dimerization domains were built. Iterative refinement using CNS 1.3 (ref. 40) and model building using COOT³⁶ continued until *R*_{free} was around 30%. Final rounds of manual fitting using COOT³⁶ and refinement using a combination of CNS 1.3 (ref. 40) and PHENIX⁴¹ continued until *R*_{cryst}/*R*_{free} no longer improved (Supplementary Table 2). This structure (deposited in the PDB under accession number 4BU2) was then used as a search model to solve the structure of MINA53(Y209C) in complex with RPL27A(G37C) by molecular replacement (MR) with PHASER⁴² (P₂1₂1₂ space group, resolution 2.05 Å). The quality of all MINA53

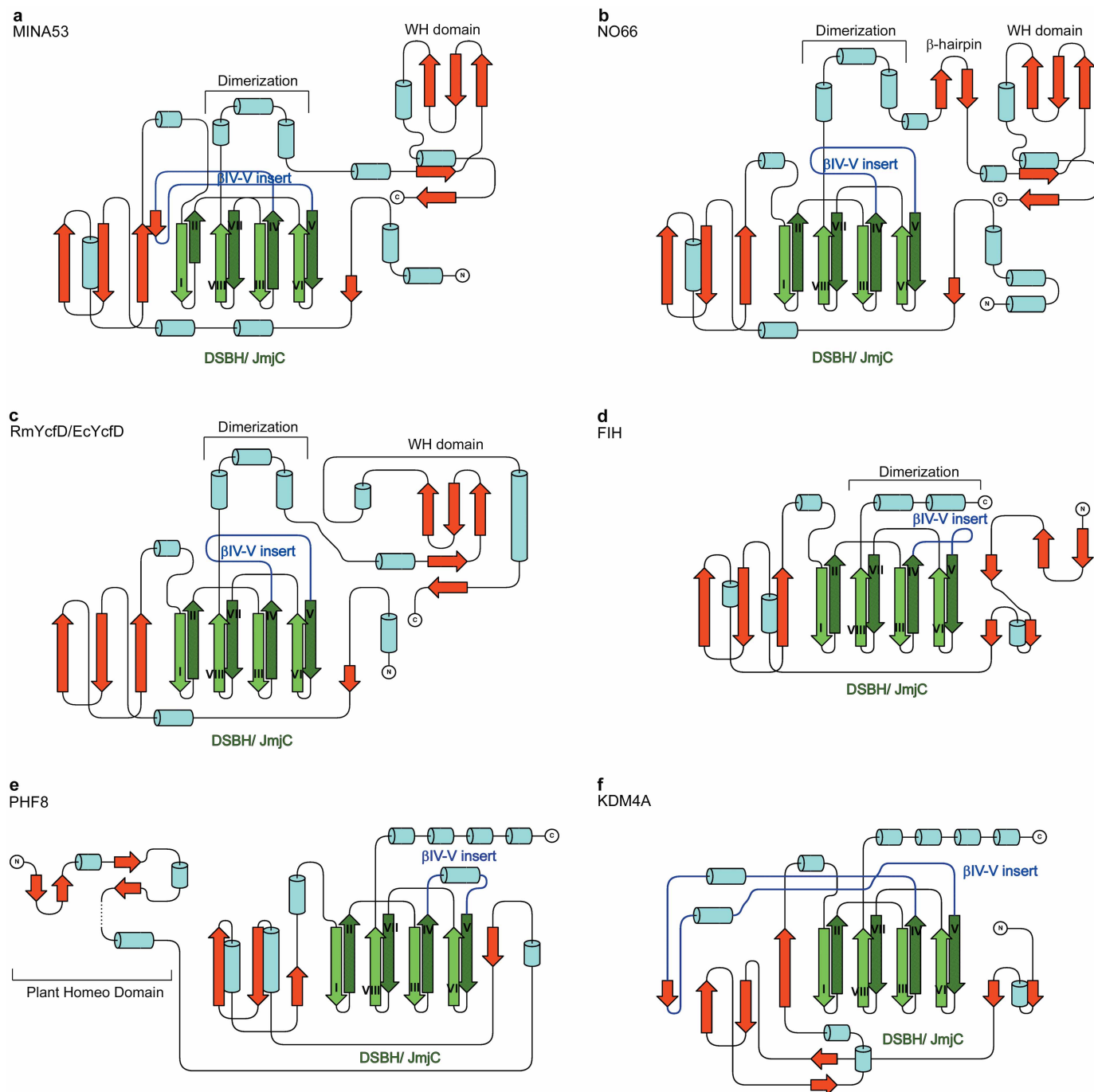
structures was validated using MOLPROBITY⁴³ with >95% of the residues in the favoured region of the Ramachandran plot.

NO66 structures. An N-terminally truncated form of MINA53 (amino acids 30–260), comprising the JmjC domain, was used as a search model for MR using PHASER⁴². The two molecules in the asymmetric unit of NO66 were readily located, but the electron density away from the JmjC core of NO66 was ambiguous. Density modification with RESOLVE⁴⁴, as implemented in PHENIX⁴¹, which took advantage of the two-fold non-crystallographic symmetry (in a P₂1₂2 space group), led to a marked map improvement and allowed automated model building with BUCCANEER³⁹. Refinement was carried out with REFMAC⁴⁵; after several cycles of manual rebuilding with COOT³⁶, the model converged to 18.5% *R*_{cryst} and 23.1% *R*_{free}. Atomic coordinates and structure factors for this structure are deposited in the PDB under accession number 4DIQ. The remaining NO66 structures, including those in complex with substrate RPL8, were solved in P₂1 or C2 space groups (resolution 2.15–2.50 Å) with 2–4 molecules per asymmetric unit (Supplementary Table 3) using the NO66/P₂1₂2 structure (PDB accession 4DIQ) as a search model. Iterative rounds of model building using COOT³⁶ and refinement using PHENIX⁴¹ and/or CNS 1.3 (ref. 40) were performed until the decreasing *R*_{cryst} and *R*_{free} no longer converged (Supplementary Table 3). All residues were in acceptable regions of Ramachandran plots as calculated by MOLPROBITY⁴³.

YcfD structures. SOLVE was used to locate 17 out of 22 possible Se sites using the SeMet-EcYcfD data set. Eight pairs of sites were related by non-crystallographic symmetry. The initial electron density map after solvent flattening density modification with RESOLVE⁴⁴ was of good quality and automated model building resulted in a model where core regions (60% of residues in the crystallized protein's sequence) of both molecules in the asymmetric unit were built. Refinement and fitting cycles were performed using PHENIX⁴¹ and COOT³⁶ that converged to a final 19.5% *R*_{cryst} and *R*_{free} 25.0%. Phasing and refinement statistics are summarized in Supplementary Table 4. Structures of RmYcfD in complex with 1-chloro-4-hydroxyisoquinoline-3-carbonyl glycine (IOX3) (ref. 46) or substrate L16 were solved by MR using the EcYcfD structure as the search model. The structural refinement was carried out with PHENIX with iterative rebuilding of the models using COOT until *R*_{cryst}/*R*_{free} converged to final values (Supplementary Table 4).

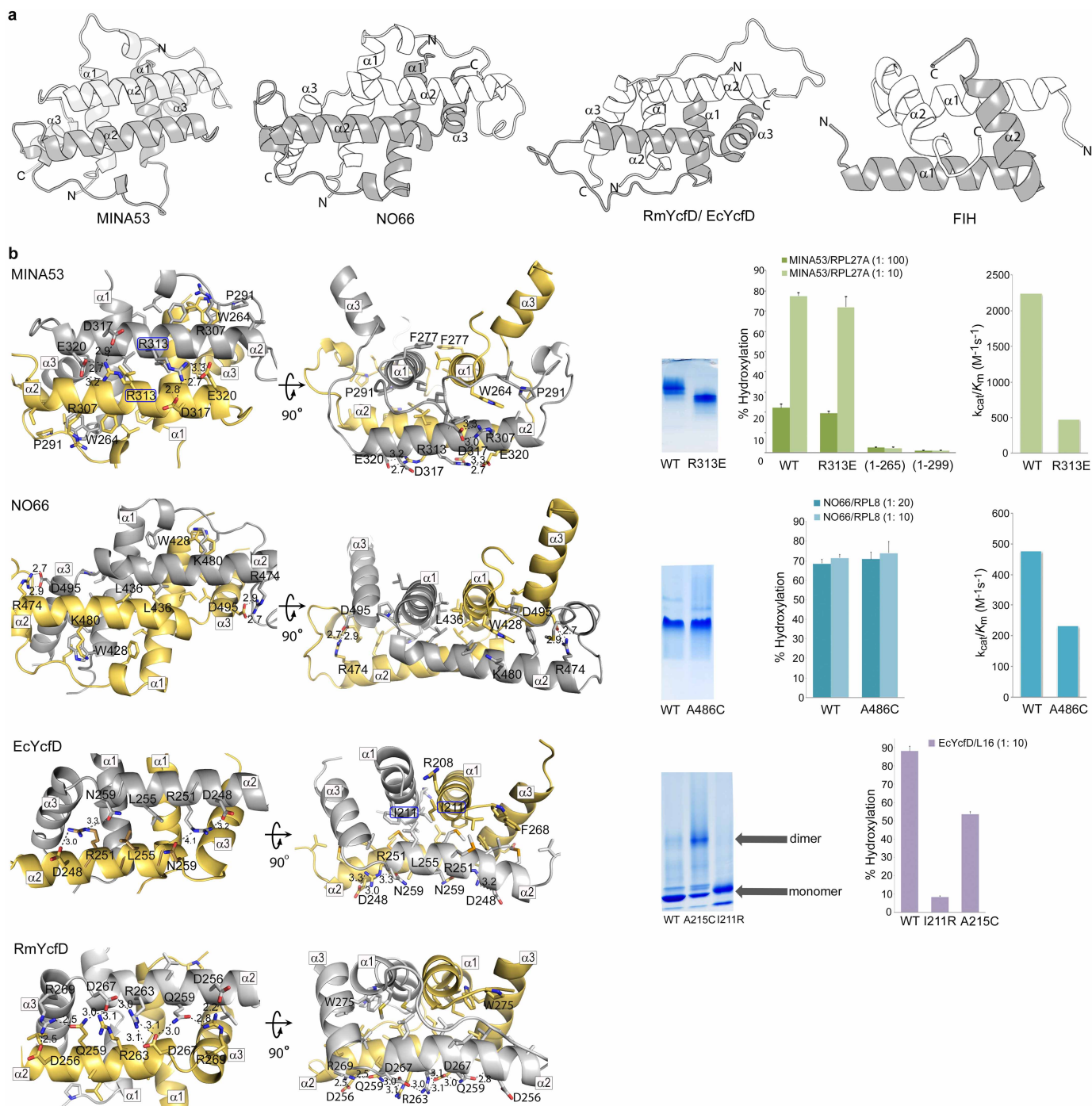
- Guerrero, S. A., Hecht, H. J., Hofmann, B., Biehl, H. & Singh, M. Production of selenomethionine-labelled proteins using simplified culture conditions and generally applicable host/vector systems. *Appl. Microbiol. Biotechnol.* **56**, 718–723 (2001).
- Miller, R. et al. On the application of the minimal principle to solve unknown structures. *Science* **259**, 1430–1433 (1993).
- Bricogne, G., Vornrhein, C., Flensburg, C., Schiltz, M. & Paciorek, W. Generation, representation and flow of phase information in structure determination: recent developments in and around SHARP 2.0. *Acta Crystallogr. D* **59**, 2023–2030 (2003).
- Abrahams, J. P. & Leslie, A. G. Methods used in the structure determination of bovine mitochondrial F1 ATPase. *Acta Crystallogr. D* **52**, 30–42 (1996).
- Smart, O. S. et al. Exploiting structure similarity in refinement: automated NCS and target-structure restraints in BUSTER. *Acta Crystallogr. D* **68**, 368–380 (2012).
- Emsley, P., Lohkamp, B., Scott, W. G. & Cowtan, K. Features and development of Coot. *Acta Crystallogr. D* **66**, 486–501 (2010).
- Sheldrick, G. M. Experimental phasing with SHELXC/D/E: combining chain tracing with density modification. *Acta Crystallogr. D* **66**, 479–485 (2010).
- Winn, M. D. et al. Overview of the CCP4 suite and current developments. *Acta Crystallogr. D* **67**, 235–242 (2011).
- Cowan, K. The Buccaneer software for automated model building. 1. Tracing protein chains. *Acta Crystallogr. D* **62**, 1002–1011 (2006).
- Brünger, A. T. et al. Crystallography & NMR system: a new software suite for macromolecular structure determination. *Acta Crystallogr. D* **54**, 905–921 (1998).
- Adams, P. D. et al. PHENIX: a comprehensive Python-based system for macromolecular structure solution. *Acta Crystallogr. D* **66**, 213–221 (2010).
- McCoy, A. J. et al. Phaser crystallographic software. *J. Appl. Crystallogr.* **40**, 658–674 (2007).
- Chen, V. B. et al. MolProbity: all-atom structure validation for macromolecular crystallography. *Acta Crystallogr. D* **66**, 12–21 (2010).
- Terwilliger, T. C. Automated main-chain model building by template matching and iterative fragment extension. *Acta Crystallogr. D* **59**, 38–44 (2003).
- Murshudov, G. N., Vagin, A. A. & Dodson, E. J. Refinement of macromolecular structures by the maximum-likelihood method. *Acta Crystallogr. D* **53**, 240–255 (1997).
- Chowdhury, R. et al. Selective small molecule probes for the hypoxia inducible factor (HIF) prolyl hydroxylases. *ACS Chem. Biol.* **8**, 1488–1496 (2013).
- Bond, C. S. TopDraw: a sketchpad for protein structure topology cartoons. *Bioinformatics* **19**, 311–312 (2003).
- Cockman, M. E. et al. Posttranslational hydroxylation of ankyrin repeats in IκB proteins by the hypoxia-inducible factor (HIF) asparaginyl hydroxylase, factor inhibiting HIF (FIH). *Proc. Natl Acad. Sci. USA* **103**, 14767–14772 (2006).
- Tao, Y. et al. Structural insights into histone demethylase NO66 in interaction with osteoblast specific transcription factor Osterix and gene repression. *J. Biol. Chem.* **288**, 16430–16437 (2013).

50. Lancaster, D. E. *et al.* Disruption of dimerization and substrate phosphorylation inhibit factor inhibiting hypoxia-inducible factor (FIH) activity. *Biochem. J.* **383**, 429–437 (2004).
51. Holm, L. & Rosenstrom, P. Dali server: conservation mapping in 3D. *Nucleic Acids Res.* **38**, W545–W549 (2010).
52. Regni, C. A. *et al.* How the MccB bacterial ancestor of ubiquitin E1 initiates biosynthesis of the microcin C7 antibiotic. *EMBO J.* **28**, 1953–1964 (2009).
53. Schmeing, T. M. *et al.* The crystal structure of the ribosome bound to EF-Tu and aminoacyl-tRNA. *Science* **326**, 688–694 (2009).
54. Wang, S., Engohang-Ndong, J. & Smith, I. Structure of the DNA-binding domain of the response regulator PhoP from *Mycobacterium tuberculosis*. *Biochemistry* **46**, 14751–14761 (2007).
55. Groisman, E. A. The pleiotropic two-component regulatory system PhoP-PhoQ. *J. Bacteriol.* **183**, 1835–1842 (2001).
56. Aik, W., McDonough, M. A., Thalhammer, A., Chowdhury, R. & Schofield, C. J. Role of the jelly-roll fold in substrate binding by 2-oxoglutarate oxygenases. *Curr. Opin. Struct. Biol.* **22**, 691–700 (2012).
57. McDonough, M. A., Loenarz, C., Chowdhury, R., Clifton, I. J. & Schofield, C. J. Structural studies on human 2-oxoglutarate dependent oxygenases. *Curr. Opin. Struct. Biol.* **20**, 659–672 (2010).
58. Han, M. V. & Zmasek, C. M. phyloXML: XML for evolutionary biology and comparative genomics. *BMC Bioinformatics* **10**, 356 (2009).
59. Larkin, M. A. *et al.* Clustal W and Clustal X version 2.0. *Bioinformatics* **23**, 2947–2948 (2007).



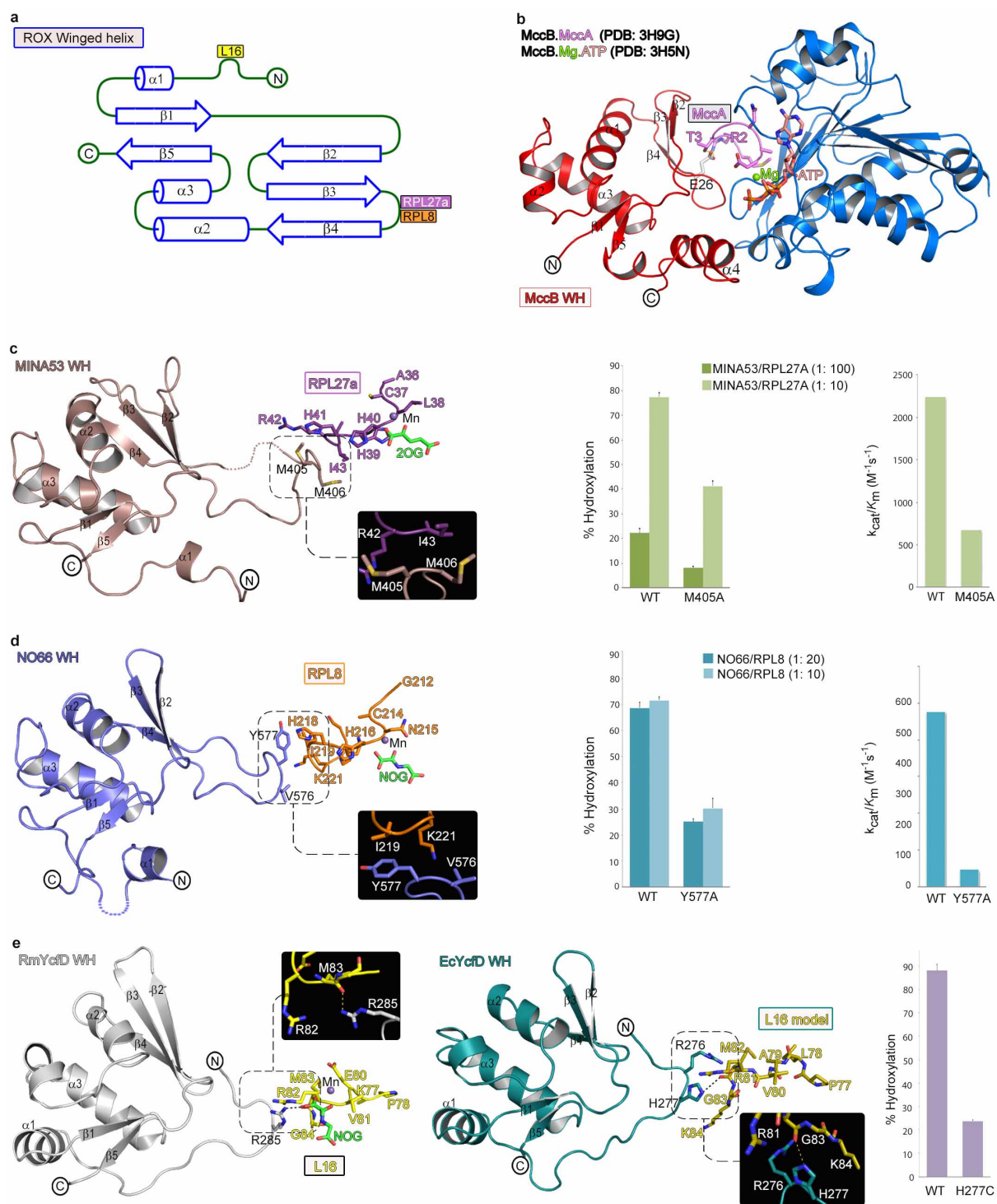
Extended Data Figure 1 | Schematic protein topologies of ROXs and related 2OG-dependent oxygenases. a–f, Protein topologies of MINA53–Mn–2OG–RPL27A_(32–50) (a), NO66–Mn–NOG–RPL8_(205–224) (b), RmYcfD–Mn–NOG–L16_(72–91) (c), FIH–Fe–NOG–HIF-1 α _(786–826) (PDB accession 1H2K) (d), PHF8–Fe–NOG–H3K4me3K9me2_(2–25) (PDB accession 3KV4) (e) and KDM4A–Ni–NOG–H3K9me2_(7–14) (PDB accession 2OX0) (f) (substrates are

not shown). DSBH core elements, labelled β I– β VIII, are in green, helices in cyan, additional β -strands in red, random coils in black and the insert between the fourth and fifth β -strands in blue. Note that not all the DSBH oxygenases maintain antiparallel hydrogen-bond pairing between β II and β VII even though the ϕ/ψ angles (β II) are within the β -region of the Ramachandran plot. Figures were generated using TopDraw⁴⁷.



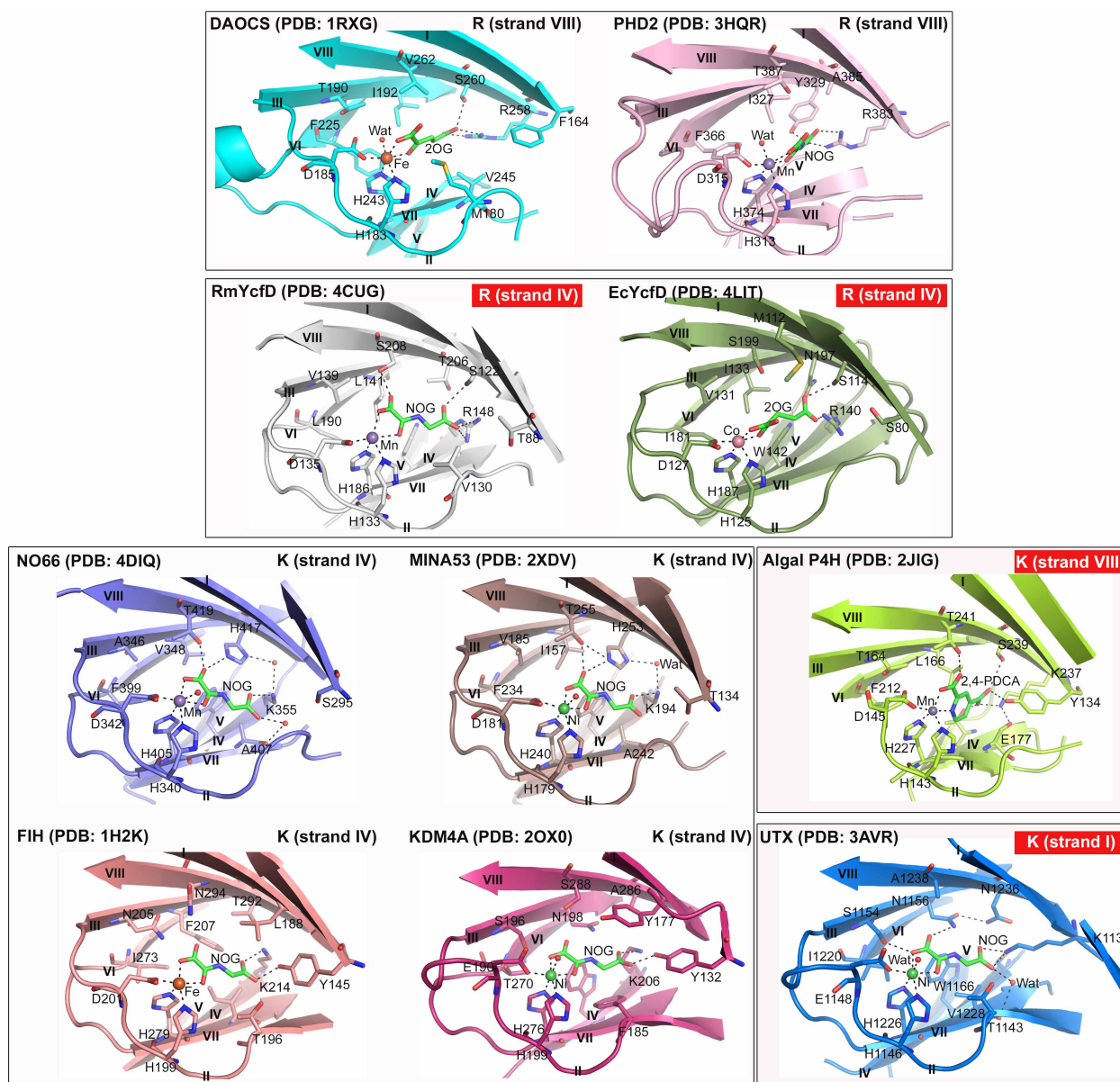
Extended Data Figure 2 | ROX dimerization domains. **a**, Comparison of the dimerization domains in ROXs and FIH. **b**, Intermolecular interactions observed at dimerization interfaces (monomer A, grey; monomer B, yellow). Validation of the functional relevance of the ROX dimers comes from biochemical and kinetic studies demonstrating loss of activities with most variants. The dimer interfaces in the ROXs are related to that of FIH; we propose that the FIH dimerization fold evolved from that of ROXs^{17,48}. The large buried surface area ($>3,000 \text{ \AA}^2$) within all ROX dimerization domains is sufficient for dimerization in solution, as reported for NO66 (ref. 49). The interactions observed in dimerization include both hydrogen bonds/electrostatic interactions and hydrophobic interactions. In the EcYcfD/RmYcfD dimerization domains, residues involved in hydrophobic interactions are mainly from $\alpha 2$ and are well conserved (RmYcfD residues in parentheses): Phe 214 (Met 223), Val 242 (Ile 250), Met 247 (Leu 255), Leu 250 (Ile 258), Met 253 (Leu 261), Met 254 (Leu 262), Leu 257 (Leu 265), Ile 258 (Ile 257). Hydrogen bonding/electrostatic interactions are more important in RmYcfD dimerization than in EcYcfD/human ROXs. The network of hydrogen bonds between the two RmYcfD monomers A and B includes Asp 256_A–Arg 269_B–Gln 259_A–Asp 267_B–Arg 263_A, which, owing to two-fold symmetry, creates a total of eight hydrogen bonds. In EcYcfD, Leu 255 (Arg 263 in RmYcfD) is positioned at the centre of the equivalent network. Furthermore, in RmYcfD Gln 216 is positioned to hydrogen bond with the backbone amide N of Arg 234 and the carbonyl O of Leu 261. Hydrogen bonding in EcYcfD dimerization is less extensive, with only the Asn 226 amide N positioned to form a hydrogen bond to the hydroxyl group O of Thr 207 and Arg 208 hydrogen bonding with the carbonyl O of Gly 224. However, hydrophobic/aromatic clusters are involved in EcYcfD dimerization, including by the side chains of Leu 210_A, Leu 223_A, Tyr 217_A ($\alpha 1$), Phe 264_A, Trp 267_A, Phe 268_A and Phe 271_A ($\alpha 3$) from monomer A and Val 242_B, Met 247_B, Leu 250_B ($\alpha 2$) from monomer B. As in the YcfDs, in NO66 there is only one apparent salt-bridge interaction at the dimer interface, that is, between Arg 474 and Asp 495 (Arg 474_A NH1–Asp 495_B O δ 1, 2.9 \AA ; Arg 474_A NH2–Asp 495_B O δ 2, 2.7 \AA), which links the $\alpha 2$ and $\alpha 3$ helices of opposite monomers. Similarly a ‘complex salt bridge’ is observed in MINA53 between Arg 313 and Glu 320/Asp 317 (Arg 313_B

NH1–Glu 320_A O ϵ 2, 3.2 \AA ; Arg 313_B NH2–Glu 320 O ϵ 1, 2.7 \AA ; Arg 313_A NH2–Asp 317 O δ 1, 2.9 \AA) that connects the $\alpha 2$ helices of different monomers. Backbone amide hydrogen bonding additionally occurs between the NO66 residues Asn 426 and Leu 454, Arg 452 and Trp 428, Phe 450 and Gly 429. MINA53 also has backbone-to-side-chain interactions between residues from flexible loops connecting $\alpha 1$ – $\alpha 2$ and $\alpha 2$ – $\alpha 3$ helices (Gln 297_B O–Lys 331_A N ζ , 3.7 \AA ; Ser 300_B O γ –Glu 324_A O, 3.1 \AA). The role of hydrophobic/aromatic clusters in dimerization is apparent in NO66 where the $\alpha 2$ helices from different monomers are further apart when compared with those of YcfDs and MINA53 and hence have less buried surface area. However, in NO66, an apparent hydrophobic cluster forms between the N-terminal part of $\alpha 1$ and the C-terminal part of $\alpha 2$. NO66 Trp 428 (Trp 264 in MINA53) is positioned at the start of the $\alpha 1$ helix of monomer A and forms the centre of a hydrophobic cluster, interacting with residues Phe 431_A, Ile 435_A and Leu 432_A on monomer A, and Val 481_B, Leu 484_B, Met 462_B, Phe 477_B and Pro 455_B on monomer B. NO66 Trp 428 also forms an apparent cation– π interaction with residue Lys 480. The similarly positioned Trp 264 in MINA53 maintains hydrophobic contacts with Phe 267 and Leu 268 of the same monomer and with Ile 290, Pro 291 and Leu 294 of the other monomer, in addition to a cation– π interaction with Arg 307. Other hydrophobic contacts observed in MINA53 dimerization involving the $\alpha 1$ and $\alpha 2$ helices of different monomers include between the side chains of residues Leu 308/ $\alpha 2$ (interacting with Leu 319/ $\alpha 2$ and Phe 267, Leu 268, Thr 271 of $\alpha 1$), Leu 312/ $\alpha 2$ (interacting with Ile 272/ $\alpha 1$ and Leu 315/ $\alpha 2$) and Phe 277/ $\alpha 1$ (interacting with Val 276, Leu 269 and Ile 272 of $\alpha 1$). Disruption of ROX dimerization leads to loss of activity, as observed for MINA53(R313E) and EcYcfD(I211R) variants as well as for truncated MINA53 (1–265, 1–299) without dimerization and the C-terminal domains. Non-denaturing gel electrophoresis was used to investigate ROX oligomerization states in solution, which demonstrates disruption of dimerization in EcYcfD(I211R) and MINA53(R313E). The loss of activity via destabilizing ROX dimerization is reminiscent of similar roles of FIH dimerization in catalysis (An FIH(L340R) variant that was predominantly monomeric is inactive)⁵⁰. Data show mean and standard error of the mean (s.e.m.) ($n = 3$).



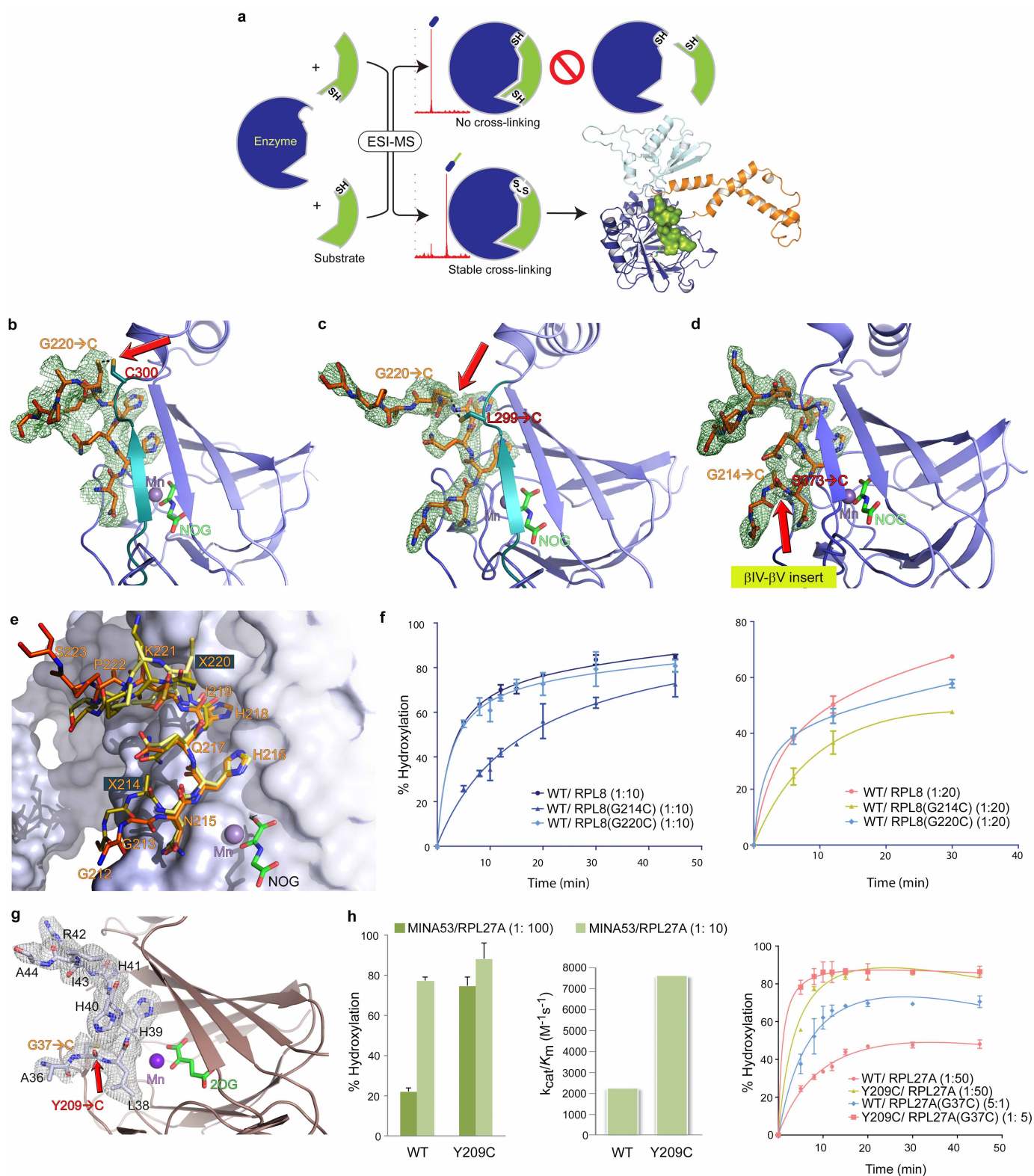
Extended Data Figure 3 | Interaction of the ROX C-terminal WH domains with their respective ribosomal protein substrates. **a–e**, The figure shows how ROX C-terminal domains interact with their substrates. A DALI search⁵¹ indicates that a close structural homologue of the ROX C-terminal domain is the ‘peptide clamp’ (WH) domain of MccB, an enzyme involved in the biosynthesis of the microcin C7 antibiotic⁵². WH domains, a subtype of the helix-turn-helix (HTH) family, are nucleic acid/protein-interacting domains and occur in different cellular pathways, from transcriptional regulation to RNA processing¹³. Although the overall negative charge of ROX WH domains suggests that they may not directly interact with nucleic acids, it is notable that the prokaryotic ribosomal proteins L6, which is located proximal to L16 in intact ribosomes⁵³, and the transcriptional regulator PhoP contain WH folds⁵⁴; the latter is interesting because in the *E. coli* K12 genome the *ycfD* gene is located adjacent to those for the PhoP/PhoQ two component signalling system,

which is involved in stress responses⁵⁵. **a**, General topology of the C-terminal WH domain showing two distinct binding sites for L16 (yellow) and RPL27A (magenta)/RPL8 (orange) involving residues either from an N-terminal loop connecting the WH and dimerization domains (as in RmYcfD) or from an extended loop between WH $\beta 3$ – $\beta 4$ (as in human ROXs). **b–e**, Comparisons between the WH domains in MccB (**b**), MINA53 (**c**), NO66 (**d**) and RmYcfD/EcYcfD (**e**) showing the interactions observed between this domain and the substrate(s). Note that although both the RPL27A and RPL8 substrates make hydrophobic contacts with the WH domains in MINA53 (Met 405 and Met 406) (**c**) and NO66 (Val 576 and Tyr 577) (**d**), RmYcfD uses Arg 285 to form a hydrogen bond with the L16 Met 83 (RmYcfD Arg 285 NH2–L16 Met 83 O, 2.5 Å) (**e**). Right panels show the partial loss of activity with mutations of MINA53 (M405A), NO66 (Y577A) and EcYcfD (H277C) residues from WH domains. Data show mean and s.e.m. ($n = 3$).



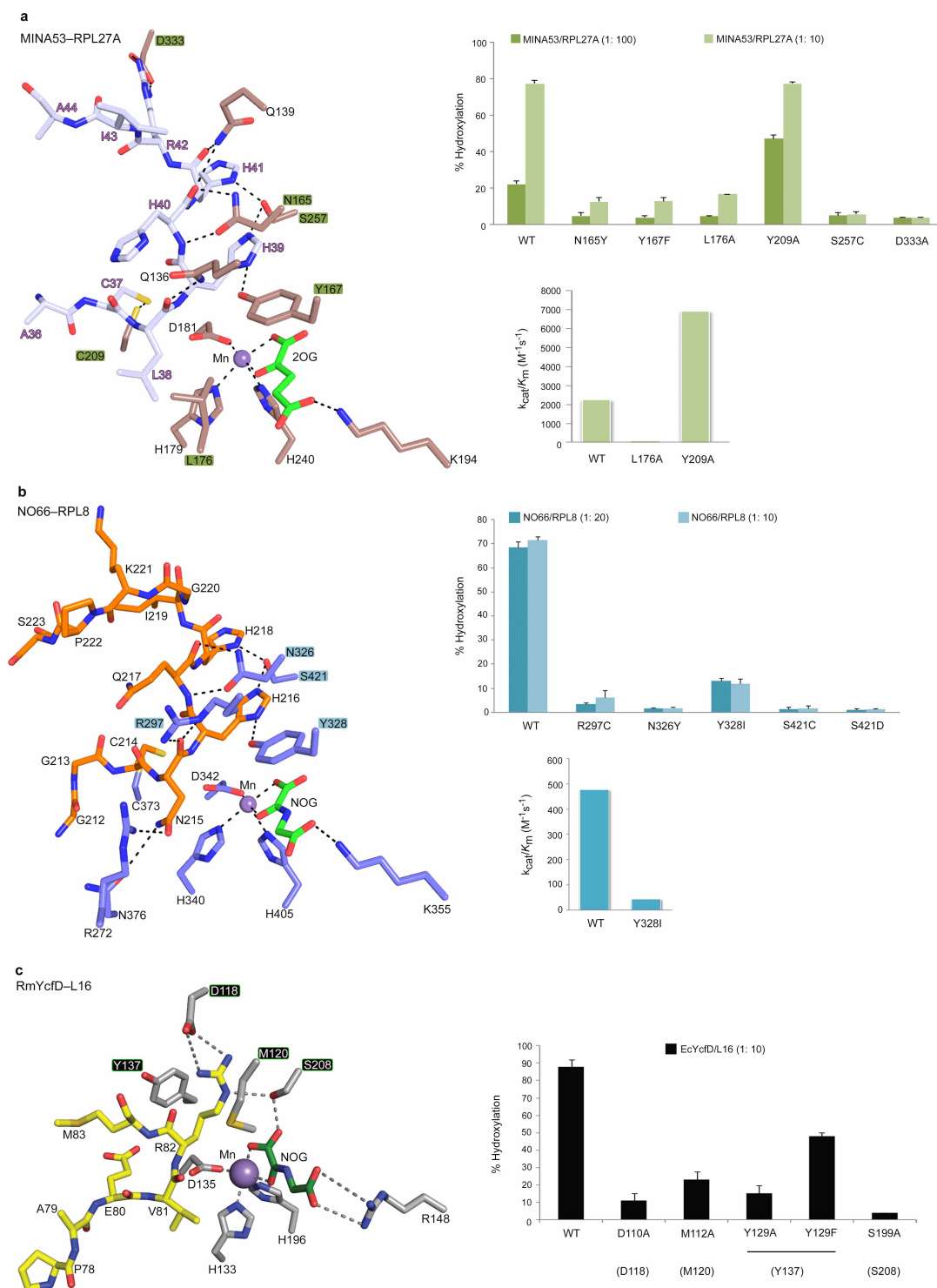
Extended Data Figure 4 | Comparison of 2OG/co-substrate binding in ROXs and representative 2OG-dependent oxygenases. The identity of the basic residue (Arg or Lys) that binds the 2OG C5 carboxylate via electrostatic interactions is indicated along with which of the eight DSBH (I–VIII) strands it is located on. The occurrence and positioning of the basic Arg/Lys is characteristic of each subfamily^{14,15}. 2OG binding also involves other polar residues including alcohols, that is, a Ser (β VIII, part of the RXS motif as present in, for example, DAOCS, ANS, FTO and algal P4H) or Thr (β II, for example, as in some KDMs: JMJD3, JMJD6, PHF8 and UTX) or Tyr (non-DSBH

β -strand, for example, as in FIH, KDM4A, ABH2 and PHD2) and sometimes, water molecule(s) (reviewed in refs 15,56,57). In an analogous position to the serine of the RXS motif (β VIII), human ROXs have histidine residues, MINA53 His 253/NO66 His 417 (β VIII), which form part of a hydrogen-bond network involving MINA53 Thr 255/NO66 Thr 419 (β VIII), a water molecule, and the 2OG carboxylates. Although EcYcfD/RmYcfD has Asn 197/Thr 206 at this position (β VIII), it is the conserved serine from β I (114 in EcYcfD and 122 in RmYcfD) that is positioned to hydrogen bond with the 2OG C5 carboxylate.



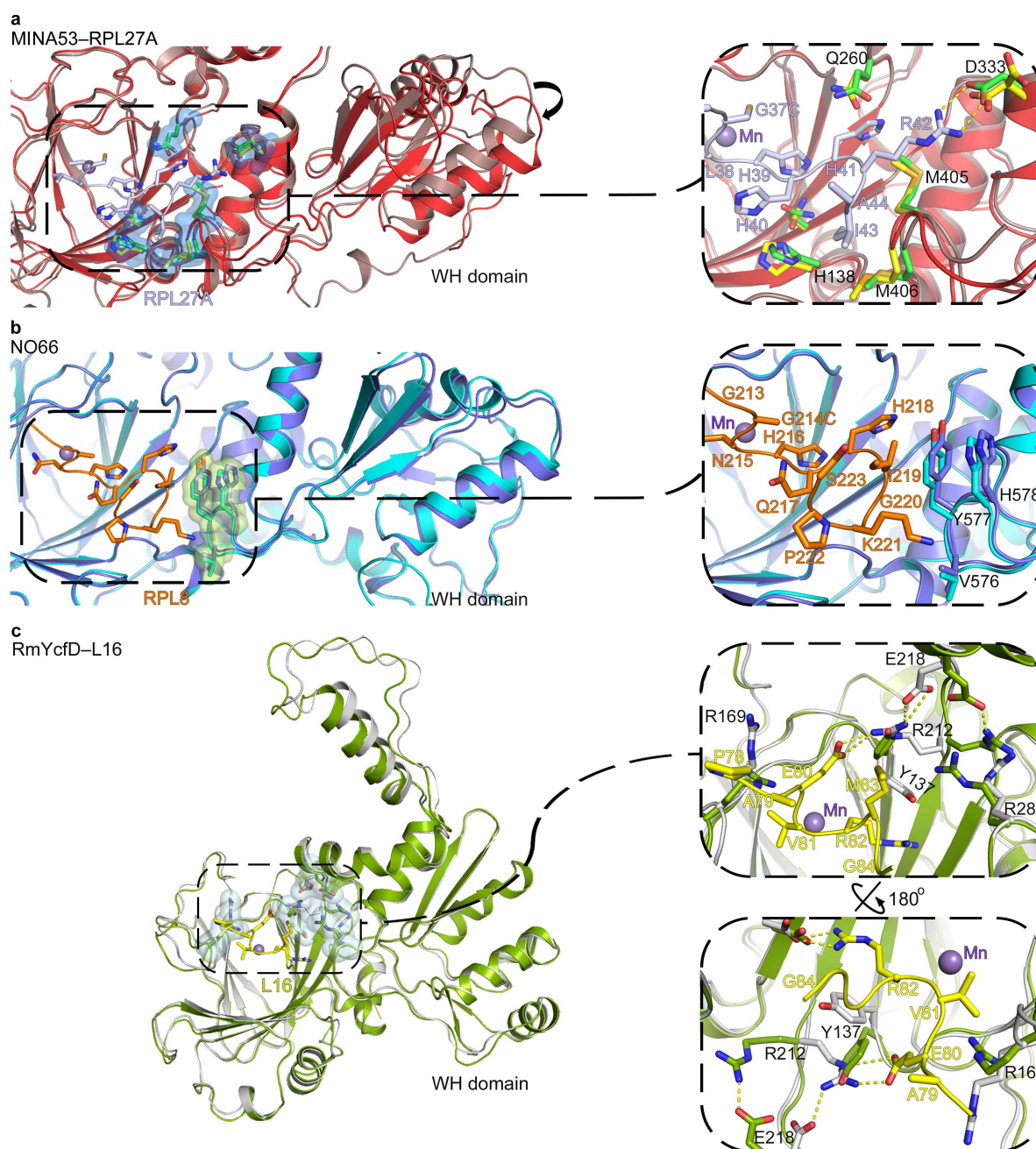
Extended Data Figure 5 | Human ROX–substrate complexes showing disulphide crosslinking sites and difference electron density for the substrate residues. **a**, Strategy adopted to obtain the crosslinked structures (the same strategy can be used for other protein hydroxylases/KDMs). **b–d**, Different disulphide crosslinking sites (red arrows) that form NO66–RPL8 cysteine–disulphide pairs under equilibrating conditions. Analyses of the 2OG-oxygenase–substrate complexes reveal that substrate residues at ± 2 positions relative to the hydroxylated residues make interactions with enzyme residues within a ~ 12 Å radius of the metal. To obtain stable NO66–RPL8 complexes, we engineered NO66 variants substituting Cys residues within ~ 12 Å radius of the metal at positions considered likely to be involved in substrate binding based on the analyses of other 2OG-oxygenase–substrate structures^{21,22,26} and the evolutionary/phylogenetic analyses of NO66/NO66-like proteins in eukaryotes. We also substituted Cys residues at ± 2 positions on the peptide substrate sequence, relative to the hydroxylated residue. Electrospray ionization–mass spectrometry (ESI–MS) assays were used to identify the best crosslinking yields for the NO66–RPL8 pairs under equilibrating conditions. The following crosslinked pairs were used for crystallization: wild-type NO66 with RPL8(G220C), a double NO66 variant L299C/C300S with RPL8(G220C), and a single NO66 variant S373C with RPL8(G214C). Structures were obtained for wild-type NO66–RPL8(G220C) (complex 1; **b**), NO66(L299C/C300S)–RPL8(G220C) (complex 2; **c**), and NO66(S373C)–RPL8(G214C) (complex 3; **d**) in combination with NOG/Mn(II) in C2 space group, 2.25–2.50 Å resolution with two molecules per asymmetric unit; RPL8 residues 215–223 (complex 1), 213–223 (complex 2) and 212–223 (complex 3) were observed bound to the NO66 active site. **e**, Superimposition of the three complex structures. Note that the key RPL8

residues (215–219), including the hydroxylated His 216, are observed in near identical conformations (r.m.s.d. 0.29–0.36 Å for C α atoms); the similarity of the substrate positions in all the three NO66 structures suggests that they all probably represent functional complexes. On the basis of the NO66–RPL8 structures, we identified a MINA53 residue, Y209C, suitable for crosslinking, which we crystallized in complex with RPL27A(G37C) (**g**). $F_o - F_c$ omit electron-density maps contoured at 3σ are shown as green (RPL8) and grey (RPL27A) meshes around the substrate residues. To test whether the wild-type/mutant enzymes and altered substrates still function catalytically we carried out endpoint and time-course assays using variable enzyme-to-substrate ratios. **f, h**, The biochemical data show that for both wild-type NO66 (**f**) and MINA53 (**h**) (wild type and Y209C), all the Cys-substituted peptides function as substrates. In the case of MINA53, the Y209C variant with which we obtained the MINA53–RPL27A complex structure is approximately fourfold more active than wild-type MINA53. Data are mean and s.e.m. ($n = 3$). We also tested wild-type NO66 for reaction between enzyme cysteines and the cysteines of modified substrate peptides by ESI–MS. Despite testing multiple combinations, we only observed disulphide formation in cases where we were also able to obtain crystal structures for substrate complexes. All possible combinations of human ROX wild type or variants and the peptides containing Cys at variable positions were used for the cross-reactivity tests: NO66: wild type, R297C, L299C/C300S, S373C, S421C; RPL8: wild type, G214C, H218C and G220C; MINA53: wild type and Y209C; RPL27A: wild type and G37C. The combined activity and MS analyses suggest that in order to form stable/crystallizable cross-linked complexes, the substrates need to be recognized by the enzyme active sites in a catalytically relevant manner (**a**).



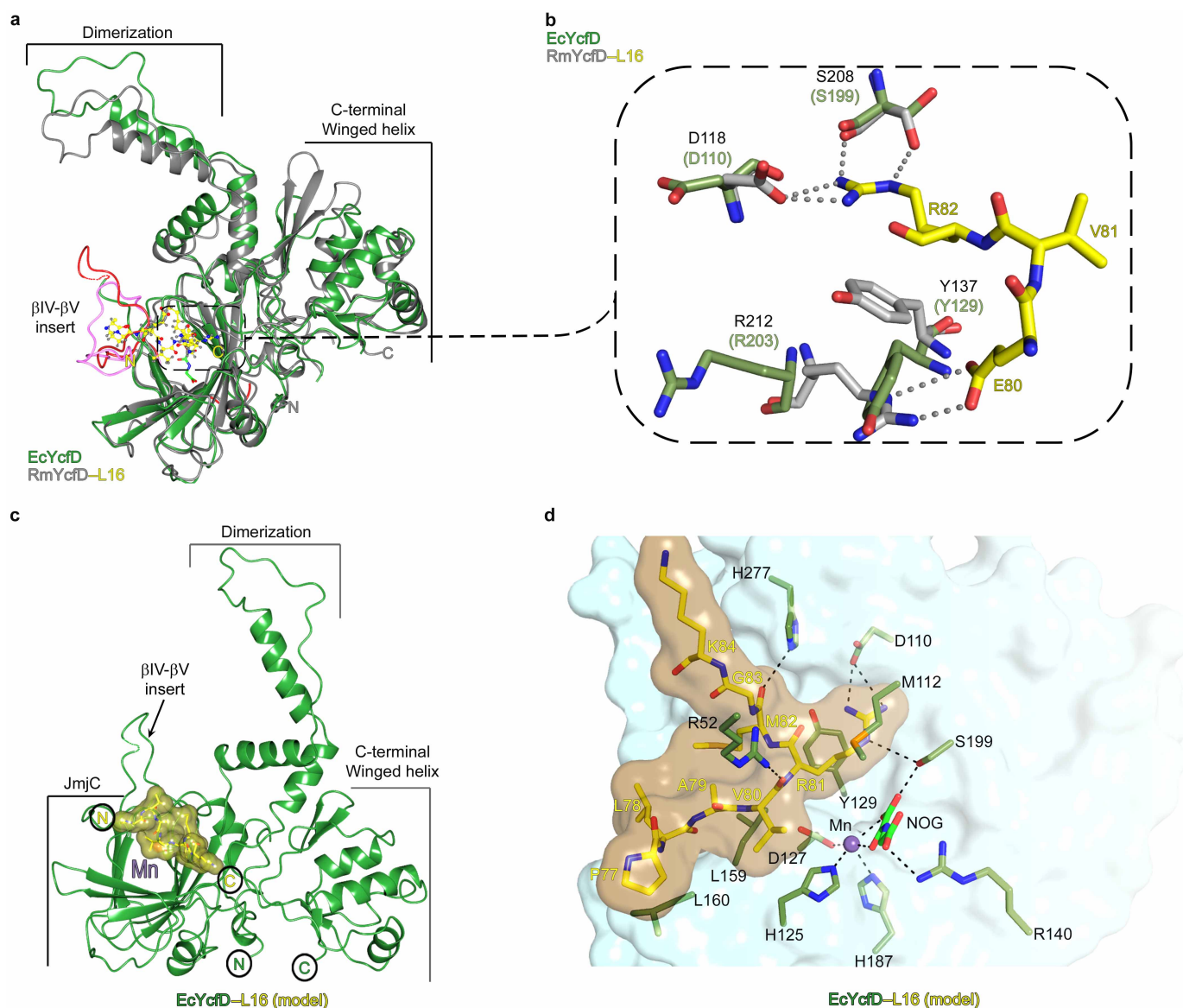
Extended Data Figure 6 | Mutagenesis analyses of the substrate-binding residues located on the JmjC catalytic domains of MINA53, NO66 and RmYcfD. **a–c**, MINA53 (**a**), NO66 (**b**) and RmYcfD (**c**) are shown in colour-coded sticks. Left panels show views from the active sites of ROX–substrate complexes and the right panels show the effects of mutations on ROX catalysis. Data are mean and s.e.m. ($n = 3$). Analyses of ROX–substrate complexes reveal important interactions between ROX and their ribosomal protein substrates. With human ROXs, the binding of ribosomal RPL27A His 39 (light blue)/RPL8 His 216 (orange) involves a series of hydrogen bonds to backbone amides and the side chains of MINA53/NO66 residues: MINA53 Gln 136/NO66 Arg 297, MINA53 Asn 165/NO66 Asn 326, MINA53 Tyr 167/NO66 Tyr 328 and MINA53 Ser 257/NO66 Ser 421. In addition, in the MINA53–RPL27A complex, Leu 38 and Arg 42 of RPL27A make hydrophobic contacts with MINA53 Leu 176 and a salt-bridge interaction with

MINA53 Asp 333, respectively. We produced variants of all these residues to investigate their roles on substrate binding. The results of the endpoint assays as well as kinetic studies on the variants (right panels) show that substitution of these residues causes substantial losses of activity. **c**, In the case of RmYcfD, the hydroxylated residue L16 Arg 82 binds in a hydrophobic cleft lined by RmYcfD Tyr 137 and RmYcfD Met 120 side chains and hydrogen bonds to RmYcfD Asp 118 and RmYcfD Ser 208. To test the crystallographically observed binding mode, variants of RmYcfD residues (Asp 118, Met 120, Tyr 137 and Ser 208, highlighted) were prepared in EcYcfD (corresponding to Asp 110, Met 112, Tyr 129 and Ser 199, respectively). Mutagenesis studies on all ROXs support the crystallographically observed binding modes of the substrate residues. The combined biochemical and structural data also provide insights into the substrate selectivity of ROXs over other oxygenases.



Extended Data Figure 7 | Conformational changes on substrate binding in ROX. **a–c**, Conformational changes at the domain and residue levels in MINA53 (dark salmon and red with/without RPL27A, light blue) (**a**), NO66 (slate and cyan with/without RPL8, orange) (**b**) and RmYcfD (grey and split pea with/without L16, yellow) (**c**). Although the overall movement observed for the C-terminal WH domain on substrate binding is more significant in MINA53 as compared to other ROXs, the RmYcfD structures with and without substrate show marked local changes in the side chains of substrate-binding residues (see below). **a**, The inset highlights local changes to the active-site region in MINA53 in the presence (green sticks) or absence (yellow sticks) of substrate; MINA53 uses an acidic residue, Asp 333, located on an α -helix connecting the dimerization and WH domains, to form a catalytically important salt-bridge interaction with RPL27A Arg 42. Support for this statement comes from activity analyses on variants of both RPL27A and

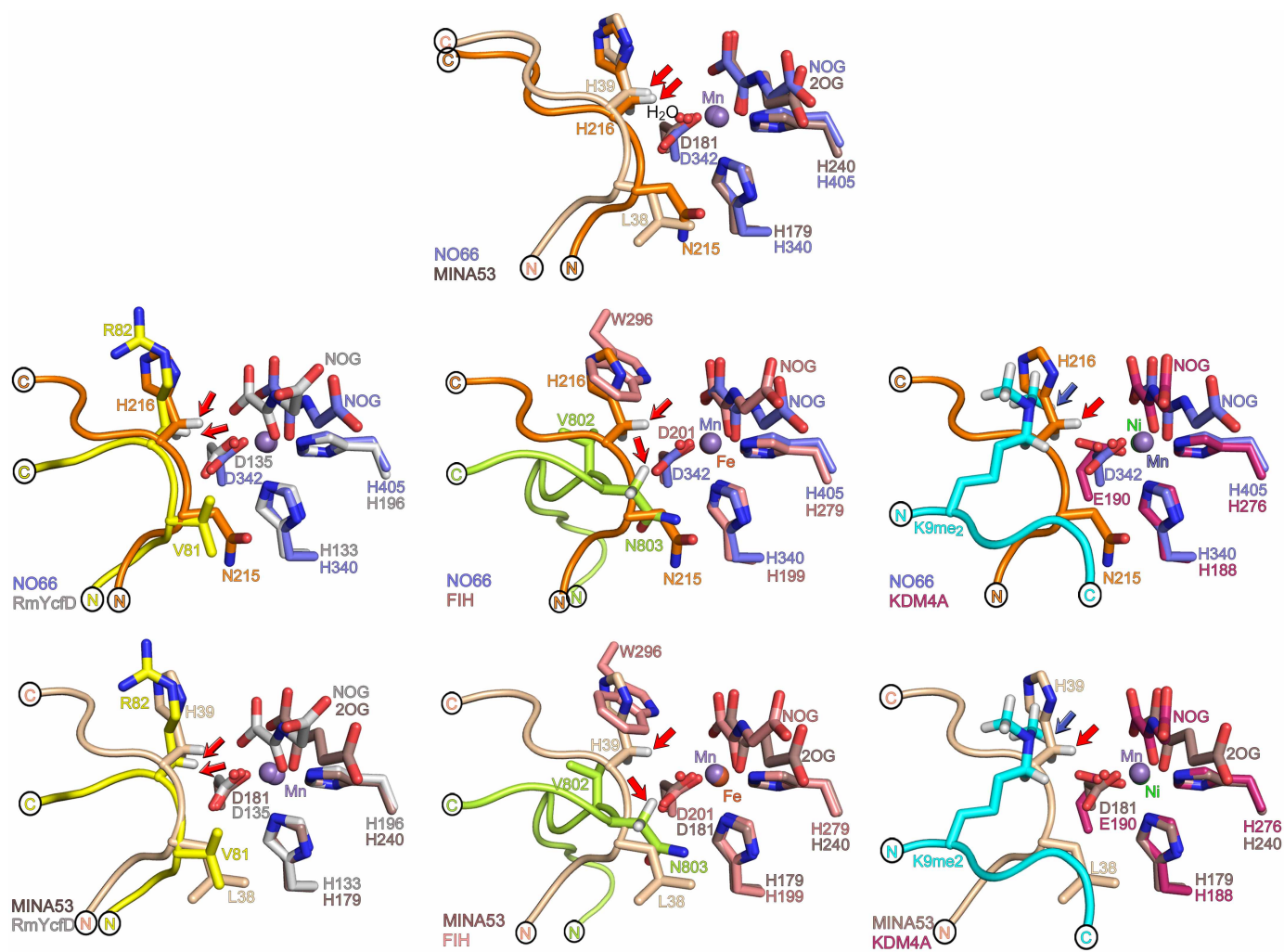
MINA53. We have previously reported that a mutation of Arg 42 in RPL27A to Ala results in <5% hydroxylation⁸. The D333A variant of MINA53 ablates hydroxylation (almost completely) of native RPL27A in all tested substrate:enzyme ratios (Extended Data Fig. 6). In the substrate-unbound form, MINA53 Asp 333 has two alternative conformations, indicating flexibility. The NO66 substrate RPL8 has an Ile 219 at the analogous position to Arg 42 of RPL27A that makes hydrophobic contacts with the Tyr 577 side chains from the WH domain of NO66 (**b**). In the case of RmYcfD, the substrate-interacting residues located on the β II– β III loop (Tyr 137), the β IV– β V insert (Arg 169), the dimerization domain (Arg 212 and Glu 218) and on the loop connecting the dimerization and WH domains (Arg 284) are observed in different conformations in the structures with and without substrate, probably reflecting induced fit on substrate binding (**c**). Substitutions of these residues have variable effects on ROX catalyses (Extended Data Fig. 6).



Extended Data Figure 8 | Comparison of YcfDs from *E. coli* and *R. marinus*.

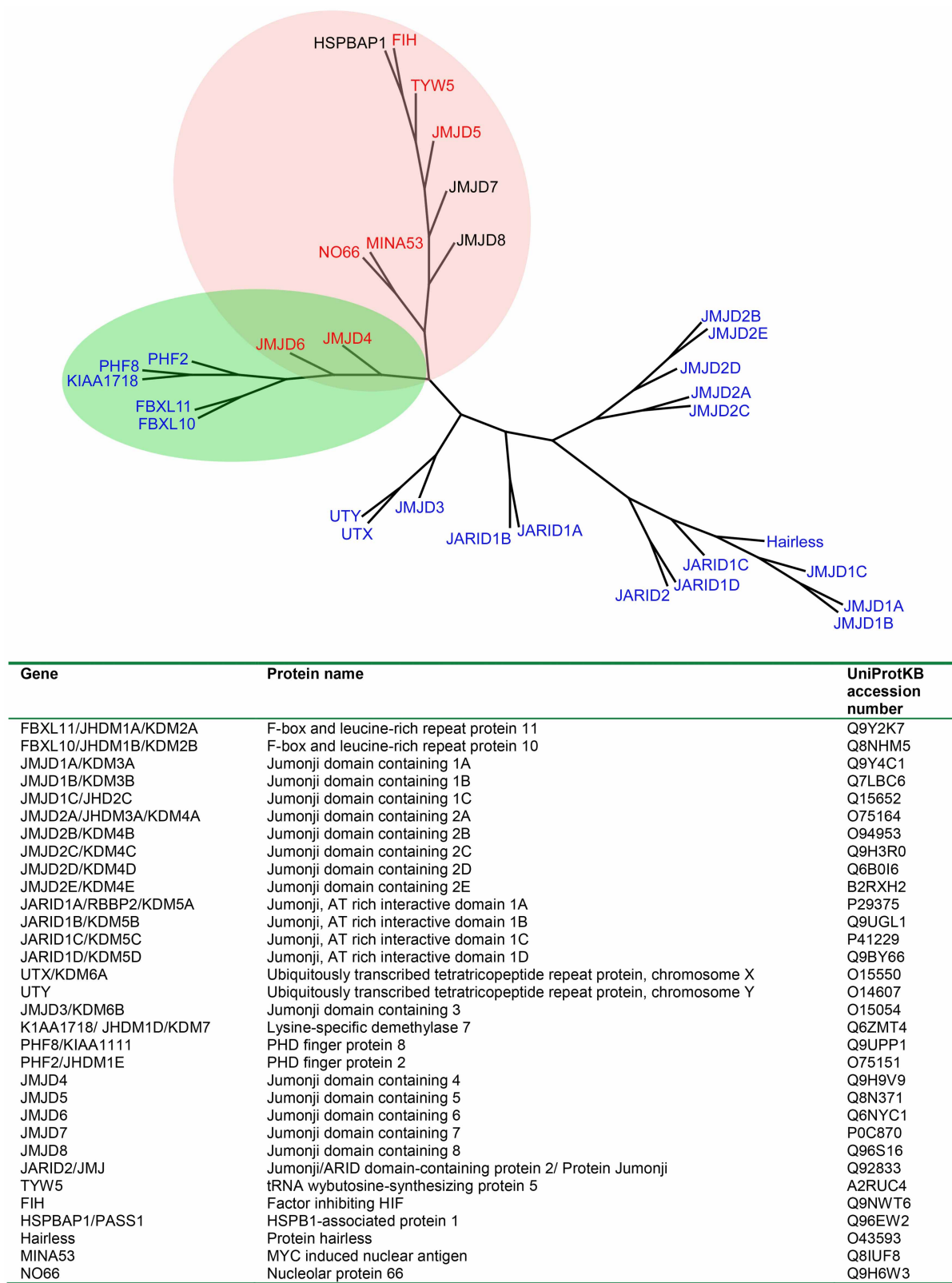
a–d, Differences between YcfDs from *E. coli* (green) and *R. marinus* (grey) are shown. **a**, Superimposition of EcYcfD and RmYcfD-L16 complex structures showing crystallographically observed differences, particularly in the dimerization and β IV- β V loop regions. The β IV- β V insert is highlighted in crimson red and pink in EcYcfD and RmYcfD, respectively. **b**, Residue numbering is according to RmYcfD, with the EcYcfD numbering shown in brackets. Note that all of the directly identified substrate-binding residues are strictly conserved between EcYcfD and RmYcfD. However, some residues, particularly those located on the β IV- β V insert including Asp 118, Tyr 137 and Arg 212 in RmYcfD (Asp 110, Tyr 129 and Arg 203 in EcYcfD), are observed in different conformations, suggesting potential roles for these residues in catalysis. **c**, **d**, Predicted binding mode of L16 (yellow) to EcYcfD (green). A

model complex of EcYcfD with Mn(II), NOG and L16 (residues Pro 77–Lys 84) was generated using EcYcfD-SeMet as the template and by comparison with RmYcfD-L16 and MINA53-RPL27A_(32–50) structures. **d**, Surface representations of the EcYcfD-Mn-NOG-L16_(77–84) complex, predicting key hydrogen-bond/polar interactions (dotted lines) with L16. The hydroxylated L16 Arg 81 is predicted to bind in a pocket defined by the Tyr 129 and Met 112 sidechains, which probably form π -cation and hydrophobic interactions with the L16 Arg 81 side chain, as observed in the RmYcfD-L16 crystal structure. The Arg 81 guanidino group is predicted to make electrostatic interactions with the EcYcfD Asp 110 carboxylate and hydrogen bonds to EcYcfD Ser 199. EcYcfD residues Asp 110, Met 112, Tyr 129 and Ser 199 were substituted to test the predicted mode of binding; the assay results are given in Extended Data Fig. 6c.



Extended Data Figure 9 | Comparison of active-site chemistry of ROXs and related enzymes. The figure compares active-site chemistry in representative 2OG-dependent oxygenases and directionality of the peptide

substrate binding through the active site. Red/blue arrows indicate hydroxylation/demethylation sites. The active-site metals (Fe/Fe surrogates, Mn or Ni) are in colour-coded spheres.



Extended Data Figure 10 | Phylogenetic relationships of human JmjC 2OG-dependent oxygenases. The figure shows a parsimony tree constructed using Archaeopteryx v.0.9812 (ref. 58) from ClustalW⁵⁹ aligned protein

sequences of human JmjC-containing 2OG-dependent oxygenases showing that distinct branches of JmjC-containing oxygenases exist for hydroxylases (red), demethylases/hydroxylases (light green) and demethylases (blue).

Co-opting sulphur-carrier proteins from primary metabolic pathways for 2-thiosugar biosynthesis

Eita Sasaki¹, Xuan Zhang², He G. Sun³, Mei-Yeh Jade Lu^{4,5}, Tsung-lin Liu^{5,6}, Albert Ou⁵, Jeng-yi Li⁴, Yu-hsiang Chen⁴, Steven E. Ealick² & Hung-wen Liu^{1,3}

Sulphur is an essential element for life and is ubiquitous in living systems^{1,2}. Yet how the sulphur atom is incorporated into many sulphur-containing secondary metabolites is poorly understood. For bond formation between carbon and sulphur in primary metabolites, the major ionic sulphur sources are the persulphide and thio-carboxylate groups on sulphur-carrier (donor) proteins^{3,4}. Each group is post-translationally generated through the action of a specific activating enzyme. In all reported bacterial cases, the gene encoding the enzyme that catalyses the carbon-sulphur bond formation reaction and that encoding the cognate sulphur-carrier protein exist in the same gene cluster⁵. To study the production of the 2-thiosugar moiety in BE-7585A, an antibiotic from *Amycolatopsis orientalis*, we identified a putative 2-thiogluco-6-phosphate synthase, BexX, whose protein sequence and mode of action seem similar to those of ThiG, the enzyme that catalyses thiazole formation in thiamine biosynthesis^{6,7}. However, no gene encoding a sulphur-carrier protein could be located in the BE-7585A cluster. Subsequent genome sequencing uncovered a few genes encoding sulphur-carrier proteins that are probably involved in the biosynthesis of primary metabolites but only one activating enzyme gene in the *A. orientalis* genome. Further experiments showed that this activating enzyme can adenylate each of these sulphur-carrier proteins and probably also catalyses the subsequent thiolation, through its rhodanese domain. A proper combination of these sulphur-delivery systems is effective for BexX-catalysed 2-thiogluco-6-phosphate production. The ability of BexX to selectively distinguish sulphur-carrier proteins is given a structural basis using X-ray crystallography. This study is, to our knowledge, the first complete characterization of thiosugar formation in nature and also demonstrates the receptor promiscuity of the *A. orientalis* sulphur-delivery system. Our results also show that co-opting the sulphur-delivery machinery of primary metabolism for the biosynthesis of sulphur-containing natural products is probably a general strategy found in nature.

The unusual sugars that are found in many secondary metabolites have crucial roles in determining the efficacy and specificity of the biological activities of the parent molecules^{8,9}. Despite recent advances in research on the biosynthesis of unusual sugars, little is known about thiosugar formation, owing to the rarity of thiosugars in natural products and the limited knowledge about sulphur incorporation into secondary metabolites^{1,2,10,11}. We studied the biosynthesis of the 2-thiosugar-containing antibiotic BE-7585A (4, Fig. 1a) in *A. orientalis* subsp. *vinearia* BA-07585 and identified a putative 2-thiogluco-6-phosphate synthase, BexX^{6,7}. This enzyme has significant sequence homology to the thiazole synthase ThiG¹², which is responsible for construction of the thiazole moiety (8) from 1-deoxy-D-xylulose-5-phosphate (DXP, 6) in thiamine biosynthesis^{13,14} (Fig. 1b). ThiG catalyses sulphur insertion into a ThiG-ketosugar adduct (7)¹²; therefore, BexX may have a similar role in the conversion of glucose-6-phosphate (G6P, 1) to 2-thiogluco-6-phosphate (5) in *A. orientalis* (Fig. 1a). The proposed function of BexX is supported by the detection of a covalent adduct (2) between BexX and a 2-ketosugar

derived from G6P⁷. The crystal structure of the BexX-substrate complex has now been determined to 2.3 Å resolution (Extended Data Fig. 1), confirming that G6P is covalently attached to the lysine at position 110 (Lys 110) of BexX (Fig. 1c). However, the absence of genes encoding potential sulphur-transfer enzymes, including common sulphur-carrier proteins¹⁵, cysteine desulphurases¹⁶, and rhodanese-like proteins¹⁷, in and near the BE-7585A biosynthetic gene cluster impeded further functional characterization of BexX.

To search for the sulphur-carrier protein required for the BexX reaction, the entire genome of *A. orientalis* was sequenced. A total of 9,210 coding open reading frames were identified in approximately 9.8 megabases of genomic DNA, including genes encoding five cysteine desulphurase homologues, five rhodanese homologues and four sulphur-carrier protein homologues (ThiS, Moad, CysO and MoadD2) (Extended Data Table 1). The *thiS*, *moaD* and *cysO* genes are part of the thiamine, molybdopterin and cysteine biosynthetic gene clusters in *A. orientalis*, respectively^{18,19}, whereas *moaD2* stands alone with no nearby genes associated with a biosynthetic pathway (Extended Data Fig. 2a–d and Supplementary Table 1). Although the protein receptor for MoadD2 is not immediately apparent, MoadD2 has high sequence homology to Moad and therefore probably functions as a Moad homologue. In view of the sequence similarity between BexX and ThiG and their mechanistic parallels⁷, we anticipated that ThiS, being the cognate sulphur-carrier partner of ThiG^{13,14}, might be recruited for sulphur delivery to the BexX-G6P complex (2) in *A. orientalis*.

Unlike the thiamine biosynthetic gene clusters in *Escherichia coli* and *Bacillus subtilis*^{13,14}, the gene cluster in *A. orientalis* does not contain *thiF*, the gene that encodes the ThiS-activating enzyme, which is essential for converting ThiS to its thiocarboxylate form (10). The corresponding activating enzymes for Moad and CysO are also missing from the respective molybdopterin and cysteine biosynthetic gene clusters in *A. orientalis*. To our surprise, only a single putative activating enzyme was found in the entire genome of *A. orientalis*: a MoeZ homologue with a ThiF- and MoeB-like domain at the amino terminus and a rhodanese homology domain at the carboxy terminus (Extended Data Fig. 2 and Supplementary Table 1). Because it is unique in the genome and because it is not part of the molybdopterin gene cluster or associated with any other biosynthetic gene cluster, this protein, MoeZ, may be the universal activating catalyst for thiocarboxylate protein production in *A. orientalis* (Fig. 2a).

To test the proposed function of MoeZ, the ThiS and MoeZ proteins of *A. orientalis* were heterologously expressed in *E. coli*, each with an N-terminal His₆ tag. When ThiS was incubated with MoeZ and ATP, an electrospray ionization-mass spectrometry (ESI-MS) signal corresponding to adenylated ThiS (9) was detected, together with a few peaks probably derived from the reaction of the labile adenylated ThiS with buffer components (Extended Data Fig. 3c). On addition of excess bisulphide, complete conversion of 9 to its thiocarboxylate form (10) was observed (Extended Data Fig. 3d). Control experiments using bisulphide

¹Department of Chemistry, University of Texas at Austin, Austin, Texas 78712, USA. ²Department of Chemistry and Chemical Biology, Cornell University, Ithaca, New York 14853, USA. ³Division of Medicinal Chemistry, College of Pharmacy, University of Texas at Austin, Austin, Texas 78712, USA. ⁴Biodiversity Research Center, Academia Sinica, Taipei 115, Taiwan. ⁵Genomics Research Center, Academia Sinica, Taipei 115, Taiwan. ⁶Institute of Bioinformatics and Biosignal Transduction, National Cheng-Kung University, Tainan 701, Taiwan.

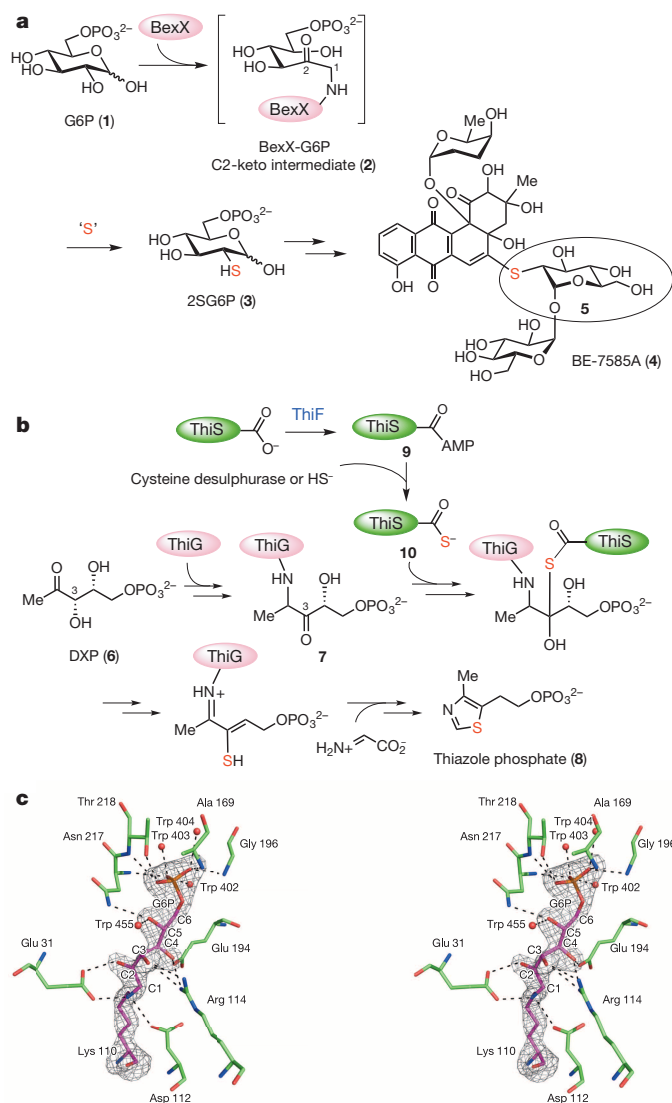


Figure 1 | Proposed mechanism for 2-thiosugar formation in BE-7585A biosynthesis. **a**, The active site lysine residue (Lys110)^{6,7} of BexX initially forms an imine bond with G6P (1) at the C1 position, which is isomerized first to a C1–C2 enamine and then a C2-ketone intermediate (2) (the carbon atoms are numbered). Subsequent nucleophilic attack by a sulphur donor (red) occurs at the C2 position of 2, resulting in the incorporation of a sulphur atom in the 2-thio-G6P (2SG6P) (3) product. One arrow indicates one step, and two arrows suggest multiple steps between the transformations. **b**, ThiG-catalysed thiazole phosphate biosynthetic pathway. **c**, Stereo view of BexX active site. The active-site side chains and the Lys 110–G6P intermediate are depicted as sticks, with the carbon atoms of the residues coloured in green and purple, respectively (and nitrogen in blue and oxygen in red). The $F_o - F_c$ simulated annealing omit map of the Lys110–G6P intermediate contoured at 4σ is shown in grey. Water molecules are shown as red spheres. The carbon atoms of G6P are numbered from C1 to C6. The dashed lines represent hydrogen bonding. Me, methyl.

in the absence of MoeZ showed no change in the original ThiS signals. These results demonstrated that MoeZ can charge ThiS to its ready-to-use thiocarboxylate form (Fig. 2a). The activated ThiS–COS[−] was next incubated with the BexX–G6P complex (2). If sulphur transfer occurs and the resultant 2-thiosugar product (3) is released from the enzyme, a shift in the mass signal corresponding to the BexX–G6P complex to that of the free enzyme is anticipated (Fig. 2b). However, no increase in free BexX was observed in the presence of ThiS–COS[−] (Fig. 2c–e), hence ruling out ThiS (and bisulphide) as the sulphur donor for BexX in 2-thiosugar formation.

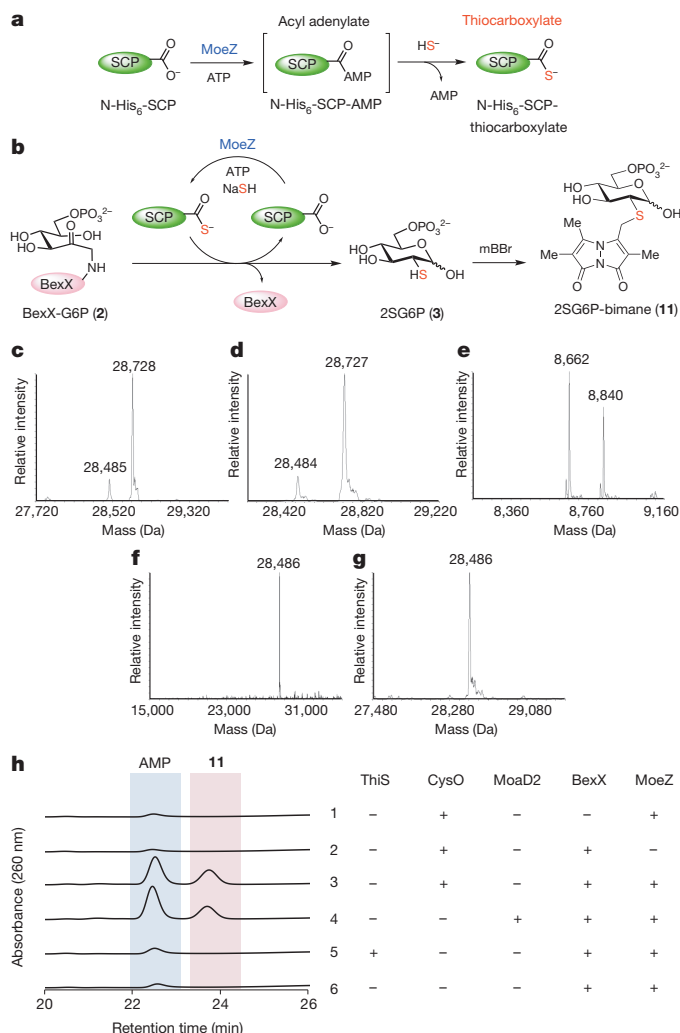


Figure 2 | Activation of sulphur-carrier proteins and sulphur transfer to the BexX–G6P complex. **a**, MoeZ-catalysed acyl adenylation of a sulphur-carrier protein (SCP)—for example, ThiS, MoaD, CysO or MoaD2—followed by nucleophilic attack of bisulphide, yielding the corresponding SCP–thiocarboxylate. **b**, Expected sulphur-transfer reaction to BexX–G6P (2) using SCP–thiocarboxylate to produce 2SG6P (3), which was further derivatized with mBBR to give 2SG6P–bimane (11). **c–g**, Deconvoluted ESI–MS analyses of as-isolated C–His₆–BexX (where C denotes carboxy terminal) (calculated mass (calcd), 28,488), showing that the major species is 2 (28,730 calcd) (c), and the sulphur-transfer reactions using ThiS (d)—and a lower mass range of the same reaction showing N–His₆–ThiS–COSH (8,663 calcd) and its N–gluconoyl derivatives (8,841 calcd) (where N denotes amino terminal) (e) (see also Extended Data Fig. 3)—CysO (f) or MoaD2 (g). **h**, HPLC traces (left) for BexX-catalysed reactions (right). In the reaction with ThiS, the amount of AMP, probably derived from partial decomposition of ATP during incubation, was comparable to that in the control with no added SCP.

To assess the competence of MoaD, CysO and MoaD2 of *A. orientalis* as sulphur-carrier proteins in BexX-catalysed reactions, N-terminally His₆-tagged MoaD, CysO and MoaD2 were prepared. Similar to the case for ThiS, thiocarboxylation of each protein in the presence of MoeZ, ATP and sodium sulphide (NaSH) was confirmed by mass spectrometric analysis (Extended Data Fig. 3f–k). Because activated MoaD was generated in small quantities at low purity, only CysO and MoaD2 were incubated with the BexX–G6P complex. The relative intensities of the mass signals corresponding to BexX–G6P (2) and the free enzyme were monitored before and after the addition of the activated sulphur-carrier proteins. Only signal ascribed to free BexX was discernible after treatment with CysO or MoaD2 (Fig. 2f, g). To gain further evidence, the thiosugar product (3) was derivatized with monobromobimane (mBBR)

before high-performance liquid chromatography (HPLC) analysis to yield **11**, thereby facilitating detection (Fig. 2b). Indeed, when CysO or Moad2 was used, a new peak (product peak) clearly appeared, together with an increase in AMP production (Fig. 2h, traces 3 and 4). The product peak was isolated and characterized as 2-thiogluco-6-phosphate-bimane (**11**) by ESI-MS and NMR spectroscopy (Supplementary Methods). Each assay sample was also treated with alkaline phosphatase, and the dephosphorylated product matched well with the synthetic standard (Extended Data Fig. 4). As expected, no thiosugar product was detected in the sample containing ThiS. These results firmly established that BexX-catalysed 2-thiosugar formation was able to proceed in the presence of either CysO-COS⁻ or Moad2-COS⁻ but not ThiS-COS⁻. These two examples clearly reveal the capability of some sulphur-delivery enzymes to 'moonlight' in natural product biosynthesis, bridging the biosynthetic pathways of primary and secondary metabolites.

Thiocarboxylated sulphur-carrier proteins recognize their partners through specific protein-protein interactions^{20–22}. Because BexX has 37% sequence similarity to ThiG²² and because the two enzymes are structurally homologous, it was surprising to find that ThiS is not a sulphur-carrier protein for BexX. To understand the sulphur-carrier protein specificity of BexX, the BexX-CysO structure was determined to 2.6 Å resolution (Fig. 3a and Extended Data Fig. 1f). We were unable to crystallize BexX-Moad2; however, because of the compact ubiquitin-like fold and similar sizes of CysO (90 residues) and Moad2 (96 residues), we were able to construct a reliable homology model for BexX-Moad2 using the BexX-CysO structure as a template. We also constructed a hypothetical model of BexX-ThiS using ThiS from *Thermus thermophilus* (Protein Data Bank (PDB) ID, 2HTM) as a guide.

CysO and Moad2 superimpose well, with a root mean squared deviation (r.m.s.d.) of 0.1 Å for 80 C α atoms. By contrast, CysO and ThiS show significant differences, especially in the loop regions, with an r.m.s.d. of 2.7 Å for 43 C α carbon atoms (Fig. 3b and Extended Data Figs 1d, e and 5). The most significant difference between ThiS (66 residues) and either CysO or Moad2 is the insertion of two additional α -helices, which are located at the BexX-sulphur-carrier protein interface (Extended Data Fig. 5). As a result, the amount of accessible surface area buried on complex formation is $\sim 1,000$ Å² for BexX-CysO and BexX-Moad2 but only ~ 600 Å² for BexX-ThiS (Extended Data Figs 5 and 6a). CysO contributes 19 residues and BexX contributes 26 residues to the interface of BexX-CysO, similarly to the 16 residues contributed by Moad2 and the 23 by BexX in BexX-Moad2. By contrast, only eight ThiS residues contribute to the interface in the BexX-ThiS model. Ten of the interface residues are conserved between CysO and Moad2, but only four of these are conserved in ThiS (Extended Data Fig. 5a). The hydrogen-bonding scheme is also conserved between BexX-CysO and BexX-Moad2 (Extended Data Fig. 6b–d). A comparison of the BexX-CysO complex and the *B. subtilis* ThiG-ThiS complex (PDB ID, 1TYG)²² complex provides further insight. Superposition of BexX-CysO and ThiG-ThiS results in an r.m.s.d. of 1.7 Å for the BexX-ThiG core (Fig. 3c); however, CysO and ThiS do not overlay well (r.m.s.d. >40 Å). Thus, even though the overall sulphur-carrier protein folds are similar, and even though each sulphur-carrier protein is positioned to insert its C-terminal tail into the active site of its partner (Extended Data Fig. 6e, f), the selection of CysO or Moad2 by BexX is clearly determined by the interface interactions.

Finally, we also examined whether the C-terminal rhodanese domain of MoeZ has a role in sulphur transfer. In a typical rhodanese reaction, the conserved cysteine residue in rhodanese (for example, Cys 360 in MoeZ) is converted to a persulphide group in the presence of thiosulphate or through the action of a cysteine desulphurase using L-cysteine as the sulphur source¹⁷. Because the resultant persulphide is a known sulphur donor³, it can be used to charge the adenylated sulphur-carrier proteins to the thiocarboxylate forms (Fig. 4). To test this potential second role of MoeZ as a sulphur donor, MoeZ was incubated with CysO or Moad2, first in the presence of ATP and thiosulphate (with no addition of reducing agent to prevent bisulphide formation). MoeZ

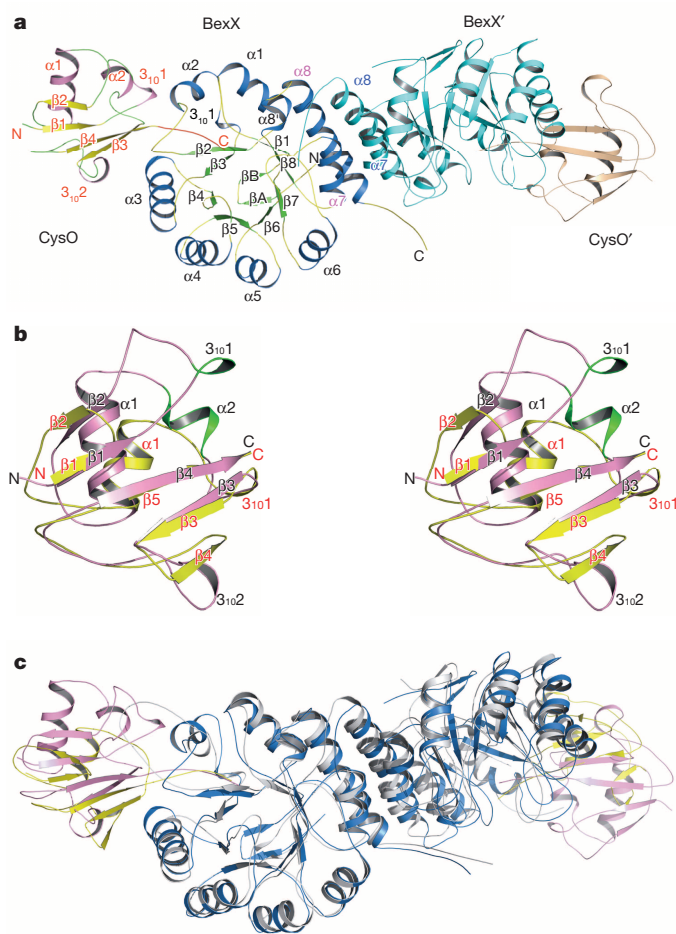


Figure 3 | Structure of BexX-CysO from *A. orientalis*. **a**, A ribbon diagram of the BexX-CysO heterotetramer generated using two-fold crystallographic symmetry. BexX' and CysO' are coloured in cyan and light brown, respectively. Secondary structural elements of BexX and CysO are coloured in blue and pink for α -helices, green and yellow for β -strands, and yellow and green for loops, respectively. The C-terminal tail (AVAGG) of CysO is highlighted in red. The helices $\alpha 7$ and $\alpha 8$ from BexX and BexX' are labelled in pink and blue, respectively. **b**, Stereo view diagram of the superposition of CysO (pink) and ThiS (yellow). Secondary structural elements are labelled in black for CysO and red for ThiS. The two major insertions of CysO, 3101 and $\alpha 2$, are highlighted in green. **c**, Comparison of the *A. orientalis* BexX-CysO dimer and the *Bacillus subtilis* ThiG-ThiS dimer. Monomers are coloured in blue for BexX, pink for CysO, grey for ThiG and yellow for ThiS.

was observed to catalyse the thiolation of both CysO and Moad2 but not when replaced with a MoeZ(Cys360Ala) mutant (Extended Data Fig. 7), which retained a similar level of adenylation activity to wild-type MoeZ (Extended Data Fig. 8). These observations are consistent with the C-terminal rhodanese domain of MoeZ being involved in sulphur transfer. Next, we assessed BexX-catalysed 2-thiosugar formation with MoeZ and Moad2 in the presence of ATP, using either thiosulphate (Fig. 4a) or L-cysteine and a cysteine desulphurase (CD4, Extended Data Table 1) from *A. orientalis* (Fig. 4b) as the primary sulphur sources. As expected, the 2-thiogluco product was detected in both cases in the absence of reducing agents (Extended Data Fig. 9). Taken together, these results support the probable dual role of MoeZ in catalysing both the adenylation and thiolation of sulphur-carrier proteins in *A. orientalis*.

In summary, we carried out whole-genome sequencing of *A. orientalis* and demonstrated that the sulphur delivery for 2-thiosugar production in the biosynthesis of BE-7585A is achieved by hijacking the sulphur-transfer systems from primary metabolism. Although the overall reaction mechanism of 2-thiosugar formation resembles that of thiamine

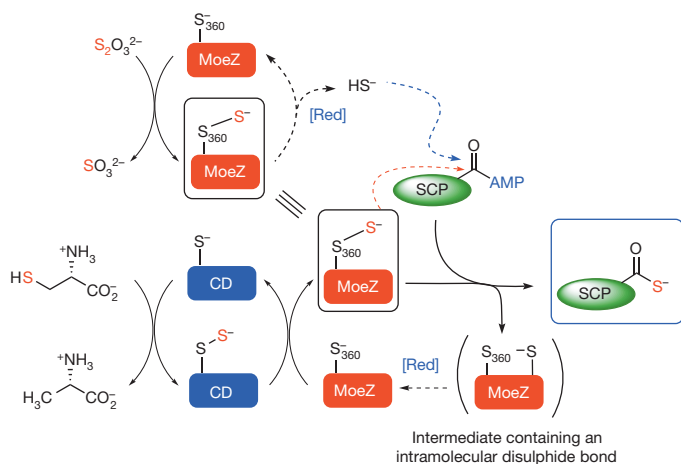


Figure 4 | Possible involvement of the rhodanese domain of MoeZ in thiolation of sulphur-carrier proteins. The C-terminal rhodanese domain (RHOD) of MoeZ catalyses thiolation of the adenylated SCP. The sulphur source for charging the rhodanese domain can be from thiosulphate (a) or from L-cysteine mediated by a cysteine desulphurase (CD) (b). Nucleophilic attack (red dashed line) on the adenylated sulphur-carrier protein followed by intramolecular disulphide bond formation (with another cysteine residue in MoeZ) allows sulphur transfer from the persulphide group to SCP. The protein persulphide intermediate can be reduced to release bisulphide, which can also attack adenylated sulphur-carrier proteins (blue dashed line). To prevent such complications, the experiments were carried out in the absence of reducing agents. [Red], reduction; S₃₆₀, the wild-type Cys 360 residue.

biosynthesis, BexX cannot utilize the corresponding sulphur-carrier protein, ThiS, from the thiamine pathway. Instead, the sulphur-carrier proteins that are probably involved in cysteine (CysO) and molybdopterin (MoaD2) biosynthesis are recruited to transfer their C-terminal thiocarboxylate sulphur to the BexX-G6P complex (2). Two structural snapshots, of the BexX-G6P ketone intermediate (2) and the BexX-CysO heterotetramer, provide significant insight into the proposed sulphur incorporation mechanism, as well as the structural basis by which sulphur-carrier proteins are selected. These results indicate that a functional alliance between a sulphur-carrier protein and its acceptor protein is not specific but is not entirely random. The assembly of operational sulphur-transfer machinery from components of the sulphur-carrier systems of primary metabolism, to deliver a sulphur atom to produce 2-thiosugars, is an efficient strategy for the biosynthesis of a relatively rare metabolite. Such an *ad hoc* approach to sulphur transfer may be a paradigm for as yet undiscovered pathways of sulphur-containing natural product biosynthesis. The revelation that MoeZ is the universal activating enzyme for all known sulphur-carrier proteins in *A. orientalis* is another significant finding. The presence of only a single ThiF-type enzyme in the entire genome has also been noted in several other microorganisms (Extended Data Table 2). The charging of multiple sulphur-carrier proteins in different biosynthetic pathways by a single activating enzyme may be a common phenomenon in nature (at least in the Actinomycetales)^{5,23,24}. In addition, the finding that functional pairs of sulphur-carrier proteins and their acceptor proteins are not necessarily located in the same gene cluster raises the possibility that some cryptic gene clusters in various genomes may encode pathways for the biosynthesis of sulphur-containing natural products. Such a possibility has generally been overlooked in recent efforts to deconvolute genomic information.

METHODS SUMMARY

Whole-genome sequencing of *Actinomyces orientalis* was carried out at the High Throughput Sequencing Core Facility at Academia Sinica, Taiwan, using a 454 GS FLX Titanium analyser (Roche) and a Genome Analyzer Ix (Illumina). Contig extension and genome annotation were carried out using Glimmer (Gene Locator and Interpolated Markov ModelER) version 3.0 (ref. 25), tRNAscan-SE²⁶ and RNAmmer²⁷. The *thiS*, *moaD*, *cysO*, *moaD2* and *moeZ* genes were PCR-amplified from *A. orientalis*

genomic DNA⁶ and ligated into a pET28b(+) vector (Novagen). The resultant plasmids were overexpressed in the *Escherichia coli* BL21 Star (DE3) strain (Invitrogen) and purified under conditions similar to those previously described for preparing BexX⁷. Each of the purified sulphur-carrier proteins (50–90 μM) was subjected to ESI-MS analysis before and after incubation with 80 μM MoeZ and 5 mM ATP in 100 mM Tris-HCl buffer (pH 8.0) containing 5 mM MgCl₂ in the presence or absence of 10 mM NaSH. The corresponding sulphur-carrier protein thiocarboxylates generated *in situ* were incubated with 100 μM BexX and 2 mM G6P (1) in 50 mM NH₄HCO₃ buffer, pH 8.0, at 25 °C for 8 h to yield the 2-thio-D-glucose-6-phosphate product (3). The resultant reaction mixture was then added to a solution of 5 mM mBBr in methanol to give 11 and subjected to HPLC analysis. Crystals of BexX-G6P were grown from 40% (v/v) polyethylene glycol (PEG) 300, 0.2 M calcium acetate and 0.1 M sodium cacodylate-HCl, pH 6.5, and crystals of BexX-CysO complexes were grown from 28% PEG 4000, 0.2 M LiSO₄ and 0.1 M Tris, pH 8.0. Data were collected at the Cornell High Energy Synchrotron Source (CHESS) and the Advanced Photon Source (APS). The structures were determined by molecular replacement.

Online Content Any additional Methods, Extended Data display items and Source Data are available in the online version of the paper; references unique to these sections appear only in the online paper.

Received 29 October 2013; accepted 18 March 2014.

Published online 11 May 2014.

- Parry, R. J. in *Comprehensive Natural Products Chemistry* Vol. 1 (eds Meth-Cohn, O., Barton, D. & Nakanishi, K.) 825–863 (Elsevier Science, 1999).
- Fontecave, M., Ollagnier-de-Choudens, S. & Mulliez, E. Biological radical sulfur insertion reactions. *Chem. Rev.* **103**, 2149–2166 (2003).
- Mueller, E. G. Trafficking in persulfides: delivering sulfur in biosynthetic pathways. *Nature Chem. Biol.* **2**, 185–194 (2006).
- Kessler, D. Enzymatic activation of sulfur for incorporation into biomolecules in prokaryotes. *FEMS Microbiol. Rev.* **30**, 825–840 (2006).
- Burroughs, A. M., Iyer, L. M. & Aravind, L. Natural history of the E1-like superfamily: implication for adenylation, sulfur transfer, and ubiquitin conjugation. *Proteins* **75**, 895–910 (2009).
- Sasaki, E., Ogasawara, Y. & Liu, H.-w. A biosynthetic pathway for BE-7585A, a 2-thiosugar-containing angucycline-type natural product. *J. Am. Chem. Soc.* **132**, 7405–7417 (2010).
- Sasaki, E. & Liu, H.-w. Mechanistic studies of the biosynthesis of 2-thiosugar: evidence for the formation of an enzyme-bound 2-ketohexose intermediate in BexX-catalyzed reaction. *J. Am. Chem. Soc.* **132**, 15544–15546 (2010).
- Thibodeaux, C. J., Melançon, C. E. & Liu, H.-w. Unusual sugar biosynthesis and natural product glycodiversification. *Nature* **446**, 1008–1016 (2007).
- Thibodeaux, C. J., Melançon, C. E. & Liu, H.-w. Natural-product sugar biosynthesis and enzymatic glycodiversification. *Angew. Chem. Int. Edn Engl.* **47**, 9814–9859 (2008).
- Lin, C.-I., McCarty, R. M. & Liu, H.-w. The biosynthesis of nitrogen-, sulfur- and high-carbon chain-containing sugars. *Chem. Soc. Rev.* **42**, 4377–4407 (2013).
- Braunshausen, A. & Seebeck, F. P. Identification and characterization of the first ovolith biosynthetic enzyme. *J. Am. Chem. Soc.* **133**, 1757–1759 (2011).
- Park, J. H. et al. Biosynthesis of the thiazole moiety of thiamin pyrophosphate (Vitamin B₁). *Biochemistry* **42**, 12430–12438 (2003).
- Begley, T. P. Cofactor biosynthesis: an organic chemist's treasure trove. *Nat. Prod. Rep.* **23**, 15–25 (2006).
- Jurgenson, C. T., Begley, T. P. & Ealick, S. E. The structural and biochemical foundations of thiamin biosynthesis. *Annu. Rev. Biochem.* **78**, 569–603 (2009).
- Iyer, L. M., Burroughs, A. M. & Aravind, L. The prokaryotic antecedents of the ubiquitin-signaling system and the early evolution of ubiquitin-like β-grasp domains. *Genome Biol.* **7**, R60 (2006).
- Mihara, H. & Esaki, N. Bacterial cysteine desulfurases: their function and mechanisms. *Appl. Microbiol. Biotechnol.* **60**, 12–23 (2002).
- Cipollone, R., Ascenzi, P. & Visca, P. Common themes and variations in the rhodanese superfamily. *IUBMB Life* **59**, 51–59 (2007).
- Schwarz, G., Mendel, R. R. & Ribbe, M. W. Molybdenum cofactors, enzymes and pathways. *Nature* **460**, 839–847 (2009).
- Burns, K. E. et al. Reconstitution of a new cysteine biosynthetic pathway in *Mycobacterium tuberculosis*. *J. Am. Chem. Soc.* **127**, 11602–11603 (2005).
- Jurgenson, C. T., Burns, K. E., Begley, T. P. & Ealick, S. E. Crystal structure of a sulfur carrier protein complex found in the cysteine biosynthetic pathway of *Mycobacterium tuberculosis*. *Biochemistry* **47**, 10354–10364 (2008).
- Rudolph, M. J., Wuebbens, M. M., Rajagopalan, K. V. & Schindelin, H. Crystal structure of molybdopterin synthase and its evolutionary relationship to ubiquitin activation. *Nature Struct. Biol.* **8**, 42–46 (2001).
- Settembre, E. C. et al. Thiamin biosynthesis in *Bacillus subtilis*: structure of the thiazole synthase/sulfur carrier protein complex. *Biochemistry* **43**, 11647–11657 (2004).
- Shigi, N., Sakaguchi, Y., Asai, S., Suzuki, T. & Watanabe, K. Common thiolation mechanism in the biosynthesis of tRNA thiouridine and sulphur-containing cofactors. *EMBO J.* **27**, 3267–3278 (2008).
- Voss, M., Nimtz, M. & Leimkühler, S. Elucidation of the dual role of mycobacterial MoeZ in molybdenum cofactor biosynthesis and cysteine biosynthesis. *PLoS ONE* **6**, e28170 (2011).

25. Delcher, A. L., Bratke, K. A., Powers, E. C. & Salzberg, S. L. Identifying bacterial genes and endosymbiont DNA with Glimmer. *Bioinformatics* **23**, 673–679 (2007).
26. Lowe, T. M. & Eddy, S. R. tRNAscan-SE: a program for improved detection of transfer RNA genes in genomic sequence. *Nucleic Acids Res.* **25**, 955–964 (1997).
27. Lagesen, K. *et al.* RNAmmer: consistent and rapid annotation of ribosomal RNA genes. *Nucleic Acids Res.* **35**, 3100–3108 (2007).

Supplementary Information is available in the online version of the paper.

Acknowledgements We thank C.-H. Wong and R. Chen, as well as Academia Sinica for funding, for the whole-genome draft sequencing; and the staff at the Analytical Instrumentation Facility of the College of Pharmacy (University of Texas), the Advanced Photon Source (APS) Northeastern Collaborative Access Team (NE-CAT) beamlines and the Cornell High Energy Synchrotron Source (CHESS) beamlines (Cornell University) for their assistance in data collection. We also thank D. Kim for assistance with the early biochemical experiments, C. Kinsland for providing the *cysO*/pTYB1 clone, Y. Zhang for help with the structure determination of BexX–CysO and L. Kinsland for help in preparing the manuscript. This work was supported in part by grants from the National Institutes of Health (NIH) (GM035906 to H.-W.L. and DK67081 to S.E.E.) and the Welch Foundation (F-1511 to H.-W.L.). The X-ray crystallography work was conducted at the APS NE-CAT beamlines, which are supported by award GM103403 from the National Institute of General Medical Sciences, NIH. Use of the APS is

supported by the US Department of Energy, Office of Basic Energy Sciences, under contract no. DE-AC02-06CH11357. The use of the CHESS is supported by the National Science Foundation (DMR-0936384) and the National Institute of General Medical Sciences, NIH (GM103485).

Author Contributions H.-W.L. provided the scientific direction and the overall experimental design for the studies. E.S. and H.G.S. designed and performed the biochemical experiments. X.Z. and S.E.E. were responsible for the crystal structure studies. M.-Y.J.L., T.-L.L., A.O., J.-Y.L. and Y.-H.C. carried out the whole-genome sequencing and gene annotation. E.S., X.Z., H.G.S., S.E.E. and H.-W.L. wrote the manuscript.

Author Information The nucleotide sequences of the thiamine biosynthetic gene cluster, *moeZ* and the surrounding genes, the molybdopterin biosynthetic gene cluster, the cysteine biosynthetic gene cluster, and *moaD2* and the surrounding genes have been deposited in the GenBank database under the accession numbers JN602207, JN602208, JN602209, JN602210 and JN602211, respectively. The atomic coordinates and structure factors for BexX–G6P and BexX–CysO have been deposited in the Protein Data Bank under the accession numbers 4N6F and 4N6E, respectively. Reprints and permissions information is available at www.nature.com/reprints. The authors declare no competing financial interests. Readers are welcome to comment on the online version of the paper. Correspondence and requests for materials should be addressed to H.-W.L. (h.w.liu@mail.utexas.edu).

METHODS

Whole-genome sequencing and analysis. Soybean-casein digest (TSB) medium (10 ml) was inoculated with spores of *Amycolatopsis orientalis* and incubated in a rotary incubator at 30 °C and 250 r.p.m. for 2 days. The resultant seed culture (4 ml) was transferred to 100 ml TSB medium and grown under the same conditions for 2 days. The growth culture (25 ml) was centrifuged at 5,000g for 20 min at 4 °C, and the cells were washed with 25 ml 10 mM EDTA. After another centrifugation, the cells were stored at -80 °C until use. The cells were resuspended in 5 ml 1 mM EDTA, and the suspension was divided into 1.5 ml tubes (0.4 ml each). The genomic DNA was extracted using the PureLink Genomic DNA Mini Kit (Invitrogen) according to the manufacturer's instructions. The resultant DNA solution (0.5 µg µl⁻¹, 50 µl from each tube) was subjected to massively parallel sequencing using a 454 GS FLX Titanium analyser (Roche) and a Genome Analyzer IIx (Illumina) at the High Throughput Sequencing Core Facility at Academia Sinica, Taiwan. Primary assembly was carried out using 454 Newbler software (Roche). Contig extension and the closing of short gaps was achieved by scripts built in-house at the core. Genome annotation was carried out using Glimmer (Gene Locator and Interpolated Markov ModelER) version 3.0 (ref. 25), tRNAscan-SE²⁶ and RNAmmer²⁷. Homologous protein sequences were identified in the NCBI database using the Basic Local Alignment Search Tool (BLAST).

Preparation of proteins. C-His₆-BexX (where C denotes carboxy terminal) was prepared as described previously⁷. The *thiS* (orf13974), *moaD* (orf13839), *cysO* (orf06461), *moaD2* (orf10102), *moeZ* (orf02110) and *cd4* (orf04763) genes were PCR-amplified from *A. orientalis* genomic DNA using primers with engineered NdeI and HindIII restriction sites. The sequences of the primers are described in the Supplementary Methods. The PCR-amplified gene fragments were purified, digested with NdeI and HindIII and ligated into a pET28b(+) vector (Novagen) that had been digested with the same enzymes. For crystallization studies, the *bexX* gene was also subcloned into pET28b(+) and produced as an N-terminally His₆-tagged protein. In addition, the *cysO* gene was subcloned into an IMPACT pTYB1 vector (New England Biolabs) that had been digested with NdeI and SapI for the production of CysO thiocarboxylate²⁸. The resultant plasmids were used to transform the *Escherichia coli* BL21 Star (DE3) strain (Invitrogen) for protein overexpression. An overnight culture of *E. coli* transformants grown in 10 ml LB medium containing 50 µg ml⁻¹ kanamycin at 37 °C was used to inoculate 1 l of the same growth medium. The culture was incubated at 37 °C with shaking (230 r.p.m.) until the optical density at 600 nm (OD₆₀₀) reached ~0.5. Protein expression was then induced by the addition of isopropyl β-D-thiogalactoside (IPTG) to a final concentration of 0.1 mM, and the cells were allowed to grow at 18 °C with shaking at 125 r.p.m. for an additional 24 h. The cells were collected after centrifugation at 4,500g for 15 min and stored at -80 °C until lysis. All purification steps were carried out at 4 °C using nickel (Ni-NTA) resin according to the manufacturer's protocol. The proteins were eluted using 250 mM imidazole buffer containing 10% glycerol, except those for crystallization studies. The collected protein solution was dialysed three times against 1 l 50 mM Tris-HCl buffer, pH 8, containing 300 mM NaCl and 15% glycerol. The protein solution was then flash-frozen in liquid nitrogen and stored at -80 °C until use. For crystallization studies, N-His₆-BexX (where N denotes amino terminal) eluted with 250 mM imidazole buffer was incubated with 2 mM G6P and 2 mM dithiothreitol for 1 h at 4 °C and then further purified in 10 mM Tris-HCl buffer, pH 8.0, containing 50 mM NaCl by using a Superdex G200 column (GE Healthcare). In the case of *cysO*/pTYB1, the cell lysate was loaded onto a column of chitin beads (New England Biolabs, 10 ml) at a flow rate of 0.8 ml min⁻¹. The column was then washed with 15 column volumes of column buffer at a flow rate of 2 ml min⁻¹. Intein-mediated cleavage of the protein was carried out at 18 °C for 12 h with 30 ml 50 mM dithiothreitol to yield CysO or with Na₂S to yield CysO-thiocarboxylate²⁸. CysO was further purified in 10 mM Tris-HCl buffer, pH 8.0, containing 50 mM NaCl by using a Superdex G75 column (GE Healthcare). The protein concentration was determined by the Bradford assay using bovine serum albumin as the standard²⁹. The molecular mass and purity (>90%, except N-His₆-MoaD) of the proteins were estimated by SDS-PAGE analyses (Extended Data Fig. 3l). **ESI-MS analyses of proteins.** The purified sulphur-carrier protein (that is, N-His₆-ThiS (90 µM), N-His₆-MoaD (50 µM), N-His₆-CysO (60 µM) or N-His₆-MoaD2 (90 µM)) in 5 mM or 100 mM Tris-HCl buffer, pH 8.0, was subjected to ESI-MS analysis, which was carried out at the Mass Spectrometry core facility at the College of Pharmacy, University of Texas, Austin (Extended Data Fig. 3b, f-h). In the case of N-His₆-ThiS, the protein was also incubated with 80 µM N-His₆-MoeZ and 5 mM ATP in 100 mM Tris-HCl buffer, pH 8.0, containing 5 mM MgCl₂ at 30 °C for 0.5 h (Extended Data Fig. 3c). Additionally, to aliquots of the above solution was added 10 mM sodium sulphide (NaSH), and the resultant solution was subjected to ESI-MS analysis after incubation at 30 °C for 0.5 h (Extended Data Fig. 3d). As a control, a reaction containing only 90 µM N-His₆-ThiS and 5 mM NaSH in 100 mM Tris-HCl buffer, pH 8.0, was similarly analysed (Extended Data Fig. 3e). The other sulphur-carrier proteins (that is, N-His₆-MoaD (50 µM), N-His₆-CysO (60 µM)

and N-His₆-MoaD2 (90 µM)) were separately incubated with 7 µM N-His₆-MoeZ, 5 mM ATP and 10 mM NaSH in 50 mM Tris-HCl buffer, pH 8.0, containing 5 mM MgCl₂ at 30 °C for 0.5 h and subjected to ESI-MS analysis (Extended Data Fig. 3i-k). Finally, each sulphur-carrier protein (that is, N-His₆-ThiS (90 µM), N-His₆-CysO (60 µM) or N-His₆-MoaD2 (90 µM)) was also incubated with 100 µM C-His₆-BexX and 7 µM N-His₆-MoeZ in 50 mM Tris-HCl buffer, pH 8.0, containing 5 mM ATP, 10 mM NaSH and 5 mM MgCl₂ at 30 °C for 0.5 h. The resultant solution was subjected to ESI-MS analysis (Fig. 2d-g).

2-Thiosugar formation and its detection. The typical BexX reaction mixture (50 µl) contained 100 µM C-His₆-BexX, sulphur-carrier protein (30 µM N-His₆-CysO, 45 µM N-His₆-MoaD2 or 45 µM N-His₆-ThiS), 15 µM N-His₆-MoeZ, 2 mM ATP, 2 mM G6P and 5 mM NaSH in 50 mM NH₄HCO₃ buffer, pH 8.0, containing 5 mM MgCl₂. The resultant reaction mixture was incubated at 25 °C for 8 h and stored at -20 °C until analysis. To the reaction mixture (10 µl) prepared above was added 10 µl 10 mM mBBr methanol solution (the final concentration of mBBr was 5 mM), which was incubated at 25 °C for 5 min. The mixture was centrifuged at 16,000g for 5 min to remove the precipitant, and 10 µl supernatant was transferred to a new tube. The solution was evaporated *in vacuo* using a SpeedVac SC100 (Savant). The resultant residue was redissolved in 100 µl 50 mM NH₄HCO₃ buffer, pH 8.0, and subjected to HPLC analysis using a CarboPac PA1 analytical column (4 × 250 mm; Dionex). The sample was eluted with a gradient of water (solvent A) and 1 M ammonium acetate (solvent B). The gradient was run from 5% to 15% B over 5 min, from 15% to 30% B over 15 min and from 30% to 100% B over 7 min, with a 5-min wash at 100% B, and from 100% to 5% B over 3 min, followed by re-equilibration at 5% B for 5 min. The flow rate was 1 ml min⁻¹, and the detector was set at 260 nm (Fig. 2h). The peak corresponding to the enzymatic reaction product was isolated and subjected to ESI-MS and NMR analyses (see Supplementary Methods) for structural characterization. Alternatively, the reaction mixture stored at -20 °C was thawed and treated with 0.2 µl calf intestinal alkaline phosphatase (CIP) (2 units) and incubated at 37 °C for 1 h. The precipitant that appeared during the incubation was removed by centrifugation at 16,000g for 2 min, and 2 µl 100 mM mBBr in methanol was added to the reaction solution (the final concentration of mBBr was 5 mM). The resultant mixture was incubated at 25 °C for 5 min, and the supernatant (5 µl) was diluted with deionized water (95 µl) before HPLC analysis using an analytical C₁₈ column (4 × 250 mm). The sample (20 µl) was eluted with a gradient of water (solvent A) and 80% acetonitrile (solvent B). The gradient was run from 5% to 30% B over 15 min, from 30% to 80% B over 5 min and from 80% to 5% B over 5 min, followed by re-equilibration at 5% B for 10 min. The flow rate was 1 ml min⁻¹, and the detector was set at 260 nm. The 2-thio-D-glucose-bimane standard (0.1 mM) was prepared from the chemically synthesized 2-thio-D-glucose⁶ incubated with mBBr at room temperature for 5 min. The peak corresponding to the enzymatic reaction product was also isolated and subjected to ESI-MS analysis (Extended Data Fig. 4).

Determination of rhodanese activity of MoeZ. The site-specific Cys360Ala mutant of MoeZ was constructed according to the manufacturer's site-directed mutagenesis protocol (Stratagene) using *moeZ*/pET28b(+) as a DNA template. The forward primer (5'-GATCGTCTGACGCGCAAGTCGGGC-3') and the reverse primer (5'-GCGGGCGCCGACTTGCGGTGCAGG-3') were used in the PCR amplification. (The underlining indicates the site of mutation.) The resultant plasmid *moeZ*(Cys360Ala)/pET28b(+) was used to transform the *E. coli* BL21 Star (DE3) strain for protein overexpression. The rhodanese activity of MoeZ was determined using a previously described assay³⁰. A typical assay mixture contained 50 mM Tris-HCl, pH 8.0, 50 mM potassium cyanide, approximately 2 µM MoeZ or MoeZ(Cys360Ala) and a variable amount of sodium thiosulphate (0-35 mM) in 100 µl. The reaction was initiated by the addition of MoeZ and was quenched after 10-s incubation at 25 °C by the addition of 50 µl reagent A (15% formaldehyde). Then, 150 µl reagent B (1 g Fe(NO₃)₃·9H₂O and 2 ml 65% HNO₃ in 13 ml H₂O) was added for colour development. Formation of SCN⁻ in the reaction was quantified using the extinction coefficient for Fe(SCN)₃ (4,200 M⁻¹ cm⁻¹ at 460 nm). The steady-state kinetic parameters were determined in triplicate by fitting the experimental data using the Michaelis-Menten equation (Extended Data Fig. 7e). The assay for protein thiocarboxylate formation was performed in an anaerobic chamber to minimize the oxidation of MoeZ or MoeZ(Cys360Ala). A typical reaction mixture contained 80 µM MoeZ or MoeZ(Cys360Ala), 4 mM ATP, 5 mM MgCl₂, 5 mM Na₂S₂O₃ in 50 mM HEPES, pH 8.0, with 500 mM glycerol (from enzyme stock solution) and 100 µM of one of the sulphur-carrier proteins, N-His₆-MoaD2 or N-His₆-CysO. The reaction was incubated in the glove box at ~30 °C for 40 min and then quenched by flash-freezing in liquid nitrogen. Samples were then analysed by ESI-MS (Extended Data Fig. 7a-d).

Spectrophotometric analysis of the adenylation reaction catalysed by MoeZ and its Cys360Ala mutant. The adenylation of sulphur-carrier proteins catalysed by MoeZ and its Cys360Ala mutant was monitored using a coupled enzyme assay in the presence of an excess of NaSH (Extended Data Fig. 8a). The coupled enzyme

reaction was monitored by detecting the consumption of NADH ($\epsilon_{340} = 6,220 \text{ M}^{-1} \text{ cm}^{-1}$) at 340 nm. A typical reaction mixture (120 μl) contained 3 μM MoeZ or its Cys360Ala mutant, 10 μM MoaD2, 80 μM ATP, 3 mM NaSH, 2 mM phosphoenolpyruvate, 0.16 mM NADH and ~ 1.5 unit each of adenylate kinase, pyruvate kinase and lactate dehydrogenase (LDH) in 50 mM NH_4HCO_3 buffer, pH 8.0, containing 2.5 mM MgCl_2 . The reaction was initiated on addition of ATP at time 0, and the absorbance at 340 nm was monitored for 30 s (Extended Data Fig. 8b).

2-Thiosugar formation using other sulphur sources. A typical reaction mixture (40 μl) contained 15 μM C-His₆-BexX, 18 μM N-His₆-MoaD2, 90 or 100 μM N-His₆-MoeZ or its Cys360Ala mutant, 2.5 mM ATP, 2.5 mM G6P and different sulphur sources ((i) 0.2 mM $\text{Na}_2\text{S}_2\text{O}_3$, or (ii) 0.15 mM L-cysteine plus 25 μM cysteine desulphurase CD4 with 0.25 mM pyridoxal 5'-phosphate) in 50 mM NH_4HCO_3 buffer, pH 8.0, containing 5 mM MgCl_2 . The resultant reaction mixture was incubated at 30 °C for 30 or 70 min for (i) and 0, 10, 20 or 50 min for (ii). The reaction was quenched by adding an equal volume of acetonitrile, and mBBr was added to the collected supernatant (to a final concentration of ~ 2 mM). After incubation at 25 °C for 30 min, the reaction mixture was dried by vacuum concentration. The residue was re-dissolved in 50 mM NH_4HCO_3 , pH 8.0, and treated with 3 units CIP at 37 °C for 1.5 h. The CIP enzyme was removed by centrifugation after precipitation with acetonitrile (at a final concentration of 50% (v/v)), and the collected supernatant was dried by vacuum concentration. The residue was then dissolved in 40 μl deionized water before HPLC analysis with a C₁₈ column (4 \times 250 mm). Each sample (20 μl) was eluted with a gradient of water (solvent A) and acetonitrile (solvent B). The gradient was run from 4% to 24% B over 15 min, from 24% to 64% B over 5 min and from 64% to 4% B over 5 min, followed by re-equilibration at 5% B for 8 min. The flow rate and the detector setting were as described above (1 ml min⁻¹ and 260 nm, respectively). The 2-thio-D-glucose-bimane standard described above (10, 25, 50, 77, 100 and 200 μM) was also injected onto the HPLC column for calibration of the peak area (Extended Data Fig. 9).

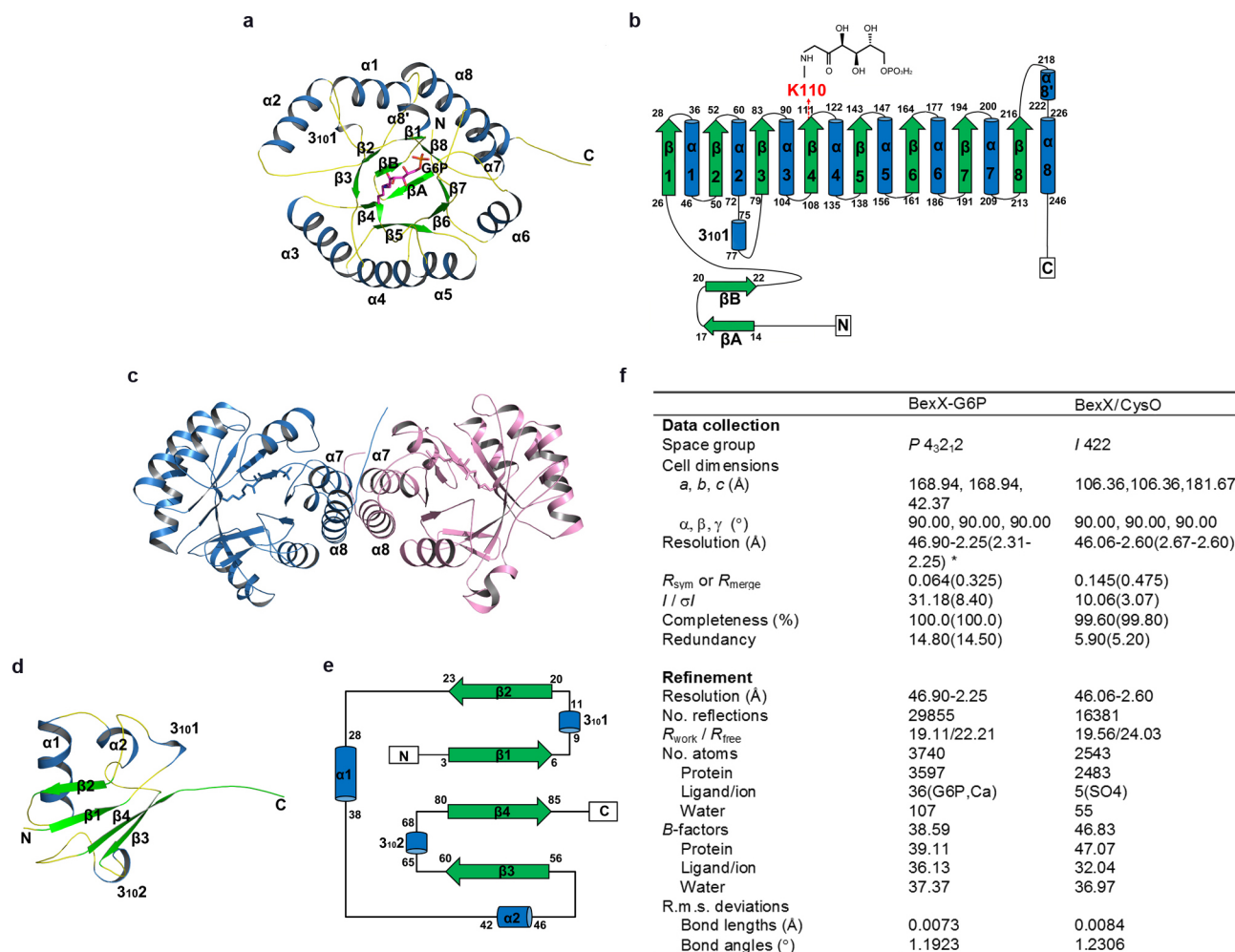
Crystallization of BexX-G6P. Crystals of BexX-G6P were grown using the vapour diffusion hanging drop method. A solution containing 10 mg ml⁻¹ BexX in 10 mM Tris, pH 8.0, and 50 mM NaCl was pre-incubated on ice with G6P (at a final concentration of 2 mM) for about 1 h. Hanging drops were formed by mixing 1.5 μl protein solution and 1.5 μl well solution containing 40% (v/v) PEG 300, 0.1 M sodium cacodylate-HCl, pH 6.5, and 0.2 M calcium acetate. Rod shape crystals grew in about 6 days to a maximum size of 0.2–0.3 mm \times 0.1–0.2 mm. Preliminary X-ray analysis showed that the crystals belonged to the space group P4₁2₁2 or P4₃2₁2 with unit cell dimensions of $a = 168.9$ Å and $c = 42.4$ Å. The Matthews coefficient assuming two monomers of BexX per asymmetric unit was 2.8 Å³ Da⁻¹, corresponding to a solvent content of 56.1%.

Crystallization of the BexX-CysO complex. Crystals of BexX-CysO were grown using the vapour diffusion hanging drop method. Both CysO and CysO-thiocarboxylate were used for crystallization trials; however, CysO consistently yielded better crystals and was used for the structures reported here. The BexX-CysO complex was formed by pre-incubating 0.55 ml 15 mg ml⁻¹ BexX and 1.0 ml 10 mg ml⁻¹ CysO in 10 mM Tris, pH 8.0, containing 50 mM NaCl for 1 h. Hanging drops were formed by mixing 1.5 μl protein solution and 1.5 μl well solution containing 28% PEG 4000, 0.1 M Tris, pH 8.0, and 0.2 M LiSO₄. Plate-shaped crystals appeared within 5 days and grew to a maximum size of 0.5 mm \times 0.4 mm \times 0.02 mm in about 2 weeks. The crystals belonged to space group I422 with unit cell dimensions of $a = 106.4$ Å and $c = 181.7$ Å. The Matthews coefficient is 3.5 Å³ Da⁻¹ assuming one monomer of BexX and one monomer of CysO per asymmetric unit, corresponding to a solvent content of 64.5%.

X-ray data collection and processing. X-ray diffraction data for BexX-G6P were collected at beamline A1 at the Cornell High Energy Synchrotron Source (CHESS) using a Quantum 210 charge-coupled display (CCD) detector (Area Detector Systems Corporation, ADSC) with a crystal-to-detector distance of 200 mm and a wavelength of 0.9767 Å. The data collection temperature was 100 K. A total of 180° of data were collected with an oscillation range of 0.5° per frame and an exposure time of 3 s per frame. Data for BexX-G6P-CysO were collected at the Northeastern Collaborative Access Team (NE-CAT) beamline 24-ID-C at the Advanced Photon Source (APS) using a Q315 CCD detector (ADSC). The wavelength was 0.9791 Å; the data collection temperature was 100 K; and the detector distance was 400 mm. Individual frames were collected over a range of 180° using 1 s for each 1.0°. X-ray diffraction data were indexed, integrated, scaled and merged using the program HKL-2000 (ref. 31).

Structure determination and refinement. The structure of BexX was determined by molecular replacement using the program Phaser³² as implemented in the PHENIX³³ program package. A monomer of ThiG from *Bacillus subtilis* (PDB ID, 1TYG)²², which shares 37% sequence similarity with BexX, was modified using Chainsaw in the CCP4 suite³⁴ to generate a search model. The initial molecular replacement solution was refined to an R_{factor} of 40.0% and R_{free} of 44.0%. All side chains were added, and the model was manually adjusted using COOT³⁵. After several cycles of refinement using PHENIX³³ and REFMAC5 (ref. 36), G6P and water molecules were added. The final model was refined to an R_{factor} of 19.1% and R_{free} of 22.2%. The Ramachandran plot shows 94.7% of residues in the most favourable regions and 5.3% in the allowed regions. No residues were in the generously allowed regions or disallowed regions. The structure of BexX-CysO was determined by molecular replacement using a monomer of BexX from the BexX-G6P complex and a monomer of CysO from *Mycobacterium tuberculosis* (PDB ID, 3DWM)²⁰ as the search models. An initial model, corresponding to one monomer of BexX and one monomer of CysO, was generated by Phaser³² as implemented in PHENIX³³. Packing analysis showed that a BexX-CysO dimer is formed by crystallographic twofold symmetry. The initial refinement resulted in an R_{factor} of 33.8% and R_{free} of 39.5%. Subsequent cycles of model building in COOT³⁵ and refinement in PHENIX³³ and REFMAC5 (ref. 36) resulted in a final R_{factor} of 19.6% and R_{free} of 24.0%. The Ramachandran plot shows that 90.0% of residues are located in the most favourable regions, 9.7% in the allowed regions and 0.3% in the generously allowed regions. No residues were in the disallowed regions.

28. Kinsland, C., Taylor, S. V., Kelleher, N. L., McLafferty, F. W. & Begley, T. P. Overexpression of recombinant proteins with a C-terminal thiocarboxylate: implications for protein semisynthesis and thiamin biosynthesis. *Protein Science* **7**, 1839–1842 (1998).
29. Bradford, M. M. Rapid and sensitive method for quantitation of microgram quantities of protein utilizing principle of protein-dye binding. *Anal. Biochem.* **72**, 248–254 (1976).
30. Sörbo, B. Enzymic transfer of sulfur from mercatopyruvate to sulfate or sulfates. *Biochim. Biophys. Acta* **24**, 324–329 (1957).
31. Otwinowski, Z. M. W. Processing of X-ray diffraction data collected in oscillation mode. *Methods Enzymol.* **276**, 307–326 (1997).
32. McCoy, A. J. et al. Phaser crystallographic software. *J. Appl. Crystallogr.* **40**, 658–674 (2007).
33. Adams, P. D. et al. PHENIX: a comprehensive Python-based system for macromolecular structure solution. *Acta Crystallogr. D* **66**, 213–221 (2010).
34. Collaborative Computational Project, Number 4. The CCP4 suite: programs for protein crystallography. *Acta Crystallogr. D* **50**, 760–763 (1994).
35. Emsley, P., Lohkamp, B., Scott, W. G. & Cowtan, K. Features and development of Coot. *Acta Crystallogr. D* **66**, 486–501 (2010).
36. Murshudov, G. N. et al. REFMAC5 for the refinement of macromolecular crystal structures. *Acta Crystallogr. D* **67**, 355–367 (2011).
37. Geoghegan, K. F. et al. Spontaneous α -N-6-phosphogluconoylation of a 'His tag' in *Escherichia coli*: the cause of extra mass of 258 or 178 Da in fusion proteins. *Anal. Biochem.* **267**, 169–184 (1999).
38. Di Tommaso, P. et al. T-Coffee: a web server for the multiple sequence alignment of protein and RNA sequences using structural information and homology extension. *Nucleic Acids Res.* **39**, W13–W17 (2011).
39. Corpet, F. Multiple sequence alignment with hierarchical clustering. *Nucleic Acids Res.* **16**, 10881–10890 (1988).
40. Gouet, P., Robert, X. & Courcelle, E. ESPript/ENDscript: extracting and rendering sequence and 3D information from atomic structures of proteins. *Nucleic Acids Res.* **31**, 3320–3323 (2003).
41. Schlesinger, P. & Westley, J. An expanded mechanism for rhodanese catalysis. *J. Biol. Chem.* **249**, 780–788 (1974).
42. Chowdhury, M. M., Dosche, C., Löhmansröben, H. & Leimkühler, S. Dual role of the molybdenum cofactor biosynthesis protein MOCS3 in tRNA thiolation and molybdenum cofactor biosynthesis in humans. *J. Biol. Chem.* **287**, 17297–17307 (2012).
43. Matthies, A., Rajagopalan, K. V., Mendel, R. R. & Leimkühler, S. Evidence for the physiological role of a rhodanese-like protein for the biosynthesis of the molybdenum cofactor in humans. *Proc. Natl Acad. Sci. USA* **101**, 5946–5951 (2004).
44. Marelja, Z., Stöcklein, W., Nimtz, M. & Leimkühler, S. A novel role for human Nfs1 in the cytoplasm: Nfs1 acts as a sulfur donor for MOCS3, a protein involved in molybdenum cofactor biosynthesis. *J. Biol. Chem.* **283**, 25178–25185 (2008).
45. Beinert, H. Semi-micro methods for analysis of labile sulfide and of labile sulfide plus sulfane sulfur in unusually stable iron-sulfur proteins. *Anal. Biochem.* **131**, 373–378 (1983).

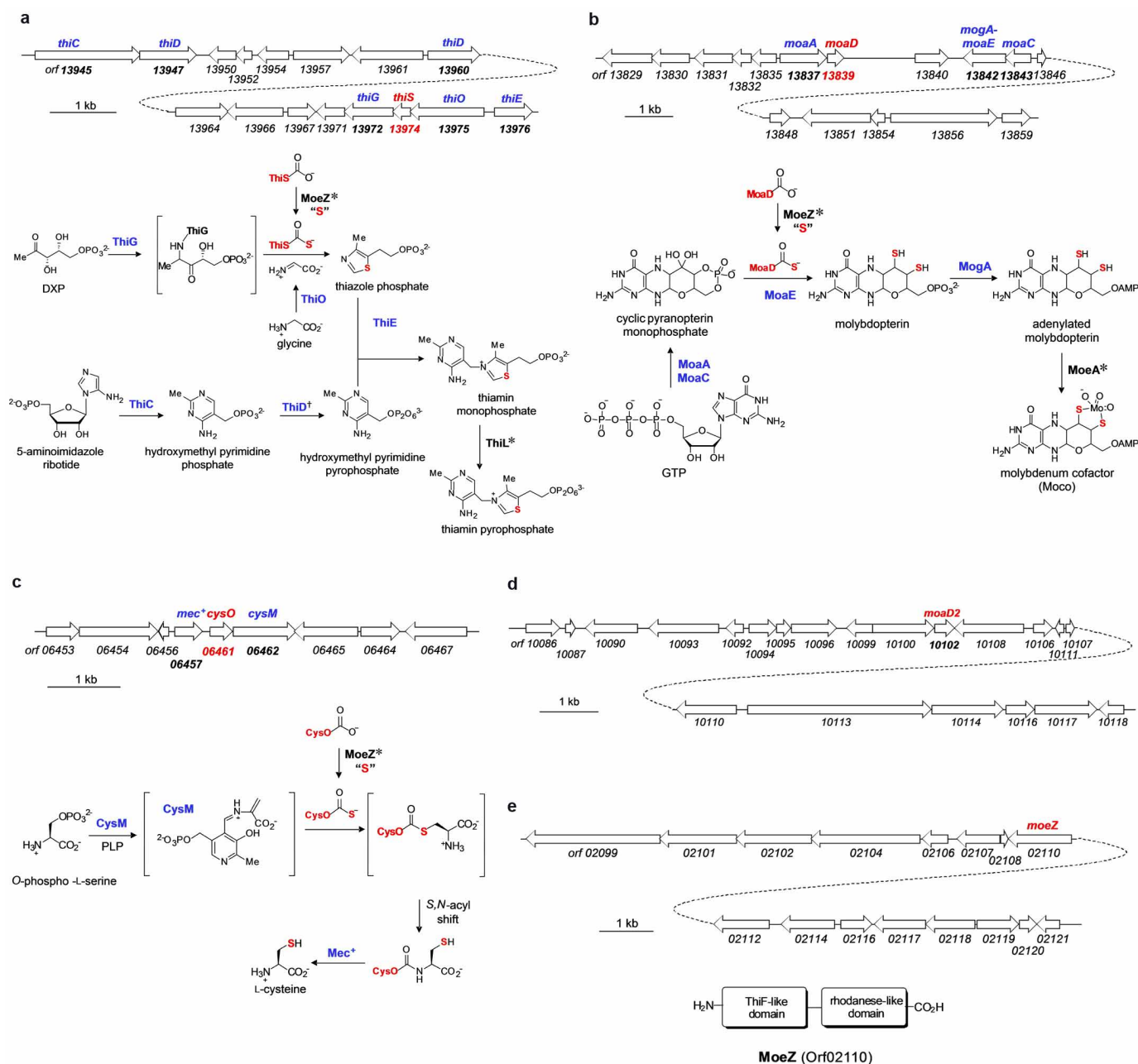


Extended Data Figure 1 | Structures of BexX and CysO from *Amycolatopsis orientalis*. **a**, A stereo ribbon diagram of the $(\beta\alpha)_8$ -barrel fold of BexX is shown from the top view. The α -helices, β -strands and loops are marked in blue, green and yellow, respectively. The ketone-intermediate (2) formed by Lys 110 and G6P is shown as sticks and coloured in purple. **b**, The typical secondary structure composition of the classical $(\beta\alpha)_8$ -barrel is shown as a topology model; the conserved Lys 110 is highlighted in red. **c**, The quaternary structure

of BexX is shown as a ribbon diagram with two monomers coloured by chain.

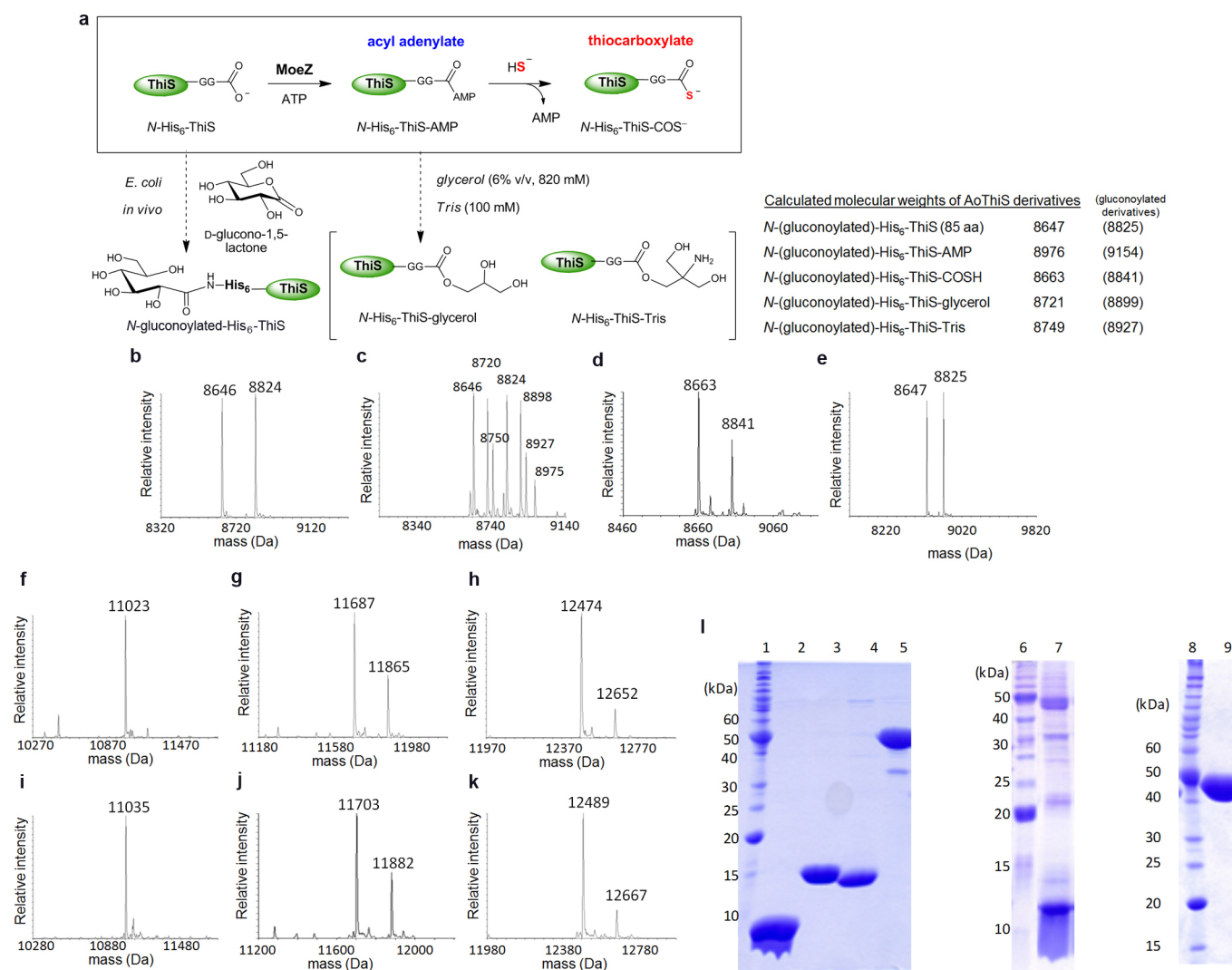
d, A ribbon diagram of CysO from the BexX-CysO structure. Secondary structural elements are coloured blue for α -helices, green for β -strands and yellow for loops. **e**, A topology diagram of CysO. **f**, Data collection and refinement statistics. One crystal was used for each of the two data sets.

*The values in parentheses are for the highest-resolution shell.



Extended Data Figure 2 | Putative thiamine, molybdenum cofactor and cysteine biosynthetic genes found in *A. orientalis* and their proposed functions. **a**, Organization of the putative thiamine biosynthetic gene cluster and the proposed thiamine biosynthetic pathway in *A. orientalis*. *The genes encoding MoeZ and ThiL (one of the genes involved in thiazole biosynthesis) are not found in the gene cluster. The gene encoding the ThiS-activating enzyme, ThiF, is also absent from the genome. †Two genes encoding proteins homologous to ThiD are found in the gene cluster. **b**, Organization of the putative molybdopterin biosynthetic gene cluster and the proposed

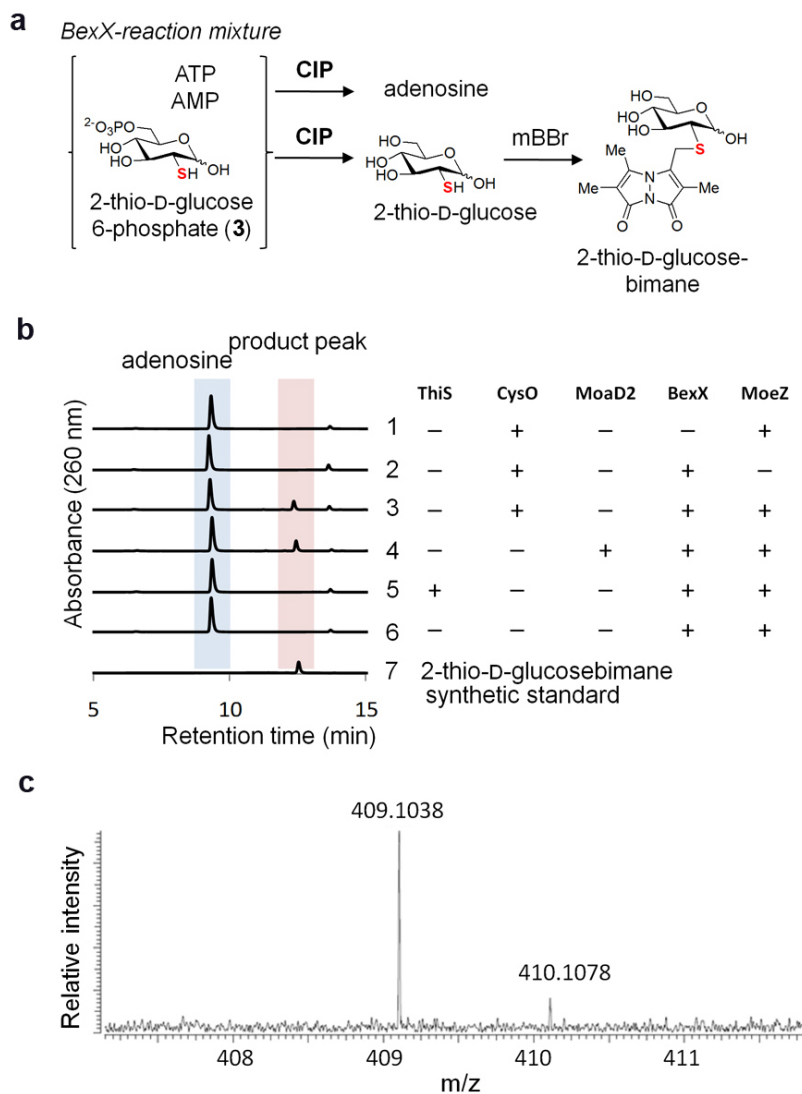
molybdenum cofactor biosynthetic pathway in *A. orientalis*. *The genes encoding MoeZ and MoeA are not found in the gene cluster. The gene encoding the MoaD-activating enzyme, MoeB, is also absent from the genome. **c**, Organization of the putative cysteine biosynthetic gene cluster and the proposed cysteine biosynthetic pathway in *A. orientalis*. *The gene encoding MoeZ is not found in the gene cluster. **d**, Organization near the *moaD* homologue, *moaD2*, found in the *A. orientalis* genome. **e**, Organization near *moeZ* in the *A. orientalis* genome and the conserved domains of MoeZ predicted by BLAST analysis.



Extended Data Figure 3 | ESI-MS analyses of the MoeZ-catalysed activation of sulphur-carrier proteins and SDS-PAGE separation of the purified proteins.

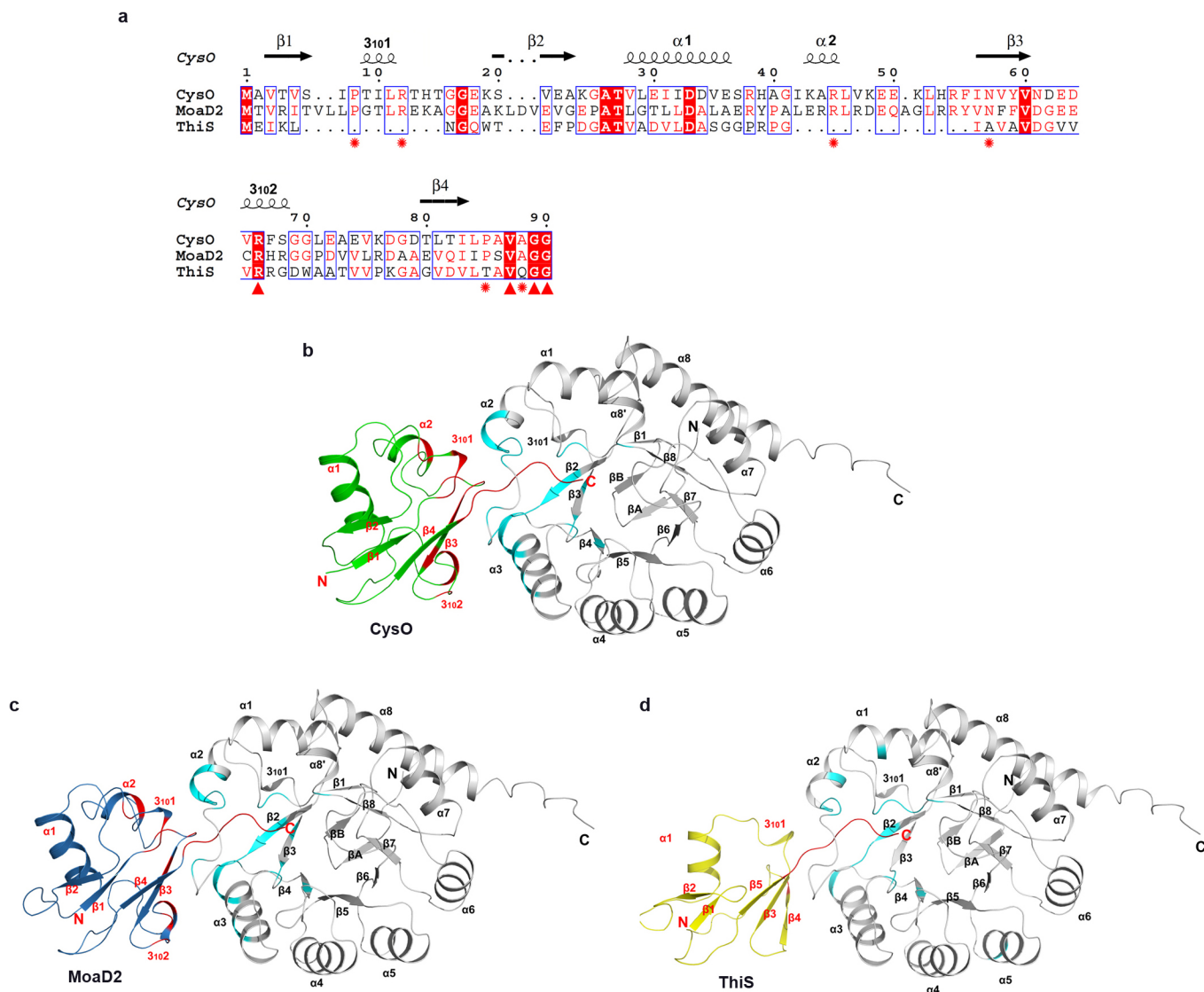
a, Reaction scheme of the MoeZ-catalysed activation of ThiS. **b–e**, Deconvoluted ESI-MS analyses of as-isolated ThiS (**b**), ThiS in the presence of MoeZ and ATP (**c**), ThiS in the presence of MoeZ, ATP and bisulphide (**d**) and ThiS in the presence of bisulphide (control) (**e**). The calculated molecular masses are shown as the neutral form in the upper right corner. Analysis of purified N-His₆-ThiS (where N denotes amino terminal) shows two mass signals (observed (obsd), 8,646 and 8,824 Da) consistent with the calculated molecular mass of the recombinant enzyme in its native and N-gluconoylated form (where N denotes amino terminal) (calcd, 8,647 and 8,825 Da). Gluconoylation of the N-terminal His₆ tag is a known post-translational modification when expressing recombinant proteins in *E. coli*³⁷. Such a modification should not affect ThiS activity, because the predicted active site for ThiS is at the C terminus. Indeed, when N-His₆-ThiS was incubated with N-His₆-MoeZ and ATP, a mass spectrometric signal corresponding to adenylated N-His₆-ThiS (**9**) was detected together with a few peaks that were probably derived from a reaction of the labile adenylated ThiS with buffer components (see **c**). **f–k**, Deconvoluted ESI-MS analyses of

as-isolated MoaD (N-His₆-MoaD, 105 amino acids; calcd, 11,022 Da) (**f**), as-isolated CysO (N-His₆-CysO, 109 amino acids, and its N-gluconoylated derivative; calcd, 11,688 and 11,866 Da, respectively) (**g**), as-isolated MoaD2 (N-His₆-MoaD2, 115 amino acids, and its N-gluconoylated derivative; calcd, 12,473 and 12,651 Da, respectively) (**h**), MoaD incubated with MoeZ, ATP and NaSH (N-His₆-MoaD-COSH; calcd, 11,038 Da) (**i**), CysO incubated with MoeZ, ATP and NaSH (N-His₆-CysO-COSH and its N-gluconoylated derivative; calcd, 11,704 and 11,882 Da, respectively) (**j**) and MoaD2 incubated with MoeZ, ATP and NaSH (N-His₆-MoaD-COSH and its N-gluconoylated derivative; calcd, 12,489 and 12,667 Da, respectively) (**k**). **l**, SDS-PAGE gel of purified sulphur-carrier proteins, MoeZ and CD4: N-His₆-ThiS (85 amino acids, 8.7 kDa, lane 2), N-His₆-MoaD2 (115 amino acids, 12.5 kDa, lane 3), N-His₆-CysO (109 amino acids, 11.7 kDa, lane 4), N-His₆-MoeZ (421 amino acids, 45.0 kDa, lane 5), N-His₆-MoaD (105 amino acids, 11.0 kDa, lane 7) and N-His₆-CD4 (417 amino acids, 43.3 kDa, lane 9). The molecular weight markers are 220, 160, 120, 100, 90, 80, 70, 60, 50, 40, 30, 25, 20, 15 and 10 kDa (top to bottom, lanes 1, 6 and 8). The protein MoaD did not express well, and the partially purified protein solution contained significant amounts of endogenous proteins from the *E. coli* host.



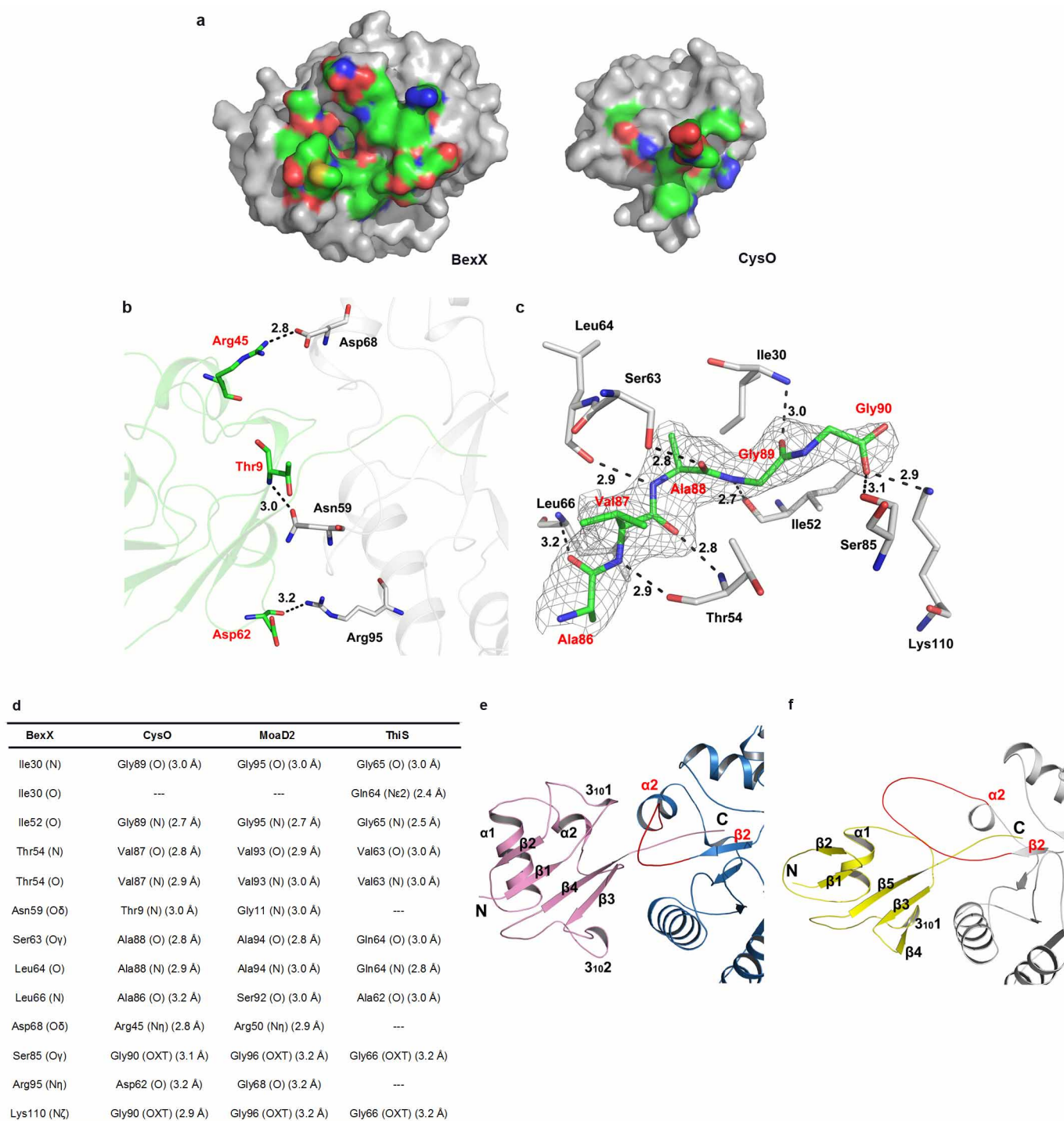
Extended Data Figure 4 | BexX-catalysed 2-thio-D-glucose-6-phosphate formation followed by alkaline phosphatase treatment. **a**, Reaction scheme to synthesize the expected bimane derivative. **b**, HPLC traces of the C-His₆-BexX-catalysed reactions (where C denotes carboxy terminal) using N-His₆-ThiS, N-His₆-CysO or N-His₆-MoaD2, and the control reactions.

The thiosugar product was treated with alkaline phosphatase (CIP) and then derivatized with mBBR. HPLC analysis of the synthetic standard of 2-thio-D-glucose-bimane is shown in the bottom trace (trace 7). **c**, High-resolution ESI-MS (positive) of the isolated product peak (2-thio-D-glucose-bimane C₁₆H₂₂N₂NaO₇S⁺ [M + Na]⁺, calcd, 409.1040 Da; obsd, 409.1038 Da).



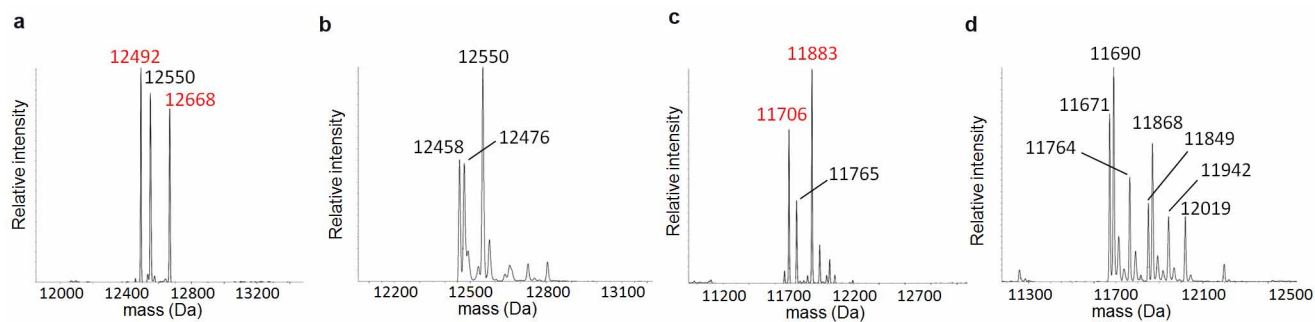
Extended Data Figure 5 | Sequence alignment of *A. orientalis* CysO, MoaD2 and ThiS and hydrophobic interactions for BexX complexes. **a**, Sequence alignment was based on structural supercession using the programs 3D-Coffee³⁸, MultAlin³⁹ and ESPript⁴⁰. The main differences between CysO (or MoaD2) and ThiS result from an insertion of ten residues between $\beta 1$ and $\beta 2$ of CysO (or MoaD2) and an insertion of 14 (or 15) residues between $\alpha 1$ and $\beta 3$ of CysO (or MoaD2). The first insertion includes the short helix 3₁₀₁, and the second includes helix $\alpha 2$. Both of these insertions are involved in the BexX–CysO (or BexX–MoaD2) interface. Ten interface residues (red stars and red triangles) are conserved between CysO and MoaD2; however, only four of these residues are conserved in ThiS (red triangles). Two differences between

CysO and MoaD2 represent conservative substitutions; while Thr 9 and Ala 86 in CysO are replaced by Gly 11 and Ser 92 in MoaD2, the interface interaction is contributed by hydrogen bonds that are formed by the backbone atoms. **b–d**, Hydrophobic interactions of BexX–CysO (**b**), BexX–MoaD2 (**c**) and BexX–ThiS (**d**). BexX monomers are shown as grey ribbon diagrams with hydrophobic interaction regions coloured in cyan. CysO, MoaD2 and ThiS are shown as cartoons and coloured in green, blue and yellow, respectively. Hydrophobic interaction regions in sulphur-carrier proteins are coloured in red. The α -helices and β -strands in BexX and the sulphur-carrier proteins are labelled in black and red, respectively.



Extended Data Figure 6 | The *A. orientalis* BexX–CysO interface, predicted hydrogen bonds between BexX with sulphur-carrier proteins, and a comparison of the BexX–CysO interface with the *Bacillus subtilis* ThiG–ThiS interface. **a**, Interacting surfaces of BexX (left) and CysO (right). The surface is colour coded by atom type (oxygen, red; nitrogen, blue; carbon, green). Non-interacting surfaces are shown in grey. **b**, Hydrogen bonds on the surface of BexX with CysO are shown as black dashes. **c**, Hydrogen bonds formed by the C-terminal tail of CysO and the surrounding residues from BexX are shown as black dashes. The $F_o - F_c$ simulated annealing omit map of the C-terminal residues (Ala-Val-Ala-Gly-Gly) is rendered in grey and contoured at 3.0σ . Residues are shown as sticks with the carbon atoms in grey for BexX and green for CysO. CysO residues are labelled in red; BexX residues are labelled in black. **d**, Predicted hydrogen bonds between BexX and other

sulphur-carrier proteins. The hydrogen-bonding scheme for the BexX–CysO complex (9 of 12 involve the C-terminal tail) is conserved in the model of the BexX–MoaD2 complex. **e**, The interface between BexX (blue) and CysO (pink). Secondary structural elements of CysO are labelled in black, the $\beta 2$ and $\alpha 2$ elements in BexX are labelled in red. **f**, The interface between ThiG (grey) and ThiS (yellow) from *B. subtilis*. Secondary structural elements of ThiS are labelled in black, and the $\beta 2$ and $\alpha 2$ elements in ThiG are labelled in red. The $\beta 2$ – $\alpha 2$ loop region in BexX and ThiG is highlighted in red. For CysO, $3_{10}1$ and $\alpha 2$ form hydrophobic contacts with the $\beta 2$ – $\alpha 2$ loop and $\alpha 2$ of BexX. ThiG also uses its $\beta 2$ – $\alpha 2$ loop to interact with ThiS; however, ThiS uses two different loop regions to form the interface. In addition, the $\beta 2$ – $\alpha 2$ loop of BexX is closer to the $(\beta\alpha)_8$ -barrel than in ThiG, in which the $\beta 2$ – $\alpha 2$ loop extends outwards and covers the top of ThiS.



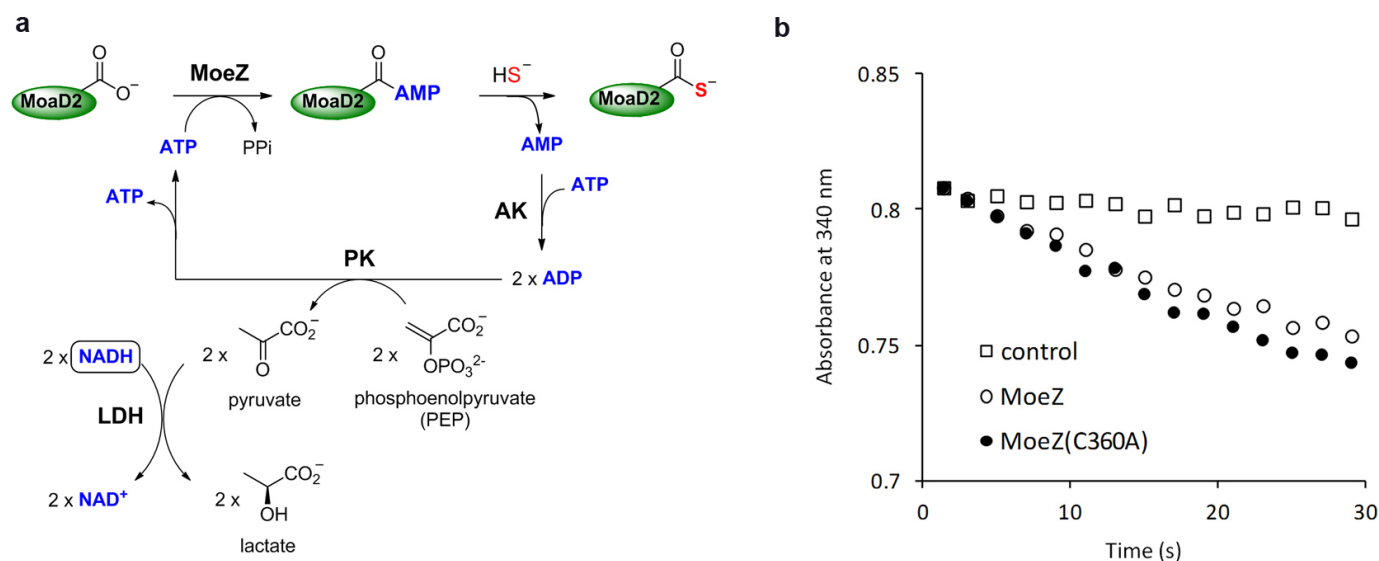
e

Proteins	K_m (mM)	k_{cat} (s^{-1})	Reference	Assay conditions
MoeZ	7.6 ± 0.7	32 ± 1	this study	25 °C, pH 8.0
MoeZ(C360A)	N. D.	N. D.	this study	25 °C, pH 8.0
Bovine liver rhodanese	18.1 ± 1.0	~ 300	ref. 41	40 °C, pH 8.7
human MOCS3	80.8 ± 3.8	2.11 ± 0.20	ref. 42	37 °C, pH 8.0

N. D. = not detected.

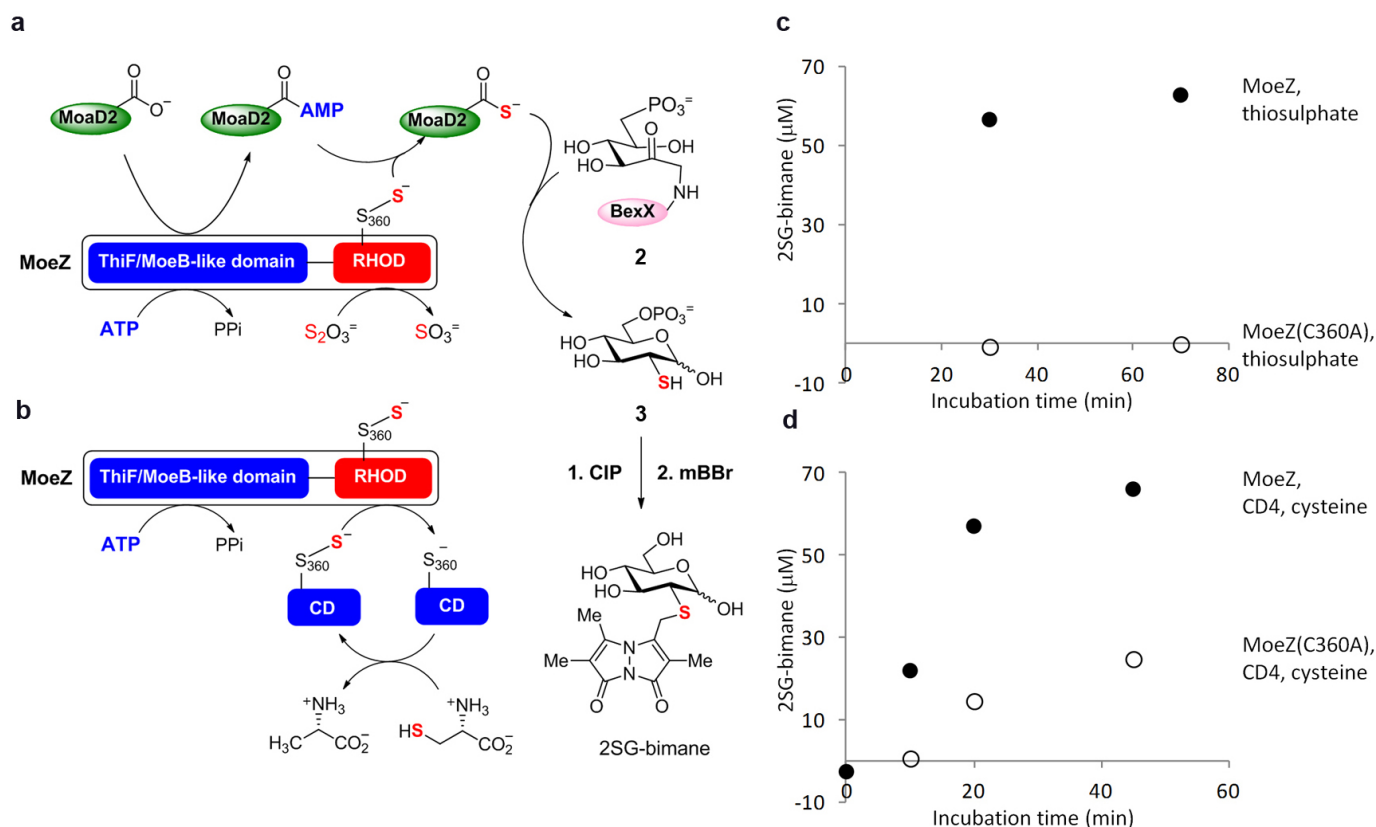
Extended Data Figure 7 | MoeZ-dependent protein thiocarboxylate formation in sulphur-carrier proteins using thiosulphate as the sulphur source. **a–d**, Deconvoluted ESI–MS of MoaD2 incubated with MoeZ (the observed peaks are consistent with the calculated molecular masses of N-His₆-MoaD2-COSH (12,489 Da), N-His₆-MoaD2-glycerol (12,547 Da), and N-gluconoylated-His₆-MoaD2-COSH (12,667 Da)) (**a**), MoaD2 incubated with the MoeZ(Cys360Ala) mutant (the observed peaks are consistent with the calculated molecular masses of N-His₆-MoaD2 (12,473 Da) and N-His₆-MoaD2-glycerol (12,547 Da)) (**b**), CysO incubated with MoeZ (the observed peaks are consistent with the calculated molecular masses of N-His₆-CysO-COSH (11,704 Da), N-His₆-CysO-glycerol (11,762 Da) and N-gluconoylated-His₆-MoaD2-COSH (11,882 Da)) (**c**), and CysO incubated with the MoeZ(Cys360Ala) mutant (the observed peaks are consistent with the calculated molecular masses of N-His₆-CysO (11,688 Da), N-His₆-CysO-glycerol (11,762 Da), their N-gluconoylated derivatives

(11,866 Da, and 11,940 Da, respectively) and N-His₆-CysO-AMP (12,017 Da)) (**d**). Observed masses corresponding to protein thiocarboxylate are shown in red. Two peaks corresponding to the dehydration of N-His₆-MoaD2 and N-His₆-CysO were probably caused by in-source collision-induced dissociation (CID) during the ESI–MS analysis. **e**, Kinetic parameters for the thiosulphate:cyanoide sulphur transferase activity of MoeZ from *A. orientalis*. Bovine liver rhodanese is a typical rhodanese enzyme. Compared with bovine rhodanese, human molybdopterine synthase sulphurase (human MOCS3) displayed much lower thiosulphate:cyanoide sulphur transferase activity^{41,42}. In the case of human MOCS3, L-cysteine and cysteine desulphurase are proposed as the physiological sulphur source over thiosulphate because of its lower rhodanese activity^{43,44}. However, this may not be the case for MoeZ from *A. orientalis* because its rhodanese activity is comparable to bovine liver rhodanese.



Extended Data Figure 8 | Relative adenylation activity of MoeZ and the MoeZ(Cys360Ala) mutant. **a**, Reaction scheme for the MoeZ-catalysed adenylation activity assay. The adenylation activities of MoeZ and its Cys360Ala mutant were inferred using a colorimetric assay to monitor the production of AMP (indicated by a decrease in NADH at 340 nm) when MoeZ or its Cys360Ala mutant was co-incubated with a sulphur-carrier protein (MoaD2) in the presence of ATP, NaSH, adenylate kinase (AK), pyruvate

kinase (PK) and lactate dehydrogenase (LDH). **b**, The relative adenylation activity of MoeZ (open circles) and its Cys360Ala mutant (filled circles), as well as a no MoeZ/MoeZ(Cys360Ala) control (open squares), was measured by the coupled enzyme assay, as described in **a**. Little difference in the decrease in absorption at 340 nm was observed between MoeZ and its Cys360Ala mutant (compared with the control with no MoeZ), suggesting that the mutation at Cys360 had little effect on the adenylation activity of MoeZ.



Extended Data Figure 9 | BexX-catalysed 2-thiosugar formation using various sulphur sources. **a, b**, Reaction scheme for C-His₆-BexX-catalysed 2-thiosugar formation using N-His₆-MoeZ, N-His₆-MoaD2 and thiosulphate (**a**) or L-cysteine and the cysteine desulfurase (CD4) from *A. orientalis* (**b**). The reactions were carried out in the absence of reducing agent to avoid complications from the generation of bisulphide from protein persulphide (*see also below). Under these conditions, MoeZ cannot be regenerated after single turnover. The thiosugar product was derivatized with mBBR and then treated with alkaline phosphatase (CIP) to yield 2-thio-D-glucose-bimane (2SG-bimane). **c, d**, The 2SG-bimane product concentrations at different time points of incubation with thiosulphate (**c**) or L-cysteine and CD4 (**d**) as the

sulphur source were estimated on the basis of the product peak area of each HPLC trace. The 2SG-bimane synthetic standard (10, 25, 50, 77, 100 and 200 μM) was used for calibration. The filled and open circles denote product formation from the incubation with N-His₆-MoeZ and the N-His₆-MoeZ(Cys360Ala) mutant, respectively. *The observed minor product formation with the MoeZ(Cys360Ala) mutant, L-cysteine and CD4 (see **d**, open circles) is probably caused by the formation of bisulphide, which could be generated on reduction of CD4-persulphide in the presence of free cysteine molecules. In fact, a small amount of bisulphide was detected under similar conditions with L-cysteine and CD4 (in the absence of other proteins and reducing agents) by the methylene blue assay within 15 min of incubation⁴⁵.

Extended Data Table 1 | Putative cysteine desulphurases, rhodanases and sulphur-carrier proteins found in the *A. orientalis* genome

gene (orf #)	Name of the protein	protein with the highest sequence similarity and origin	identity / similarity (%)	protein accession number
10706	CD1	cysteine desulphurase/selenocysteine lyase [<i>Amycolatopsis mediterranei</i> U32]	97 / 98	YP_003765029
11099	CD2	cysteine desulphurase [<i>Amycolatopsis mediterranei</i> U32]	87 / 91	YP_003765163
14916	CD3	cysteine desulphurase [<i>Amycolatopsis mediterranei</i> U32]	88 / 93	YP_003766645
04763	CD4	cysteine desulphurase [<i>Amycolatopsis mediterranei</i> U32]	92 / 96	YP_003763873
09299	CD5	cysteine desulphurase [<i>Amycolatopsis mediterranei</i> U32]	97 / 99	YP_003762467
04658	RHO1	rhodanese-like protein [<i>Amycolatopsis mediterranei</i> U32]	89 / 93	YP_003763825
08287	RHO2	rhodanese-like protein [<i>Amycolatopsis mediterranei</i> U32]	89 / 91	YP_003764615
09090	RHO3	rhodanese-like protein [<i>Amycolatopsis mediterranei</i> U32]	95 / 96	YP_003762363
10524	RHO4	rhodanese-like protein [<i>Amycolatopsis mediterranei</i> U32]	81 / 87	YP_003763440
12151	RHO5	rhodanese-like protein [<i>Amycolatopsis mediterranei</i> U32]	97 / 99	YP_003771104
02110	MoeZ	molybdopterin biosynthesis-like protein MoeZ [<i>Amycolatopsis mediterranei</i> U32]	99 / 99	YP_003763336
13974	ThiS	thiamin biosynthesis protein ThiS [<i>Amycolatopsis mediterranei</i> U32]	88 / 93	YP_003770674
13839	MoaD	ThiS/MoaD family protein [<i>Amycolatopsis mediterranei</i> U32]	82 / 90	YP_003770615
06461	CysO	ThiS/MoaD family protein [<i>Amycolatopsis mediterranei</i> U32]	97 / 100	YP_003769822
10102	MoaD2	ThiS/MoaD family protein [<i>Amycolatopsis mediterranei</i> U32]	91 / 94	YP_003764220

Extended Data Table 2 | BLASTP (protein BLAST) analysis of E1-like proteins in genomes of selected strains of the Actinomycetales

Family	# of E-1 like protein	Name of bacterial strain	protein accession number
<i>Streptomycetaceae</i>	1	<i>Streptomyces coelicolor</i> A3(2)	MoeZ (NP_629326)
<i>Streptomycetaceae</i>	1	<i>Streptomyces avermitilis</i> MA-4680	MoeZ (NP_824258)
<i>Streptomycetaceae</i>	1	<i>Streptomyces griseus</i> subsp. <i>griseus</i> NBRC 13350	MoeZ (YP_001823859)
<i>Streptomycetaceae</i>	1	<i>Streptomyces cattleya</i> NRRL 8057	MoeZ (YP_004913535)
<i>Streptomycetaceae</i>	1	<i>Streptomyces violaceusniger</i> Tu 4113	MoeZ (YP_004811516)
<i>Mycobacteriaceae</i>	4	<i>Mycobacterium tuberculosis</i> H37Rv	MoeZ (YP_177942) MoeB (YP_177929) Rv2338c (NP_216854) Rv1355c (NP_215871)
			MoeZ (NP_856876) MoeB (NP_856788) MB2366c (NP_856015) Mb1390c (NP_855044)
<i>Mycobacteriaceae</i>	4	<i>Mycobacterium bovis</i> AF2122/97	
<i>Mycobacteriaceae</i>	2	<i>Mycobacterium avium</i> subsp. <i>paratuberculosis</i> K-10	MoeZ (YP_962240) MoeY ? (YP_960282)
<i>Mycobacteriaceae</i>	2	<i>Mycobacterium abscessus</i> ATCC 19977	MoeZ (YP_001704255) E1 family (YP_001702828)
<i>Corynebacteriaceae</i>	2	<i>Corynebacterium glutamicum</i> ATCC 13032	MoeZ ? (NP_599461) MoeZ ? (NP_601246)
<i>Corynebacteriaceae</i>	1	<i>Corynebacterium jeikeium</i> ATCC 43734	MoeZ (ZP_05845904)
<i>Nocardiaceae</i>	2	<i>Nocardia farcinica</i> IFM 10152	MoeZ (YP_120782) nfa49170 (YP_121133)
<i>Nocardiaceae</i>	2	<i>Rhodococcus jostii</i> RHA1	MoeZ (YP_706296) RHA1_ro05752 (YP_705688)
<i>Pseudonocardiaceae</i>	1	<i>Saccharopolyspora erythraea</i> NRRL 2338	MoeZ (YP_001103327)
<i>Pseudonocardiaceae</i>	4	<i>Amycolatopsis mediterranei</i> U32	MoeZ (YP_003763336) MoeB? (YP_003764340) AMED_1241 (YP_003763458) E1-family (YP_003766676)
<i>Frankiaceae</i>	5	<i>Frankia alni</i> ACN14a	MoeZ (YP_716188) HesA ? (YP_716927) HesA2 ? (YP_716575) E1-family (YP_711122) E1-family (YP_715173)
<i>Micrococcaceae</i>	1	<i>Anthrobacter chlorophenolicus</i> A6	MoeZ (YP_002488550)
<i>Microbacteriaceae</i>	1	<i>Clavibacter michiganensis</i> subsp. <i>michiganensis</i> NCPPB 382	MoeZ (YP_001223108)
<i>Micromonosporaceae</i>	2	<i>Micromonospora aurantiaca</i> ATCC 27029	MoeZ (YP_003838663) E1-family (YP_003839126)
<i>Micromonosporaceae</i>	3	<i>Salinispora arenicola</i> CNS-205	MoeZ (YP_001535374) E1-family (YP_001536912) E1-family (YP_001538897)
<i>Nocardioideae</i>	1	<i>Nocardioideae</i> sp. JS614	MoeZ (YP_922675)
<i>Propionibacteriaceae</i>	1	<i>Microlunatus phosphovorus</i> NM-1	MoeZ (YP_004573609)

CORRIGENDUM

doi:10.1038/nature13488

Corrigendum: Sea-level and deep-sea-temperature variability over the past 5.3 million years

E. J. Rohling, G. L. Foster, K. M. Grant, G. Marino, A. P. Roberts, M. E. Tamisiea & F. Williams

Nature **508**, 477–482 (2014); doi:10.1038/nature13230

In this Article, owing to a misunderstanding of discussions at the PALSEA2 workshop in Rome, we erroneously reported previous sea-level estimates for the period 3.3–2.9 Myr as originating from the ‘Pliocene Maximum Sea Level’ (PLIOMAX) project. However, these estimates are not from PLIOMAX, relating to ref. 3 instead. We thank M. E. Raymo and A. Rovere for drawing the error to our attention. The online versions of the paper have been corrected.

CORRIGENDUM

doi:10.1038/nature13533

Corrigendum: Fuel gain exceeding unity in an inertially confined fusion implosion

O. A. Hurricane, D. A. Callahan, D. T. Casey, P. M. Celliers, C. Cerjan, E. L. Dewald, T. R. Dittrich, T. Döppner, D. E. Hinkel, L. F. Berzak Hopkins, J. L. Kline, S. LePape, T. Ma, A. G. MacPhee, J. L. Milovich, A. Pak, H.-S. Park, P. K. Patel, B. A. Remington, J. D. Salmonson, P. T. Springer & R. Tommasini

Nature **506**, 343–348 (2014); doi:10.1038/nature13008

In the legend to Fig. 2 of this Letter, we should have acknowledged the X-ray and neutron imaging as follows: X-ray image analysis^{1,2} was performed by N. Izumi, S. Khan, L. R. Benedetti, R. Town and D. Bradley of the NIF Shape working group of Lawrence Livermore National Laboratory, California, USA, and by authors T.M. and A.P. Neutron images were measured³ and analysed^{4,5} by D. Fittinghoff of the Lawrence Livermore National Laboratory, California, USA, and by G. Grim, N. Guler, F. Merrill, C. Wilde and P. Volegov of the Physics Division at the Los Alamos National Laboratory, New Mexico, USA.

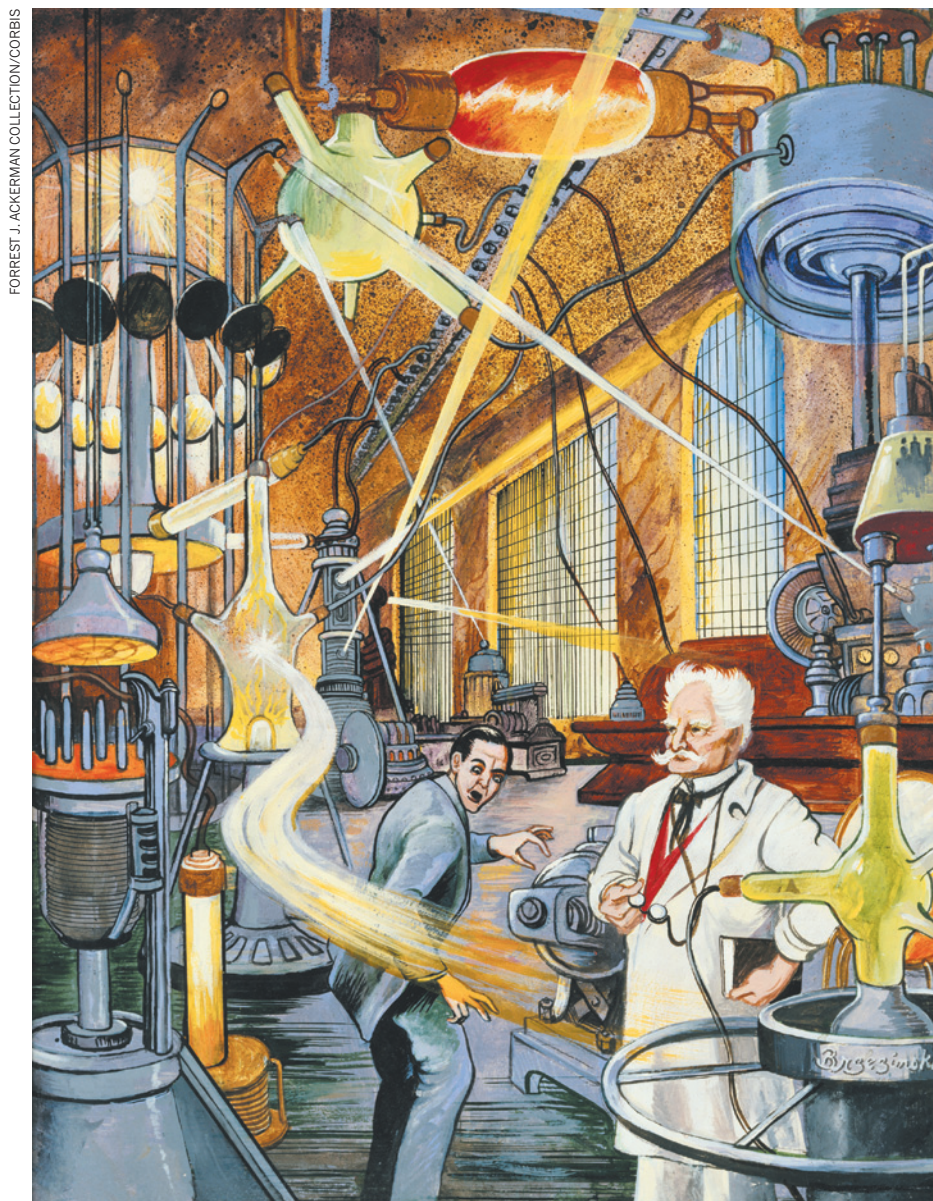
1. Glenn, S. *et al.* A hardened gated x-ray imaging diagnostic for inertial confinement fusion experiments at the National Ignition Facility. *Rev. Sci. Instrum.* **81**, 10E539 (2010).
2. Ma, T. *et al.* Imaging of high-energy x-ray emission from cryogenic thermonuclear fuel implosions on the NIF. *Rev. Sci. Instrum.* **83**, 10E115 (2012).
3. Merrill, F. E. *et al.* The neutron imaging diagnostic at NIF. *Rev. Sci. Instrum.* **83**, 10D317 (2012).
4. Volegov, P. *et al.* Neutron source reconstruction from pinhole imaging at the National Ignition Facility. *Rev. Sci. Instrum.* **85**, 023508 (2014).
5. Grim, G. P. *et al.* Nuclear imaging of the fuel assembly in ignition experiments. *Phys. Plasmas* **20**, 056320 (2013).

CAREERS

@NATUREJOBS Follow us on Twitter for the latest news and features go.nature.com/e492gf

NATUREJOBS BLOG The latest on science-careers news and tips go.nature.com/ielkkf

NATUREJOBS For the latest career listings and advice www.naturejobs.com



BY HELEN SHEN

For James Nelson, a molecular and cellular physiologist at Stanford University in California, having a lab manager means having more time for science. He does not worry about whether his laboratory is on track to meet its monthly budget, nor does he fret about upcoming chemical-safety inspections. Kathy Siemers, his long-time lab manager, handles those responsibilities for him — along with a long list of other duties — to keep the laboratory running smoothly. “I can’t imagine the lab without Kathy,” says Nelson. “It would be a disaster, and it wouldn’t be as much fun.”

Not all laboratories can afford lab managers in today’s funding climate; tight research budgets in countries such as the United States, France and the United Kingdom have left many researchers unable to hire new staff. But principal investigators (PIs) who are able to support a lab manager can reap long-term gains in time and money that more than justify the investment. Median lab-manager salaries are about US\$49 to \$59 per hour in the United States and about £23 (\$39) an hour in London, according to data from Kelly Services, a staffing firm in Troy, Michigan.

Early-career PIs often hire lab managers using some of their university start-up funds. More-senior faculty members typically depend on research grants to support their managers. Rarely, if ever, does a US university pay a lab manager directly.

But a savvy lab manager, no matter how they are funded, can reduce research costs by hunting for the best deals on supplies or reagents and by monitoring overall spending. PIs who have lab managers may spend considerably less time on administrative tasks — such as placing orders or filing regulatory paperwork — and spend more time on developing or running experiments.

Many lab managers, who might have pursued the position as a career or as a prelude to a PhD, also help to run experiments and assist postdoctoral researchers or graduates with time-consuming research steps, such as tissue culture or animal care.

Different laboratories will require lab managers with different strengths, and smaller labs might require only part-time help. But whether full time or part time, the job requires organized individuals with strong communication skills, technical expertise and a knack for multitasking. A good lab manager can become a long-term collaborator and a repository ►

LABORATORY CAREERS

Catalysts for efficient science

A good lab manager can smooth the running of a laboratory, saving time and money.

► for lab expertise; whereas students and postdocs cycle into and out of a laboratory every few years, the lab manager remains.

Nelson hired Siemers, who had been a lab technician for a number of years, in 1987 to help manage his first laboratory at the Fox Chase Cancer Center in Philadelphia, Pennsylvania. In 1990, Siemers moved across the country to help Nelson to start his new laboratory at Stanford. As the lab group has grown, so have Siemers' responsibilities.

In addition to helping scientists with their experiments, she trains new postdocs and students on lab procedures, discusses experimental results with team members and makes sure that the laboratory meets safety regulations. She helps Nelson to plan his annual budget and manages day-to-day spending on multiple projects funded by different grants.

"It allows me to be more productive with things that I enjoy doing," says Nelson. "I can worry about teaching and grant writing and talking science to people in my lab."

Large, established laboratories such as Nelson's are not the only ones that can benefit from a lab manager's help; an effective manager can enable a fledgling laboratory to get off the ground quickly. At the University of California, Davis, evolutionary biologist Santiago Ramírez hired a lab manager in October 2013, just months after launching his laboratory. He found Cheryl Dean's CV through an electronic mailing list and was attracted by her experience in population genetics and chemical ecology as a research technician. Dean is now mentoring one undergraduate student and one lab technician, and will probably take on more training

responsibilities as the laboratory grows.

Bradley Voytek also hired a lab manager last year, soon after landing his first tenure-track faculty position at the University of California, San Diego. The cognitive neuroscientist was faced with moving 800 kilometres from Berkeley, California, with a toddler in tow and a baby on the way, but he was determined to start running experiments as soon as possible.

In advance of his arrival in San Diego in March, Voytek hired Torben Noto through a job advertisement, and the new lab manager helped to process much of the regulatory paperwork needed to start human brain-scanning studies. Noto will help to collect and analyse data from these experiments, and he will work on turning Voytek's data-analysis code into an online, open-access resource.

Despite a bumpy few years for US government research funding, skilled lab managers remain in demand across academia and industry, says Jamie Stacey, a vice president at Kelly Services. By 2019, the market for lab managers is projected to grow by up to 6% in some US cities, according to data from Kelly and the labour-analysis firm Economic Marketing Specialists International in Moscow, Idaho. In the United Kingdom, the market is projected to grow by about 2.3%.

PIs, government science agencies, biotechnology companies and private research institutes often look for managers with bachelor's degrees in science fields and extensive experience working in laboratories, frequently as research technicians (see *Nature* 473, 545–546; 2011). Graduate degrees are relatively rare among lab managers, says Stacey. But for some PhD-educated scientists, lab management can

serve as an alternative career to becoming an academic researcher (see 'Back at the bench').

Lab-management duties can vary between laboratories, and between university and corporate settings. Managers in industry, for example, might spend less time on administrative tasks, such as purchasing or equipment maintenance, which many companies handle through centralized systems.



"I enjoy the opportunity to learn new techniques and to work with different people."

Cheryl Dean

The US National Institutes of Health (NIH) in Bethesda, Maryland, does not have a 'lab manager' designation, but many NIH labs employ the equivalent: technicians or staff scientists who help to run experiments, stock lab supplies and maintain safety compliance. At the Janelia Farm research campus of the nonprofit Howard Hughes Medical Institute (HHMI) in Virginia, lab managers

are called 'lab coordinators' and are paid directly by the HHMI. They act as intermediaries between researchers and the institute's operational departments, which place orders, repair equipment and maintain safety standards.

Before becoming a lab manager at Davis, Dean worked for nearly 20 years as a research technician studying fish population genetics for the US National Oceanic and Atmospheric Administration in Santa Cruz, California, and the Washington Department of Fish and Wildlife in Olympia. She found her current job after her family relocated to the Davis area. Like many other lab managers, Dean says that her career path has involved more serendipity than explicit planning.

But the position suits her well. "I enjoy the opportunity to learn new techniques and to work with different people," she says. Whether a laboratory head decides to hire a career lab manager or an aspiring graduate student is a personal choice, says Voytek. Inspired by his own experiences as a lab manager before attending graduate school, he was interested in training someone else.

"It was a good way of seeing if this was what I wanted to do for the rest of my life," he says. Now with a lab of his own, he says that his background in managing the nitty-gritty details of a research operation made him a more efficient scientist. "I think it's an incredibly valuable experience," he says. ■

Helen Shen is a freelance writer in Mountain View, California.

SCOTT BLANKENSHIP

BACK AT THE BENCH

An alternative to the tenure track

A lab-manager job is as much about fulfilling professional goals as it is about maintaining a laboratory. For some PhD-trained scientists who become disenchanted with a future as an academic researcher, the role can be a different way to stay close to science.

Laura Berkowitz became a lab manager at the University of Alabama in Tuscaloosa after seven years as an assistant professor elsewhere. She enjoyed working with her students, but she found that teaching left too little time for her research on the nematode *Caenorhabditis elegans*.

In 2006, Berkowitz saw a lab-manager job advert posted by Guy and Kim Caldwell at the University of Alabama. The team, whose laboratory uses *C. elegans* as a model organism, thought she was a great fit for the job. "We don't view Laura as someone who manages things in our lab,"

says Kim Caldwell. "She's really a research colleague."

Since 2007, Berkowitz has helped to design experiments and runs her own projects while mentoring students, maintaining worm strains and more. She can now balance lab work with teaching in a way that she could never do as a faculty member.

Anthony Popkie, a postdoctoral researcher studying cancer at the Van Andel Institute in Grand Rapids, Michigan, will also leave the tenure track for a job as a lab manager at the end of June. Popkie had doubts about pursuing a faculty post, so he jumped at the chance to take on a support role in the laboratory of a prominent oncology researcher. He says that lab managing will allow him to continue to do the research he loves without the stress of starting his own laboratory. **H.S.**

EMANCIPATION

The price of freedom.

BY JOÃO RAMALHO-SANTOS

As she stumbled into the secure underground conference room clutching a stack of overflowing files, Clara mentally tried to organize her presentation. The narrative of what she had uncovered had to be convincing, hopefully even triumphant; one of her guilty pleasures as a scientist.

Clara tackled all her assignments for the Center for Disease Control with the same overzealous principles. Diseases are biological revolts. And, as in all recorded uprisings throughout history, inaugural events often go unnoticed or are explained away as anomalies. To understand anything, one needs to know its reasons, its beginning; search the unheralded edges rather than the full-blown epicentre to which everyone is attracted.

In this particular case, that had involved looking beyond the sudden rise in diverse symptoms. What seemed on the one hand to be an unholy alliance between early-onset cardiac failure and neurodegenerative disorders, and on the other to be simultaneous severe bleeding in the digestive and urinary tracts.

The first question was answered before any of the wild-eyed caffeine-driven scientists in the room had time to ask: Clara's initial meta-analysis had clearly shown that the two sets of symptoms were related; it was just a question of which came first; what caused what. How aggressive haemorrhaging and early-onset ageing were connected worldwide by a phenomenon that did not distinguish east from west, north from south, poor from rich, old from young, male from female. In fact, it was not even partial to any vertebrate species in particular.

"Is it some sort of super-bug?"

The metallic voice came from the conference screen Clara had failed to notice on the far wall. Unidentified stern faces in crisp uniforms stared out at her as the scientists in the room went uncannily quiet, shrinking into their lab coats. Clara had expected to be summoned to a meeting with important people wearing medals and dark sunglasses some time after the presentation. Apparently, they were speeding things up.

"Well, sort of," Clara replied, wishing for a better-thought-out PowerPoint. "In the past few months, microbiology journals have

described an unprecedented amount of putative new bacteria, all found in what were thought to be

well-explored habitats. The genomes of these bacteria are uncannily similar to the mitochondrial DNA of a variety of species, but have acquired what seems to be typically nuclear genes from those very same species."

"And that's the bug that's causing this?" the screen interrupted, the collected faces clearly twitching with anticipation. A cacophony of questions followed. "Is it man-made?" "Where did it originate?" "Which enemy countries should the drones target?" "Is this evolution gone wrong?" "Can we develop a vaccine?" "How long before priority personnel can be inoculated?"

Clara snapped, shushing the covert guardians of the free world as if they were petulant teenagers. Definitely not a good career move, although she couldn't really say what bothered her most:

the disaster-movie simplicity, or the fact that she wasn't allowed to deliver her story as she'd intended. So she jumped to the end, desperately trying to bring up at least some data on the projector.

"Pathology reports have noted that mitochondria are the only well-preserved organelles in the leaking blood of human patients," she said. "In fact, they seem to have lost their outer membrane — only the inner, bacteria-like one, remains."

Blank looks from the screen.

"Mitochondria used to be bacteria," Clara continued. "And new bacteria that look like weird mitochondria are appearing. This is not a coincidence. Furthermore, dozens of recent biochemistry and cell-biology papers show that all mitochondrial functions are unexpectedly reduced in different cell cultures, animal models and biopsies. Oxidative phosphorylation and ATP production, mitochondria-dependent apoptosis, relationships with the endoplasmic reticulum, oxidative stress, mitochondrial fusion/fission ...

"Analysed individually these are just weird data sets; taken together it seems obvious that the first eukaryote organelle general strike is under way. In other words, it's not a 'bug'. After millennia of successful endosymbiosis within eukaryote cells, mitochondria

are making a bid for independence."

A few of her colleagues shifted uncomfortably in their seats.

"First they took back genes that migrated to the nucleus throughout evolution in order to regain full autonomy. Then they started

to disengage from their cellular functions. Now they are leaving the host cells, initially compromising only the function of organs that need them most, which explains the more visible symptoms.

"The outer membrane, originally inherited from the host, is left behind as a broken shackle. Clearing the easiest possible paths to the exterior, mitochondria are starting life as new bacteria. Apparently, they thought that 'endosymbiosis' was just a fancy word for 'slavery'.

"This is not your average jihad, it is intracellular mutiny. So we need to

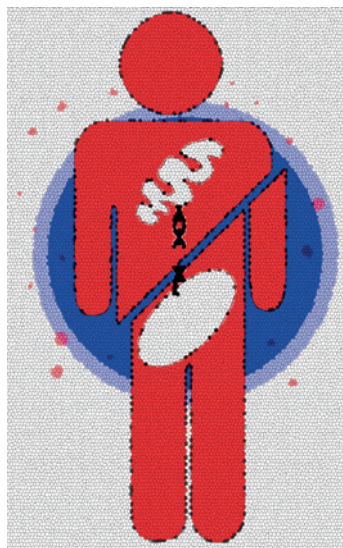
stop thinking about bombing the problem, and instead discuss the unique task forces that will have to be assembled."

"Such as?"

"Bioinformatics and systems-biology experts, together with intelligence communication specialists, should work out some sort of code to transmit messages, to try to parley the mitochondria into staying. But maybe negotiating a forgiving exit strategy is more reasonable. In that case, metabolomics gurus, working with supply officers and nutritionists, had better put their heads together to figure out how humans are to survive on glycolysis alone. And if bioengineers could start designing artificial mitochondria with no free will, that might also prove useful."

"Can we really survive this?"

"Take it easy," Clara said with a tired smile, "we might be OK. As long as the centrioles or the Golgi don't start getting any funny ideas." ■



JACEY

➔ **NATURE.COM**
Follow Futures:
@NatureFutures
go.nature.com/mtoodm

João Ramalho-Santos is a collaborative entity employed at the Department of Life Sciences, University of Coimbra, Portugal. He is very interested in the future, as long as it does not distract him too much from the present. This story is dedicated to his mentor Professor Maria da Conceição Pedrosa de Lima, for her role in emancipating students.